United States Department of Commerce
National Institute of Standards and Technology

NIST Special Publication 804

Chemistry of Electronic Ceramic Materials

Peter K. Davies and Robert S. Roth, Editors

NIST Special Publication 804

Chemistry of Electronic Ceramic Materials

Proceedings of the International Conference on the Chemistry of Electronic Ceramic Materials, August 17–22, 1990 held at Jackson, WY

Edited by

Peter K. Davies
University of Pennsylvania

Robert S. Roth
National Institute of Standards and Technology

Editorial Assistant

Mary A. Clevinger
National Institute of Standards and Technology

Sponsored by

NIST
NASA
ONR
DuPont
Idaho National Engineering Laboratory
University of Pennsylvania

January 1991

U.S. Department of Commerce
Robert A. Mosbacher, Secretary

National Institute of Standards and Technology
John W. Lyons, Director

National Institute of Standards
and Technology
Special Publication 804
Natl. Inst. Stand. Technol.
Spec. Publ. 804
513 pages (Jan. 1991)
CODEN: NSPUE2

U.S. Government Printing Office
Washington: 1991

For sale by the Superintendent
of Documents
U.S. Government Printing Office
Washington, DC 20402

PREFACE

The International Conference on the Chemistry of Electronic Ceramic Materials was held at The Sojourner Inn, in the Teton Village, Jackson Hole, Wyoming from August 17-22, 1990. In an attempt to maximize the development of this rapidly moving, multidisciplinary field, this conference brought together major national and international researchers to bridge the gap between those primarily interested in the pure Chemistry of Inorganic Solids and those interested in the Physical and Electronic Properties of Ceramics. With the many major discoveries that have occurred over the last decade, one of the goals of this meeting was to evaluate our current understanding of the Chemistry of Electronic Ceramic Materials, and to assess the state of a field that has become one of the most important areas of Advanced Materials Research.

The conference consisted of 18 extended invited lectures, 10 contributed oral presentations, and 37 poster presentations. The meeting was attended by scientists from a broad spectrum of fields based at universities, industries, and national laboratories. Approximately one-third of the attendees were from outside the United States and represented 10 different countries. In addition to the quality of the science, the meeting was also memorable for the large number of family members who were able to attend, resulting in many new friendships.

The scientific presentations covered many topics including new methods for the synthesis of ceramics, the structures and properties of dielectric and ferroelectric materials, crystal chemistry, surface chemistry, high-T_c superconductors, and theory and modeling. The papers appearing in these proceedings provide an up-to-date review of many aspects of these areas. For most of the oral presentations the discussions following the paper were successfully transcribed. Edited versions appear in these proceedings after each paper. In addtion to clarifying certain aspects of the material covered in the lecture, the unedited comments, transcribed by a local court reporting service, also provided considerable amusement for the editors and speakers.

The success of a meeting depends on many parameters ranging from the science to the weather. One of the most important is sponsorship and support. For this we are grateful to NIST, NASA, ONR, DuPont, the Idaho National Engineering Laboratory, and the University of Pennsylvania. The smooth running of a meeting also depends upon considerable work by those who often receive little recognition. In this respect we were truly fortunate to have Mary Clevinger as our conference coordinator who has also ensured that these proceedings appeared in an accurate form in a timely manner. We would also like to thank Audrey Roth and Kathy Davies for organizing an outstanding activities program for the many family members who attended the meeting. Thanks are also due to Denice Gilbert, Nancy Dickinson, and Tony Kostick in the Materials Science Department at Penn, who assisted in many typing duties and several tedious budgetary matters.

We hope that these proceedings will contribute to the development of the Chemistry of Electronic Ceramic Materials and, judging from the enthusiastic response of all who attended this meeting, we look forward to the Second International Conference sometime in the not too distant future.

October 1990

Peter K. Davies (Univ. of Pennsylvania)
Robert S. Roth (NIST)

TABLE OF CONTENTS

IV. CRYSTAL CHEMISTRY

V. SUPERCONDUCTORS

I. DIELECTRIC CERAMICS

National Institute of Standards and Technology Special Publication 804, Chemistry of Electronic Ceramic Materials, Proceedings of the International Conference held in Jackson, WY, August 17-22, 1990, issued January 1991.

CHEMICAL REACTION CONTROLLED MICROSTRUCTURES AND PROPERTIES OF FERROELECTRIC CERAMICS

D. Kolar

"J. Stefan" Institute, University of Ljubljana, Ljubljana, Yugoslavia

ABSTRACT

Electronic ceramic components are usually manufactured from complex mixtures of oxides or partially prereacted compounds. During sintering at high temperatures, chemical reactions take place which influence the kinetics and mechanism of densification and development of ceramic microstructure. The densification process is also critically dependent on minor impurities. It is recognised that the inadequate control of chemical reactions frequently does not allow generalisation of research results and is the main reason for poor reproducibility in manufacture of electronic ceramics. The present review is concentrated on interdiffusion phenomena and growth in presence of minor amounts of reactive liquid.

1. INTRODUCTION

Ceramic ferroelectrics are extensively used for manufacture of important electronic devices, notably ceramic capacitors, nonlinear resistors and piezo elements. More than 40 years of extensive investigation of ferroelectric phenomena resulted in a good understanding of the fundamental physical principles underlying the function and performance of various devices.

The principles and latest achievements in the field of ceramic capacitors were thoroughly discussed in recent reviews by Payne (1), Goodman (2), Hennings (3) and Kahn et al. (4).

At present, two families of materials are used in manufacture of multilayer capacitors: barium titanate based compositions and lead niobate based com-

positions, known as relaxors. The barium titanate family remains the major component for manufacture of MLC dielectrics with permittivity above 1000 to 15000, and above.

In spite of extensive development, several problems remain to be solved. The present review stresses the importance of chemical reactions during sintering at high temperatures on the microstructure development and electrical properties of $BaTiO_3$ based dielectric ceramics.

2. THE IMPORTANCE OF CHEMICAL REACTIONS AT HIGH TEMPERATURES

High resistivity ceramic capacitors with low temperature coefficients of capacitance are chemically inhomogeneous materials in metastable thermodynamic equilibrium.

Due to this thermodynamic instability, the technology is rather demanding and requires careful control of manufacturing parameters, such as chemical composition, initial homogeneity, powder grain size and morphology, homogeneity of the formed body, heating rate, sintering temperature and time.

In general, maintainance of chemical heterogeneity demands a low sintering temperature and short sintering times to limit solid state diffusion, which causes homogenisation. A low sintering temperature is also required to allow the use of less expensive electrodes in multilayer devices.

On the other hand, sintering time and temperature must assure densification to low and closed porosity. Porous bodies exhibit a low dielectric constant, low breakdown strength and high loss due to water permeability.

High density at lower sintering temperatures is usually achieved with additives which promote densification by forming liquid phase at sintering temperature, as will be discussed later. Sintering additives dilute the high dielectric constant phase, therefore the amount should be as small as possible.

The third deciding parameter which determines electrical properties is ceramic microstructure. Small grain size with narrow size distribution is normally required for most applications. Liquid phase sintering with small amounts of liquid phase frequently results in coarse microstructure with broad size distribution.

It is clear that carefull optimization of chemical composition and processing parameters is needed to achieve the best compromise, i.e. dense, fine grained and chemically heterogeneous ceramics.

3. LIQUID PHASE SINTERING OF BARIUM TITANATE BASED COMPOSITIONS

The basic approach to preparing high capacitance material is to shift the $BaTiO_3$ Curie peak close to room temperature and to broaden it. Shifting is accomplished with solid solution additives, for instance alkaline-earth titanates, lead titanate, various stannates and zirconates (2).

Broadening of the Curie temperature maximum is achieved by compositional inhomogeneity. Inhomogeneity causes a diffuse phase transition (DPT). A simple model of the inhomogeneous ceramic is that it consists of a symmetric compositional distribution of micro regions, each having a Curie point temperature characteristic of its composition (5).

In accordance with the model, the width of the distribution of Curie temperature maxima may serve as an indication of the homogeneity of the dielectric (6).

Barium titanate with solid solution additives are refractory compounds which demand high sintering temperatures, 1350°C and above.To decrease the high sintering temperature, which favours homogenisation and yet to enable densification to closed porosity, barium titanate compositions contain sintering aids,which form a liquid phase at sintering temperatures. The liquid phase formed by the presence of small amounts of sintering additives in the basic composition accelerates densification and grain growth by rearrangement and solution-precipitation processes (7).

A common liquid phase forming aid in $BaTiO_3$ based compositions is TiO_2. The well known phase diagrams by Negas et al (8) and O'Bryan and Thomson (9) indicate a eutectic in $BaTiO_3$-excess TiO_2 compositions at 1320 and 1312°C, respectively. This temperature is further lowered to 1240°C by the presence of impurities such as SiO_2 and Al_2O_3 (10). The liquid phase triggers discontinuous grain growth which results in a coarse structure. Such structures can lead to low breakdown strength and mechanical weakness (11).

Discontinuous grain growth is characterised by rapid growth of a limited amount of grains to sizes much larger than those of the average grain population (7). It may originate from many possible causes such as wide initial particle size distribution, a small amount of liquid phase, chemical heterogeneity, heterogeneous density distribution, intrinsic boundary properties (preferential grain boundary mobility) and others.

The discontinuous grain growth observed to occur in the presence of a small amount of liquid phase is beleived to be caused by the combined effects of the heterogeneous distribution of the limited amount of liquid, and the presence of

grains much larger than the average population. The growth mechanism is described as Ostwald ripening caused by the difference in solubility for particles of different size, which causes matter to be transported from the smaller to the larger particles. Discontinuously growing grains grow at a constant rate, until they impinge on other rapidly growing grains and the growth rate abruptly slows down to a value encountered in normal grain growth. Thus, the resulting grain size after prolonged sintering is controlled only by the number of secondary grains that are nucleated and not by the time of heating (12).

Barium titanate is one of the first ceramic materials for which discontinuous grain growth was recorded (12). When triggered, discontinuous growth is very rapid. Growth rates on the order of 10 μm per minute were observed directly under a heating microscope (13). Since the final coarse grain size may be quite homogeneous, discontinuous grain growth may go unnoticed when only final microstructures were examined. Fig. 1. illustrates rapid growth and shows typical microstructures developed during sintering of $BaTiO_3$ with 2 mol % excess TiO_2.

Extensive grain growth by a solution-preciptation process helps in rapid chemical homogenisation, decreases permittivity below the Curie point maximum and increases temperature dependence of the maximum. Therefore, special additives are usually incorporated in dielectric compositions to prevent grain growth. However, liquid phase sintering is in general difficult to control. The effect of additives may depend on processing conditions, as demonstrated in $BaTiO_3$-$SrTiO_3$ and $BaTiO_3$-$CaTiO_3$ systems (14).

Figs 2a-2c show the influence of 8 mol % $CaTiO_3$ and $SrTiO_3$ additions, respectvely, on the microstructure of $BaTiO_3$ - 2 mol % $Ba_6Ti_{17}O_{40}$ ceramics sintered 24 hours at 1350°C. The addition of $CaTiO_3$ strongly increases the final grain size, and the addition of $SrTiO_2$ reduces it. Whereas reduction of grain size due to additives is a common phenomenon in ceramics, the coarsening influence of $CaTiO_3$ is unusual. In contrast, it was reported (15) that $CaTiO_3$ addition to PTCR ceramics based on a $BaTiO_3$-$PbTiO_3$ solid solution containing, besides Y_2O_3 dopant, 2 mol % SiO_2 and 0.5 mol % TiO_2 inhibits the grain growth. It is obvious that the influence of $CaTiO_3$ on microstructure development depends on the grain growth mechanism, firing conditions and composition.

Examination of microstructures after short sintering times revealed that the addition of 8 mol % $CaTiO_3$ to the $BaTiO_3$-$Ba_6Ti_{17}O_{40}$ composition greately reduced the nucleation rate of discontinuously growing grains. These grains could grow unhindered to comparatively large size, the maximum size of the grains exceeding 300 μm. On the other hand, addition of 8 mol % $SrTiO_3$ caused a high nucleation rate with consequent early impingement of discontinuously

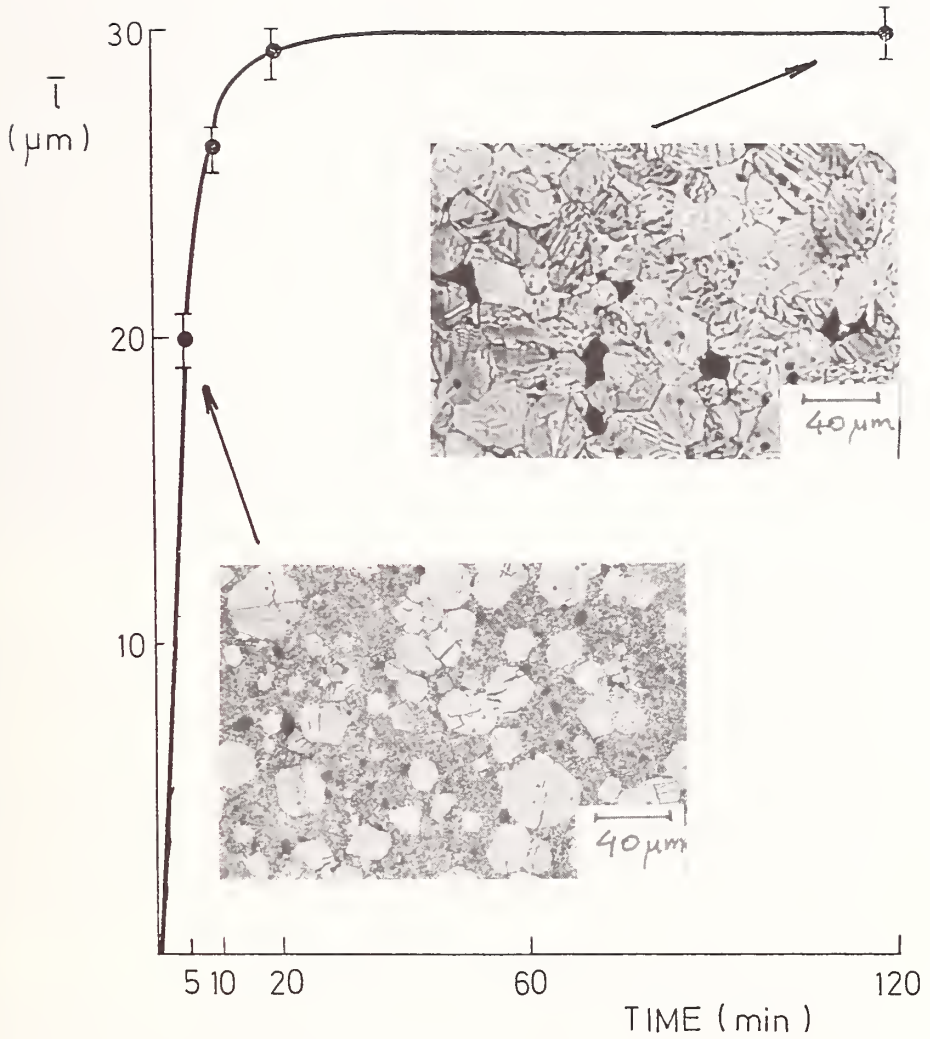

Fig. 1: Average intercept length vs. sintering time and corresponding microstructures for $BaTiO_3$ - TiO_2 excess ceramics, sintered at 1350°C

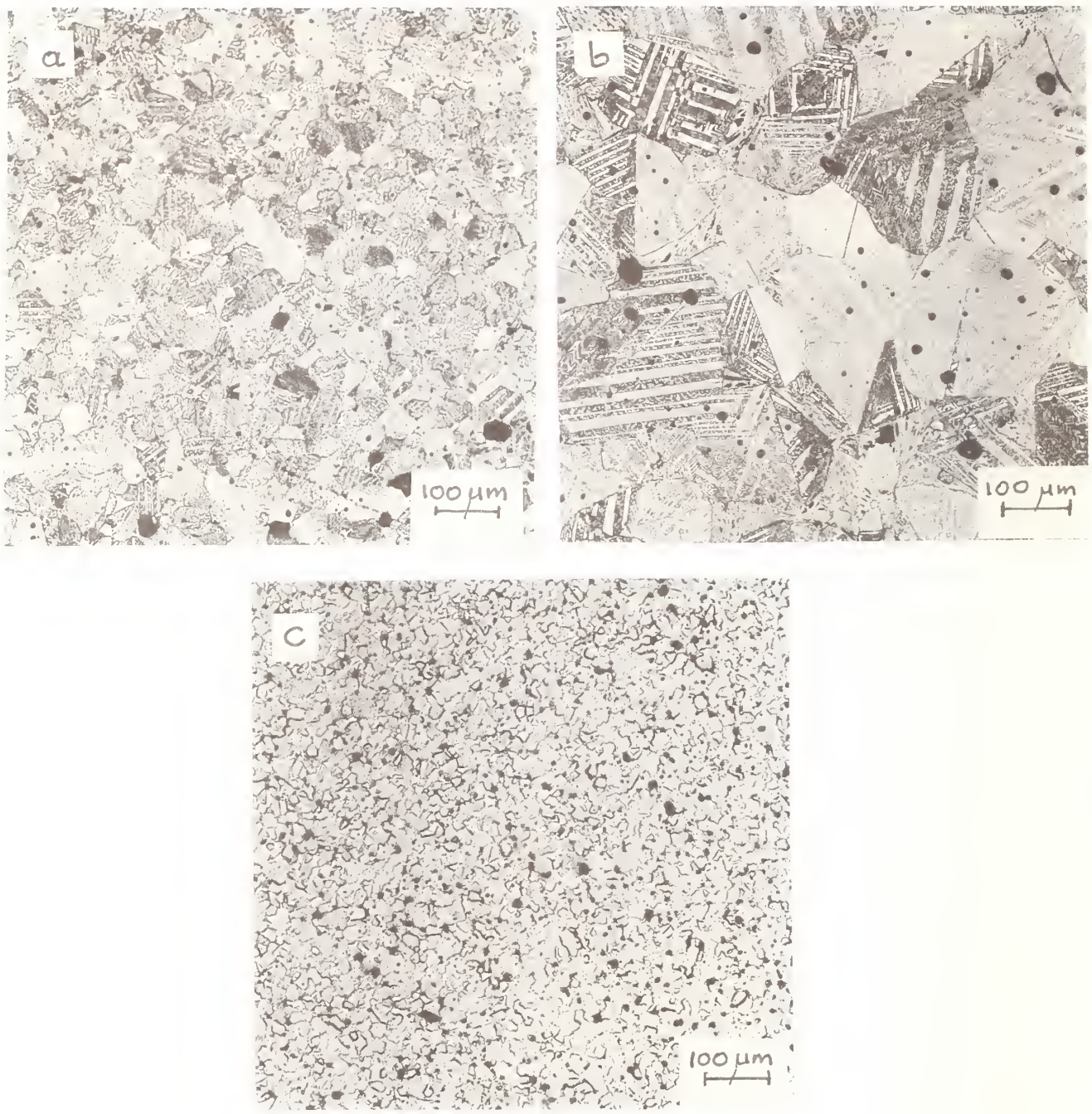

Fig. 2: Microstructures of $BaTiO_3$ ceramics after heat treatment 24 hours at 1350°C (a) $BaTiO_3$-2 mol % $Ba_6Ti_{17}O_{40}$, (b) $BaTiO_3$ - 2 mol % $Ba_6Ti_{17}O_{40}$ - 8 mol % $CaTiO_3$, (c) $BaTiO_3$ - 2 mol % $Ba_6Ti_{17}O_{40}$ - 8 mol % $SrTiO_3$

growing grains. The microstructure remained fine grained even after prolonged sintering.

The final grain size is influenced by the relative values of the rate of nucleation N and the rate of growth of nuclei G. If the ratio of N to G is large, the final grain size will be small. Conversely, if the ratio of N to G is small, the final grain size will be large. Both rates strongly depend on processing parameters such as the composition, the amount of liquid phase and temperature.

Analysis of microstructure evolution in undoped and doped $BaTiO_3$ samples at various temperatures revealed that the grain growth rate was not particularly sensitive towards increase in temperature, whereas the nucleation rate strongly increased, as already noted (16). Consequently, the ratio N/G increases with temperature resulting in finer final microstructures. It was demonstrated that a finer grain size may be achieved by avoiding the critical temperature region in which ratio N/G is low. Similar temperature dependence of grain growth was reported by Matsuo and Sazaki (10), who observed exaggerated grain growth in $BaTiO_3$ doped with TiO_2, SiO_2 and Al_2O_3 in the temperature region of 1240-1250°C. In their case, the eutectic temperature was estimated to be at 1240°C.

The reason for contrasting influences of $SrTiO_3$ and $CaTiO_3$ addition on the nucleation rate of discontinuously growing grains in TiO_2-excess $BaTiO_3$ ceramics seems to be the different chemistry in the $BaTiO_3$-TiO_2-$SrTiO_3$ and $BaTiO_3$-TiO_2-$CaTiO_3$ systems.

The systems differ from each other in several aspects. Relevant for this discussion are the facts that whereas $BaTiO_3$ and $SrTiO_3$ exhibit solid solubility at all compositions, $BaTiO_3$ and $CaTiO_3$ are soluble only to a limited extent. The second major difference is the existence of a Ca-stabilized $Ba_2Ti_5O_{12}$ phase in the BaO-CaO-TiO_2 system, which was not found in the BaO-SrO-TiO_2 system (17).

TEM analysis of sintered $BaTiO_3$ - 2 mol % $Ba_6Ti_{17}O_{40}$ - 8 mol % $SrTiO_3$ and $BaTiO_3$ - 2 mol % $Ba_6Ti_{17}O_{40}$ - 8 mol % $CaTiO_3$ revealed the presence of a Ca-stablized $Ba_2Ti_5O_{12}$ phase in the Ca-containing ceramics. Such a phase could not be identified in Sr- containig ceramics.

It was proposed that the close similarity of $BaTiO_3$ and Ca- stabilised $Ba_2Ti_5O_{12}$ causes absorption of the Ca-containing phase on the surface of $BaTiO_3$ grains thus diminishing the nucleation rate. In the concentration range studied, the effect is the same as that caused by the decrease in the amount of $Ba_6Ti_{17}O_{40}$-$BaTiO_3$ eutectic, which accounts for the coarse grained structure after prolonged sintering. On the other hand, addition of $SrTiO_3$ does not destabilize the $Ba_6Ti_{17}O_{40}$ phase; it causes a monotonic decrease in the grain size of the $(Ba,Sr)TiO_3$ ceramic by accelerating the nucleation rate.

Besides TiO_2 a large number of other additives which form a liquid phase at lower temperatures have been investigated. In early work various low melting glasses were found very effective in decreasing the sintering temperatures at the expense, however, of considerable lowering of permittivity. Later on, glass compositions were adjusted to titanates to permit some grain growth during sintering. During grain growth, partial homogenisation of the constituents takes place by dissolution of some ions from the glass into the titanate lattice, thereby lowering the volume fraction of the low dielectric constant phase. By this means, several low fired MLC dielectrics with permittivity around 4000 were prepared (18).

4. EFFECTS OF CHEMICAL HETEROGENEITY ON SINTERING AND GRAIN GROWTH IN FERROELECTRIC CERAMICS

In preparation of dielectric ceramics from chemically heterogeneous mixtures care should be taken to minimise the effects of high temperature reactions on sintering and grain growth. In general, volume changes and microstructure development during sintering of chemically heterogeneous compacts are mainly controlled by interdiffusion. Analysis of diffusion phenomena which lead to solid solution and compound formation in solid state sintering of initially heterogeneous mixtures revealed that counterdiffusion with equal diffusion rates such as described by Wagner (19) is merely a special case. In general, diffusion coefficients of interdiffusing species in chemically heterogeneous systems are not equal. Differences in diffusion fluxes cause formation of vacancies on the side of the atoms whose diffusivity is larger. Excess vacancies precipitate at contacts between the particles and form additional porosity in the powder compact during sintering. The effect is more pronounced in sintering of large particles. Formation of additional porosity may cause swelling of the compact instead of shrinkage during sintering.

In perovskite systems, swelling was observed during sintering of compacts made of $PbTiO_3$-$PbZrO_3$ powder mixtures, which form a complete solid solution (20).

Expansion was more extensive when coarse powders of $PbTiO_3$ were used. Many small cavities were seen to exist in the structure. It was suggested that preferential diffusion of Ti occured during firing and the expansion was qualitatively explained as a Kirkendall effect.

EPMA analysis of $PbTiO_3$-$PbZrO_3$ diffusion couples after firing at 900^oC confirmed preferential diffusion of Ti ions into $PbZrO_3$ (21). Since line analysis did not show an appreciably higher PbO concentration of TiO_2 depleted $PbTiO_3$, it was concluded that PbO is transported with Ti ions, most probably

through the gas phase. This is supported by the fact that a liquid phase could not be detected in sintered samples. If present in excess, PbO should be detected locally.

In sintering of $BaTiO_3$-$SrTiO_3$ mixtures (22), preferential diffusion of Ba ions caused formation of the nonequilibrium polytitanate phase $Ba_6Ti_{17}O_{40}$ which in turn gave rise to a low temperature eutectic liquid with $BaTiO_3$. Transient eutectic liquid was proposed as a reason for discontinuous grain growth, which was observed at contacts between sintered $SrTiO_3$-$BaTiO_3$ powder layers at temperatures well below the liquid phase formation temperature in the $BaTiO_3$-$SrTiO_3$ system. Large $Sr_{1-x}Ba_xTiO_3$ solid solution grains such as shown on Fig. 3. are believed to be flux grown. In spite of liquid phase formation, $BaTiO_3$-$SrTiO_3$ compacts sintered to lower final density than pure compounds.

Expansion instead of shrinkage was also observed in sintering of a $BaTiO_3$-$BaZrO_3$ mixture. Analysis of neck areas formed during sintering of $BaTiO_3$ spheres on a $BaZrO_3$ plate by EPMA revelaed preferential diffusion of Ti^{4+} into $BaZrO_3$ (Fig. 4).

As in the case of sintering of $BaTiO_3$-$SrTiO_3$ mixtures, nonequilibrium phases and additional porosity are formed because of unequal diffusion rates. It is interesting to note that X-ray powder examination of the sintered mixture indicated preferential diffusion in the opposite direction, i.e., Zr^{4+} into $BaTiO_3$. After heating 1:1 mole $BaTiO_3$-$BaZrO_3$ mixtures for 15 minutes at $1100^{o}C$, X-ray reflections belonging to $BaTiO_3$ almost disappeared, while the intensity of pure $BaZrO_3$ reflections remained strong.

High temperature firing resulted in complete solid solution. It may be easily shown that the type of unreacted material depends on the ratio of the grain sizes of $BaTiO_3$ and $BaZrO_3$. In drawing up such conclusions, it must be remembered that average grain size may be misleading. Even a small amount of coarse $BaZrO_3$ particles, say 10 %, when present, may remain unreacted after a prolonged sintering time, giving rise to a false impression of predominant diffusion of Zr^{4+} ions (23).

5. REACTION SINTERING AND MICROSTRUCTURE DEVELOPMENT IN $BaTiO_3$-$CaZrO_3$ MIXTURES

Among the most widely used compositions for achieving a permittivity of 6000 and above are those based on the system $BaTiO_3$-$CaZrO_3$ (2,24-27). Both compounds are not compatible. On heating, $BaTiO_3$ and $CaZrO_3$ react to form a barium zirconate phase with some Ca and Ti in solid solution and a calcium

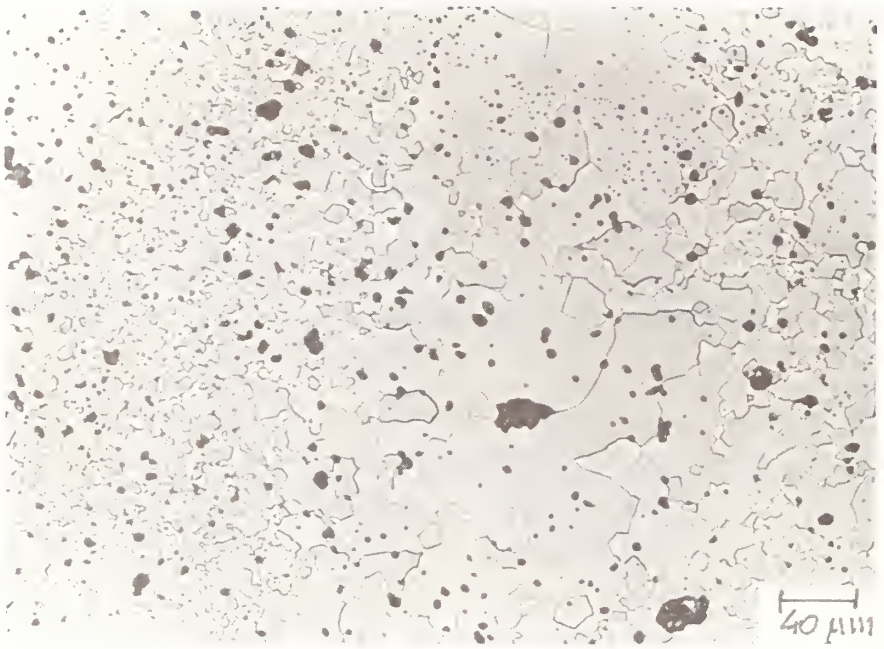

Fig. 3: Discontinuous grain growth in 95 w/o $SrTiO_3$ - 5 w/o $BaTiO_3$ ceramic sintered at 1450°C, 3 hours

titanate phase with some dissolved $BaTiO_3$ (29). $BaTiO_3$-$BaZrO_3$ form a solid solution $Ba(Ti_{1-y}Zr_y)O_3$ over the whole composition range. The solubility of Ca in the $Ba_{1-x}Ca_x$ $Ti_{1-y}Zr_yO_3$ solid solution was reported to be 17,5 mol % at 1300°C (25) and increases to 28 mol % at 1600°C (28). Zr^{4+} ions shift the Curie temperature maximum to the vicinity of room temperature, whereas Ca^{2+} ions are effective in broadening the maximum (27).

In our experiments (29), reaction between $BaTiO_3$ and $CaZrO_3$ was detectable by X-ray analysis already after 1 hour's heating at 1100°C. At this temperature, reaction is slow and no heat effect could be detected on DTA curves. It was demonstrated by dilatometric analysis that chemical reaction interferes with the sintering process. Shrinkage curves presented in Fig. 5 show that $BaTiO_3$ started sintering at around 1100°C and sintered to high density in the temperature region 1300-1350°C; $CaZrO_3$, being more refractory needed higher sintering temperatures. It began to shrink at around 1250°C and sintered to high density in the temperature region 1450-1500°C. $BaTiO_3$ - 16 mol % $CaZrO_3$ started to shrink at approximately the same temperature as $BaTiO_3$; however, after a few % shrinkage the kinetics slowed down and temperatures of 1550-1600°C were needed for densification. Microstructural examinations showed high porosity which was ascribed to the Kirkendal effect due to differences in the diffusion coefficients of various constituents in the $BaTiO_3$- $CaZrO_3$ ternary mixture.

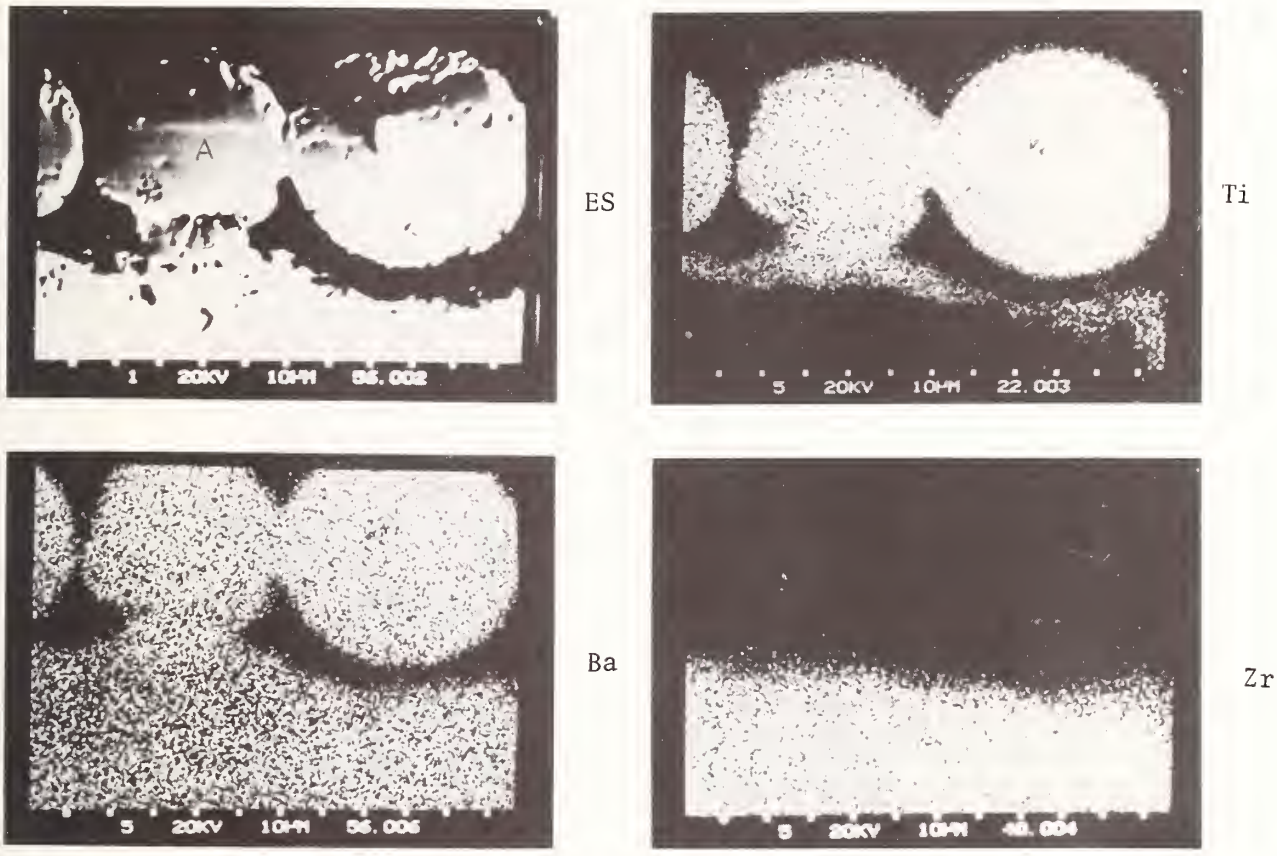

Fig. 4: Microprobe analysis of $BaTiO_3$ spheres sintered to $BaZrO_3$ plate at 1400°C, 3 hours. ES electron image, Ti, Ba, Zr X-ray image

Sinterabiltiy was improved by avoiding solid state diffusion. As shown on Fig.5, sinterability of $BaTiO_3$ - 16 mol % $CaZrO_3$ - 2 mol % TiO_2 was improved by reactive liquid formation so that sintering temperatures of 1350-1380°C were sufficient to achieve high density - above 95 % of theoretical value in 1 hour firing time. Common additives which lowered the eutectic temperatures (i.e. SiO_2 and Al_2O_3), decreased sintering temperature to below 1300°C. 16 mol % $ZrTiO_3$ effectively reduced discontinuous grain growth to an average intercept length 3-4 μm (Fig.6). The solution- precipitation process resulted in a core-shell type structure (1,3,30,31), as shown on Fig. 7. It is believed that the compositional inhomogeneities within the grains is related to the known flattening of the dielectric constant vs. temperature characteristic of $BaTiO_3$-$CaZrO_3$ dielectric ceramics. Compositions are sensitive to firing conditions. Small increases in sintering temperature and time increase the permittivity and its temperature dependence due to diffusional homogenisation.

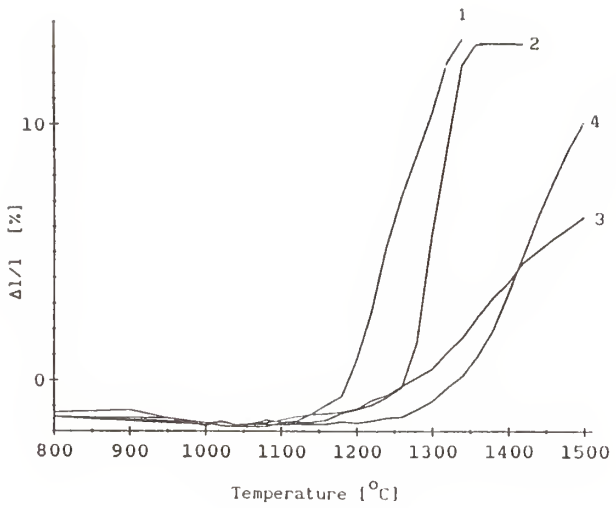

Fig. 5: Dilatometric curves for (1) $BaTiO_3$ - 2 mol % TiO_2 (2) $BaTiO_3$ - 2 mol % TiO_2 - 8 mol % $CaZrO_3$ (3) $BaTiO_3$ - 8 mol % $CaZrO_3$ (4) $CaZrO_3$. Heating rates 10°C/min

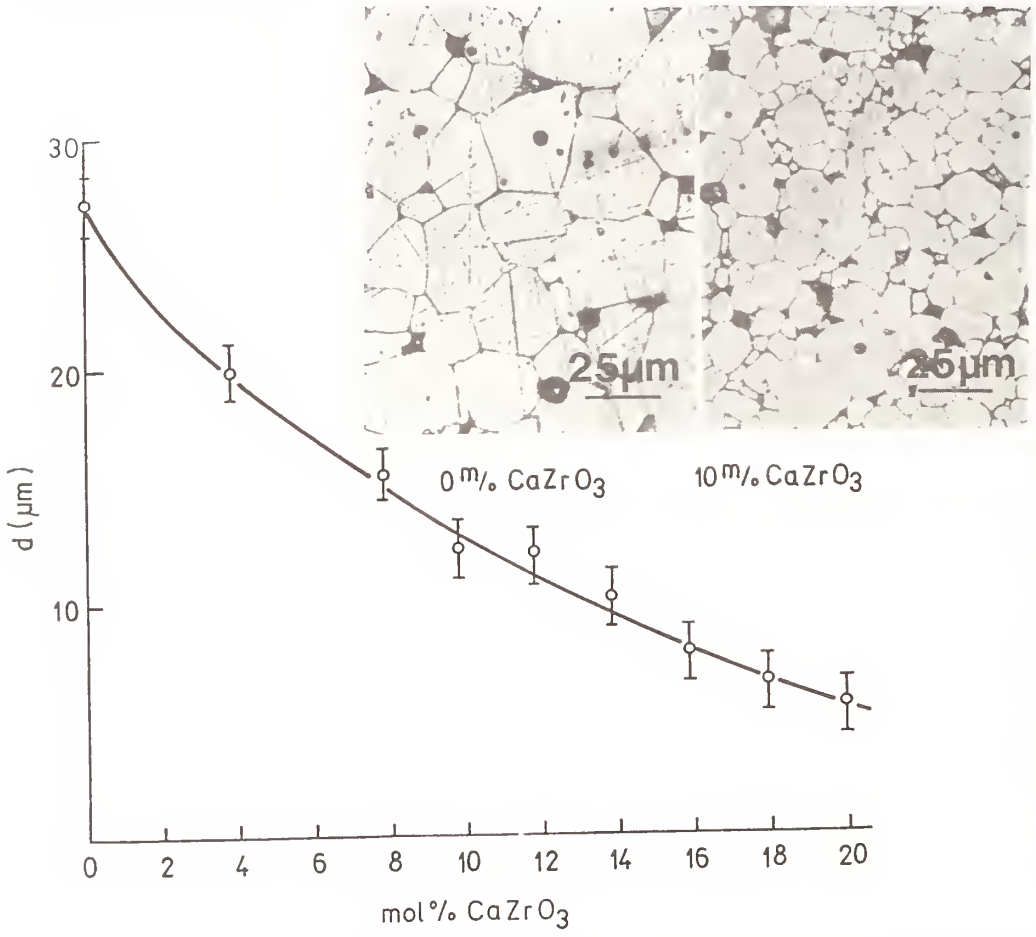

Fig. 6: Average grain size vs. composition in $BaTiO_3$ - 2 mol % TiO_2-$CaZrO_3$ ceramics sintered 1 hour at 1360°C

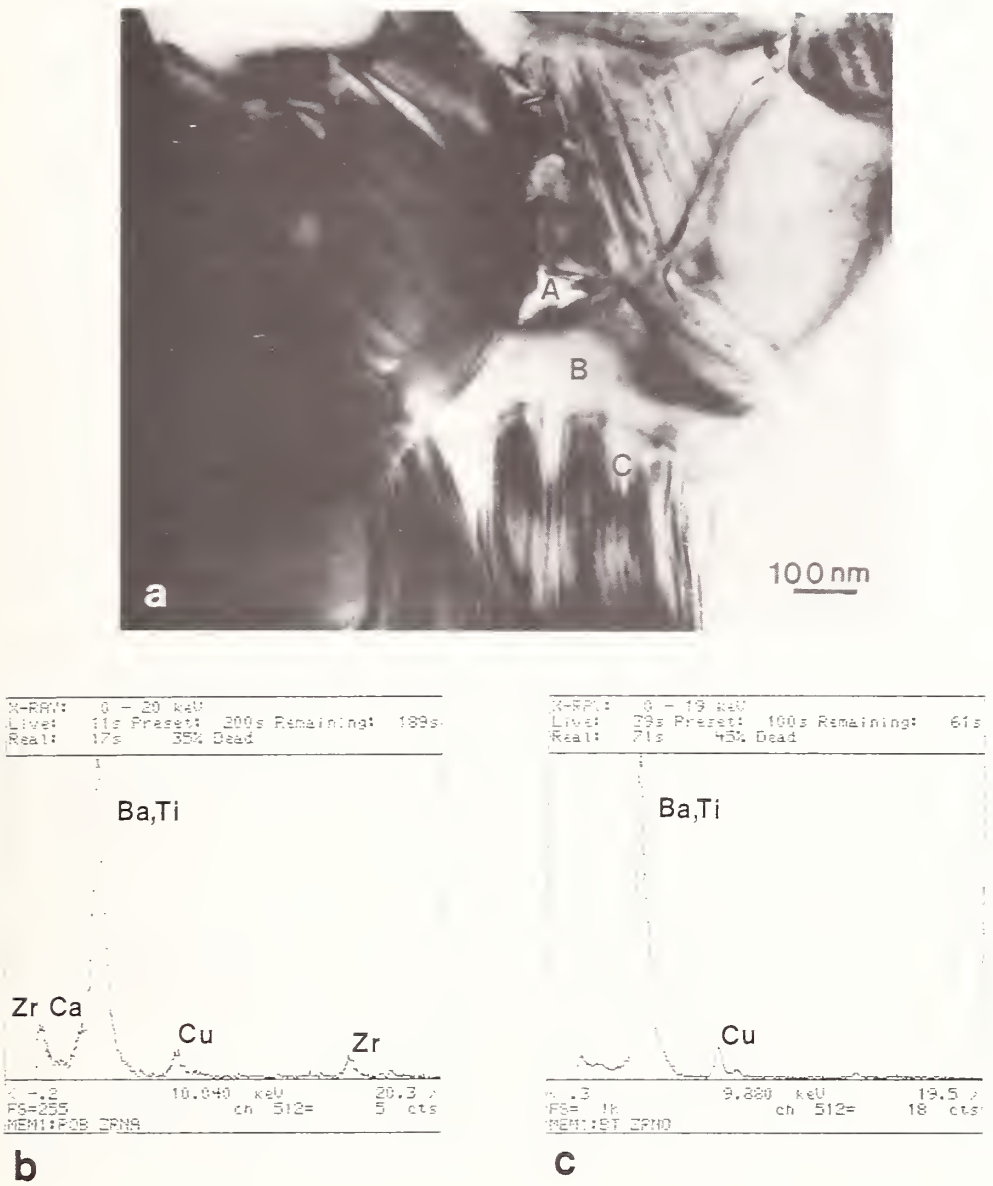

Fig. 7: TEM photomicrograph and corresponding EDS spectra of 90 mol % $BaTiO_3$-8 mol % $CaZrO_2$ - 2 mol % TiO_2 ceramic, fired 2 hours at 1260°C. (A) Solidified TiO_2-rich phase at grain corners and along grain boundaries, (B) Ca and Zr modified domain free region and (C) ferroelectric grain core.

REFERENCES

1. D.A.Payne, pp 413-431 in Processing of Heterogeneous Ceramics for Dielectric Applications, Mat.Sci.Res. 20 Plenum New York 1986
2. G.Goodman, Ceramic Capacitor Materials, pp 79-138 in Ceramic Materials for Electronics, ed. by R.C. Buchanan, Marcel Dekker, New York 1986
3. D.Hennings, Barium Titanate Based Ceramic Materials for Dielectric Use, Int.J.High Technology Ceramics 3 91-111 (1987)
4. M.Kahn, D.P. Burks, I.Burn and W.A.Schulze, Ceramic Capacitor Technology, pp 191-274 in Electronic Ceramic, ed. by L.M.Levinson, Marcel Dekker, New York 1988
5. G.A.Smolenskii, J.Phys.Soc.Jpn.Suppl. 28, 26 (1970)
6. S.M.Neirman, The Curie Point Temperature of $Ba(Ti_{1-x}Zr_x)O_3$ Solid Solutions, J.Mat.Sci. 23 3973-3980 (1988)
7. W.D.Kingery, H.K.Bowen, D.R.Uhlmann, Introduction to Ceramics, Wiley, New York 1976 498-
8. T.Negas, R.S.Roth, H.S.Parker and D.Minor, Subsolidus Phase Relations in the $BaTiO_3$-TiO_2 System, J.Solid State Chem. 9, 297 (1974)
9. H.M.O'Bryan Jr. and J.Thomson Jr., Phase Equilibria in the TiO_2-Rich Region of the System BaO-TiO_2, J.Am.Ceram.Soc. 57 (12) 522-526 (1974)
10. Y.Matsuo, H.Sasaki, Exaggerated Grain Growth in Liquid Phase Sintering of $BaTiO_3$, J.Am.Ceram.Soc 54 (9) 471 (1971)
11. J.M.Herbert, Ceramic Dieletrics and Capacitors, Gordon and Breach Publ., New York 1985, p 86
12. J.E.Burke, "Grain Growth in Ceramics", pp 109-116 in Kinetics of High Temperature Processes, ed. by W.D.Kingery, Wiley, New York 1959
13. H.Heydrich, quoted by H. Schmelz and H. Thomman, cfi/Ber. DKG 61, No. 4/5 199-205 (1984)
14. D.Kolar, V.Kraševec, "Influence of Additives on Discontinuous Grain Growth During Liquid Phase Sintering of Barium Titanate", pp 375-380 in Sintering '89, ed. by S.Somiya, M.Shimada, M.Yoshimura and R.Watanabe, Elsevier, Amsterdam 1988
15. W.Y.Howng and C.McCutcheon, "Electrical Properties of Semiconducting $BaTiO_3$ by Liquid Phase Sintering", Cer. Bull 62, 231-243 (1983)
16. D.Hennings, "Recrystallization of Barium Titanate Ceramics", Sci. Ceram., 12 405-409 (1984)
17. W.Kwestroo, H.A.M. Paping, "The Systems BaO-SrO-TiO_2, BaO- CaO-TiO_2 and SrO-CaO-TiO_2", J.Am.Cer.Soc. 42 (6) 292-299 (1959)
18. I.Burn, Flux-Sintered $BaTiO_3$ Dielectrics, J.Mat.Sci. 17 1398-1408 (1982)

19. C.Wagner, J.Phys.Chem. B 34 209 (1936)
20. Y.Nakamura, S.Chandratreya and R.M.Fulrath, "Expansion During the Reaction Sintering of PZT", Ceramurgia Int. 6 57-60 (1980)
21. M.Kosec and D.Kolar, "PZT Solid Solution Formation from $PbZrO_3$ and $PbTiO_3$", pp 421-427 in "Ceramic Powders", ed. by P.Vincenzini, Elsevier, Amsterdam 1983
22. D.Kolar, M.Trontelj and Z.Stadler, "Influence of Interdiffusion on Solid Solution Formation and Sintering in the System $BaTiO_3$-$SrTiO_3$", J.Am.Cer.Soc. 65 470 (1982)
23. D.Kolar, "Sintering in Chemically Heterogeneous Systems", Ceramic Transactions, in print
24. M.McQuarrie and F.W.Behncke, "Structural and Dielectric Studies in the System (Ba,Ca)(Ti Zr)O_3, J.Am.Cer.Soc. 37 539-543 (1954)
25. G.H.Jonker, Kondensatormaterialien mit Hoher Dielektrizitätskonstante, Philips Tech. Rundschau 17 127-135 (1955)
26. O.Drexler, B.R.Schatt, "Development of Ceramic Materials With a Dielectric Constant of 10000 at Room Temperature", Science of Ceramics 1, 239-254 (1962)
27. H.J.Hagemann, D.Hennings and R.Wernicke, "Ceramic Multilayer Capacitors", Philips Tech.Rev. 41, No 3, 89-98 (1983/84)
28. D.Hennings and H.Schreinemacher, "Temperature Dependence of the Segregation of Calcium Titanate from Solid Solutions of (Ba,Ca) (Ti Zr)O_3 and its Effect on the Dielectrics Properties", Mat.Res.Bull. 22, 1221-1226 (1977)
29. D.Suvorov and D.Kolar, "Sintering and Dielectric Properties on the System $BaTiO_3$-$CaZrO_3$", pp 2.314-2.318 in Euro-Ceramics 2, ed. by G. de With, R.A.Terpstra and R.Metselaar, Elsevier 1989
30. B.S.Rawal, M.Kahn, and W.R.Buessem, "Grain Core - Grain Shell Structures in Barium-Titanate Based Dielectrics", pp 172-88 in Advances in Ceramics, Vol. 1, Am.Cer.Soc., Columbus, Ohio 1981
31. D.Hennings and G.Rosenstein, Temperature-Stable Dielectrics Based on Chemically Inhomogeneous $BaTiO_3$, J.Am.Cer.Soc. 67, 4, 249-254 (1984)

DISCUSSION

R. J. Cava: Did you imply we do not understand the reasons for the effect of grain sizes upon the dielectric constant?

D. Kolar: I did not imply this. It is commonly observed that with decreasing grain size in $BaTiO_3$ and $BaTiO_3$-based dielectric ceramics, the dielectric constant below the Curie temperature increases whereas the maximum at the Curie temperature decreases and broadens. The dielectric constant increase below the Curie temperature with decreasing grain size is attributed to increasing internal stress due to a smaller number of domains per grain. A decrease in the Curie point dielectric maximum and a broadening of the peak width in small grain size ceramics is attributed to lower degree of crystallinity, amorphous outer layers and local chemical inhomogeneity of the grains.

What I commented was that the experimental data vary. Whereas most of the authors find very shallow dielectric maximum in small grain size ceramics (about 1 mm), a high dielectric maximum of ~ 11000 was also reported (K. Kinoshita and A. Yamaji, J. Appl. Phys. 47, 371 (1976)).

J. Nowotny: The effect of the grain size can also be discussed in terms of the different stoichiometry of the grain boundary layers, which in the case of oxides has a certain thickness. Now, as the grain size decreases the ratio of the boundary layer to the bulk increases. When we speak about the different grain sizes we should also consider the segregation of certain ions to the boundary, the grain boundaries.

For example, titanium has a tendency to segregate. But that's not the end of the story because there is also a structural rearrangement of the boundary layer, and, for example, it is possible that the bulk grains remain tetragonal whereas the boundary layers may be stabilized with a cubic structure.

D. Kolar: It was also reported (D. Hennings and A. Schnell, J. Am. Ceram. Soc., 65, 539-544 (1982)) that in small grain size $BaTiO_3$ based ceramics, the structure may remain cubic below the Curie temperature or that the cubic, tetragonal and orthorhombic phases coexist.

A. Sleight: I want to be clear about the explanation for the liquid phase that you gave. Were you just postulating this disproportionation from 1:1 to 1:2 and 2:1 phases or have you some observation of the real cause of the liquid phase.

D. Kolar: Would you please repeat that? I'm not quite sure I understand the question.

A. Sleight: My question is do you have evidence that the liquid phase is caused by going from the 1:1 compound to 1:2 plus 2:1 compounds? Is there experimental evidence, and can you quench these phases and see them in the specimens?

R. Roth: Did you actually see the polytitanate?

D. Kolar: In some cases we detected in $BaTiO_3$-$SrTiO_3$ compositions after firing faint x-ray diffraction lines corresponding to polytitanate $(Ba,Sr)_6Ti_{17}O_{40}$ solid solution. Other evidence of polytitanate was grain morphology and size of $(Ba,Sr)TiO_3$ solid solution grains, which were typical for flux growth.

R. Roth: Did you also observe lines from the 2:1 compound?

D. Kolar: Faint diffraction lines of $(Ba,Sr)_2TiO_4$ were also detected. However, the main evidence for the existence of 2:1 compound was obtained by microprobe analysis which showed Sr-rich layer in the boundary region between $BaTiO_3$ and $SrTiO_3$ in hot pressed $BaTiO_3$-$SrTiO_3$ diffraction couple according to the reference (D. Kolar, M. Trontelj, and Z. Stadler, J. Am. Ceram. Soc., 65 [10] 470-474 (1982).

R. Newnham: The key point you seem to be making at the end was that barium has a higher diffusion coefficient.

D. Kolar: Yes.

R. Newnham: Higher than strontium, it seems counter-intuitive since barium is a larger ion than strontium.

D. Kolar: Yes.

R. Newnham: At least it seems unusual if we think of the diffusion expected in a pure crystal. Do you believe that this is related to the defect structure? It's known, for instance, that in barium titanate sometimes the surface of barium titanate is barium deficient depending on the preparation technique of the material. This could give a very high surface diffusion rate for barium. Or do you think it's through the bulk that this is happening?

D. Kolar: The pictures which I presented demonstrate surface diffusion of barium over the $SrTiO_3$ sphere. They also demonstrate bulk diffusion of Ba into $SrTiO_3$. $SrTiO_3$ was coarse grained and Ba diffused along grain boundaries and into the bulk of the grains. I agree that one would expect faster diffusion of Sr ions, however, the experiments showed the opposite.

National Institute of Standards and Technology Special Publication 804, Chemistry of Electronic Ceramic Materials, Proceedings of the International Conference held in Jackson, WY, August 17-22, 1990, issued January 1991.

CHEMISTRY AND PROPERTIES OF TEMPERATURE COMPENSATED MICROWAVE DIELECTRICS

T. Negas, G. Yeager, S. Bell, and R. Amren
Trans-Tech, Inc.
Adamstown, Maryland

ABSTRACT

Modern microwave detection and communication devices rely on high dielectric constant (E'), low loss (high Q), temperature stable oxide ceramics that can be grouped into four major classes. These are $(Zr,Sn)(Ti,Sn)O_4$, $Ba_2Ti_9O_{20}$, BaLnTi-oxides (Ln = Nd, Sm), and $Ba_3Ta_2MeO_9$ (Me = Zn or Mg). This report focuses on relevant chemistry/structure-property-processing features for ceramics in or derived from the last three classes.

INTRODUCTION

The past decade has seen the emergence of diverse microwave technologies that operate in the 0.4-30GHz band. Typical systems presently encompass cellular telephones, satellite communications of many types, and frequency sensors. Global positioning systems for personal use and high resolution/digital communication devices loom in the near future. Oxide ceramics, developed and improved over the past 30 years, are critical elements in these microwave circuits. By simple coupling and frequency tuning techniques, they store, filter, and /or transfer electromagnetic energy in a circuit with minimal loss because of their high Q. They diminish the size of a device because of their high E'. They minimize frequency drift when temperature fluctuates due to the environment and/or to circuit heating because of their small temperature coefficients of dielectric constant (T_E'), resonant frequency (T_f), and capacitance (T_c). The industry requires that these chemically complex ceramics be held to stringent electrical (and dimensional) tolerances, typically $\pm$0.5-1ppm/°C and $\pm$0.25% for specified T_f and E', respectively. Yet, the market demands low cost for parts ranging from a few samples to millions per year. Thus, the message to the ceramist, an implicit theme of this report, is old but worth repeating. Make processing more efficient, minimize technical problems, and, thereby, increase product yield and lower expenses. Therefore, know your crystallochemical system, understand how it is influenced by processing, and design processes accordingly within technical/economic constraints. Comprehend the sampling and electrical measurement methodologies but be aware that subtle microstructural details, often process or raw material dependent, can yield unexpected property results. Routine microwave measurements are especially sensitive to microstructural/chemical details but the evidence gained is indirect and, therefore, must be linked either to empirical models of a chemical system that can be tested experimentally or, if time/resources permit, to direct observations at the submicron level.

Three well established classes of ceramics are discussed. Our objective is to help consolidate the technical base for each by detailing some simple but pertinent features that either are alluded to or not recognized in the open literature.

$Ba_2Ti_9O_{20}$ (B_2T_9) and $BaTi_4O_9$ (BT_4); Q, T_f

$ZrTiO_4$:SnO_2 ceramics, developed in the late 1970's to early 1980's, have gained acceptance by the industry because of their high Q (>10K, 4.5GHz), high E' (35-40), and low, adjustable T_f. The earlier candidates, B_2T_9 and BT_4, forwarded by work in (1) and the pioneering efforts in (2-6), lost favor primarily because Q was "too low" and, secondarily, because T_f could not be adjusted easily. Typical literature Q's range from 5K-10K (4.5 GHz), while 2-5 and 14-20ppm/°C are approximate T_f's reported for B_2T_9 and BT_4, respectively. Periodically, the literature informed us that Q for B_2T_9 can be improved by thermal annealing, by "chemical treatment" of powders (2-5), and/or by additions of Mn-oxide (7). Most recently (8), we learn that for unclear reasons WO_3 additions increase Q for B_2T_9 and BT_4. We have concluded that two simple chemical factors, apart from ill-defined intrinsic loss mechanisms related to crystal structure, really control Q. Figures 1 and 2 demonstrate that the Q of BT_4 and B_2T_9 is extremely high when certain raw materials are avoided. Modest Q ceramics are obtained through the use of titanias of 99.5+% purity (LP), typically anatase that contains silica or phosphate at levels near 0.1%. When 99.9+% rutile (HP) is used, Q (4.5 GHz) exceeds 13K and 12K for BT_4 and B_2T_9, respectively, even in routine production. Well controlled laboratory specimens yield Q as high as 14.8K. Indeed, the data show that BT_4 has a Q somewhat higher than B_2T_9 and that both rival, if not exceed, the best Q's reported for $ZrTiO_4$:SnO_2. We speculate that for nominally "pure" ceramics, silicates or phosphates of very low Q develop during densification and these reside primarily in the grain boundary region. O'Bryan (9) broached this very issue and suggested for the case of phosphorus that crystalline Ba-Ti-P or glassy Ti-P oxides are formed. They diminish bulk Q disproportionately to their small apparent volume fraction and are easily detected by the microwave measurement. If this conclusion is nearly correct some deliberate additives (e.g. Mn-oxide, WO_3) may improve a normally low Q ceramic simply by scavenging the detrimental impurities and "improving" the grain boundary region. Our work indicates that when the system is "clean", Q is high and additives only diminish it. Process contaminants such as milling media [e.g. Al_2O_3 (10)] and sodium impurities in many cellulose binders also deteriorate Q. We return to this argument below.

Oxygen loss, particularly for B_2T_9, at densification temperatures, 1325-1375°C, is the second major factor that influences Q. The process, operative for almost all titanate-based ceramics, is manifested by a darkened, semiconducting interior or "core", particularly within ceramics that are of high density and large cross-section. When coring is present, Q is low. Figure 3 (top) shows slices of B_2T_9 ceramics densified at 1330°C, air. High purity (HP) and lower purity (LP) end-members (see Fig. 2) were air-quenched from 1330°C. The HP ceramic is uniformly blue-grey, while the LP material is not as dark near exposed surfaces. The lower set of B_2T_9 parts in Fig. 3 have compositions given in Fig. 2. They were densified at 1330°C in air, then cooled 50°C/hr to RT. Note the progressive increase in "cored" volume from LP to HP ceramics and refer to

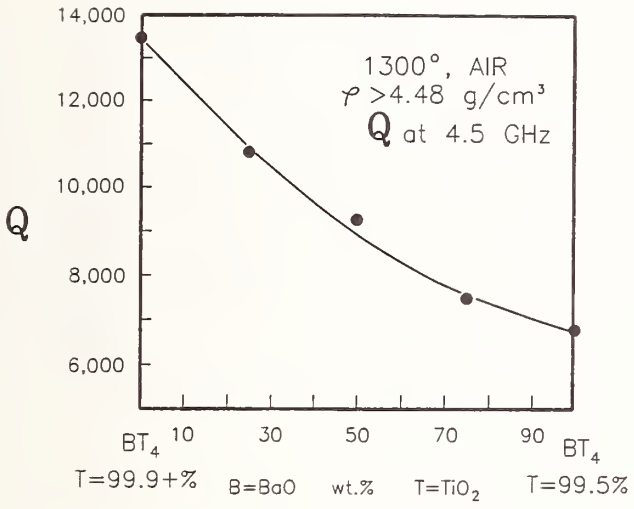

Fig. 1. Q of $BaTi_4O_9$ ceramics versus TiO_2 raw material content. Temperature in °C.

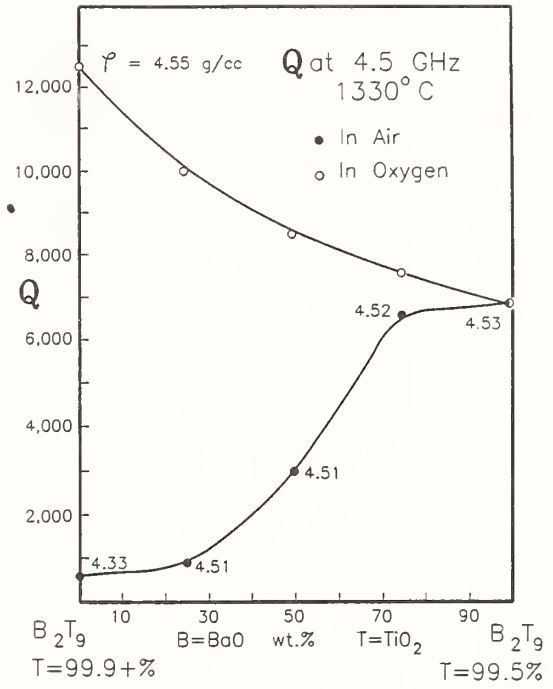

Fig. 2. Q of $Ba_2Ti_9O_{20}$ ceramics versus TiO_2 raw material content and processing in O_2/air. 99.9+ %TiO_2 = HP and 99.5 %TiO_2 = LP in text.

Fig. 2 for corresponding Q in air. Bulk density is not a variable in the coring since it remains high and constant (Fig. 2) except for the most extensively cored HP end-member which, interestingly, has a much lower density. When ceramics are processed in oxygen, coring is eliminated and Q increases accordingly (Fig. 2).

Speculation regarding the influence of the grain boundary region on Q is given greater validity when considered within the context of the coring observations. First, B_2T_9 reduces in air during densification, >1325°C. Second, reoxidation occurs during cooldown but the penetration depth of oxygen (Fig. 3) clearly is a function of impurity content. LP end-member parts completely reoxidize, while coring volume increases as the HP content increases. Given constant bulk density and grain size (3-6 μm) for the ceramics, the physical/chemical nature of the grain boundaries must control the reoxidation kinetics. Wider, "dirty" boundaries, perhaps dominated by defects, provide avenues for faster oxygen transport that eliminate coring, but the penalty is low Q. Tighter, "cleaner" boundary regions decrease the reoxidation rate and parts core. Therefore, more stringent processing is required to avoid

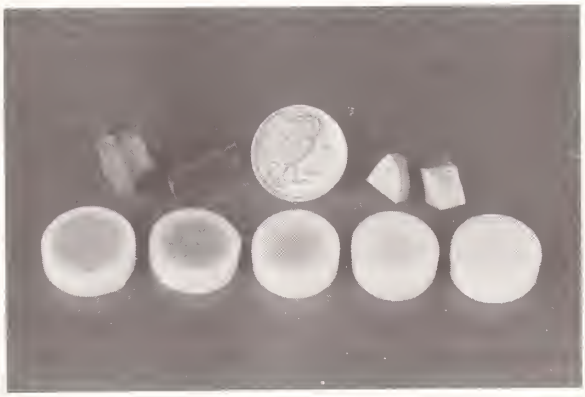

Fig. 3. Cored $Ba_2Ti_9O_{20}$ ceramics (1330°C, air). Slow cooled (bottom); air quenched (top); compositions from left to right correspond to materials in Fig. 2, left to right.

reduction and attain high Q. In a pertinent HRTEM study (11), unsuccessful attempts were made to "explain the poorly understood variations in dielectric loss" of $Ba_2Ti_9O_{20}$ materials including a low Q ceramic from Trans-Tech. An argument was made that loss seems to "result from different degrees of polytypic intergrowth" (within B_2T_9 grains). This may be correct for overall intrinsic loss but the Q of real ceramics also is influenced by extrinsic contributions such as from grain boundaries. Indeed in (11), one HR-image is shown for a grain boundary region and the writers remark that it is characterized by a Ti-O framework and extended rows of vacancies (i.e. "missing" Ba). It is this observation that meshes with our data. Impurities probably help generate the defects and provide for localized charge compensation. In turn, the overall concentration of defects/impurities controls Q and reoxidation kinetics. HRTEM images for low or high Q BT_4 do not show intracrystalline extended defects but they do exist in ceramics of high and low Q B_2T_9 (12). Such defects, therefore, are of marginal importance in Q considerations. However, Q for BT_4 is a function of impurity content (Fig. 1), again suggesting that the grain boundary region is critical. Reoxidation kinetics are not relevant since BT_4 does not reduce in the practical densification range, 1275-1350°C, air.

The ability to chemically tune the T_f of dielectrics to be device specific without diminishing Q or changing E' by more than several units is a practical requirement. BT_4 would be the perfect candidate to tune because of processing ease. Unfortunately, the most obvious substitutions for Ba and/or Ti (e.g. Sr,Ca,Zr) do not budge T_f from a plateau in the 13-16ppm/°C range. Solubility appears too limited to produce the desired effect. Even Sn solubility (see below) is less than given in (1) and is not useful. Thus, the next most attractive option is to drive T_f toward 4ppm/°C by making composites of BT_4 with B_2T_9. Figure 4 summarizes the results. Unexpectedly, a T_f minimum, ~2ppm/°C, near 30m.%BT_4 is observed but its significance is not clear. We suspect that the electrical data are reflecting a limited homogeneity region for B_2T_9 not unlike that proposed in (4). A second practical aspect of Fig. 4 is amplified in Fig. 5. For many applications, the designer often requires a T_f approximately "linearized" over the range -30 to 60°C. Conventional $ZrTiO_4$:SnO_2 ceramics show significant departure from linearity. For example, a T_f that holds at 6ppm/°C from 25-60°C changes to 9-10ppm/°C from -30 to 25°C. Figure 5 shows that BT_4-B_2T_9 composites retain good linearity and, indeed, traverse near perfect linearity in the 75-60m.% BT_4 range.

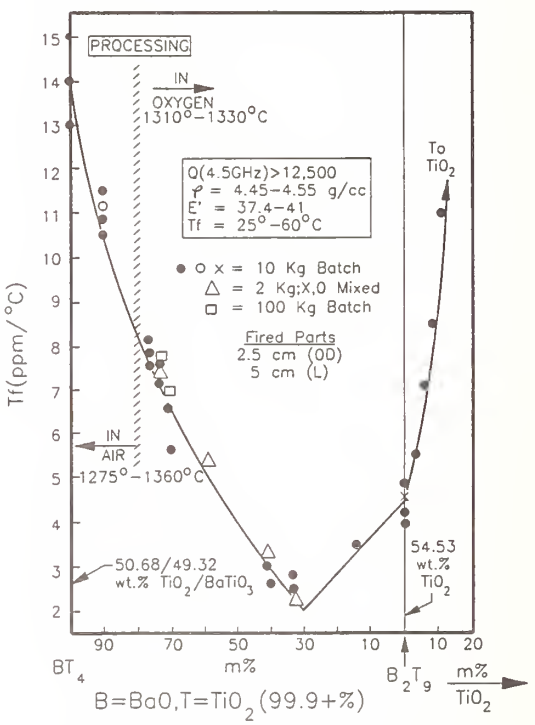

Fig. 4. T_f (25-60°C) for the system $BaTi_4O_9$-$Ba_2Ti_9O_{20}$-TiO_2.

BT_4 ceramics can be forced to assume T_f values 10-15ppm/°C higher than the normal 13-16ppm/°C without chemical adjustments. The most obvious microstructural feature that directly correlates is the presence of anomalous/discontinuous grain growth introduced into the ceramics by deliberate bad processing practices. When random grain growth is extensive and quite visible (1-6 mm long, anisotropic crystals), T_f is highly positive. Details of this work are reserved for the future but are mentioned only to target a potential pitfall for researchers. BT_4/B_2T_9 composites, however, never show massive discontinuous grain growth (B_2T_9 >15 mol.%) and unusually large T_f indicating that B_2T_9 is an effective inhibitor.

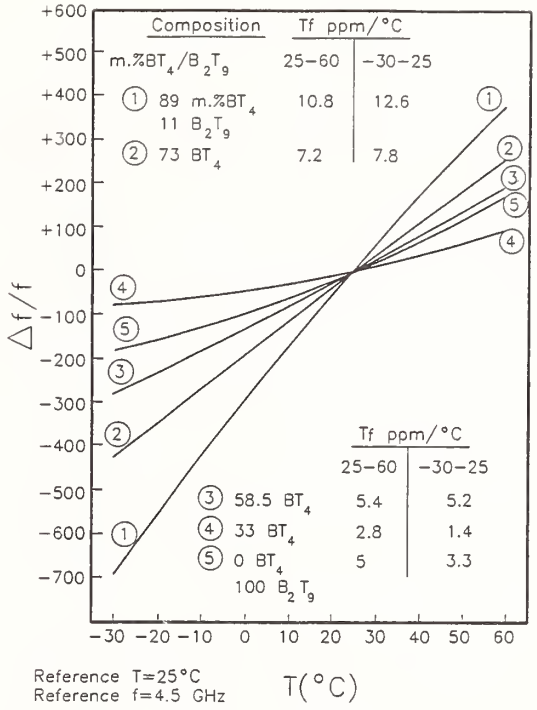

Fig. 5. $\Delta f/f$ versus temperature ($T_f = \Delta f/f\Delta T$) for compositions in Fig. 4; 25-60, -30-25 in °C.

The last need is to produce BT_4/B_2T_9 composites with T_f less positive than 2ppm/°C. Work in (5) shows that SnO_2 substitutions in/near B_2T_9 diminish T_f. Figure 6 illustrates T_f isopleths for solid solutions in the system $Ba_2Ti_9O_{20}$-$BaTi_4O_9$-"$BaTi_{3.5}Sn_{0.5}O_9$"-"$Ba_2Ti_8SnO_{20}$". The latter two are not single phase. Our results for B_2T_9 are consistent with the T_f data in (5). SnO_2 enters into solid solution primarily with B_2T_9 as indirectly reflected by the electrical data. Microstructural evidence (Fig. 7) from a ceramic with near zero T_f combined with qualitative EDS (S. G. Mhaisalkar, Ohio State Univ.) confirms that B_2T_9 grains contain most of the SnO_2. The composition shown by the data point at "$BaTi_{3.7}Sn_{0.3}O_9$" consists of B_4T_{13}, BT_4, and TiO_2 with SnO_2 concentrated primarily in the latter. Q is very low, ~600. Thus, at high SnO_2 content, two-phase solid solution tie-lines (not shown) must traverse compositional space from northwest to southeast in Fig. 6. Note particularly in Fig. 6 the broad trough of low T_f that appears to be related to the minimum on the BT_4/B_2T_9 join. As SnO_2 content is increased for any starting Ti/Ba ratio, Q progressively decreases from a >12.5K plateau towards about 10.5K (4.5 GHz). Large pucks (2.5" OD x 1.25" t) of several SnO_2-containing ceramics were dissected to obtain numerous randomly oriented test parts (0.5" OD x 0.25" t) that sampled surface and interior volumes. Uniform electrical properties were measured indicating that the ceramics are not anisotropic and that vaporization of SnO_2 is not a significant problem.

Figure 8 shows that good T_f linearity is maintained for B_2T_9 materials with SnO_2 and other substitutions. ZrO_2 substitutions are not very effective in decreasing T_f; coupled substitutions, for example, of Ni/Ta for Ti, effectively increase T_f of B_2T_9. The coupled substitution approach appears attractive but requires further work (e.g. Me^{2+}/Ta, Nb; Me = Mg, Zn, Co, etc. combinations).

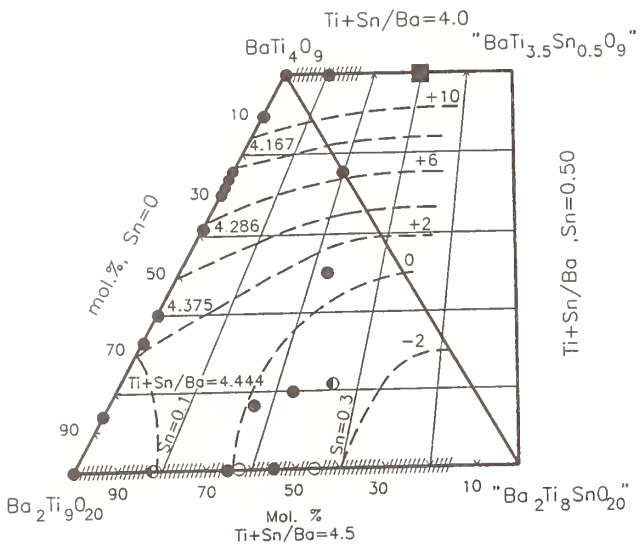

Fig. 6. T_f isopleths (approximate) for the system $BaTi_4O_9$-$Ba_2Ti_9O_{20}$ and SnO_2-containing solid solutions (1330-1350°C,O_2). Hatching depicts approximate limits of solid solubility after (1) and this work (■, not single phase). Open circles are after (5).

Fig. 7. Microstructure of $BaTi_4O_9/Ba_2Ti_9O_{20}$ composite; each phase contains SnO_2; $T_f \approx +1$ppm/°C (Fig. 6). Defective grains are B_2T_9.

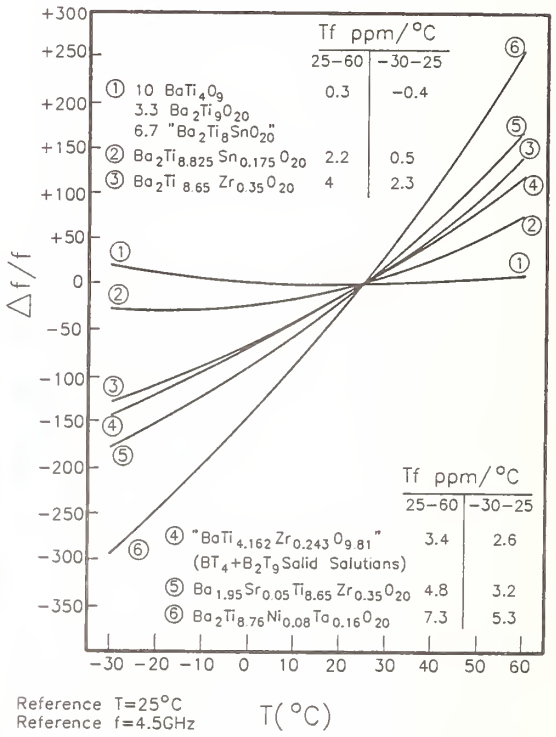

Fig. 8. Δf/f versus temperature ($T_f = \Delta f/f\Delta T$) for ceramics based on $Ba_2Ti_9O_{20}$ that contains various cation substitutions; 25-60, -30-25 in °C.

High E' (smaller size) ceramics of modest Q are used in many applications in the 0.4 to ~3GHz band. Development of products lay dormant until spurred by market needs in the early 1980's. The technical foundation for renewed efforts resides in work by Bolton (13), but subsequent literature, including a plethora of patents, never acknowledges the study. Bolton examined the system, $BaTiO_3$-Ln_2O_3-TiO_2, Ln = didydium. A composite with low loss (1MHz), small temperature coefficient of capacitance (T_c), and high E' ~62 was found when "pure" Nd_2O_3 was used. More importantly, a broad region of higher E' (>80) and very negative T_c was delimited and shown to result from a phase X plus a phase Y. Figure 9 summarizes developments to

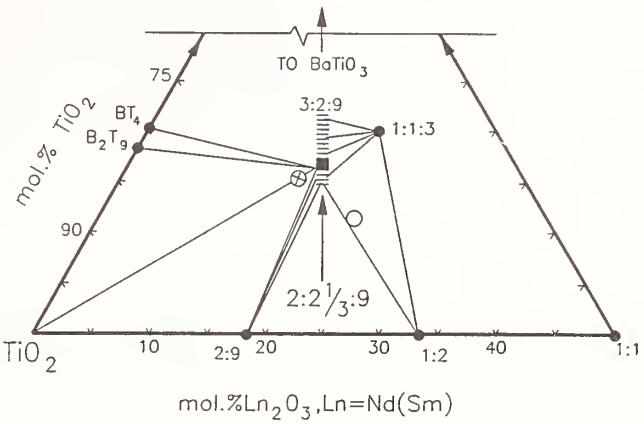

Fig. 9. Present knowledge of the $BaTiO_3$-TiO_2-Ln_2O_3 system. Solid solution (hatched) is after (20). O, low Tc, high E' material after (13). ■, 1:1:4 composition (Nd_2O_3) of special focus in (14,15,16). ⊗, 1:1:5 composition to 1:1:4 (Sm_2O_3) of special emphasis in (17) and this work. Tie-lines from Ln_2T_9 to 1:1:4 solid solution do not exist for the Sm_2O_3 system [2:9(Sm) not stable].

date. Kolar et al. (14) completely characterized the electrical properties (1MHz) of the system containing Nd_2O_3 and later (15) showed that additions of $Bi_4Ti_3O_{12}$ to the compositions 1:1:5 ($BaO:Nd_2O_3:TiO_2$) and 1:1:4 yield high E' (88-105) ceramics with low $T_{E'}$. Wakino et al. (16) next demonstrated that in the vicinity of the 1:1:4 composition (Nd), ceramics with high E' (85-88), modest Q (~2K, 3GHz), and near-zero T_f can be obtained by substituting some Pb for Ba. Parallel work in (17), and at Trans-Tech focused on Sm-variants which yield ceramics with negative T_f, E≈80, and higher Q≈3K-4K (3GHz). The former tuned T_f through zero by substituting some Sr for Ba. We tune T_f simply by adjusting TiO_2 content along the join TiO_2 - 1:1:4. Meanwhile, crystal chemists were attempting to define phase equilibrium and structural details for these materials. Kolar et al. (18) reported on the Nd compounds 1:1:3 and "1:1:5". Matveeva et al. (19) determined a preliminary crystal structure for a Pr-analogue near this compositional region. Finally, in (20) we learn that the high E' compound(s) are members of a solid solution region that extends from about 3:2:9 through 1:1:4 to about 2:2 1/3:9 (Fig. 9). The 3:2:9 end-member is Bolton's phase X, while his phase Y is close to the 1:1:3 compound. Today, the chemistry-property cycle has been nearly

closed, but one major factor has been overlooked and it casts doubt on the ability of researchers to reproduce the available property data. In every study and patent promulgated to date, samples were made by uniaxial pressing of prereacted powders. It will be demonstrated below that this methodology complicates the electrical data.

In (19), 1:1:4-type materials are shown to have a structure that contains perovskite-like building blocks and that crystals with orthorhombic symmetry grow with acicular habit. During our work with 1:1:4 (Sm), we observed that a given batch of powder, 1200°C calcine, can yield highly variable T_f depending on the forming process used and on the method of sampling the ceramic for electrical testing. We conjectured that, since 1:1:4 crystals/grains are anisotropic, electrical properties should be anisotropic. If so, the observed T_f variation must somehow be related to dimensional crystalline anisotropy. However, this requires at least partial preferred orientation of crystallites in the finished ceramics. Qualitative microstructural examination and quantitative XRD analysis (J. Simmins, Alfred Univ.) of typical ceramics do not reveal obvious preferred orientation, albeit lath/acicular crystals are present (Fig. 10). Consequently, a series of experiments was designed to address the issue.

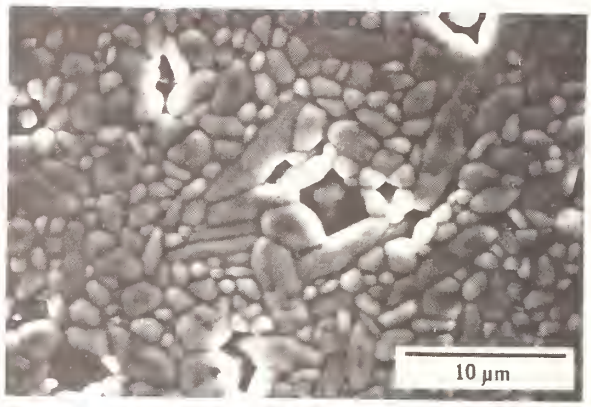

Fig. 10. Microstructure of ceramics in the vicinity of 1:1:4-1:1:5 (Sm_2O_3).

Five large, dimensionally precise pucks were formed [~1:1:4.5(Sm) composition] each at a different uniaxial pressure. Pucks were cut in half, and one set of halves was isostatically overpressed, >100MPa. All ten pieces were densified (>5.70 g/cc, <2% porosity) at 1330°C. Figure 11 gives initial green densities and shows anisotropy in fired shrinkage which we will not discuss other than to indicate that uniaxial pressing imposes some type of "memory" to the powder that is not erased by isostatic overpressing and is carried into densification. Figure 12 illustrates subsequent methodology and T_f data for the fired parts. Every half-puck was machined to obtain a minimum of two orthogonal sets of test parts for T_f measurement using cavity methods and the $TE_{01\delta}$ mode (21).

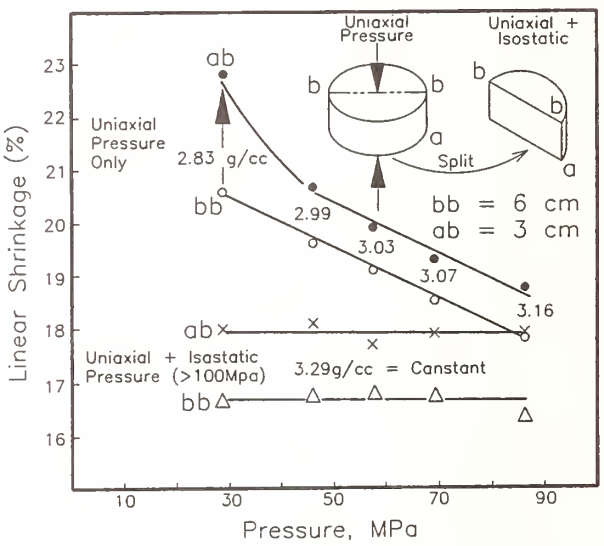

Fig. 11. Pressing methodology of ~1:1:4.5(Sm) powder (plus green densities) showing anisotropy in fired shrinkage.

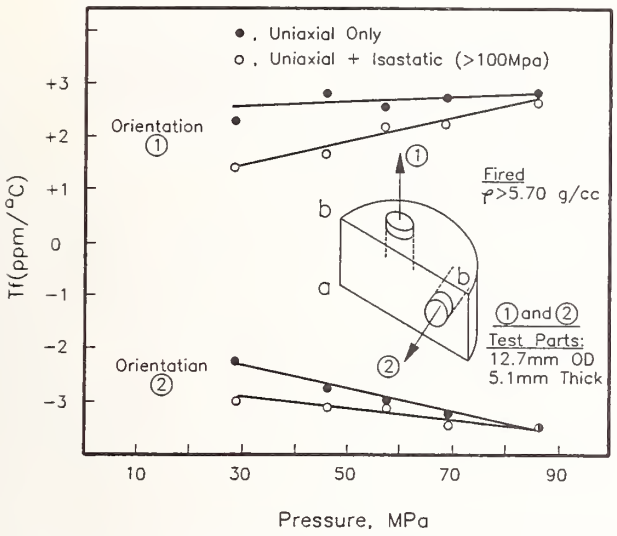

Fig. 12. T_f of fired ceramics versus methodology of pressing (Fig. 11) and extraction of oriented test parts for electrical measurement.

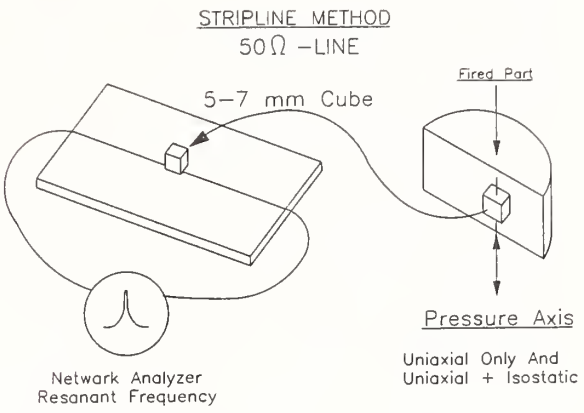

Fig. 13. Method to detect E' anisotropy in ceramics of Fig. 12.

Alternatively, orthogonal TE and TM modes for only one set of identically oriented parts may be used to test for T_f, but this complicates procedural logistics and increases possible error. Figure 12 demonstrates that ceramics show anisotropy in T_f that widens in magnitude as uniaxial pressure increases. Isostatically overpressed parts retain the anisotropy imposed by the initial uniaxial pressing. Ceramics that are isostatically pressed only do not display anisotropy and yield $T_f \approx 0 \pm 1$ppm/°C. Anisotropy in E' was examined using the same test pieces and the parallel plate method (22). Small variations near the limit of error were observed, so a more sensitive but indirect method was developed, Fig. 13. Cubes containing the uniaxial pressing direction as a unique 4-fold axis were precisely extracted and machined from all half-puck ceramics. These were coupled to a 50 Ω stripline, and resonant frequency (F_r) was measured at six different cube orientations, i.e. each 4-fold axis, (+) and (-) direction, brought to the vertical position. If E' is isotropic, F_r should remain constant for all cube orientations. Figure 14 shows an E' anisotropy of ~0.4 units, and the unique uniaxial pressing direction is easily discernable. The extensive data collected show that Sm-ceramics display anisotropy in T_f of about 6ppm/°C and in E' of 0.4-0.7 units. The magnitude of the anisotropy within the 1:1:4-1:1:5-1:1:5 (+2 wt% TiO_2) compositional region examined remains constant provided uniaxial pressure also is constant. This indicates that secondary phases (e.g. TiO_2) contribute little

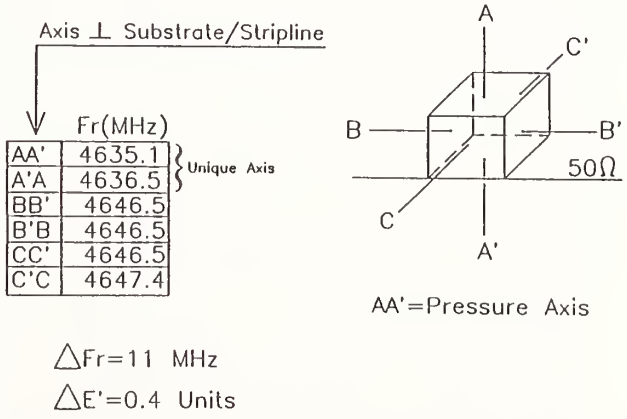

Fig. 14. Methodology and example measurements to determine E' anisotropy by the "cube technique", Fig. 13.

to the anisotropy. The largest E' and most positive T_f are observed when the $TE_{01\delta}$ field during measurement is normal to the pressing direction. Almost within measurement error (±5% maximum), Q seems to remain constant but systematic trends in the data suggest that slightly lower Q is associated with the more positive T_f orientation. The ceramic in Fig. 15 contains 0.2 wt% less TiO_2 than the materials illustrated above. Uniform but directional properties are clearly evident and note sample 8 which was extracted inclined to the pressing direction.

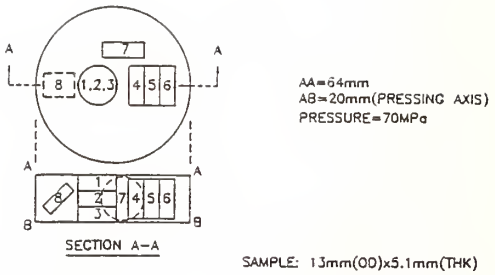

SAMPLE	Q(2.9GHz)	T_f	E'	DENSITY(g/cc)
1	3480	−0.7	80.1	5.72
2	3525	−0.5	79.6	5.71
3	3410	−0.5	79.7	5.72
4	3710	−6.5	79.2	5.71
5	3710	−6.3	79.2	5.71
6	3710	−6.3	79.4	5.72
7	3670	−6.1	79.4	5.72
8	3700	−2.0	79.5	5.72

Fig. 15. Uniaxially pressed and fired ceramic [~1:1:4(Sm) composition], dissected to demonstrate anisotropic electrical properties but good overall uniformity.

Several samples of dense, commercial 1:1:4(Nd):PbO pucks were made available and these were tested as above. The pucks must have been pressed uniaxially because anisotropy in T_f of 14ppm/°C and in E' of ~0.7 units are evident (Q≈2300, 3GHz). Bi_2O_3-containing materials of the 1:1:4(Nd)-type (15) were fabricated by isostatic and by uniaxial pressing, then densified. The latter show anisotropy of 22ppm/°C and ~3 units in T_f and E', respectively. These data might be further influenced by a Bi-ferroelectric phase that exists as domains and/or at grain boundaries. Solubility of Bi_2O_3 in 1:1:4 also requires definition. Isopressed parts are relatively uniform, $T_f \approx$ 10ppm/°C and E' ≈ 91 (Q ≈ 1800, 3GHz).

Electrical properties and processing for the high E' materials can be considered within the context of an oversimplified empirical model. First, it is assumed that powder, calcined at 1200°C and milled to an average particle size near 2 μm, contains nuclei of 1:1:4 that have lath/acicular habit. XRD reveals that the powder consists of B_2T_9, TiO_2, $Sm_2Ti_2O_7$, and 1:1:4 but definitive identification of nuclei could not be obtained by SEM. Second, we speculate that some fraction of the nuclei is aligned during uniaxial forming with their long axis (or axes) perpendicular to the pressing direction. Most of the alignment is accomplished at the lowest pressures. Isostatic pressing (only) does not cause preferred orientation. When it is applied to uniaxially pressed parts of low green density, the alignment of nuclei is preserved with only minor disruption (Figs. 11,12). During densification, preoriented nuclei grow in the plane normal to the initial pressing direction at the expense of smaller 1:1:4 particles and of adjacent secondary phases as chemical equilibrium is attained. The rest of the ceramic also undergoes similar changes, but they are directionally random. The resultant product consists of a matrix of random crystallites plus a small volume fraction of oriented grains that are not easily resolved by routine methods. However, the sensitive microwave measurements detect the anisotropy. It is useful to reflect on one final experiment. The model assumes that nuclei of 1:1:4 exist in processed powder. Therefore, their availability and concentration should be dictated by the magnitude of the initial calcination temperature. Consider the extreme, no calcination and no nuclei. $BaTiO_3$, Sm_2O_3, and TiO_2 (rutile) raw materials (see bulk

composition pertinent to Fig. 15) were blended in alcohol, dried, and reblended. Samples of this powder were pressed uniaxially and isostatically (90 MPa) and these were densified, 1330°C. Fired densities were 5.60g/cc (<4% porosity) sufficient to yield E' ≈ 77 and Q = 3.2K (3GHz). Both ceramics gave T_f = -3.1ppm/°C and the cube test showed no frequency variation indicating complete lack of anisotropy. Although we grant that for these powders microstructural evolution is controlled by a completely different set of densification/reaction mechanisms and kinetics, the assumption for the need of 1:1:4 precursors appears to have some validity.

Exact details for the model require further work and it would be useful to have electrical data from 1:1:4 single crystals. We recognize that electrical and dimensional anisotropy are discussed using the simple case of two primary axes. Since 1:1:4 is orthorhombic, a third axis must influence the observed properties and add complexity to the model. Many other experiments need to be performed to address questions involving numerous variables such as calcination and densification temperature/time, extent of grain growth, the influence of pore size/shape, etc. versus electrical anisotropy. We note, however, that for 1:1:4(Sm) ceramics the experimental options are limited by a narrow effective densification range, 1330±15°C, without introducing other problems. Nevertheless, some practical processing approaches can be derived from the limited data. Anisotropy initiated by forming methods such as uniaxial pressing, extrusion, etc., can be managed by imposing strict controls in powder calcining through densification operations. Alternatively, parts can be formed exclusively by isostatic pressing but this is not always cost effective nor applicable to shapes such as substrates. Finally, the nuclei in powder can be eliminated. Reactive sintering of well blended raw materials (see above) is appropriate provided high density, target E', and control of large shrinkage are obtained. Calcining the blended raw materials at a temperature slightly lower than that required to form 1:1:4 crystallites is particularly attractive since powder homogeneity is enhanced by preliminary reaction and subsequent milling. The 1050-1100°C range is optimal.

High E' materials mildly reduce during densification in air. High density, Sm-ceramics show distinct cores, while Nd variants have cores that are masked by their intrinsic bluish color. Coring diminishes Q to almost unmeasureable values but processing in oxygen, 1330±15°C, avoids the problem when using conventional powders.

MICROWAVE PEROVSKITES

As applications entered the 10-30GHz band, ceramics with super Q (>>10K, 10GHz) and small E' (<30) were demanded. During the 1980's, it was demonstrated that the well-known perovskite family, $Ba_3Ta_2MeO_9$ (Me = Zn or Mg), has these requisite properties (8,23,24) when octahedral cations are ordered (1:2 type) to near perfection. However, this seemingly simple need has important practical engineering consequences. Multiple octahedral substitutions (Ni,Co,Mn,Zr,Sn, etc.) often are used to tune T_f. As an example, Fig. 16 illustrates ordered perovskite solid solutions in the system $Ba_3Ta_{2-2/3x}Zn_{1-1/3x-y}Ni_yZr_xO_9$. Since ordering is diffusion controlled, many obvious

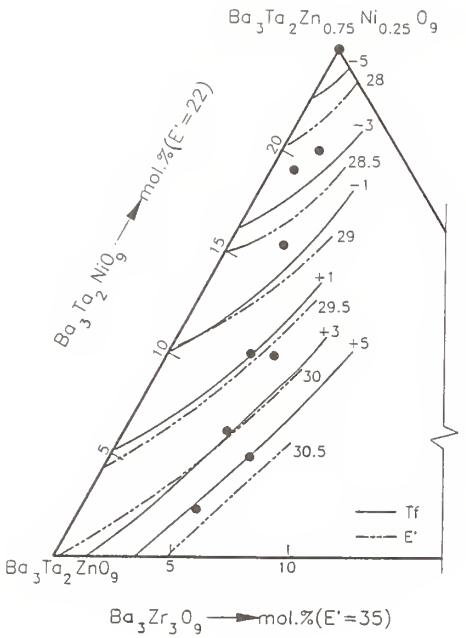

Fig. 16. T_f and E' isopleths (approximate) for ordered perovskite ceramics in the system $Ba_3Ta_2ZnO_9$-$Ba_3Ta_2NiO_9$-$Ba_3Zr_3O_9$. Ten Kg batches were made; fired densities are >7.70 g/cc.

factors limit the kinetics. Of these, the "mundane" blending of raw materials is the least appreciated and, in our judgment, the most crucial yet most difficult to quantify. For the example given, $BaCO_3$, Ta_2O_5, ZnO, NiO, and ZrO_2 powders having diverse physical properties are blended by high shear wet mixing. To test "homogeneity", samples are reacted at 1250°C. Dark agglomerates are observed when homogeneity is "poor". XRD reveals that these products are "$BaNiO_3$"-type oxides and BaNi-oxycarbonates (25); when present, even after rehomogenization by milling, pressed ceramics rarely reach target E' or Q after firing. When the calcined blend lacks these and appears "uniform", there is considerable batch to batch variation in the time required for pressed parts to attain the high Q ordered state. Typically, 12 to 100 hr at 1450-1500°C are necessary indicating that perfect blending is elusive. Much better uniformity is achieved when the Zn, Ni, and Zr are added to a $BaCO_3/Ta_2O_5$ slurry as nitrate and/or acetate solutions. In this case, the high Q state is obtained within 25 hours.

The association of high Q with insulating, non-ferroelectric, perovskites prompted us to explore other systems. $Ba_8Ta_6Li_2O_{24}$ ceramics were fabricated and without special efforts to optimize, a material was obtained with E' = 28, T_f = 26ppm/°C, and Q = 14.5K (5.5GHz). This perovskite-like phase features ordered Ta/Li octahedra that share corners and faces (26). Complex perovskites also were explored in work for a radar-related project that required a dielectric with E' = 50±5, T_f = 0±20ppm/°C, and Q > 5K (4GHz). Unpublished records at Trans-Tech describe a ceramic, nominally $La_{2/3}TiO_3$, which the literature shows (27) should consist of $La_2Ti_2O_7$ (LT_2) plus $La_4Ti_9O_{24}$ (L_2T_9). Properties, reproduced in Fig. 17, reveal some peculiar correlations with processing. At constant fired density, E' increases and Q improves each time the powder is calcined/milled. Figure 18 shows our XRD traces for the actual products. When E' = 45 and Q is low, the ceramic is a composite of LT_2 and L_2T_9 plus a third

phase that dominates when E' = 68 and Q is high. This product is an ordered orthorhombic perovskite (~3.8 x 3.8 x 7.6Å) similar to $La_{2/3}TiO_{3-x}$ reported in (28). Additional details indicate that the powder was milled with Al_2O_3 media and up to ~2 wt.% "pickup" was experienced. Furthermore, the perovskite ceramics were "cored" and of low Q unless annealed at 1100°C. Thus, it appeared that perovskite formation could be favored by incorporation of Al_2O_3 according to $La_{2/3+x/3}Ti_{1-x}Al_xO_3$. Two compositions, $La_{2/3}TiO_3$ + 2 wt.%Al_2O_3 (A) and x = 0.10 (B) were formulated (10g) from pure (>99.9%) oxides which were heated in Al_2O_3 crucibles at 1200°, at 1350°, and finally at 1400°C, air. After each heating, samples were cooled 200°C/hr to RT and remixed. XRD showed that (A) consists of L_2T_9 plus perovskite and (B) is single-phase, ordered perovskite. Although the evidence suggests that Al_2O_3 helps "stabilize" the structure, it is not sufficient to clarify the importance of reduction. Since ceramics core, mild reduction must occur but the perovskite can be reoxidized without causing decomposition. More work is necessary to elucidate equilibrium details including solid solution toward $LaAlO_3$. Subsequently, the system La_2O_3-TiO_2-MgO was examined in the hope of finding a similar perovskite, $La_{2/3+x/3}Ti_{1-1/2x}Mg_{1/2x}O_3$, with smaller E' and T_f. In the vicinity of $La_{2/3}TiO_3 \pm MgO$, the phase was obtained again but ceramics were not

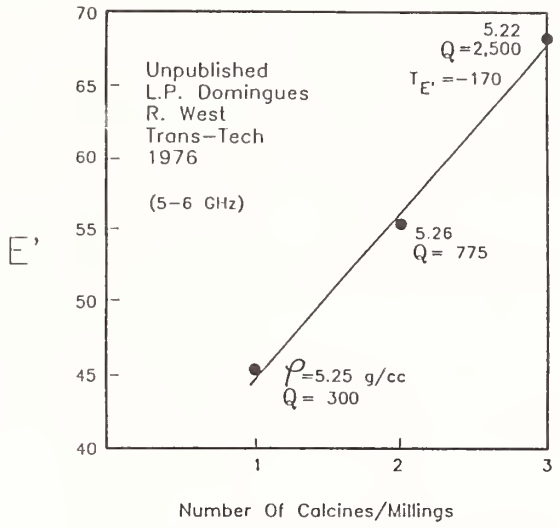

Fig. 17. "Processing" versus E' for "$La_{2/3}TiO_3$" composition.

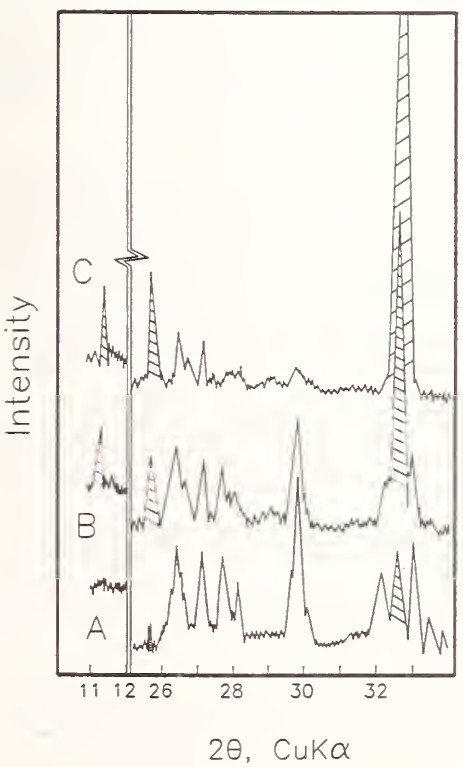

Fig. 18. XRD tracings for ceramics in Fig. 17 (A,B,C correspond to E' = 45, 55, 68, respectively). A = LT_2 + L_2T_9 + trace ordered perovskite (P, shaded); B = LT_2 + L_2T_9 + P; C = L_2T_9 + P (trace LT_2). LT_2 = $La_2Ti_2O_7$; L_2T_9 = $La_4Ti_9O_{24}$.

fabricated since the XRD data from powders were plagued by many uncertainties. Fortunately, at x=1, $LaTi_{1/2}Mg_{1/2}O_3$ (LTM) was found to be an orthorhombic perovskite similar to $GdFeO_3$. Ceramics yield E' = 33, $T_f \approx$ -100ppm/°C, and Q ~ 8K (5GHz). Possible LTM-$CaTiO_3$ (E' $\approx$ 150, $T_f \approx$ 800ppm/°C) solid solutions thus became obvious candidates and at 44 mol.% LTM an orthorhombic perovskite was obtained with E' = 47, T_f = 0, and Q = 7.4K (3.8GHz). All properties met project requirements.

ACKNOWLEDGMENT

We thank all the employees of Trans-Tech that made this report possible. D. Cronin, L. P. Domingues, R. West, and R. Huntt contributed valuable discussions. A. Arnold, D. Huntt, and K. Anderson (with his swamp group) provided their machining, forming, and powder preparation expertise. Appreciation is extended to M. Clevinger of NIST for organizing and preparing this manuscript.

REFERENCES

1. G. H. Jonker and W. Kwestroo, J. Am. Ceram. Soc. 41, 390 (1958).
2. H. M. O'Bryan, Jr., J. K. Pluorde, and J. Thomson, U.S. Patent 3,938,064 (1976).
3. H. M. O'Bryan, Jr. and J. Thomson, U.S. Patent 4,337,446 (1982).
4. H. M. O'Bryan, Jr. and J. Thomson, J. Am. Ceram. Soc. 66, 66 (1983).
5. H. M. O'Bryan, Jr., J. K. Pluorde, and J. Thomson, U.S. Patent 4,563,661 (1986).
6. D. W. Readey, E. A. Maguire, C. P. Harting, and D. J. Masse', Raytheon Co., Contract DAAB07-69-C-0455 (1971).
7. S. Nomura, Ferroelectrics 49, 61 (1983).
8. S. Nishigaki, S. Yano, H. Kato, T. Hirai, and T. Nonomura, J. Am. Ceram. Soc. 71, C-11 (1988).
9. H. M. O'Bryan, Jr., Am. Ceram. Soc. Bull. 66, 677 (1987).
10. S. G. Mhaisalker, W. E. Lee, and D. W. Readey, J. Am. Ceram. Soc. 72, 2154 (1989).
11. P. K. Davies and R. S. Roth, J. Solid State Chem. 71, 490 (1987).
12. S. G. Mhaisalker, Masters Thesis, Ohio State Univ. (1987) and personal communication.
13. R. L. Bolton, Dissertation, Univ. Ill. (1968).
14. D. Kolar, Z. Stadler, S. Gaberscek, and D. Suvorov, Ber. Dt. Keram. Ges. 55, 346 (1978).
15. D. Kolar, S. Gaberscek, Z. Stadler, and D. Suvorov, Ferroelectrics 27, 269 (1980).
16. K. Wakino, K. Minai, and H. Tamura, J. Am. Ceram. Soc. 67, 278 (1984).
17. S. Nishigaki, H. Kato, S. Yano, and R. Kamimura, Am. Ceram. Soc. Bull. 66, 1405 (1987).
18. D. Kolar, S. Gaberscek, B. Volavsek, H. S. Parker, and R. S. Roth, J. Solid State Chem. 38, 158 (1981).
19. R. G. Matveeva, M. B. Varfolomeev, and L. S. Il'yushchenko, Russ. J. Inorg. Chem. 29, 17 (1984).
20. F. Beech, K. Davis, A. Santoro, R. S. Roth, J. L. Soubeyroux, and M. Zucchi, Abstract 251-B-87, Ann. Meeting Am. Ceram. Soc. (April 1987).
21. D. Kajfez and P. Guillon, Dielectric Resonators, Artech House, Norwood, MA, 1987 (pp. 539).
22. E. Courtney, IEEE Trans. Mic. Th. and Tech. MTT-18, 476 (1970).
23. S. Kawashima, M. Nishida, I. Ueda, and H. Ouchi, J. Am. Ceram. Soc. 66, 421 (1983).
24. K. Matsumoto, T. Hinga, K. Takada, and H. Ichimura, Proc. 6th IEEE Int'l. Symp. App. of Ferroelectrics, p. 118 (June 1986).
25. T. Negas and R. S. Roth, NBS Spec. Publ. 364, 233 (1972).
26. T. Negas, R. S. Roth, H. S. Parker, and W. S. Brower, J. Solid State Chem. 8, 1 (1973).
27. J. B. McChesney and H. A. Sauer, J. Am. Ceram. Soc. 45, 416 (1962).
28. M. Abe and J. Uchino, Mat. Res. Bull. 9, 147 (1974).

D. Smyth: I'd like to suggest another effect of purity on your oxidation problem. Most of the naturally occurring impurities have a lower valence, impurities like iron, aluminum, and these are acceptor impurities. As the acceptor impurity content increases, the transition from oxygen excess insulating material to oxygen deficient semiconductor material is shifted to lower oxygen activities. So, you essentially have shifted your reduction problem to a lower oxygen activity.

T. Negas: I'll buy that.

D. Smyth: And there is another bonus to that. Because acceptor impurities are compensated by oxygen vacancies and these increase your reoxidation kinetics you obtain a double advantage. That would be a bulk effect as opposed to your grain boundary effect.

T. Negas: I indicated that I used 99.9 plus percent rutile which contains very low levels of aluminum impurities. It actually is a very good, clean titania that results in very high Q ceramics. The ceramics with less pure titania show faster reoxidation kinetics but are of low Q.

D. Smyth: That's what I'm suggesting. The less pure material behaves better because it contains more acceptor impurities.

T. Negas: I understand what you're saying.

D. Kolar: Is it possible that your impure material was simply not reduced as much as the pure?

T. Negas: Okay, that's a good point. If I can have the overhead. You wish to know what x is in the $Ba_2Ti_9O_{20-x}$ ceramics. There it is (overhead shows $X < 0.001$) and it is difficult to measure either the pure or impure material with conventional TGA. One has to fill a crucible with a hundred grams of powder, then quench it and reoxidize the powder. Both show low levels of reduction -- the x value is very small even though you see highly darkened material, very small.

D. Kolar: The simple way to show this would be to cool down your darkened materials in a neutral atmosphere.

T. Negas: We have also done that.

D. Kolar: Yes? It's dark, this impure material?

T. Negas: Of course.

D. Kolar: Okay.

T. Negas: $Ba_2Ti_9O_{20}$--you cool it down in nitrogen or argon and it is dark. When you pull it out of the kiln--straight out--it's blue. The less pure material starts to reoxidize and the edges, the leading edges of the ceramic start turning a lighter color but the interior is blue. However, the high purity material is all blue. Again, it's the reoxidation kinetics as related to the grain boundary region that control the reoxidation process which in turn relates to the overall Q of the material. The two are related, the impurities, the oxidation phenomenon. I think they're really tightly correlated.

P. Davies: On the dirty materials that people use, bismuth or lead are added to affect the temperature coefficient of resonant frequency. Does it generally drop, and if so, can you give me a crystal chemical explanation as to why that happens to go in that direction? Is there a good chemical reason why they have that particular effect?

T. Negas: You mean in tuning the temperature coefficient of resonant frequency?

P. Davies: Yes.

T. Negas: In these sort of things, theoretical approaches are practically useless as far as I'm concerned. There aren't that many but we have a lot of empirical data; measurements, a lot of measurements for many materials. For example, if you look at lead titanate, the temperature coefficient of dielectric constant is something like plus 5600 ppm/°C. It stands to reason that if you have a highly negative material, I could put in lead titanate, for example, in solid solution using simple mixing rules. You can adjust chemical composition such that the temperature coefficient of dielectric constant and resonant frequency go to zero. So you pick and choose materials, pick and choose based on what you know about crystal chemistry and what you know about available properties because there isn't much theory around. There is some, but it's not theory that guides you. Unfortunately, it always comes afterward.

You can talk about Q and theoretial views on Q looking at optical frequency resonances and gamma factors which are related to lattice vibrations and crystal structure. We can talk about that, but these are summation kind of things--a summation over all atoms, all molecules, all of the grain boundary regions, etc. It's tough and you get some guidance--but it's the measurements, I feel that count, at least in the short term.

R. Roth: I have one question. Back in about 1980 we obtained specimens of the tetratitanate from Trans-Tech. When looked at with high resolution electron microscopy the material was highly defective and showed a lot of polytypic defects. The materials you showed did not show the defects. Are you implying that the difference between what we saw in Trans-Tech material in 1980 and what you see in 1988 or 1989 may be due to differences in purity of starting materials?

T. Negas: You are not looking at a difference in impurity content because the tetratitanate grains, despite what raw materials you use, remain clear. We do not see, at

least a group at Ohio State does not see, this gross defectiveness in the tetratitanate. On the other hand, I should caution you about samples that you used.

R. Roth: But these came from Trans-Tech.

T. Negas: Right. You have to remember that if you really look into what you got, it is the standard Trans-Tech low Q tetratitanate material. It is not pure barium tetratitanate. It's about 90 mole percent barium tetratitanate, 10 mole percent barium nonatitanate. Going through and looking at the high resolution TEM you have to make sure you're looking at the right grains because there is 10 mole percent barium nonatitanate. I know you showed me pretty pictures of polytypism and defects, but until you guys publish that and convince me, I'll stand pat.

R. Roth: I noticed that Peter Davies published the paper on the 1:5 and 2:9 compounds but never wrote up the 1:4.

P. Davies: It was definitely 1:4. There is no doubt about it.

T. Negas: I believe you also have had similar discussions with the group from Ohio State and I guess you guys seem to be in some disagreement. I'm stuck in the middle and I've seen the microstructures that have been taken with the TEM, and the evidence there seemed to be that, at least the limited number of pictures that I've seen, the tetratitanate seems to be fairly defect free. Perhaps the resolution isn't that great. I don't know.

R. Roth: Maybe what we should do is look at your materials.

T. Negas: I've been wanting you guys to do that but I did go to the Ohio State group. Here, I'll give you a sample now. Here's my high Q composite, and there you should see tetratitanate and nonatitanate grains--both types. But let me tell you. Peter and Bob had a beautiful paper on lattice imaging or high resolution work on nonatitanate. I read the paper in 1987 and I was looking at beautiful pictures. I went from figures 1 through 13 and I kept saying, golly, get me to the grain boundary region. Finally in figure 14 in that publication they show this region and then say a few words about it, then drop it. You had it right there, I think. They showed in the grain boundary region strings of titanium, oxygen and a lot of missing barium. More than likely this area is charge compensated by impurities but they dropped the discussion after that. This is precisely what I'm talking about, the reoxidation kinetics being controlled by the grain boundary region. I think your data are in line with, at least, our very simplistic observations.

National Institute of Standards and Technology Special Publication 804, Chemistry of Electronic Ceramic Materials, Proceedings of the International Conference held in Jackson, WY, August 17-22, 1990, issued January 1991.

TUNABLE TRANSDUCERS: NONLINEAR PHENOMENA IN ELECTROCERAMICS

Robert E. Newnham
Materials Research Laboratory
Pennsylvania State University
University Park, PA 16802

ABSTRACT

The concept of a fully tunable transducer is developed as an example of a very smart material whose sensing and actuating functions can be tuned to optimize behavior. By constructing the composite transducer from an elastically nonlinear material (rubber) and an electrically nonlinear material (relaxor ferroelectric), most of its key properties can be adjusted over wide ranges by applying DC bias fields or mechanical prestress. These properties include resonant frequency, acoustic and electric impedance, damping factors, and electromechanical coupling coefficients.

The origins of nonlinear properties are considered briefly using electrostriction as an example. The nonlinearities usually involve phase transformations and size-dependent phenomena on the nanometer scale.

INTRODUCTION

Much of the recent interest in nonlinear phenomena stems from the desire to build "smart materials" for intelligent systems. The words "smart materials" have different meanings for different people, and can be smart in either a passive sense or an active sense. Passively smart materials incorporate self-repair mechanisms or stand-by phenomena which enable the material to withstand sudden changes in the surroundings.

Ceramic varistors and PTC thermistors are passively smart materials. When struck by lightning or otherwise subjected to high voltage, a zinc oxide varistor loses its electrical resistance and the current is bypassed to ground. The resistance change is reversible and acts as a stand-by protection phenomenon. Barium titanate PTC thermistors show a large increase in electrical resistance at the ferroelectric phase transformation near 130°C. The jump in resistance enables the thermistor to arrest current surges, again acting as a protection element. The

R(V) behavior of the varistor and the R(T) behavior of the PTC thermistor are both highly nonlinear effects which act as standby protection phenomena, and make the ceramics smart in a passive mode.

A smart ceramic can also be defined with reference to sensing and actuating functions, in analogy to the human body. A smart ceramic senses a change in the environment, and using a feedback system, makes a useful response. It is both a sensor and an acutator. Examples include vibration damping systems for space structures and energy-saving windows for homes and factories. The new electronically-controlled automobile suspension systems using piezoelectric ceramic sensors and actuators constitutes an actively smart material.

By building in a learning function, the definition can be extended to a higher level of intelligence: A very smart ceramic senses a change in the environment and responds by changing one or more of its property coefficients. Such a material can tune its sensor and actuator functions in time and space to optimize behavior. The distinction between smart and very smart materials is essentially one between linear and nonlinear properties. The physical properties of nonlinear materials can be adjusted by bias fields or forces to control response.

TUNABLE TRANSDUCER

To illustrate the concept of a very smart material, we describe the tunable transducer recently developed in our laboratory. Electromechanical transducers are used as fish finders, gas igniters, ink jets, micropositioners, biomedical scanners, piezoelectric transformers and filters, accelerometers, and motors.

Four important properties of a transducer are the resonant frequency f, the acoustic impedance Z_A, the mechanical damping coefficient Q, the electromechanical coupling factor k, and the electrical impedance Z_E. The resonant frequency and acoustic impedance are controlled by the elastic constants and density, as discussed in the next section. The mechanical Q is governed by the damping coefficient (tan δ) and is important because it controls "ringing" in the transducer. Electromechanical coupling coefficients are controlled by the piezoelectric coefficient which, in turn, can be controlled and fine-tuned using relaxor ferroelectrics with large electrostrictive effects. The dielectric "constant" of relaxor ferroelectrics depends markedly on DC bias fields, allowing the electrical impedance to be tuned over a wide range as well. In the following sections we describe the nature of nonlinearity and how it controls the properties of a tunable transducer.

ELASTIC NONLINEARITY: TUNING THE RESONANT FREQUENCY

Information is transmitted on electromagnetic waves in two ways: amplitude modulation (AM) and frequency modulation (FM). There are a number of advantages to FM signal processing, especially where lower noise levels are important.

Signal-to-noise ratios are also important in the ultrasonic systems used in biomedical and nondestructive testing systems, but FM-modulation is difficult because resonant frequencies are controlled by stiffness (c) and sample dimensions (t):

$$f = \frac{1}{2t}\sqrt{c / \rho}$$

Neither c, t, or the density ρ can be tuned significantly in most materials, but rubber is an exception. To tune the resonant frequency of a piezoelectric transducer, we have designed and built a composite transducer incorporating thin rubber layers exhibiting nonlinear elasticity.

Rubber is a highly nonlinear elastic medium. In the unstressed compliant state, the molecules are coiled and tangled, but under stress the molecules align and the material stiffens noticeably. Experiments carried out on rubber-metal laminates demonstrate the size of the nonlinearity. Young's modulus ($E = 1/s_{1111}$) was measured for a multilayer laminate consisting of alternating steel shim and soft rubber layers each 0.1 mm thick. Under compressive stresses of 200 MN/m^2, the stiffness is quadrupled from about 600 to 2400 MN/m^2. The resonant frequency f is therefore double, and can be modulated by applied stress.

Rubber, like most elastomers, is not piezoelectric. To take advantage of the elastic nonlinearity, it is therefore necessary to construct a composite transducer consisting of a piezoelectric ceramic (PZT) transducer, thin rubber layers, and metal head and tail masses, all held together by a stress bolt.

The resonant frequency and mechanical Q of such a triple sandwich structure was measured as a function of stress bias. Stresses ranged from 20 to 100 MPa in the experiments. Under these conditions the radial resonant frequency changed from 19 to 37 kHz, approximately doubling in frequency as predicted from the elastic nonlinearity. At the same time the mechanical Q increases from about 11 to 34 as the rubber stiffens under stress.

The changes in resonance and Q can be modeled with an equivalent circuit in which the compliance of the thin, rubber layers are represented as capacitors coupling together the larger masses (represented as inductors) of the PZT transducer and the metal head and tail masses. Under low stress bias, the rubber is very compliant and effectively isolates the PZT transducer from the head and tail masses. At very high stress, the rubber stiffens and tightly couples the metal end pieces to the resonating PZT ceramic. For intermediate stresses the rubber acts as an impedance transformer giving parallel resonance of the PZT - rubber - metal -radiation load.

It is interesting to compare the change in frequency of the tunable transducer with the transceiver systems used in the biological world. The biosonar system of the flying bat is similar in frequency and tunability to our

tunable transducer. The bat emits chirps at 30 kHz and listens for the return signal to locate flying insects. To help it differentiate the return signal from the outgoing chirp, and to help in timing the echo, the bat puts an FM signature on the pulse. This causes the resonant frequency to decrease from 30 to 20 kHz near the end of each chirp. Return signals from the insect target are detected in the ears of the bat where neural cavities tuned to this frequency range measure the time delay and flutter needed to locate and identify its prey. Extension of the bat biosonar principle to automotive, industrial, medical and entertainment systems is obvious.

PIEZOELECTRIC NONLINEARITY: TUNING THE ELECTROMECHANICAL COUPLING COEFFICIENT

The difference between a smart and a very smart material can be illustrated with piezoelectric and electrostrictive ceramics. PZT (lead zirconate titanate) is a piezoelectric ceramic in which the ferroelectric domains are aligned in a poling field. Strain is linearly proportional to electric field in a piezoelectric material which means that the piezoelectric coefficient is a constant and cannot be electrically tuned with a bias field. Nevertheless it is a smart material because it can be used both as a sensor and an actuator.

PMN (lead magnesium niobate) is not piezoelectric at room temperature because its Curie temperature lies near O°C. Because of the proximity of the ferroelectric phase transformation, and because of its diffuse nature, PMN ceramics exhibit very large electrostrictive effects. The nature of this large nonlinear relationship between strain and electric field, and of its underlying atomistic origin, will be described later.

Electromechanical strains comparable to PZT can be obtained with electrostrictive ceramics like PMN, and without the troubling hysteretic behavior shown by PZT under high fields. The nonlinear relation between strain and electric field in electrostrictive transducers can be used to tune the piezoelectric coefficient and the dielectric constant.

The piezoelectric d_{33} coefficient is the slope of the strain-electric field curve when strain is measured in the same direction as the applied field. Its value for Pb $(Mg_{0.3}Nb_{0.6}Ti_{0.1})$ O_3 ceramics is zero at zero field and increases to a maximum value of 1300 pC/N (about three times larger than PZT) under a bias field of 3.7 kV/cm.

This means that the electromechanical coupling coefficient can be tuned over a very wide range, changing the transducer from inactive to extremely active. The dielectric constant also depends on DC bias. The polarization saturates under high fields causing decreases of 100% or more in the capacitance. In this way the electrical impedance can be controlled as well.

Electrostrictive transducers have already been used in a number of applications including adaptive optic systems, scanning tunneling microscopes, and precision micropositioners.

To summarize, two types of nonlinearity are utilized in the fully tunable transducer: elastic nonlinearity and piezoelectric nonlinearity. By incorporating thin rubber layers in an electrostrictive transducer several important properties can be optimized with bias fields and bias stresses. Electromechanical coupling coefficients and electric impedance are tuned with electric field, and mechanical damping, resonant frequency, and acoustic impedance with stress bias.

RELAXOR FERROELECTRICS

In the three remaining sections we consider the atomistic origin of nonlinear behavior in ceramics. The magnesium - niobium distribution in PMN ceramics have been studied by transmission electron microscopy. Images formed from superlattice reflections show that the size of the regions with 1:1 ordering is approximately 3 nm (=30Å). The ordered regions are small islands separated by narrow walls of niobium - rich PMN.

A simple energy argument explains the scale of the ordered regions. The chemical formula of PMN can be divided into 1:1 ordered regions with niobium-rich coatings as follows:

$$Pb_3MgNb_2O_9 = (Pb_2MgNbO_6)^- + (PbNbO_3)^+$$

assuming all ions have their usual valence states, the ordered regions will be negatively charged and the coatings positive. The ordering must therefore be on a very fine scale in order to minimize coulomb energy.

A cubes model is adopted to estimate the size of ordered islands. Let each island be a cube n unit cells on edge. Then there will be $n^3/2$ Mg atoms and $n^3/2$ Nb atoms within the island. This means that $n^3/2$ Nb atoms are excluded from the island because the Mg:Nb ration is 1:1 in the ordered island and 1:2 in the chemical formula. We assume the excluded niobiums form a thin monolayer coating on the cubes then $n^3/2 = 3n^2$, where $3n^2$ is the number of surface atoms per cube, neglecting edges and corners. By keeping the coating as thin as possible, charge is neutralized on a local scale, and electrostatic energy is minimized.

Solving the equation gives n=6, or 24Å, surprisingly close to the 30Å observed by TEM. It is also interesting to compare this result with the behavior observed of small ferroelectric particles. X-ray studies of very fine-grained $PbTiO_3$ show that the polar tetragonal phase becomes unstable below about 200Å, the so-called ferroelectric - superparaelectric transformation. Relaxor ferroelectrics like PMN exhibit many of the characteristics of superparaelectric solids where the dipole moments are strongly coupled to one another, but not to a

crystallographic axis. The coupled electric dipoles oscillate in orientation and respond readily to applied fields giving rise to large dielectric constants and massive electrostriction coefficients.

SEVEN MISCONCEPTIONS ABOUT ELECTROSTRICTION

Perhaps the best way to describe the basic features of nonlinear physical properties is to first dispel some of the common misconceptions. Some of the key ideas are described in this section using electrostriction as an example.

Misconception #1: Electrostrictive strain is proportional to the square of the electric field.

When an electric field E is applied to an insulator it develops a polarization P and a strain ε. In tensor notation the strain can be written as a power series in E or in P.

$$(1)\quad \varepsilon_{ij} = d_{ijk}E_k + M_{ijkl}\,E_kE_l + \ldots .$$

$$(2)\quad \varepsilon_{ij} = d_{ijk}P_k + Q_{ijkl}\,P_kP_l + \ldots .$$

The first term in both equations represents piezoelectricity, the second electrostriction. Piezoelectricity is a third rank tensor property found only in noncentrosymmetric materials. It is absent in most ceramic materials, but electrostriction is not. The electrostriction coefficients M_{ijkl} or Q_{ijkl} constitute a fourth rank tensor which, like the elastic constants, are found in all materials, regardless of symmetry. In the discussion which follows, we deal with centrosymmetric media for which the piezoelectric coefficients are zero.

Returning to equations (1) and (2), which of these equations is the correct way to describe electrostriction, or can both be used? For normal low permittivity materials, the polarization P is proportional to the applied electric field E, and therefore both expressions are correct, but for high permittivity solids only one is correct. Under high fields, the polarization saturates in high permittivity materials, especially in ferroelectric ceramics just above T_c, the Curie temperature. In capacitor dielectrics, it is not unusual to observe a decrease in dielectric constant of 100% under high electric fields. In this situation P is not proportional to E, and therefore electrostrictive strain cannot be proportional to both E^2 and P^2.

When strain is plotted as a function of electric field for PMN-PT, a typical electrostrictive transducer ceramic, it is not proportional to E^2 except for small fields where the shape is parabolic. When plotted as function P^2, a straight line is obtained for the $\varepsilon(P^2)$ relationship. Therefore the correct way to formulate electrostriction is

(3) $$\boxed{\varepsilon_{ij} = Q_{ijkl}P_kP_l} \quad (i,j,k,l = 1,2,3)$$

The M_{ijkl} coefficients in eq. (1) are not good constants except in linear dielectrics.

It is instructive to convert the fourth rank tensor coefficients to the more manageable matrix form

(4) $\varepsilon_i = Q_{ij}P_j^2 \quad (i,j = 1\text{-}6)$

When written out in full for cubic point group m3m, this becomes

$$(5) \quad \begin{matrix} \varepsilon_1 \\ \varepsilon_2 \\ \varepsilon_3 \\ \varepsilon_4 \\ \varepsilon_5 \\ \varepsilon_6 \end{matrix} = \begin{matrix} Q_{11} & Q_{12} & Q_{12} & 0 & 0 & 0 \\ Q_{12} & Q_{11} & Q_{12} & 0 & 0 & 0 \\ Q_{12} & Q_{12} & Q_{11} & 0 & 0 & 0 \\ 0 & 0 & 0 & Q_{44} & 0 & 0 \\ 0 & 0 & 0 & 0 & Q_{44} & 0 \\ 0 & 0 & 0 & 0 & 0 & Q_{44} \end{matrix} \begin{matrix} P_1^2 \\ P_2^2 \\ P_3^2 \\ P_2P_3 \\ P_3P_1 \\ P_1P_2 \end{matrix}$$

In this expression ε_1, ε_2 and ε_3 represent tensile strains along the [100], [010], and [001] axes, respectively. ε_4, ε_5 and ε_6 are shear strains about the same three axes.

To understand the structure-property relationship underlying electrostriction, it is helpful to visualize the atomistic meaning of coefficients Q_{11}, Q_{12}, and Q_{44}. The high temperature structure of $PbTiO_3$ is pictured in Fig. 1 a. Lead ions are located at the corners of the cubic unit cell, titanium ions at the body-centered position, and oxygens at the face-center positions.

When an electric field is applied along [100], polarization component P_1 develops along the same axis. This in turn causes the unit cell to elongate by an amount Δa, and the resulting tensile strain is $\varepsilon_1 = \Delta a/a$. Electrostrictive coefficient Q_{11} is equal to ε_1/P_1^2. The drawing in Fig. 1b makes it clear why electrostrictive strain is proportional to electric polarization rather than electric field. Polarization and strain are both controlled by atomic displacement.

The atomistic meaning of Q_{12} and Q_{44} are pictured in figs. 1 c and 1 d, respectively.

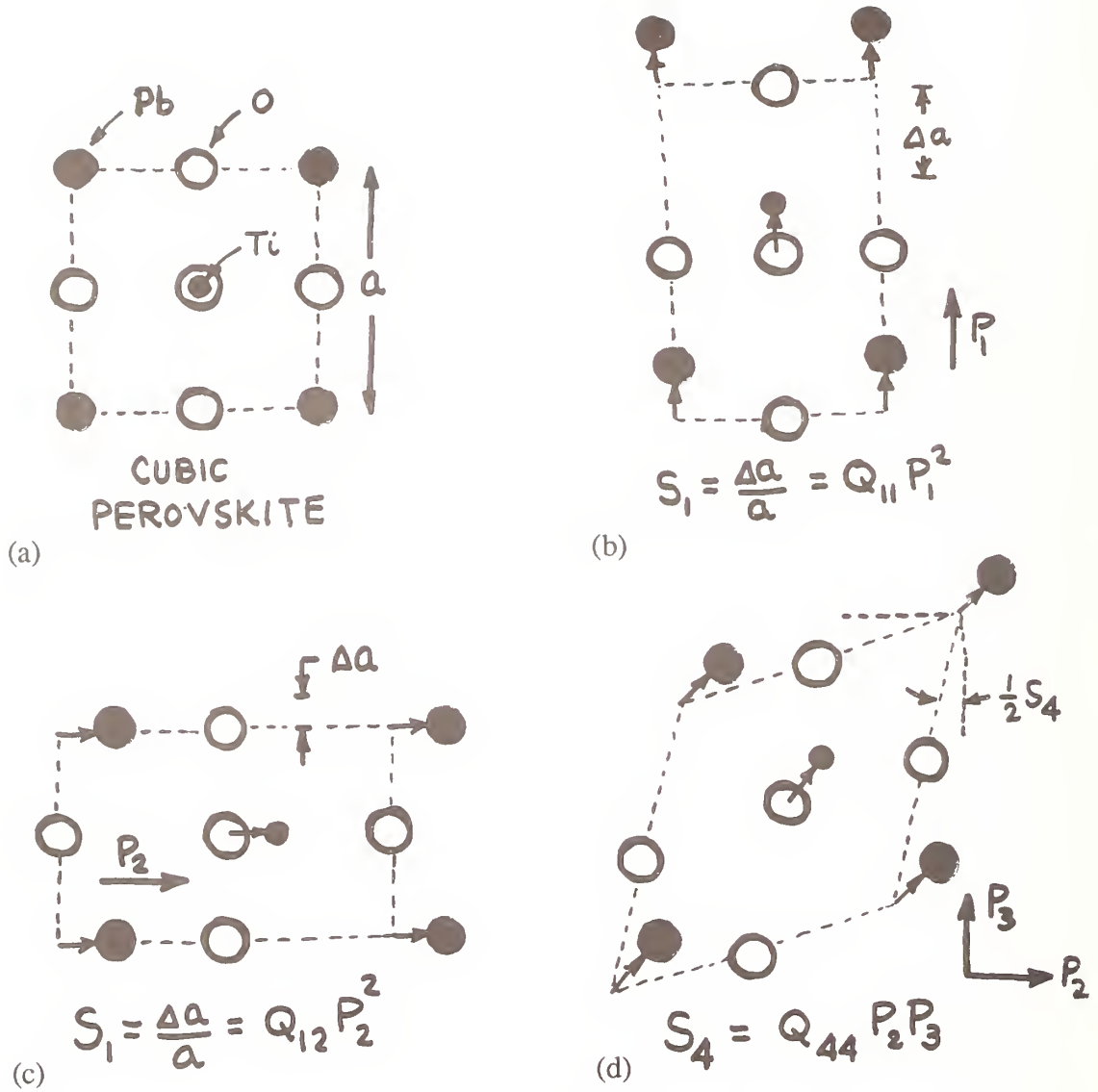

Fig. 1 Electrostriction in cubic pervoskite showing the physical origin of coefficients Q_{11}, Q_{12}, and Q_{44}.

Misconception #2. Large voltages are required to observe electrostriction.

This misconception arises from the fact that historically, the first electroceramics were high voltage insulators made from low permittivity oxides such as porcelain, glass, steatite, and alumina. To prevent breakdown, the insulators were fabricated in large sizes, typically with 1-10 cm separation between electrodes. Under these conditions the voltages required to induce measurable electrostriction are huge, but the picture has changed in the last decade.

Two factors have made the difference: sma'ler electrode separation and higher permittivity. The introduction of thin and thick film technology, together with tape-casting, has reduced the thickness of the dielectric constants to less than 50 μm with corresponding increases in the electric field levels. Fields of megavolts/meter are common under these circumstances. At the same time, new ferroelectric ceramics with dielectric constants in excess of 10,000 have raised the polarization levels to new heights, further contributing to electrostriction strain. As a result, strains of 10^{-3} to 10^{-2} are observed with relatively modest voltages.

Misconception #3 Electrostriction coefficients are about the same size for all materials.

Misconception #4 Electrostriction coefficients are largest in ferroelectric solids with high dielectric constants.

Q_{11} coefficients measured for normal oxides are several orders of magnitude or more larger than those of ferroelectrics.

	Q_{11} (m^4/C^2)
Silica	+12.8
Barium Titanate	+0.11
Lead Magnesium Niobate	+0.009

Misconception #5 Materials with large electrostrictive coefficients produce the biggest strains.

The Q coefficients are largest for non-ferroelectrics but relaxor ferroelectrics like PMN have the largest strains. The following table lists typical values of the electrostriction coefficients Q, the dielectric constant K, and electrostrictive strain ε computed for a field of 1 MV/m.

	Q	K	ε
non-ferroelectric	~10	~10	$\sim 10^{-7}$
normal ferroelectric	$\sim 10^{-1}$	$\sim 10^{3}$	$\sim 10^{-5}$
relaxor ferroelectric	$\sim 10^{-2}$	$\sim 10^{4}$	$\sim 10^{-4}$

Note that the product QK~100 m^4/C^2 is approximately a constant for all three classes. To see why this is so, consider the following argument based on the atomistic models in Fig 1.

Under the action of an applied electric field, the cations and anions in a crystal structure are displaced in opposite directions by an amount Δr. It is this displacement which is responsible for electric polarization (P), the dielectric constant K, and the electrostrictive strain ε. To a first approximation, all three are proportional to Δr. The electrostriction coefficient Q is therefore proportional to 1/K:

$$Q = \frac{E}{P^2} \sim \frac{(\Delta r)}{(\Delta r)^2} = \frac{1}{\Delta r} \sim \frac{1}{K}$$

This means then, that QK is approximately constant, as indicated earlier. Materials with high permittivity have small electrostriction coefficients but large electrostrictive strain.

Misconception #6. Unlike piezoelectricity there is no converse electrostriction effect.

In the direct piezoelectric effect an applied mechanical stress σ_{kl} produces an electric polarization $P_i = d_{ijk}\ \sigma_{kl}$. The converse effect relates mechanical strain to applied electric field, $\varepsilon_{ij} = d_{ijk}\ E_k$. The piezoelectric coefficients d_{ijk} are identical in the direct and converse effect because both originate from the same term in the fill energy function:

$$F = \ldots . + d_{ijk}\ P_i\ \sigma_{jk} + \ldots .$$

Electrostriction and its converse effects arise from the free energy term

$$F = \ldots . + Q_{ijkl}\ P_i\ P_j\ \sigma_{kl} + \ldots .$$

Taking the partial derivatives in different order leads to three equivalent effects. The first is the normal electrostriction effect, the variation of strain with polarization:

$$\frac{\partial}{\partial P_i}\left(\frac{\partial}{\partial P_j}\left(\frac{\partial F}{\partial \sigma_{kl}}\right)\right) = \frac{\partial^2 \in_{kl}}{\partial P_i\, \partial P_j} = Q_{ijkl}$$

The second is the stress dependence of the dielectric stiffness β_{ij}, better known as the reciprocal electric susceptibility:

$$\frac{\partial}{\partial \sigma_{kl}}\left(\frac{\partial}{\partial P_i}\left(\frac{\partial F}{\partial P_j}\right)\right) = \frac{\partial \beta_{ij}}{\partial \sigma_{kl}} = Q_{ijkl}$$

The third effect is the polarization dependence of the piezoelectric voltage coefficient g_{jkl}:

$$\frac{\partial}{\partial P_i}\left(\frac{\partial}{\partial \sigma_{kl}}\left(\frac{\partial F}{\partial P_j}\right)\right) = \frac{\partial g_{jkl}}{\partial P_i} = Q_{ijkl}$$

Thus there are <u>two</u> converse effects for electrostriction, and there are three ways of evaluating the electrostrictive coefficients.

The three effects are used in three different applications: (1) the electrostrictive micropositioner, (2) a capacitive stress gauge, and (3) a field-tunable piezoelectric transducer.

Misconception #7 Thermal expansion effects make electrostrictive micropositoners and stress gauges impractical.

This is true for normal oxide insulators but not for relaxor ferroelectrics. For a normal oxide such as silica, the electrostrictive coefficient $Q \sim 10 m^2/C^2$, the dielectric constant $K \sim 10$, and the thermal expansion coefficient $\alpha \sim 10^{-5} K^{-1}$. For such a material the strain produced by an electric field of 1 MV/m is about 10^{-7}, which is equivalent to a temperature change of only 10^{-2} degrees. This would pose severe problems in an actuator or micropositioner, but the situation is quite different for a ferroelectric.

For PMN, $Q \sim 10^{-2}$, $K \sim 10^4$ and $\alpha \sim 10^{-6} K^{-1}$. Therefore the electrostrictive strain for a field of 1 MN/m is about 10^{-3} which is equivalent to a temperature rise of 1000°! Relaxor ferroelectrics sometimes have an abnormally low thermal expansion coefficient near the diffuse phase transformation where the dielectric constant and the electrostrictive strain are unusually large. Micropositioners made from ferroelectric ceramics are not troubled by small variations in temperature.

ORIGINS OF NONLINEARITY

What do nonlinear materials have in common? The passively-smart PTC thermistor and ZnO varistor have grain boundaries a few nm thick, insulating barriers that can be obliterated by the polarization charge accompanying a ferroelectric phase transformation, or, in the case of the varistor, insulating boundaries so thin they can be penetrated by quantum mechanical tunneling.

Small size is also key factor in the nonlinear behavior of semiconductors. The thin gate region in a transistor allows charge carriers to diffuse through unimpeded. The p-region in an n-p-n transistor is thin compared to the diffusion length in single crystal silicon. Similar size-related phenomena are observed in quantum well structures made from GaAs and $Ga_{1-x}Al_xAs$. Planar structures with nm-thick layers show channeling behavior of hot electrons in clear violation of Ohm's law. Current - voltage relationships are highly nonlinear in many submicron semiconductor structures. Ohm's law is a statistical law which relies upon the assumption that the charge carriers make a sufficiently large number of collisions to enable them to reach a terminal velocity characteristic of the material. When the size of the conduction is sufficiently small, compared to the mean free path between collisions, the statistical assumption breaks down, and Ohm's law is violated.

Nonlinear behavior is also observed in thin film insulators where even a modest voltage of 1-10 volts can result in huge electric fields of 100 MV/m or more. This means that thin film dielectrics experience a far larger field than do normal insulators, and causing the polarization to saturate and electric permitivity to decline. Because of the high fields, electric breakdown becomes a greater hazard, but this is partly counteracted by an increase in breakdown strength with decreasing thickness. This comes about because the electrode equipotential surfaces on a thin film dielectric are extremely close together, thereby eliminating the asperities that lead to field concentration and breakdown.

The influence of nanometer-scale domains on the properties of relaxor ferroelectrics has already been made plain. Here the critical size parameter is the size of the polarization fluctuations arising from thermal motions near the brood ferroelectric phase transformation in PMN and similar oxides. The ordering of Mg and Nb ions in the octahedral site of the PMN structure results in a chemical inhomogeneous structure on a nm-scale, and this, in turn, influences the size of the polarization fluctuations. Tightly coupled dipoles within each Nb-rich portion of this self-assembling nanocomposite behave like a superparaelectric solid. The dipoles are strongly coupled to one another but not to the crystal lattice, and thus they reorient together under the influence of temperature or electric field. this in turn causes the large electric permittivities and large electrostrictive effects found in relaxor ferroelectrics.

The importance of nanometer-scale fluctuations and the instabilities associated with phase transformations is also apparent in the nonlinear elasticity of rubber and other polymeric materials. The thermally-assisted movement of the randomly oriented polymer chains under tensional stress results in large compliance coefficients, but rubber gradually stiffens as the chains align with the stress into pseudo-crystalline regions. The increase in stiffness with stress gives rise to sizeable third order elastic constants in many amorphous polymers. The effect depends markedly on temperature. On cooling, to lower temperatures rubber and other amorphous polymers transform from a compliant rubber-like material to a brittle glass-like phase which is of little use in nonlinear devices.

Nonlinear behavior is also observed in magnetic and optical systems. Superparamagnetic behavior, analogous to the superparaelectric behavior of relaxor ferroelectrics, is found in spin glasses, fine powder magnets, and magnetic cluster materials. As in PMN, the magnetic dipoles are strongly coupled to one another in nanometer-size complexes, but are not strongly coupled to the lattice. Superparamagnetic solids display nonlinear magnetic susceptibilities and unusual "ΔE" effects in which Young's modulus E can be controlled by magnetic field. The effect is especially large in metallic glasses made from Fe-Si-B-C alloys. The cluster size in spin glasses is in the nanometer range like those in PMN.

Lead lanthanum zirconate titanate (PLZT) perovskites can be prepared as transparent ceramics for electrooptic modulators. Quadratic nonlinear optic behavior are observed in pseudocubic regions of the phase diagram which show relaxor-like properties.

In summary, the nonlinear properties of electroceramics are often associated with nanometer-scale structure and diffuse phase transformations. Under these circumstances the structure is poised on the verge of an instability and responds readily to external influences such as electric or magnetic fields, or mechanical stress.

The ready response of nonlinear ceramics allows the properties to be tuned in space or time to optimize the behavior of the sensor-actuator systems referred to by some as "very smart ceramics."

ACKNOWLEDGEMENTS

Numerous discussions with Q.C. Xu, M. Blaskewiecz, L.E. Cross, K. Uchino, S.J. Jang and S. Yoshikawa are gratefully acknowledged. Carol Foster typed the manuscript with great skill.

P. Davies: Concerning the relaxor ferroelectric with cation ordering in the nanodomains, the charge imbalance between the ordered and disordered regions bothers me a little bit. Are we sure there are no oxygen deficiencies in these domains? Why are the ordered domains stable?

R. Newnham: Well, that's a good question. If you examine various ordered configurations, say by model-building, you find the one-to-one pattern goes together very nicely because there are six unit cells around each perovskite unit cell, making it easy to pair things off. If you try, two-to-one ordering corresponding to the overall composition, you find it is necessary to position niobium ions in neighboring octahedral sites. This violates Paulings electrostatic valence rule and leads to charge imbalance on the atomic scale.

What I'm pointing out is that if you look at other possible ordering schemes there are problems with them, too, so it comes down to which is least unfavorable.

P. Davies: Are we sure there are no oxygen deficiencies in the domains?

R. Newnham: Well, I'll let Prof. Smyth comment on that, but I can tell you that these relaxors are excellent insulators which will withstand very high voltages, and I think if there were a lot of oxygen vacancies which were present we would be seeing conduction and degradation phenomena which are not observed.

D. Smyth: Well, that's a question of continuity. You might have some motion within the domain, but whether it would transport throughout the entire system, I don't know. I don't think we have any direct evidence on that because it is difficult to probe these very small areas.

D. Kolar: What is the effect of grain size?

R. Newnham: The samples we have prepared have normal grain sizes on the micron scale. There have been studies of small grain sizes in ferroelectric ceramics and studies of nanocomposite materials showing transitions from the multidomain regime, to single domain, and to the superparaelectric regime. You have to ask in what temperature range and in which size regime are you operating. In the high temperature regime, the electrostrictive material behaves like a normal paraelectric, then on cooling, there is a broad diffuse phase region with relaxor phenomena, and then at low temperatures it is a normal ferroelectric with normal domain structure. Then PMN behaves pretty much like other ferroelectrics, but it is this broad diffuse range which comes about because of nanometer scale structure, and which we think is analogous to similar phenomena observed when ferroelectrics are prepared in very small particle sizes. This is what is often called superparaelectricity with very large dielectric constants and very large electrostrictive effects.

National Institute of Standards and Technology Special Publication 804, Chemistry of Electronic Ceramic Materials, Proceedings of the International Conference held in Jackson, WY, August 17-22, 1990, issued January 1991.

STRUCTURAL AND ELECTRONIC PROPERTIES OF SOME PEROVSKITES

P.D. BATTLE
INORGANIC CHEMISTRY LABORATORY
SOUTH PARKS ROAD
OXFORD OX1 3QR
ENGLAND

INTRODUCTION

The perovskite structure is one of the best known structures in oxide chemistry. It is adopted by compounds having the general formula ABO_3 where A is usually (but not always) an alkaline earth or one of the larger lanthanides and B is usually a transition metal or one of the smaller lanthanides. It is possible to have more than one element occupying the A or B sites in a compound; for example, in $BaLaNiRuO_6$ the A sites and B sites are respectively occupied by random distributions of Ba/La and Ni/Ru. These compounds can be represented by the general formula $AA'BB'O_6$. In this paper we shall focus on the coordination geometry around the B site cations. In an ideal cubic perovskite (Figure 1) these cations occupy an octahedral site, 6-coordinated by oxygen. (The larger A-site cations are 12 coordinated by oxygen.) I shall regard the BO_6 octahedron as the basic building block of these structures. The cubic perovskite structure can then be built up by the corner-sharing of these units. There are other compounds, having hexagonal symmetry, which also have the basic formula ABO_3. The B site cation is again 6-coordinated and these compounds are usually referred to as hexagonal perovskites. However, in these compounds the octahedra are linked together by both corner-sharing and face-sharing. Figure 2 shows the structure of $SrMnO_3$ which contains both types of octahedral linkage. The B-O bond length in these compounds is of the order of 2Å; the B-B distance is thus ~4Å when the octahedra are linked by corner-sharing and ~2.5Å when they are linked by face-sharing. The extent of face sharing increases as the ratio of the ionic radii r_A/r_B increases.

The electronic properties of perovskites are very variable. For example, $SrFeO_3$ is a metallic antiferromagnet, $SrCoO_3$ is a metallic ferromagnet, $LaFeO_3$ is an insulating antiferromagnet and $LaNiO_3$ is a metallic Pauli paramagnet. The transition metals in perovskites can all take more than one oxidation state. This leads to the possibility of non-stoichiometry on the oxygen sublattice, i.e. the formation of ABO_{3-y}. The oxygen content of the Sr-Co-O system, for example, can vary from $SrCoO_3$ (Co^{4+}) to $SrCoO_{2.5}$ (Co^{3+}). The variation in the number of d electrons on the transition metal cation can have a profound effect on the electronic properties of the system, as demonstrated by the change from metallic

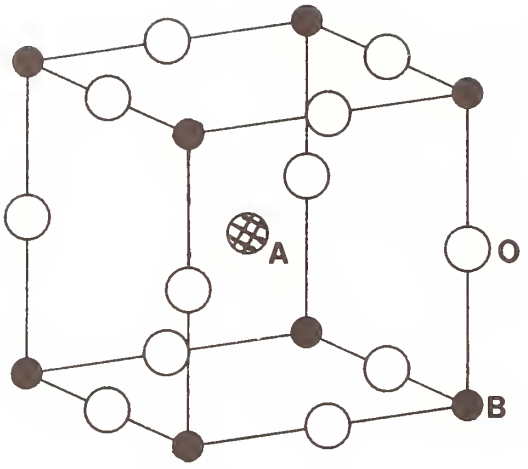

Figure 1: The perovskite structure

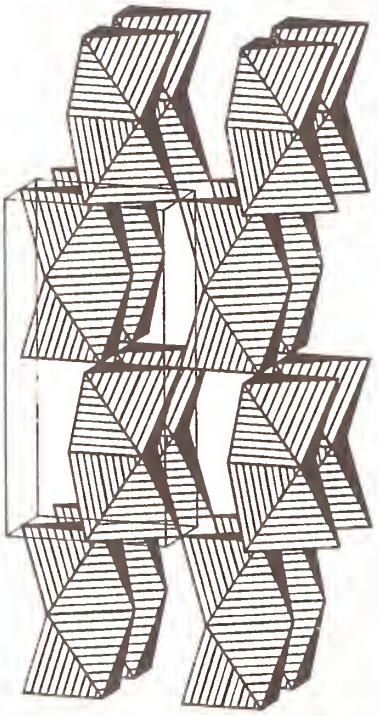

Figure 2: The crystal structure of $SrMnO_3$

ferromagnetism in $SrCoO_3$ to insulating antiferromagnetism in $SrCoO_{2.5}$. The variation is governed by the oxygen content, which is itself governed by the method of preparation. In other words, the electronic properties of perovskites are controlled by chemistry.

$SrCoO_{3-y}$

The points made above are well illustrated by a more detailed discussion of the phases in the system $SrCoO_{3-y}$. These are all prepared from the reaction

$$3SrCO_3 + Co_3O_4 + nO_2 \rightarrow 3SrCoO_{3-y} + 3CO_2$$

but under a variety of conditions as described below:

(i) heat at 1200°C in air and quench to room temperature gives $SrCoO_{2.5}$ (y=0.5) i.e. Co^{3+} only

(ii) heat at 1200°C and slow cool in air gives $SrCoO_{2.63}$ i.e. Co^{3+} and Co^{4+}

(iii) heat as in (i), but then heat at 800°C under argon gives $SrCoO_{2.5}$ still

The crystal structure of the product from (i) is that of a brownmillerite - essentially an oxygen deficient perovskite with the anion vacancies ordered in such a way as to give alternate layers of 6- and 4-coordinate cations. The crystal structure of the product from (ii) and (iii) is a 'rhombohedral' phase which will be discussed in more detail later in this paper. The magnetic properties of the three products are as described below:

brownmillerite $SrCoO_{2.5}$ - antiferromagnetic at room temperature

'rhombohedral' $SrCoO_{2.5}$ - antiferromagnetic below 25K

'rhombohedral' $SrCoO_{2.63}$ - paramagnetic at 4.2K

The dependence of the magnetic properties on the crystal structure and the oxygen content, both determined by the conditions of synthesis, is thus clear.

I write inverted commas around "rhombohedral" because although many groups have made this phase of $SrCoO_{2.5}$, nobody has ever got a satisfactory unit cell for it, never mind a crystal structure. The X-ray powder diffraction pattern strongly suggests rhombohedral symmetry, but the fit between observed and calculated line positions is less than satisfactory. EXAFS measurements have been able to shed some light on this structural problem. Figure 3 shows the orthorhombic brownmillerite structure of high temperature $SrCoO_{2.5}$. Although anion vacancies are present, the structure is still very similar to that of a perovskite with a B-O distance of ~1.9-2.0Å, B-A at ~3.4Å and B-B distance of ~4Å. The observed and calculated Co K-edge EXAFS of this phase are shown in

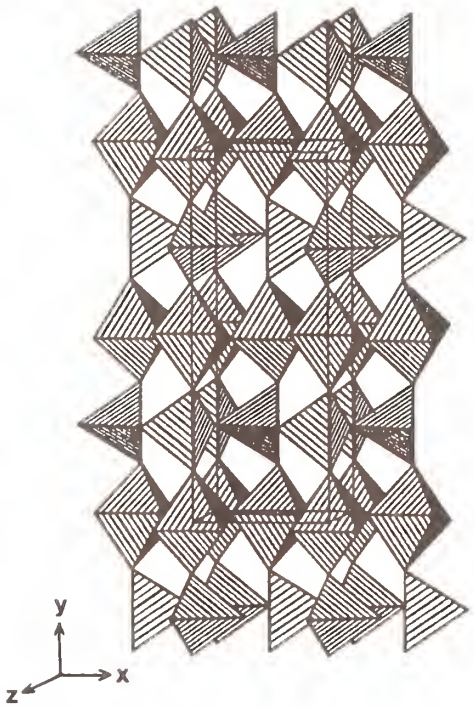

Figure 3: The brownmillerite structure

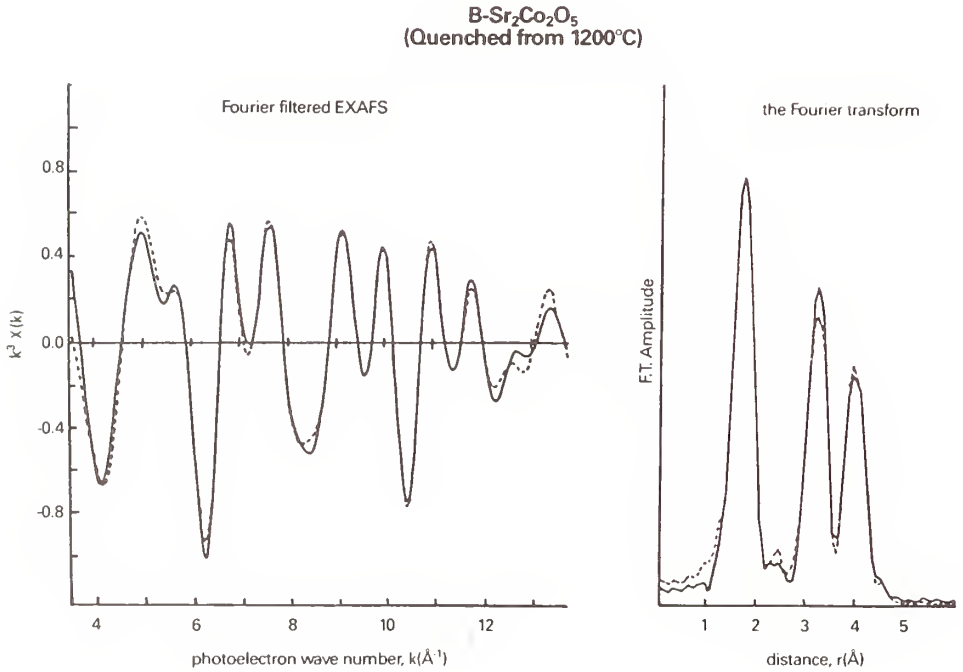

Figure 4: The Co-K EXAFS spectra of brownmillerite $SrCoO_{2.5}$

Figure 4, along with their Fourier transforms, and it is clear that the coordination geometry described above is consistent with the observed data. The EXAFS data on 'rhombohedral' $SrCoO_{2.5}$ are shown in Figure 5. The most striking difference between the environments of the Co atoms in the two phases is the presence of a coordination shell at a radius of 2.46Å in the rhombohedral phase. Figure 6 shows the observed and calculated Fourier-filtered EXAFS from this shell, modelled with the assumption that the back-scattering atom is Co. These data thus show a Co-Co distance of 2.46Å in the low temperature phase of $SrCoO_{2.5}$, suggesting that, in contrast to the high temperature brownmillerite form, face sharing octahedra are present in this phase. The EXAFS of the partially oxidised composition $SrCoO_{2.56}$ show an additional coordination shell at ~2.8Å, consistent with the presence of edge-sharing octahedra, although this is not well-established (1). The structural complexities of $SrCoO_{3-y}$ are still not fully resolved, but it is clear that EXAFS can make an important contribution in some cases when diffraction methods fail.

$Sr_2LaFe_3O_{8+y}$

$Sr_2LaFe_3O_{8+y}$ is another perovskite-like system showing a wide range of electronic behaviour. The end member (y=0) $Sr_2LaFe_3O_8$ is an Fe^{3+} compound which is antiferromagnetic at room temperature. It can be prepared by firing stoichiometric quantities of $SrCO_3$, La_2O_3 and Fe_2O_3 under vacuum at 1200°C (2). The crystal structure (Figure 7) is intermediate between those of brownmillerite and perovskite, consisting of double octahedral layers separated by single tetrahedral layers. When the reaction mixture is heated in air and slow cooled to room temperature the product has the composition $Sr_2LaFe_3O_{8.94}$ (3). The average oxidation state of the Fe atoms in this compound is 3.63. The Mössbauer spectrum (Figure 8) suggests that above 230K all the iron atoms are electronically equivalent. This is consistent with the crystal structure refined from neutron powder diffraction data collected at room temperature (4), which contains only one crystallographic site for Fe in a perovskite which has undergone a small rhombohedral distortion. The observed and calculated diffraction patterns are shown in Figure 9. The Mössbauer spectra collected below 230K suggest that the material orders magnetically at 220K and that the Fe simultaneously disproportionates into two oxidation states, ideally described as Fe^{3+} and Fe^{5+}.

i.e. $$3Fe^{3.66+} \rightleftharpoons 2Fe^{3+} + Fe^{5+}$$

The areas of the two sextets in the low temperature spectrum are consistent with this interpretation. We expected this disproportionation to produce a structural distortion and we therefore repeated our neutron diffraction experiments at 50K. The observed and calculated diffraction patterns are shown in Figure 10. Additional Bragg scattering is apparent, particularly at low angle, because of the presence of long-range antiferromagnetic order at 50K. The crystal structure could still be defined in the same rhombohedral space group with only one Fe site, suggesting that, perhaps surprisingly, there was no ordering of the Fe^{3+} and Fe^{5+} cations. However, consideration of the magnetic Bragg scattering shows this to be a false conclusion. Perovskites are known to order magnetically in a number of different ways, each of which gives rise to a characteristic neutron

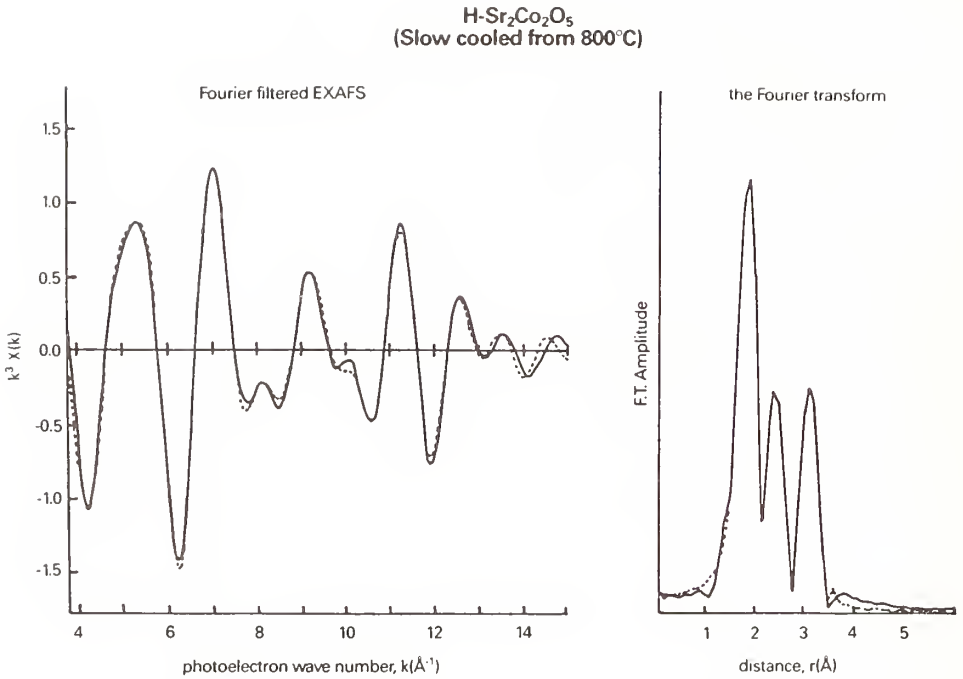

Figure 5: The Co-K EXAFS spectra of 'rhombohedral' $SrCoO_{2.5}$

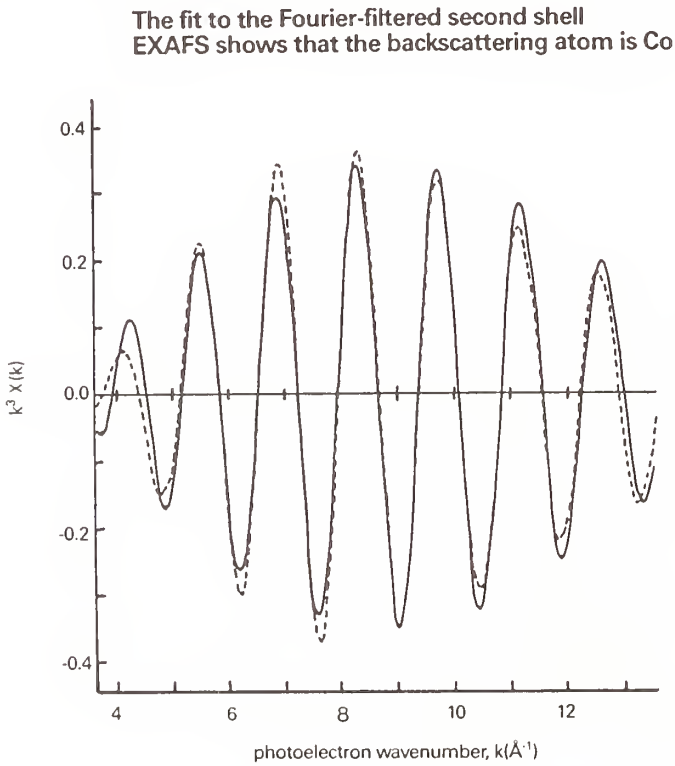

Figure 6: The Fourier-filtered EXAFS of the second coordination shell in 'rhombohedral' $SrCoO_{2.5}$

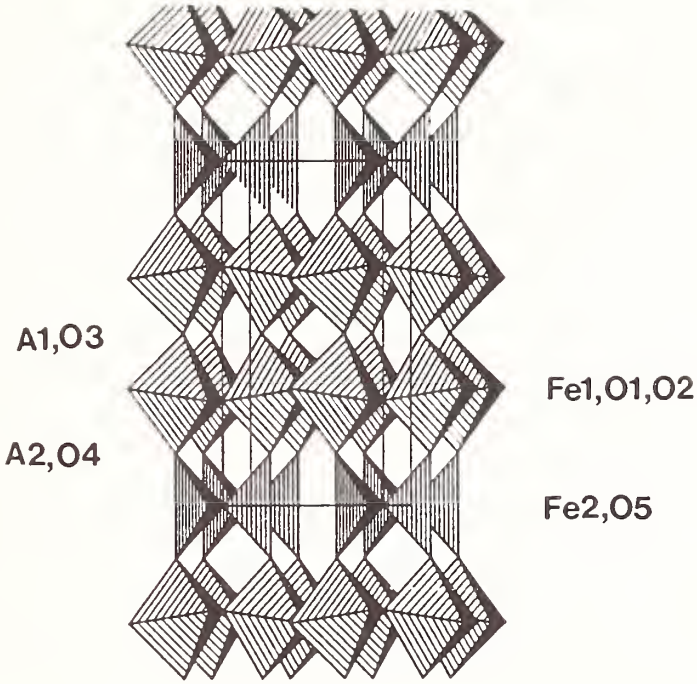

Figure 7: The crystal structure of $Sr_2LaFe_3O_8$

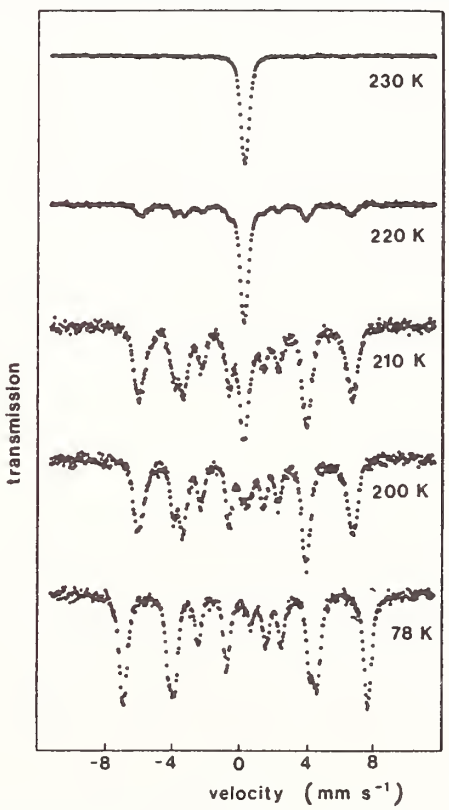

Figure 8: Mössbauer spectra of $Sr_2LaFe_3O_{8.94}$ as a function of temperature

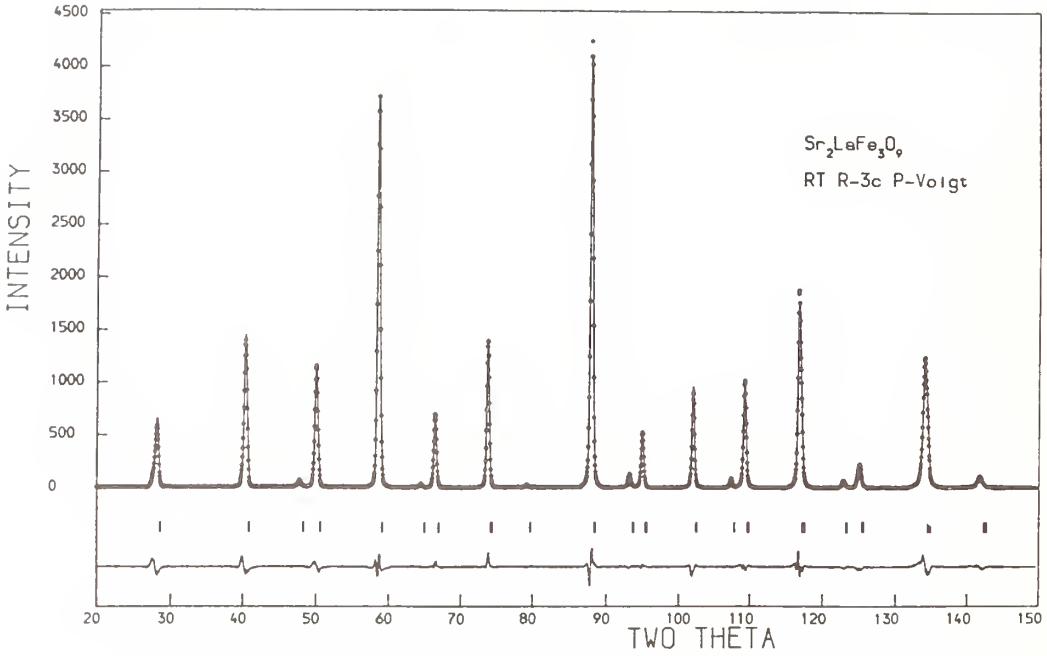

Figure 9: Neutron diffraction pattern of $Sr_2LaFe_3O_{8.94}$ at room temperature

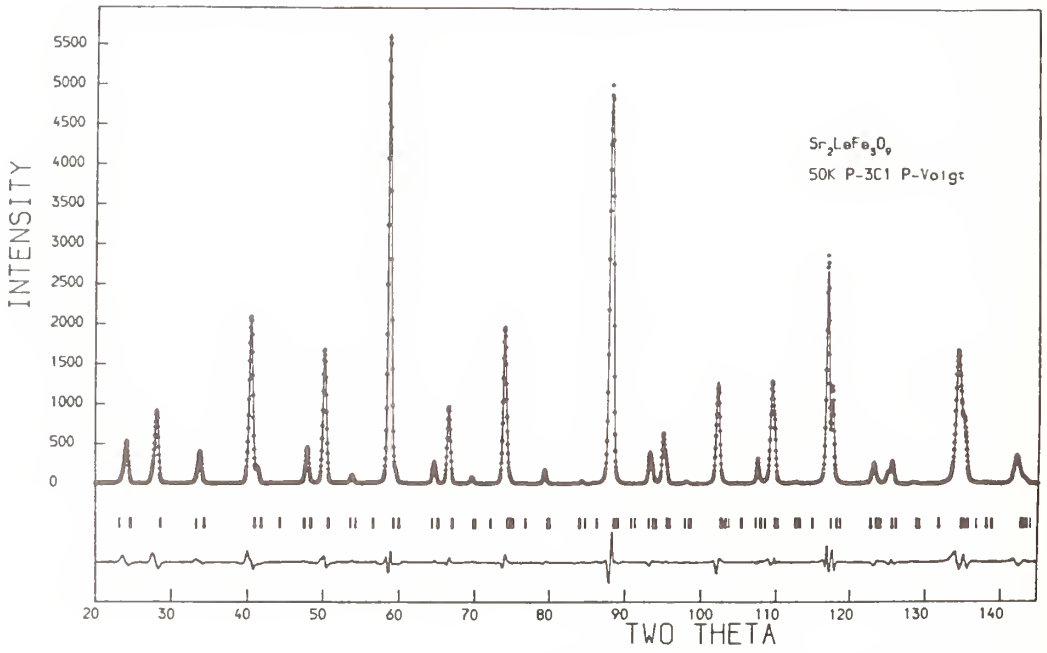

Figure 10: Neutron diffraction pattern of $Sr_2LaFe_3O_{8.94}$ at 50K

diffraction pattern. The distribution of magnetic scattering in the diffraction pattern of $Sr_2LaFe_3O_{8.94}$ differed from these standard forms, and was eventually accounted for using the magnetic structure shown in Figure 11. The diagram shows a network of corner sharing FeO_6 octahedra with the [111] axis of the rhombohedral unit cell running from top to bottom. The magnetic ordering involves the formation of ferromagnetic sheets perpendicular to this axis. The magnetic moment per cation is not the same in all sheets, and those with the larger moment (3.61 μ_B) are assumed to contain Fe^{3+} cations whilst those with the smaller moment (2.72 μ_B), which are only half as numerous, are assumed to contain Fe^{5+}. The relative orientations of the magnetic moments in neighbouring sheets is such as to ensure antiferromagnetic coupling between pairs of Fe^{3+} ions, but ferromagnetic coupling between Fe^{3+} ions and Fe^{5+} ions. This is consistent with the different electronic configurations of the two ions (Fe^{3+}:$3d^5$, Fe^{5+}:$3d^3$). The surprising conclusion to emerge from these results is that the magnetic diffraction data indicate that the Fe^{3+} and Fe^{5+} ions are ordered (into sheets perpendicular to [111]) despite the fact that there is no crystallographic distortion. It is likely that the description of this compound in terms of integral oxidation states is an oversimplification, and we are really dealing with $Fe^{(4-\lambda)+}$ and $Fe^{(4+\lambda)+}$. The electronic structure of the transition metal sublattice can then be described in terms of spin- and charge-density waves, but it is still surprising not to find an accompanying periodic structural distortion. It is possible that such a distortion is quenched by the presence of disorder among the Sr and La atoms on the A site of the perovskite structure.

The behaviour of $BaLaFe_2O_{5.91}$ in some ways resembles that of $Sr_2LaFe_3O_{8.94}$, but in other ways it differs (5). Mössbauer spectroscopy indicates that a high temperature, average valence state does undergo a charge disproportionation into oxidation states that can be approximated by Fe^{3+} and Fe^{5+} in a 3:1 ratio, and the crystal structure is always that of a primitive cubic perovskite, indicating an absence of ordering among the transition metal cations. However, the low temperature magnetic structure is that of a G-type antiferromagnet, perhaps the most common type of magnetic ordering found in simple perovskites and consistent with the presence of a disordered arrangement of Fe^{3+} and Fe^{5+} in this compound, unlike the behaviour of $Sr_2LaFe_3O_{8.91}$ where an ordering of the spin density was found.

$SrMn_{1-x}Co_xO_{3-y}$

The existence of both hexagonal and cubic perovskites leads to a number of interesting questions, for example if $SrCoO_3$ is a cubic, metallic ferromagnet and $SrMnO_3$ is a hexagonal antiferromagnetic insulator, what are the properties of the solid solution $SrMn_{1-x}Co_xO_{3-y}$? Our attempts to prepare this compound in air (6) led to the discovery of an unusual incommensurate hexagonal phase for $0.4<x<0.55$. The lines in the X-ray powder diffraction pattern could be indexed using the relationship

$$\frac{1}{d^2} = \frac{4}{3a^2}(h^2+k^2+hk) + \frac{(l+j\delta)^2}{c^2}$$

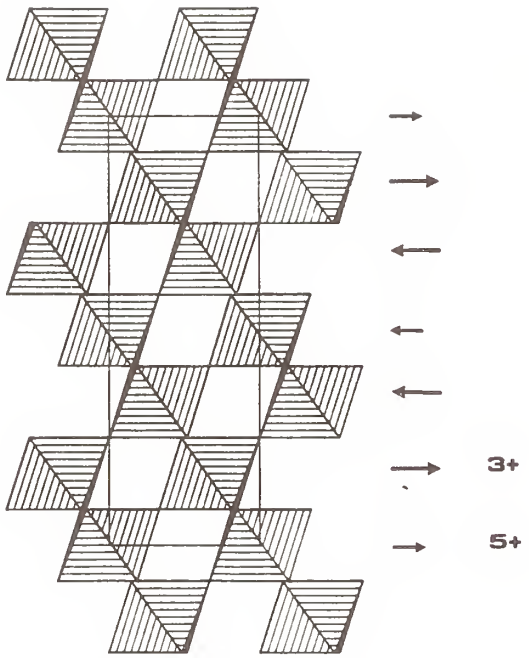

Figure 11: The magnetic structure of $Sr_2LaFe_3O_{8.94}$

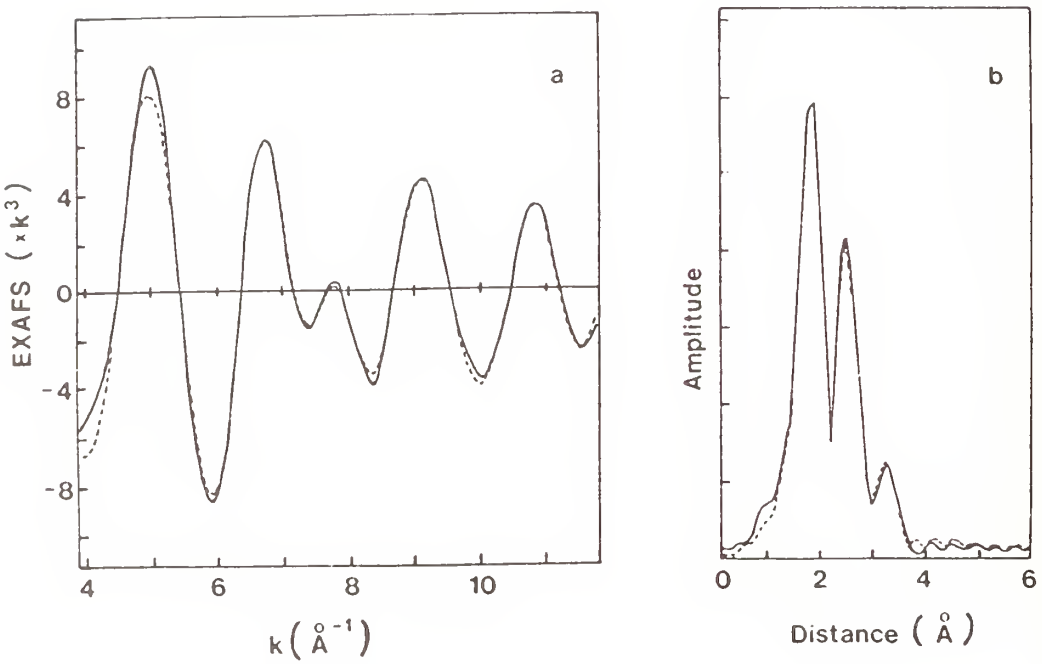

Figure 12: The Mn K-edge EXAFS of $SrMn_{0.55}Co_{0.45}O_{2.55}$

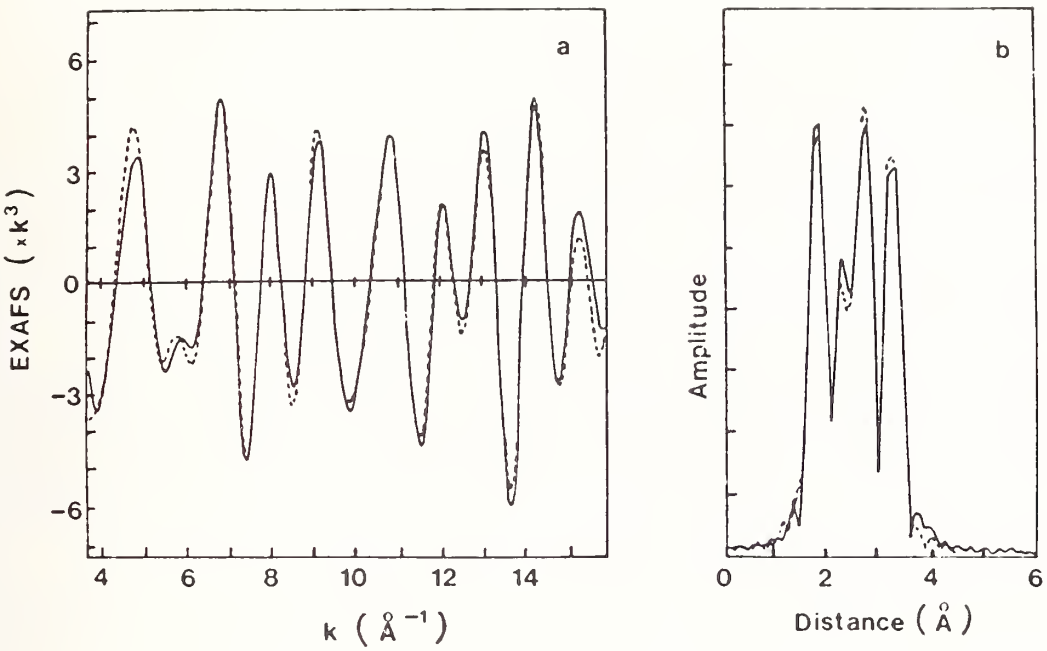

Figure 13: The Co K-edge EXAFS of $SrMn_{0.55}Co_{0.45}O_{2.55}$

where $\delta = \delta(x)$: $\delta_{0.4}$~0.194, $\delta_{0.55}$~0.135. The value of y is ~0.45 for all values of x. The origin of this incommensuration is unclear, but again EXAFS has thrown some light on the problem. The Mn and Co EXAFS from a sample having x = 0.45 are shown in Figures 12 and 13 respectively. The Mn data show an oxygen shell at a radial distance of 1.88Å from the central Mn atom, a transition metal shell at a distance of 2.53Å, and a Sr shell at 3.21Å. The Co data are somewhat more complex. the oxygen shell is again followed by a transition metal shell, but there is then an additional Co shell at 2.87Å before the Sr shell at 3.21Å. The presence of a shell at ~2.5Å in both data sets indicates that both the Co and Mn cations occupy, at least in part, face sharing octahedra. The shell at 2.87Å, observed only in the Co data, suggests the presence of edge sharing Co containing octahedra, and is reminiscent of our results, described above, on $SrCoO_{2.56}$. It may be that there is a link between the structure of this incommensurate phase and that of 'rhombohedral' $SrCoO_{3-y}$.

ACKNOWLEDGEMENTS

Dr. T.C. Gibb (Leeds University) played a major role in this work, particularly in the collection and analysis of Mössbauer data. Drs. A.T. Steel and R. Strange played an equally important part in the EXAFS work. The work has been funded by the SERC.

REFERENCES

1. P.D. Battle, T.C. Gibb and A.T. Steel
   J.Chem.Soc.Dalton Trans., 1987, 667

2. P.D. Battle, T.C. Gibb and P. Lightfoot
   J. Solid State Chem., **84**, 237 (1990)

3. P.D. Battle, T.C. Gibb and S. Nixon
   J. Solid State Chem., **77**, 14 (1988)

4. P.D. Battle, T.C. Gibb and P. Lightfoot
   J. Solid State Chem., **84**, 271 (1990)

5. P.D. Battle, T.C. Gibb, P. Lightfoot and M. Matsuo
   J. Solid State Chem., **85**, 38 (1990)

6. P.D. Battle, T.C. Gibb and R. Strange
   J. Solid State Chem., **81**, 217 (1989)

M. Takano: Did you make EXAFS measurements at low temperatures?

P. Battle: On the Co system, no, we didn't. We haven't done any EXAFS measurements on those systems at all.

R. Newnham: You have spin glass behavior in that $3^+/5^+$ phase, don't you?

P. Battle: In the Ba-La one it's what physicists call a Mattis spin glass where you have a random arrangement of Fe^{3+} and Fe^{5+} in the 3:1 ratio which is governed by the oxygen content. And, the value of the magnetic moment you get from the neutron data is again consistent with antiferromagnetic coupling between Fe^{3+} pairs, antiferromagnetic coupling between Fe^{5+} pairs, but ferromagnetic coupling between 3+ and 5+.

M. Takano: Did you say it's a spin glass?

P. Battle: It's what physicists, I believe, call a Mattis spin glass, Physics Letters, 56A, 421 (1976).

M. Takano: Did you make magnetization measurements?

P. Battle: No, we haven't done that measurement yet.

A. Navrotsky: Do you need Fe^{3+} to stabilize Fe^{5+}? That is, can you replace Fe^{3+} with something trivalent of similar size such as, for example, aluminum or gallium, and still maintain the Fe^{5+}?

P. Battle: There is that compound La_2LiFeO_6 which is an Fe^{5+} perovskite made by Hagenmuller's group which doesn't have any other oxidation states of iron present. That was done in about 1982.

K. Poppelmeier: Getting back to this explanation of no atomic displacement. Is it associated with the fact that you have two different A cations.

P. Battle: I think so, yes. I think the sort of variation in the strain field caused by having disordered arrangements of strontium and lanthanum quenches the structural distortion that you would otherwise expect to see.

A. Sleight: Just to follow up on that. That might be a good explanation for this one but it doesn't solve the problem of the calcium iron oxide.

P. Battle: That's the one that shows the charge disproportion. It's not clear. Has anybody actually done the structure of $CaFeO_3$ at low temperature?

M. Takano: No, just simple powder X-ray diffraction.

A. Sleight: I want to go back to the strontium cobalt system. This pseudo-rhombohedral phase you were talking about. What I was curious about and you didn't mention, is it single phase?

P. Battle: We tried to index the extra peaks as other likely impurities or second phases and got nowhere. We did think about the possibility that there was something else in there. I suspect it may be an incommensurate phase.

D. Smyth: Are these powder samples?

P. Battle: Yes.

D. Smyth: Are you sure that when you go through these various quenchings and slow coolings, and so forth that you have really homogeneous oxygen stoichiometries?

P. Battle: The way we made the $O_{8.94}$ was to cool it very slowly and then leave it at 200°C for 24 hours. So, I believe we came very close to homogeneity.

D. Smyth: But there is a continuous tendency to pick up oxygen as you cool down and at some point you'll have a kinetic problem.

P. Battle: Yes, but I think we did it in what I think was a thorough way, and I'm satisfied. From memory I can't describe everything we did. But I know at the time I believed it was thorough.

D. Smyth: I would like to see a long equilibration at a fixed condition in the quench.

P. Battle: That's essentially what we did. We cooled it slowly from high temperatures to 200°C to give it a chance to pick up what it wanted to. We held it at 200 and then quenched it. You get the same result from 400 as 200. We did that just to prove that point.

National Institute of Standards and Technology Special Publication 804, Chemistry of Electronic Ceramic Materials, Proceedings of the International Conference held in Jackson, WY, August 17-22, 1990, issued January 1991.

FERROELECTRIC AND FERROELASTIC DOMAIN STRUCTURES IN PIEZOELECTRIC CERAMICS

L.A. Bursill and Peng JuLin
School of Physics
The University of Melbourne
Parkville 3052 Victoria
Australia

ABSTRACT

There exist a hierarchy of domain textures in both single crystal and polycrystalline piezoelectrics. Considerable effort has to be made to develop imaging techinques which allow the different contributions to be distinguished; e.g. ferroelectric and/or ferroelastic domains, discommensurations versus antiphase boundaries, extended versus localized chemical defects and multiphase versus grain boundaries.

The present paper presents a discussion of the results of conventional and high-resolution high-voltage electron microscopic studies of two important ferroelectrics, barium sodium niobate (BNN) and lead zirconium titanate (PZT). The first case is relatively well-characterized whereas the latter reveals the complexity of a commercial piezoelectric ceramic.

BARIUM SODIUM NIOBATE (BNN; $Ba_2NaNb_2O_{15}$)

BNN has essentially a tetragonal-tungsten bronze type framework superstructure with the corner-shared octahedral sites fully-occupied by Nb (Fig. 1a). The room temperature phase has cell parameters a = 35.18Å, b = 35.24Å, c = 7.99Å, space group Im2a [1]. The pentagonal and square tunnels are fully-occupied by Ba and Na respectively. A high-resolution electron micrograph (Fig. 1b) shows all of the cations imaged for the [001] projection. Since the point group of the paraelectric phase (4/m2/m2/m) has order 16 compared with the room temperature ferroelectric phase which has point group mm2 of order 4 then we expect two ferroelectric variants and two ferroelastic variants [2]. Physically we may say the polarization vector lies either parallel or antiparallel to the c axis whereas the orthorhombic a axis lies either parallel to $[110]_t$ or $[1\bar{1}0]_t$ of the tetragonal paraelectric phase.

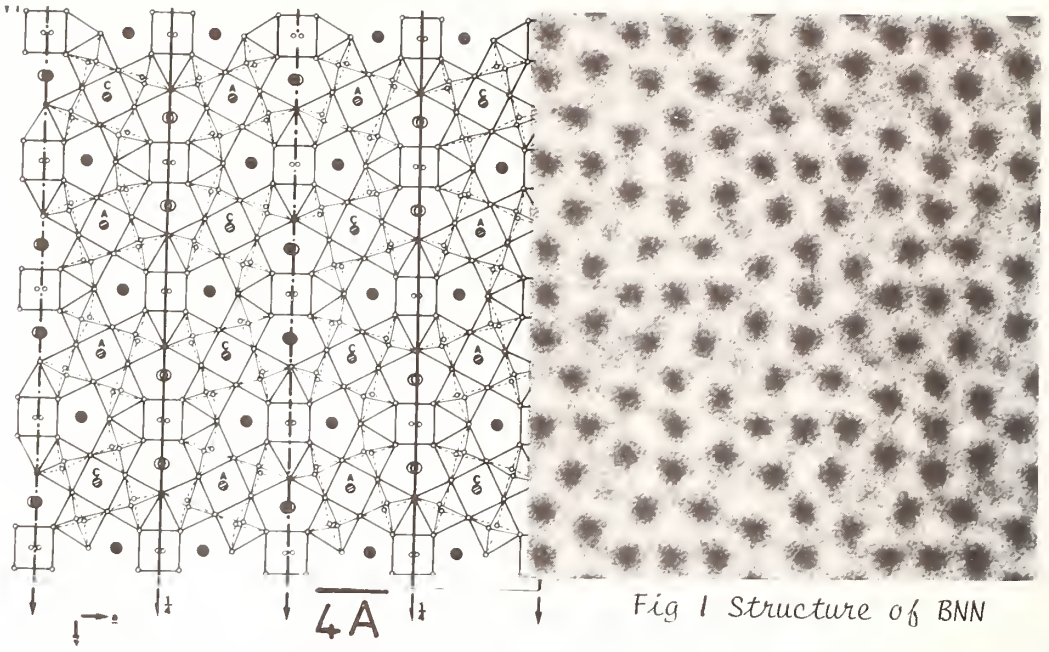

Fig 1 Structure of BNN

(a) Ferroelectric domains. Fig. 2a shows 180° domain walls in as grown BNN at room temperature. Note the irregular nature of the walls, which may be ribbon-like at low magnification. The fringe pattern shows the "black-white" contrast (α-fringes) typical of inversion boundaries in ferroelectric materials. On approaching the thin edge of the specimen these domains become typically lenticular in shape (Fig. 2b). In this high-resolution dark-field image asymmetrical excitation of 001 systematic reflections gave rise to a background change, whereas interference between subcell and supercell reflections maintained a lattice image. Thus it can be seen that the wall thickness is virtually zero. These walls are elongated in the direction of the ferroelectric c-axis. Sub-lattice steps have been visualized clearly in many areas. The lenticular nature of these domains, with c alternately parallel and antiparallel to the crystal surface may indicate the considerable influence of surface depolarization mechanisms on the domain wall topology. Crystallographic studies [3] show that all the metal cations in BNN are displaced along c, in the same sense, away from the nearest mean plane of oxygen atoms, which provides the origin of the ferroelectricity and determines the macroscopic polarization vector.

Other more complex domains, including zig-zag and tightly-curved patterns, represent alternative surface depolarization mechanisms. Here the domain texture is strongly dependent on the orientation of the polarization vectors with respect to the surface and edge directions of the wedge-shaped crystals used typically for electron microscopy. Any electric fields due to charging of the specimen serve only to complicate the domain texture. Thus focussing the electron beam to an intense spot may induce rapid rearrangements of the surface domains.

Fig 2a Wavy 180° domains in BNN

Fig 2b Lenticular 180° ferroelectric domains in BNN

(b) Ferroelastic/ferroelectric domain walls. The room temperature phase of BNN is both ferroelectric and ferroelastic, but the spontaneous polarization and strain appear to remain uncoupled, with the configuration of the ferroelastic domain not strongly coupled to the 180° ferroelectric domain walls. Two sets of ferroelectric-ferroelastic domains are observed with domain walls approximately parallel to $[100]_t$ or $[010]_t$ directions, referred to the tetragonal subcell axes (see Fig. 3). These 90°-ferroelastic/ferroelectric domains present distinct contrast for appropriate bright- or dark-field imaging conditions. They also show essentially planar walls, quite unlike the 180° domain walls, i.e. the surface energy would appear to be much higher, due to the piezoelectric induced strain across the walls.

(c) Commensurate superlattice domain walls (or discommensurations). Incommensurate superlattice phases of BNN were studied by X-ray difffraction [4]. The commensurate/incommensurate transition near 561K gives a phase having a double c axis and an incommensurate modulation along $[110]_t$ tetragonal axis, yielding orthorhombic

Fig. 3 Discommensurations, ferroelastic domains and wavy ferroelectric domains in BNN

symmetry for the average structure. It has been suggested theoretically [5] that the incommensurate phase is composed of commensurate domains separated by out-of-phase domains or discommensurations. Bear in mind that the results of the present section all refer to the commensurate phase, which is stable at room temperature. Dark-field diffraction contrast images were obtained using the commensurate superlattice reflections (inset in Fig. 3). Very faint streaking parallel to [110] was also included (not visible). A special tilt condition was required, to enhance those weak reflections to produce observable contrast. A distinct array of ribbonlike domain contrast was then observed, accompanied usually by 180°-ferroelectric domain walls as well as 90°-ferroelastic domains. These new features are relatively very rough (stepped) and irregular compared to the smooth wavy 180° walls, or the essentially planar 90° walls (cf. Figs. 2). Fig. 3 refers to a crystal orientation tilted a few degrees away from the tetragonal c-axis. A second imaging condition was obtained close to the orthogonal $[110]_t$ projection, which gave discommension images which were elongated essentially parallel to the c-axis. These were again easily distinguished from the 180° and 90° domains, which could be extinguished for this projection by appropriate choice of dark-field imaging conditions. Thus the discommensuration domain walls are elongated along c but have an irregular, chaotic cross-section, perhaps best described as irregular prismatic in shape. Close inspection of the discommensuration morphology reveals a predominance of quadruple modes when they intersect (see Fig. 4) confirming that at least four translation variants exist in the room temperature phase.

Referring to our Fig. 1 , note the sequence of rotated octahedra C A A C along both [100] and [010]. Thus there are four possible sequences generated by a discommensuration which interupts the normal sequence (Fig. 5) corresponding to four phase shifts which are multiples of $\pi/2$. The discommensuration density increases dramatically on approaching the commensurate to incommensurate phase transition [6,7].

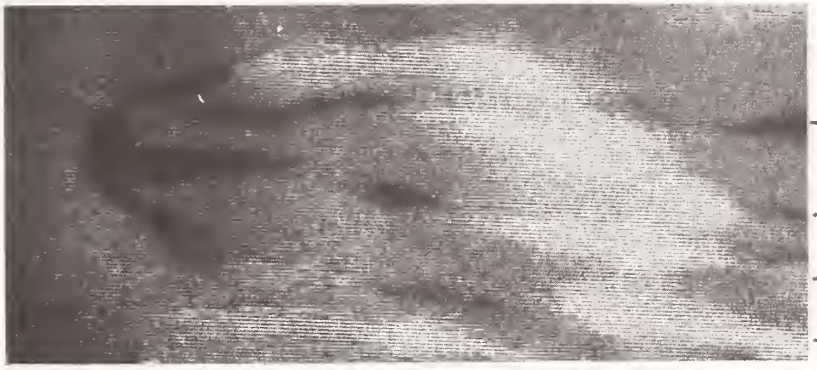

Fig 4 Four-fold discommensuration node in BNN

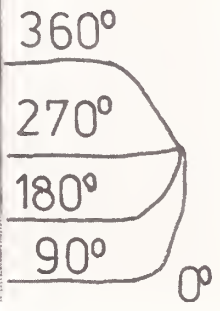

Fig 5 Phase changes at four-node in BNN

(d) Chemical defects. The isostructural phase strontium barium niobate (SBN ; $Ba_xSr_{1-x}Nb_2O_5$; $0.25 \leq x \leq 0.75$) exhibits a further domain texture, due to short-range ordering associated with the mixed occupancy of Ba and Sr along the [001] tunnels [8].

(e) Conclusions. Use of highly perfect single crystals of BNN has enabled the hierarchy of domain textures to be sorted out using a combination of high-resolution and conventional bright- and dark-field electron optical techniques.

LEAD ZIRCONIUM TITANATE (PZT; $Pb(Zr_{1-x}Ti_x)O_3$)

The phase diagram of the $PbZrO_3$-$PbTiO_3$ system shows a complete solid solution at high temperature [9] with Zr and Ti distributed randomly over the octahedral sites of the cubic perovskite structure. On cooling there is a displacive phase transformation into a distorted perovskite structure. Titanium-rich compositions favour a tetragonal modification with significant elongation along [001] and a large spontaneous polarization in the same direction. There are six equivalent polar axes in the tetragonal state, corresponding to the <100> directions of the cubic paraelectric state. A rhombohedral ferroelectric state is favoured for zirconium-rich compositions. Here the distortion and polarization are along the [111] directions, giving rise to eight possible domain states, corresponding to the eight <111> directions of the cubic paraelectric phase. The compositions which pole best are near the morphotropic boundary between the rhombohedral and tetragonal ferroelectric phases. Thus, for $x \simeq 0.5$ there may be up to 14 poling directions over a wide temperature range. We note that the piezoelectric coefficients are largest near the R-T phase boundary.

Domain walls are an important source of dielectric loss for temperature below T_c [9]. Under applied fields, domain wall motion takes place, dissipating energy. A number of different types of walls are expected in PZT. Tetragonal PZT has 180° walls, and both charged and uncharged 90° walls. Charged walls are important only in conducting ceramics, where currents can flow, neutralizing the charge. The 180° walls are generally more mobile than 90° walls because of the mechanical strain associated with the latter. The magnitudes of the piezoelectric coefficients depend markedly on dopants and defect structure because of their influence on domain wall motion, due to alignment of defect dipoles against spontaneous polarization below the Curie temperature (~350°C) [9]. Oxygen vacancy diffusion is believed to be the predominant relaxation mechanism contributing to dielectric losses [9].

The aim of the present work was to observe submicron texture for PZT ceramics of commercial interest. Bright- and dark-field TEM images were used to characterize the ferroelectric and ferroelastic twin domains in both tetragonal and rhombohedral phases of PZT. Attempts have also been made to apply atomic resolution electron microscopy to investigate domain wall widths (charged walls may be diffuse, whereas uncharged walls are sharp [10,11], as well as interactions between twin variants and dislocations. The grain texture is also accessible to high-voltage instruments (say $\geq$300 kV). Results are reported here for a pure tetragonal PZT, i.e. $Pb(Zr_{0.53},Ti_{0.47})O_3$ and a rhombohedral doped PZT + 6 mol.% $NiNbO_3$. Thin specimens were prepared by mechanical grinding and dimpling, followed by ion-beam thinning using argon. Thin edges were carefully aligned with <001>, <011> and <111> pseudocubic vectors parallel to the electron beam. A JEOL-4000EX instrument was used, operated at 400 keV.

(a) $Pb(Zr_{0.53}, Ti_{0.47})O_3$. Low magnification shows grain size about 7 μm. Complex intersecting fringe contrasts, indicative of multiple polysynthetic twin lamellae give rise to textural detail within each grain on the scale ~50 nm. Fig. 6 shows a whole grain, containing lath-like domains parallel to [110], as well as fringe contrasts due to extended defects inclined to the projection axis. The overwhelming complexity of the domain texture, and the fine scale have so far prevented a systematic identification of the many possible combinations of ferroelectric and ferroelastic twins in this material.

Fig 6 Edge-on (left) and inclined (right) ferroelectric domains in tetragonal PZT

High-resolution images showed areas of perfect perovskite-type structure with changes of image detail and symmetry occuring on the scale of ~10 nm. Such changes are consistent with the existence of coherent domain walls. This specimen closely ressembled $BaTiO_3$ and $KNbO_3$ in its behaviour in the electron beam. Thus the specimens often showed charging effects.

(b) $Pb(Zr_{0.53}, Ti_{0.47})O_3$ + 6 mol.% $NiNbO_3$. This rhombohedral specimen was relatively very stable in the electron microscope, showing no charging effects. Fig. 7 shows a typical grain again showing complex domain textures. Some grain boundaries showed precipitates. High-resolution images again showed local changes of periodicity (doubling) and symmetry implying a fine-scale coherent microdomain texture, with fluctuations on the scale of 5~10 nm (Fig. 8). This texture was remarkably similar to results obtained previously for silver ion-exchanged lithium tantalate [12,13], proton- and Fe-doped lithium niobates [14,15]. The papers [12-14] should be consulted for a discussion of the coherency and structural relationships between various pseudocubic and rhombohedral perovskite phases.

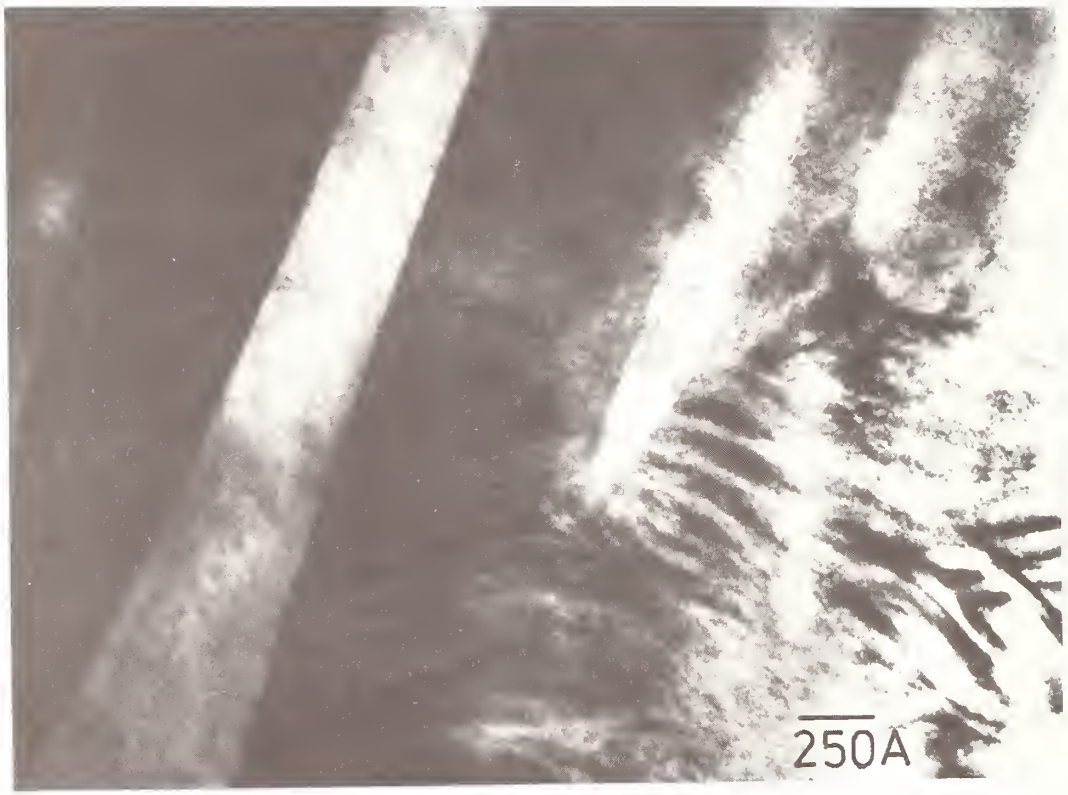

Fig 7 Ferroelastic and ferroelectric domains in rhombohedral PZT

Fig 8 HREM image showingchanges in lattice images on crossing ferroelastic domains in PZT

(c) Conclusion. The present results demonstrate that knowledge of the interaction between stoichiometry, processing routes, microstructure and piezoelectric characteristics is rather primitive, due largely to the complexity of PZT. It is clear however that there is a rich variety of microstructural information accessible in PZT, using high-voltage HREM and TEM techniques

ACKNOWLEDGEMENTS

This work was supported financially by the Australian Research Council, the Victorian State Government and The University of Melbourne, through the National Advanced Materials Analytical Center.

We are grateful for the collaboration of Dr J.R. Sellar, ICI Australian Research Laboratories.

REFERENCES

[1] Peng JuLin and L.A. Bursill, Acta Crystallogr. B 47, 504 (1987).
[2] V. Janovec and V. Dvorak, Ferroelectrics 66, 169 (1986).
[3] P.B. Jamieson, S.C. Abrahams and J.L. Bernstein, J. Phys. Chem. Sol. 49, 4352 (1969).
[4] J. Schneck, J.C. Toledano, C. Joffrin, T. Aubree, B. Joukoff and A. Gabelotard, Phys. Rev. B 25, 1766 (1982).
[5] W.L. McMillan, Phys. Rev. B 14, 1496 (1976).
[6] G. van Tendelloo, J. van Landuyt and S. Amelinckxz, (J.F. Scott and N.A. Clark (Eds.) "Incommensurate Crystals, Liquid Crystals and Quasicrystals", NATO A.S.I. Series, Plenum Press, NY, (1987).
[7] Feng Duan, Cryst. Latt. Defects and Amorp. Mat. 12, 229 (1985).
[8] L.A. Bursill and Peng JuLin, Acta Crystallogr. B 43, 49 (1987).
[9] R. E. Newnham, Rep. Prog. Phys. 52, 123 (1989).
[10] L.A. Bursill, Peng JuLin and Feng Duan, Phil. Mag. 48, 953 (1983).
[11] Peng JuLin and L.A. Bursill, Phil. Mag. 48, 251 (1983).
[12] L.A. Bursill and Peng JuLin, Ferroelectrics 76, 175 (1987).
[13] Peng JuLin and L.A. Bursill, Ferroelectric 77, 69 (1988).
[14] Yan Yong, Feng Duan, Peng JuLin and L.A. Bursill, Ferroelectrics 77, 91 (1988).
[15] L.A. Bursill and Peng JuLin, Ferroelectrics 77, 81 (1988).

National Institute of Standards and Technology Special Publication 804, Chemistry of Electronic Ceramic Materials, Proceedings of the International Conference held in Jackson, WY, August 17-22, 1990, issued January 1991.

CATION SUBSTITUTION IN BARIUM TITANATE FOR DIELECTRIC CERAMIC APPLICATIONS.

F.Batllo[a], A.Beauger[c], B.Jannot[b], J.C.Jules[a], M.Laurent[c], M.Maglione[b], J.C.Niepce[a].

[a] *Laboratoire Réactivité des Solides - CNRS URA 23*
[b] *Laboratoire de Physique du solide - CNRS URA 785*
Université de Bourgogne - BP 138 - 21004 DIJON Cedex, France.
[c] *Laboratoire Recherche et Développement - Thomson LCC*
Avenue du Col. Prat - 21850 Saint Apollinaire, France.

A small amount of foreign element is able to modify drastically the properties of a material but the understanding of these modifications is not always well established.
When a partial substitution on a cation site is carried out in a crystalline material the substituting cation may differ from the substituted cation by the mass, the volume, the electric charge, the oxydo reduction potential,...
At the present time it is not possible to give a full explanation of the modifications of the properties of the material resulting of the various substitutions with reference to the above features only. Nevertheless we would like to show, on barium titanate as an example, how some of these features can be taken into account to influence the properties of a material.
It will be shown and explained how some of the dielectric properties of $BaTiO_3$ are modified with various substitutions. Particularly, with reference to some of the above features, the manufacture of $BaTiO_3$ based material able to be cosintered with a non noble metal will be described.

INTRODUCTION

Barium titanate is the main dielectric material component of class II ceramic capacitors. Due to particular characteristics such as its crystalline structure, insulating properties and phase transitions, $BaTiO_3$ exhibits a very large relative dielectric constant ε_r at the ferroelectric-paraelectric transition. For these reasons, $BaTiO_3$, used as main dielectric material

component of class II ceramic capacitors, allows the highest volumic capacitance for this kind of capacitors among all the capacitor species.
The manufacture of ceramic capacitors under certain pressure and temperature conditions could lead to an important drop in $BaTiO_3$ dielectric properties. For these reasons it is always necessary to modify the chemical composition of the material in order to anneal the effects of such processing.
To fully understand the chemical modifications of $BaTiO_3$ prior to its elaboration as a ceramic capacitor a review of the point defect chemistry at high temperature of the material should be made.

INTRINSIC POINT DEFECT IN $BaTiO_3$

Figure 1 shows the point defect chemistry outlines of pure $BaTiO_3$ evidenced by electrical conductivity measurements upon a large range of oxygen pressure [1][2]. Three different regions can be defined.

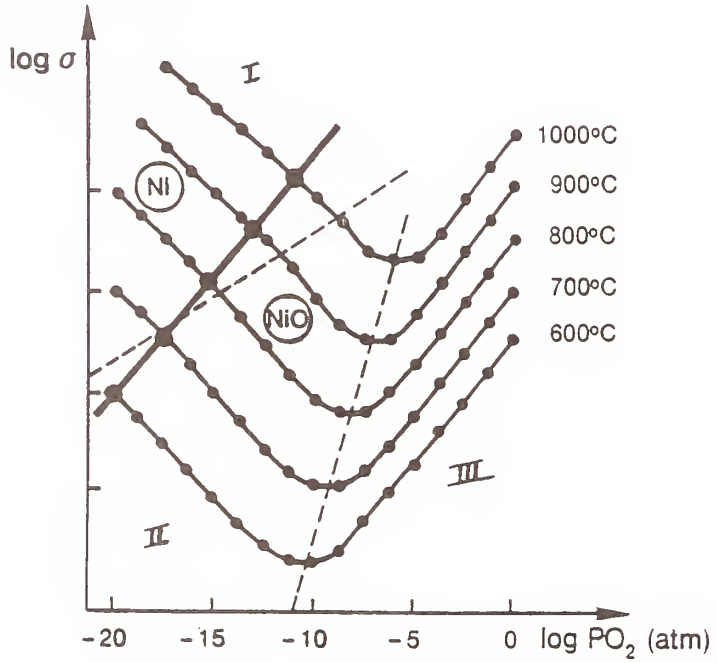

Figure 1: •—•—•— Equilibrium electrical conductivity versus oxygen pressure for undoped $BaTiO_3$ [1].
•—•—•— Equilibrium line between the stability fields of Nickel and Nickel oxide in a P_{O2} vs. T diagram [2].

- Region I is located at very low oxygen pressure and high temperature. The point defect chemistry of $BaTiO_3$ in this region is governed by the departure of oxygen from the structure and the creation of oxygen vacancies associated with the release of 2 electrons. These 2 electrons eventually remain weakly bonded to the titanium sites and lead to a partial reduction of Ti(IV) cations. This behavior can be described by the reaction :

$$O_O + 2Ti_{Ti} \leftrightarrow 1/2O_2 + V_O^{\cdot\cdot} + 2Ti_{Ti}' \qquad (1)$$

- The point defect chemistry in region II and III have been subject to controversies among the different authors. However the most widely accepted view is that of Smyth et al.[1] who suggest that oxygen vacancies $V_O^{\cdot\cdot}$ resulting from the presence of extrinsic point defects and in particular acceptors (i.e. cations with lower valency than normal cations) are still preponderant in these regions.

ELABORATION OF MULTILAYER CERAMIC CAPACITORS

One of the most used type of capacitor is the multilayer ceramic capacitor (MLC). The MLC consists in the alternated superposition of dielectric and metallic electrode layers as shown figure 2.

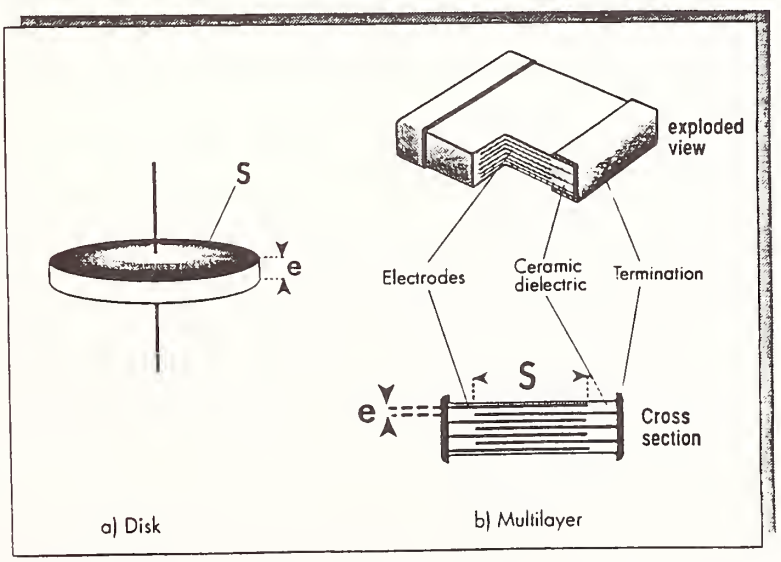

Figure 2: Ceramic Capacitors

This particular processing allows a larger volumic capacitance than classical capacitors. In order to lower the MLC cost price, non noble metal such as nickel is likely to be used as internal electrodes.
An important stage during the manufacture of the MLC is the cosintering of the dielectric material and the Ni electrodes at high temperatures.
Figure 1 shows that in order to avoid an oxidation of the nickel and the loss of its conductive properties, the MLC must be sintered under reducing conditions ($P_{O2} < 10^{-11}$atm). These pressure and temperature conditions coincide with the reducing region of $BaTiO_3$ (region I). The sintering under low oxygen pressure results in the departure of oxygen from the material and the reduction of Ti(+IV) cations into Ti(+III) cations. The ceramic is no longer an ideal dielectric but presents the characteristics of a n type semi conductor with large dielectric losses at room temperature (figure 3) [3].

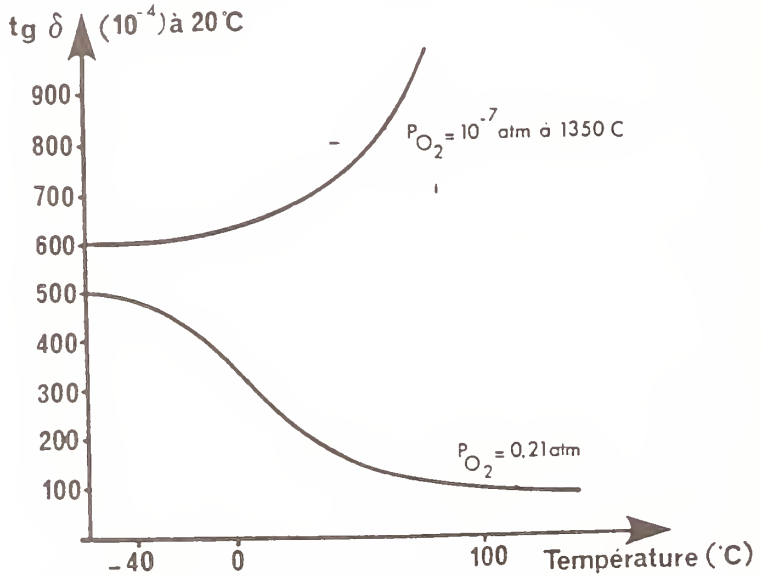

Figure 3: Influence of the oxygen partial pressure during the sintering of a Z5U material with general formula $Ba_{1-x}\ Ca_x\ Ti_{1-y}\ Zr_y\ O_3$ [3].

To avoid the reduction of Ti(+IV) cations, one solution is to trap the electrons on a more reducible cation than Ti(+IV). Figure 4 represents the free enthalpy variation of the reaction :

$M + n/4O_2 \rightarrow MO_{n/2}$ (2) for different elements [4]. This figure shows that manganese is less oxidizable than titanium and consequently oxidized Mn is more easily reduced than oxidized titanium. This confirms that Mn(+IV) and Mn(+III) cations are able to trap the electrons produced during the sintering of the MLC. Moreover, due to the fact that Mn cations are statistically far from one another ([Mn] ≃ 0.1%), the trapped electrons are unable to jump from site to site.
The large decrease of the dielectric losses with the increase of Mn concentration in $BaTiO_3$ shown figure 5 [2], confirms the role of Mn as an electron trapper.

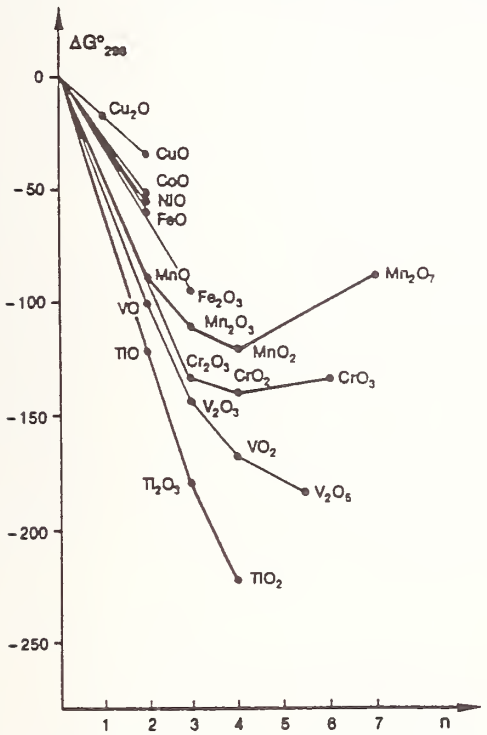

Figure 4: Oxidation state diagram of the metal of the phase transition series [4] (established with reference to the free enthalpy ΔG^0_{280} of formation of the oxides [7],[8]).

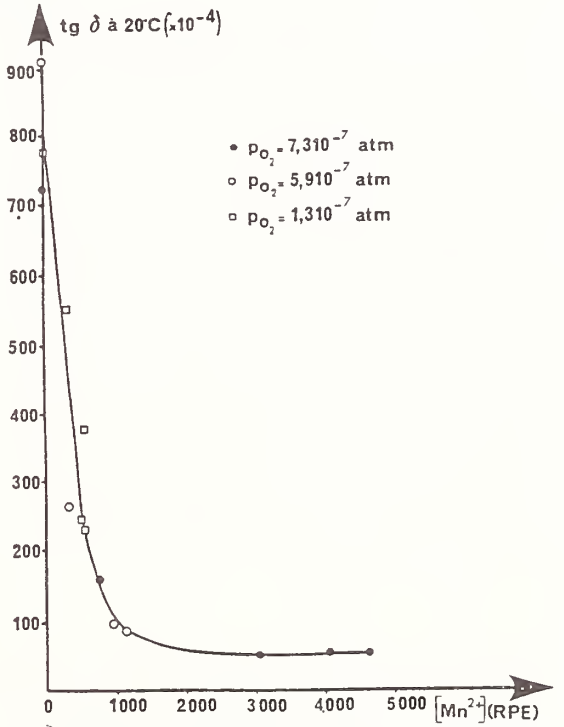

Figure 5: Dielectric losses at Room Temperature as a function of Mn(+II) concentration in a $BaTiO_3$ based Z5U material [2].

Another unwanted effect of the sintering at low P_{O2} is the appearance of oxygen vacancies (reaction (1)). In addition the

introduction of acceptors in the lattice like Mn(+III) in place of Ti(+IV) is also source of oxygen vacancies through the reaction:

$$BaO + (1-y)TiO_2 + y/2\ Mn_2O_3 \rightarrow$$

$$(Ba_{Ba})\ (Ti_{Ti})_{1-y}\ (Mn'_{Ti})_y\ (O_O)_{3-y/2}\ (V_O^{\cdot\cdot})_{y/2} \quad (3)$$

Because of their mobility when T increases, the presence of oxygen vacancies inside the lattice induces a very poor stability of the dielectric material during accelerated life tests as shown figure 6 [3].

To prevent the appearance of oxygen vacancies a substitution of Ti(+IV) and/or Ba(+II) cations by donors i.e., cations with higher electric charge, can be made. For example, the introduction of Ce(+III) cations in place of Ba(+II) lead to the appearance of $Ce_{Ba}^{\cdot}$ which compensates for 1/2 $V_O^{\cdot\cdot}$.

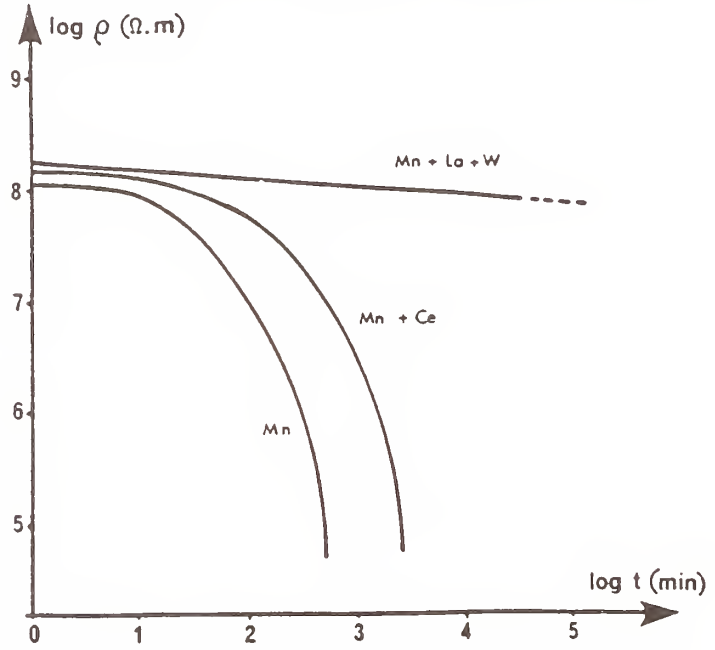

Figure 6: Resistivity of $BaTiO_3$ based Z5U material as a function of various doping during life test (1.7V/µm and 280°C) [3].

The double substitution,in a convenient proportion, by both donors and acceptors like Ce(+III) in Ba(+II) sites and Mn(+III) in Ti(+IV) sites can be described by the following reaction:

$$(1-x)BaO + x/2Ce_2O_3 + (1-x)TiO_2 + x/2Mn_2O_3 \rightarrow$$

$$(Ba_{Ba})_{1-x}\ (Ce_{Ba}^{\cdot})_x\ (Ti_{Ti})_{1-x}\ (Mn_{Ti}')_x\ (O_O)_3 \quad (4)$$

The resulting material no longer contains vacancies. However this substitution must be made in such a way that the oxygen vacancies generated by the departure of oxygen during the sintering have to be compensated prior to the sintering.

Figure 6 shows the effect of a triple substitution on the accelerated life test evolution of a $BaTiO_3$ ceramic capacitor in time. Mn has been added as Mn(+III) and Mn(+IV) on Ti(+IV) sites to trap the electrons generated by the oxygen departure. La(+III) and W(+VI) are added in substitution for Ba(+II) and TI(+IV) in order to compensate the oxygen vacancies generated by both the acceptor substitution and the oxygen departure [3],[5],[6].
The resulting composition can be written:
$(Ba_{Ba})_{1-x}\ (La_{Ba}^{\cdot})_x\ (Ti_{Ti})_{1-y-z}\ (Mn_{Ti}^{'})_y\ (W_{Ti}^{\cdot\cdot})_z\ (O_O)_3$

In conclusion, despite the chemical complexity of a material resulting from different substitutions, we have shown that it is possible to modify in a convenient way some of the dielectric properties of a material by considering parameters such as: relative electric charges and oxydo reduction potential of the substituting cation with reference to the substituted cation.
However, we would not try to explain completely the behavior of a substituted material by considering only these parameters. Nevertheless they can be a good guide.

References:

[1] D.M. SMYTH. Prog.Solid.State Chem., 15, (145-171) 1984.
[2] F.BATLLO. Thesis DIJON (France), 1987.
[3] M.LAURENT. Thesis CNAM DIJON (France), 1989.
[4] A.MORELL and J.C.NIEPCE. J.Mat.Education, (in press.), 1991.
[5] Patent of "Inst. Nat. Prop. Indust. Français", nº 8817081, (23/12/88).
[6] Patent of "Inst. Nat. Prop. Indust. Français", nº 8807404, (03/06/88).
[7] O.KUBACHEVSKI and E.EVANS. "La Thermochimie en Metallurgie". Gauthiers Villars Edit. Paris. 1964.
[8] L.BREWER. Chem. Rev., 52, 1,1953.

National Institute of Standards and Technology Special Publication 804, Chemistry of Electronic Ceramic Materials, Proceedings of the International Conference held in Jackson, WY, August 17-22, 1990, issued January 1991.

LIQUID PHASE SINTERING OF LiF-FLUXED $BaTiO_3$

Sea Fue Wang, Wayne Huebner, and Clive Randall
Materials Research Laboratory
Penn State University
University Park, PA 16802

INTRODUCTION

Reduction of the firing temperature of $BaTiO_3$-based multilayer capacitors (MLC's) is typically achieved using fluxing agents such as CuO, ZnO, CdO, LiF, or Bi-compounds[1-6]. Most of these fluxes enhance densification due to liquid phase sintering. Liquid phase formation in these systems is either due to melting of the flux, or by the formation of a eutectic liquid between the flux and $BaTiO_3$. Although the flux reduces the sintering temperature, it may also introduce undesirable effects such as lowering the dielectric constant and mechanical strength, and increasing the aging rate. These effects are most noticeable in systems in which the flux remains as a continuous second phase in the grain boundary, or enters into solid solution with the $BaTiO_3$ and hence alters the defect chemistry.

LiF is an effective sintering aid for both MgO and many perovskites[2-6]. Small additions of LiF (0.5-3wt%) may yield > 98% dense $BaTiO_3$ at temperatures as low as 850°C[3-5]. Changes in stoichiometry dramatically impact this behavior: Ba-excess compositions exhibit the highest densities. Desgardin et al.[4,6] proposed that an intermediate composition of the fired ceramic is an oxyfluoride, $BaTi_{1-x}Li_xO_{3-3y}F_{3y}$, but this was difficult to prove due to the fact that Li and F are not readily detectable by simple spectroscopic techniques.

The dielectric behavior of flux-sintered $BaTiO_3$ cannot be simply understood through the application of standard mixing rules. Although these rules effectively describe the dielectric behavior for multiple component systems, for flux-sintered $BaTiO_3$ strong variations in the chemical homogeneity (and its impact on the phase transition temperatures) and the defect chemistry demand a more complex analysis. Few systematic studies on the microstructural evolution of flux-sintered $BaTiO_3$ and a direct correlation to the resultant dielectric properties have been performed.

The purpose of our investigations is to clarify the interaction of $BaTiO_3$ with Li-compounds during liquid phase sintering, the chemical inhomogeneity of the resulting microstructure, and the microstructure-property relationships.

EXPERIMENTAL PROCEDURE

The effects of two flux systems are reported here: $LiF+BaCO_3$, and $BaLiF_3$. The LiF and $BaCO_3$ were obtained from Aldrich. The $BaLiF_3$ was prepared by mixing stoichiometric amounts of BaF_2 and LiF for 24 hours with a shaker mill. Powders were milled in methyl alcohol using polyethylene jars and ZrO_2 media. After drying, these powders were transferred to a Pt crucible, reacted at 850°C, and quenched. The powder was then dry-milled and sieved through a 320 mesh screen. XRD analysis confirmed $BaLiF_3$ formation.

TAM-HPB $BaTiO_3$ was used in this study. Fluxes were mixed/milled with the $BaTiO_3$ as described above. Milled powders had an average particle of 0.7 μm as determined by light scattering. To prepare the powders for pressing, they were mixed with DuPont 5200 binder using acetone as a solvent, dried, pulverized using a motor and pestle, and then sieved through a 120 mesh screen. Disks were prepared by uniaxial-pressing at 15000 psi. Green densities were ≈ 64% theoretical. These disks were calcined for 2 h at 500°C, followed by sintering in a closed crucible at temperatures ranging from 800 to 1150°C for two hours. A 6°C/min heating rate was used throughout.

Sintered densities were measured using a displacement technique with xylene as the liquid medium. Fired samples were mounted in an epoxy, ground, polished and etched using a 10 wt% HCl, 90 wt% H_2O solution with several drops of HF. Microstructural observations were carried out on etched surfaces using an SEM, and on ion-milled samples with a TEM.

After sputtering on Pt electrodes, the dielectric properties of sintered samples were measured as a function of temperature and frequency using an HP 4274 RLC bridge. Measurements were taken during cooling from 200 to -50°C, over a frequency range from 100 Hz to 100 kHz.

RESULTS AND DISCUSSION

Figure 1 shows the densification curves for 2wt% LiF+2m% $BaCO_3$, and 3 and 7w% $BaLiF_3$. For temperatures ≥850°C the densities for 2wt% LiF+2m% $BaCO_3$ and 7w% $BaLiF_3$ samples are all ≈95%. The 3w% $BaLiF_3$ flux did not densify as well, which is probably due to an insufficient amount of liquid phase. Since the melting temperature of LiF is 846°C, a eutectic liquid must have formed in order to explain the onset of densification for T≤800°C. Results from DTA studies on mixtures of $BaTiO_3$ and 20 wt% LiF with or without $BaCO_3$, and $BaTiO_3$ and 20 wt% $BaLiF_3$ are shown in Figure 2. Endothermic peaks corresponding to eutectic liquid formation appear at 700°C for $BaTiO_3$ and LiF, and 610°C with the addition of $BaCO_3$. This correlates well with studies which have shown LiF additions to Ba-excess $BaTiO_3$ (adjusted by $BaCO_3$) lower the sintering temperature[4,5]. The DTA results also show that mixture of $BaTiO_3$ and $BaLiF_3$ did not exhibit any liquid formation other than the incongruent melting of $BaLiF_3$ at ≈840°C. This result is consistent with the sintering behavior which shows

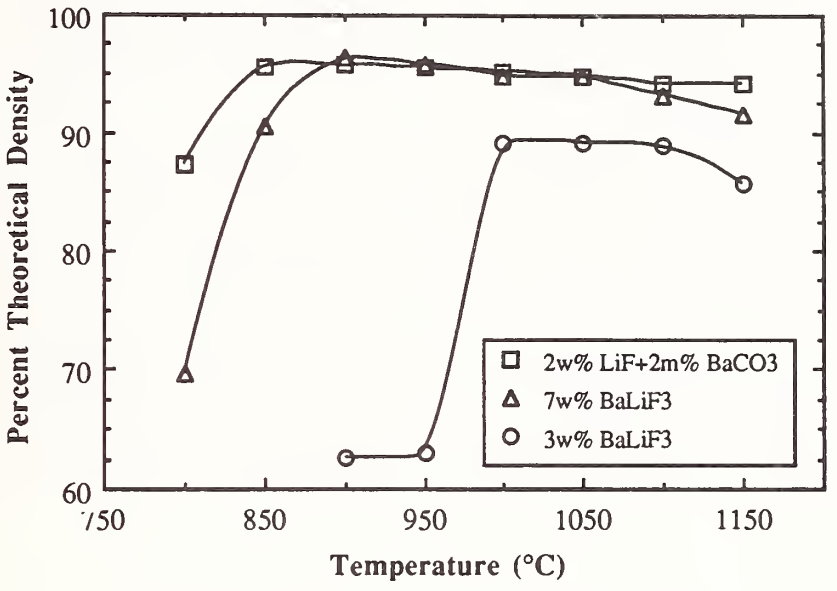

Figure 1: Densification behavior of $BaTiO_3$ sintered with LiF and $BaLiF_3$

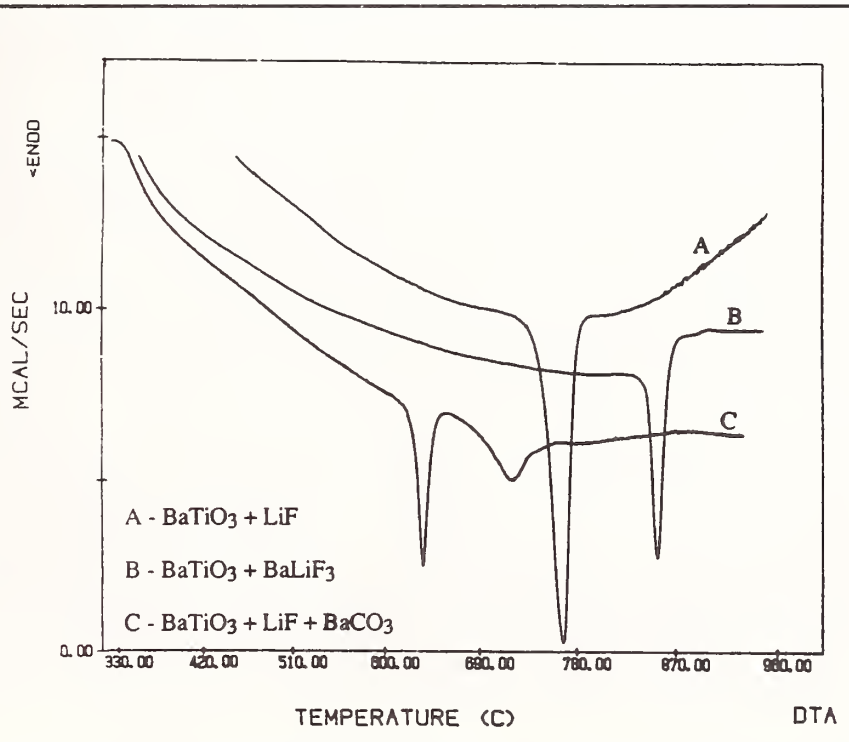

Figure 2: DTA results for mixtures of LiF and $BaLiF_3$ with $BaTiO_3$.

significant densification occurs for T >850°C; i.e. the onset of densification is coincident with liquid phase formation. Some authors[6] have proposed that the mechanism for densification in the LiF system is due to intermediate formation of $BaLiF_3$. However, our results show $BaLiF_3$ is only effective at higher temperatures.

XRD analysis on identical mixtures heated and quenched at temperature from 600 to 900°C indicate : a) no $BaCO_3$ or LiF peaks are observed at temperatures above the eutectic temperature, b) for T>800°C there are no detectable differences in phase formation for mixtures of $BaTiO_3$ and LiF with and without $BaCO_3$, and c) only $BaTiO_3$ peaks exist when the $BaLiF_3$ mixture is heated at T>900°C.

Based on these DTA and XRD results, liquid formation at the eutectic temperature of $BaTiO_3$-LiF-$BaCO_3$ at 610°C is responsible for the lower densification temperatures observed for Ba-excess compositions. Since only $BaTiO_3$ peaks are indicated in XRD pattern of $BaTiO_3$ and $BaLiF_3$ mixture, this confirms that the formation of a perovskite solid solution $BaTi_{1-x}Li_xO_{3-3y}F_{3y}$ from $BaTiO_3$ and $BaLiF_3$.

Figures 3a and b contain SEM micrographs of 2 wt% LiF-$BaTiO_3$ (Ba/Ti=1.02) sintered at 900°C and 1100°C for 2 hours. For the sample sintered at 900°C, the grain size is ≈ 1-2 μm. For samples sintered at 1100°C the micrograph shows faceted grains of an average diameter >50 μm, and the presence of many <111> twins. This microstructure is similar to that obtained when Ti-excess $BaTiO_3$ is sintered at T> 1312°C. Figure 4 contains a representative TEM micrograph of a sample sintered at 900°C. A grain core-shell microstructure is observed, with both 90° and 180° domain walls inside the core region, and line and dislocation loops located at the core-shell interface. Heating and cooling the sample in-situ and observing the disappearance and appearance of the domains confirmed the core was pure $BaTiO_3$. Importantly, the shell bears an epitaxial relationship to the core, and the size of the core is roughly equal to the original starting powder size prior to the liquid phase sintering. A residual glass phase was also observed at grain boundaries and triple points. These results indicate that the shell is the perovskite solid solution, $BaTi_{1-x}Li_xO_{3-3y}F_{3y}$, which formed due to a solution-reprecipitation process. The interface is due to the lattice mismatch associated with the discontinuous Li-concentration.

The permittivity response of a LiF-$BaCO_3$-$BaTiO_3$ sample sintered at 900° for 2 hours is shown in Figure 5, with the corresponding Curie-Weiss plot in Figure 6. A broad peak in the dielectric constant is observed at ≈10°C, and a slight peak at ≈120°C. The dielectric loss is high and dispersive. These results correlate well with the hypothesis that the shell is a $BaTi_{1-x}Li_xO_{3-3y}F_{3y}$ solid solution. The peak at ≈10°C is associated with the decrease in the cubic-tetragonal transition, while the broadness is associated with spatial variation in x and y. The linearity of the Curie-Weiss plot for T>125°C is due to the pure $BaTiO_3$ core. The high, dispersive dielectric loss most likely indicates the shell region exhibits a high conductivity

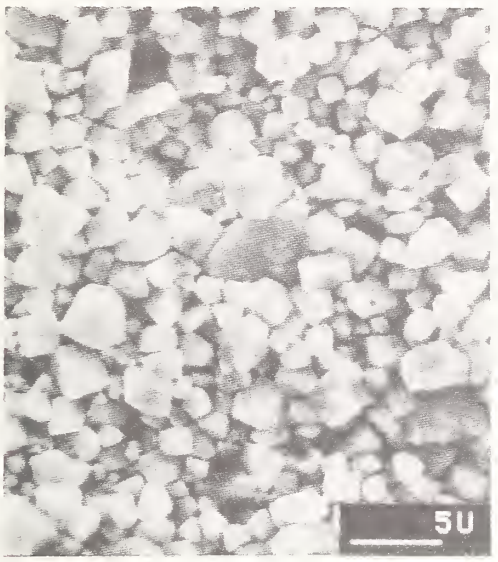

900°C

1100°C

Figure 3: SEM micrographs of 2 wt% LiF-$BaTiO_3$ (Ba/Ti=1.02) sintered at 900°C and 1100°C for 2 hours.

Figure 4: TEM micrograph of a 2wt% LiF-$BaTiO_3$ (Ba/Ti=1.02) sample sintered at 900°C.

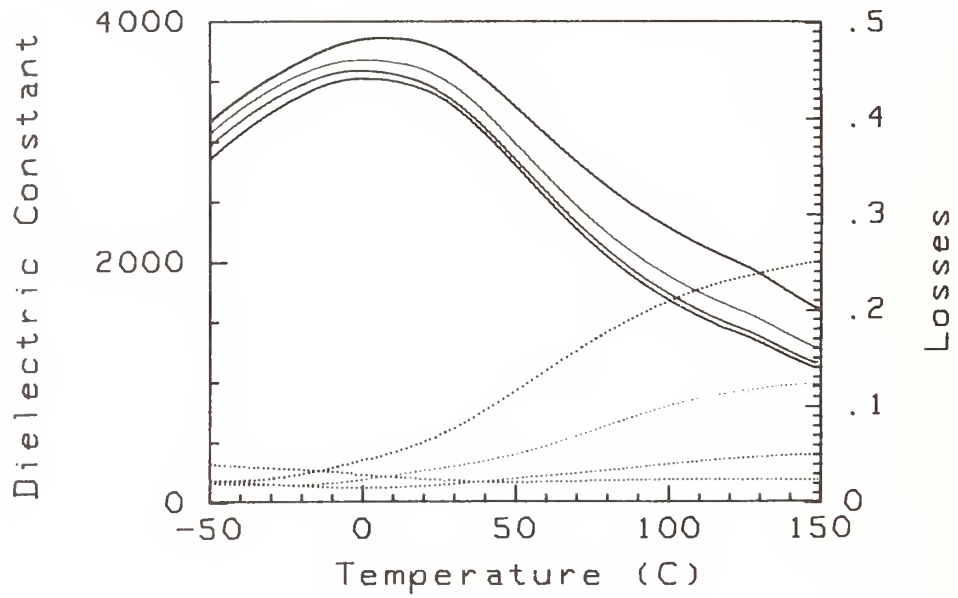

Figure 5: Dielectric behavior of a 2wt% LiF-$BaTiO_3$ (Ba/Ti=1.02) sample sintered at 900° for 2 h.

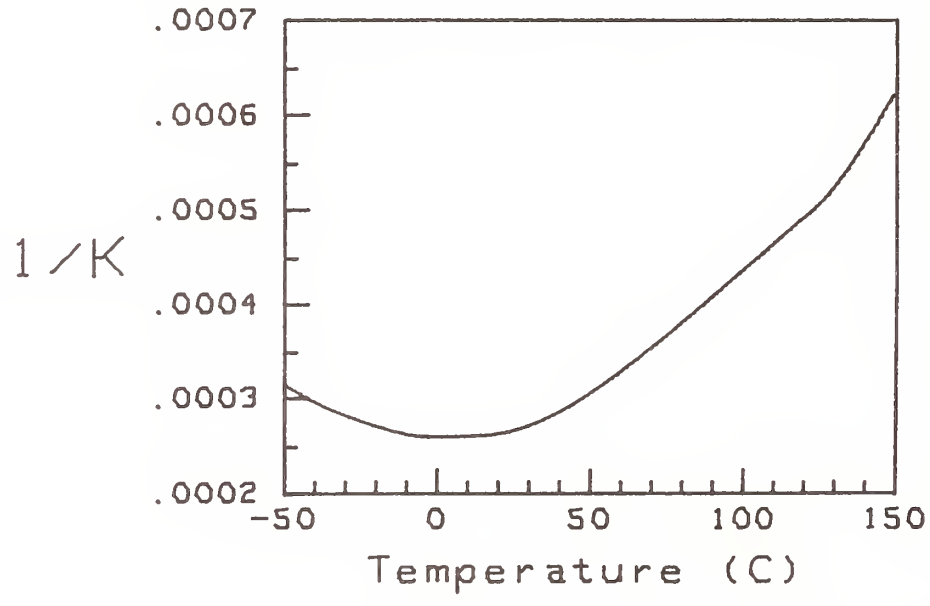

Figure 6: Curie-Weiss plot of the dielectric behavior exhibited in Figure 5.

associated with either ionic conductivity of Li or F ions, or due to an enhanced electronic conductivity associated with an altered defect chemistry.

SUMMARY

1. The onset of densification in the flux systems studied can be directly correlated with the temperatures at which a eutectic liquid forms. The lower sintering temperatures of Ba-excess compositions (due to $BaCO_3$) is clearly due to the eutectic liquid which forms at 610°C, compared to 700°C when $BaCO_3$ is not present.

2. TEM micrographs reveal $BaTiO_3$ sintered with 2 wt% LiF (Ba/Ti=1.02) at 900°C for 2 hours results in a grain core(tetragonal)-shell(cubic) structure. The shell region is most likely the perovskite solid solution $BaTi_{1-x}Li_xO_{3-3y}F_{3y}$, which is formed due to a solution-reprecipitation process. The temperature dependence and dispersive behavior of the dielectric properties confirm this hypothesis.

REFERENCES

1. I.Burn, "Flux-Sintered $BaTiO_3$ Dielectrics," *J. Matr. Sci.*, **17**[5], 1398-1408 (1982).

2. M. W. Benecke, N. E. Olson, and J. A. Pask, "Effect of LiF on the Hot-Pressing of MgO," *J. Am. Ceram. Soc.*, **50**[7], 365-368 (1967).

3. A. Potten, J. Ravez, and J. P. Bonnet, "STEM Study of the Sintering Mechanism of $BaTiO_3$ with LiF," High Tech Ceram., edited by P. Vincenzini, 1525-1532 (1987).

4. J.M. Haussonne, G. Desgardin, P.H. Bajolet, and B. Raveau, "Barium Titanate Perovskite Sintered with Lithium Fluoride," *J. Am. Ceram. Soc.*, **66**[11], 801-807 (1983).

5. D. A. Tolino and J. B. Blum, "Effect of Ba:Ti Ratio on Densification of LiF-Fluxed $BaTiO_3$," *J. Am. Ceram. Soc.*, **68**[11], C-292-C-294 (1985).

6. G. Desgardin, I. Mey, and B.Raveau, "$BaLiF_3$-A New Sintering Agent for $BaTiO_3$-Based Capacitors," *Am. Ceram. Soc. Bull.*, **64**[4] 563-70 (1985).

National Institute of Standards and Technology Special Publication 804, Chemistry of Electronic Ceramic Materials, Proceedings of the International Conference held in Jackson, WY, August 17-22, 1990, issued January 1991.

A REAL SPACE ANALYSIS OF SHORT RANGE ORDER IN FERROELECTRIC $Pb(Mg_{1/3}Nb_{2/3})O_3$

H. D. Rosenfeld and T. Egami
(Department of Materials Science and Laboratory for Research on the Structure of Matter, University of Pennsylvania, Philadelphia, PA 19104, USA)

A. Bhalla
(Materials Research Laboratory, Pennsylvania State University, University Park, PA 16802, USA)

ABSTRACT

The local atomic structure of $Pb(Mg_{1/3}Nb_{2/3})O_3$ (PMN) was investigated using pulsed neutron powder diffraction. Changes in nearest neighbor distances were studied by pair-distribution function, or real space, analysis. We find a decrease in the number of intermediate Mg/Nb-O and Pb-O pair distances below the Curie temperature due to interatomic correlations. These correlated displacements may be related to the onset of bulk ferroelectricity. We find evidence supporting the existence of ferroelectric cells above T_c in PMN.

INTRODUCTION

Short range order in the relaxor ferroelectric lead magnesium niobate $Pb(Mg_{1/3}Nb_{2/3})O_3$ (PMN) has been a subject of considerable interest, since the ferroelectric transition may be attributed to local deviations of the atomic structure from that of an ideal perovskite [1]. Bonneau et al. [2] have suggested a disorder model in which Pb and Nb atoms are displaced along the cubic [100], [110] and [111] directions, and Smolenskii and Agranovskaya [1,3] have discussed the distribution of Mg and Nb ions as a means of explaining the diffuse nature of the ferroelectric phase transition. Recently Husson et al. [4] have reported the results of a Raman spectroscopy study of short range

order in PMN suggesting the existence of ferroelectric cells above the -7°C Curie temperature.

We have studied short range order in PMN by Rietveld and pair-density function (PDF), or real space, analysis of neutron powder diffraction data. The results of the Rietveld refinement have been reported elsewhere [5]. PDF or real space analysis provides extensive insight into the local atomic structure of a material, and provides a simple and direct means of connecting trial structures of materials not possessing long range order to diffraction experiments. The pair-density function $\rho(r)$ is the Fourier transform of the structure factor $S(q)$. Periodicity of the structure need not be assumed in calculating the PDF and non-periodic structures may be treated exactly. The PDF is sensitive to details of the local structure, whereas Rietveld analysis is best suited to studying long range order in periodic structures. Neutron diffraction was chosen owing to the relative uniformity of neutron scattering lengths which makes it possible to refine the positions of Mg, Nb and O atoms in the presence of Pb.

EXPERIMENTAL METHODS

Neutron diffraction data were collected using the Time-of-Flight method on the Special Environment Powder Diffractometer (SEPD) at the Intense Pulsed Neutron Source (IPNS), Argonne National Laboratory. A burst of highly energetic neutrons is produced at time t_o. A liquid methane moderator placed close to the target produces a neutron wavelength spectrum with a large Maxwellian thermal component in addition to an epithermal portion, producing a continuous spectrum of neutrons with wave vectors ranging from 0.3Å^{-1} to 30Å^{-1}. Assuming elastic scattering, the magnitude of the wave vector k may be determined by measuring the time required, Δt, for the neutron to traverse the flight path from target to detector, D, via

$$k=2\pi mD/h\Delta t \quad . \qquad (1)$$

The sample is located 14m from the target and is surrounded at a distance of 2m by detector banks at angles of 2θ equal to 15°, 30°, 60°, 90° and 150°. The magnitude of the scattering vector q is related to k by

$$q=2k\ \sin(\theta)\,. \qquad (2)$$

S(q) was obtained over q equal to 0.5-50Å^{-1}. Obtaining the structure factor S(q) to such large values of q minimizes termination errors when Fourier transformed to produce the pair-density function. The lack of energy resolution in this experiment implies an integration over all neutron energies during data collection. In interpreting the data, this integration was assumed taken at constant scattering vector q. A correction for this approximation, the Placzek correction [6], was applied to the data. In addition corrections were made for absorption, background and incident spectrum (see for example [6]). S(q) is related to the corrected intensity by

$$S(q) = \frac{I(q)}{\ll b \gg^2} + \frac{\ll b \gg^2 - \ll b^2 \gg}{\ll b \gg^2}\,. \qquad (3)$$

10.37g of powdered PMN was placed in a vanadium can and mounted in a Displex in SEPD. Diffraction data were collected at three temperatures, 10K, 200K and 295K. Detector counts were typically 32000 per bank. Scattering from the empty vanadium can and empty Displex were measured for absorption and background corrections. Scattering from a vanadium standard was also measured to determine the incident spectrum.

PDF ANALYSIS

The pair-density function $\rho(r)$ is related to the structure factor S(q) by the Fourier transform,

$$\rho(\vec{r})-\rho_0 = \frac{1}{(2\pi)^3}\int d\vec{q}\,[S(\vec{q})-1]e^{i\vec{q}\cdot\vec{r}} \qquad (4)$$

where ρ_o is the average atomic number density and q is the scattering vector [7]. It should be noted that S(q) is the square of F(q), the structure factor conventionally used in crystallography. If S(q) is isotropic as in an amorphous material, or as the result of powder averaging, the integral in (4) reduces to

$$\rho(r)-\rho_0 = \frac{1}{(2\pi^2 r)}\int dq\,[S(q)-1]q\sin(qr)\,. \qquad (5)$$

The physical interpretation of $\rho(r)$ may be understood by considering the single and two particle density functions. In general the two particle density function is not equal to the product of the two single particle density functions, due to interatomic correlations, rather

$$n^{(2)}(r_1, r_2) = n^{(1)}(r_1)\ \rho_o\ g(r) \qquad (6)$$
$$r = r_1 - r_2$$

where

$$g(r) = \rho(r)/\rho_o \qquad (7)$$

is the pair-distribution function. As r approaches infinity, interatomic correlation becomes negligible and $g(r)$ tends to unity or $\rho(r)$ tends to ρ_o.

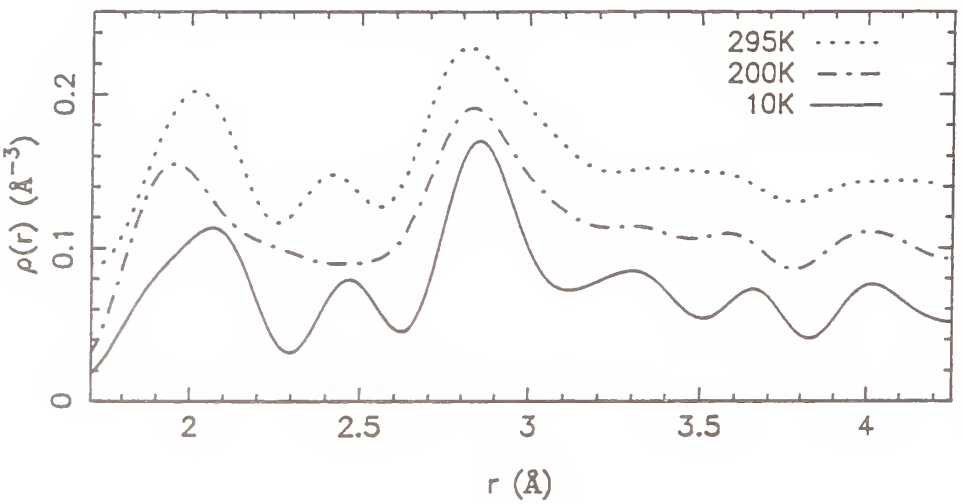

Figure 1. PMN Pair-distribution functions at 295K(dot), 200K(dot-dash) and 10K(solid).

The PDF's determined from neutron powder diffraction at 10K, 200K and 295K are shown in figure 1. In the ideal perovskite we would expect peaks at 2.02Å corresponding to Mg(Nb)-O pairs, 2.86Å corresponding to Pb-O and O-O pairs, 3.51Å due to Mg/Nb-Pb pairs and 4.05Å the unit cell size. Rietveld analysis [5] suggests displacements of Pb, Mg and Nb along the cubic [111] and of oxygen along [112]. These displacements account for the

additional peaks near 2.47Å and 3.30Å observed most clearly in the 10K data. Peak positions, integrated intensities and contributing pairs at the temperatures studied are given in table 1. The aforementioned displacements, when not constrained by the requirement of translational invariance, do not produce single pair separations at the peak centers, but rather produce a range of distances about the peak positions. This accounts for the broad nature of the peaks, a phenomenon approximated in Rietveld refinement by anomalously large thermal factors. That these broad peaks are composed of multiple pair distances may be seen in the Mg(Nb)-O peak. At 10K the maximum is at 2.06Å, but the peak shape suggests the presence of a second peak near 1.9Å. At 200K the maximum has shifted to 1.95Å, however substantial intensity is observed near 2.06Å. In the 295K data only a single broad peak may be seen at 2.02Å, between the 10K and 200K peak positions. Lead-oxygen distances are distributed over three ranges. The first range centered near 2.45Å, the second covers 2.8Å-3.0Å and the third centered near 3.3Å. At 200K the number of short Pb-O distances decreases in favor of

peak position			integrated intensity			contributing pairs
295K	200K	10K	295K	200K	10K	
2.02	1.95	2.06	4.282	4.279	4.281	Mg/Nb-O
2.42	2.45[1]	2.47	1.826	1.742	1.924	Pb-O
2.82	2.83	2.85	5.782	5.692	5.452	Pb-O, O-O
3.37	3.30	3.30	2.888	2.904	2.978	Pb-O
3.6[1]	3.57	3.65	1.851	1.830	1.882	Pb-Pb, Mg/Nb-Pb

1. No distinct peak observed.

Table 1. Nearest neighbor peak positions and integrated intensities.

long and, to a lesser extent, intermediate Pb-O distances as indicated by the integrated intensities. At 10K the intermediate range has been depleted in favor of both short and long Pb-O nearest neighbor distances.

CONCLUSIONS

We find significant temperature dependent shifts in the distribution of both Mg/Nb-O and Pb-O nearest neighbor distances, the trend being toward a decrease in the number of intermediate pair separations as the temperature is reduced below the Curie temperature. We

believe the increase in number of extreme Mg/Nb-O and Pb-O nearest neighbor distances below the Curie temperature is responsible for bulk ferroelectricity in PMN. The presence of these short and long pair separations at all temperatures suggests that PMN is locally ferroelectric above T_c.

Acknowledgements

The authors would like to acknowledge Prof. S. K. Kurtz for the suggestion of applying the real space method to relaxor ferroelectrics, Brian Toby and Prof. P. K. Davies for useful discussions and Jiu-qi Huang for assisting with analysis. Work at the University of Pennsylvania was supported by the National Science Foundation through the MRL Grant DMR-8819885. The Intense Pulsed Neutron Source is operated as a user facility by the U.S. Department of Energy, Division of Materials Sciences, under contract W-31-109-Eng-38.

REFERENCES

[1] L. E. Cross, "Relaxor Ferroelectrics," Ferroelectrics, Vol. 76, pp. 241-267, 1987.

[2] P. Bonneau, P. Garnier, E. Husson and A. Morrell, "Structural Study of PMN Ceramics by X-ray Diffraction Between 297 and 1023 k," Mat. Res. Bull., Vol. 24, pp. 201-206, 1989.

[3] G. A. Smolenskii and A. I. Agranovskaya, Soviet Physics Solid State, pp. 1429, 1959.

[4] E. Husson, L. Abello and A. Morell, "Short Range Order in $PbMg_{1/3}Nb_{2/3}O_3$ Ceramics By Raman Spectroscopy," Mat. Res. Bull., Vol. 25, pp. 539-545, 1990.

[5] H. D. Rosenfeld, T. Egami and A. Bhalla, "A Neutron Powder Diffraction Study of Short Range Order in Ferroelectric $Pb(Mg_{1/3}Nb_{2/3})O_3$," (To Be Published)

[6] IPNS Note 19, IPNS, Argonne National Laboratory.

[7] B. E. Warren, X-ray Diffraction. Reading, Mass.: Addison-Wesley, 1969, ch. 10, pp. 120-130.

National Institute of Standards and Technology Special Publication 804, Chemistry of Electronic Ceramic Materials, Proceedings of the International Conference held in Jackson, WY, August 17-22, 1990, issued January 1991.

MECHANISM OF PNN BASED PEROVSKITE CERAMICS FORMATION

Yukichi Sasaki, Akira Nagai, Tetsuo Yoshimoto
Odawara Research Center,Nippon Soda Co.,Ltd.
345 Takada Odawara Kanagawa, 250-02 JAPAN

Introduction

It is well known that multicomponent lead perovskite materials are promising candidates for applications in multilayer-capacitor. $Pb(Mg_{1/3}Nb_{2/3})O_3$ (PMN), $Pb(Ni_{1/3}Nb_{2/3})O_3$ (PNN), $PbTiO_3$ (PT) are representatives of lead perovskite materials. The dielectric constant for the three component solid-solution system of PNN-PMN-PT is about 20,000 to 23,000 and the value of T.C.C(Thermal Coefficient of Capacitance) for the solid-soluton satisfies the requirements of the Y5V specification by the E.I.A.

When that solid solution is prepared by the conventional oxide mixing process, lead-based pyrochlore phases mainly occur at first. However, it is reported that the columbite precursor method is very effective restraining the formation of the pyrochlore phase. The calcination reactions were studied in detail to confirm the relationship between the crystal structure and the calcining temperature which is much influenced by powder processing. The XRD studies showed many differences in the calcination reaction between PNN and PMN in spite of having the same crystal structure which has the general fomula $Pb(B1_{1/3}B2_{2/3})O_3$. Therefore, for PMN there was little pyrochlore phase produced by the columbite process, but for PNN the pyrochlore phase was formed as much as in the conventional oxide process even when the columbite process was used. And also the sintered pellets of the conventional oxide mixing process often contained inclusions in the grains. The microstructure and the chemical compositions of the inclusions were determined by SEM-WDS and TEM-EDS.

Experimental Procedure

(1)Powder preparations

The material composition we used for this experiment was ternary multicomponent lead perovskite system, with the chemical formula $20Pb(Mg_{1/3}Nb_{2/3})O_3$-$60Pb(Ni_{1/3}Nb_{2/3})O_3$-$20PbTiO_3$. Powders were prepared using three different methods and the flowcharts for those three methods are given in fig.1.

(2)Studies of the calcination reaction

To investigate the calcination reaction each powder was heat-treated at 600-900℃, using a magnesia crucible in a closed atmosphere. These calcined powders were identified by X-ray diffraction at a scanning rate of 2.4° /min.
Furthermore, PMN and PNN, which are the main components of this solid solution, were investigated individually.

(3)Microstructure of sintered pellet

The microstructure of these sintered pellets were observed by TEM-EDS and SEM-WDS. The samples were polished and etched with 20wt% phosphoric acid solution before SEM observation.

Then for each polished sintered pellet(10mmφdisk), 16 points on the surface were analyzed by high resolution SEM-WDS and the measured values were statistically calculated in order to investigate the homogeneity of the constituent elements.

Results and Discussion

(1)Calcination reaction of PNN-PMN-PT system (fig.2)

①Conventional oxide process

The calcination reaction on the conventional oxide process occurs approximately as follows.

$PbO+NiO+MgO+TiO_2+Nb_2O_5$

$\sim 600℃ \rightarrow$ Pyrochlore(1)+NiO+MgO+$PbTiO_3$ <1>

$650\sim 700℃ \rightarrow$ Pyrochlore(1)+Pyrochlore(2)+PbO +(NiO+MgO+$PbTiO_3$) <2>

$\sim 750℃ \rightarrow$ Pyrochlore(2)+PbO+(NiO+MgO+$PbTiO_3$) <3>

$800\sim 850℃ \rightarrow$ Pyrochlore(2)+PbO+Perovskite*+(NiO+MgO) <4>

$\sim 900℃ \rightarrow$ Perovskite* <5>

Pyrochlore(1):$Pb_{14}Nb_{10}O_{39}$	┐ NiO and/or MgO
Pyrochlore(2):$Pb_3Nb_4O_{13}$	┘ are solid-solved
Perovskite* :PNN-PMN-PT solide-solution	

In this reaction, most of the PbO,Nb_2O_5 and TiO_2 were changed to pyrochlore(1) and $PbTiO_3$ at about 600℃. XRD peaks of the Nb_2O_5 and PbO vanished at that temperature, and a part of pyrochlore(1) decomposed to pyrochlore(2) and PbO at 650~700℃. Then, the PbO was reproduced again in this system. The decomposition reaction is $Pb_{14}Nb_{10}O_{39} \rightarrow 5/2Pb_3Nb_4O_{13} + 13/2PbO$, and it was accelerated at 700~750℃. At 800~850℃ other perovskite compounds were produced and formed a solid solution with the $PbTiO_3$. Finally the reaction product was changed to single phase. On the other two processes, this three component solid solution was produced under the similar reaction mechanism, but there were some differences from the conventional oxide process.

②Columbite precursor process

1. The amount of reproduced PbO was less in the columbite precursor process than in the conventional oxide process, and little PbO was observed at 800℃.
2. It is possible to obtain a single phase of perovskite in the columbite process at about 50℃ lower than in the conventional oxide process.

③Alkoxide process

1. The same amount of PbO was reproduced during the calcining reaction in both the alkoxide process and the conventional oxide process, but the PbO was not observed at 800℃.
2. The mechanism of the calcination reaction for the alkoxide process was the same as for the conventional oxide process up to 750℃, but in the alkoxide process the reaction proceeded quickly, and the complete monophase material was obtained at 800℃.

(2)Calcination reaction of PNN and PMN

The calcination reaction was examined for PNN and PMN individually in order to investigate the influence of the powder processing in more detail (fig.2).

As the result it was confirmed that the mechanism of the calcination reaction depended on the process for preparing the PMN. When the PMN was prepared by the conventional

oxide process, that reaction proceeded like <1>~<5> reaction. But, by the columbite precursor process the PMN perovskite phase was produced directly in the calcination reaction and little pyrochlore phase appeared. On the other hand, PNN did not depend on the powder processing, and even though the previously prepared $NiNb_2O_6$ was reacted with PbO, the pyrochlore phase was appeared. The difference between the $NiNb_2O_6$ and $MgNb_2O_6$ in the reaction with the PbO is supposed as follows.

PMN: $3PbO+MgNb_2O_6 \rightarrow 3Pb(Mg_{1/3}Nb_{2/3})O_3$ <6>

PNN: $3PbO+NiNb_2O_6 \rightarrow$ Pyrochlore(1)+NiO <7>
$\rightarrow$ Pyrochlore(2)+PbO+NiO <8>
$\rightarrow$ Perovskite <9>

Thus, the PMN and PNN are the same $Pb(B1_{1/3}B2_{2/3})O_3$ perovskite compounds, but there is a difference in the calcination reaction according to the powder preparation processes between the PMN and the PNN.

(3)Microstructue study

Moreover, to confirm the above presumption the microstructure of the sintered pellets was observed by SEM and TEM. After thermal and chemical etching, we could see small circular traces in SEM images. Since some of those traces were not falling off and remained, we considered that these were not pores or defects but inclusions which were observed in the sintered grains by SEM (fig.3)

These inclusions were seen in both the conventional oxide process and the columbite precursor process. In the alkoxide process we could not see such inclusions as those observed in the oxide process or columbite process, and by TEM-EDS study, it is understood that the chemical composition of these inclusions was different between the oxide process and the columbite process. Namely, the inclusions in the conventional oxide process pellets were composed of NiO and MgO but those in the columbite process pellets were composed of only NiO (fig.4). The reason of this difference is considered as follows.

1.In the conventional oxide process, the PbO reacted with Nb_2O_5 more preferably than NiO or MgO, and the pyrochlore phase formed prior to the perovskite phase. So some of the free NiO and MgO remained as inclusions in the grains or between the grains after perovskite formation was finished.

2.In the columbite process, $MgNb_2O_6$ columbite reacted with PbO to form the perovskite phase directly but $NiNb_2O_6$ columbite reacted with PbO to decompose its structure and to form NiO and the pyrochlore phase to some extent. So NiO only was observed for the inclusion in the sintered pellet.

Then we studied the compositional homogeneity of the sintered pellets by SEM-WDS analysis. The homogeneity of B-site ion constituents is not good in the oxide and is very good in the alkoxide process. For the columbite process the medium value between the oxide process and the alkoxide process was obtained. Therefore, it is supposed that this compositional homogeneity measured by SEM-WDS has a close relation with the presence of the inclusions in the sintered pellets.

Conclusion

(1)There is a large difference in the formation reaction mechanism between PMN and PNN in spite of having the same $Pb(B1_{1/3}B2_{2/3})O_3$ perovskite structure. For PMN it is easy

to form the perovskite single-pahse compounds by using the columbite process. But for PNN it is difficult to form the perovskite phase even if columbite process is used.

(2)The reaction mechanism of PNN-PMN-PT ternary solid solution formation varies with the powder processing method, and this is attributed mainly to the reaction mechanisms of the PMN formation.

(3)The chemical composition of the inclusions in the sintered pellets varies with the powder processing methods, and this inclusion formation has a strong influence on the compositional homogeneity of the sintered pellets.

References

1.S.L.Swartz, T.R.Shrout Mat.Res.Bull., 17 (1982) 1245-1250

2.T.R.Shrout, Arvind Halliyal Am.Ceram.Soc.Bull., 66[4] (1987) 704-711

3.M.Backhaus-Ricoult, D.Ricoult J.Materials Sience, 23 (1988) 1309-1316

4.A.Nagai, Y.Sasaki, T.Yoshimoto Ferroelectrics, 102 (1990) 117-127

5.J.P.Guha, H.U.Anderson J.Am.Ceram.Soc., 70[3] (1987) C-39 - C-40

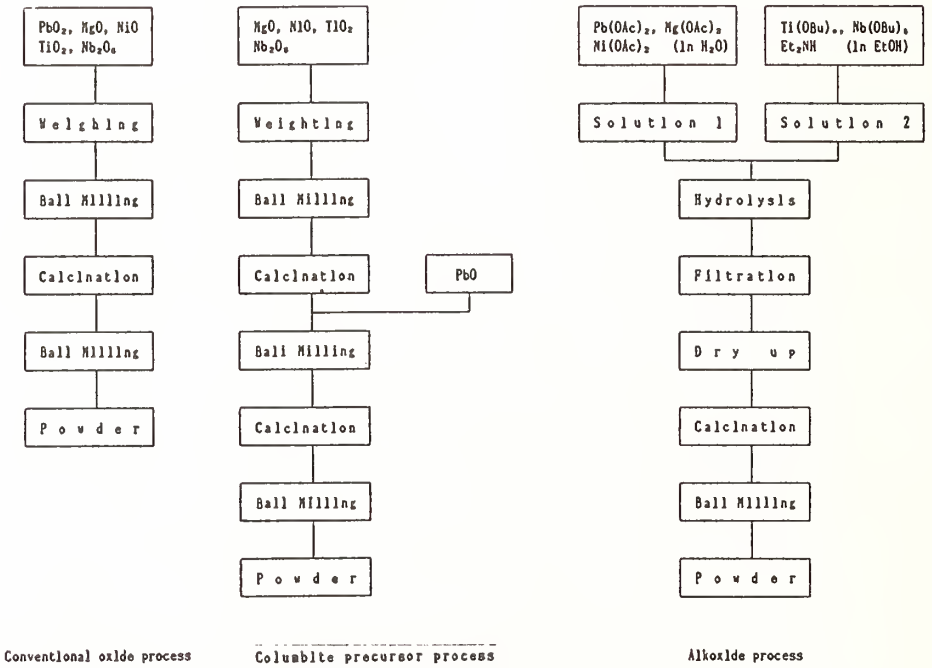

Figure 1 Processing flowchart for powder preparation.

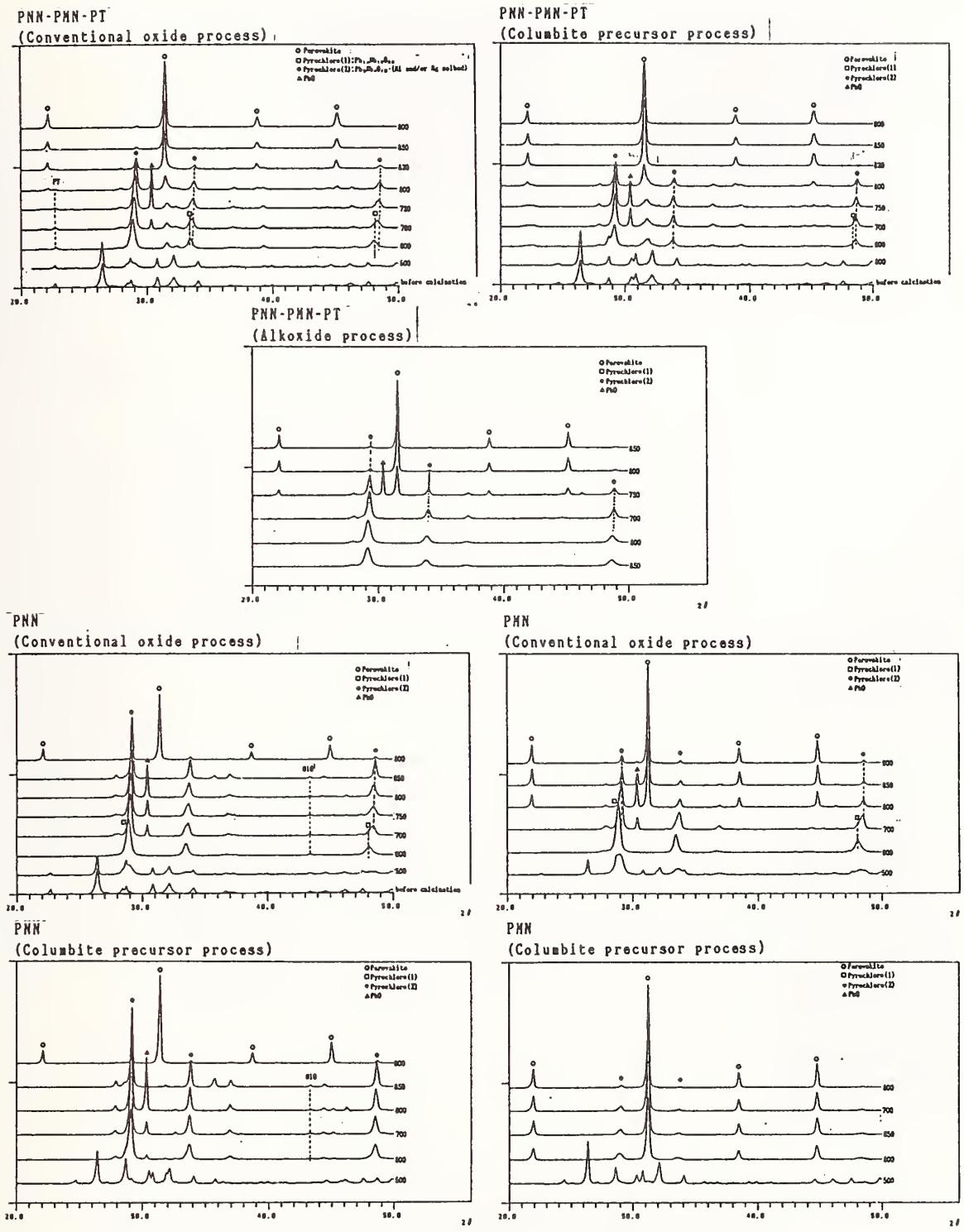

Figure 2 X-ray diffraction patterns of the calcined powder.

Figure 3 SEM photographs of the etched surfaces. The surface was chemically etched by 20wt% phosphoric acid after thermal etching.

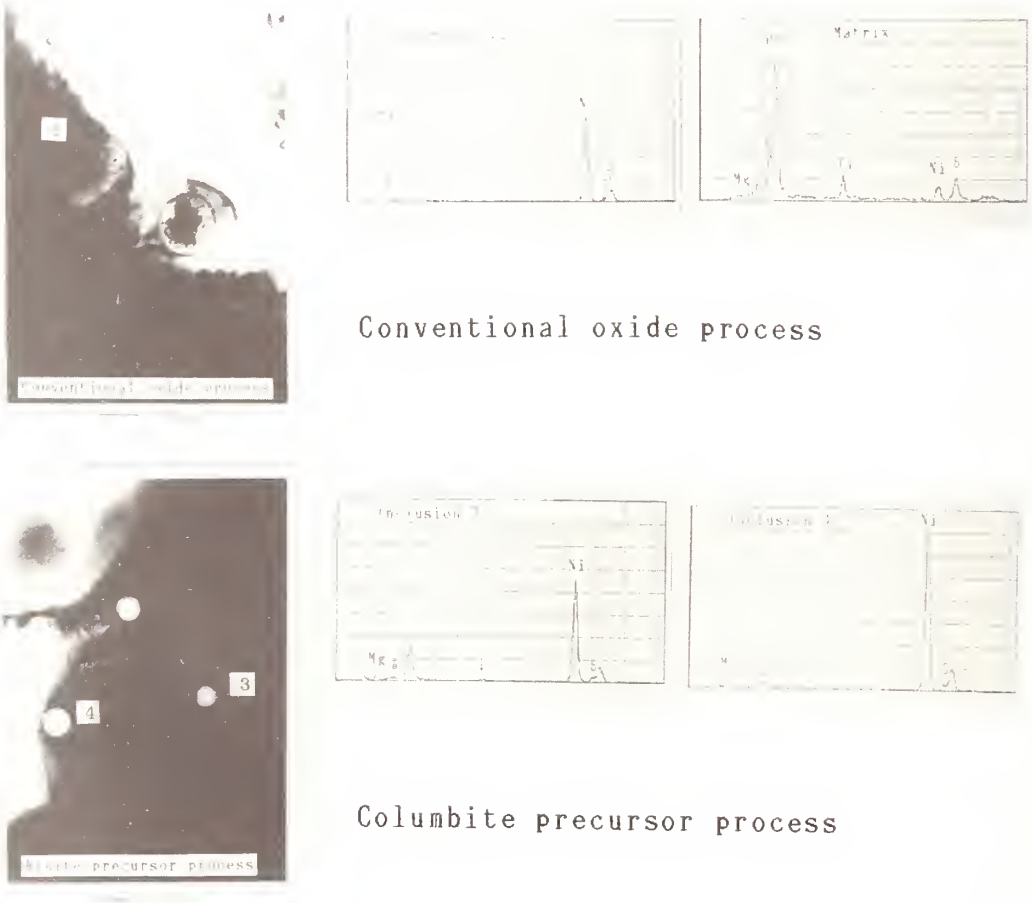

Figure 4 TEM photographs and EDS spectrums of sintered pellets.

National Institute of Standards and Technology Special Publication 804, Chemistry of Electronic Ceramic Materials, Proceedings of the International Conference held in Jackson, WY, August 17-22, 1990, issued January 1991.

CONVENTIONALLY PREPARED SUBMICRON ELECTRO-CERAMIC POWDERS BY REACTIVE CALCINATION

Thomas R. Shrout
Pennsylvania State University
Materials Research Laboratory
University Park, PA 16802

ABSTRACT

It is the physiochemical nature of lead-based perovskites $Pb(B)O_3$ that upon reaction of the component oxides a large volumetric expansion occurs. In addition to perovskites, Pb- and Bi-based pyrochlores ($A_2B_2O_7$) and the layered structure compound $Bi_4Ti_3O_{12}$ also exhibit similar physiochemical behavior. At the temperature of maximum expansion, the associated morphological development results in a porous skeletal type structure consisting of fine particulates that can be readily broken down further by milling. The level of expansion and ease of comminution was shown to be strongly dependent on the starting powder size, using perovskite $Pb(ZrTi)O_3$ as the example. Using this concept of "reactive calcination," the state of optimum soft agglomeration and subsequent milling can allow for fully reacted powder with submicron particle size.

INTRODUCTION

With the continuing miniaturization of electronics including ceramic devices such as multilayer capacitors, ultrasonic transducers, sensors, piezo motors, and electrostrictive actuators, the importance of fine and phase pure starting powders becomes ever so more evident. Such powders also allow the potential for novel applications such as ferro-fluids which require finely dispersed submicron powders in a liquid medium.[1] Fundamentally, submicron to nano-sized powders are of interest in the understanding of the role of "scale" on intrinsic physical phenomena such as ferroelectricity and related behavior.[2]

Numerous methods to produce submicron powders have been developed with emphasis on the perovskite ABO_3 family of materials. Methods include chemical synthesis techniques such as co-precipitation of alkoxides, molten salt, and hydrothermal. However, most chemical synthesis techniques are relatively costly and do not lend themselves for mass production.

Recently, submicrometer powders of Pb-based perovskites including $PbTiO_3$, $PbZrO_3$, $Pb(Zr_{.53}Ti_{.47})O_3$ and $Pb(Mg_{1/3}Nb_{2/3})O_3$ were prepared by a reactive calcination process.[3] Using only reagent-grade raw materials and conventional processing techniques, highly reactive powders were produced by reacting the materials near the temperature of maximum volumetric expansion. At this point, the associated morphological development results in a skeletal-type

structure consisting of ultra-fine particulates than can be readily broken down by milling (see Fig. 1). Powder sizes < 0.1 μm were produced allowing enhanced densification and correspondingly small grain sizes.[4,5]

The objective of this work was to further optimize the "reactive calcination" process of lead-based perovskite through control of the starting powder characteristics. It was a further objective to explore the potential of reactive calcination in non-PbO perovskites and other electro-ceramic structural families through knowledge of their physiochemical behavior.

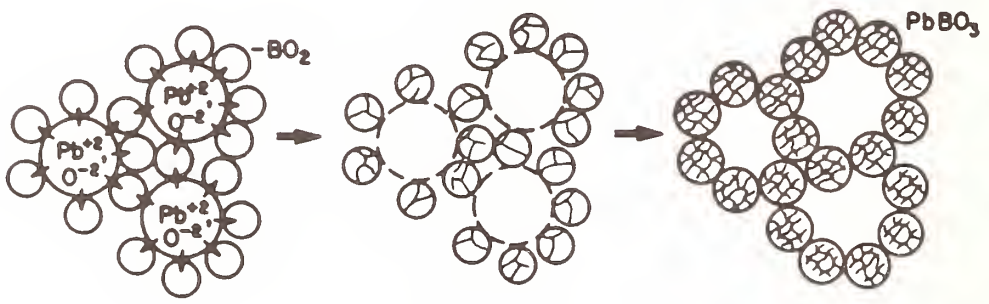

Figure 1. Schematic representation of the perovskite $PbBO_3$ formation and associated morphological changes.[3]

EXPERIMENTAL PROCEDURE

The Pb-based perovskite material chosen to examine the role of component powder characteristics on reactive calcination was the solid solution $Pb(Zr_{.53}Ti_{.47})O_3$ (PZT). Non-perovskite materials investigated included the pyrochlores $Pb_2Nb_2O_7$ and $Bi_2Ti_2O_7$ and $Bi_4Ti_3O_{12}$ layer structure compound. The non-PbO perovskite $(Na_{1/2}Bi_{1/2})TiO_3$ was also studied.

Reagent-grade raw materials were used to prepare the compounds as described in ref. 3. The component powders were characterized by determining their as-received surface area and particle size.

Since intermediate reactions occur in the formation of the complex perovskite PZT, the B-site precursor method developed by Swartz and Shrout[6] was used whereby the ZrO_2 and TiO_2 oxide were pre-reacted prior to reaction with PbO as follows:

$$0.53\ ZrO_2 + 0.47\ TiO_2 \xrightarrow{\sim 1400\ ^\circ C\ /\ 4hr} Zr_{.53}Ti_{.47}O_2 \quad \text{(rutile)} \qquad [1]$$

$$PbO + Zr_{.53}Ti_{.47}O_2 \rightarrow PZT \quad \text{(perovskite)} \qquad [2]$$

Variations in particle sizes of both the PbO and Zr,TiO_2 oxides were prepared by vibratory or attrition milling. The powder size schemes for reactive calcination of PZT are schematically shown in Fig. 2.

Stoichiometric mixtures of the component oxides for all the compounds studied were prepared by vibratory mixing in ethyl alcohol or de-ionized H_2O and polyelectrolyte dispersant at a pH where minimal dissolution of Pb^{+2} occurs.(7) Upon drying, the powders were pressed into disks of similar packing densities.

The possibility and/or extent of reactive calcination was determined by the degree of volumetric expansion and corresponding temperature reaction range. This was performed by placing pressed disks in a furnace (open air) and heated at a rate of ~ 100°C/hr. Above 500°C, disks were quenched at 25 to 50°C intervals by being pulled directly from the furnace and allowed to cool in air. Sample geometries were used to determine the degree of volumetric expansion or shrinkage. The disks were then crushed and powder XRD analysis performed to determine the amount of phase reaction and subsequent particle characteristics. SEM microstructural analysis of selected powder compacts (before and after crushing) were also examined to examine morphological development during reaction.

Based on these results, large quantities of (~ 1 kg) PZT packed powders were prepared. The powders were calcined for 4 hrs approximately 50°C below the maximum expansion (to allow for kinetics) and at higher temperatures to demonstrate the point of optimum skeletal formation and subsequent consequence on milling efficiency. Slurries of the calcined powders were prepared as before and attrition milled while samples were removed at various intervals. The milled powders were then characterized by specific surface area. The primary particle size was determined through the equation

$$D = \frac{6}{\rho SA} \qquad [3]$$

where ρ is the theoretical density, SA the surface area, and D the calculated primary particle size.

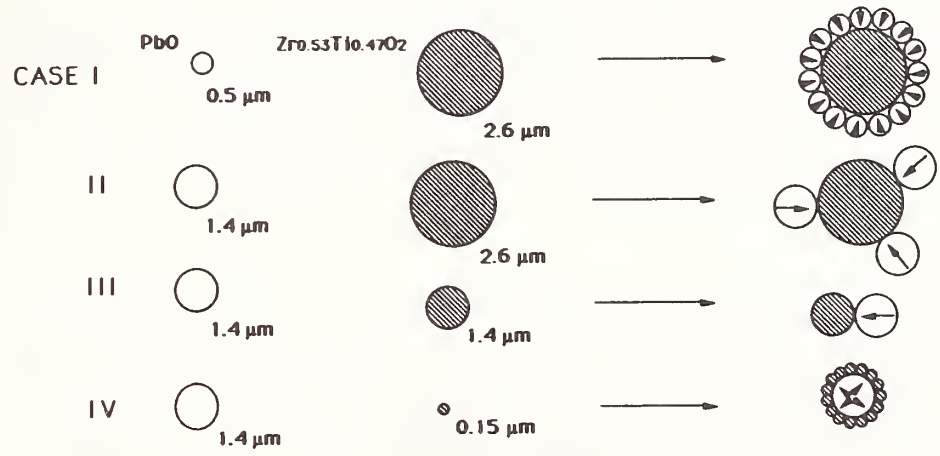

Figure 2. Component powder size schemes for the formation of perovskite PZT.

RESULTS AND DISCUSSION

Instinctively, one expects that ceramic powder compacts should shrink on reaction as a consequence of higher product densities, as found for non-PbO perovskites. The volumetric expansion observed during the formation of Pb-based perovskites is reportedly the result of molar volume differences in the component oxides and subsequent perovskite phase. Attempts to predict relative volume expansions for various compounds clearly suggests the expansion behavior is also dependent on the particle packing and size characteristics as proposed in Fig. 2.

The importance of particle characteristics on reactive calcination is clearly evident in Fig. 3, showing the impact of PbO particle size on the volume expansion during the formation of perovskite PZT. As presented, fine PbO (Case I) resulted in shrinkage prior to a relatively small volume expansion and associated formation of the perovskite phase. The shrinkage is believed to be the result of the highly reactive nature of the fine PbO particle/agglomerates which sinter prior to reaction with the coarser Zr,TiO_2 particles. The impact of Zr,TiO_2, particle size, clearly shows that the finer material enhanced the formation of perovskite PZT, but the reactive nature of the fine powder and less open skeletal structure lead to densification at relatively low temperatures (Case IV). For Case III, where PbO and Zr,TiO_2 are of similar size, resulted in the largest volume expansion. Of particular interest is that once the skeletal structure was formed, densification did not occur even up to temperatures of 1000°C. Hence, inhomogeneous densification (low coordination number of reaction regions) was optimized. The importance of this behavior is clearly evident in Fig. 4, whereby the ease in which the skeletal structures can be broken down is given in terms of a milling factor. As shown, the skeletal sructure associated with Case III was readily broken down by milling with an order of magnitude decrease in particle size in only one hour. A large volume change found over an extensive temperature range (Case III), thus, allows for a broader calcination process window. Further implications of the morphological development of these materials will be presented in the summary.

The morphological behavior presented above was not found to be unique to Pb-perovskites but was also observed in the Pb-based pyrochlore phase $Pb_2Nb_2O_7$ as shown in Fig. 5. Analogous to Pb, the Bi-based perovskite $Na_{0.5}Bi_{0.5}TiO_3$, pyrochlore $Bi_2Ti_2O_7$ and layer structure $Bi_4Ti_3O_{12}$ compounds also exhibited similar behavior, but to a lesser degree. It is important to note that at the point of maximum volumetric expansion corresponds to the formation of the expected phase.

CONCLUSION

The volumetric expansion and morphological development associated with the formation of Pb-based perovskites was found to be strongly dependent on the starting powder characteristics, using perovskite $Pb(ZrTi)O_3$ as the example. The resulting porous skeletal structure of perovskite particulates was found to be readily broken down into submicron particles by milling. In addition to Pb-based perovskites, Pb- and Bi-based pyrochlores ($A_2B_2O_7$), the layered structure compound $Bi_4Ti_3O_{12}$ and $(Na_{1/2}Bi_{1/2})TiO_3$ perovskite were also found to exhibit

similar physiochemical behavior. Using this concept of "reactive calcination" the point of maximum expansion can be used as a characterization tool to determine the optimum state of soft agglomeration to provide highly reactive powders.

Further investigation and modeling of particle size and packing effects on reactive calcination are still required.

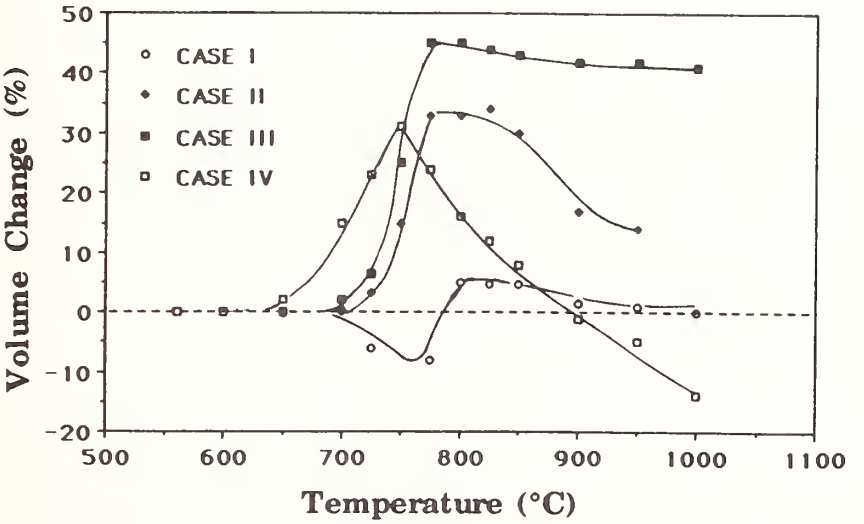

Figure 3. Volumetric expansion-shrinkage characteristics of PZT as a function of temperature for various component sizes.

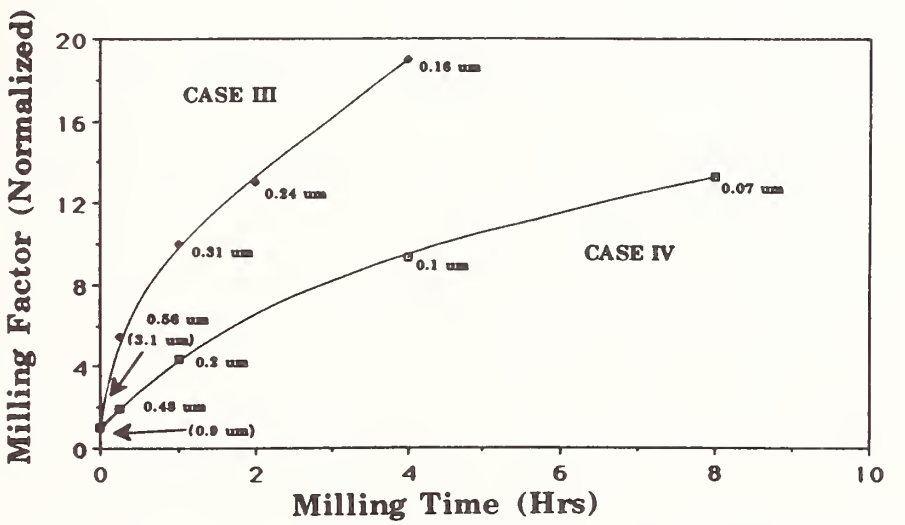

Figure 4. Milling factor (normalized) for reactively calcined PZT (Cases III (3.1 μm) and IV (0.9 μm)) as a function of milling (attrition) time.

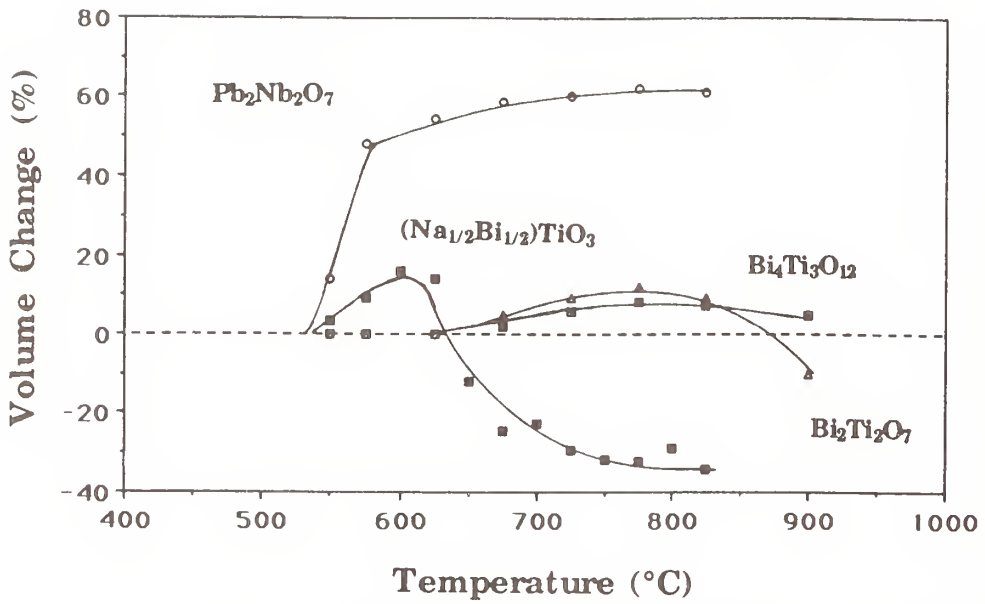

Figure 5. Volumetric expansion-shrinkage characteristics of $Pb_2Nb_2O_7$, $Bi_2Ti_2O_7$ (pyrochlore), $Na_{0.5}Bi_{0.5}TiO_3$ (perovskite) and $Bi_4Ti_3O_{12}$ (larger structure).

ACKNOWLEDGEMENTS

The author wishes to thank Beth Jones for her technical skills and Drs. Venkataramani, G.S. Lee, and J.H. Adair for their helpful discussions.

REFERENCES

1. J.U. Muller and K. Barner. "Polydisperse Suspensions of $BaTiO_3$ Particles," *Ferroelectrics*, 108, 83-88 (1990).

2. K. Uchino, E. Sadamaga, and T. Hirose. "Dependence of the Crystal Structure on Particle Size in Barium Titanate," *J. Am. Ceram. Soc.*, 72[8], 1555-1558 (1989).

3. T.R. Shrout, P. Papet, S. Kim, and G.S. Lee. "Conventionally Prepared Submicrometer Lead-Based Perovskite Powders by Reactive Calcination," *J. Am. Ceram. Soc.*, 73[3], 1862-1867 (1990).

4. P. Papet, J.P. Dougherty, and T.R. Shrout. "Particle and Grain Size Effects on the Dielectric Behavior of the Relaxor Ferroelectric $Pb(Mg_{1/3}Nb_{2/3})O_3$," (to be published in *J. Mat. Res.*).

5. S. Kim, G.S. Lee, and T.R. Shrout. "Fabrication of Fine Grain Piezoelectric Ceramics Using Reactive Calcination," (to be published in *J. Mat. Sci.*).

6. S.L. Swartz and T.R. Shrout. "Fabrication of Perovskite Lead Magnesium Niobate," *Mater. Res. Bull.*, 17, 1245-1250 (1982).

7. M. Pourbaix. Atlas of Electrochemical Equilibria in Aqueous Solutions, National Association of Corrosion Engineers (1974).

II. LOW-TEMPERATURE SYNTHESIS AND CHARACTERIZATION

National Institute of Standards and Technology Special Publication 804, Chemistry of Electronic Ceramic Materials, Proceedings of the International Conference held in Jackson, WY, August 17-22, 1990, issued January 1991.

PREPARATION OF $YBa_2Cu_3O_{7-\delta}$ FROM HOMOGENEOUS METAL ALKOXIDE SOLUTION; SYNTHESES OF MIXED-LIGAND COPPER (II) ALKOXIDES

D. M. Millar* and D. A. Payne
Department of Materials Science and Engineering,
Materials Research Laboratory, Beckman Institute,
and Science and Technology Center for Superconductivity,
University of Illinois at Urbana-Champaign, Urbana, IL 61801

ABSTRACT

Mixed-ligand copper (II) alkoxides of the type $(C_5H_7O_2)_2Cu_2(\mu\text{-}OR)_2$, $C_5H_7O_2$ = 2,4-pentanedionate, R = $CH_2CH_2OCH_3$ (**1**) and n-C_4H_9 (**2**), have been synthesized as precursors for the preparation of superconducting $YBa_2Cu_3O_7$ thin layers. Crystallization from n-butanol yielded crystals of **2** suitable for x-ray structure determination. The molecule consists of two approximately planar n-butoxy-bridged dimers $(C_5H_7O_2)Cu(\mu\text{-}OC_4H_9)_2Cu(O_2C_5H_7)$ linked by four apical Cu-O bonds (2.443(4)Å) involving each of the n-butoxy-oxygen atoms. The dimers are situated such that the two Cu_2O_2 units are rotated 90° with respect to each other. Comparison of the IR spectra of compounds **1** and **2** suggest that in **1**, dimer linkage also occurs between one pentanedionate oxygen atom of each unit and a copper atom of the opposing dimer. This dual coordination of the pentanedionate prevents subsequent reactions of this ligand with barium alkoxides, making compound **1** a suitable precursor for formation of 1:2:3 Y:Ba:Cu solutions. Superconducting thin-layers have been prepared from these solutions by spin-casting methods.

INTRODUCTION

Ever since Bednorz and Müller[1] first reported the unusually high temperature superconductivity in $(La,Ba)_2CuO_4$, increased attention has been focussed on a broad class of high T_c ceramic superconductors. In addition to attempts to increase T_c by new oxide compositions, much work has been directed towards processing superconducting oxides such as $YBa_2Cu_3O_{7-\delta}$ into technologically useful forms.[2] Of particular interest has been the preparation of thin layers due to their potential applications on semiconductor and electronic devices. Preparation of such layers by rf sputtering,[3] electron beam de-composition,[4] or metal-organic chemical vapor deposition[5] methods have been successfully demonstrated. However, these techniques require sophisticated equipment and

---

* Currently with Central Research, The Dow Chemical Company, Midland, MI, 48674

extreme processing conditions. Deposition of $YBa_2Cu_3O_{7-\delta}$ layers from solutions of the corresponding alkoxides offers the possibility of avoiding these extreme processing conditions, [6,7] as well as the potential for preparing highly homogeneous products.

As part of a larger effort of research on the chemical processing of electrical ceramic materials, we have investigated the preparation of $YBa_2Cu_3O_{7-\delta}$ thin layers and powders from homogeneous metal-alkoxide solutions. This paper describes the synthesis and characterization of a series of unique mixed-ligand copper (II) alkoxides of the type $(C_5H_7O_2)_2Cu_2(\mu\text{-}OR)_2$.

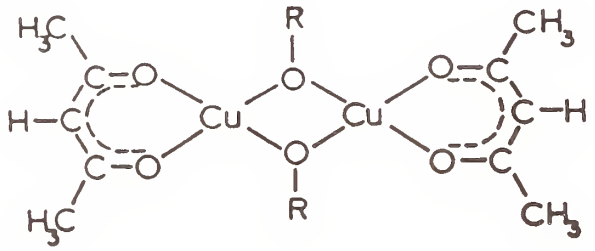

This system avoids the usual oligomerization of copper (II) alkoxides, and the subsequent insolubility by filling two copper coordination sites with a chelating ß-diketonate, 2,4-pentanedionate ($C_5H_7O_2$). The remaining coordination sites about the copper atoms are filled with doubly bridging alkoxy groups. Of particular interest is the system where these bridging alkoxides are derived from 2-methoxyethanol, R = $CH_2CH_2OCH_3$. Reaction of this readily soluble material with the corresponding yttrium and barium alkoxides results in homogeneous 1:2:3 Y:Ba:Cu solutions from which thin layers or powders can be obtained.

EXPERIMENTAL

REAGANTS, SOLVENTS AND GENERAL PROCEDURES

The following chemicals were purchased from commercial sources and used without further purification: $Cu(NO_3)_2 \cdot 2H_2O$ (Mallinkrodt) 2,4-pentanedione (Aldrich); NH_4OH (Mallinkrodt); CH_3OH (Baker); KOH (Fischer); n-butanol (Aldrich); barium granules (Alfa); yttrium isopropoxide (Alfa). HPLC grade 2-methoxyethanol (Aldrich) was obtained in Sure-Seal bottles and transferred and stored under dry nitrogen.

Sapphire wafers (1.5 cm diameter, 350 µm thickness, one side polished, 0001 axis parallel to surface) (Insaco, Inc.) and platinum substrates (12 mm x 12 mm x 0.5 mm) were cleaned by sequential ultrasonication in trichlorethylene, acetone, and 2-methoxyethanol, then air dried.

Thin layers were prepared as described below by spin-casting onto the substrates using a Headway Research Photoresist Spinner.

ANALYTICAL PROCEDURES. Elemental Analyses were carried out by the University of Illinois School of Chemical Sciences Analytical Laboratory. Mass Spectrometry was done in the School of Chemical Sciences Mass Spectrometry Laboratory. FTIR spectra were obtained from KI pellets using an IBM IR/32 spectrometer. Single-crystal X-ray diffraction studies were carried out by Dr. Scott Wilson in the School of Chemical Sciences X-ray Diffraction Laboratory.

PREPARATION OF $(C_5H_7O_2)_2Cu$ (II).[8] A 1L flask was fitted with a pressure-equalizing addition funnel and loaded with 50 g (0.224 mol) $Cu(NO_3)_2 \cdot 2H_2O$ and 500 mL deionized water, followed by 75 mL concentrated NH_4OH. To the rapidly stirred, deep blue solution, 55 mL (0.534 mol) 2,3-pentanedione were added dropwise over a 1 hr period. Pale blue $(C_5H_7O_2)_2Cu$ was collected as a wet precipitate by vacuum filtration 30 minutes after complete addition. This material was dissolved in 900 mL $HCCl_3$ and a clear colorless, aqueous layer separated from the deep blue organic phase in a separatory funnel. The volume of the $HCCl_3$ solution was reduced one-third by removal of the solvent by distillation. Upon slow cooling to room temperature, dark blue crystalline $(C_5H_7O_2)_2Cu$ was obtained and collected by vacuum filtration. This procedure was repeated until no further crystalline product was obtained. A total of 46.17 g (0.178 mol) were collected, a yield of 80% based on the original amount of Cu(II). IR (KI pellet, 1400-400 cm^{-1}) 1356(s), 1275(s), 1190(m) 1020(s), 937(s), 783 (vs), 685(m), 654(m), 613(m), 455(vs), 430(w).

PREPARATION OF $(C_5H_7O_2)_2Cu_2(\mu\text{-}OCH_3)_2$ (1).[9] A 1L flask fitted with a pressure equalizing addition funnel and a reflux condensor vented to a Nujol bubbler was loaded with 5.4 g (20.9 mmol) $(C_5H_7O_2)_2Cu$ and 500 mL CH_3OH. The addition funnel was charged with a methanolic KOH solution (1.2 g KOH in 50 mL CH_3OH). This solution was added dropwise to the refluxing $(C_5H_7O_2)_2$ Cu suspension over a 2 hr period. Thirty minutes after complete addition, heating was stopped and the mixture cooled to room temperature. Vacuum filtration of the resulting suspension produced 3.18 g (8.2 mmol) violet $(C_5H_7O_2)_2$ $Cu2(\mu\text{-}OCH_3)_2$, a yield of 79% based on the original amount of Cu(II). Anal. Calcd for $C_6H_{10}O_3Cu$:C,37.21; H,5.21; Cu, 32.81. Found: C,37.14; H,5.23; Cu,32.91. IR (KI pellet, 1400-400cm^{-1}, bands in addition to those for $(C_5H_7O_2)_2$ Cu) 1071 (s), 554 (vs).

PREPARATION OF $(C_5H_7O_2)_2Cu_2(\mu\text{-}OCH_2CH_2OCH_3)_2$ (2) A 100 mL flask was loaded with 1.0 g (2.58 mmol) of 1 and 40 mL 2-methoxyethanol added by syringe. A reflux condensor vented to a N_2 inlet/Nujol bubbler was added and the slurry heated in a 90°C oil bath. After 1.5 hr at this temperature, all volatiles were removed under vacuum. Turquoise-solid 2 was obtained as a fine powder and 1.19 gl (2.50 mmol) were collected, a yield of 97% based on the original amount of Cu(II). Anal. Calcd for $C_8H_{14}O_4Cu$: C,40.42; H. 5.95; Cu, 26.73. Found: C, 40.23; H, 5.99; Cu, 26.62. MS. m/z = 476 (M^+). IR (KI pellet, 1400-400 cm^{-1}, bands in addition to those for $(C_5H_7O_2)_2$ Cu) 1240 (w), 1123 (s), 1075 (s), 966 (m), 901 (m) 839 (w), 764 (m) 588 (m) 575 (w), 513 (m), 450 (m).

PREPARATION OF $(C_5H_7O_2)_2Cu_2(\mu\text{-}OC_4H_9)_2$ (3) This compound was prepared identically to 2 above using n-butanol as the solvent. Blue-green 3 was obtained as a fine powder with 1.21 g (2.56 mmol) collected, an essentially quantitative yield. IR (KI pellet, 1400-400 cm^{-1}, bands in addition to those for $(C_5H_7O_2)$ Cu) 1240 (w), 1117 (m), 1073 (s), 950 (w), 840 (w), 768 (m), 630 (w), 552 (m), 507 (m).

PREPARATION OF $Ba(OC_4H_9)_2$ SOLUTION. In a glove box, an oven-dried 50mL flask was loaded with 3.43 g (25.0 mmol) Ba granules, and an oven-dried addition funnel and reflux condensor with N_2 inlet added. In a fume hood, 10mL Na_2SO_4 dried pentane was added by syringe and the suspension stirred vigorously. To this mixture, 25 mL (25.0 mmol) n-butanol was added over 1.5 hours. Stirring at room temperature was continued until gas evolution ceased and no solids remained, about 18 hours. Removal of pentane under vacuum yielded a cloudy, viscous solution. The final clear solution was obtained after filtration through a 0.45 μm filter and dilution to 25 mL volume with n-butanol. Analysis for Ba determined a final concentration of 0.90 M.

PREPARATION OF 1:2:3 Y:Ba:Cu SOLUTIONS. In a typical preparation, an oven-dried 25 mL flask was charged with 300 mg (0.631 mmol) of 2, thoroughly purged with dry nitrogen, and 10 mL 2-methoxyethanol added. To this clear, deep blue solution, 631 μL of a 1M $Ba(OCH_2CH_2OCH_3)_2$ (0.631 mmol) 2-methoxyethanol solution were added and the homogeneous solution stirred rapidly at room temperature. Over the next 1.5 hours, finely divided $Cu(OCH_2CH_2OCH_3)_2$ precipitated and was removed by filtration of the solution by cannula. Addition of 0-90 equivalents (based on yttrium) of deionized water was followed after 30 minutes by addition of 315 μL of a 1M $Y(OCH_2CH_2OCH_3)_3$ (0.315 mmol) 2-methoxyethanol solution. After vigorous stirring for 2 hours at room temperature, the clear solution was filtered by cannula and stored in a refrigerator (5°C) for 24 hours. Analysis for Y, Ba, and Cu determined a ratio usually on the order of 1:2.2:2.9.

PREPARATION OF LAYERS ON PT. Prior to deposition, each solution was filtered through a 0.2 μm filter. Twelve sequential layers were deposited with a 10 second, 300°C heat treatment between layers and a final 30 second, 300°C heat treatment upon completion. Layers were spun at 2000 rpm for 50 seconds.

PREPARATION OF LAYERS ON SAPPHIRE. Similarly, layers were spin-cast from solutions filtered through a 0.2 μm filter for 50 seconds at 2000 rpm. Between layers, substrates were placed in a 630°C box furnace (Lindburg) for 15 seconds, then quickly cooled to room temperature. Ten layers per substrate were deposited in this manner and the resulting specimens stored in a desiccator.

RESULTS AND DISCUSSION.

Although the alkoxide chemistry of copper (II) has been well explored, [10] such products are generally non-volatile and insoluble in common organic solvents. These properties, a direct consequence of the oligomeric nature of copper (II) alkoxides, can be ascribed to the strong tendency of the metal for higher coordination. These coordination requirements can partially be satisfied by chelation of the copper

(II) with ß-diketonate ligands such as 2,4-pentanedionate, $C_5H_7O_2$. I. In this manner, soluble mixed-ligand copper (II) alkoxides can be prepared.

In 1965, Bertrand and Kaplan[9] first reported the synthesis of a dimeric 2,4-pentanedionate, methoxy-bridged compound formulated as $(C_5H_7O_2)_2Cu_2(\mu\text{-}OCH_3)_2$ (**1**) based on spectroscopic and molecular weight measurements. This basic dimeric structure was later confirmed by Andrew and Blake[11] as the essential unit in the solid state structure of $(C_5H_7O_2)_2Cu_2(\mu\text{-}OCH_2C_6H_5)_2$, prepared by alcohol exchange of **1** with benzyl alcohol. This compound was not found to crystallize as discrete Cu_2-dimers, but rather as strongly associated pairs of dimers. The authors also reported the synthesis by alcohol exchange of the ethoxy and n-propoxy-bridged compounds. Based on the spectroscopic similarities observed between these systems, it was suggested that compounds of the type $(C_5H_7O_2)_2Cu_2(\mu\text{-}OR)_2$ possess a similar associated-dimer solid state structure. In addition, each of these compounds shows some solubility in the parent alcohol, as well as limited solubility in other polar organic solvents.

As detailed in the experimental section, the methoxy-bridged dimer **1** readily undergoes alcohol exchange to produce, in addition to those compounds just described, products of the type $(C_5H_7O_2)_2Cu_2(\mu\text{-}OR)_2$ (R = $OCH_2Ch_2OCH_3$ (**2**), n-C_4H_9 (**3**)) according to reaction 1:

$$(C_5H_7O_2)_2Cu_2(\mu\text{-}OCH_3)_2 + 2ROH \xrightarrow[90°C]{} (C_5H_7O_2)_2Cu_2(OR) + 2CH_3OH \qquad 1.$$

Although compounds **1, 2,** and **3** share the same dimeric formulation, they differ markedly in their solubility in the parent alcohol, and in the case of **2** and **3,** in their subsequent reactivity with $Ba(OCH_2CH_2OCH_3)_2$. Violet solid **1** is sparingly soluble in methanol, whereas turquoise dimer **2** demonstrates good room temperature solubility in 2-methoxyethanol. Blue solid **3** is soluble in room temperature n-butanol, but is an order of magnitude less soluble in this solvent than **2** is in 2-methoxyethanol.

The range of solubilities and disparate reactivities for compounds **2** and **3** could be a simple consequence of the nature of the bridging alkoxide, or they may reflect more subtle structural differences, such as a different degree of dimer association. Consequently, attempts were made to determine the solid-state structures of compounds **1, 2,** and **3.** Single crystals of **3** were readily obtained from solutions of hot n-butanol, however, no suitable solvent for the crystallization of **1** was found. Crystals obtained of **2** using a variety of crystallization procedures and solvent systems, were consistently twinned and unsuited for X-ray analysis.

Figure 1 shows the results of a single-crystal X-ray determination for crystals of dimer **3.**[12] The structure consists of two approximately planar n-butoxy-bridged dimers $(C_5H_7O_2)_2Cu(\mu\text{-}OC_4H_9)_2Cu(O_2C_5H_7)$ joined by four apical Cu-O bonds involving each of the n-butoxy oxygen atoms. Each copper atom possesses approximately square-planar coordination. The dimers are situated such that the two Cu_2O_2 units are rotated 90° with respect to each other. This unit is essentially planar

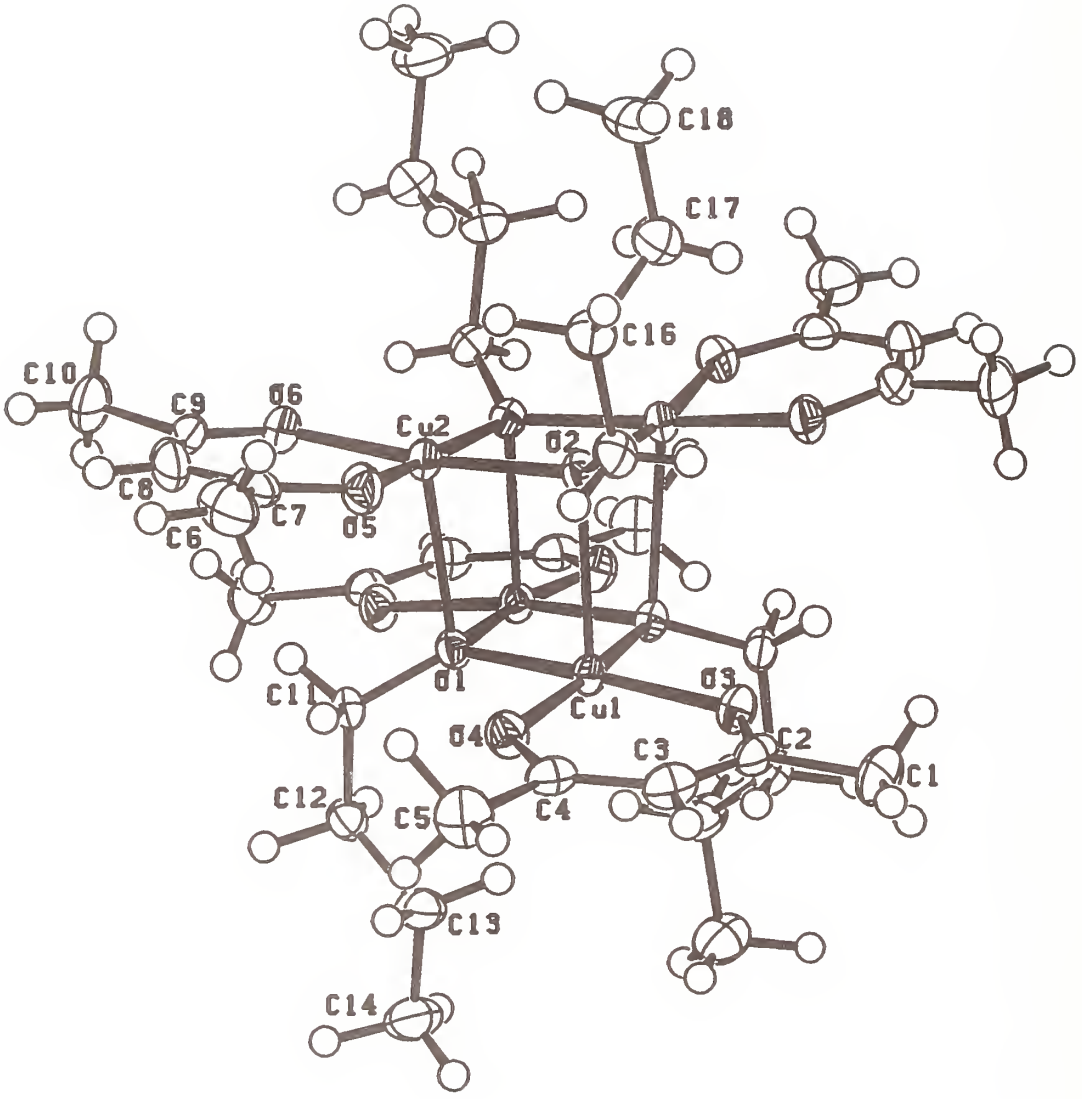

Figure 1. Perspective view of compound **3** with atoms labeled. Thermal ellipsoids are drawn at the 35% probability level for the non-hydrogen atoms.

in each dimer with mean Cu-O bond lengths of 1.94Å and are linked by 2.44Å apical Cu-O bonds. The planes of the dimers containing the 2,4-pentanedionate ligands are slightly bent away from each other with the n-butoxy groups extending perpendicular to these planes. Distances and angles within the 2,4-pentanedionate and n -butoxy ligands are as expected.

The structure of **3** can be contrasted with that reported by Andrew and Blake[12], the only other structurally characterized $(C_5H_7O_2)_2Cu(\mu\text{-}OR)_2$ system reported. Both structures are similar in that they consist of apically associated dimers. However, in the structure of the benzoxy product, the dimers are linked by Cu-O bonds involving one benzoxy and one 2,4-pentanedionate oxygen atom of each dimer. Consequently, the two dimers lie above and below each other without rotation of the Cu_2O_2 units. Within each Cu_2O_2 unit, the two Cu-O bonds to the three-coordinant bridging oxygens are significantly shorter (1.88 Å) than those to the four-coordinant bridging oxygens (1.94 Å).

In the absence of single crystal data for compounds **1** and **2**, information regarding their molecular structures can be inferred by comparison of their infrared spectra with those of **3** and the benzoxy-bridged product, Figure 2. Absorptions assigned to the $(C_5H_7O_2)_2Cu$ unit[13] are indicated. Of particular interest is the region of Cu-O absorptions found between 570 and 420 cm^{-1}. In the spectrum of compound 3, Figure 2c, three distinct Cu -O absorptions are observed and assigned to 455 cm^{-1}, Cu-O (2,4-pentanedionate); 507 cm^{-1}, Cu-O (intramolecular bridged alkoxide); 552 cm^{-1}, cu-O (intermolecular bridged alkoxide). These Cu-O assignments are based on the relative bond lengths (1.94A-intramolecular vs. 2.44Å-intermolecular) of the corresponding units.

Examination of the Cu-O absorption region in the spectrum of $(C_5H_7O_2)_2Cu_2(\mu\text{-}OCH_2C_6H_5)_2$, Figure 2d, shows the metal-oxygen bands consistent with the molecular structure reported. As described earlier, the two dimer units are linked through one of the two bridging benzoxy- and one of the chelating ß-diketonate ligands. As a result, two distinct Cu-0 (2,4-pentanedionate) absorptions, 451 and 448 cm^{-1}, and two Cu-O (intramolecular bridged alkoxide) bands 580 and 548 cm^{-1}, are observed. In addition, a weak absorption in the region assigned to the dimer-linking Cu-O (intermolecular bridged alkoxide) bond, 490cm^{-1}, is observed. No band could be assigned to the second type of dimer-linking Cu-O (2,4-pentanedionate) band seen in the structure.

In comparison with the IR spectra of **3** and the benzoxy-bridged dimer, the spectra obtained of dimers **1** and **2**, Figures 2a and 2b respectively, show similarities and significant differences. In the spectrum of **1**, only two metal-oxygen absorptions are observed. The lower frequency band, 455 cm-1, falls in the region assigned to the Cu-O bond to an unperturbed 2,4-pentanedionate ligand, as in $(C_5H_7O_2)_2$ Cu[13] and dimer **3**. By analogy with the group assignments previously made, the absorption at 554 cm^{-1} is assigned to the Cu-O bond of an intermolecular bridged methoxide ligand. The absence of any bonds in the intermolecular bridged alkoxide region suggests that compound **1** does exist as a singular, unassociated methoxy-bridged dimer as originally formulated.

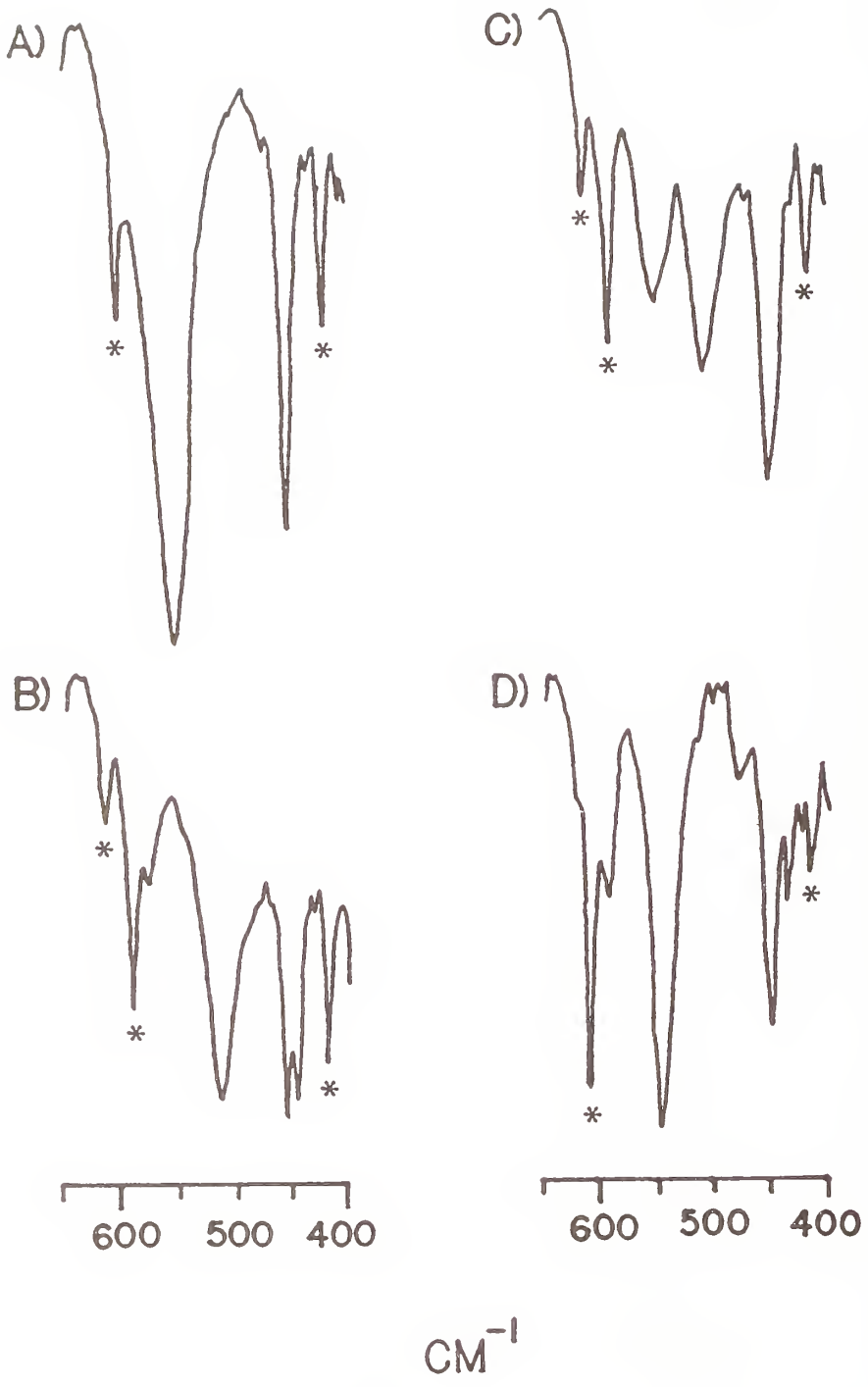

Figure 2. FTIR spectra (650-400 cm^{-1}) of KI pellets of A) compound **1**, B) compound **2**, C) compound **3**, and D) $(C_5H_7O_2)_2Cu_2(\mu\text{-}OCH_2C_6H_5)_2$.

Interestingly, the IR spectrum of the methoxyethoxy bridged dimer **2**, Figure 2b, exhibits characteristics observed in both **3** and the benzoxy-compound. As seen in these systems, bands are present which correspond to both intramolecular, 561 cm^{-1}, and intermolecular 512 cm^{-1}, bridged alkoxides. It must be noted that in contrast to the phenoxy-system, only one of each type of absorption is found. However, an additional band at 433 cm^{-1} is observed with the 455 cm^{-1} Cu-O (2,4-pentanedionate) moiety suggesting a linkage of dimers through an oxygen of the ß-diketonate. These results suggest that dimer **2** may well possess a solid state structure similar to that found for $(C_5H_7O_2)_2Cu_2(\mu\text{-}OCH_2C_6H_5)_2$. These studies clearly demonstrate that generalization of the molecular structure for these types of alkoxy-bridged dimers cannot be made based solely on observed physical behavior.

As was stated earlier, the differences between dimers **2** and **3** extend beyond their relative solubilities and structures. Most significant is the behavior of **2** is such that homogeneous 1:2:3 Y:Ba:Cu solutions can be prepared, whereas they cannot by using **3**. Solutions of Y:Ba:Cu with stoichiometries of 1:2:3 were obtained by reaction of **2** with 1M 2-methoxyethanol solutions of $Ba(OCH_2CH_2OCH_3)_2$, and $Y(OCH_3CH_2OCH_3)_3$ in the ratio 2:2:1 (see Experimental Section). This stoichiometry was required due to reaction of **2** with the barium alkoxide which resulted in the precipitation of one equivalent of $Cu(OCH_2CH_2OCH_3)_2$ Attempts to characterize this reaction and to identify the soluble barium and copper species using NMR spectroscopy were complicated by the presence of paramagnetic copper (II). As a result, resonances for species other than the solvent employed were not observed. A similar reaction between **3** and the corresponding barium alkoxide also produces copper precipitation as $Cu(OC_4H_9)_2$, however all of the copper and 80% of the barium are lost from solution. Similar destructive reactions between **2** or **3** with the yttrium alkoxide solutions were not observed.

Solutions of Y, Ba, and Cu suitable for deposition of thin layers and preparation of powders were prepared according to reaction 2, where R = $OCH_2CH_2OCH_3$ and n = 9-90:

$$Y(OR)_3 + 2\ Ba(OR)_2 + 2(C_5H_7O_2)_2Cu_2(\mu\text{-}OR)_2 + nH_2O \rightarrow \qquad 2.$$

Characterization of layer deposited on platinum and sapphire wafers has been reported.[14] From such layers, superconducting films of $YBa_2Cu_3O_7$ have been obtained.

CONCLUSIONS

Two unique mixed-ligand copper (II) alkoxides, $(C_5H_7O_2)_2Cu_2(\mu\text{-}OCH_2CH_2OCH_3)_2$. and $(C_5H_7O_2)_2Cu_2(\mu\text{-}OC_4H_5)_2$.were synthesized by alcohol exchange of $(C_5H_7O_2)_2Cu_2(\mu\text{-}OCH_3)_2$. A single crystal X-ray diffraction study determined the structure of the n-butoxy bridged dimer to be two apically associated dimers linked by Cu-O bonds to each of the two bridging alkoxide oxygen atoms. The Cu_2O_2 units of each dimer are rotated 90° with respect to each other. Comparison of the FTIR spectra of methoxy- and methoxyethoxy-bridged dimers with the n-

butoxy and benzoxy-bridged products suggested that $(C_5H_7O_2)_2Cu_2(\mu\text{-}OCH_3)_2$ exists as discrete, unassociated dimers in the solid state. Similar comparison suggests that $(C_5H_7O_2)_2Cu_2(\mu\text{-}OCH_2CH_2OCH_3)2$ and $(C_5H_7O_2)_2Cu_2(\mu\text{-}OCH_2C_6H_5)_2$ possess similar solid state structures.

Homogeneous solutions of Y:Ba:Cu can be obtained with stoichiometries of 1:2:3 by reaction of $(C_5H_7O_2)_2Cu_2(\mu\text{-}OCH_2CH_2OCH_3)_2$ with 1M solutions of $Ba(OCH_2CH_2OCH_3)_2$ and $Y(OCH_2CH_2OCH_3)_3$. Hydrolysis of these solutions with 9-90 equivalents of water per equivalent of yttrium results in homogeneous solutions from which both powders and thin layers can be prepared.

ACKNOWLEDGEMENTS

This work was supported by the U.S. Department of Energy, Division of Materials Sciences, under contract DE-ACO2-76ER01198. We gratefully acknowledge the assistance of S. R. Wilson for X-ray diffraction studies, and with W. G. Fahrenholtz for ceramic processing.

REFERENCES

1. Bednorz, J. G.; Müller, K. A., J. Phys. ß-Condensed Matter, 1986, 64, 189.
2. See, for example, Advanced Ceramic Materials, 1987, 2 (3B), 267.
3. Adachi, H.; Setsune, K.; Mitsuyu, T.; Hirochi, K.; Ichikawa, Y.; Kamada, T.; Wasa, K. Jap. J. App. Phys. 1987, 26 (5), 709.
4. Naito, N. submitted to J. Mat. Res.
5. Chandhari, P.; LeGoues, F. K.; Segmuller, A., Science, 1987, 1238, 342.
6. Kramer, S.; Wu, Ki; Kordas, G., Mat. Res. Soc. Proc. 1988, 9, 323.
7. Hirano, S.; Hayashi, T.; Miura, M.; Tomonaga, H. Presented at the 90th Annual Meeting of the American Ceramic Society, May, 1988, Cincinnati, OH.
8. Jones, M. M., J. Am. Chem. Soc., 1959, 81, 3188.
9. Bertrand, J. A.; Kaplan, R. I.; Inorg. Chem., 1965, 4 (11), 1657.
10. Singh, J. V., Baranwal, B. P.; Mehrotra, R C. Z Anorg. Allg. Chem., 1981, 477, 235.
11. Andrew, J. E.; Blake, A. B.; J. Chem. Soc. Dalton, 1973, 1102.
12. Data were collected at -75°C. The structure was solved by direct methods (SHELXS-86); correct positions for copper, oxygen and 12/18 carbon atoms were deduced from an E-map. Subsequent least squares-difference Fourier calculations gave positions for the remaining carbon and hydrogen atoms. The final difference Fourier map had no significant features. Final agreement factor, R = 0.0033.
13. Nakamoto, K., Infrared Spectra of Inorganic and Coordination Compounds; J. Wiley and Sons, Inc., NY, 1978.
14. (a) Fahrenholtz, W. G.; Millar, D. M.; Payne, D. A., Ceramic Superconductors III Research Update 1989, M. Y. Yan, Editor, 141, Am. Ceram. Soc.
(b) Fahrenholtz, W. G., M. S. Thesis, University of Illinois, 1989.

National Institute of Standards and Technology Special Publication 804, Chemistry of Electronic Ceramic Materials, Proceedings of the International Conference held in Jackson, WY, August 17-22, 1990, issued January 1991.

MOLECULAR CHEMISTRY AND THE SYNTHESIS OF PRECURSORS TO ELECTRONIC CERAMIC MATERIALS

J. J. Ritter, J. F. Kelly, D. E. Newbury[1], and D. B. Minor
NIST
Ceramics Division
Gaithersburg, MD 20899

ABSTRACT

The use of molecular chemical reactions to generate precursors to ceramic materials has been the subject of considerable study for more than three decades. This approach, in many cases, offers distinct advantages over conventional high-temperature syntheses particularly in the areas of improved homogeneity, purity, particle size regulation and amenability to intelligent processing control. Generally, within the broad spectrum of chemical schemes available for ceramic precursor synthesis, the molecular processes are poorly understood. Moreover, the reactions are often interpreted either through "chemical intuition" or by analogy to similar chemistries, rather than from measurements on the relevant systems. An additional complicating factor arises from our lack of knowledge about the mechanisms operating during the conversion of precursors to ceramic phases.

This presentation elaborates on several chemical routes which have been used to synthesize ceramic precursors. The discussion includes systems where control over the molecular architecture may lead to ceramic phases at low temperatures. Other systems, which essentially deliver random, intimately mixed assemblies of the elements, are also examined. The various approaches are illustrated with examples from research programs at NIST which have focused on the chemical synthesis of precursors to barium polytitanates, metal carbides and borides, electrically conductive oxides and nitrides, and the YBCO high-temperature superconductor.

INTRODUCTION

Molecular chemical reactions have been used for more than 30 years to generate precursors to ceramic materials. In many cases, these approaches offer advantages over conventional high-temperature syntheses in the areas of homogeneity, purity, particle size regulation, and amenability to intelligent processing control.

Synthetic methods reported in the literature include the hydrolysis of metal alkoxides, the reductive dehalogenation of elemental halides (RDEH), the formation and pyrolysis of organometal ion complexes, and the coprecipitation of insoluble salts. Some of these methods e.g., alkoxide hydrolysis and RDEH offer the potential for control of protostructural development. The concept of protostructural development may be viewed as

[1] Center for Analytical Chemistry, NIST

the placement of atoms in a precursor in nearly the same locations they will have in the final ceramic phase. Alternatively, one can envision the fabrication of a precursor structure whose favored decomposition pathway gives the desired ceramic phase through a facile relocation of atoms. From the molecular chemist's viewpoint, control for protostructural development can be approached by altering the reaction mode of participating molecules through changes in substituents, solvent systems, pH, etc.. Recent publications by Phule and Risbud[1,2] describe work related to this concept with the synthesis of barium titanates from the hydrolysis of modified Ba and Ti alkoxides. Protostructural precursors generally will require only a little additional energy to promote their conversion. Other synthesis methods such as coprecipitation and the decomposition of organometal complexes usually provide only an intimately mixed, random assembly of atoms which require relatively more additional energy to form the ceramic material.

The use of metal alkoxides to produce oxide ceramic powders has been reviewed extensively in the literature[3]. NIST work on barium polytitanates derived from alkoxide routes has also been published previously[4,5]. This presentation will focus on RDEH as a route to carbides and borides, organometal complex routes to a conductive ceramic powder, and a copreciptation route to the YBCO superconductor.

SYNTHESIS OF PRECURSORS TO CARBIDES AND BORIDES BY REDUCTIVE DEHALOGENATION

Background: Electrical and electronic devices of the future will be expected to operate reliably in a variety of increasingly adverse environments. To meet these requirements, designers are seriously considering nonoxide ceramic materials for certain applications. For example, silicon carbide has been proposed as a microchip substrate, boron carbides may have applications as high-temperature semiconductors, while titanium nitride has been shown to perform well as an electrical contact material. The development of molecular chemical routes to these and other nonoxide ceramic materials continues to gain momentum. I shall describe here the application of an inorganic redox chemistry, known to chemists for more than 100 years, for the synthesis of precursors to carbide and boride powders. Schematically, for silicon carbide, the reaction may be represented as follows:

$$SiCl_4 + CCl_4 + 8Na \xrightarrow[130°C]{\text{n-heptane}} \underset{\text{(precursor)}}{\text{"SiC"}} + 8NaCl \quad (1)$$

The precursor to boron carbide is synthesized from a n-heptane solution of BCl_3 and CCl_4, whereas precursors to TiC and TiB_2 are generated from $TiCl_4$ and CCl_4 or BCl_3, respectively. The reaction chemistry is general for any combination of elemental halides which can be reduced by alkali metals and have at least some solubility in the solvent system used.

Synthesis and Characterization: The details of the reaction procedures have been given previously[6]. In brief, a dilute solution of the elemental halides in n-heptane is added dropwise to a vigorously stirred suspension of molten sodium in the same solvent, under vacuum. Potassium

can be substituted for Na, or if Na/K alloy is used, the reaction proceeds at room temperature. Under these carefully controlled conditions, the normally explosive reaction between elemental halides and alkali metals is smooth and only mildly exothermic. However, it is recommended that only personnel familiar with handling reactive materials attempt these procedures and that maximum safety precautions be implemented. After removal of the solvent by distillation, the alkali halide is separated from the precursor by vacuum sublimation at ~900 °C. Silicon carbide and boron carbide precursors require further heating in vacuum at 1400, and 1900 °C, respectively, to crystallize, while TiC and TiB2 crystallize at ~900 °C, during the removal of the alkali halide. The materials are identified by x-ray powder diffraction (XRPD) and morphology determined by scanning electron microscopy (SEM). Surface areas are measured with N_2 by the standard B.E.T. method.

Results and Discussion: Characterization data are summarized in table I. In most cases, the precursors are pyrophoric and must be handled in vacuum or under argon (< lppm water and oxygen) in a glove box. The powders are recovered with moderate-to high-surface areas while some, particularly the boron carbide, contain a few percent excess carbon. The use of Na/K with concomitant lower reaction temperatures reduces the excess carbon problem. The TiC produced by this process is readily converted to TiN by heating to ~900 °C in N_2.

While the dehalogenation reaction mechanism has not been extensively investigated, it is thought to be of the Wurtz-Fittig nucleophilic displacement type well known in organic chemistry[7]. It is proposed that the initial interaction of an elemental halide, MX_4, with an alkali metal forms a nuleophile, X_3M^-, and an alkali halide, e.g., NaX, as shown in eq(2).

$$MX_4 + 2Na \longrightarrow Na^+ {}^-MX_3 + NaX \qquad (2)$$

Due to the electronegativities of halogen substituents, the central atom, M, in MX_4-type molecules bears a partial positive charge. Thus,the nucleophile initially forms a complex,(I), with the central atom of another elemental halide molecule, e.g., $M'X_4$, and in so doing displaces a halogen from this receptor molecule. The coupled M-M' product (II) and another molecule of NaX are produced, as shown in eq(3).

$$X_3M^- \cdot \cdot \cdot \cdot \cdot M'X_3 \longrightarrow X_3M\text{-}M'X_3 + NaX \qquad (3)$$

$$Na^+ \quad : \quad X$$

(I) (II)

Each halogen and M site on the coupled product (II) is subject to attack by either Na or another nucleophile with the final result that all of the halogens are removed and a three-dimensional M-M' matrix is developed. This three-dimensional M-M'matrix is the ceramic precursor. To a first approximation, the manner in which this precursor is built up can be influenced by varying the substituents, X, on M and M'. Changes in the substituents will affect the electron densities of the M and M' centers,

and thus, their susceptibility to nucleophilic attack. In practice, control of protostructure development can be realized by changing halogens, using a mixed halogen system, introducing a precoupled moiety similar to (II) as a reactant, or perhaps even substituting pseudohalogens. Another approach would involve adding the alkali metal in carefully measured increments which are designed to control the coupling reactions in a sequential manner.

Table I

Characterization data for boride and carbide powders

	silicon carbide		boron carbide		titanium diboride	
	P	C	P	C	P	C
color	black	grey	black	black	black	black
B.E.T Surface Area (m^2/g)	65.5	26.4	-----	215.6	-----	29.5
morphology (SEM)	sponge-like	whiskers & crystallites	sponge-like	agglomerated irregular particles	sponge-like	irregular particles 1-5μm
XRPD	amorphous	cubic (8F) & hexagonal (4H)	amorphous	B_4C, excess C	amorphous	TiB_2
Residual Cl (wt%)	0.090	0.086	-----	-----	-----	------

P = precursor C = crystallized powder

ORGANOMETAL COMPLEX SYNTHESIS OF A CONDUCTIVE OXIDE CERAMIC POWDER

Background: Current practice in the construction of cathodes for alkaline fuel cells involves the coating of small polytetrafluoroethylene (PTFE) particles with 2-5 nm gold particles at such loadings to assure Au-Au contact for electrical conductivity. While fine gold particles are a good electrocatalyst for the cathodic reduction reaction, they tend to sinter when cell temperatures exceed ~80 °C, with a concomitant loss in electrocatalytic activity. A new generation of cathodes is under consideration, wherein the PTFE will be replaced by a "conductive particle" lightly loaded with gold. The elimination of extensive Au-Au contact is expected to greatly alleviate the loss of activity at elevated temperatures. Alternatively, if the "conductive particles" show electrocatalytic activity, they could be used directly without the Au deposition. The requirements for these "conductive particles" include, electrical conductivity in the 10^3-10^5/ohm-cm range, 20-70 nm particle size, resistance to chemical attack by 40% aqueous KOH at ~100 °C, and stability under cell reduction potentials in the range 0.4-1.2 V, Reversible Hydrogen Electrode. Among the candidates considered for this application is a lithium-doped lanthanum nickelate, $La(Li)NiO_x$[2].

[2] Investigation suggested by Dr. Joseph Singer, NASA-Lewis Research Center, Cleveland, OH.

The synthetic challenge was to effectively substitute 1 mol % Li for Ni while maintaining the required particle size.

Synthesis and Characterization: The known solubility of many lithium compounds in water and other common solvents suggested that coprecipitation would be inappropriate to assure the quantitative inclusion of Li in the product. Thus, an alternative organometal complex approach to prepare initial samples of the nickelate was selected. Three options were investigated, a citric acid-ethylene glycol route[8], a glycine complex route[9] and a citric acid route[10]. In each case, aqueous nitrate solutions of the metals with molar ratio La : Ni : Li = 1.0 : 0.99 : 0.01, were combined with 1 mol of complexing agent per mole of metal ion. Solvent was removed thermally until polymerization occurred. The resultant polymers were calcined up to 500 C, and the desired phase formed at 600-650 °C in O_2. Phases were identified by XRPD, surface areas determined with N_2 on a commercial B.E.T. apparatus, Li analysis conducted by flame emission spectroscopy (FES), while powder morphology was examined by SEM. Small portions of the powder were ultrasonicated in 2%(v/v) acetic acid, in an attempt to increase surface area.

Results and Discussion: All three methods generate the desired material which contains, in all cases, a few percent of NiO. However, experimentally, the simplest approach is the citrate route. Surface area measurements on citrate-derived powders by standard B.E.T. methods give values typically in the 3-6 sq m/g range. Results from FES verified that Li is present at the intended 1 mole % level, whereas examination of the material by SEM shows a matrix of fused ~100 nm particles. After ultrasonication in 2% acetic acid, only 20% of the powder is recovered. However, this recovered material exhibits a surface area of ~15 sq m/g. Examination by SEM indicates considerable erosion of the connective "necks" between particles but general retention of the connective structure. Lithium assay by FES indicates that more than 80% of the original Li is retained.

Studies by Delmon and Droguest[11], suggest that the polymerization of citric acid-metal complexes form a vitreous phase which contains the metal ions in a random array. It is unlikely that the polymer formation can be controlled to develop a "protostructure" to the ceramic phase, but its chief advantage is in its ability to retain ions in a relatively homogeneous dispersion. For the synthesis of the Li-doped lanthanum nickelate, the citrate complex route has the demonstrated advantage of incorporating Li quantitatively. The high Li content of the powder after vigorous acetic acid treatment suggests that a major portion of this dopant is part of the nickelate crystal structure.

SYNTHESIS OF A COPRECIPITATED HYDROXYCARBONATE PRECURSOR TO THE YBCO SUPERCONDUCTOR

Background: Within the past few years, a large number of chemical procedures for the synthesis of precursors to the YBCO superconductor have been published. The coprecipitation approach to be considered here has particular merit in that it is a water-based process, uses relatively

inexpensive chemicals, and is readily adapted to continuous production methods with intelligent processing control.

In conventional practice, coprecipitation reactions are often conducted by adding one reactant solution to another in a dropwise fashion with some attendant nominal stirring. This approach favors the formation of large concentration gradients in the vicinity of the entering reactant solution causing significant initial inhomogeneities in the formation of the coprecipitate. Moreover, the ionic concentrations are subject to continuous change as the addition proceeds, resulting in a continuous change of the reaction rate. In addition, the ever increasing bulk of coprecipitated material captive in the receiving vessel acts as an occlusion trap for unreacted species, thus both slowing down the coprecipitation process, and increasing the probability for inhomogeneous precipitation. The latter problems become particularly serious in the final stages of addition when the viscous slurries become difficult to stir.

Alternative methods of combining reactant solutions have been developed, but these are infrequently used in the research laboratory. For example, it is well known that a fluid moving under laminar flow conditions within a straight tube develops a parabolic flow velocity profile. Fluid near the center of the tube travels at twice the average fluid velocity, while fluid near the walls travels much more slowly. Samples of reaction fluid taken along a laminar flow tube radius will have very different residence, reaction and thermal histories. Thus, since a laminar flow tube provides practically no radial mixing, it is a poor choice for a chemical reactor. The flow profile, and thus the radial mixing can be improved somewhat by increasing the Reynolds number of the system to $>10^4$ so that the fluid experiences turbulent flow.

However, within the past two decades, a technology has been developed in the chemical process industry which provides efficient mixing even under laminar flow conditions. This advance, often referred to as "motionless" or "fixed-element" mixing, incorporates a series of carefully designed, stationary, geometric elements within a tube of flow. The shape and placement of these elements is such that they interact with the moving fluid causing it to divide, swirl and recombine in a mathematically predictable fashion to impart an effective radial mixing. The overall effect is to give all of the flowing material nearly the same velocity, residence time and degree of radial mixing. As a result, each increment of fluid emerging from the flow tube has the same uniform mixing history. The output of a well-designed "fixed-element" mixer very closely approximates that of an ideal plug flow reactor(12)

The chemical flow reactor used at NIST is a commercially available research model. It consists of a series of 52 helical elements, each of aspect ratio 1.6, stacked within a flow tube with their respective ends oriented at 90 °C to each other. Each element is placed so that its "twist," clockwise or counterclockwise, is opposite to that of its precedent. The number of divisions experienced by an increment of fluid in its passage through the reactor is given by 2^n, where n is the number of elements in the tube. For this reactor the value is 2^{52}. The two reactant solution streams are combined in a region of confluence at the first helical element

in the tube. With proper adjustment of flow rates and reactant concentrations, the efficiency of this system allows, for most precipitation reactions, an effective blending of the solutions within the induction period of the reaction. As a result, many discrete nuclei are formed and particles grow from these nuclei until the reactants within the immediate vicinity are consumed. With suitable modifications to the plumbing, the flow reactor is equally adaptable to either batch or continuous powder syntheses as shown in figures 1 and 4b, respectively.

Synthesis and Characterization: The reaction of a solution of Y, Ba, and Cu acetates with solution of potassium carbonate can be written schematically as follows:

$$Y^{3+} + 2Ba^{2+} + 3Cu^{2+} \xrightarrow[H_2O]{CO_3^{2-}} [Y(OH)CO_3 : 2BaCO_3 : 2Cu(OH)_2 : CuCO_3]. \quad (4)$$

The details of conducting this coprecipitation in the conventional manner and evidence for the composition of the hydroxycarbonate product shown in eq(4) have been described previously[13].

A schematic diagram of the chemical flow reactor arranged for batch coprecipitation is shown in figure 1.

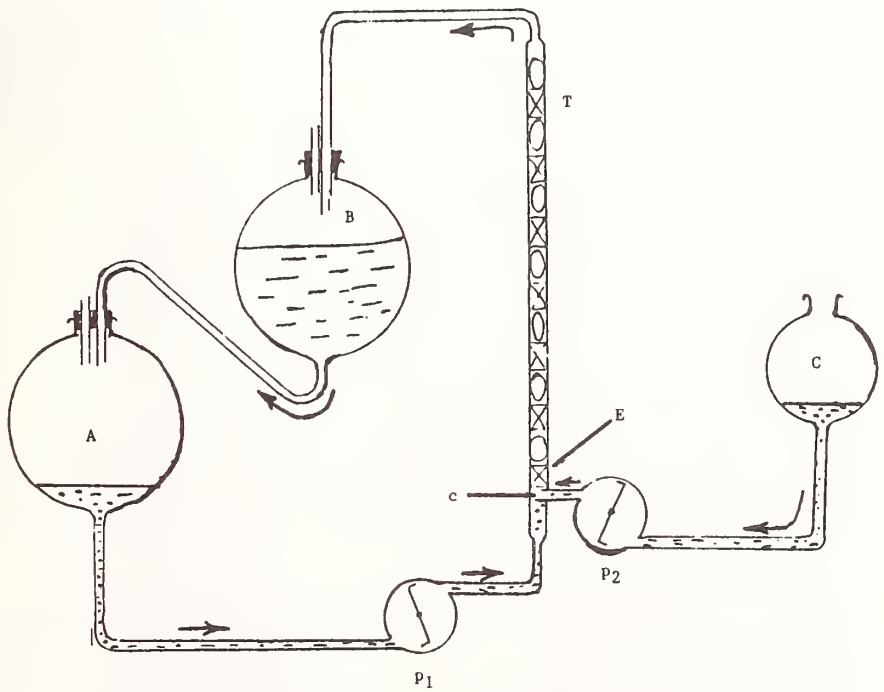

Figure 1. Chemical Flow Reactor Schematic

A reactant reservoir p_1 mainstream pump E helical mixing element
B slurry reservoir p_2 sidestream pump c stream confluence area
C reactant reservoir T mixing tube

A water solution of K_2CO_3 with $[CO_3^{2-}] = 0.30$ M is contained in reservoir A and delivered to the reactor, T, by gear pump p_1 at a velocity of 56 cm/s. Simultaneously, a water solution of Y, Ba, and Cu acetates with $[Y^{3+}] =$

0.05 M, $[Ba^{2+}]$ = 0.10 M and $[Cu^{2+}]$ = 0.15 M, is contained in reservoir C and delivered to the reactor by gear pump p_2 at a velocity of 110 cm/s. The two process streams are combined in an area of confluence, c, at the leading edge of the first helical mixing element, E. The solution volumes and flow rates from reservoirs A and C are such that they become empty at nearly the same instant. At this point, the product slurry which has been accumulating in reservoir B, has reached a sufficient height to initiate a self-siphoning action into reservoir A. Pump p_1 now serves to circulate the slurry through the reactor, while p_2 is shut down. The recirculation process is continued for some minutes before the slurry is removed. The coprecipitated hydroxycarbonates are separated from the liquid phase by centrifugation, and washed several times with water followed by several ethanol washings.

The washed coprecipiates from both conventional and flow reactor routes are initially air dried and finally calcined at temperatures between 300-500 °C for various periods of time(cf. fig. 5). Samples of the as-precipitated and calcined materials were subjected, as appropriate, to examination by SEM, Transmission Electron Microscopy (TEM), and by High Resolution Analytical Electron Microscopy (HRAEM).

Results and Discussion: The SEM micrograph shown in figure 2a shows that the coprecipitated material generated at low, ionic concentrations is highly segregated. Moreover, earlier work indicates that this segregation is independent of pH in the range from 8-11[14] Energy Dispersive X-Ray (EDX) analyses indicate that the spherical particles are rich in both Y and Cu while the dendritic structures are rich in Ba. This data, when combined with previous evidence available on the precipitation forms of Y, Ba, and Cu, indicates that the spherical particles are a yttrium-copper hydroxycarbonate, while the dendrites are barium carbonate[13].

Figure 2b shows material coprecipitated at higher ionic concentrations. No morphological distinctions between particles are apparent and, to the resolution of the SEM EDX (~1 micrometer), no elemental segregation is detected.

Figure 3 shows the morphology of Y, Ba, and Cu hydroxycarbonates as coprecipitated in the chemical flow reactor. Note that the individual particles, although catenated, are 20-30 nm in size in contrast to the 100-300 nm sized particles derived from the conventional precipitation route and depicted in Figure 2b.

Figure 4 shows the results of HRAEM Y, Ba, and Cu mapping on conventional and flow reactor coprecipitated powders, respectively. Since the resolution of the HRAEM is of the order of 10-20 nm, different portions of individual small particles may be assayed for composition. While EDX mapping of powder conventionally coprecipitated at high ionic concentrations shows no segregation, the higher resolution data from HRAEM indicates substantial inhomogeneities in this material. In contrast, the flow reactor powder exhibits a rather close grouping of the data points, indicating a higher degree of homogeneity.

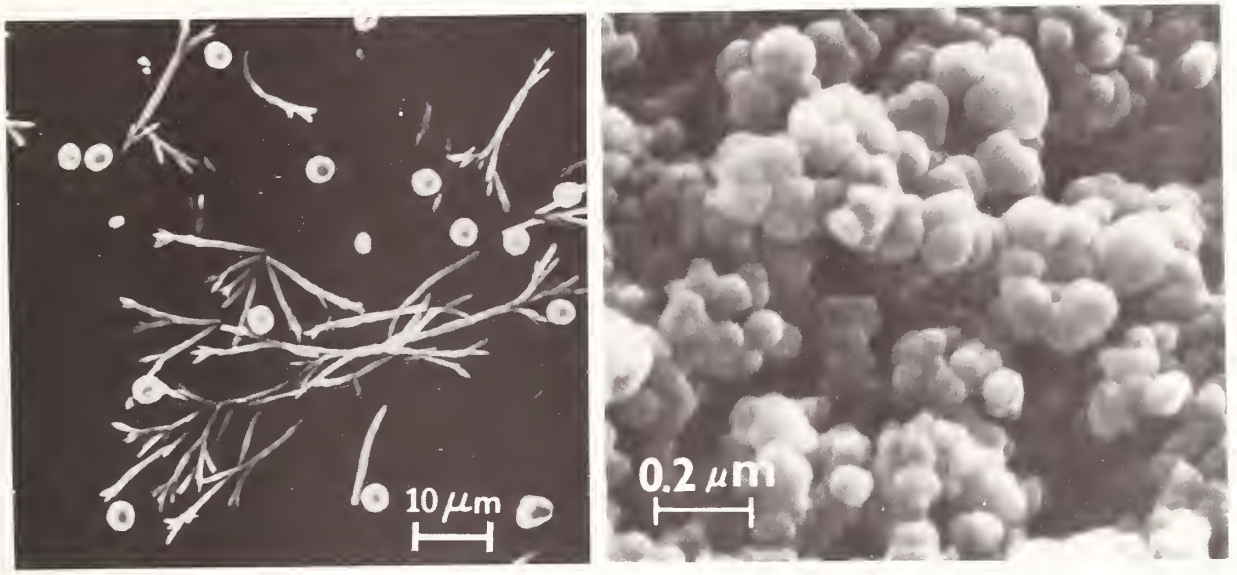

(a) (b)

Figure 2. SEM micrographs of hydroxycarbonates conventionally coprecipitated at low-and high-ionic concentrations

a. pH = 10, $[Y^{3+}]$ = 0.0033M, $[Ba^{2+}]$ = 0.0066M, $[Cu^{2+}]$ = 0.0099M, $[CO_3^{2-}]$ = 0.02M

b. pH = 10, $[Y^{3+}]$ = 0.05M, $[Ba^{2+}]$ = 0.10M, $[Cu^{2+}]$ = 0.15M, $[CO_3^{2-}]$ = 0.30M

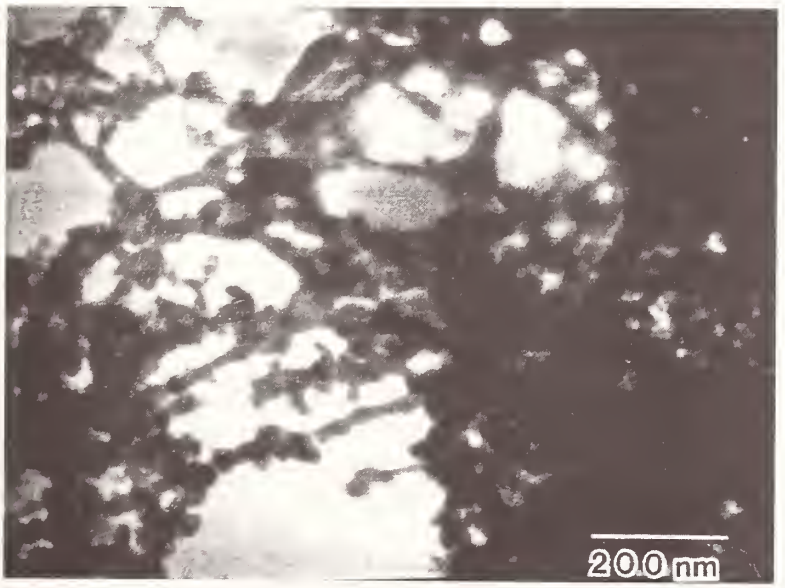

Figure 3. TEM micrograph of Y, Ba, and Cu hydroxycarbonates as coprecipitated in the chemical flow reactor.

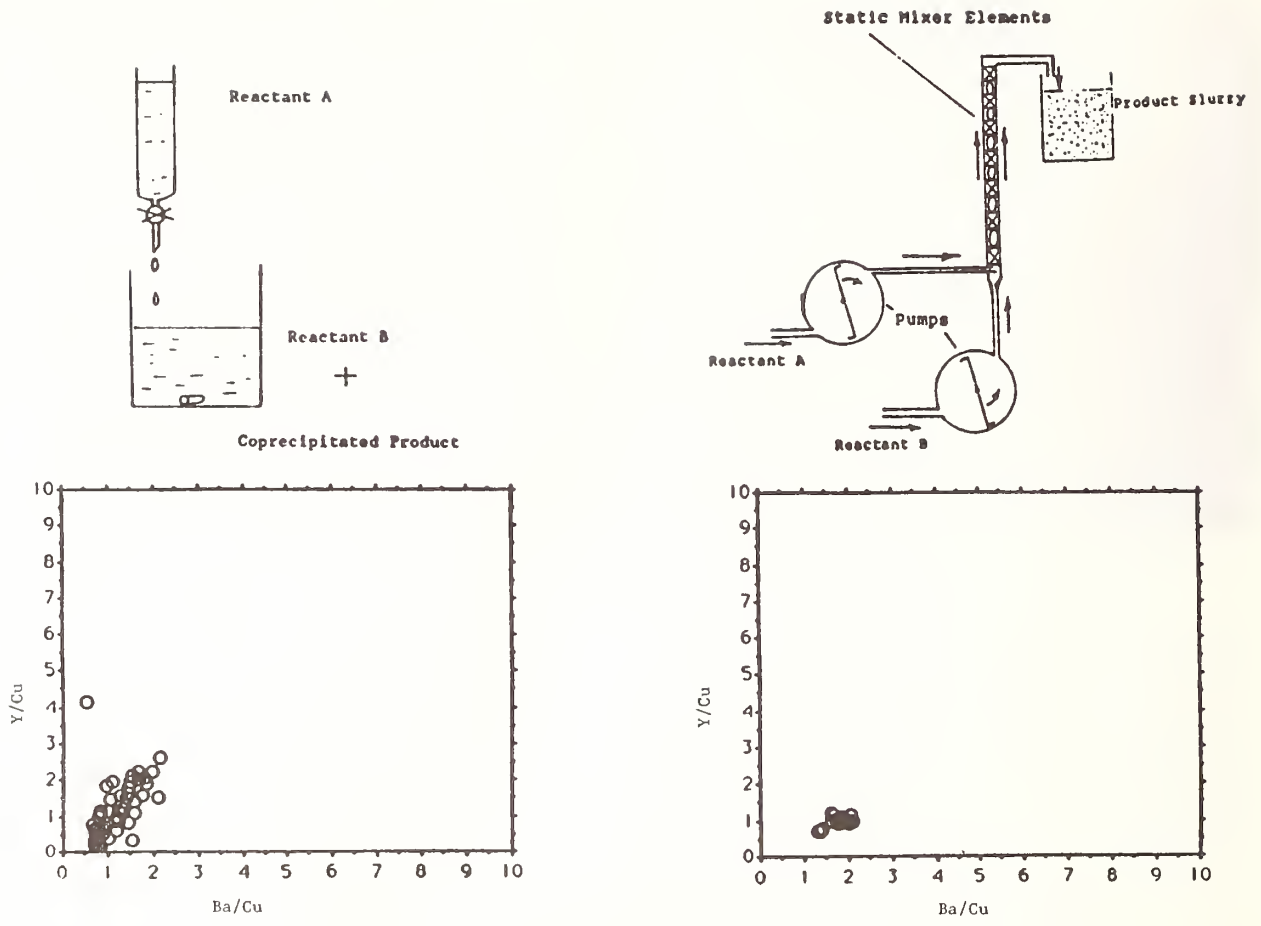

(a) (b)

Figure 4. Apparatus schematics and respective Y/Cu and Ba/Cu concentration ratios (wt %) as determined by HRAEM.

a. Conventional coprecipitation b. Flow reactor coprecipitation
Flow reactor configured for continuous powder synthesis

A consideration of the precipitating forms of the respective metallic elements in a highly basic carbonate environment leads to some interesting speculations. As shown in equation (4), both Y and Cu precipitate as hydroxycarbonates, for which no solubility data have been found in the literature. Barium precipitates predominantly as barium carbonate. In the light of a recent publication by Livage[15], it is suggested that Y and Cu ions undergo "olation" processes, i.e., the linking of these ions through the formation of hydroxyl bridges. Thus, Y and Cu readily coprecipitate. However, Ba ions, with their strong affinity for carbonate, are not chemically incorporated into the Y-OH-Cu network. This differential precipitation phenomenon is manifested macroscopically at low-ionic concentrations as shown in figure 2a. At higher ionic concentrations, or under the very efficient mixing regime offered within the flow reactor, the same phenomenon persists but on a very different scale. Thus, one can

envision a Y-OH-Cu network encapsulating smaller and smaller clusters of barium carbonate according to the relative rates of precipitation prevailing under the ionic concentrations and the mixing regime used.

Figure 5 a-d summarizes the results of HRAEM studies on flow reactor powders calcined under various conditions. The initial high degree of homogeneity deteriorates as calcining times and temperatures increase, suggesting that "flash" calcining procedures may be advantageous for this system. However, recent <u>in situ</u> phase development studies by high-temperature x-ray techniques[16] have shown that even flow reactor powders with a calcining history similar to that shown in figure 5d, convert readily to tetragonal YBCO at low O_2 partial pressures between 600 and 800 °C.

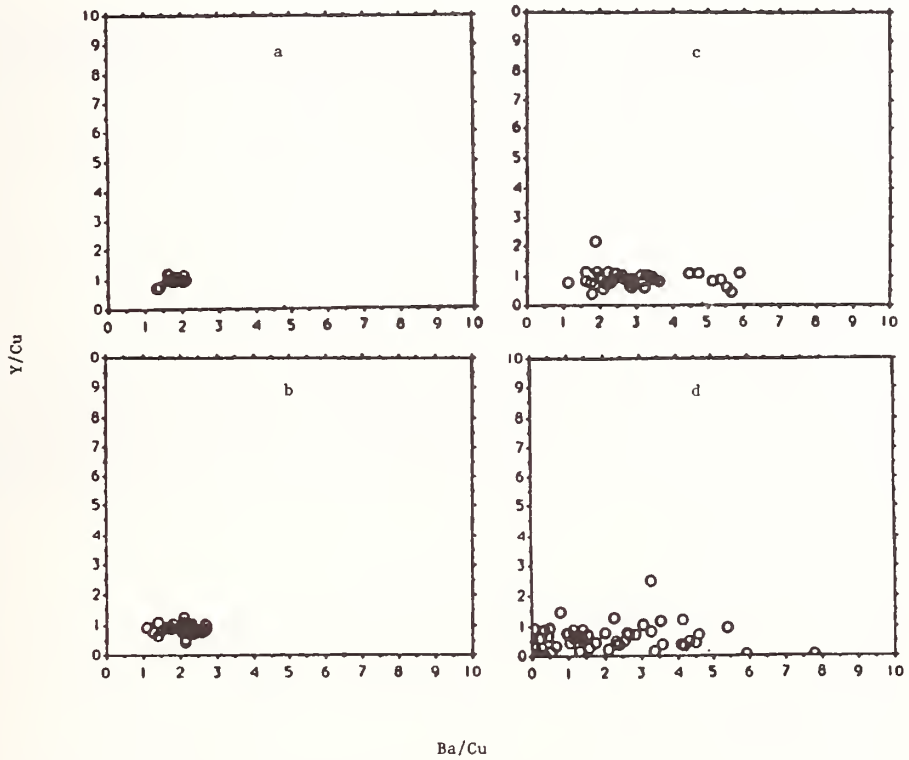

Figure 5. Y/Cu and Ba/Cu concentration ratios(wt %) for as-precipitated and calcined flow reactor powders.

a. as coprecipitated; b. 315°C, 5 min; c. 500°C, 5min; d. 450°C, 16.5h

SUMMARY

This presentation has indicated how molecular chemical routes to ceramic precursors are of practical utility to obtain desired ceramic phases often at low to modest temperatures. Methods such as RDEH and alkoxide hydrolysis, which have the potential for protostructure control, are quite complex and difficult to study. In the area of alkoxide hydrolysis, for example, much of the work has focussed on silicon-based materials[17], with very little emphasis on the more complex transition metal alkoxides or mixed-element alkoxides. As a result, progress towards "designing"

protostructures in multicomponent precursors has been minimal. Both the RDEH reactions and alkoxide hydrolyses are thought to be of the nucleophilic displacement type. The recent work of Livage(15) outlining procedures for estimating partial charges on metal atoms in molecules as a function of substituents should be quite useful in predicting at least the initial stages of these displacement reactions.

Organometal complexing has been shown to be useful in the synthesis of lithium-doped lanthanum nickelate. Although the procedure does not produce a high-surface area material directly, acetic acid treatment improves the surface area by a factor of five and produces a textured structure. The textured structure may offer subsequent benefits when the nickelate is fabricated into electrodes.

Homogeneity in the coprecipitation of Y, Ba, and Cu as hydroxycarbonates has been shown to be a function of the precipitation method, with the most homogeneous material obtained by using the chemical flow reactor. Unfortunately this homogeneity deteriorates during calcining, but our experimental results suggest that "flash" calcining procedures may minimize the segregation.

ACKNOWLEDGEMENTS

Research on conductive oxides was supported by the NASA-Lewis Research Center, under contract number C-30010-M. The authors would like to thank NIST scientists Dr. Eric Steel for the TEM micrograph and Dr. M. Epstein for the FES analyses.

REFERENCES

1. P.P. Phule and S.H. Risbud, Mater. Sci.& Eng., B3,(1989), 241.

2. P.P. Phule and S.H. Risbud, Mat. Res. Symp. Proc., 121, Materials Research Society, (1988), p. 275.

3. David W. Johnson Jr., Am. Cer. Bull., 64,(1985), 1597.

4. J.J. Ritter, R.S. Roth, and J.E. Blendell, J. Amer. Cer. Soc., 69, (1986), 155.

5. R.S. Roth, J.J. Ritter, H.S. Parker, and D.B. Minor, J. Amer. Cer. Soc., 69, (1986), 858.

6. J.J. Ritter, Advances in Ceramics: Ceramic Powder Science, G.L. Messing, K.S. Mazdiyasni, J.W. McCauley, and R.A. Haber, eds., Amer. Cer. Soc., Westerville, OH, (1987), p. 21.

7. E. Earl Royals, Advanced Organic Chemistry, Prentice Hall Inc., NJ,(1959), p. 117.

8. Paul A. Lessing, Ceramic Bulletin, 68, (1989), 1002.

9. L.A. Chick, J.L. Bates, L.R. Pederson, and H.E. Kissinger, Proc. 1st Int'l Symp.; Solid Oxide Fuel Cells, Subhash C. Singhal, ed., (1989), p. 170.

10. H.-M. Zhang, Y. Teraoka, and N. Yamazoe, Chem. Soc., Japan, Chem. Lett., (1987), 665.

11. B. Delmon and J. Droguest, Fine Particles; 2nd Int'l Conf., Wm. E. Kuhn, ed., Electrochem Soc. Monograph, (1974), p. 24.

12. Chemical Reaction Engineering, 2nd ed., Octave Levenspiel, J. Wiley & Sons, Inc., NY, (1972), p. 107.

13. J. J. Ritter and J. F. Kelly, High Temperature Superconducting Compounds: Processing and Properties, S. H. Whang and A. DasGupta, eds., Minerals, Metals and Materials Society, Warrendale PA, (1989), p. 303.

14. J. F. Kelly and J. J. Ritter, to be published.

15. J. Livage, Sol-Gel Science and Technology, M.A. Aegerter, M.J. Jafelicci Jr., D.F. Souza and E.D. Zanotto, eds., World Scientific, N.J., (1989), p. 111.

16. J.P. Cline, R.S. Roth, and J.J. Ritter, to be published.

17. R.C. Mehrotra, Sol-Gel Science and Technology, M.A. Aegerter, M.J. Jafelicci Jr., D.F. Souza and E.D. Zanotto, eds., World Scientific, N.J., (1989), p. 40.

R. Roth: I would like to make some comments about some of this superconductor precursor Joe was talking about. We've done quite a bit of high-temperature x-ray characterization of some of his products. As any of you who've been playing with the copper oxide, 123 (or 213) compound know, there are problems with respect to carbon dioxide in this compound. Starting with a carbonate precursor you might think that's not the way to go if you're worried about carbonating the product. But we have found that if you calcine this precursor in a high temperature x-ray, at 700 degrees in pure oxygen you get a beautiful join of yttrium oxide and 2:3 barium cuprate. We know from earlier work that the 2:3 barium cuprate doesn't form in the presence of carbon dioxide at all. Consequently, with the proper procedures you can get rid of all of the carbonate in this mixture when you heat it. So it's really, in my opinion, a good way to go. I wouldn't have thought so too long ago. Joe, you agree?

J. Ritter: I would say one thing in general. While we can synthesize good powders chemically, we have a very poor understanding how to process them after we make them, and that's Bob's point.

B. A. Scott: I'm curious about the reduction chemistry to form silicon carbide. It would seem that you're sort of at the mercy of kinetics of those reduction processes, so you get a lot of wrong bonds as well as the ones you want.

J. Ritter: Yes.

B. A. Scott: So, is that something that you can circumvent?

J. Ritter: Let me put it this way. We demonstrated that the chemistry works. We have not demonstrated how to control it. I think there is potential, but the approach needs a lot of additional work.

P. Davies: With regard to Bob's point, on the stability of the $Ba_2Cu_3O_5$ phase. If your goal is to make homogeneous 123 with as small a particle size as possible you really need to avoid firing anywhere below 700 or 750 °C. It seems desirable to heat straight to 800-850 °C as quickly as possible; otherwise, you're going to undo all your initial homogeneity, start to form the 2:3 phase and yttria with reasonable particle sizes, which will then have to resinter.

R. Roth: Oh, no, Peter, that depends on the P_{O2}. If you do this at .5% oxygen in the nitrogen mixture then you get your 123 to form at 600 °C.

P. Davies: Without seeing any 2:3?

R. Roth: Without seeing that phase at all.

National Institute of Standards and Technology Special Publication 804, Chemistry of Electronic Ceramic Materials, Proceedings of the International Conference held in Jackson, WY, August 17-22, 1990, issued January 1991.

ION EXCHANGE REACTIONS OF LAYERED PHOSPHATOANTIMONIC ACIDS : A ROUTE FOR NEW CATALYSTS AND LUMINESCENT MATERIALS

Yves PIFFARD
Laboratoire de Chimie des Solides,
IPCM UMR CNRS n° 110, Université de Nantes
2, rue de la Houssinière, 44072 NANTES CEDEX 03, France.

I - INTRODUCTION

It is now more than thirty years since the ion exchange behavior of zirconium phosphate gels was first reported [1,2]. Since that time many investigations into the nature of this and similar compounds have continued, leading to the discovery of many other layered groups (IV) and (V) phosphates and arsenates. The most important results dealing with these studies have been summarized in various review articles and books [3-7]. As already pointed out [8,9] the layered structure of α-zirconium phosphate (α-ZrP) and related materials exhibit a remarkable analogy with that of smectite clays, leading to similar chemical behaviors. These analogies have motivated considerable research on crystalline forms of α-ZrP-like materials and in the recent past, exciting new developments have taken place in the areas of catalysis, electrochemistry and fast ion conduction [7].
Prior to our work in this domain several attempts to prepare phosphatoantimonic acids have been reported [10-14], but there was only one material : $HSb(PO_4)_2.xH_2O$ for which the Sb/P ratio was well defined and whose structure, even not completely determined, was known since it is closely related to that of α-ZrP [15-16]. However it must be mentioned that, for this compound prepared from $SbCl_5$ and concentrated phosphoric acid, some disagreements exist about its characterization [10,12,17] (water content, decomposition temperature, amorphous character). As part of a search for new phosphatoantimonic acids [18] $HSb(PO_4)_2.xH_2O$ has been prepared through a new route along with an other layered phosphatoantimonic acid (LPA) : $H_3Sb_3P_2O_{14}.xH_2O$. This route involves the synthesis by solid state reaction of potassium phosphatoantimonates and ion exchange reactions in acidic medium. After a description

of the crystal structure of the parent potassium compounds, the preparation and characterization (thermal behavior, water content) of the LPA will be examined. Then, it will be shown through two examples how new catalysts and luminescent materials can be prepared by taking advantage of the ion exchange properties of these acids.

II - PARENT POTASSIUM PHASES

II.1 - $KSb(PO_4)_2$

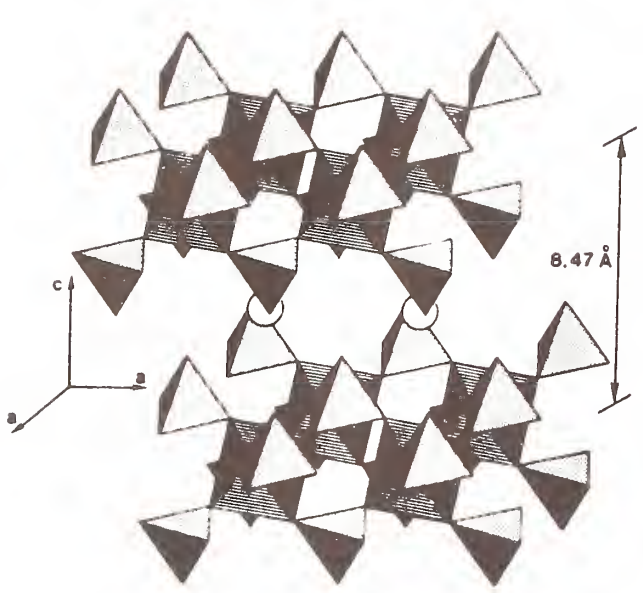

Fig. 1 - Perspective drawing of two $(Sb(PO_4)_2^-)_n$ layers showing two potassium atoms in the interlayers space.

This compound crystallizes in the rhombohedral system, space group $R\bar{3}$, with a = 4.7623(4)Å, c = 25.409(4)Å, Z = 3 [19]. It has a layered structure (fig 1). The $(Sb(PO_4)_2^-)_n$ infinite layers are built up from SbO_6 octahedra and PO_4 tetrahedra sharing corners. Three oxygen atoms of each tetrahedral phosphate are linked to three antimony atoms so that each antimony is octahedrally coordinated with six oxygen atoms of six different phosphate groups. The fourth oxygen of each phosphate group is unshared and points into the interlayer space. These layers are very similar to the $(Zr(PO_4)_2^{2-})_n$ layers in the α-ZrP compound. Each potassium atom is octahedrally coordinated to six of the unshared oxygen atoms (fig 1).

II.2 - $K_3Sb_3P_2O_{14}.xH_2O$

This compound crystallizes in the rhombohedral system, space group $R\bar{3}m$, with a = 7.147(1)Å, c = 30.936(6)Å, Z = 3 [20]. It is a layered material (fig 2 and 3). The $(Sb_3P_2O_{14}^{3-})_n$ layers are built up from SbO_6 octahedra and PO_4 tetrahedra sharing vertices. The SbO_6 octahedra are linked together in the same way as the WO_6 octahedra in the (001) plane of the hexagonal tungsten bronze. The phosphate groups are linked to these layers of octahedra via three

of their vertices. The fourth, which is unshared, points into the interlayer space wherein potassium atoms are situated. In the unit cell, there are nine potassium atoms distributed over twelve possible positions which are therefore occupied at an average of 75%. This compound, prepared by solid state reaction at 1000°C, is hydrated at room temperature (RT) [21].

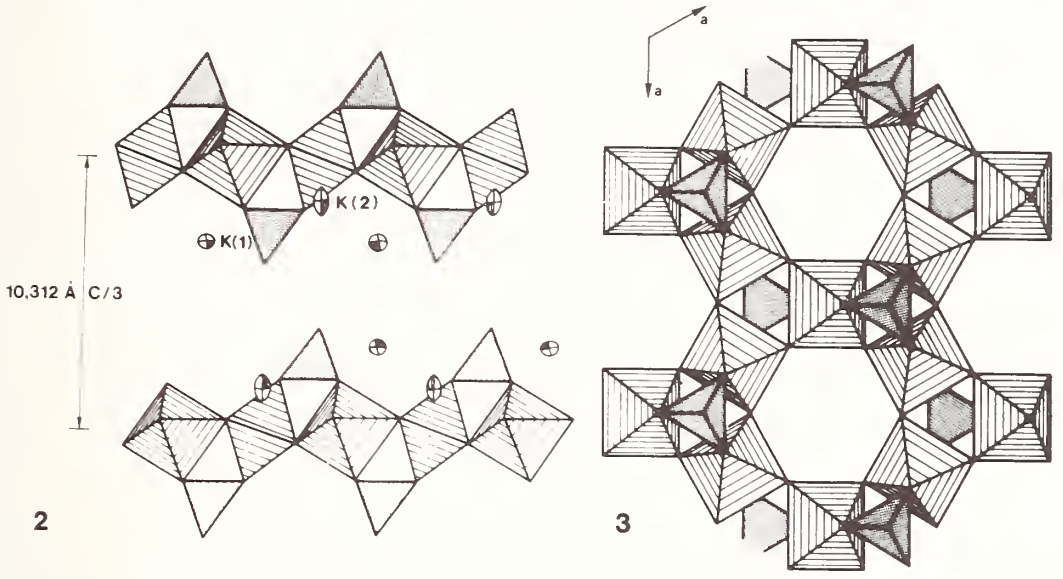

Fig. 2 - $K_3Sb_3P_2O_{14}$: projection of the structure on (110).

Fig. 3 - [001] view of a $(Sb_3P_2O_{14}^{3-})_n$ layer.

III - THE LPA $H_nSb_nP_2O_{3n+5}.xH_2O$ (n=1,3) : PREPARATION, WATER CONTENT AND THERMAL BEHAVIOR

III.1 - Preparation

The potassium compounds have been ion exchanged in a 8N nitric acid solution at 50°C [22,23]. The solution to solid ratio was 100ml/g of alkali material. After 3 stages, with renewal of the acidic solution between each 2hr stage, the extent of exchange is at least 99% and the hydrolysis has proved to be very weak, with less than 1% by weight. Electron and X-ray powder diffraction studies show unambiguously that the covalent layers which have been evidenced in the potassium phases are still present in the LPA.

III.2 - Water content, interlayer distance and protonic conductivity versus relative humidity (RH) at 20°C.

The LPA are hydrated compounds and their water content at RT strongly depends on the partial pressure of water vapor. The RH

influence on the composition, interlayer distance and protonic conductivity has then been studied at 20°C [24]. The main results of these studies have been summarized on fig. 4. Since the lattice parameters parallel to the layers are very close to those of the parent potassium compound, one can calculate the increase of volume per formula unit of the interlayer space simply by considering the evolution of the interlayer distance. It is then possible to estimate if the corresponding increase of the water content can be associated, entirely or partly, to crystallization water.

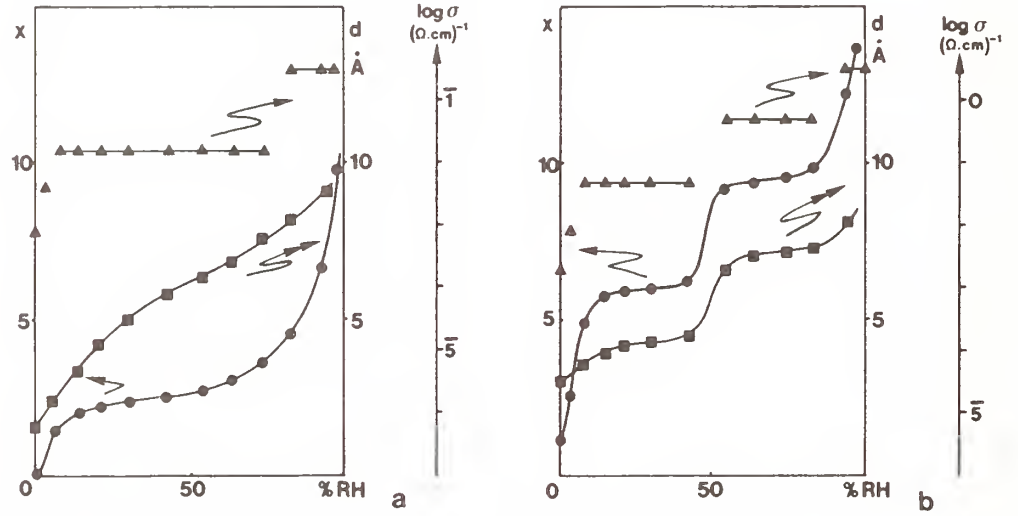

Fig. 4 - Adsorption isotherm of water, evolution of the water content x, of the interlayer distance d and of the conductivity, as a function of the relative humidity at 20°C for a) $HSb(PO_4)_2.xH_2O$ b) $H_3Sb_3P_2O_{14}.xH_2O$.

For $HSb(PO_4)_2.xH_2O$ the adsorption isotherm (fig. 4a) shows a sigmoïd-like evolution and the volume increase of the interlayer space with RH cannot account for the total increase of the water content ; then one must assume that part of it refers to water molecules adsorbed on the grain boundaries or at the surface. The conductivity strongly depends on the water content but its variation is too important to be only due to the intercalation of water. Generally speaking the evolution of the conductivity and the behavior towards hydration recall those observed for particle hydrates [25].

For $H_3Sb_3P_2O_{14}.xH_2O$ the protonic conductivity is closely related to the water content (fig. 4b). Each plateau corresponds to a fixed x value and to a particular interlayer distance. Therefore, this evolution shows a true "bulk-type" conductivity in agreement with the fact that, from volume considerations, the water content can be associated with crystallization water over almost the whole range of RH.

III.3 - Thermal behavior

In hydrates, properties related with the water content are strongly dependent on the temperature. The thermal behavior of the LPA has then been studied with use of TGA, DTA, DSC and X-ray thermodiffraction techniques [22,23]. Typical TG curves for both LPA are represented on fig. 5. They show that the LPA are rather stable : the dehydration process is reversible up to 560°C for $HSb(PO_4)_2.xH_2O$ and 300°C for $H_3Sb_3P_2O_{14}.xH_2O$.

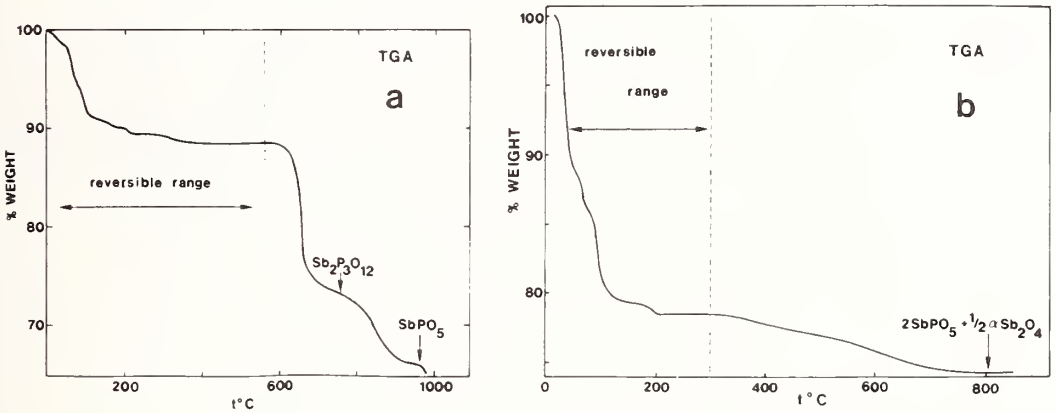

Fig. 5 - Weight loss versus temperature for a) $HSb(PO_4)_2.xH_2O$ b) $H_3Sb_3P_2O_{14}.xH_2O$.

IV - ACIDIC AND ION EXCHANGE PROPERTIES OF THE LPA

IV.1 - Acidic character

Vibrational spectroscopies, infrared absorption and Raman diffusion, are well adapted to the characterization of inorganic acids and especially to infer valuable information about protonic species. It is, however, essential to identify first the various vibrations corresponding to the atoms of the covalent layers. The LPA have then been studied at 20°C in comparison with the parent potassium compounds for which an assigment of the observed frequencies has been done [26,27] and more particularly for the stretching P-O and Sb-O domains.

For both acids, only slight changes are observed [28] in the vibrational spectra of the covalent layers with respect to those of the parent potassium phases, and this is true, in particular, for frequencies assigned to the antisymmetric stretching vibration involving the terminal P-O bonds ; i.e those bonds which point into the interlayer space and correspond to unshared oxygen atoms. It is then clear that the interaction between acidic protons, as well as all protonic species, and covalent layers is relatively weak. Strongly self-associated HPO_4^{2-} groups similar to those observed in α-ZrP do not exist in the LPA in which acidic protons belong to H_3O^+ oxonium groups ; that means that they are stronger acids than α-ZrP and related compounds.

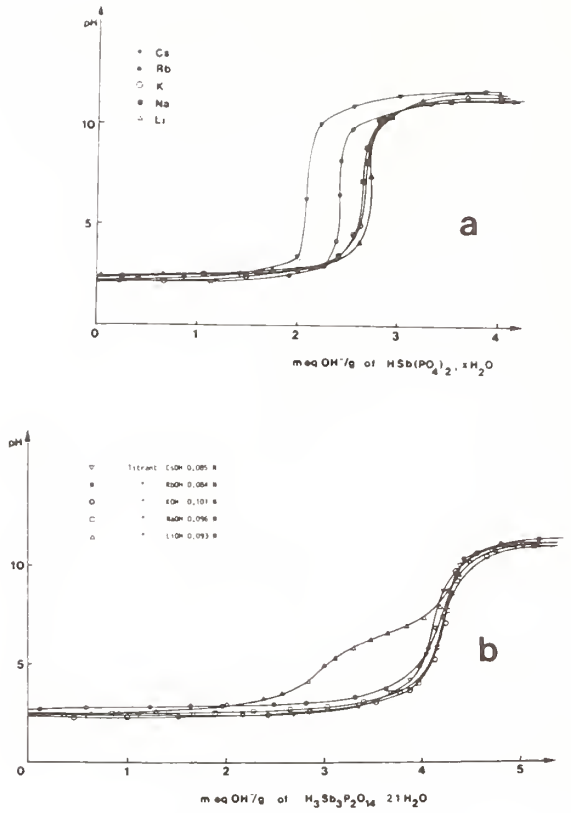

Fig. 6 - Potentiometric titration curves for alkali cations on a) $HSb(PO_4)_2.xH_2O$ b) $H_3Sb_3P_2O_{14}.xH_2O$.

In addition the LPA exhibit a swelling behavior similar to that of smectite clays. When suspended in water they readily undergo infinite swelling leading to a sol- or a gel-like solution from which a film can be obtained after removal of the solvent. This is a remarkable difference with the α-ZrP like acids which require a preintercalation of amines to give colloïdal suspensions. Such a difference can be attribued to the fact that the charge of the anionic layer in α-ZrP is higher than that of layers in the LPA or in montmorillonite [8].

IV.2 - Ion exchange behavior

The ion exchange behavior of the LPA is illustrated by the titrations with alkali hydroxide solutions (fig. 6) [23,24] and also by ion exchange isotherms such as those represented in fig. 7 for $H_3Sb_3P_2O_{14}.xH_2O$ (isotherms with $HSb(PO_4)_2.xH_2O$ are similar).

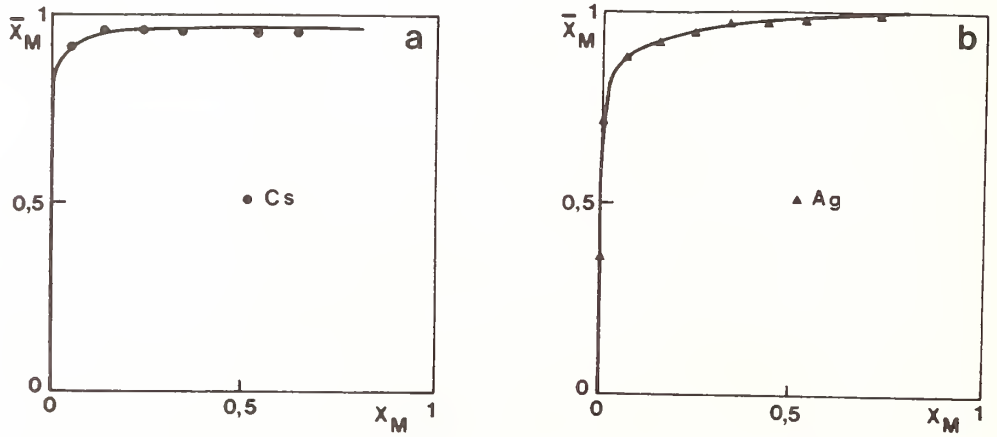

Fig. 7 - a) Cs^+/H^+ b) Ag^+/H^+ ion exchange isotherm on $H_3Sb_3P_2O_{14}.xH_2O$.

The ordinate of these plots, X_M, is the equivalent fraction of the M^+ ion in the exchanger and the abscissa, X_M, is the equivalent fraction of the M^+ ion in the solution. Both curves show that the selectivity coefficients of the Cs^+/H^+ and Ag^+/H^+ systems with the LPA are very high.

V - THE LPA AND SOME OF THEIR ION EXCHANGE DERIVATIVES AS ACIDIC CATALYSTS.

In order to evaluate their catalytic properties, the LPA and some of their ion exchange derivatives have been studied in a test reaction which corresponds to the conversion of isopropanol (IPA) into propene, diisopropylether and acetone according to the following reaction :

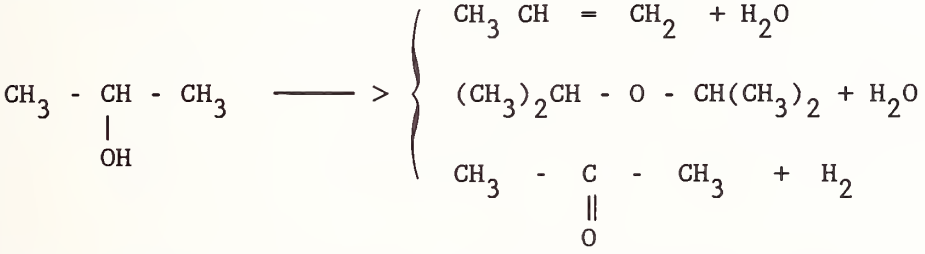

This reaction is not of industrial interest ; however since it can give rise either to dehydrations (intra- and/or inter-molecular) or to a dehydrogenation, it appears as a valuable catalytic test.

Cu^{II}-, Ni^{II}- and La^{III}- derivatives with various metal-ion loadings have been prepared by ion exchanging the LPA with solutions containing either $Cu(SO_4).5H_2O$, $Cu(NO_3)_2.3H_2O$, $Ni(NO_3)_2.6H_2O$ or $La(NO_3)_3.6H_2O$.

The best results have been obtained with $HSb(PO_4)_2.xH_2O$ and its ion exchange derivatives. In all cases, compounds resulting from the dehydration (propene and diisopropylether) are the majority products, indeed even exclusive with a clear selectivity towards propene. This is not surprising since acidic sites from the catalyst promote the carbocation formation occuring in the dehydration process as follows :

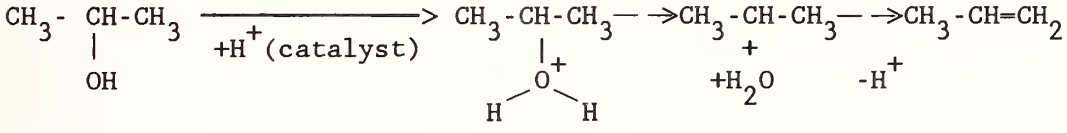

The selectivity towards propene is better when ion exchange derivatives are used and the carbon yield is close to 1. This result can be explained by the fact that when metallic ions are introduced, the density of acidic sites at the surface of the catalyst is decreased, therefore :

- desorption of products is promoted and, as a consequence, their polymerization (coke formation) is avoided.
- a monomolecular dehydration process is favored with respect to a bimolecular one since the distance between acidic sites is sufficiently large.

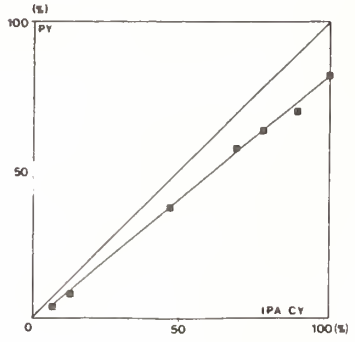

Fig. 8 - Disactivation curve (Propene Yield as a function of the IPA Conversion Yield) for $H_3Sb_3P_2O_{14}.xH_2O$.

Disactivation curves obtained with some of our catalysts can be interpreted in a similar way. They represent the propene yield (PY) as a function of IPA conversion yield (CY) (fig. 8). The ideal curve (diagonal straight line with slope 1) corresponds to a situation in which all the IPA is converted in propene. The fact that the experimental curve is a straight line indicates that propene- and coke-formation occur on the same sites and that the disactivation corresponds to a decrease on the number of active sites. When ion exchange derivatives are used the disactivation process is very slow, indeed even non observable, as in the case of $Cu_{0.35}Sb(PO_4)_2$ which has been more extensively studied. For this catalyst the IPA CY has been represented in fig. 9 as a function of time. Starting at about 95% the CY first decreases down to 75% and then increases up to 100% (after 120 hr) for a reaction temperature (T_R) of 200°C.

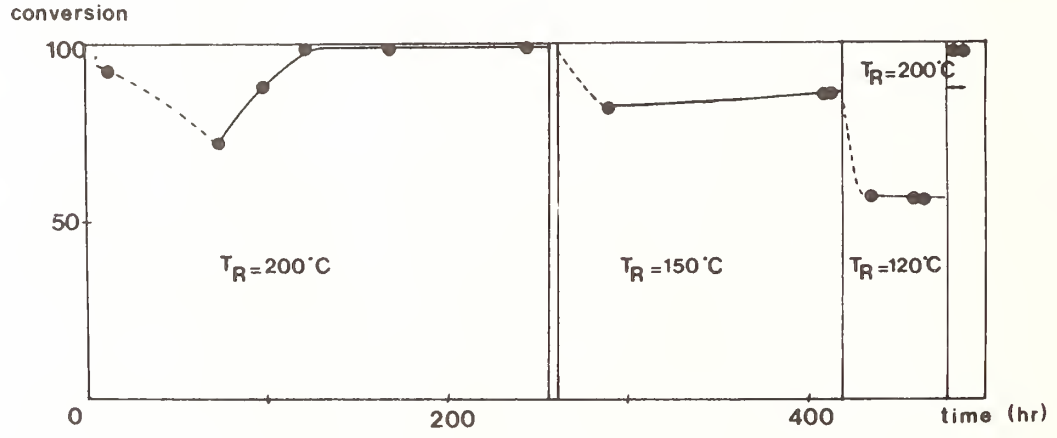

Fig. 9 - IPA Conversion Yield versus time with $Cu_{0.35}Sb(PO_4)_2$.

This step allowing the catalyst to reach is working regime is observed only if the catalyst is prepared from $Cu(SO_4).5H_2O$ (not with $Cu(NO_3)_2.3H_2O$). This effect of residual SO_4^{2-} ions is not understood but it is clear that it promotes the activity of acidic

sites since the specific activity, for the same copper content, is three times as much as that of a catalyst prepared with $Cu(NO_3)_3.3H_2O$ (Table I). In the working regime at 200°C the CY remains very stable (close to 100%). If T_R is decreased, the CY decreases (fig. 10, see steps at T_R=150°C and T_R=120°C). However, coming back to T_R=200°C a CY of about 100% is restored and maintained throughout the test, i.e over more than 500 hr.

TABLE I - Influence of the Cu^{II} content ($Cu_yH_{1-2y}Sb(PO_4)_2$) on the IPA conversion

y	0	0.35*	0.35**	0.10**	0.01**
Specific activity (g IPA g^{-1} h^{-1})	0.287	1.24	0.432	0.619	2.18
Selectivity (C%)					
Propene	91	100	100	100	99
Diisopropylether	9	-	-	-	1
Acetone	-	-	-	-	-

* prepared from $CuSO_4.5H_2O$

** prepared from $Cu(NO_3)_2.6H_2O$

Conditions of the test - T_R : 200°C
- Total pressure : 1.4 bar
- IPA mass flow : 0.134 g h^{-1}
- W.H.S.V. : 1.25 h^{-1}

Various tests involving different copper contents and other ion exchange derivatives of $HSb(PO_4)_2.xH_2O$ have been performed. The main results have been summarized in tables I and II. It can be seen from table I that even for small copper contents (y = 0.01), the ion exchange derivatives exhibit a greater specific activity and a better selectivity than those of the acidic compound. It must be mentioned however that, for a given selectivity, the evaluation of a catalyst is not limited to its specific activity, but it includes the disactivation rate. If traces of copper promote the activity, larger quantities are necessary to maintain it for a long time. Table II shows the influence of the cation type on the catalytic reaction for a given substitution ratio. The specific activities are similar but the selectivities are different. In addition it must be mentioned that the Ni- and La- catalysts disactivate rapidly (a few tens hr).

TABLE II - Influence of M ($M^{z}_{y}H_{1-yz}Sb(PO_4)_2$ with yz = 0.7) on the conversion (conditions for the test similar to those given in table I).

M_y	H	$Cu_{0.35}$	$Ni_{0.35}$	$La_{0.23}$
Specific activity (g IPA g^{-1} h^{-1})	0.287	0.432	0.435	0.426
Selectivity (C%)				
Propene	91	100	97.3	99.6
Diisopropylether	9	-	2.7	0.4
Acetone	-	-	-	-

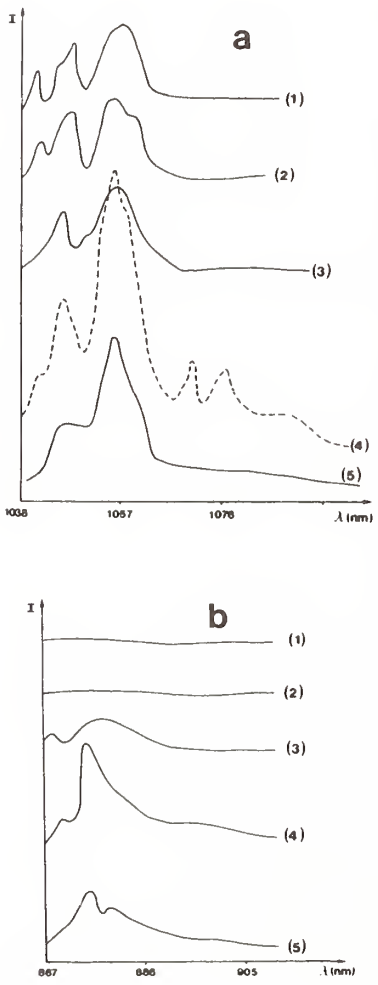

VI - THE LPA AS STARTING COMPOUNDS FOR THE PREPARATION OF LUMINESCENT MATERIALS

When ion exchange reactions with $HSb(PO_4)_2,xH_2O$ are carried out with Ln^{3+} cations (Ln=Nd,Eu) the extent of exchange is at least 98% with solutions containing an excess of these cations [22]. When the amount of Ln^{3+} in the solution is less than the theoretical exchange capacity of the acid, the cation uptake is maximum and leads to $(Ln_yH_{1-3y})Sb(PO_4)_2.x'H_2O$ compounds. Their thermal decomposition occurs above 850°C leading to the isomorphous series $Ln_{x/2}Sb^{III}_{(1-x)/2}Sb^{V}_{3/2}(PO_4)_3$ whose structure is isotypic with that of $Bi^{III}_{1/2}Sb^{V}_{3/2}(PO_4)_3$ [29]. In this latter compound the shortest Bi-Bi distance is 8.5Å. This feature is of great interest since it corresponds to the shortest Nd-Nd distance in compounds for which the Nd concentration can reach $2.2x10^{21}cm^{-3}$ when x=1.

Fig. 10 - Emission spectra of the $Nd_{x/2}Sb^{III}_{(1-x)/2}Sb^{V}_{3/2}(PO_4)_3$ compounds (1) x=0.05, (2) x=0.10, (3) x=0.15, (4) x=0.25, (5) x=0.30 corresponding to the transitions a) $^4F_{3/2} \rightarrow {}^4I_{11/2}$ b) $^4F_{3/2} \rightarrow {}^4I_{9/2}$

As a matter of fact, it has been shown that the degree of concentration quenching in Nd-laser materials is determined by the linkage between the NdO_y polyhedra [30], and especially by the Nd-Nd distance.
Preliminary luminescence experiments have been undertaken on powder samples of $Nd_{x/2}Sb^{III}_{(1-x)/2}Sb^{V}_{3/2}(PO_4)_3$ compounds at RT. Typical emission spectra, corresponding to the $^4F_{3/2}$ -> $^4I_{11/2}$ and $^4F_{3/2}$ -> $^4I_{9/2}$ transitions of Nd^{3+} are given in fig. 10. It can be seen that the Nd concentration strongly influences the intensity of the emission lines which reaches a maximum for x=0.25 thus giving a rather narrow band. According to this result, single crystal corresponding to this particular composition (x = 0.25) would be adequate for a mini laser application.

The LPA prepared by ion exchange in acidic medium are rather well defined compounds in terms of structure, water content and thermal behavior. Their swelling behavior similar to that of smectite clays and their strong acidity make them efficient ion exchangers from which new materials can be prepared. Those include catalysts and luminophors but other ones such as pillared layered materials could be thought up.

REFERENCES

[1] K.A. KRAUS and H.O. PHILIPS, J. Am. Chem. Soc., 1956, 78, p. 644
[2] C.B. AMPHLETT, L.A. DONALD and M.J. REDMAN, Chem. In. (London), 1964, p. 1314
[3] V. VESELY and V. PEKAREK, Talanta, 1972, 19, p. 219
[4] A. CLEARFIELD, G.H. NANCOLLAS and R.H. BLESSING, J.A. MARINSKY and Y. MARCUS Eds., M. Dekker, New York, 1973, Chap. 1
[5] G. ALBERTI and U. COSTANTINO, J. Chromatogr., 1974, 102, p. 5
[6] G. ALBERTI, Acc. Chem. Res., 1978, 11, p. 163
[7] A. CLEARFIELD, C.R.C. Press Inc, Boca Raton, 1982
[8] A.DYER and D.LEIGH, J. Inorg. Nucl. Chem., 1972, 34, p. 369
[9] S.YAMANAKA and M. KOIZUMI, Clays Clay Min., 1975, 23, p. 477
[10] A. WINKLER and E. THILO, Z. Anorg. Allg. Chem., 1966, 346, p. 92
[11] A. WINKLER and E. THILO, J. Polymer. Sci., 1969, 16, p. 4283
[12] J.P. JOLIVET and J. LEFEBVRE, Bull. Soc. Chim., 1975, p. 2409
[13] J.P. JOLIVET and J. LEFEBVRE, Bull. Soc. Chim., 1975, p. 2420
[14] N.G. CHERNORUKOV, I.A. KORSHUNOV, N.P. EGOROV, A.I. ZABELIN and T.A. GALANOVA, Izv. Akad. Nauk S.S.S.R., Neorg. Mater., 1981, 17, p. 1058.

[15] J.M. TROUP and A. CLEARFIELD, Inorg. Chem., 1977, 16, p. 3311
[16] J. ALBERTSON, A. OSKARSSON, R. TELLGREN and J.O. THOMAS, J. Phys. Chem., 1977, 81, p. 1574
[17] N. MIURA, Y.OZAWA and N.YAMAZOE, Denki Kagaku, 1985, 53, p. 338
[18] M. TOURNOUX and Y. PIFFARD, French Patent 85-01839, 1985
[19] Y. PIFFARD, S. OYETOLA, S. COURANT and A.LACHGAR, J. Solid State Chem., 1985, 60, p. 209
[20] Y. PIFFARD, A. LACHGAR and M. TOURNOUX, J. Solid State Chem., 1985, 58, p. 253.
[21] A. LACHGAR, S. DENIARD-COURANT and Y. PIFFARD, J. Solid State Chem., 1988, 73, p. 572
[22] Y. PIFFARD, A. VERBAERE, A. LACHGAR, S. DENIARD-COURANT and M. TOURNOUX, Eur. J. Solid State Inorg. Chem., 1989, 26, p. 113
[23] Y. PIFFARD, A.VERBAERE, A. LACHGAR, S. DENIARD-COURANT and M. TOURNOUX, Rev. Chim. Min., 1986, 23, p. 766.
[24] S. DENIARD-COURANT, Y. PIFFARD, P. BARBOUX and J. LIVAGE, Solid State Ionics, 1988, 27, p. 189
[25] P. BARBOUX, R. MORINEAU and J. LIVAGE, Solid State Ionics, 1988, 27, p. 211
[26] E. HUSSON, A. LACHGAR and Y. PIFFARD, J. Solid State Chem., 1988, 74, p. 138
[27]E. HUSSON, F. GENET, A. LACHGAR and Y. PIFFARD, J. Solid State Chem., 1988, 75, p. 305
[28] E. HUSSON, M. DURAND-LE FLOCH, C. DOREMIEUX-MORIN, S. DENIARD-COURANT and Y. PIFFARD, Solid State Ionics, 1989, 35, p. 133
[29] S. OYETOLA, A. VERBAERE, D. GUYOMARD and Y. PIFFARD, J. Solid State Chem., 1988, 77, p. 102
[30] M.S. HWANG, H. Y.-P. HONG, M.C. CHENG, and Y. WANG, Acta Crystallogr. Sect. C., 1987, 43, p. 1241.

P. Battle: Have you looked at the protonic conductivity at higher temperature, in the reversible regime?

Y. Piffard: No, we didn't study the protonic conductivity at higher temperature. We only looked at the conductivity at room temperature because I think that since it is very likely that the protonic conductivity is related to a diffusion of protons on a hydrogen bonded network within the interlayer space, if you remove water molecules you will lower the conductivity very, very quickly. It's almost always true for this type of mechanism.

K. Poeppelmeier: Following up on your earlier point where you convinced us that the proton was not tightly bound to the terminal oxygen but associated with the water between the layer. Through your dehydration studies it appeared you could reach a state where you have only $HSb(PO_4)_2$.

Y. Piffard: Yes.

K. Poeppelmeier: If you do the infrared analyses on that compound is the proton then tightly bound to the terminal oxygen?

Y. Piffard: In that case, the situation is probably different, yes.

K. Poeppelmeier: This is the sort of material that probably is important at elevated temperatures for reactions when you're studying solid acids.

Y. Piffard: At higher temperatures, yes.

R. Roth: When you're ion exchanging those layered structures with Rb and Cs, I would assume the Rb and Cs ions go in place of the water molecules structurally. Do these compounds then hydrate as much as the potassium phase ($K_3Sb_3P_2O_{14}\cdot 5H_2O$) does?

Y. Piffard: I don't remember exactly what is the number of water molecules, but I know that it is smaller.

R. Roth: They still do hydrate?

Y. Piffard: Yes, but the water content is less.

A. Jacobson: You mentioned that, in the swelling behavior with water, they looked like, and behaved like smectite clays?

Y. Piffard: Yes.

A. Jacobson: Have you looked at ion exchange reactions with large cations like polyhydroxycations, for example, to see if you can pillar them?

Y. Piffard: We are looking at this problem at the moment. I can indicate that it's very easy to ion exchange with amines, for example, even with long chain amines. We don't need any preintercalation processes as in the case of α-ZrP-like acids.

K. Poeppelmeier: I have a general question; maybe for the audience, too. This difference between sulfate and nitrate anions. One of the things we've been looking at is something we've been calling salt inhibition and I was wondering if the geochemists in the audience have observed this phenomenon. In these fairly open structures there are sites for both anions and cations, and literally both are incorporated. It has been observed in zeolites. I was wondering if this phenomenon wouldn't be enhanced on the near surface when you do these partial exchanges with copper and observe the effect of the anion. That in fact, there is incorporation of both cations and anions and the sulfate anion would be different from the nitrate anion. This isn't ion exchange but the incorporation of a cation and corresponding anion. Do you have any thoughts about that? Have others seen effects like this?

Y. Piffard: I don't think so because when a cation exchange reaction is concerned you don't think, a priori, of any difference associated with the anion.

K. Poeppelmeier: But it would be very difficult, I think, to detect a small additional incorporation of both cations and anions. It isn't really equivalent to the ion exchange process. It might be one explanation for the difference in the effect on these anions.

A. Navrotsky: To address that from the geochemical point of view there are a number of minerals that incorporate cations and anions in different amounts and certainly cordierites and scapulites and so on will incorporate nitrate, sulfate and carbonate ions. I think very little is known about the mechanisms of whether they're coupled, but I think you're probably right. It's probably kinetically controlled.

K. Poeppelmeier: It may be an important reaction to think about when you are studying these reactions.

National Institute of Standards and Technology Special Publication 804, Chemistry of Electronic Ceramic Materials, Proceedings of the International Conference held in Jackson, WY, August 17-22, 1990, issued January 1991.

MIXED METAL OXIDES WITH THE PYROCHLORE STRUCTURE AS CATALYSTS FOR METHANE OXIDATIVE COUPLING

A. J. Jacobson, J. T. Lewandowski, C. A. Mims*, R. B. Hall and G. R. Myers
Exxon Research and Engineering Company, Annandale, NJ 08801
*Department of Chemical Engineering, University of Toronto, Toronto, M5S 1A4, Canada

ABSTRACT

A new series of bismuth tin pyrochlore oxides have been synthesized by precipitation from aqueous potassium hydroxide and calcination at 400°C. The low temperature synthesis method leads to the formation of compounds with compositions $Bi_2(Sn_{2-x}Bi_x)O_{7-x/2}$ ($0.05<x<0.86$) in which bismuth is present on both the A and B sites of the pyrochlore structure. The bismuth rich pyrochlores decompose at temperatures between 500°C and 700°C, depending on the specific composition, to Bi_2O_3 and $Bi_2Sn_2O_7$. The phase separated compositions are good catalysts for the direct conversion of methane to higher hydrocarbons via oxidative coupling.

INTRODUCTION

A variety of metal oxides have been studied as catalysts for the direct conversion of methane to higher hydrocarbons via oxidative coupling[1]. Following the initial work of Keller and Bhasin[2], many different types of oxides have been found to be effective catalysts at temperatures above 600°C. Examples include simple binary systems such as the alkaline and rare earth oxides, PbO, SnO_2 and Bi_2O_3, often promoted with alkali metals to improve selectivities[2 - 8]. In particular, lithium promoted MgO[5, 6], samarium oxide[7, 8] and supported manganese oxides[9] have been examined in detail. More complex mixed metal oxides, for example, $LiNiO_2$[10, 11], the perovskites $BaPbO_3$[12] and $SrCeO_3$[13], kentrolite $Pb_2Mn_2Si_2O_9/SiO_2$[14] and bismuth oxyhalides $ABi_3O_4Cl_2$ (A = Li, Na, K and Ag)[15, 16] all show good selectivities (40 - 80%) at moderate conversions.

Although considerable variations in specific activity and selectivity are observed between different oxides, the reaction mechanism is thought to be similar for all catalysts. The hydrocarbon products are formed by coupling of methyl radicals which are generated by hydrogen abstraction from methane by an active oxygen site on the catalyst surface.

The active oxygen site is regenerated by oxidation and the elimination of water from the oxide surface. In order to study systematically the influence of chemical substitution on the chemistry of these reactions, we have studied mixed metal oxides of general composition $A_2B_2O_7$ with the pyrochlore structure which can be synthesized for a wide range of A,B combinations provided the radius ratio, r_A/r_B, is greater than approximately 1.4[17]. The catalytic performance of the pyrochlore oxides, $Ln_2Sn_2O_7$[18] has recently been found to show variations which were related to the ease of oxidation or reduction of the specific rare earth cation. In this paper, we focus on one specific set of pyrochlore oxides based on the compound $Bi_2Sn_2O_7$ and describe the synthesis and stability of a range of compositions together with some preliminary data on their performance as catalysts for oxidative coupling of methane.

The compound $Bi_2Sn_2O_7$ was first reported by Roth[19] and subsequently further studied by Gattow[20], Shannon et al. [21]and Vetter[22]. The compound has a tetragonal structure related to pyrochlore at room temperature with cell constants 21.328 and 21.545 Å. At 140°C the α form converts to the cubic β structure with a unit cell parameter of 21.40Å at 200°C. Both the α and β form have unknown non-centric crystal structures. At 680°C the β structure transforms to the γ phase with the ideal pyrochlore structure and a cell parameter of 10.73Å at 700°C. The phase transitions observed in $Bi_2Sn_2O_7$ are sensitive to impurities or small amounts of dopants on either the A or B sites in the pyrochlore structure. Impurities and dopants lower the transition temperatures and for many samples the α to β transition is not observed. The high temperature phase diagram shows the existence of the single stoichiometric composition $Bi_2Sn_2O_7$.

High surface area compounds with the pyrochlore structure containing bismuth or lead as the A site cation and ruthenium or iridium as the B site cation have been prepared previously by crystallization at mild conditions (<100°C) from concentrated alkali hydroxide solutions [23, 24]. Compounds were prepared with Bi^{3+} occupying both the A and B cation sites in the pyrochlore structure by control of the synthesis conditions (solution composition, pH and temperature). The $Bi_2Ru_{2-x}Bi_xO_{6.5}$ compositions have been called 'expanded' pyrochlores because their cubic lattice constants increase linearly with composition with increasing levels of substitution on the B cation site. A similar series of phases is observed when bismuth is replaced by lead. We have extended this solution synthesis approach to prepare a new series of bismuth tin expanded pyrochlore compositions $Bi_2(Sn_{2-x}Bi_x)O_{7-x/2}$ and examined their catalytic behavior. The end member of the series, $Bi_2Sn_2O_7$, has previously been found to be an average catalyst for methane coupling[25]. Mixed Bi_2O_3 - SnO_2 phases have also been studied at lower temperatures (500°C) as catalysts for methane conversion using N_2O as the oxidant and observed to be selective for the formation of formaldehyde at low (<3%) conversion[26].

EXPERIMENTAL

In a typical synthesis, $Bi(NO_3)_3 \cdot 5H_2O$ (12.129g, Alfa) was dissolved in 100ml of water and 30ml of concentrated nitric acid. Tin was added to the solution as $SnCl_4 \cdot 5H_2O$

(8.763g, Aldrich) followed by 250ml of 2M KOH solution. The pH and the total solution volume were then adjusted by further addition of KOH solution and water. A white amorphous precipitate was formed at this stage of the synthesis. The slurry was then heated at 75 to 100°C for typically 2 to 5 days to complete the reaction. The final product was separated by filtration, washed with water and dried at 100°C. The effects of changes in the total reactant concentrations from 0.0313M to 0.0625M in tin, the solution pH values from 10 to 14 and Bi/Sn ratios from 1:1 to 3:1 were examined.

A Dupont 1090 thermal analyzer was used to determine the water contents of samples by heating them in air to 1000°C at 10°C min^{-1}. Elemental analysis for alkali metals, bismuth and tin was carried out by Galbraith Laboratories. Surface area measurements were made by N_2 adsorption using an Omicron Omnisorb 360.

Powder X-ray diffraction data were measured on an automated Siemens D500 diffractometer using Cu Kα radiation. Samples were loaded into 2mm deep aluminum sample trays. Diffraction profiles were scanned in ω - 2θ mode over the range $2.0 \leq 2\theta \leq 90.0°$ in steps of 0.02°, with count times of 2s at each point. In a few cases, data over a wider angular range ($2.0 \leq 2\theta \leq 122.0$) with higher statistical precision were obtained at count times of 30s per 0.02° step (see Figure 3.). Lattice constants were obtained from the powder X-ray diffraction data by least squares refinement of peak positions or for many of the samples by full matrix Rietveld analysis of the diffraction profiles[27].

The full matrix least squares Rietveld refinements were achieved using a locally modified version of the DBW3.2 code of Wiles and Young[28]. The background was treated by linear interpolation between a set of estimated points that were updated periodically. The peak shapes were described by the pseudo-Voigt function. Scattering factors for the species Bi^{3+}, Sn^{4+} and O^{-1} were used. The space group Fd3m(No. 227 [29]) was assumed.

The thermal stability of the expanded pyrochlore phases with different compositions was determined X-ray diffraction measurements both 1) at room temperature after annealing to each of a series of temperatures for 16h, and also 2) at high temperatures. The high temperature X-ray measurements were made on samples contained in quartz capillaries using a wavelength of 0.97203Å at the X10A beam line at Brookhaven National Laboratories .

The performance of the materials as catalysts for methane oxidative coupling was evaluated using a small downflow quartz reactor. Samples of the catalysts consisting of 80-120 mesh particles were prepared by pressing into pellets, followed by grinding and sieving. A standard reactant gas mixture of $CH_4 : O_2 : Ar = 2 : 1 : 5$ (stoichiometric for ethylene production) at one atmosphere total pressure was used. By variations in in the reactant flow rate (50-150 ml/min) and sample size (0.3-3g), we were able to vary the gas residence time , and therefore the methane conversion at constant temperature. Reaction temperatures from 500°C to 900°C were investigated and the products were analyzed by gas chromatography.

RESULTS

The final compositions of the bismuth tin pyrochlore phases when prepared by the solution synthesis route depend on the pH of the syntheses, the reaction temperature, the ratios of the reactants and the total concentration of bismuth and tin. The formation of a pure pyrochlore phase directly from solution at 100°C depends critically on the pH of the synthesis solution. For example, at a ratio of reactants Bi/Sn =1 and a total solution concentration 0.0625 molar in tin, a pure pyrochlore phase is obtained only in a narrow pH range close to 13. At high pH values, a mixture of the pyrochlore phase and a second crystalline composition is obtained. At these conditions, the second phase (D*) is obtained in pure form at pH >13.3. Close to pH = 14, Bi_2O_3 appears as a second phase together with D*. As the concentration of the solution is decreased, D* persists to lower pH as a pure phase and coexists with the pyrochlore to a pH as low as 12.65 in the most dilute reaction solutions (0.0313 molar). Below pH = 12.5, a new poorly crystalline phase is formed in addition to pyrochlore. On calcination, materials containing this poorly crystalline phase convert to a mixture of a pyrochlore and an amorphous component.

The average composition of D* determined for four different samples by elemental and thermogravimetric analysis corresponds to a Bi/Sn ratio of 2.5. Thermogravimetric analysis data show the absence of coordinated water molecules but show a small (2.8 - 3.1%) reproducible weight loss at 300°C suggesting the presence of hydroxyls. On complete dehydroxylation the product is a pure pyrochlore phase. The weight loss and the chemical analysis data indicate a composition $Bi_5Sn_2O_9(OH)_5$. All the reflections in the X-ray powder pattern of D* can be indexed with an orthorhombic unit cell and cell constants a = 7.613(2)Å, b = 10.564(3)Å and c = 6.734(2)Å. The systematic absences in the powder data suggest that the space group is $P2_12_12_1$(No. 19[29]). Further work to obtain crystals of D* large enough for structural analysis is in progress.

On calcination at 400°C, pure pyrochlore phases are observed for all of the products of the 100°C solution syntheses which are pyrochlore, D* or mixtures. The surface areas of the pure pyrochlore phases as prepared from solution are typically in the range of 50 to 100 m^2/g and reduce to 30 to 50 m^2/g on calcination at 400°C. In contrast, D* phases and pyrochlore samples made from them have surface areas in the 1-6 m^2/g range.

The extent of bismuth substitution in the pyrochlore phases $Bi_2(Sn_{2-x}Bi_x)O_{7-x/2}$ can be varied by adjusting the various synthesis parameters such as the pH and the concentration of the reactants. The detailed influence of all of the various synthesis parameters has not yet been fully evaluated though some of the general trends are clear. For example, Figure 1 shows the influence of the ratio and concentration of the bismuth and tin components on the product composition. The solution volumes of 400, 600, and 800 ml indicated on the Figure, correspond to solution concentrations which are 0.0625, 0.0417 and 0.0313 molar in tin. The composition of the product becomes more bismuth rich both as the reactant Bi/Sn ratio increases and as the synthesis solutions become more dilute. The latter effect is due to the greater solubility of tin relative to bismuth in alkaline solutions.

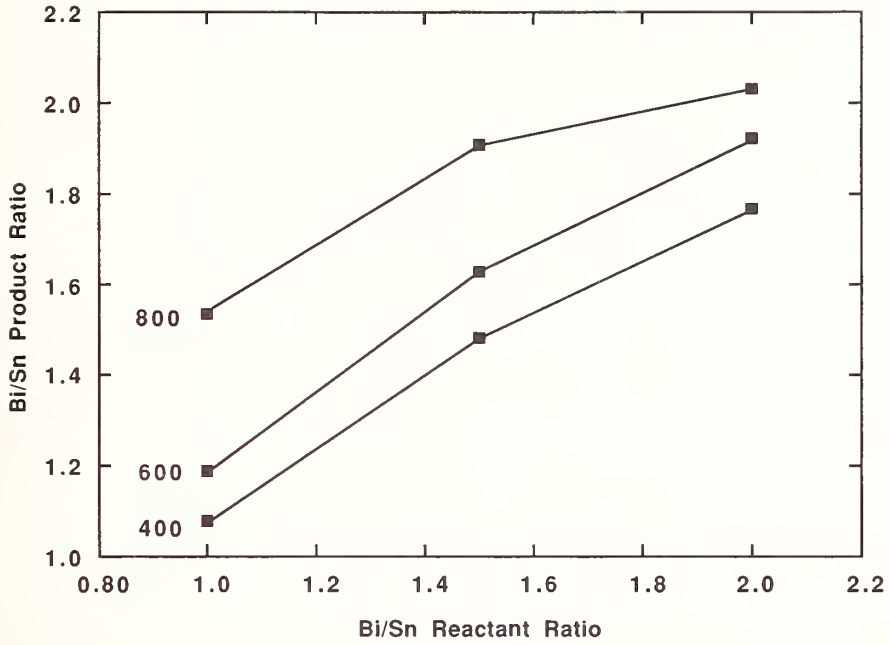

Figure 1. The dependence of the Bi/Sn ratio in $Bi_2(Sn_{2-x}Bi_x)O_{7-x/2}$ on the ratio of the reactants and their concentrations used in the synthesis.

The analytical data for samples which after calcination in air at 400°C appear to be pure pyrochlore phases by X - ray diffraction fall in the composition range $0.05 \leq x \leq 0.86$. The products also usually contain small amounts of residual potassium which corresponds to 0.01 to 0.05 K/Bi. The excess potassium is presumably adsorbed on the surface of the high surface area particles since it can be easily removed by further washing with dilute nitric acid. The X ray diffraction data for all of the compositions show considerable line broadening consistent with particle sizes of approximately 80 -100Å and the measured surface areas. Lattice parameters were determined from the positions of the strong fluorite subcell peak positions or by fitting the entire profile. The lattice parameters as a function of composition are shown in Figure 2. The scatter in the data is primarily due to uncertainties in determining lattice parameters from broad diffraction peaks and inhomogeneities in sample composition. Nevertheless, the data show a well defined trend of increasing lattice parameter with increasing bismuth content consistent with the substitution of the larger Bi^{3+} cation for the smaller Sn^{4+} cation on the octahedral B site of the pyrochlore structure. A similar trend is observed for the ruthenium containing pyrochlores[23, 24].

The X-ray powder diffraction pattern for a sample calcined at 400°C with $x = 0.64$ is shown in Figure 3. The data were fit by Rietveld analysis to the simplest cubic pyrochlore structure with space group Fd3m though little evidence is observed in the data for superlattice reflections corresponding to the doubling of the fluorite sub-cell. Close

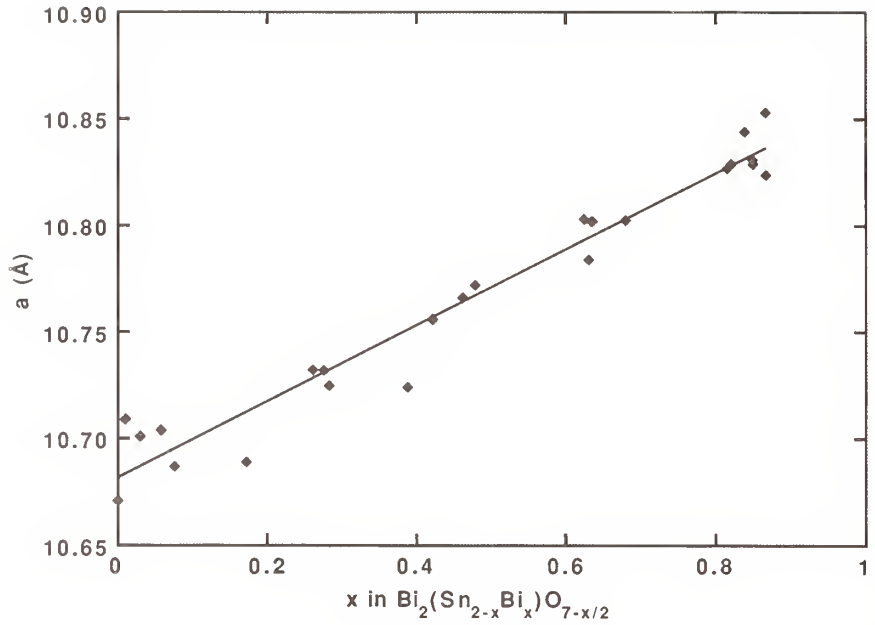

Figure 2. Lattice Parameter vs. Composition for $Bi_2(Sn_{2-x}Bi_x)O_{7-x/2}$.

inspection of the data, however, does show the presence of weak reflections resulting from the ordering of bismuth and tin cations on the A and B sites of the pyrochlore structure. Similar results are obtained across the entire composition range. The data for the sample with x = 0.64 were refined assuming that all of the excess bismuth substitutes for tin on the B sites and that the cation charge deficiency is compensated by oxygen atom vacancies. The refinement converged to give values of 5.2%, 6.9% and 1.9% for the profile, weighted profile and Bragg intensity R factors respectively. The calculated superlattice reflections with this model are predicted to be very weak and appear to be broadened more than the main fluorite subcell reflections suggesting significant disorder. The thermal parameters are large as a consequence of disorder and possibly also reflect deviations from the ideal pyrochlore structure, known to be present at the pure 1:1 composition. The oxygen positional parameter refines to a value of 0.3230(9), close to the value of 0.3175 for an ideal octahedral B site. A model assuming a random distribution of cations between both sites fits almost as well as the pyrochlore model, as expected from the weak intensities of the superlattice reflections. In contrast, a random model fit with the ideal fluorite oxygen position (x = 0.375) gives a significantly poorer fit. The presence of the superlattice reflections is confirmed in samples which have been heated to higher temperature and have consequently larger particle sizes and sharper lines. Figure 4 compares X - ray diffraction data for a sample with x = 0.06 at 400°C and at 685°C. The superlattice reflections (with h,k,l all odd) become sharper and more easily discernable at the higher temperature, confirming that these phases are pyrochlores though substantially disordered and possibly

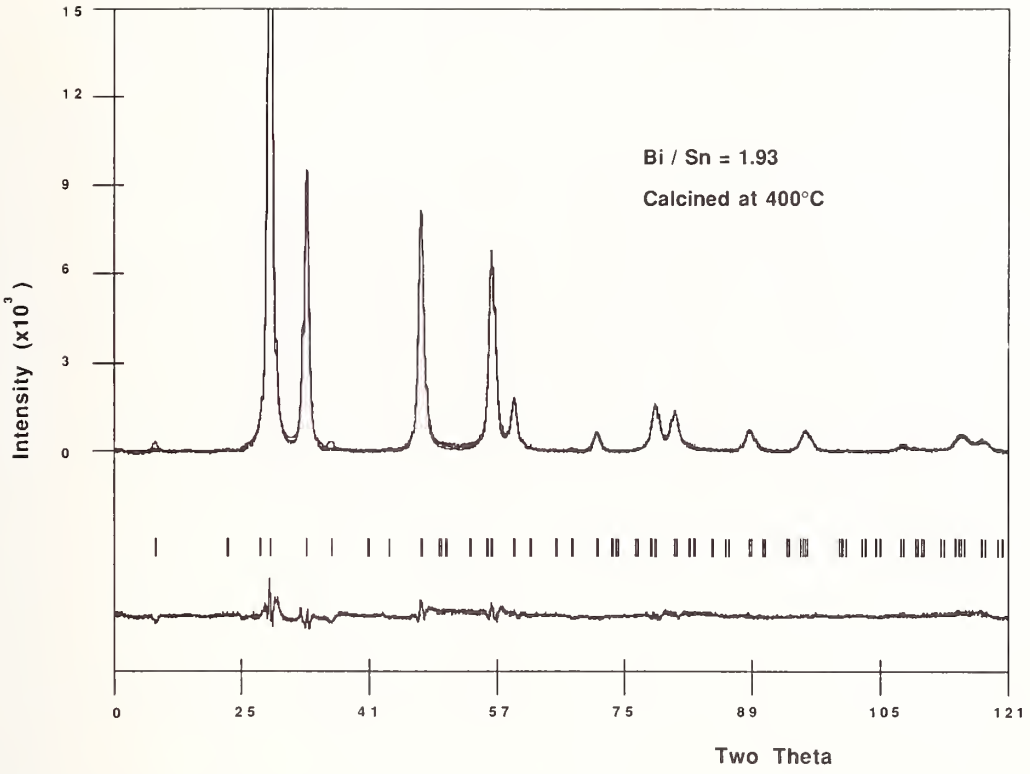

Figure 3. A room temperature powder X-ray diffraction pattern of a $Bi_2(Sn_{2-x}Bi_x)O_{7-x/2}$ phase with Bi/Sn = 1.9. The observed and calculated data are shown together with a difference plot. The vertical lines mark the positions of the contributing Bragg reflections.

of lower than Fd3m symmetry.

The compound $Bi_2Sn_2O_7$ is the only stable phase at high temperature[22] and consequently all of the expanded compositions decompose when heated to higher temperatures. The decomposition temperature depends on the composition and varies from approximately 700°C when x = 0.06 to 500°C at x = 0.86. A differential thermal analysis scan (10°C/min to 800°C) on a sample with x = 0.64 is featureless but on cooling shows a sharp endotherm at 642°C. On reheating, a sharp exotherm is observed at 673°C, and on recooling, the endotherm is observed to occur again at 642°C. The thermal behavior is characteristic of Bi_2O_3 which is formed by decomposition of the expanded composition on the first heating cycle. X - ray diffraction patterns from the products confirm the presence of bismuth oxide together with the stoichiometric pyrochlore phase $Bi_2Sn_2O_7$. The latter is observed to have the doubled cubic unit cell previously reported[21].

Catalytic results for one sample of $Bi_2(Sn_{2-x}Bi_x)O_{7-x/2}$ with x = 0.71 are shown in Figure 5. The top part of the figure shows the distribution of the major products CO, CO_2,

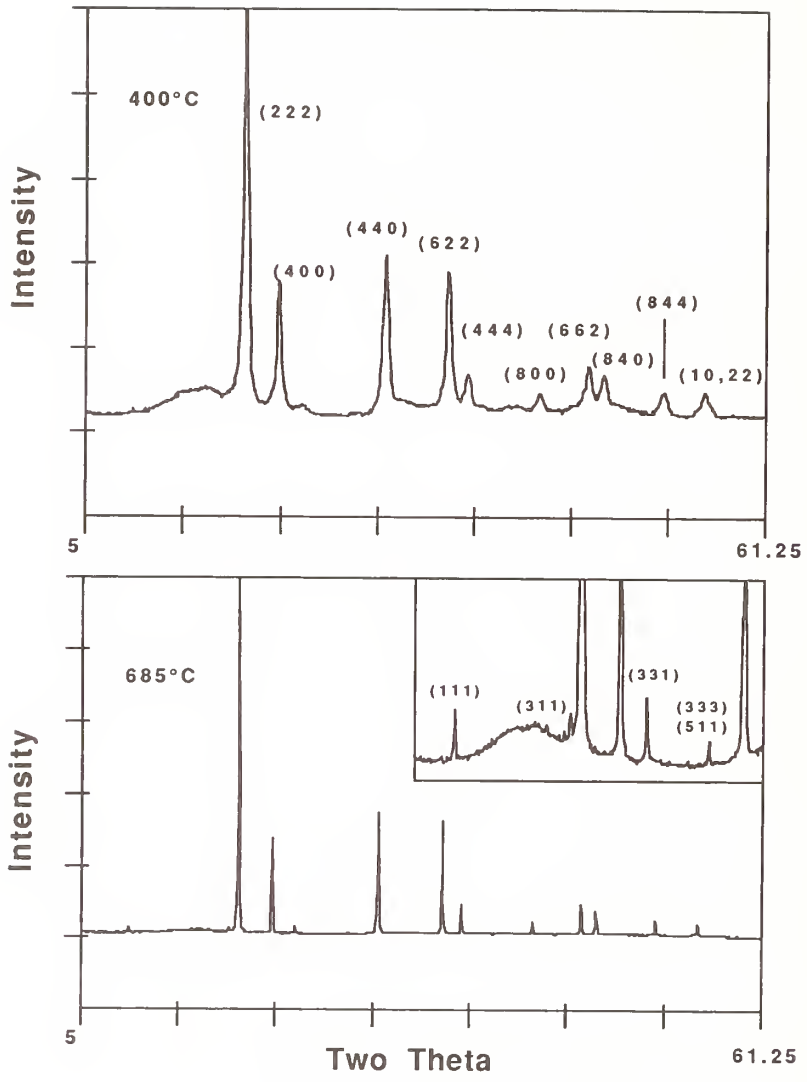

Figure 4. Comparison of the X-ray diffraction patterns for $Bi_2(Sn_{2-x}Bi_x)O_{7-x/2}$ with Bi/Sn =1.06 at 430 and 685°C.

C_2H_6, C_2H_4 and higher hydrocarbons (mostly C_3) at different conversions. The residence times required to achieve these conversions are shown in the bottom part of the Figure. The general form of the data is the same for other bismuth - tin pyrochlore based catalysts examined, though there are some indications that the hydrocarbon selectivity increases by a small amount as x increases. For the specific catalyst used to obtain the data in Figure 5, the selectivity is 60.2% at 1.4% methane conversion and rises to a maximum of 68.3% at 17.7% conversion. The maximum yield (selectivity x conversion) is 21.4 at 40.8% methane and 87.3% oxygen conversions respectively for this set of data. In most respects

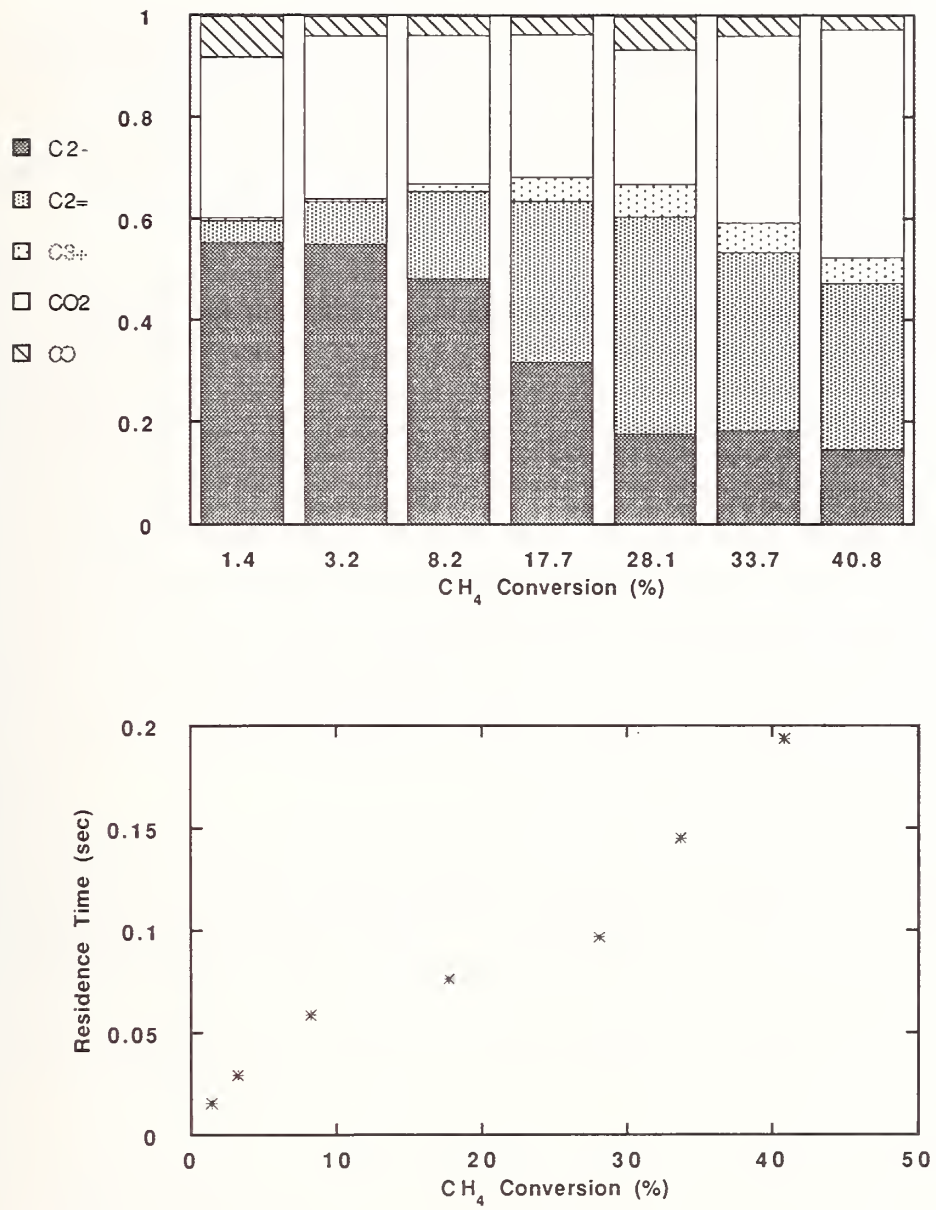

Figure 5. Product distribution at different conversions for a $Bi_2(Sn_{2-x}Bi_x)O_{7-x/2}$ catalyst with x = 0.71 at 850°C and $CH_4 : O_2 : Ar = 2 : 1 : 4$ (top); residence time vs. conversion for the same catalyst (bottom).

the data resemble results for other good oxide catalytic systems. Little CO is observed and the major deep oxidation product is CO_2. The ethylene to ethane ratio increases with increasing conversion and the higher hydrocarbons reach about 10% of the total hydrocarbon product.

At the the reaction temperatures used, the expanded pyrochlore compositions are not stable and decompose to Bi_2O_3 and $Bi_2Sn_2O_7$. However, physical mixtures of the two components with comparable surface areas do not give catalysts with comparable selectivities and the individual components have been shown to be only average catalysts. At this time, the nature of the interaction between the phase separated bismuth oxide and the $Bi_2Sn_2O_7$ pyrochlore which leads to enhancement of the catalytic performance is not understood.

The bottom panel of Figure 5 deserves further comment. The data show a non-linear dependence of the methane conversion on the residence time. An initial period of lower rate (below approximately 10% conversion) is followed by a period of decidedly faster rate. This rapid increase is a consequence of the buildup of a gas phase flame radical pool which augments the surface methane activation rate. Such autocatalytic behavior is common in gas phase hydrocarbon oxidations and pyrolysis[30]. At longer residence times and higher conversions the system becomes limited by the oxygen availability. At the high temperature of the experiments (850°C), a model of the gas phase radical chemistry can provide an adequate description of most of the features of the hydrocarbon product distribution[31]. The catalyst provides a source for methyl radical generation and catalyses the oxidation of CO to CO_2. A detailed model of the gas phase chemistry involved in methane conversion chemistry and comparison with experimental data on product distributions and isotopic labelling experiments will be presented elswhere[32].

CONCLUSIONS

A new series of bismuth tin pyrochlore oxides, $Bi_2(Sn_{2-x}Bi_x)O_{7-x/2}$, ($0.05<x<0.86$) have been synthesized by precipitation from aqueous potassium hydroxide and calcination at 400°C. The bismuth rich pyrochlores decompose to Bi_2O_3 and $Bi_2Sn_2O_7$ at temperatures in the range 700°C to 500°C. The compounds with higher x values decompose at the lower temperatures. The phase separated compositions are good catalysts for the direct conversion of methane to higher hydrocarbons via oxidative coupling.

REFERENCES

1. Hutchings, G.J., Scurrell, M.S. & Woodhouse, J.R.; Chem. Soc. Rev. **18**, 251-283 (1989).
2. Keller, G.E. & Bhasin, M.M.; J. Catal. **73**, 9-19 (1982).
3. Hinsen, W., Bytyn, W. & Baerns, M.; Proc. 8th Int. Congr. Catalysis, Berlin, **3**, 581-592 (1984).
4. Hinsen, W. & Baerns, M.; Chem.-Ztg **107**, 223 (1983).
5. Ito, T. & Lunsford, J.H.; Nature **314**, 721-722 (1985).
6. Ito, T., Wang, J.-X., Lin, C.-H. & Lunsford, J.H.; J. Amer. Chem. Soc. **107**, 5062-5068 (1985).
7. Otsuka, K., Jinno, K. & Morikawa, A.; Chemistry Letters 499-500 (1985).

8. Otsuka, K., Jinno, K. & Morikawa, A.; J. Catal. **100**, 353-359 (1986).
9. Jones, C.A., Leonard, J.J. & Sofranko, J.A.; J. Catal. **103**, 311-319 (1987).
10. Hatano, M. & Otsuka, K.; Inorg. Chim. Acta **146**, 243-247 (1988).
11. Hatano, H. & Otsuka, K.; J. Chem. Soc. Faraday Trans. I **85**, 199-206 (1989).
12. Kharas, K.C.C. & Lunsford, J.H.; J. Amer. Chem. Soc. 2336 (1989).
13. Machida, K. & Enyo, M.; J. Chem. Soc. Chem. Commun. 1639-1640 (1987).
14. Thomas, J.M., Kuan, X. & Stachurski, J. J.; Chem. Soc. Chem. Commun. 162-163 (1988).
15. Thomas, J.M. & Ueda, W.; J. Chem. Soc. Chem. Commun. 1148-1149 (1988).
16. Thomas, J.M. & Ueda, W.; Proc. 9th Int. Cong. Catalysis, Calgary, **4**, 960-967 (1988).
17. Subramanian, M., Aravamudan, G. & Subba Rao, G.V.; Prog. Solid St. Chem. **15**, 55-143 (1983).
18. Ashcroft, A.T., Cheetham, A.K., Green, M.L.H., Grey, C.P. & Vernon, P.D.F.; J. Chem. Soc. Chem. Commun. 1667-1669 (1989).
19. Roth, R.S.; J. Res. Nat. Bur. Standards **56**, 18-27 (1956).
20. Gattow, G. & Fricke, H.; Z. anorg. allg. Chem. **324**, 287296 (1963).
21. Shannon, R.D., Bierlein, J.D., Gillson, J.L., Jones, G.A. & Sleight, A.W.; J. Phys. Chem. Solids **41**, 117-122 (1980).
22. Vetter, G., Queyroux, F. & Gilles, J.-C.; Mater. Res. Bull. **13**, 211-216 (1978).
23. Horowitz, H.S., Longo, J.M. & Lewandowski, J.T.; Mater. Res. Bull. **16**, 489-496 (1981).
24. Horowitz, H.S., Longo, J.M., Horowitz, H.H. & Lewandowski, J.T.; ACS Symposium Series, Eds. Grasselli, R.K. & Bradzil, J.F. **279**, 143-163 (1985).
25. Roos, J.A., Bakker, A.G., Bosch, H., van Ommen, J.G. & Ross, J.R.H.; Catalysis Today **1**, 133-145 (1987).
26. Solymosi, F., Tombacz, I. & Kutsan, G.; J. Chem. Soc. Chem Commun 1455-1456 (1985).
27. Rietveld, H.M.; J. Appl. Cryst. **2**, 65-72 (1969).
28. Wiles, D.B. & Young, R.A.; J. Appl. Cryst. **14**, 149-151 (1981).
29. International Tables for Crystallography, D. Reidel, Dordrecht, Holland, (1983).
30. Pyrolysis: Theory and Industrial Practice; Albright, L.F., Crynes, B.L., Corcoran, W.H., Eds.; Academic Press: New York, (1983)
31. Labinger, J.A. & Ott, K.C.; J. Phys. Chem. **91**, 2682-2684 (1987).
32. Mims, C.A., Dean, A.M. & Hall, R.B.; to be published (1990).

S. Roth: It appears to me that based on the faster surface exchange reaction with CO_2 than oxygen, a good way to carry out this reaction would be to use CO_2 and then still get methyl radical coupling but also make CO and H_2; is that possible?

A. J. Jacobson: The use of CO_2 as an oxidant for methane conversion in this process has been considered but I'm not aware of a good catalytic route.

A. Navrotsky: Still on the subject of rapid CO_2 exchange I don't remember the details precisely, but there has been a lot of geochemical work on oxygen exchange between phases, and I remember considerable work that suggests that carbonates and silicates exchange oxygen much more rapidly than silicate/silicate pairs. That may be additional evidence.

A. J. Jacobson: I'd be very interested to see that, Alex, because the exchange is an interesting result which was unexpected.

A. Navrotsky: I'll try to dig that out.

National Institute of Standards and Technology Special Publication 804, Chemistry of Electronic Ceramic Materials, Proceedings of the International Conference held in Jackson, WY, August 17-22, 1990, issued January 1991.

SOFT CHEMICAL SYNTHESIS OF METASTABLE TITANIUM, VANADIUM, AND MOLYBDENUM OXIDES

T.P. Feist and P.K. Davies, Dept. of Materials Science, University of Pennsylvania, Philadelphia, PA 19104

ABSTRACT

Low temperature synthetic methods have been used to prepare metastable transition metal oxides from a variety of layered precursors. Aqueous ion exchange of several alkali metal titanates followed by heating at temperatures less than 500°C leads to the formation of TiO_2(B) and other metastable titanates. Acid treatment of layered brannerite-type phases $AVMoO_6$ (A=Li,Na) has been used to synthesize new compounds $A'_{0.13}V_{0.13}Mo_{0.87}O_3$ (A'=H,Na) with the "hexagonal molybdenum oxide" structure. Methods of synthesis are presented, and mechanisms of the transformations of the various layered starting materials to new framework structures are discussed.

INTRODUCTION

Many transition metal oxides are of great interest for catalytic and electrochemical applications, and metastable structures often demonstrate new or enhanced properties compared to their thermodynamically stable forms. These materials can often be prepared at low temperatures by electrochemical intercalation, inorganic ion exchange, or organic precursor methods. A specific example is the preparation of TiO_2(B), a metastable form of TiO_2, from the layered titanate $K_2Ti_4O_9$ (fig. 1) using soft chemistry. (1) The new material demonstrated several interesting properties, including enhancement of the catalytic activity of V_2O_5 when used instead of anatase as the catalyst support and facile intercalation

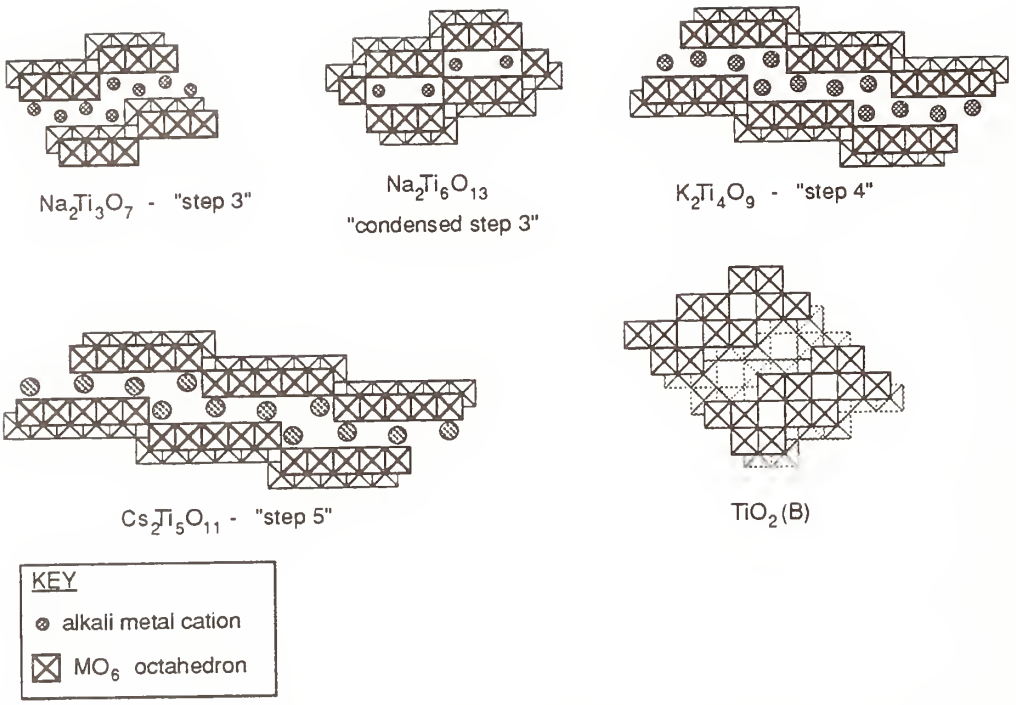

Figure 1. The structures of several alkali metal titanates and TiO_2(B)

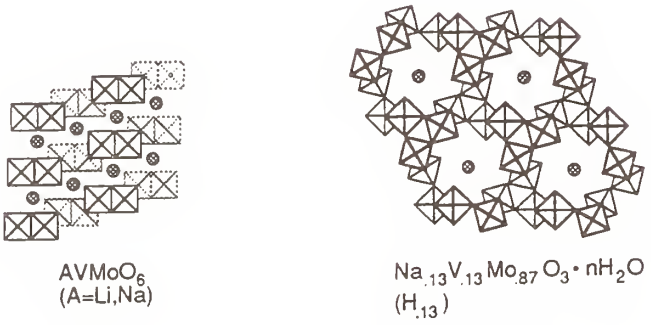

Figure 2. The structures of brannerite (a) and hexagonal molybdenum oxide (b).

by alkali metal cations and hydrogen to form a mixed valence titanium oxide bronze (2).

Subsequent work has shown that TiO_2(B) can be prepared from a variety of other titanate structures (3,4). but the mechanistics of the transformation from layered titanate to TiO_2(B) have remained poorly understood. It is the goal of the present work to investigate the intermediate structures observed during the dehydration of the different starting materials in order to better understand the mechanistics of the reaction and the stability of TiO_2(B).

In the second portion of the paper we report the synthesis in aqueous acid of $A'_{0.13}V_{0.13}Mo_{0.87}O_3$ (A'=H,Na) from the compounds $AVMoO_6$ (A=Li,Na) which have the layered brannerite structure. (fig. 2a) The framework of the new structure is isotypic with the hypothetical hexagonal tunnel structure of MoO_3 (5) shown in figure 2b. Conventional synthesis techniques have been used to stabilize this structure by incorporating large cations into the tunnels, but there have been no reports of the preparation of the structure containing empty tunnels. If such a material could be prepared, it would likely be a candidate for a variety of intercalation and catalytic reactions. We report here the synthesis and characterization of new hexagonal MoO_3-type tunnel structures by a novel soft chemical route of acid treatment and dehydration of alkali brannerites.

EXPERIMENTAL

Alkali metal titanates were prepared by solid state reaction of TiO_2 (anatase) and alkali metal carbonates or nitrates as reported previously. (4) Acid exchange of the layered titanates (fig. 1a) was achieved by stirring the pulverized titanate in 1M HCl (200-fold excess) for 24-72 hours at 60°C. Acid exchange of the tunnel structure $Na_2Ti_6O_{13}$ (fig. 1) was achieved by immersing the powder in molten NH_4NO_3 for 5 days at 200°C. Thermogravimetric analysis was used to investigate weight loss behavior of acid exchanged materials, and TGA/Mass Spectroscopy confirmed that the

only species evolved during heating was H_2O. Differential scanning calorimetry (DSC) was used to examine the energetics of the dehydration reactions, and X-ray diffraction (XRD) was used to probe the structure of intermediates isolated during the formation of TiO_2(B).

Lithium and sodium brannerites were prepared by solid state reaction of AVO_3 (A=Li,Na) and MoO_3 as reported by Galy et al. (6). The Na brannerite was stirred in 0.25M HCl for 12 hours at 60°C, and the solid was recovered by vacuum filtration. The process was repeated to insure complete conversion of the brannerite to the tunnel structure. $LiVMoO_6$ was immersed in 0.25M HCl for 36 hours with stirring at 60°C. The solution was then acidified with 1M HCl and stirred for 2 hours before isolating the product by vacuum filtration. The products were analyzed by TGA, XRD, and atomic absorption spectroscopy.

RESULTS AND DISCUSSION

(1) TITANATES

The TGA curves for each of the acid exchanged layered titanates (fig. 3a) show multistep weight loss behavior, indicating the possible formation of stable intermediate structures. The final dehydration product in each case is TiO_2(B). X-ray diffraction confirms that intermediate structures can be isolated during the dehydration reactions. Figure 3b shows the powder diffraction patterns of materials isolated during the transformation of the trititanate $H_2Ti_3O_7$ to TiO_2(B). The pattern of the first intermediate is very similar to that of the condensed structure $Na_2Ti_6O_{13}$, and the weight loss associated with the formation of the intermediate is equal to 1 mole of water per 2 moles of $H_2Ti_3O_7$. The reaction can be formulated:

$$2H_2Ti_3O_7 \rightarrow H_2Ti_6O_{13} + H_2O\uparrow$$

which corresponds to a topotactic condensation of the initial layered structure. Upon elimination of water, layers join through the previously unshared oxygen atoms at the corner of each "step". DSC shows that this process is endothermic (fig. 4), which is consistent

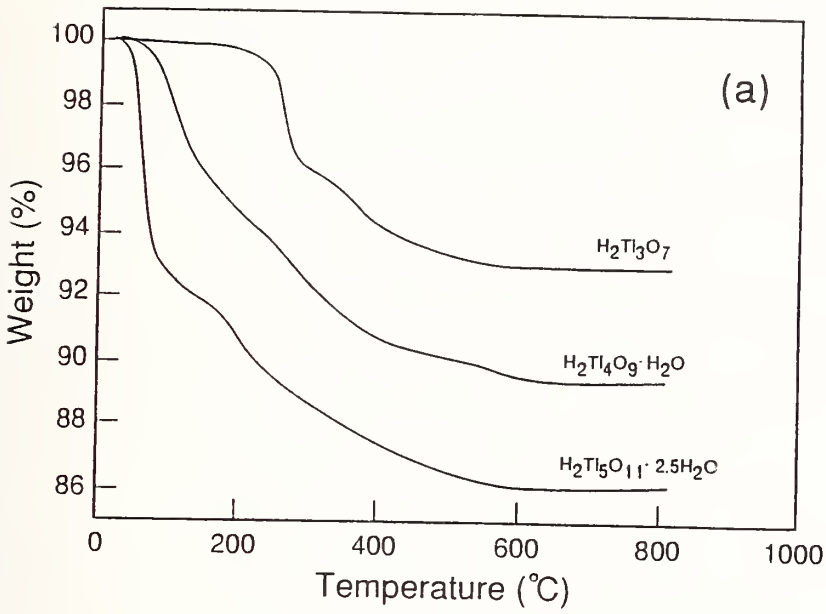

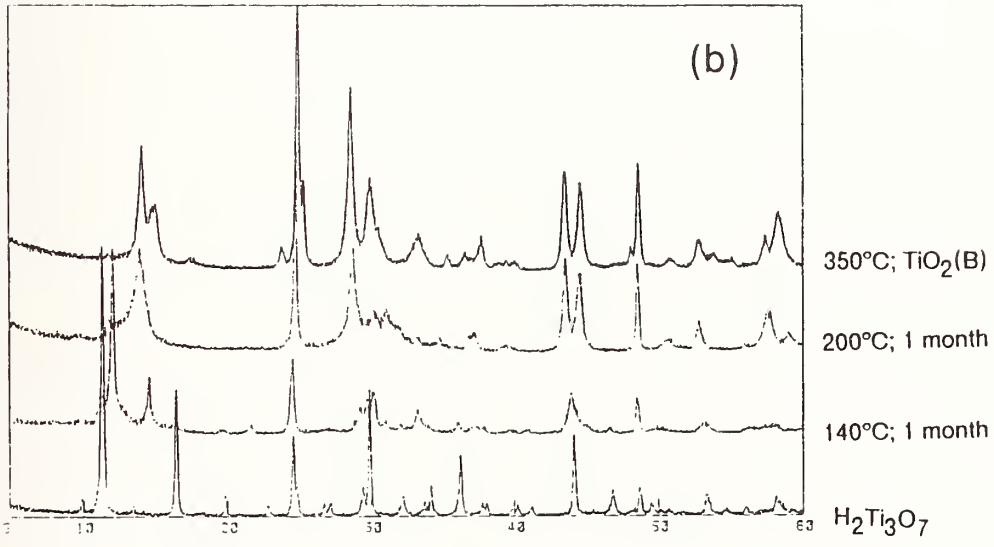

Figure 3. (a) Thermogravimetric analysis of layered titanates.
(b) Powder X-ray diffraction of $H_2Ti_3O_7$ dehydration products.

with its topotactic nature. XRD and DSC indicate that the other layered titanates behave similarly to $H_2Ti_3O_7$. $H_2Ti_6O_{13}$, which has also been prepared by direct acid exchange of the tunnel structure $Na_2Ti_6O_{13}$, does not show any low temperature endotherm because the structure is already condensed. (fig. 4)

X-ray diffraction shows that the next step results in the formation of an intermediate which is structurally similar to TiO_2(B) and is independent of starting titanate structure. Although the powder pattern could not be indexed, electron diffraction indicated that the new structure has a *C*-centered monoclinic cell with approximate lattice parameters of $a \approx 14$Å, $b \approx 3.75$Å, and $c \approx 20$Å. β is not known. DSC shows the formation of this structure, in contrast to the previous topotactic step, is accompanied by a strong exothermic heat effect. This leads us to postulate that the intermediate which immediately precedes TiO_2(B) forms by nucleation and growth from the condensed structures. TiO_2(B) then forms in a single, final step that shows no strong heat effect, presumably because the structure of the last intermediate is very similar to that of TiO_2(B).

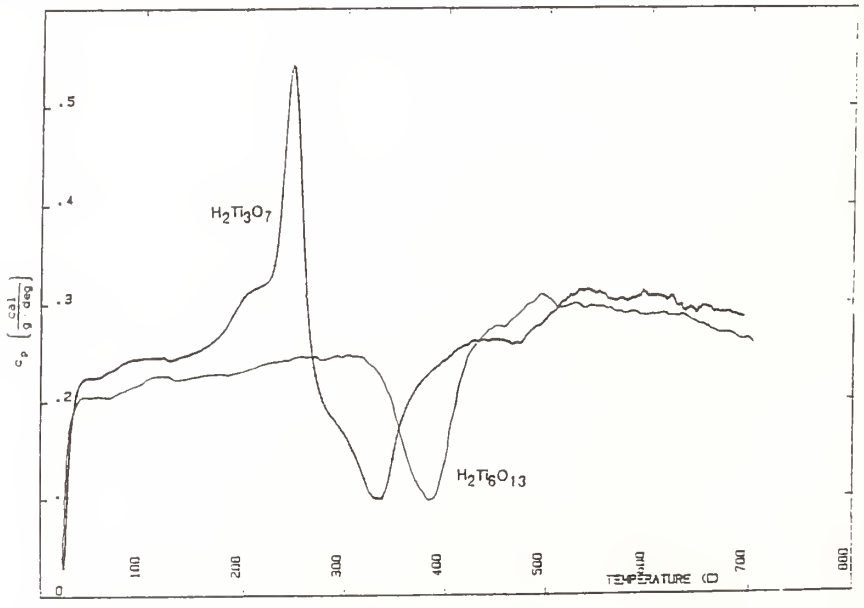

Figure 4. Differential scanning calorimetry of acid exchanged "step 3" titanates.

(2) VANADIUM-MOLYBDENUM OXIDES

The reactions which lead to the formation of the hexagonal MoO_3-type structure from alkali metal brannerites are quite different than the chemistry of layered titanates. Because vanadium and molybdenum have appreciable solubility in dilute acid, the sodium and lithium brannerites do not ion exchange, but instead undergo "leaching" reactions. Vanadium is preferentially dissolved from the brannerite, and a new structure crystallizes. In the case of Na brannerite, the process proceeds though a two-phase mixture of the starting structure and the tunnel structure, with no evidence of other phases. The final product, $Na_{0.13}V_{0.13}Mo_{0.87}O_3 \cdot 0.26H_2O$ can be dehydrated at 400°C but rehydrates immediately upon cooling. (fig 5a) The tunnels, with a minimum diameter of 3.2Å, are too large for Na^+ to occupy without coordination by water molecules. Therefore, the rapid rehydration observed during cooling suggests that sodium remains in the tunnels. XRD confirms that the tunnel structure is maintained throughout the dehydration/ rehydration process.

The Li brannerite behaves much differently. Upon immersion in dilute HCl, the material dissolves, leaving only a small amount of amorphous residue. (fig. 6) As the solution continues to be stirred at 60°C, the hexagonal tunnel structure begins to crystallize from solution. Acidification of the solution is used to remove any amorphous phase remaining after 36 hours, and the final product is single phase with yellow needle-like particles 1-10μm in length. Atomic absorption shows that the Mo:V ratio is 6.7:1 and the material contains little lithium. The final stoichiometry is $H_{0.13}V_{0.13}Mo_{0.87}O_3 \cdot nH_2O$. Subsequent dehydration of the hexagonal tunnel structure without residual alkali metal ions allows preparation of the material with empty tunnels. The TGA (fig. 5b) indicates that after the loss of surface water, the water molecules which are presumably located in the tunnels are removed, leading to the formation of $H_{0.13}V_{0.13}Mo_{0.87}O_3$ at approximately 225°C. During the final weight loss, which corresponds

to 0.065(H_2O), the residual protons are apparently abstracted from the structure with a small amount of oxygen from the framework, leaving a sample with the stoichiometry $V_{0.13}Mo_{0.87}O_{2.935}$. This yellow-green material retains the hexagonal MoO_3 structure, and neutron diffraction refinements have confirmed the absence of any species in the tunnels. Preliminary experiments indicate that this new material can be ion-exchanged with a variety of divalent cations, and it also undergoes insertion reactions with H^+, Li^+, and Na^+. Further experiments are currently being performed to clarify the mechanisms of these unusual formation reactions and to utilize the wide variety of reactions exhibited by brannerites in order to form new compounds with potential applications as catalysts and electronic ceramics.

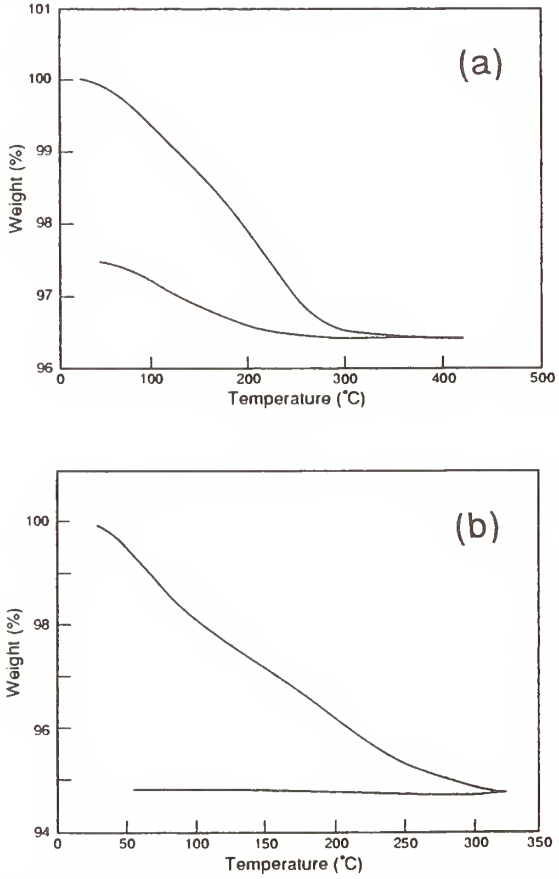

Figure 5. Thermogravimetric analysis of acid treated sodium brannerite (a) and lithium brannerite (b).

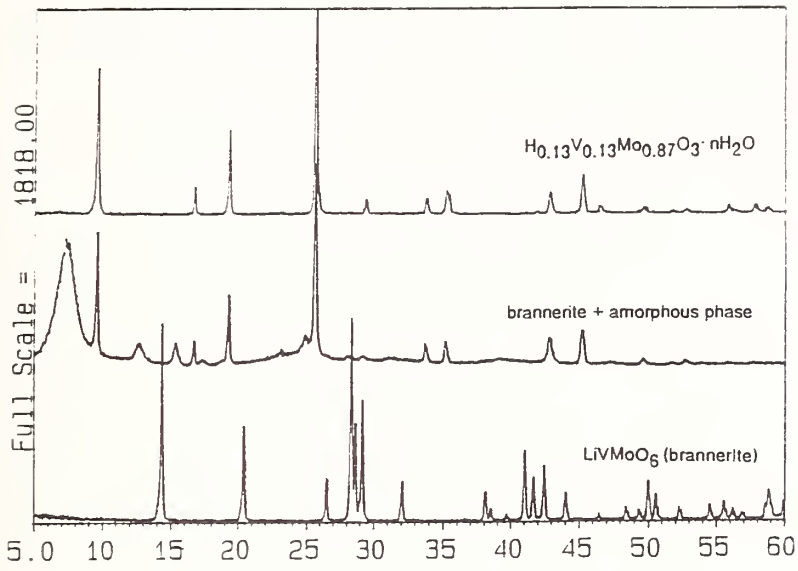

Figure 6. Powder X-ray diffraction of acid treated $LiVMoO_6$.

CONCLUSION

We have presented the formation of TiO_2(B) from several different starting layered titanates and have considered mechanistic aspects of the transformation from layered structures to a three-dimensional framework. We have also presented a novel synthesis of a hexagonal vanadium/molybdenum tunnel structure with empty tunnels. The electrochemical and catalytic properties of this material are currently being studied.

ACKNOWLEDGMENTS

The authors gratefully acknowledge the support of Exxon Research and Engineering Corp., International Business Machines Corp., and the National Science Foundation (DMR-88-19885).

REFERENCES

1. Marchand, R., Brohan, L., and Tournoux, M., *Mat. Res. Bull.*, 15, 1129-1133 (1980).
2. Tournoux, M., Marchand, R., and Brohan, L., *Prog. Solid St. Chem.*, 17, 33-52 (1986).
3. Mocarski, S.J., Master's Thesis, University of

Pennsylvania (1986).
4. Feist, T.P., Mocarski, S.J. Davies, P.K., Jacobson, A.J., and Lewandowski, J.T., *Solid State Ionics*, 28-30, 1338-1343 (1988).
5. Caiger, N., Crouch-Baker, S., Dickens, P., and James, G., *J. Sol.St. Chem.*, 369-373 (1987).
6. Galy, J., Darriet, J., and Darriet, B., *C.R. Acad. Sc. Paris, Série C*, 264, 1477-1480 (1967).

National Institute of Standards and Technology Special Publication 804, Chemistry of Electronic Ceramic Materials, Proceedings of the International Conference held in Jackson, WY, August 17-22, 1990, issued January 1991.

PRELIMINARY SOLID-STATE MULTINUCLEAR NMR OF TITANIUM AND ZIRCONIUM OXIDE CERAMICS AND PRECURSORS

John J. Fitzgerald* and Sang-sub Han
Department of Chemistry
South Dakota State University
Brookings, SD 57007

and

Steven F. Dec, Mark F. Davis,
Charles E. Bronnimann and Gary E. Maciel
Department of Chemistry
Colorado State University
Fort Collins, CO 80523

ABSTRACT

Preliminary solid-state multinuclear NMR studies of selected titanium and zirconium oxide electronic ceramic powders and precursors are described. ^{1}H CRAMPS NMR has been used to examine the metal-hydroxide and metal-hydrate protons sites in a range of hydrolyzed titanium(IV) and zirconium(IV) salts which may serve as solution precursors of Zr(IV) and Ti(IV) oxide ceramic materials. High-field (14.1 T) magic-angle spinning (MAS) ^{47}Ti, ^{49}Ti and ^{91}Zr spectra are reported for a range of Ti(IV) and Zr(IV) oxides including TiO_2 (anatase), $CaTiO_3$, $SrTiO_3$, $BaTiO_3$, $SrZrO_3$ and $BaZrO_3$. In addition, MAS ^{137}Ba NMR results are also reported for BaO, $BaTiO_3$ and $BaZrO_3$. These initial investigations suggest the potential of solid-state NMR approaches to advance our fundamental knowledge of the structure, metal ion environments, and reactions of a wider range of titanium and zirconium oxide electronic ceramics and related precursors of current interest.

*Author to whom correspondence should be sent.

INTRODUCTION

A diverse range of electronic ceramics containing titanium(IV) and zirconium(IV) ions in perovskite-type oxide lattices are of importance in materials science.[1-3] Barium titanate ($BaTiO_3$), and various alkaline earth titanates and zirconates, have found important uses in micro-electronic packaging and thin film capacitor applications.[1-7] The utility of titanium oxide-containing ceramics such as PZTs (lead zirconate titanate ($Pb_xZr_yTi_{1-y}O_3$)) and PLZTs (lead lanthanum zirconate titanate ($Pb_{1-x}La_xZr_yTi_{1-x})_{1-x/4}O_3$)) powders lie in their widespread use as high quality transparent electrooptic and piezoelectric materials.[1-3,8,9,13]

The synthesis and processing of Ti(IV) and Zr(IV)-oxide containing ceramics employ solid-state mixed oxide reactions, the thermal decomposition of metal hydroxide and metal chelate precursors, and metal alkoxide sol-gel methods.[4-9] For example, $BaTiO_3$ powders and ceramics can be synthesized by numerous reactions involving a variety of precursor materials:

$$BaO + TiO_2 \text{ -----> } BaTiO_3 \quad (1)$$

$$BaCO_3 + TiO_2 \text{ -----> } BaTiO_2 + CO_2 \quad (2)$$

$$Ba(OH)_2 + TiO_2 \text{ -----> } BaTiO_3 + H_2O \quad (3)$$

$$BaTiO(Ox)_2 \bullet 2H_2O \xrightarrow{\Delta} BaTiO_3 + 2CO_2 + 2H_2O \quad (4)$$

$$Ba(OR)_2 + Ti(OR)_4 \text{ -----> Sol-Gel Precursor} \quad (5)$$

$$\text{Sol-Gel Precursor} \xrightarrow{dry} \xrightarrow{sinter} BaTiO_3$$

Similarly, the synthesis of PZT and PLZT has been reported[8,9,13] using solid-state oxide or carbonate mixtures of the various metal ion constituents and synthetic approaches using various hydrolysis precursors such as $ZrOCl_2 \bullet 8H_2O$ or $TiOSO_4$ solutions.[7,8]

The structural characterization of Ti(IV) and Zr(IV) oxide ceramics, their synthetic precursors and the detailed examination of these synthesis reactions are of major significance to our understanding of both their chemistry and functional properties.

Solid-state multinuclear nuclear magnetic resonance (NMR) represents a unique and important spectroscopic technique with tremendous potential to advance our fundamental knowledge of the structure and reactivity of titanium and zirconium oxide ceramics and their related precursors. This report describes the applications of solid-state multinuclear NMR approaches to examine selected titanium and zirconium oxide ceramic precursors and powdered materials. ^1H CRAMPS NMR[10] has been used to examine titanium and zirconium hydroxide-containing complexes. MAS ^{47}Ti, ^{49}Ti, ^{91}Zr and ^{137}Ba NMR has been used to examine the M(II) and M(IV) metal ion environments in mixed metal oxides such as $BaTiO_3$ and $BaZrO_3$[11,12].

EXPERIMENTAL

Solid-state MAS ^{47}Ti, ^{49}Ti, ^{91}Zr and ^{137}Ba NMR were obtained on a Bruker AM-600 NMR spectrometer, using a home-built probe at spinning speeds of 5-6 kHz. ^{47}Ti and ^{49}Ti NMR spectra were obtained at 33.8 MHz, ^{91}Zr NMR at 55.8 MHz and ^{137}Ba NMR at 66.7 MHz using the external references $TiCl_4(\ell)$, $BaZrO_3(s)$ and $BaZrO_3(s)$, respectively, assigned as 0.00 ppm. Spectra were acquired using a Hahn spin echo-pulse sequence in order to eliminate artifacts from probe "ringdown."

^{1}H CRAMPS NMR were obtained on an extensively modified Nicolet NT-200 NMR spectrometer operating at 187 MHz using the BR-24 pulse sequence.[10] Samples were contained in glass tubes using a modified Gay spinner. The ^{1}H NMR chemical shifts were externally referenced to tetrakis(trimethylsilyl)methane (TTMSM) and reported here relative to TMS.

RESULTS AND DISCUSSION

<u>^{47}Ti and ^{49}Ti NMR</u>. ^{47}Ti and ^{49}Ti NMR spectra have been previously reported for only $BaTiO_3$.[11,12] A wider range of alkaline earth titanates have been examined here using MAS ^{47}Ti and ^{49}Ti NMR measurements. Titanium has two NMR-active isotopes, ^{47}Ti (I=5/2, 7.28% abundance) and ^{49}Ti (I=7/2, 5.51% abundance), both of which have very low gyromagnetic ratios and medium quadrupole moments (Q (^{47}Ti) = $0.29\times10^{-28}m^2$, Q (^{49}Ti) = $0.24\times10^{-28}m^2$). These parameters make these nuclides unattractive for NMR study except at the highest available magnetic fields (11.7 and 14.1 T).

Figure 1 shows the solid-state ^{47}Ti and ^{49}Ti MAS NMR spectra of $CaTiO_3$, $SrTiO_3$ and $BaTiO_3$ obtained at 33.840 MHz using a 14.0 T magnetic field and spinning speeds of 5-6 kHz. The NMR reference is a neat solution of $TiCl_4(\ell)$ taken as 0.0 ppm. No spectra were observed for $MgTiO_3$ under these conditions. The ^{47}Ti/^{49}Ti NMR spectra show only the central transition (1/2 <--> 1/2) resonance for both nuclides. The ^{49}Ti resonance is the most intense and narrowest signal, being about 270 ppm downfield from the ^{47}Ti signal for $SrTiO_3$. The ^{49}Ti NMR peak is much broader for both $CaTiO_3$ and $BaTiO_3$ than that observed for $SrTiO_3$. The chemical shifts of the ^{49}Ti resonance for $CaTiO_3$, $SrTiO_3$ and $BaTiO_3$ are -874, -843, and -746, respectively, and are assigned to the 6-coordinate titanium(IV) ion.[14-16] The variation in the ^{49}Ti chemical shifts is probably due to the nature of the M(II) cation in these lattices, whereas changes in the local symmetry about the Ti(IV) nucleus probably significantly affect the linewidth of the ^{47}Ti/^{49}Ti central transition resonances due to second-order quadrupolar broadening.

The MAS ^{47}Ti and ^{49}Ti NMR spectrum of the anatase form of TiO_2 is given in Figure 2. The spectrum is dominated by the ^{49}Ti central transition, which shows a second-order powder pattern with two peak maxima at -938 and -994 ppm relative to $TiCl_4(\ell)$. The ^{47}Ti resonance is upfield with observable intensity in the -1150 to -1450 ppm range, and is significantly broadened relative to the ^{49}Ti signal. The second-order powder pattern for the ^{49}Ti NMR resonance is due to the large electric field gradient about the Ti(IV) ion in this axially symmetric 6-coordinate oxide lattice site of anatase.[14,17]

^{91}Zr and ^{137}Ba NMR. The ^{91}Zr nuclide is 11.23% abundant with a nuclear spin of 5/2. To date, no solid-state NMR spectra have been reported for this nucleus. Figure 3 shows the MAS ^{91}Zr NMR spectra of $SrZrO_3$ and $BaZrO_3$ taken at 66.7 MHz using a 14.1 T magnetic field and spinning speeds of 5-6 kHz. No ^{91}Zr NMR spectra were observed for $MgZrO_3$ and $CaZrO_3$ under these conditions. The ^{91}Zr NMR show only the central transition resonance, with $BaZrO_3$ exhibiting a sharp signal taken as the chemical shift reference at 0.0 ppm. $SrZrO_3$ exhibits a broadened, unsymmetrical NMR resonance centered near -29 ppm. This resonance may be due to second-order quadrupole interactions or due to a range of chemically distinct 6-coordinate zirconium(IV) ion sites in this sample.[14]

The ^{137}Ba nuclide (I=3/2) is 11.32% abundant and has $Q=0.28x10^{-28}m^2$. NMR spectra obtained for BaO, $BaTiO_3$ and $BaZrO_3$ at 66.7 MHz in a 14.1 T magnetic field and 5-6 kHz spinning speeds are shown in Figure 4. $BaZrO_3$, which has cubic 12-coordinate Ba(II) ion sites,[14] gives the sharpest signal and is used as the reference standard. $BaTiO_3$, likewise, has a perovskite structure, although the 12-coordinate Ba(II) ion sites are distorted in the tetragonal phase at room temperature.[11] BaO has a NaCl lattice with six-coordinate barium(II) ion sites[14] and exhibits a ^{137}Ba NMR signal at 481 ppm relative to $BaZrO_3$.

^{1}H CRAMPS NMR. ^{1}H CRAMPS NMR have been reported for silica and alumina/silica materials.[10] Ceramic oxides of Ti(IV) and Zr(IV) ions are often prepared from metal hydrates, hydroxides and various other complex hydrolysis precursors containing M-OH, M-OH-M and M-OH_2 proton-containing structural moieties.

Figure 5 shows the ^{1}H CRAMPS NMR of various Ti(IV) and Zr(IV) salts obtained at 187 MHz using the BR-24 pulse sequence and 2-3 kHz spinning speeds. The spectrum of $ZrO(OH)(CO_3)$, an extensively hydrolyzed Zr(IV) complex, probably containing primarily M-OH moieties, shows a single, broad resonance at 5.7 ppm. The ^{1}H CRAMPS spectrum of $ZrOCl_2 \bullet 8H_2O$, containing the tetrameric $Zr_4(OH)_8(H_2O)_{16}^{8+}$ ion,[18] with a proton M-OH_2/M-OH ratio of 4/1, exhibits two resonances at 7.1 ppm and 9.5 ppm assigned to M-OH_2 and M-OH protons, respectively. The spectrum of crystalline $Zr(SO_4)_2 \bullet 4H_2O$, a structure with linear chains of Zr(IV) ions with bridging OH groups,[19] gives a single, sharp resonance at 8.8 ppm. The ^{1}H CRAMPS spectra of $TiOSO_4 \bullet H_2SO_4$ H_2O, a complex material containing a range of Ti-OH, Ti-OH-Ti, Ti-OH_2 moieties, exhibits a ^{1}H CRAMPS NMR spectrum consisting of four sharp resonances in the 5-10 ppm range.

CONCLUSIONS

The initial ^{47}Ti and ^{49}Ti NMR spectra reported here demonstrate the application of solid-state NMR to observe 6-coordinate Ti(IV) sites in cubic ($SrTiO_3$), tetragonal ($BaTiO_3$), and axially symmetric titanium oxide (TiO_2) materials. The ^{49}Ti chemical shifts of the ^{49}Ti NMR resonance for the alkaline earth titanates are dependent on the size and nature of the M(II) ion.

The ^{91}Zr NMR of $SrZrO_3$ and $BaZrO_3$ also demonstrate the capability of high-field solid-state NMR to observe cubic ($BaZrO_3$, $SrZrO_3$) 6-coordinate Zr(IV)

ion sites in oxide lattices. The large linewidth observed for $SrZrO_3$ relative to $BaZrO_3$ possibly indicates a significant electric field gradient at the ^{91}Zr nucleus in this perovskite lattice.

^{137}Ba NMR reported herein allow one to distinguish between 6-coordinate BaO_6 sites (in BaO) and 12-coordinate BaO_{12} sites (in $BaZrO_3$ and $BaTiO_3$). The distortions in the Ba(II) ion sites in tetragonal $BaTiO_3$ result in second-order quadrupolar peak broadening.

The ^1H CRAMPS NMR results for a series of M-OH and M-OH_2 containing Ti(IV) and Zr(IV) salts suggested that this technique will provide an important approach to examine both metal hydrolysis, metal chelate and sol-gel precursors of Ti(IV) and Zr(IV) oxide ceramics.

ACKNOWLEDGEMENTS

The authors gratefully acknowledge partial support of this work by National Science Foundation Grant RII-8902066 and the use of the Colorado State University Regional NMR Center, funded by National Science Foundation Grant CHE-8616437.

REFERENCES

1. B. Jaffe, W.R. Cook and H. Jaffe, Piezoelectric Ceramics, London, Academic Press (1979).

2. R. Buchanan, ed., Ceramic Materials For Electronics, Marcel Dekkar, Inc., New York (1986).

3. K. Wakino, "Piezoelectric and Pyroelectric Ceramics," in Fine Ceramics, S. Saito, ed., Elsevier, New York (1985), pp. 251-261.

4. A. Amin, M.A. Spears and B.M. Kulwicki, J. Am. Ceram. Soc., 66(10), 733-738 (1983).

5. T.T. Fang and H.B. Lin, J. Am. Ceram. Soc., 72(10), 1899-1906 (1989).

6. W. Hertl, J. Am. Ceram. Soc., 71(10), 879-883 (1988).

7. J.J. Ritter, R.S. Roth and J.E. Blendell, J. Am. Ceram. Soc., 69(2), 155-162 (1986).

8. K. Kezuka, Y. Hayashi and T. Yamaguchi, J. Am. Ceram. Soc., 72(9), 1660-1663 (1989).

9. G.H. Haertling and C.E. Land, J. Am. Ceram. Soc., 54(1), 1-11 (1971).

10. C.E. Bronnimann, B.L. Hawkins, M. Zhang and G.E. Maciel, Anal. Chem., 60, 1743 (1988).

11. C.E. Forbes, W.B. Hammond, N.E. Cipollini and J.F. Lynch, J. Chem. Soc. Commun., 433 (1987).

12. T.J. Bastow, J. Phys. Condens. Matter 1, 4985-4991 (1989).

13. P. Duran and C. Moure, Am. Ceram. Soc. Bull., 64(4), 575-579 (1985).

14. A.F. Wells, Structural Inorganic Chemistry, 5th Edition, Clarendon Press, Oxford (1984), pp. 564, 588.

15. H.D. MeGaw, Proc. Roy. Soc., A, 189, 261 (1947).

16. H.F. Kay and P.C. Bailey, Acta. Cryst., 10, 219 (1957).

17. P. Vousden, Acta. Cryst., 9, 141 (1956).

18. I. Clearfield and P.A. Vaughan, Acta. Cryst., 9, 555 (1956).

19. D.B. McWhan and G. Lundgren, Inorg. Chem., 5, 284 (1966).

National Institute of Standards and Technology Special Publication 804, Chemistry of Electronic Ceramic Materials, Proceedings of the International Conference held in Jackson, WY, August 17-22, 1990, issued January 1991.

POLYMERIC SYNTHESIS OF PEROVSKITE POWDERS AND FILMS

H. U. Anderson, M. M. Nasrallah, F. D. Blum and M. S. Smith
University of Missouri-Rolla

INTRODUCTION

The electronic components industry is constantly striving to make smaller components with increased reliability and faster information transfer. This requires the total integration of the components into single devices. Improvements in integrated electronic devices are directly linked to improvements in properties which, in turn, are related to processing. This can be achieved by utilizing the appropriate powder synthesis technique and a thorough understanding of its chemistry.

Recent breakthroughs in the processing of materials have increased the probability of success of electronic ceramics in component integration. These include: improved sputtering and chemical vapor deposition techniques, decreases in the sintering temperatures of substrates e.g. Al_2O_3, development of relaxor dielectrics with sintering temperatures around 900°C, and the development of organic derived sources of oxides which can be processed at lower temperatures and can be used as precursors for bulk and film devices. The latter, known as the "polymer precursor" or "liquid mix" technique, is one of the most significant and will be the focus of this work.

We have successfully used a modified liquid mix technique to synthesize doped double oxide perovskite-type powders with desirable sinterability and electrical properties. Spun-on films were also produced by this process. The synthesized perovskite powders are of the general formula ABO_3 where the A and B cations occupy 12 and 6 coordinated sites, respectively. Their electrical, magnetic and dielectric characteristics are strongly dependant on their defect structure. This, in turn, is related to the A/B ratio, the oxygen activity under which they are equilibrated, and the type and concentration of aliovalent dopants that can be preferentially added on either the A or B site. The liquid mix process appears to be very useful for production of

sinterable and homogeneous ABO_3 type powders with the required purity level and dopant content for the electronic industry. Numerous compounds have been developed in our laboratories including: donor doped Br and Sr titanates, counterdoped rutile, acceptor doped Lanthanum and Yttrium chromites, Sr doped La manganite, ferrites, cobaltites, niobates and superconductor $YBa_2Cu_3O_{7-x}$. Our discussion here will be limited to the titanates, manganites and the $YBa_2Cu_3O_{7-x}$ compounds.

The technique has the advantage of producing single phase ceramic powders with particle size as small as 50 nm and very precise chemical compositions. Further processing of these fine powders can be done at temperatures as low as 500°C. The protocol for the production of powders by this method was developed in the 1960's[1], however, no detailed study of the chemistry of these systems has been reported.

POWDER SYNTHESIS AND CHARACTERIZATION

(i) Liquid Mix Process

The liquid mix process utilizes complexing agents capable of chelation, e.g. pyroxycarboxylic acids, to form polybasic acids with various cations, e.g. Ti, Zr, Pb, Cr, Mn, Ba, La, etc. These chelates can undergo polymerization in the presence of polyhydroxyl alcohols or amines with a uniform distribution of the "chelating" cations. The formed polymer precursor retains homogeneity and stability (due to its high viscosity) and can be calcined at relatively low temperatures to yield fine oxide powders whose chemistry has been carefully controlled. The possible mechanism of polymer formation is as follows;

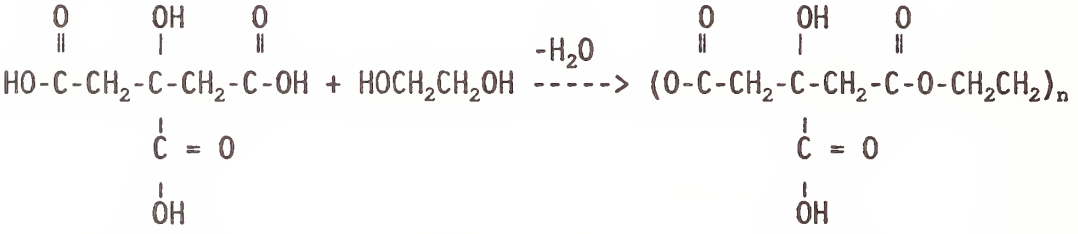

The original Pechini method involves mixing the required amounts of soluble cation salts with ethylene glycol and citric acid. The mixture is heated to about 90°C to insure complete dissolution of the cation salts. The solution is then evaporated to a polymeric residue. The metal ions are chelated to the organic chain. The organic polymer turns into a black brittle

mass as it is heated to 400°C. This is ground, screened and calcined at 600-800°C to yield a homogeneous fine particle size oxide with the required composition.

(ii) Ethylene Glycol Process

We have found that ethylene glycol oxidizes in the presence of cold nitric acid to form oxalic acid. The latter consists of two connecting functional carboxylic groups each of which loses a proton and may coordinate with the metal ion forming a ring structure as shown:

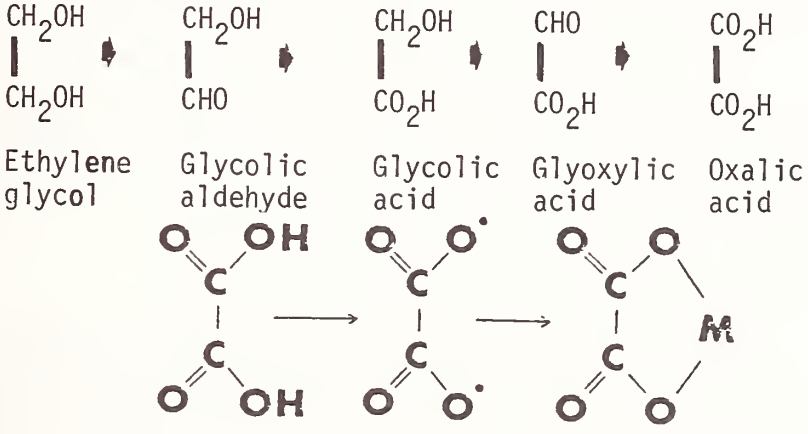

This, "modified liquid mix" process[2], was found to possess a wider range of application than was originally outlined by Pechini. Titanates, zirconates, niobates, chromites, ferrites, manganites, cobaltites and others have been successfully prepared by this process. It offers the potential of synthesizing complex double oxides with controlled stoichiometry, purity and particle size. The powder produced is initially amorphous and as the calcination temperature and time increase, crystallization gradually occurs until the crystal structure of the desired oxide is completely restored. This is detected by x-ray diffraction techniques as a function of calcination temperature. The produced powders are nearly spherical with about 0.1μm size as revealed by scanning electron microscopy.

The weight loss and changes that occur as the polymeric precursor is gradually heated are revealed by thermogravimetric analysis (TGA) and differential thermal analysis (DTA). Both techniques were carried out on the same sample. Results on $LaMnO_3$ and $BaTiO_3$ are shown in figs. 1 a and b respectively. An appreciable weight loss is observed during the early stages of calcination, this also corresponds to the DTA exothermic peak shown in fig. 1. Both samples were heated to 150°C prior to analysis to insure polymerization.

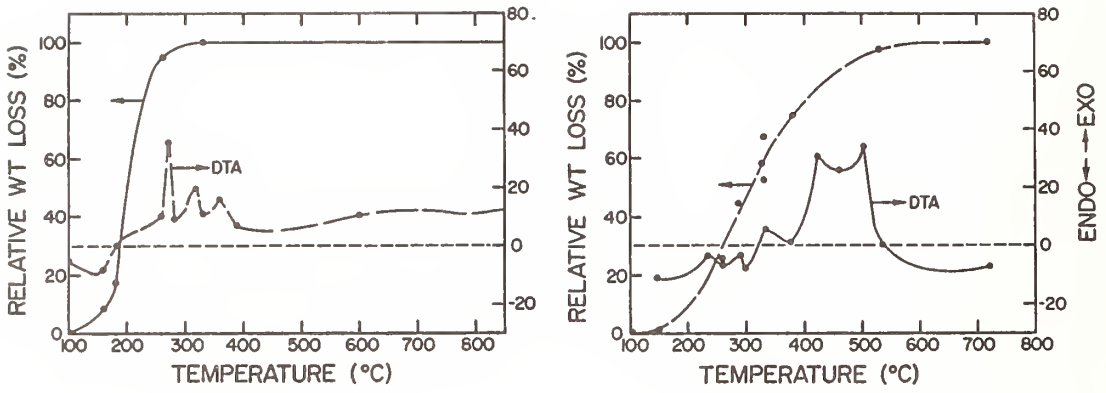

(a) (b)

Fig 1. Relative Weight Loss (TGA) and Differential Thermal Analysis (DTA) of Polymeric Precursors for (a) $LaMnO_3$. (b) $BaTiO_3$.

(iii) Ethylene Diamine Process

A major limitation of the original Pechini process is the possibility of precipitation during polymerization. This causes inhomogeneities in the resulting oxide. It is therefore essential that the mixture remains in solution throughout the polymerization process. We have found that both citric acid and ethylene diamine form chelates with the dissolved cations. The addition of ethylene diamine not only retards precipitation (through pH adjustments) but also enters the chelation process[3]. The proposed reaction sequence is as follows:

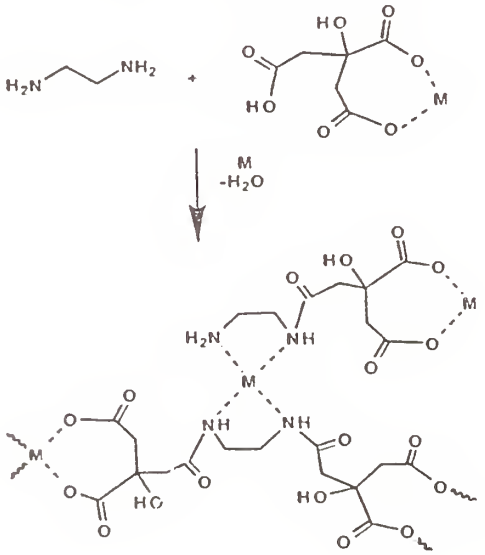

Ethylene diamine process.

Upon heating polyamidation occurs throughout the liquid medium, resulting in a homogeneous solution of metal ions attached to the organic matrix. This reaction indicates that not only citric acid, but also ethylene diamine can form chelates with dissolved metal ions increasing their concentration and the stability of the system. This process has been successfully used for synthesis of bulk and spun-on films of the superconductor $YBa_2Cu_3O_{7-x}$. The details of the process are published elsewhere[3]. Careful pH adjustment is critical to this process. The synthesized powder was calcined at temperatures ranging from 300-900°C whereby a change in structure from amorphous to the orthorhombic $YBa_2Cu_3O_{7-x}$ was observed. Fig 2 shows x-ray diffraction patterns of $YBa_2Cu_3O_{7-x}$ as a function of calcination temperature. Below 300°C a diffused pattern was observed with no characteristic crystal structure, as the temperature increased the crystalline superconducting phase appeared and became the predominant phase above 700°C. The decomposition of the polymer precursor to the desired oxide was also studied by simultaneous DTA and TGA.

Both the ethylene glycol and the ethylene diamine processes can be used for synthesis of a wide range of powders with improved chemical homogeneity, increased reactivity, high purity, and better compositional stoichiometry than other conventional techniques. However, the mechanism of these processes is not fully understood. This study is currently underway. One of the techniques used for this purpose is nuclear magnetic resonance (NMR) spectroscopy. It is based on the ability of interaction of a nuclear magnetic moment with radio frequency waves (rf) in the presence of an external magnetic field. This interaction is affected by several factors including bonding, solvent, temperature, concentration, structure, dipolar effects, etc. As a result of the interaction, one will observe a chemical shift of a particular NMR active species. The shift is defined as the difference in resonance frequency between that of the active species, due to the mentioned interactions, and that of a given standard.

Pb-207 (22.6% natural abundance) has a very large chemical shift range (~3500 ppm) and thus is very sensitive to changes in chemical environment. Preliminary results have been obtained for lead solutions in citric acid (CA) and ethylene glycol (EG). As shown in fig 3, as the Pb^{+2} concentration increases, a greater change in chemical shift is observed with (CA) as compared to (EG). Indicating that Pb^{+2} ions interact more strongly with (CA) than with (EG). When a mixture of both (CA+EG) is used, the results indicate that the (CA) association is preferred over that of (EG). This association can be interpreted in terms of Pb

chelation. We anticipate that this study will be extended to other metal ion systems in order to better understand the complexation process.

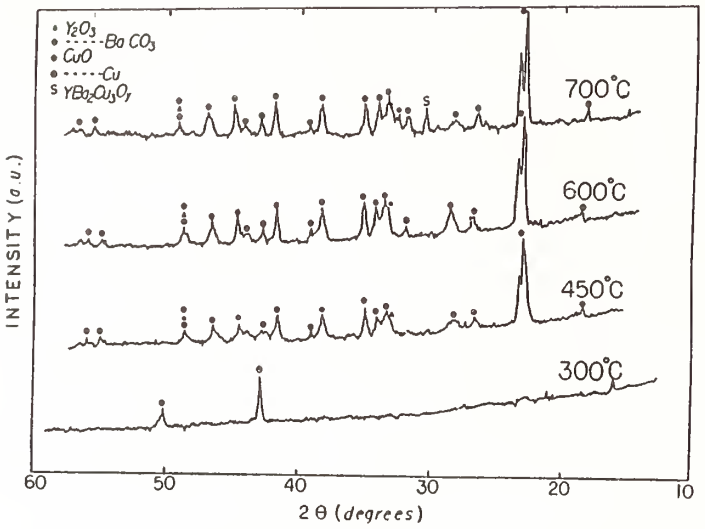

Fig. 2

X-ray diffraction as a function of calcination temperature for $YBa_2Cu_3O_{7-x}$.

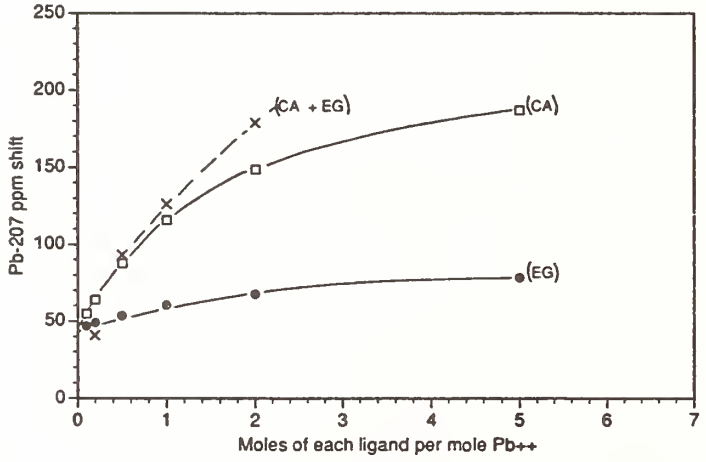

Fig. 3

Pb.207 NMR chemical shift.

REFERENCES

1. M. Pechini, U.S. Patent No. 3,330,697, July 1967.

2. N. G. Eror and H. U. Anderson, Mat. Res. Soc. Symp. Proc., Vol. 73, "Better Ceramic Through Chemistry II", Eds. C. Brinker, D. Clark and D. Ulrich, MRS, 1989.

3. C. C. Chen and H. U. Anderson, "Advanced Materials Conference II, Proc.", Ed. F. Smith, Adv. Matls. Inst., 1989.

National Institute of Standards and Technology Special Publication 804, Chemistry of Electronic Ceramic Materials, Proceedings of the International Conference held in Jackson, WY, August 17-22, 1990, issued January 1991.

ELECTRODEPOSITION OF NANOMODULATED ELECTRONIC CERAMIC THIN FILMS

Jay A. Switzer
University of Missouri-Rolla
Department of Chemistry and
Graduate Center for Materials Research
Rolla, MO 65401

ABSTRACT

Electrochemistry can be used for the atomic-level architecture of ceramic materials. In this report, ceramic superlattices based on the $Tl_aPb_bO_c/Tl_dPb_eO_f$ system were electrodeposited with individual layer thicknesses as thin as 3 nm. The superlattices were deposited from a single aqueous solution at room temperature, and the layer thicknesses were galvanostatically controlled. Substitution of Tl_2O_3 into PbO_2 appears to stabilize a face-centered cubic structure with an average lattice parameter of 0.536 nm. The lattice parameters for the $Tl_aPb_bO_c$ mixed oxides vary by less than 0.3% when the Pb/Tl ratio is varied from 0.84 to 7.3. Because the modulation wavelengths are of electron mean free path dimensions, this new class of degenerate semiconductor metal-oxide superlattices may show thickness-dependent quantum optical, electronic, or optoelectronic effects.

INTRODUCTION

We have recently demonstrated that it is possible to electrodeposit nanomodulated ceramic superlattices based on the $Tl_aPb_bO_c/Tl_dPb_eO_f$ system [1]. An idealized superlattice structure with square-wave modulation of composition and/or structure is shown in Figure 1. The thicknesses of the A and B layers are not necessarily equal, as long as the structure is periodic.

The idea of electrochemically depositing nanomodulated superlattices is not new, but it has not been applied previously to the deposition of nonmetallic materials. Several research groups have shown that compositionally modulated metallic alloys can be electrochemically deposited from

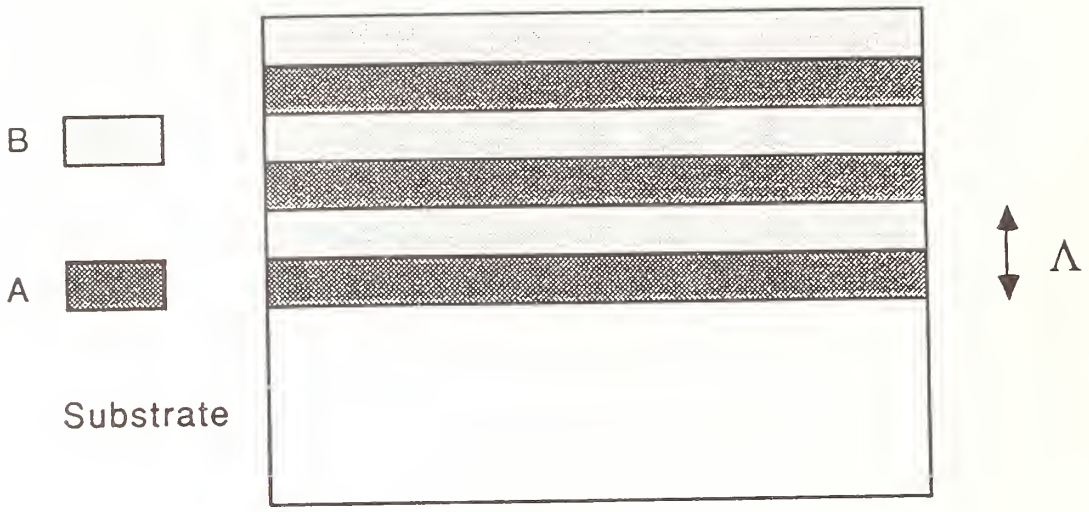

Figure 1. Idealized superlattice structure.

a single plating bath by cycling either the potential or current [2-5]. The interest in nanomodulated metallic systems stems from their enhanced mechanical and magnetic properties [3,6].

We have chosen the $Tl_aPb_bO_c/Tl_dPb_eO_f$ system for our study for several reasons: (1) during our previous work on the electrochemical and photoelectrochemical deposition of thallium(III) oxide films, we found that it was possible to deposit highly oriented films [7-9], (2) the deposition of PbO_2 [10,11] and $Pb_8Tl_5O_{24}$ [12,13] are well documented, (3) the anhydrous oxides deposit directly at room temperature and require no heat treatment, (4) there is a nearly isomorphous series of mixed thallium/ lead oxides that should grow epitaxially, and (5) the device applications of these types of materials have not been studied previously.

We expect that these materials will prove to have very interesting optical and electrical properties. The end members of the series, PbO_2 and Tl_2O_3, are both degenerate n-type semiconductors. They have the high electrical conductivity of metals, with the optical properties of semiconductors. Because of their high majority carrier concentrations ($> 10^{20}/cm^3$), they also have high reflectivity in the near-IR. Thallium(III) oxide, for instance, is a degenerate n-type semiconductor with a bandgap of 1.4 eV and a room temperature resistivity of only 70 μohm-cm [14]. Lead(IV) oxide has a larger bandgap of approximately 1.8 eV [10]. These materials are, therefore, the metal oxide analogs of semiconductors such as GaAs and AlGaAs, and they may function as multiple quantum wells when the modulation wavelength is in the nanometer range [15,16].

EXPERIMENTAL

Electrochemical depositions were performed using either a Princeton Applied Research (PAR) potentiostat/galvanostat, or a system consisting of a Stonehart BC 1200 potentiostat/galvanostat, PAR Model 175 universal programmer, and PAR Model 379 digital coulometer. Superlattices were deposited onto polycrystalline 430 stainless steel disks. The disks were housed in a PAR Model K105 flat specimen holder, so that only the front surface was exposed to the solution. The final polish on the stainless was 0.05 μm alumina. Films were deposited from aqueous solutions of 0.005 M $TlNO_3$ and 0.1 M $Pb(NO_3)_2$ in 5 M NaOH. The strong base is necessary to dissolve the $Pb(NO_3)_2$, which precipitates in 1 M NaOH as PbO. The superlattices were deposited by galvanostatically pulsing between either 5 mA or 1 mA and a lower current such as 0.05 mA. Each layer thickness was proportional to the product of current and time. Elemental analysis was done by EDS on a JEOL 35CF scanning electron microscope. The L lines of thallium and lead were used for the analysis because of the overlap of the K lines.

RESULTS AND DISCUSSION

Since Tl_2O_3 and PbO_2 can both be electrodeposited from alkaline solution, and there is considerable overlap of the deposition iV curves, it is possible to electrodeposit $Tl_aPb_bO_c$ films with compositions that are a function of applied potential or current [1]. We have carefully chosen the reactant concentrations so that it is possible to vary the Pb/Tl ratio over a wide range. Since the $TlNO_3$ concentration is only 0.005 M, and the $Pb(NO_3)_2$ concentration is 0.1 M, the deposition becomes mass-transport-limited in $[Tl^+]$ when the current is raised over about 1 mA. The Pb/Tl ratio was varied from 0.84 to 7.3, when the current was increased from 0.05 mA to 5.0 mA (see Table I).

The x-ray diffraction patterns of the $Tl_aPb_bO_c$ films are very similar to the Tl_2O_3 pattern. An important difference between the patterns is that mixed-index reflections such as (211) are not observed for the mixed oxide, but they are present for Tl_2O_3. The systematic absence of mixed index reflections is consistent with an fcc structure. This is in agreement with the assignment of Sakai et al. [12], of electrodeposited $Pb_8Tl_5O_{24}$ as an fcc fluorite-type structure with a cubic lattice parameter of 0.53331 nm. For comparison, Tl_2O_3 has a bcc bixbyite structure with a = 1.05434 nm, and PbO_2 has either an orthorhombic or tetragonal structure [17]. The lattice parameters that we measure for our mixed oxides vary by only 0.3% over the

Table I. Composition and values of the cubic lattice parameters for electrodeposited $Tl_aPb_bO_c$ films as a function of applied current (from ref. [1]).

Applied Current (mA)	Measured Potential (V vs. SCE)	Pb/Tl mole ratio	Cubic Lattice Parameter (nm)
0.05	0.06	0.84	0.536
0.5	0.12	1.9	0.535
1.0	0.14	2.5	0.537
5.0	0.27	7.3	0.535

entire composition range listed in Table I. Hence, these oxides are ideal for the epitaxial growth of nanomodulated superlattices.

A modulated structure was prepared for SEM studies by alternately pulsing the electrode at 0.05 mA for 8772 seconds and at 5.0 mA for 88 seconds. The layers were intentionally made quite thick, so that they could be easily imaged in the SEM. Cross sections of a fractured film are shown in Figure 2 for two different magnifications. The lower magnification micrograph (top) shows the strong preferred orientation of the film. We have previously reported similar columnar growth for electrodeposited thallium(III) oxide films. The higher magnification micrograph (bottom) clearly shows that the composition is modulated within each columnar grain.

Samples with much shorter modulation wavelengths and layer thicknesses were prepared by using shorter dwell times during the double-pulse galvanostatic deposition. The superlattices with modulation wavelengths in the nanometer range were characterized by x-ray diffraction. The periodicity of the superlattice manifests itself in two ways in the x-ray diffraction pattern. Bragg reflections are observed at low angles which correspond to the modulation wavelengths. These peaks at low angles would be observed even with a modulated amorphous material. At high angles the periodicity is seen as satellites around the main Bragg reflections for the material. The analysis of our superlattices was done at high angles. The modulation wavelength, Λ, can be calculated from Eq. (1), where λ is the x-ray wavelength used, L is the order of the reflection, and θ is the diffraction angle. In Eq. (1), L = 0 for the Bragg reflection, while the first

Figure 2. Scanning electron micrographs of modulated $Tl_aPb_bO_c$/ $Tl_dPb_eO_f$ films. Micrographs are low (top) and higher (bottom) magnifications of a cross-sectional view of a fractured film. Film was deposited by cycling electrode between 0.05 mA and 5 mA in a solution of 0.005 M $TlNO_3$ and 0.1 M $Pb(NO_3)_2$ in 5 M NaOH. Layer thicknesses are intentionally quite thick ($\sim$0.5 μm) so that SEM imaging is possible.

satellite at low angle has the value L = -1, and the first satellite at higher angle has the value L = +1.

$$\Lambda = \frac{(L_1 - L_2)\,\lambda}{2\,(\sin\theta_1 - \sin\theta_2)} \qquad (1)$$

The modulation wavelengths for several superlattices are listed in Table II. The x-ray modulation wavelength, Λ_F, was calculated from Faraday's law. For the Faraday's law calculation, we used ρ = 10.353 g/cm^3, n = 2, and M = 228 g/mol. This is only an approximation since the density and formula weight varies somewhat with composition. We have found, however, that for all of the compositions in Table I, approximately 1.1 to 1.2 μm of material are deposited per coulomb of anodic charge that is passed. There is remarkably good agreement between Λ_F and Λ_x in Table II considering the approximation used for Λ_F. Superlattice satellites were not observed for modulation wavelengths less than 5.9 nm.

Table II. Comparison of modulation wavelengths calculated from Faraday's law (Λ_F) and from x-ray satellite spacings (Λ_x) for ceramic superlattices deposited at various currents and dwell times. The electrode area ranged from 0.78 to 0.83 cm^3.

i_a (mA)	t_a (s)	i_b (mA)	t_b (s)	Λ_F (nm)	Λ_x (nm)
0.05	40	5.0	0.4	5.9	5.9
0.05	50	5.0	0.5	7.4	7.4
0.05	60	5.0	0.6	8.3	8.0
0.05	70	5.0	0.7	9.7	9.9
0.05	80	5.0	0.8	11.5	11.6
0.05	90	5.0	0.9	12.3	12.9

FUTURE WORK

The effect of quantum confinement on the optical and electrical properties of these materials is unknown. Quantum confinement should produce thickness-dependent blue-shifting of the optical absorption spectra,

and the development of excitonic features. We are presently studying the optical and electrical properties of these nanomodulated materials. Another important area of future research will be to study epitaxial growth in these systems by measuring nucleation and growth rate constants by transient potential-step experiments for varying degrees of lattice mismatch. These *in situ* studies should provide valuable information to architects of future superlattice structures.

ACKNOWLEDGEMENTS

The author thanks Mitsubishi Corporation for financial support through a Mitsubishi Kasei Faculty Development Award, and Unocal Corporation for donation of all of the electrochemical instrumentation used in this research.

REFERENCES

1. J. A. Switzer, M. J. Shane, and R. J. Phillips, Science, 247, 444 (1990).

2. U. Cohen, F. B. Koch, and R. Sard, J. Electrochem. Soc., 130, 1987 (1983).

3. D. Tench and J. White, Metall. Trans. A, 15, 2039 (1984).

4. J. Yahalom et al., J. Mater. Res., 4, 755 (1989).

5. D. S. Lashmore and M. P. Daniel, J. Electrochem. Soc., 135, 1218 (1988).

6. L. H. Bennett et al., J. Magn. Mater., 67, 239 (1987).

7. R. J. Phillips, M. J. Shane, and J. A. Switzer, J. Mater. Res., 4, 923 (1989).

8. J. A. Switzer, Am. Ceram. Soc. Bull., 66, 1521 (1987).

9. J. A. Switzer, J. Electrochem. Soc., 133, 722 (1986).

10. W. Mindt, J. Electrochem. Soc., 116, 1076 (1969).

11. J. C. G. Thomas and D. W. Wabner, J. Electroanal. Chem., 135, 243 (1982).

12. M. Sakai, T. Sekine, and Y. Yamazaki, J. Electrochem. Soc., 130, 1631 (1983).

13. W. Tillmetz and D. W. Wabner, Z. Naturforsch. Teil B, 39, 594 (1984).

14. V. N. Shukla and G. P. Wirtz, J. Am. Ceram. Soc., 60, 253 (1977).

15. C. R. Leavens and R. Taylor, Eds., "Interfaces, Quantum Wells, and Superlattices," (NATO Series B: Physics, Vol. 179) (Plenum, New York, 1988).

16. E. E. Mendez and K. von Klitzing, Eds., "Physics and Applications of Quantum Wells and Superlattices," (NATO Series B: Physics, Vol. 170) (Plenum, New York, 1987).

17. P. T. Moseley, J. L. Hutchison, and M. A. M. Bourke, J. Electrochem. Soc., 129, 876 (1982).

III. SOLID-STATE SYNTHESIS AND CHARACTERIZATION

National Institute of Standards and Technology Special Publication 804, Chemistry of Electronic Ceramic Materials, Proceedings of the International Conference held in Jackson, WY, August 17-22, 1990, issued January 1991.

PROPERTIES OF SOME MIXED URANIUM OXIDES

P.G. Dickens, A.V. Powell and G.P. Stuttard
University of Oxford, Inorganic Chemistry Laboratory,
South Parks Rd. Oxford U.K.

ABSTRACT

U_3O_8 and stucturally related mixed uranium/transition metal oxides UMO_5 (M=Ti, V) are examined as hosts for intercalation reactions. The location of lithium in $Li_{0.9}U_3O_8$ has been determined by neutron diffraction. Changes in the electronic properties of UVO_5 on oxidation and of $UTiO_5$ on intercalation have been investigated by XPS and magnetic susceptibility measurements.

INTRODUCTION

α-U_3O_8 is the structural archetype for a number of mixed uranium/transition-metal oxides such as UVO_5, $UTiO_5$, CuU_3O_{10} and UNb_3O_{10}, which have in common pillared-layer structures consisting of planes of edge-sharing UO_n and MO_m polyhedra connected by metal-oxygen chains running perpendicularly to the planes and providing an interplanar separation of ~4 Å. α-U_3O_8 itself, (Figs 1(a) and 4) consists of edge-sharing UO_5 pentagons connected by U-O-U chains [1]; U-O bond orders in the chain direction are higher than within the layers although no discrete uranyl groups exist. The primitive unit-cell (dashed outline) has pseudo-hexagonal symmetry ($\gamma = 119.3°$). However, powder neutron diffraction [2] indicates that above 210°C very slight atomic displacements occur to give a phase, denoted α'-U_3O_8, which has hexagonal symmetry. This phase reverts to the orthorhombic form on cooling. The relatively open structure of α-U_3O_8 provides a host matrix for intercalation reactions with Li and Na which we have described previously [3, 4].

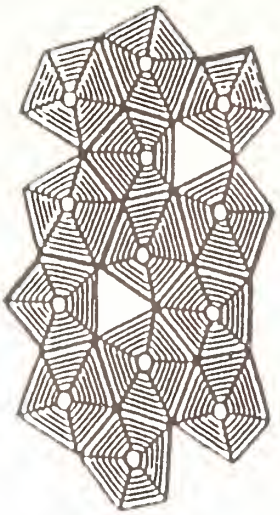

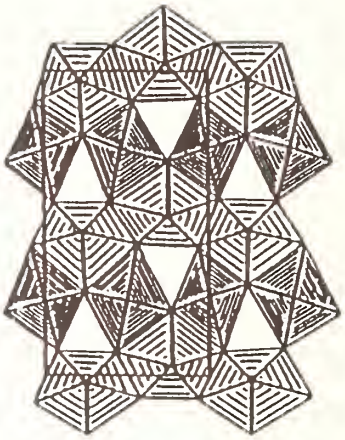

Fig 1: (a) α-U_3O_8 (b) UVO_5

The structural relationship between α-U_3O_8 and UVO_5 is shown schematically in Figs 1(a) and (b). In UVO_5 edge-sharing pentagons which form zig-zag chains are separated by single VO_5 square-based pyramids forming layers of composition $(UVO_4)_n$ [5] which in turn are linked by U-O-U chains in a similar way to those in α-U_3O_8. The V-O linkage to the oxygen at the vertex of the VO_5 square-based pyramid is very short (1.64 Å) and gives rise to IR absorption at 980 cm^{-1} characteristic of a vanadyl group. Again, the U-O-U chains perpendicular to the U/V/O layers contain no discrete uranyl groups. Oxygen coordination determined by powder neutron diffraction is illustrated in Fig 2.

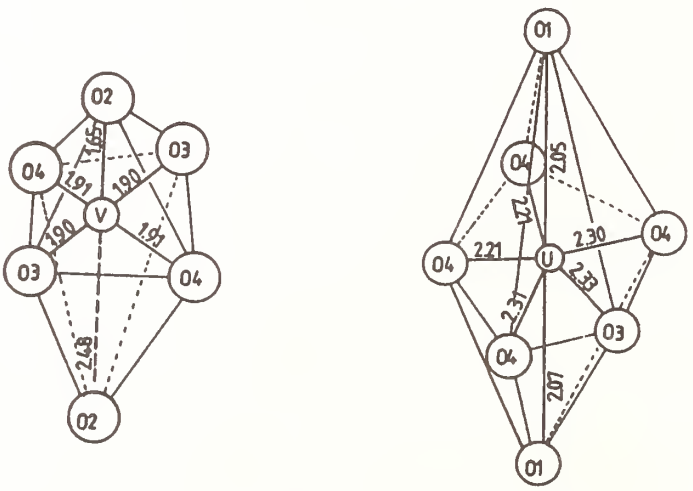

Fig 2: Oxygen Coordination About Uranium and Vanadium in UVO_5 [6]

So far, the crystal structure of $UTiO_5$ is not known in detail but comparisons of powder X-ray data strongly suggest that it and UVO_5 have similar planar metal atom arrangements which are probably also common to those of $UMoO_5$, $UNbO_5$ and $UTaO_5$. All appear to undergo similar intercalation reactions with alkali metals leading to the formation of mixed-valence compounds. In this work we describe the synthesis and characterisation of some new insertion compounds formed by U_3O_8, UVO_5 and $UTiO_5$ together with an attempt to determine their electronic structures.

EXPERIMENTAL

α-U_3O_8 was prepared, as previously described, by the thermal decomposition of $UO_4 \cdot 2H_2O$ at 720°C for 2 days. UVO_5 was prepared by conventional solid-state synthesis by reaction of V_2O_5, V_2O_3 and U_3O_8 in a sealed silica tube at 700°C for 24 hours whereas $UTiO_5$ was synthesised by heating a uranium-vanadium co-precipitate of hydrated oxides in a modification of the method described by Hoekstra and Marshall [7].

Insertion of both alkali metals and magnesium into the above three oxides was performed chemically and electrochemically (in aqueous and non-aqueous media). Chemical lithiation was accomplished by use of lithium iodide in CCl_4 in a manner that has been described previously [8]. In a similar manner, use of a magnesium iodide monoetherate complex in CCl_4 permitted the insertion of magnesium at ambient temperature. Electrochemical measurements in aqueous media were performed using a three-compartment glass cell in conjunction with a Princeton applied research potentiostat operating in a galvanostatic mode. A platinum counter-electrode was used whilst a calomel reference allowed all voltages to be referred to the standard hydrogen scale. The cathode was a mixture of the metal oxide, graphite and PTFE mixed in the ratio (by weight) 80:10:10 and pressed onto a 13mm platinum gauze disk. Electrolytes were 1M LiCL or 2M $MgCl_2$ solutions for the insertion of lithium or magnesium respectively. Non-aqueous electrochemical discharges were performed in an argon atmosphere glove-box using a Teflon cell. The cathode was as described above. The electrolyte was a solution of $LiBF_4$ in propylene carbonate and the anode a disc of lithium metal.

All products of insertion were handled in an argon atmosphere dry box. Characterisation was by powder X-ray diffraction, infra-red spectroscopy and TGA. Product compositions were determined by reducing power titration [4]. XPS measuremnts

were performed using a VG ESCALAB spectrometer. An Oxford Instruments Faraday balance was used to measure low temperature magnetic susceptibilities and measurements at room-temperature were made using a Gouy balance.

RESULTS AND DISCUSSION

(i) Insertion Reactions

(a) U_3O_8

The insertion reactions undergone by α-U_3O_8 are summarised in Fig 3. In all cases only small changes in lattice parameters relative to those of the parent oxides are observed (Table 1), strongly suggesting that insertion proceeds with retention of structure.

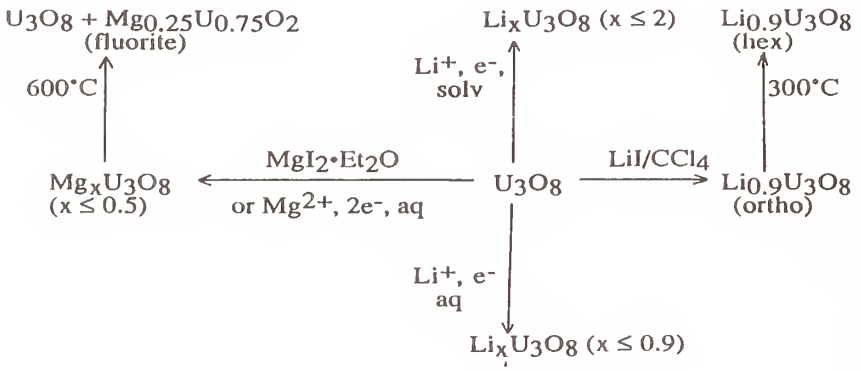

Fig 3: Insertion Reactions of α-U_3O_8

Table 1: Lattice Parameters of Some Mixed Oxides and Insertion Compounds.

	a/Å	b/Å	c/Å	
α-U_3O_8	6.715	11.968	4.143	
α-$Li_{0.88}U_3O_8$	6.727	11.953	4.188	
α'-U_3O_8	6.812	6.812	4.142	($\gamma = 120°$)
α'-$Li_{0.88}U_3O_8$	6.849	6.849	4.197	($\gamma = 120°$)
$Mg_{0.2}U_3O_8$	6.717	11.947	4.143	
UVO_5	7.207	12.364	4.123	
$Li_{1.1}UVO_5$	7.28	6.22	4.14	
$UTiO_5$	7.364	6.317	15.631	($\beta = 91°$)
$Li_{0.9}UTiO_5$	7.412	6.241	16.034	($\beta = 91°$)
$Mg_{0.15}UTiO_5$	7.387	6.270	15.667	($\beta = 91°$)

In the case of $Li_{0.88}U_3O_8$, a recent powder neutron diffraction study [9] has located the lithium positions. For material synthesised at ambient temperature the lithiums randomly occupy interlayer sites (marked A, B, C in Fig 4) in the orthorhombic α-U_3O_8 structure. These sites are of approximately trigonal bipyramidal coordination. However, on annealing in vacuum at ~573 K a transformation to the closely related hexagonal form occurs. This structure is stable at all temperatures and does not revert to the orthorhombic form on cooling. Refinement of neutron data at 595 K demonstrated that the lithiums now exclusively occupy sites of type A (2d in P62m). That this is a stable high-temperature phase, with only a limited range of stoichiometry, was demonstrated by its synthesis from the oxides, Li_2O, U_3O_8 and UO_2 in a sealed tube preparation at 500°C. This compound α'-$Li_xU_3O_8$ ($0.8 \leq x \leq 0.9$) appears to be identical with the hexagonal phase reported by Kemmler-Sack and Rüdorff [10] obtained by high temperature synthesis and formulated as $(Li_2O)_x \cdot UO_2 \cdot UO_3$ which for x = 0.33 corresponds to LiU_3O_8 a composition which is achieved by half-occupation of the sites marked 'A' in Fig 4.

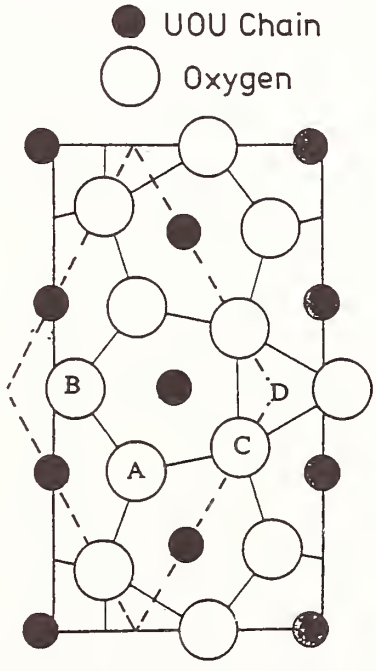

Fig 4: Sites for Insertion in α-U_3O_8 (z = 1/2)

Corresponding magnesium insertion compounds $Mg_xU_3O_8$ were prepared by reaction with $MgI_2 \cdot Et_2O$ ($x \leq 0.5$) or by galvanostatic discharge from aqueous media. The retention of structure of the orthorhombic α-U_3O_8 framework is apparent from

the data in Table 1. The thermal behaviour of this phase is quite different from that of $Li_{0.88}U_3O_8$. On heating in a sealed tube at 600°C, $Mg_{0.2}U_3O_8$ disproportionates into U_3O_8 and the stable cubic fluorite phase $Mg_yU_{1-y}O_2$ ($0 \leq y \leq 0.33$), which has been described by Kemmler-Sack and Rüdorff [11], according to;

$$Mg_{0.2}U_3O_8 = 0.8\ U_3O_8 + 0.8\ Mg_{0.25}U_{0.75}O_2$$

(b) $UTiO_5$ and UVO_5

The insertion reactions undergone by $UTiO_5$ are summarised in Fig 5. $UTiO_5$ is a versatile host lattice undergoing intercalation with the chemical reagents LiI, n-BuLi and $MgI_2 \cdot Et_2O$ and also electrochemically in both aqueous and non-aqueous media . UVO_5 also readily intercalates lithium with retention of structure.

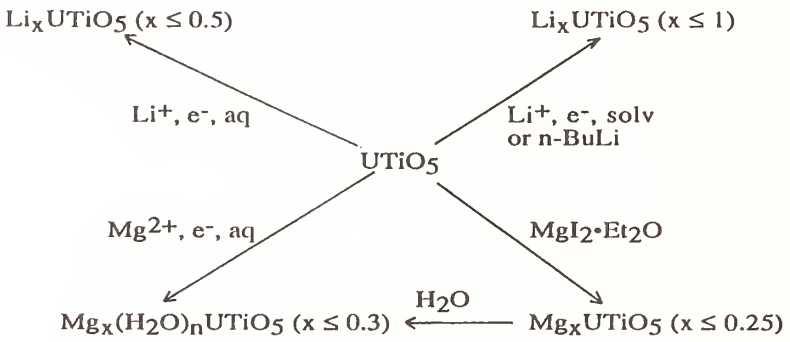

Fig 5: Insertion Reactions of $UTiO_5$

(ii) Electronic Properties

By analogy with other oxide insertion compounds it is presumed that formation of A_xUMO_5 involves transfer of valence electrons from A to metal-based orbitals in UMO_5.

$$A = A_i^{\bullet} + e'_{U \text{ or } M}$$

leading to consequential changes in electronic properties such as colour, conductivity, PE spectra and magnetism. The products described above are not metallic and their properties are compatible with localisation of the electrons at particular metal sites (small polaron model). A qualitiative $1e^-$ energy level diagram can be constructed for UMO_5 (Fig 6) which illustrates some important features of its electronic structure. In this diagram the 13 σ bonding orbitals derive from overlap between sp^n O hybrids with U

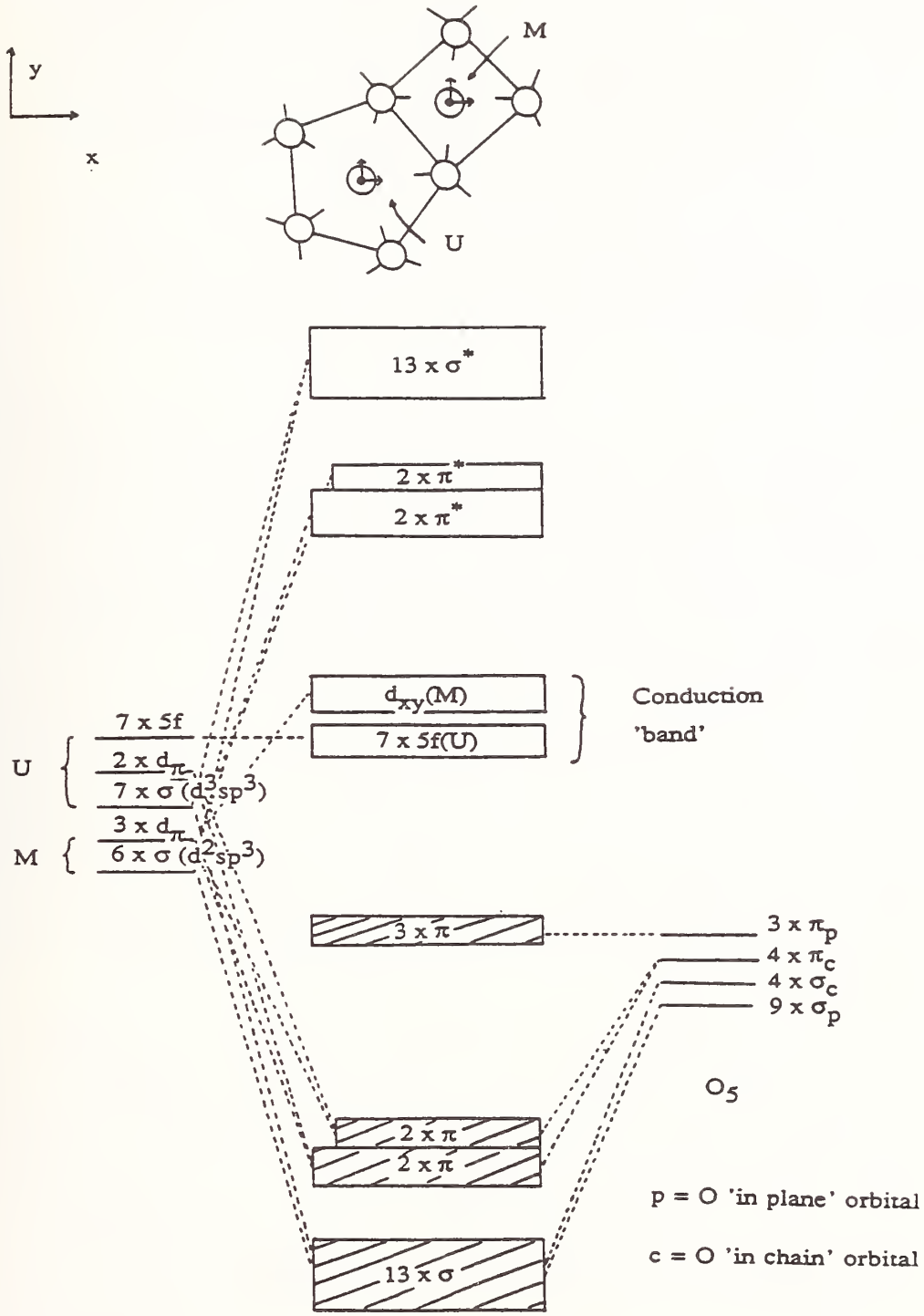

Fig 6: $1e^-$ Energy-level Diagram for UMO_5

(d^3sp^3) and M(d^2sp^3) sets, the 4π bonding orbitals from $M_{d\pi}$-$O_{p\pi}$ and $U_{d\pi}$-$O_{p\pi}$ chain interaction, and the 3π non-bonding (or weakly bonding) orbitals from O_π in-plane interactions. This places a non-bonding U(5f) set or a Md_{xy} anti-bonding orbital above the filled valence set as possible constituents of the conduction band. In $UTiO_5$ $40e^-$ completely fill the valence band. Stoichiometric $UTiO_5$ is an insulator. In UVO_5, $1e^-$ per UVO_5 unit occupies either the $V3d_{xy}$ level (V(IV)) or the uranium 5f set, U(V) and in Li_xUTiO_5 xe^- must occupy either U(V) or Ti(III).

In order to distinguish experimentally between these alternatives some preliminary studies have been made using XPS and magnetic susceptibility measurements on $UTiO_5$, Li_xUTiO_5, UVO_5 and a fully oxidised compound $UVO_{5.5}$ ($U_2V_2O_{11}$).

(a) XPS

Measurements were made by J. Kemp, S. Hawe and P.A. Cox of this laboratory and a complete account will be published elsewhere. Fig 7 shows the valence region of the XPS spectra for the samples studied. The filling of the conduction band on passing from $UTiO_5$ to $Li_{0.9}UTiO_5$ and from the fully oxidised $UVO_{5.5}$ to UVO_5 is clearly demonstrated. On oxidation, the conduction band is removed or considerably reduced in intensity due to the loss of mobile electrons .

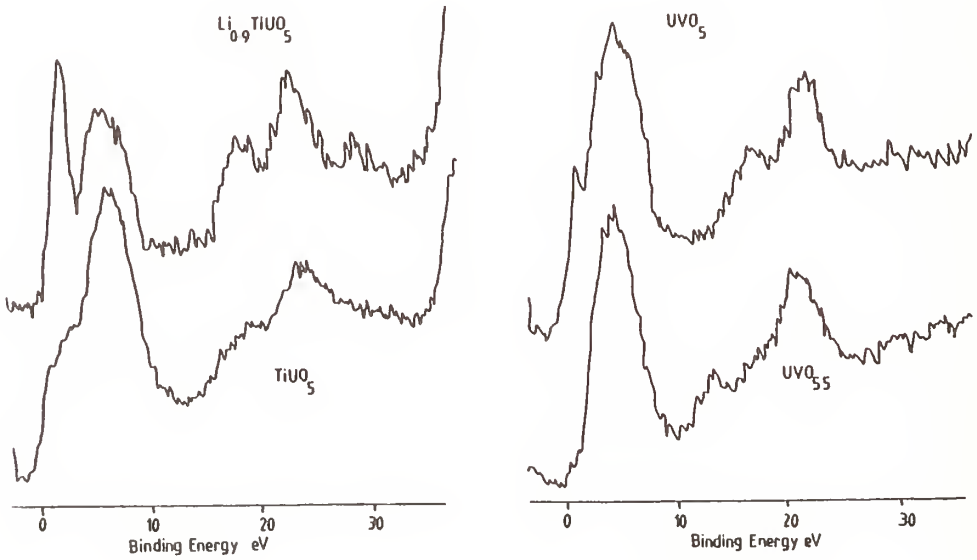

Fig 7: Valence Region of XPS

In Table 2 are shown the binding energies of the core levels of $U4f_{7/2}$, $Ti2p_{3/2}$ and $V2p_{3/2}$ and the differences between relevant pairs in the compounds studied.

Table 2: Binding Energies and Differences (eV)

Compound	$Ti2p_{3/2}$	$U4f_{7/2}$	ΔE
$Li_{0.9}UTiO_5$	459.7	382.0	77.7
$UTiO_5$	459.9	382.1	77.4
	$V2p_{3/2}$	$U4f_{7/2}$	ΔE
UVO_5	517.1	380.5	136.6
$UVO_{5.5}$	526.9	390.8	136.1

Charging effects in insulating samples, in the absence of an absolute binding energy reference, mean that only the differences ΔE in the peak positions of the relevant transition metal/uranium pairs are of significance. Oxidation raises the formal oxidation state of one or other of the metals and so leads to a shift to higher binding energy of the core line involved. The transition metal $2p_{3/2}$ line falls at a higher energy than does $U4f_{7/2}$ so that a decrease in ΔE on oxidation implies an increase of the uranium oxidation state. This is the observed direction of change for both the pairs UVO_5, $UVO_{5.5}$ and $Li_{0.9}UTiO_5$ and $UTiO_5$ and so it is concluded that in both it is the uranium which is principally reduced leading to the formulation of Li_xUTiO_5 as $Li_x^{I}U_x^{V}U_{1-x}^{VI}Ti^{IV}O_5$ and UVO_5 as $U^{V}V^{V}O_5$. Further support for this conclusion is provided by the appearance in the reduced phases of satellite lines at binding energies 7-8 eV above the $U4f_{7/2}$ core line which is a characteristic feature of U^{V} [12]. Such lines were absent in $UVO_{5.5}$ and $UTiO_5$.

(b) Magnetic Measurements

Magnetic susceptibilities of $UTiO_5$, $Li_{0.9}UTiO_5$ and $Mg_{0.25}UTiO_5$ were measured at 293 K and effective Bohr magneton numbers (per U^{V}) evaluated by using $m_{eff} = 2.82[(\chi_m - \chi_m(UTiO_5))T]^{1/2}$. The values obtained; $0.93(Li_xUTiO_5)$ and $1.08(Mg_xUTiO_5)$ are close to those found for other U^{V} compounds [13] such as $1.06(LiUO_3)$ and $1.1(UNb_3O_{10})$. They are much lower values than expected for a magnetically dilute first-row transition metal complex and support the contention that the insertion compounds contain reduced uranium rather than Ti^{III}

ACKNOWLEDGEMENTS

The assistance of J.M. Fleetwood in the preparation of samples is gratefully acknowledged. AVP thanks the CEGB for a studentship.

REFERENCES

[1] B.O. Loopstra; Acta. Cryst. 17, 651, (1964).
[2] B.O. Loopstra; J. Appl. Cryst. 3, 94, (1970).
[3] P.G. Dickens, D.J. Penny and M.T. Weller; Solid State Ionics, 18&19, 778, (1986).
[4] P.G. Dickens, A.V. Powell and A.M. Chippindale; Solid State Ionics, 28-30, 1123, (1988).
[5] R. Chevalier and M. Gasperin; Bull. Soc. Franc. Minera. Crist. 93, 18, (1970).
[6] P.G. Dickens, R.G.J. Ball, S. Patat and S.Hull; In Preparation.
[7] H.R. Hoekstra and R.H. Marshall; J. Inorg. Nucl. Chem. 27, 1947, (1965).
[8] P.G. Dickens, S.J. French. A.T. Hight and M.F. Pye; Mat. Res. Bull. 14, 1295, (1979).
[9] P.G. Dickens and A.V. Powell; Submitted to J. Solid State Chem.
[10] S. Kemmler-Sack and W. Rüdorff; Z. Anorg. Allg. Chem. 354, 255, (1967).
[11] S. Kemmler-Sack and W. Rüdorff; Z. Anorg. Allg. Chem. 354, 264, (1967).
[12] C. Miyake, H. Sakurai and S. Imoto; Chem. Phys. Lett. 36, 158, (1975).
[13] B. Kanellakopulos, E. Henrich, C. Keller, F. Baumgärtner, E. König and V.P. Desai; Chemical Physics, 53, 197, (1980).

M. Greenblatt: Have you tried any other group II elements besides magnesium?

P. Dickens: No. The only other metal we've investigated is sodium and, of course, hydrogen.

M. Greenblatt: Sodium can be inserted as well?

P. Dickens: Yes but slowly. I should have pointed out that lithium in these compounds is fairly mobile, it has a high diffusion coefficient. Sodium is much less mobile and other metals, if they do insert, are unlikely to be very mobile.

R. Newnham: Will protons go in those positions?

P. Dickens: No, they don't go in the lithium positions, but actually attach themselves as OH groups. In all the oxide insertion compounds we've studied we find that hydrogen is located as OH or OH_2 groups. So if you prepare H_xUTiO_5 the hydrogen appears as OH, but an electron, of course, is transferred to uranium to give a product isoelectronic with Li_xUTiO_5.

P. Davies: Are you able to insert protons into these structures?

P. Dickens: Yes, at least for U_3O_8, $UTiO_5$ and UVO_5. For example, for UVO_5 something like $HUVO_5$ is formed quite easily with retention of structure, but there comes a point where it begins to become amorphous. In the particular case of UVO_5, you have 3-connected oxygen and also short terminal vanadyl groups, and when the latter group begins to be attacked, the metal oxygen distance is changed quite dramatically and the parent structure is disrupted, leading to amorphization.

P. Davies: What about if you do subsequent low temperature heat treatment on a protonated compound, do you get any interesting changes?

P. Dickens: We haven't done that. We have just started doing ion exchange on some of these phases. One attraction of these materials is that they're nearly totally insoluble, particularly the niobium ones, so you can carry out reaction in aqueous media without risk of dissolution.

M. Greenblatt: The lithium content in $Li_{0.88}U_3O_8$ is a rather peculiar value, isn't it?

P. Dickens: Well, at $Li_{1.0}U_3O_8$, the A sites would just be half filled. In fact, both chemical and electrochemical preparations suggest that the phase limit for this phase lies at an x value in $Li_xU_3O_8$ below this and a completely ordered phase of $Li_{1.0}U_3O_8$ is not achieved. In the same way in Na_xWO_3 the structural limit for the cubic phase $Na_{1.0}WO_3$ is not quite reached under normal synthetic conditions.

M. Greenblatt: I see.

W. McCarroll: Can you use bond-strength, bond-length rules for checking oxidation states in these compounds?

P. Dickens: Yes. In the case of the bond lengths obtained in our recent neutron diffraction study of UVO_5, bond strength sums are consistent with $U^{V}V^{V}O_5$.

National Institute of Standards and Technology Special Publication 804, Chemistry of Electronic Ceramic Materials, Proceedings of the International Conference held in Jackson, WY, August 17-22, 1990, issued January 1991.

INVESTIGATIONS ON THE STRUCTURAL, ELECTRICAL AND MAGNETIC PROPERTIES OF $Nd_{2-x}M_xNiO_{4+\delta}$, M = Ca^{2+} AND Ba^{2+}

Brian W. Arbuckle, Zhen Zhang, and Martha Greenblatt*
Department of Chemistry, Rutgers the State University of New Jersey
Piscataway, NJ 08855-0939

*Author to whom correspondence should be addressed.

INTRODUCTION

The $Ln_2NiO_{4+\delta}$ type compounds (Ln = La, Pr, Nd) are known to possess K_2NiF_4-type structure, which can be described as alternating perovskite $LnNiO_3$ and rocksalt LnO layers stacked along the crystallographic c-axis (Figure 1). The Ni-O octahedral units form a planar array of Ni-O-Ni bonds in the ab plane. The distance between the perovskite-layers along the c direction is double the distance between the nickel ion nearest neighbors and therefore, the magnetic and electrical properties of these compounds are highly anisotropic and usually confined within the Ni-O basal plane (1-5). The influence of oxygen stoichiometry on structural, electrical transport, and magnetic properties have been found to be considerable (4,6,7). The excess oxygen has been attributed to the deviations in the metal-ion stoichiometry (8), variable formal valence of the transition metal (9), intergrowths of Ruddelesden-Popper type phases (10), and the incorporation of interstitial oxygen defects (11). Nonstoichiometric $La_2NiO_{4+\delta}$ is tetragonal at ambient temperatures and shows no long range ordering, but when reduced to nearly stoichiometric La_2NiO_4 it begins to exhibit orthorhombic distortion and long range magnetic ordering (2,4,6,12). Electrical conductivity studies on $La_2NiO_{4+\delta}$ show a semiconductor-to-metal transition between 500-620K (3,13). Orthorhombic $Nd_2NiO_{4+\delta}$ and $Pr_2NiO_{4+\delta}$ undergo a phase transition to tetragonal symmetry at 724K and 834K respectively (14). Tetragonal $La_2NiO_{4+\delta}$ does not undergo a phase transition up to 1073K. By increasing the δ value in $Nd_2NiO_{4+\delta}$ and $Pr_2NiO_{4+\delta}$ the long range magnetic ordering is suppressed, which is attributed to the decrease in structural distortion that arises with increasing δ (4).

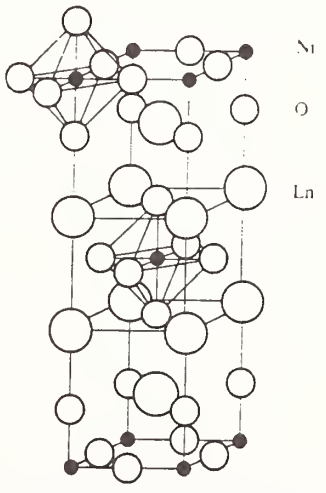

Figure 1. Tetragonal K_2NiF_4 type structure, Ln = La, Nd, or Pr

Substitution of Sr^{2+} into the Nd^{3+} sites of $Nd_2NiO_{4+\delta}$ induces a phase transition from orthorhombic to tetragonal symmetry (15). The orthorhombic samples of the solid solution series $Nd_{2-x}Sr_xNiO_{4+\delta}$ have large δ values whereas the tetragonal members ($x \geq 0.2$) are close to being stoichiometric in oxygen ($\delta \approx 0$). Samples with all values of x were semiconducting from room temperature down to 10K except $NdSrNiO_4$, which was metallic with a metal-to-semiconductor transition at 190K. The room temperature resistivity of the samples decreases as a function of increasing x. The magnetic susceptibility showed Curie-Weiss behavior with long range magnetic ordering ($T_n \approx 17K$) for the intermediate members ($0.4 \leq x \leq 0.6$). We have incorporated other group II divalent cations into $Nd_{2-x}M_xNiO_{4+\delta}$ ($M = Ca^{2+}$, Sr^{2+}, Ba^{2+}) with different sizes and electronegativities to study these effects on the physical properties.

EXPERIMENTAL

Solid solutions of $Nd_{2-x}Ca_xNiO_{4+\delta}$ ($0 \leq x \leq 0.6$) and $Nd_{2-x}Ba_xNiO_{4+\delta}$ ($0 \leq x \leq 0.5$) were prepared by co-decomposition of the metal nitrates. Stoichiometric quantities of Nd_2O_3 (Aldrich, 99.9%), NiO (Aldrich, 99.99%), $Ba(NO_3)_2$ (Aldrich, 99+%), and $CaCO_3$ (Aldrich, 99.9%) were mixed together and dissolved in concentrated nitric acid. The excess nitric acid was removed by gradual heating and the resulting green solid was calcined in air at 800°C. The products were ground and heated in air at 1150°C for 32h in alumina crucibles with two intermittent grindings. The samples were cooled to 800°C in the furnace before being quenched to room temperature. The products were ground and cold pressed into pellets. The pellets were fired in air at 1150°C for 16h and slow cooled to room temperature.

Powder X-ray diffraction (XRD) data, collected on a SCINTAG PAD V diffractometer with monochromatized CuKα radiation were used to monitor the completion of the reaction. A least-squares refinement of the observed powder diffraction data was used in the evaluation of cell parameters. The electrical resistivity of samples was measured by the standard four-probe technique in a DE202 cryostat (APD Cryogenics) from room temperature to 15K. A SQUID magnetometer (Quantum Design) was used to measure the magnetic susceptibility of samples from 2K to 370K with an applied magnetic field of 1000G. The total oxygen content was determined by hydrogen reduction using a DuPont 951 Thermogravimetric Analyzer and by iodometric titration. For TGA analysis, the material was heated on a platinum pan in flowing 5% H_2 in helium gas (0.1L/min) to 900°C at 15°C/min. For iodometric titration a 125 mg sample, after being dried at 100°C for 2 h, was dissolved in 25 mL of 0.4 mol/L aqueous HCl and 25mL of 0.15 mol/L aqueous KI solution. While under an inert atmosphere, the solution was titrated with a standardized thiosulfate solution. A few drops of a 5% starch solution were added just before the equivalence point in order to aid in the titration.

RESULTS AND DISCUSSION

Structural: Single phase specimens in the $Nd_{2-x}M_xNiO_{4+\delta}$ ($M = Ca^{2+}$ ($0 \le x \le 0.6$) and Ba^{2+}($0 \le x \le 0.5$)) solid solutions were prepared as evident by X-ray diffraction patterns. Lehmann and Müller-Buschbaum (16) have reported that $Nd_2NiO_{4+\delta}$ crystallizes with orthorhombically distorted K_2NiF_4-type structure (space group Abma). Arbuckle *et al.* (15) reported that for $x < 0.2$ in the series $Nd_{2-x}Sr_xNiO_{4+\delta}$ the samples crystallized with orthorhombically distorted K_2NiF_4-type structure at ambient temperatures and exhibited a phase transition to pseudo-tetragonal symmetry for $x \ge 0.2$. The orthorhombic distortion manifests itself in the splitting of some of the hk0 type reflections in the XRD pattern. The tetragonal samples ($x \ge 0.2$), showed no apparent splitting in the hk0 reflections. The The degree of divergence in the hk0 reflections of the orthorhombic specimens served as an indicator of the degree of distortion from tetragonal symmetry. All the samples in the series $Nd_{2-x}Ca_xNiO_{4+\delta}$ except for ($0.2 \le x \le 0.3$), appear to possess orthorhombic symmetry which is evident by the splitting of some of the hk0 reflections in the X-ray powder diffraction pattern. The XRD pattern for $0.2 \le x \le 0.3$, showed no splitting of the hk0 reflections in the range $10° < 2\theta < 60°$. The incorporation of small amounts of Sr^{2+} into the orthorhombic samples transformed the sample from orthorhombic to pseudo-tetragonal symmetry. The cell parameters as determined from least squares refinement of the XRD data are presented in Table 1. The changes in the unit cell parameters *a*, *b*, and *c* as a function of x are depicted in Figures 2A and 2B. As the Ca^{2+} content increases in $Nd_{2-x}Ca_xNiO_{4+\delta}$, the *a* and *b* cell parameters converge to form a pseudo-tetragonal unit cell at x ~ 0.20 (Figure 2A).

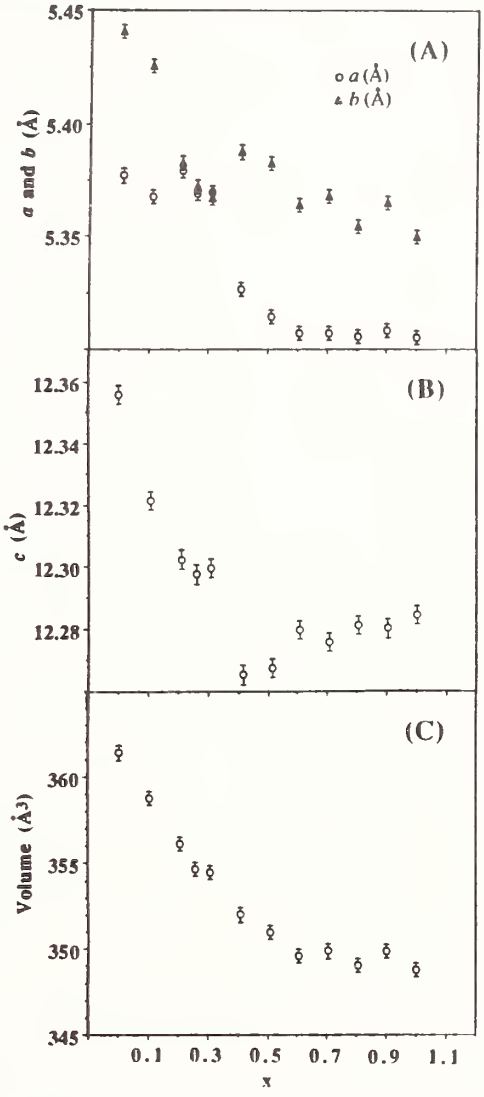

Figure 2. A) Change in the lattice parameters *a* and *b* as a function of Ca^{2+} content in $Nd_{2-x}Ca_xNiO_{4+\delta}$, B) Change in the lattice parameter *c* as a function of Ca^{2+} content in $Nd_{2-x}Ca_xNiO_{4+\delta}$, C) Change in the unit cell volume as a function of Ca^{2+} content in $Nd_{2-x}Ca_xNiO_{4+\delta}$.

Even though the $0.2 \leq x \leq 0.3$ samples can be indexed as either orthorhombic or tetragonal, only the orthorhombic unit cell parameters are listed in Table 1. The *a* and *b* cell parameters diverge for $x > 0.30$ to form what appears to be an orthorhombic unit cell. There is very little change in the unit cell parameters for $x > 0.6$, which may suggest that $x = 0.6$ is the limit of solubility of Ca^{2+} in $Nd_{2-x}Ca_xNiO_{4+\delta}$, and therefore, the samples are not single phase material but mixtures of compounds. Small impurity peaks of starting material are visible in the X-ray pattern for the $0.7 \leq x \leq 1.0$ samples. The *c* cell parameter decreases for $0 \leq x \leq 0.4$ and then increases slightly for $x > 0.4$, while the volume decreases for $0 < x \leq 0.6$ and thereafter remains fairly constant for $x > 0.6$. This is expected even though the Ca^{2+} (1.32Å, CN = (IX)), has a slightly larger effective ionic radius than Nd^{3+} (1.303 Å for CN = (IX)). The decrease in the size of nickel ions when going from

TABLE 1
Structural and Physical properties of $Nd_{2-x}Ca_xNiO_{4+\delta}$

Compound	a(Å)	b(Å)	c(Å)	volume(Å)^3	Transition Temperature (°C)
$Nd_2NiO_{4.18 \pm 0.03}$	5.378(1)	5.441(1)	12.355(1)	361.52(7)	575
$Nd_{1.9}Ca_{0.1}NiO_{4.10\pm0.03}$	5.368(1)	5.443(1)	12.333(2)	359.19(5)	240
$Nd_{1.8}Ca_{0.2}NiO_{4.12\pm0.03}$	5.385(1)	5.378(1)	12.322(3)	356.84(6)	----
$Nd_{1.75}Ca_{0.25}NiO_{4.08\pm0.03}$	5.370(1)	5.373(1)	12.298(3)	354.77(6)	----
$Nd_{1.7}Ca_{0.3}NiO_{4.01\pm0.03}$	5.370(1)	5.368(1)	12.300(1)	354.56(4)	----
$Nd_{1.6}Ca_{0.4}NiO_{3.98\pm0.03}$	5.328(1)	5.388(1)	12.266(1)	352.10(3)	380
$Nd_{1.5}Ca_{0.5}NiO_{3.96\pm0.03}$	5.327(1)	5.387(1)	12.270(1)	352.05(5)	320
$Nd_{1.4}Ca_{0.6}NiO_{3.97\pm0.03}$	5.307(1)	5.356(1)	12.281(1)	349.09(3)	180
$Nd_{1.3}Ca_{0.7}NiO_{3.97\pm0.03}$	5.309(1)	5.369(1)	12.276(1)	349.92(4)	220
$Nd_{1.2}Ca_{0.8}NiO_{3.80\pm0.03}$	5.308(1)	5.351(1)	12.284(1)	348.83(4)	180
$Nd_{1.1}Ca_{0.9}NiO_{3.79\pm0.03}$	5.310(1)	5.366(1)	12.280(1)	349.88(4)	160
$NdCaNiO_{3.68\pm0.03}$	5.307(1)	5.351(1)	12.284(1)	348.83(4)	120

Ni^{2+} to Ni^{3+}, appears to have a greater influence on the cell parameters than does the size effect of Ca^{2+} in the range $0 < x \leq 0.6$.

The $Nd_{2-x}Ba_xNiO_{4+\delta}$ samples with $x > 0.5$ show large amounts of an impurity phase(s) in the XRD pattern which have not been properly characterized so far. For this reason only samples with $x \leq 0.5$ are reported in the present study. As discussed above the extent of splitting in the hk0 reflections of the orthorhombic specimens served as an indicator of the degree of distortion from the tetragonal symmetry. From the XRD patterns it is clear that for $x \approx 0.2$, the splitting of the hk0 reflections in the range $5° < 2\theta < 60°$ are absent, indicating that a phase transition from orthorhombic to pseudo-tetragonal symmetry has occured. Even though the low angle reflections did not show any divergence in the hk0 reflections, the high angle data showed peak broadening in the corresponding reflections indicating that the actual symmetry could be lower than tetragonal. The cell parameters as determined from the least squares refinement of the XRD data are presented in Table 2. For samples with $x > 0.2$, the unit cell parameters could be indexed as orthorhombic or tetragonal, only the orthorhombic cell parameters are listed in Table 2. The changes in the unit cell parameters *a*, *b*, and *c* as a function of x are illustrated in Figures 3A and 3B. It is evident from Table 2 and Figure 3A that the orthorhombic to pseudo-tetragonal phase transition in $Nd_{2-x}Ba_xNiO_{4+\delta}$ solid solution is achieved via a rapid compression in the *b* and an expansion in the *a* unit cell parameter (Figure 3A). The *c* cell parameter and volume increase monotonically as a function of increasing x. In contrast, the a_t cell parameter (the a_t for the orthorhombic samples were calculated using the expression $a_t = ((a+b)/2\sqrt{2})$, decreases slightly as a function of increasing x for the orthorhombic samples ($x < 0.2$), but decreases more dramatically for the tetragonal samples ($0.2 \leq x \leq 0.5$). Arbuckle *et al.* (15) and

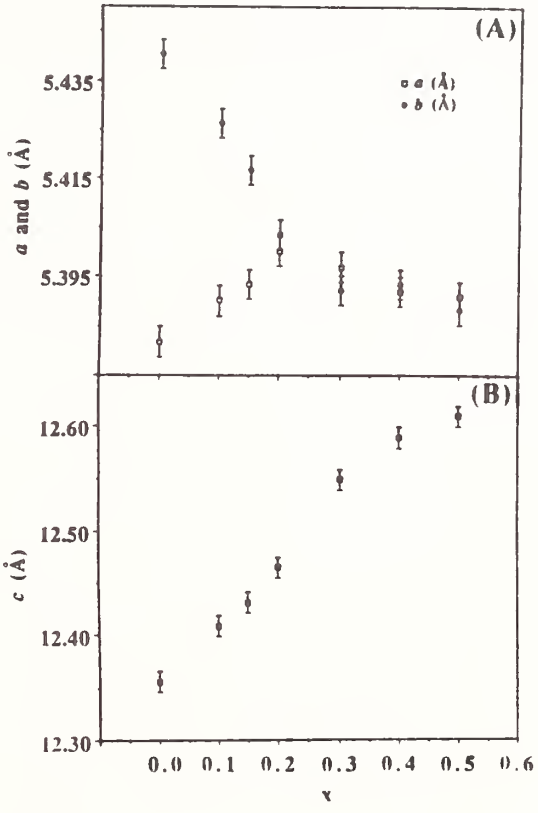

Figure 3. A) Change in the lattice parameters *a* and *b* as a function of Ca^{2+} content in $Nd_{2-x}Ca_xNiO_{4+\delta}$, B) Change in the lattice parameter *c* as a function of Ca^{2+} content in $Nd_{2-x}Ca_xNiO_{4+\delta}$.

Gopalakrishnan *et al.* (17) have reported similar trends in the a_t and c cell parameters for $Nd_{2-x}Sr_xNiO_{4+\delta}$ and $La_{2-x}Sr_xNiO_{4+\delta}$ respectively. They attributed the increase in a_t and c to the increased concentration of low-spin d^7 Ni^{3+} ($t_{2g}^6e_g^1$) and the Jahn-Teller distortion of the single electron being localized in the d_{z^2} orbital. Unlike the latter two systems, $Nd_{2-x}Ba_xNiO_{4+\delta}$ compounds show an increase in the unit cell volume with increasing x. This behavior is also observed for $La_{2-x}Ba_xNiO_{4+\delta}$ (5). If a Jahn-Teller distortion mechanism is operative here it is clear from the rate of increase in volume that the size effects of Ba^{2+} play the dominant role in the expansion of the unit cell parameters.

TABLE 2
Structural and Physical properties of $Nd_{2-x}Ba_xNiO_{4+\delta}$

Compound	a(Å)	b(Å)	c(Å)	volume(Å)^3	Transition Temperature (°C)
$Nd_2NiO_{4.18\pm0.03}$	5.378(1)	5.441(1)	12.355(1)	361.52(7)	575
$Nd_{1.95}Ba_{0.05}NiO_{4.15\pm0.03}$	5.378(1)	5.439(1)	12.381(2)	362.16(7)	515
$Nd_{1.9}Ba_{0.1}NiO_{4.13\pm0.03}$	5.389(1)	5.426(1)	12.409(1)	362.91(5)	225
$Nd_{1.85}Ba_{0.15}NiO_{4.xx\pm0.03}$	5.393(1)	5.417(1)	12.431(1)	363.16(6)	120
$Nd_{1.8}Ba_{0.2}NiO_{4.08\pm0.03}$	5.400(1)	5.403(1)	12.465(1)	363.71(4)	----
$Nd_{1.7}Ba_{0.3}NiO_{4.03\pm0.03}$	5.397(1)	5.392(1)	12.548(1)	365.17(5)	----
$Nd_{1.6}Ba_{0.4}NiO_{3.99\pm0.03}$	5.392(1)	5.393(1)	12.588(2)	366.04(4)	----
$Nd_{1.5}Ba_{0.5}NiO_{3.91\pm0.03}$	5.391(3)	5.388(1)	12.608(1)	366.22(3)	----

Tamura has reported a high temperature structural transition in $Nd_2NiO_{4+\delta}$ at 847K (18), corresponding to a structural phase transition from orthorhombic to tetragonal symmetry. Subsequent studies have confirmed this transition from high temperature X-ray diffraction and DSC studies (14). Incorporation of Sr^{2+} into the $Nd_2NiO_{4+\delta}$ structure, stabilizes the high temperature phase and thus lowers the structural transition temperature (T_t) (15). In order to understand the influence of Ba^{2+} substitution on the nature of this phase transition we have carried out high temperature X-ray diffraction and DTA studies from room temperature to 850°C in controlled oxygen atmospheres for samples with $x \leq 0.2$. Incorporation of Ba^{2+} in Nd_2NiO_4 resulted in a dramatic decrease in the T_t corresponding to the structural transformation (Table 2). We see no evidence for a structural transition above room

temperature for the pseudo-tetragonal samples corresponding to $0.2 \leq x \leq 0.5$. It is apparent that the high temperature tetragonal phase of $Nd_2NiO_{4+\delta}$ is stabilized by the incorporation of Ba^{2+}, although the exact mechanism responsible for this stabilization remains unclear at present. Incorporation of Ca^{2+} also decreases the T_t for $x \leq 0.1$. For $x \geq 0.4$ some of the hk0 reflections appear to converge which is an indication of a phase transition from orthorhombic to a pseudo-tetragonal symmetry. The orthorhombic-to-tetragonal T_t decreases anomalously as x increases (Table 1). The trend in the T_t is probably due to subtle structural changes with increasing x.

Oxygen content analysis:

In order to study the variations in the overall oxygen content as a function of x in all the samples, we have carried out TGA studies in hydrogen atmosphere and iodometric titrations. The oxygen content as determined by TGA measurement, was estimated for all samples assuming that the reduction products were nickel metal and the appropriate oxides (which was confirmed by X-ray analysis). The corresponding values are given in Table 1 for $Nd_{2-x}Ca_xNiO_{4+\delta}$ and in Table 2 for $Nd_{2-x}Ba_xNiO_{4+\delta}$.

The stability of K_2NiF_4 structures (A_2BO_4 type compound) are often described in terms of the tolerance factor defined as (19):

$$t = \frac{r_{A\text{-}O}}{\sqrt{2}\, r_{B\text{-}O}}$$

where $r_{(A\text{-}O)}$ and $r_{(B\text{-}O)}$ refer to the sum of ionic radii of A-O and B-O bond in nine and six coordination respectively. The K_2NiF_4 structure is stable over the range $0.85 < t < 1$; this is consistent with the absence of rare earth nickelates with rare earth ions smaller than neodymium. The value of t is very close to the lower limit for Ln_2NiO_4 (Ln = La, Pr, and Nd), thus explaining the deviations from the ideal tetragonal geometry. Monoclinic or orthorhombic distortion has been attributed to the low tolerance factor for Ln = Nd and Pr (20). It is possible to increase the value of t by either increasing the effective radii of A ions (through the substitution of larger divalent alkaline earth ions for Ln), or by partially oxidizing the B cations to higher valence states by suitable substitutions at both A and/or B sites. As already mentioned, the $Nd_{2-x}Sr_xNiO_{4+\delta}$ (15) compounds have orthorhombic symmetry for $x < 0.2$ and low tolerance factors. For $0 \leq x \leq 0.2$ the compounds gained stability by incorporating excess oxygen in the structure thus oxidizing some of Ni^{2+} to Ni^{3+} and therefore, increasing the tolerance factor by decreasing $r_{(B\text{-}O)}$. At $x \sim 0.2$ an orthorhombic to tetragonal phase transition was observed and the δ value decreased to zero, keeping the oxygen stoichiometry constant at around 4.0 for $0.2 \leq x \leq 1.0$. Even though the δ value remained constant at zero, the tolerance factor for these compounds increased as x increased because of the size effect of Sr^{2+} (1.45Å for CN = (IX)) versus Nd^{3+} (1.303Å for CN = (IX)). In

$Nd_{2-x}Ca_xNiO_{4+\delta}$, the Ca^{2+}(1.32Å for CN = (IX)) and Nd^{3+} ionic radii are very close in size, therefore, the size effect of Ca^{2+} should not play a significant role in influencing the tolerance factor, since the $r_{(A-O)}$ value will remain relatively unchanged as a function of x. If δ remains close to zero, then r_{B-O} will decrease and t will increase with increasing x. Based on the oxygen analysis of the samples (Table 1), the oxygen content of $Nd_{2-x}Ca_xNiO_{4+\delta}$ is high for $0 \leq x \leq 0.2$ and then it drops significantly for $0.2 < x \leq 0.3$. The δ value does remain close to zero for $0.3 \leq x \leq 0.7$ and then becomes negative for $x > 0.7$. The oxygen deficiency determined for the $x > 0.7$ samples is probably due to the impurity in these samples.

For $Nd_{2-x}Ba_xNiO_{4+\delta}$, it is clear from Table 2 that the δ values deviate from the ideal value of zero for the orthorhombic phase, and decrease, and approach zero for the tetragonal phases. As was seen for $Nd_{2-x}Sr_xNiO_{4+\delta}$ for $0 \leq x \leq 0.2$ (15), the stabilization of the K_2NiF_4 structure with orthorhombic distortion is achieved by incorporating extra oxygen in the structure. The tetragonal structure is stable with the higher concentration of Ba^{2+} and Ni^{3+} ions and does not require the extra oxygen. The oxygen discrepancy for the $x = 0.5$ sample may indicate that the impurity seen in the $x > 0.5$ samples may be present even though no impurity can be detected in the XRD pattern of the $x = 0.5$ sample.

Electrical Transport behavior:

The room temperature resistivity in the solid solution $Nd_{2-x}Ca_xNiO_{4+\delta}$ ($0 \leq x \leq 0.6$) increases as x increases (Figure 4A). This is in contrast to $Nd_{2-x}Sr_xNiO_{4+\delta}$ (15) and $La_{2-x}Ba_xNiO_{4+\delta}$ (18). For the $Nd_{2-x}Ba_xNiO_{4+\delta}$ sample where $x = 0.1$ (Figure 4B), the room temperature resistivity increases with respect to the parent compound $Nd_2NiO_{4+\delta}$ and then decreases for $0.05 < x \leq 0.5$. For the $x = 0.6$ sample which has large amounts of uncharacterized impurities present, the room temperature resistivity increases dramatically relative to the $x = 0.5$ sample. Both $Nd_{2-x}Ca_xNiO_{4+\delta}$ and $Nd_{2-x}Ba_xNiO_{4+\delta}$ solid solution series are semiconducting down to 10K. The activation energies estimated from the plots of

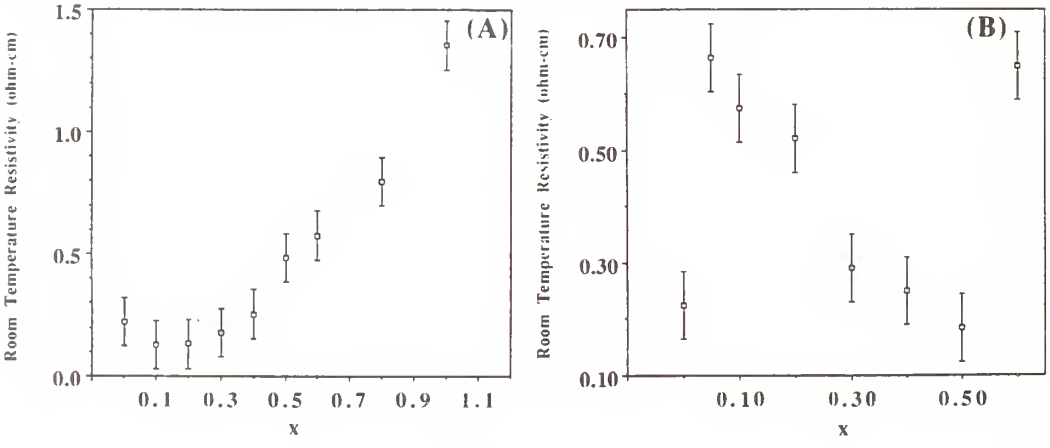

Figure 4. Room temperature electrical resistivity as a function of: A) Ca^{2+} content in $Nd_{2-x}Ca_xNiO_{4+\delta}$, and B) Ba^{2+} content in $Nd_{2-x}Ba_xNiO_{4+\delta}$.

logρ vs 1/T (125-300K) show a gradual decrease with increasing x across both series. The decreasing slope of logρ vs 1/T seen at low temperature is characteristic of an increasing dominance of extrinsic effects on the transport properties. For $Nd_{2-x}Ba_xNiO_{4+\delta}$ the decrease in the activation energies in the high temperature region appear to indicate the increased delocalization of Ni^{3+} electrons.

Magnetic Properties:

The room temperature magnetic susceptibility for $Nd_{2-x}Ca_xNiO_{4+\delta}$ and $Nd_{2-x}Ba_xNiO_{4+\delta}$ decrease with increasing x for both compounds; this can be understood by the fact that paramagnetic Nd^{3+} ions are being progressively substituted by diamagnetic M^{2+} ions. The behavior of χ_{300K} for both sets of compounds correlate well with the result reported for $Nd_{2-x}Sr_xNiO_{4+\delta}$ (15). The susceptibility data in the temperature range 220-370K can be fitted to the Curie-Weiss equation:

$$\chi = C/(T+\Theta) + \chi_o$$

Where C and Θ are the Curie and Weiss constants respectively, and the term χ_o includes the temperature independent contribution of the Pauli paramagnetic susceptibility, core diamagnetism, and the Van Vleck susceptibility.

Magnetic susceptibility as a function of temperature in the range 2-370K of representive samples are shown in Figure 5 for $Nd_{2-x}M_xNiO_{4+\delta}$ (M = Ca^{2+}, Ba^{2+}). The susceptibility values were not corrected for the core diamagnetism of component ions because of the large paramagnetic contribution from the Nd^{3+} ions. Long range magnetic ordering is observed in $Nd_{2-x}M_xNiO_{4+\delta}$ for $x \geq 0.4$ with M = Ca^{2+} (T_N = 12K), and x = 0.4, 0.5 with M = Ba^{2+} (T_N = 12K). The long range magnetic ordering observed for these samples are probably due to the Nd sublattice. No long range magnetic ordering is observed for samples with $0 \leq x \leq 0.3$ in either series. The absence of long range magnetic ordering in the orthorhombic samples with $\delta > 0$, is consistent with observations of Buttery *et al.* (4), who reported that magnetic order in $Nd_2NiO_{4+\delta}$ is suppressed with large excess of oxygen in the structure.

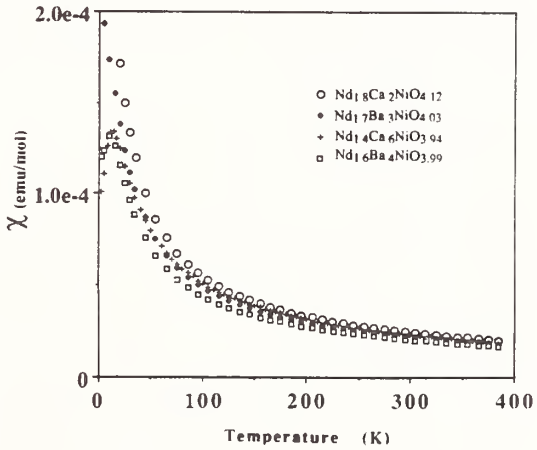

Figure 5. Magnetic susceptibility versus temperature of $Nd_{1.8}Ca_{.2}NiO_{4.12}$, $Nd_{1.7}Ba_{.3}NiO_{4.03}$, $Nd_{1.4}Ca_{.6}NiO_{3.98}$, and $Nd_{1.6}Ba_{.4}NiO_{3.99}$.

Acknowledgements:

The authors would like to thank Dr. Shu Li and Dr. K. V. Ramanujachary for helpful discussions and critical evaluation of the manuscript. The work was supported by National Science Foundation Solid State Chemistry Grant DMR-8714072.

REFERENCES

1. J.M. Bassat, P. Odier, and F. Gervais, *Phys. Rev. B*, **35**, 7126 (1987).
2. D.J. Buttrey, J.M. Honig, and C.N.R. Rao, *J. Solid State Chem.*, **64**, 287 (1986).
3. C.N.R. Rao, D.J. Buttrey, N. Otsuka, P. Ganguly, H.R. Harrison, C.J. Sandberg, and J.M. Honig, *J Solid State Chem.*, **51**, 266 (1984).
4. D.J. Buttrey, J.M. Honig, *J. Solid State Chem.*, **72**, 38 (1988).
5. A.B. Austin, L.G. Carreiro, J.V. Marik, *Mat. Res. Bull.* **24**, 639, (1989).
6. R. Saez-Puche, J.L. Rodriguez, and F. Fernandez, *Inorg. Chim. Acta.*, **140,**151 (1987).
7. R. Saez-Puche, and F. Fernández, *Solid State Commun.*, **72**, 273 (1989).
8. J.T. Lewandowski, R.A. Beyerlein, J.M. Longo, and R.A. McCauley, *J. Am. Ceram. Soc.*, **69**, 699 (1986).
9. J. Drennan, C.P. Tavares, and B.C.H. Steele, *Mat. Res. Bull.*, **17**, 621 (1982).
10. P. Odier, Y. Nigara, and J. Coutures, *J. Solid State Chem.*, **56,** 32 (1985).
11. J.D. Jorgensen, B.Dabrowski, Shiyou Pei, D.R. Richards, and D.G. Hinks, *Phys. Rev. B*, **40**, 2187 (1989).
12. J. Rodríguez-Carvajal, J.L, Martínez, J. Pannetier, and R. Saez-Puche, *Phys. Rev. B* **38,** 7148 (1988).
13. P. Ganguly and C.N.R. Rao, *Mat. Res. Bull.*, **8**, 405 (1973).
14. R. Saez-Puche, R. Fernandez, and W.S. Glaunsinger, *Mat. Sci. Monogr., (React. Solid Pt.A)*, **28A**, 607, (1985).
15. B.W. Arbuckle, K.V. Ramanujachary, Zhen Zhang, and Martha Greenblatt, *J. Solid State Chem.*, In Press.
16. U. Lehmann and Hk. Müller-Buschbaum, *Z. Natürforsch.*, **B35**, 389 (1980).
17. J. Gopalakrishnan, G. Colsmann, and B. Reuter, *J. Solid State Chem.*, **22**, 145 (1977).
18. S. Tamura, *J. Phys. Soc. Jpn.*, **33**, 574 (1972).
19. J. F. Ackerman, *Mat. Res. Bull.*, **14**, 487 (1979).
20. B. Willer and M. Dairre, *C.R. Acad. Sci. (Paris)*, C, **267**, 1482 (1968).

National Institute of Standards and Technology Special Publication 804, Chemistry of Electronic Ceramic Materials, Proceedings of the International Conference held in Jackson, WY, August 17-22, 1990, issued January 1991.

SYNTHESIS AND CHARACTERIZATION OF $La_{1-x}Sr_xTiO_3$ ($0 \le x \le 0.5$).

Susan M. Kauzlarich,* Joseph E. Sunstrom, IV* and Peter Klavins.+
Departments of Chemistry* and Physics+
University of California
Davis, California 95616

ABSTRACT

A series of compounds $La_{1-x}Sr_xTiO_3$ ($0 \le x \le .5$) have been prepared and characterized by powder X-ray diffraction, microprobe analysis, thermal gravimetric analysis and temperature dependent magnetic susceptibility. These pseudoternary compounds have been synthesized by arc-melting the stoichiometric combinations of $SrTiO_3$ and $LaTiO_3$ under argon. The compounds $La_{1-x}Sr_xTiO_3$ ($0 < x \le .3$) crystallize in the orthorhombic space group Pbnm. The compositions with $x = .4, .5$ can be indexed with a tetragonal cell. The synthesis and magnetic properties of these compounds are discussed.

INTRODUCTION

There were only a few examples of oxide superconductors[1] prior to 1986 and the discovery of superconductivity in the Cu-O system.[2] Oxide superconductors that have been discovered to date contain metals that are d^9, s^1 or d^1 ions. There have been several recent investigations of the early transition metal oxides in the search for new high temperature superconductors.[3] We are interested in the lanthanide titanates, $LnTiO_3$, a series of distorted perovskite compounds, because these materials show similar property dependence upon lanthanide cation size reminiscent of the Ln_2CuO_4 series of compounds. The influence of the size of the cation profoundly effects the magnetic and transport properties.[4] The lanthanide titanates, $LnTiO_3$, crystallize in the orthorhombic Pbnm space group ($GdFeO_3$ structure-type).[5] $LaTiO_3$ and $CeTiO_3$ are metallic (or semi-metallic) at room temperature, $PrTiO_3$ and $NdTiO_3$ are small band gap semiconductors (.03 eV), whereas the rest of the $LnTiO_3$ compounds are larger band gap semiconductors.[4] Their low-temperature magnetic properties vary from antiferromagnetic ordering for

$LnTiO_3$ (Ln = La-Pr), no apparent ordering for $NdTiO_3$, and ferromagnetic ordering for Ln = Gd-Yb, Y.[4] There are no close Ti-Ti contacts in this structure so that the properties are determined by the covalency of the Ti-O-Ti linkages. The effect of the size of the lanthanide cations is seen dramatically in the magnetic and electronic properties of the solid solutions $La_{2/3+x}TiO_3$[6] and $La_xY_{1-x}TiO_3$.[7] The substitution of an alkaline earth or alkali metal cation for the lanthanum cation will effect the density of states at the fermi level and may give rise to a superconducting state.

$LaTiO_3$ undergoes a metallic to semiconducting transition at 125 K.[8] Below 125 K antiferromagnetic ordering occurs. The magnetic structure has been determined by neutron diffraction to be type G with sublattice canting and a titanium (III) moment of 0.45(5) μ_B.[9] No structural changes are apparent at or below the transition temperature. The properties of $LaTiO_3$ have been interpreted as a result of itinerant d electrons in overlapping Hubbard bands.[4-8] A transition to an itinerant antiferromagnetic state will give rise to a gap near the Fermi level and hence the transition to semiconducting behavior.

Cation substitution of $LaTiO_3$ provides an optimal system for investigating the effects of the cation size and covalency as well as the effects of the Ti valence state upon the magnetic and transport properties in this system. The lanthanum cation is not magnetic and substitution of an alkaline earth cation for the lanthanum cation will result in holes in the valence band and metallic behavior. $LaTiO_3$ is apparently on the border of a metal-semiconductor transition and oxidation of the compound may give rise to a superconducting state. This paper briefly outlines some of our recent results on the structural and magnetic properties for the series of compounds $La_{1-x}Sr_xTiO_3$ ($0 \leq x \leq .5$).

EXPERIMENTAL

TiO_2 (99.999%) and $SrCO_3$ (99.999%) were obtained from Johnson Matthey. La_2O_3 (99.999%) was from Research Chemicals. Ti_2O_3 (99+%) was from Alfa Chemical. Ti_2O_3 and $SrCO_3$ were dried at 120°C for 24 hours prior to use. La_2O_3 and TiO_2 were dried at 1200 °C for 24 hours prior to use. Ti_2O_3 was characterized by thermal gravimetric analysis (TGA) and was determined to be $Ti_2O_{2.158(8)}$.

$LaTiO_3$ was prepared by arc melting stoichiometric amounts of La_2O_3, $Ti_2O_{2.158(8)}$ and TiO_2 in an argon atmosphere. $SrTiO_3$ was prepared by reacting a pressed pellet of well mixed $SrCO_3$ and TiO_2 in a platinum boat for 12 hours at 1200°C and then at 1400°C for an additional 12 hours. Several firings and regrindings are usually necessary in order to obtain a pure material. A large quantity of $LaTiO_3$ and $SrTiO_3$ (10 gms each) were prepared and used in the preparation of all the $La_{1-x}Sr_xTiO_3$ samples. The $La_{1-x}Sr_xTiO_3$ samples were

prepared by arc melting stoichiometric amounts of $LaTiO_3$ and $SrTiO_3$ in an argon atmosphere. The$La_{1-x}Sr_xTiO_3$ samples were dark blue-black in color.

X-ray powder diffraction data were obtained with copper radiation ($K\alpha_1$) using an Enraf-Nonius Guinier camera equipped with a Johansson monochrometer. Samples were ground and mixed with about 5-10% silicon powder and placed on a piece of cellophane tape. The positions of the five observed diffraction lines for silicon were fit to known diffraction angles by a quadratic function. The lattice constants were then calculated by least-squares fit to indexed 2θ values. The program POWDER[10] was used to calculate the expected powder pattern for $LaTiO_3$ (space group = Pbnm, $GdFeO_3$ structure-type) and $SrTiO_3$. The experimental diffraction positions and intensities agreed very well with the calculated diffraction pattern for $LaTiO_3$ and $SrTiO_3$. The lattice parameters for $LaTiO_3$ are similar those reported from neutron diffraction data ($\underline{a}$ = 5.6247(1), $\underline{b}$ = 5.607(1) and $\underline{c}$ = 7.9175(1))[5] (see Table I). The lattice parameter for $SrTiO_3$ was determined to be $\underline{a}$ = 3.9048(6). Lattice parameters for $La_{1-x}Sr_xTiO_3$ ($0 \leq x \leq .5$) are given in Table I.

Analysis of La, Sr and Ti was done on all samples using a Cameca SX50 microprobe. The data were consistent with the theoretical stoichiometry to within 2-3%. The oxygen stoichiometry was determined by TGA using a calibrated DuPont 2100 Thermal Analyzer. All the TGA measurements were done in platinum containers with an oxygen flow (50 cc/min). The heating cycle was from 20-1000°C at a rate of 5 °C/min. Table II provides the oxygen stoichiometry for $La_{1-x}Sr_xTiO_3$ samples determined from the TGA data.

Magnetic measurements were carried out on a Quantum Design SQUID magnetometer. The samples of composition $0 \leq x \leq .1$ were cooled to 5 K in a field of 10 kOe and the magnetization versus temperature data were taken at a field of 10 Oe (5 - 170 K) and 10 kOe (170 - 300 K). Compositions with x = .1, .2 did not show a magnetic transition and magnetization versus temperature data were taken at fields of 1000 Oe for T = 5 - 170K and 10 kOe for T = 170 - 300 K. Magnetic measurements on all the other compositions were taken at a field of 10 kOe.

RESULTS & DISCUSSION

A number of different reactions were performed in order to determine the most reliable method for preparing single phase $LaTiO_3$ and $La_{1-x}Sr_xTiO_3$ materials. Single phase $LaTiO_3$ was only obtained by combining stoichiometric amounts of La_2O_3, $Ti_2O_{2.158(8)}$ and TiO_2 and arc melting in an argon atmosphere. Attempts to prepare $LaTiO_3$ by reacting a pressed pellet of the same composition at 1200 °C in an evacuated silica ampoule were unsuccessful. $LaTiO_3$ is somewhat air sensitive and will react slowly with oxygen at room temperature to eventually produce $La_2Ti_2O_7$. The most satisfactory procedure for producing the Sr doped $LaTiO_3$ compositions was to arc melt mixtures in an argon atmosphere according to the equation:

$$(1\text{-}x)LaTiO_3 + xSrTiO_3 \rightarrow La_{1-x}Sr_xTiO_3$$

Table I shows the lattice parameters determined for $La_{1-x}Sr_xTiO_3$ ($0 \leq x \leq .5$). The samples prepared with $0 \leq x \leq .3$ could be indexed in the orthorhombic space group, Pbnm. This is a distorted perovskite structure ($GdFeO_3$ structure type) with the corner shared TiO_6 octahedra tilted towards the rare earth ion. As the Sr cation concentration is increased in these samples, the difference between the lattice parameters a and b decreases ($0 \leq x \leq .1$) and then increases ($.1 < x \leq .3$). This is reflected in a change in slope for a plot of Volume vs. composition, x, at $x = .1$ indicating that there is a subtle change in the structure. The diffraction peak positions and intensities agreed very well for all compositions with the calculated powder diffraction patterns based on the Pbnm, $GdFeO_3$ structure type. For the compositions $x = .4, .5$, the data could best be indexed as tetragonal. We are currently using X-ray powder diffraction Rietveld refinement to better characterize the structures.

Table I. Lattice parameters (Å) for $La_{1-x}Sr_xTiO_3$ ($0 \leq x \leq .5$).

x	a	b	c
.00	5.627(1)	5.605(1)	7.914(2)
.05	5.610(3)	5.595(1)	7.912(1)
.10	5.592(5)	5.581(2)	7.900(2)
.20	5.586(4)	5.568(3)	7.885(3)
.30	5.577(5)	5.555(3)	7.861(3)
.40	3.918(1)	3.918(1)	3.898(5)
.50	3.9140(3)	3.9140(3)	3.989(2)

Microprobe were performed on all of the samples and it appears that the materials can be prepared by this method fairly close to the desired composition. From the back scattered image of the scanning electron microscope (SEM), it is apparent that there is a small amount (not detectable by Guinier powder diffraction methods) of secondary oxidized phase at the grain boundaries. This indicates that there is some inhomogeneity in oxygen content for these samples. It was noted that the amount of this secondary phase appears to increase with Sr content. TGA data indicates that $LaTiO_3$ begins to significantly uptake oxygen at about 350°C and the strontium doped compositions at somewhat higher temperatures. As the amount of Sr cation is increased, the temperature at which the sample uptakes oxygen increases so that $La_{.5}Sr_{.5}TiO_3$ uptakes oxygen at about 650°C. Oxygen content was determined by TGA from the oxidation of $LaTiO_3$ to $La_2Ti_2O_7$ and $La_{1-x}Sr_xTiO_3$ to $La_2Ti_2O_7 + SrTiO_3$. The samples appeared to be close to stoichiometry in oxygen (Table II). Several samples have oxygen stoichiometry

apparently greater than 3.0. This is consistent with a small amount of oxidized secondary phase at the grain boundaries of these samples.

Table II. Oxygen stoichiometry for $La_{1-x}Sr_xTiO_3$ determined from TGA data.

Theoretical Stoichiometry	Experimentally Determined Stoichiometry
$LaTiO_3$	$La_1TiO_{2.98}$
$La_{.9}Sr_{.1}TiO_3$	$La_{.9}Sr_{.1}TiO_{3.00}$
$La_{.8}Sr_{.2}TiO_3$	$La_{.8}Sr_{.2}TiO_{3.01}$
$La_{.7}Sr_{.3}TiO_3$	$La_{.7}Sr_{.3}TiO_{3.02}$
$La_{.6}Sr_{.4}TiO_3$	$La_{.6}Sr_{.4}TiO_{2.99}$
$La_{.5}Sr_{.5}TiO_3$	$La_{.5}Sr_{.5}TiO_{3.01}$

Temperature dependent magnetic susceptibility was performed on all compositions. The polycrystalline samples of $LaTiO_3$ showed temperature independent paramagnetism above 150 K as reported previously by several other groups.[4-9] At 145 K, there is a sharp magnetic transition which has been attributed to a canted antiferromagnetic lattice.[9] Except for the higher onset temperature (145 K versus 125 K) for the magnetic transition, our data is comparable with literature values on single crystal samples.[8] This transition temperature is very sensitive to the La stoichiometry and small differences in either La or oxygen content could account for the difference in temperature observed for this magnetic transition.[7] For the composition, $La_{.95}Sr_{.05}TiO_3$, this magnetic transition occurs at about 125 K. This magnetic transition is completely absent for the compositions with $x \geq .1$. Figure 1 shows the temperature dependent magnetic susceptibility data for the samples $La_{1-x}Sr_xTiO_3$ ($x = 0 - .1$). The high temperature data are temperature independent paramagnetic for the compositions $0 \leq x \leq .3$ and $x = .5$. The temperature dependent magnetic susceptibility for the composition $La_{.6}Sr_{.4}TiO_3$ is more complex. The full details of the magnetic and electronic properties of these materials will be described elsewhere.

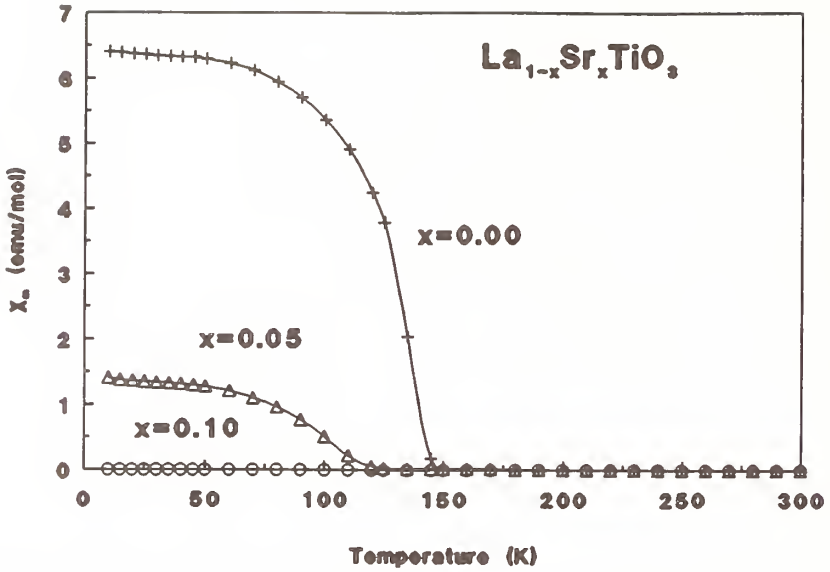

Figure 1. Magnetic Susceptibility data for $La_{1-x}Sr_xTiO_3$ x = 0, .05, .1.

ACKNOWLEDGEMENTS

We thank Robert N. Shelton for use of the TGA and the SQUID magnetometer and David J. Webb for useful discussion concerning the magnetic properties. We thank Traci Y. Kuromoto and Peter Schiffman for technical assistance with the microprobe data. This research is supported by the National Science Foundation (DMR-8913831) and UCD Committee on Research.

REFERENCES

1. (a) ($SrTiO_{3-x}$): Schooley, J. J.; Hosler, W. R.; Cohen, M. L. *Phys. Rev. Lett.* **1965**, *15*, 108. (b) ($LiTi_2O_4$): Johnston, D. C.; Prakash, H.; Zachariasen, W. H. Viswanathan, R. *Mater. Res. Bull.* **1973**, *8*, 777. (c) (A_xWO_3): Sweedler, A. R.; Raub, C.; Matthias, B. T. *Phys. Lett.* **1965**, *15*, 108.

2. (a) Bednorz, J. G.; Muller, K. A. *Z. Phys. B: Condens. Matter.* **1986**, *84*, 189. See for example the following recent reviews: (b) Sleight, A. W. *Science* **1988**, *242*, 1519. (c) Muller-Buschbaum, H. *Angew. Chem. Int. Ed. Engl.* **1989**, *28*, 1089.

3. (a) Wani, B. N.; Rao, U. R. K.; Venkateswarlu, K. S. *J. Mat. Sci. Let.* **1990**, *9*, 277. (b) Yee, K. A.; Albright, T. A.; Jung, D.; Whangbo, M. -H. *Angew. Chem. Int. Ed. Engl.* **1989**, *28*, 750.

4. (a) Greedan, J. E. *J. Less Comm. Metals* **1985**, *111*, 335. (b) Greedan, J. E. in *The Rare Earths in Modern Science and Technology Vol. 3*, McCarthy, G. J.; Silber, H. E.; Rhyne, J. J. eds. Plenum Press: New York, 1982, p. 431.

5. Eitel, M.; Greedan, J. E. *J. Less Comm. Metals* **1986**, *116*, 95.

6. Bazuev, G. V.; Makarova, O. V.; Shveikin, G. P. *Inorg. Materials* **1983**, *19*, 92.

7. Goral, J. P.; Greedan, J. E.; MacLean, D. A. *J. Sol. State Chem.* **1982**, *43*, 244.

8. MacLean, D. A.; Greedan, J. E. *Inorg. Chem.* **1981**, *20*, 1025.

9. Goral, J. P.; Greedan, J. E. *J. Magn. Magn. Mat.* **1983**, *27*, 315.

10. Clark, C. M.; Smith, D. K.; Johnson, G. J. "A Fortran IV Program for Calculating X-ray Powder Diffraction Patterns--Version V"; Department of Geosciences, The Pennsylvania State University: University Park, PA, 1973.

M. Norton: Do you plan to put any of these materials on substrates and if so do you think that you'll be able to expand the lattice parameter to get closer to 180 degrees metal-oxygen-metal linkage?

S. Kauzlarich: Actually, we talked about it, with Dave Webb in Physics (UCD), and his group is very interested in trying to put down films via sputtering. But we haven't actually done anything yet. It is premature because the bulk materials are poorly characterized at this point.

R. Roth: I have a little trouble believing your oxygen stoichiometry. $SrTiO_3$, when arc-melted in argon, is going to be considerably less than O_3. And yet you're going all the way to 50% strontium titanate and saying that it is still very close to three and in fact maybe over. What exactly are these oxygen numbers dependent upon experimentally?

S. Kauzlarich: That is a very good question. In fact, for lanthanum titanate itself we tried really hard to reduce and it does not reduce at all. And, as you put in strontium, because strontium titanate has such a wide oxygen content range, you would expect to be able to vary the oxygen content. And you would expect it to be deficient. What it could be is that these materials are very air sensitive and they oxidize very rapidly. Much more rapidly than we're being careful with or taking account of. Basically, we know looking at the $x = 0.5$ sample that we have a more oxidized second phase in there, because we saw that with SEM; whether or not the second phase came about on the grain boundaries because of the way they polish it to look at it with SEM and microprobe, is a whole debate on its own. But, we do see a second oxidized phase there and we haven't tried to reduce any of the strontium solid solution materials at all.

R. Roth: Tank argon has a P_{O2} of about 10^{-3}. You can get it down considerably if you put a little hydrogen into it. Have you tried any of that?

S. Kauzlarich: No. The only thing we tried to do is to reduce lanthanum titanate because we were worried about nonstoichiometry in that system. If you go through the literature there is a really wide disparity in the properties and so we were worried about that a lot. We only tried 6% hydrogen in nitrogen so we really didn't try very hard to reduce it but we couldn't reduce it all.

K. Poppelmeier: It's just a comment. I agree with Bob Roth that you would think you would have a lot of reduction; but one possibility that would keep it O_3 is that when you have the oxygen vacancy it would also be in the first coordination sphere of the lanthanum/strontium. That may have some effect, with the higher charge of lanthanum keeping the lattice from accommodating the oxygen defect just for local charge neutrality.

S. Kauzlarich: Yes, that is a possibility. Little is known about oxygen nonstoichiometry in this system.

National Institute of Standards and Technology Special Publication 804, Chemistry of Electronic Ceramic Materials, Proceedings of the International Conference held in Jackson, WY, August 17-22, 1990, issued January 1991.

SYNTHESIS AND CHARACTERIZATION OF PHASES IN THE SYSTEM Ba-Au-Ag-O_2

R. S. Roth, C. J. Rawn and M. D. Hill
National Institute of Standards and Technology
Gaithersburg, MD 20899

ABSTRACT

BaO_2 has been studied by heating in air, flowing O_2, and sealed Au or Pt tubes with or without excess O_2 and characterized by TGA and x-ray diffraction of quenched products. BaO_2 forms a nonstoichiometric solid solution BaO_{2-x}, with $x \leq 0.25$ at ~800°C and transforms to BaO at ~820°C in oxygen. The c-axis of the barium peroxide, CaC_2-related structure, decreases from 6.851Å to ~6.666Å with increasing x, although there is very little change in the a-axis. BaO_{2-x} has a c-axis of ~6.701Å when quenched in air from 725°C and transforms to BaO at 735 ± 2°C in air (P_{O_2} = 0.2). The reaction between BaO_{2-x} and Au or Ag which has been observed in air up to ~800°C is probably due to a hydrated melt formed by a reaction with atmospheric moisture. However, when $Ba(NO_3)_2$ is heated above its melting point (~592°C) in contact with Au, several new phases are formed. The most Ba-rich phase, presumably $Ba_6Au_2O_9$, hydrates readily on exposure to air. A second phase apparently more Au-rich, appears to be more stable. Liquid $Ba(NO_3)_2$ in contact with Ag does not decompose or react with Ag at 625°C (in flowing O_2). However, at 700°C in O_2, the $Ba(NO_3)_2$ slowly decomposes and forms single crystals of BaO_{2-x}, and no clearly discernable Ag containing phases can be identified. BaO_{2-x} and Ba-aurates have been characterized by powder and precession camera x-ray diffraction data, SEM, EDX and DTGA data. The defect structure of BaO_{2-x} is currently being investigated by neutron powder diffraction total profile (Rietveld) analyses.

INTRODUCTION

Both gold (Au) and silver (Ag) are known to react with and enter into the lattice of the copper containing high T_c superconducting oxides. When BaO is a major component of the phases, container and atmospheric reaction problems with these metals become a very important factor in synthesis. BaO reacts quickly with atmospheric moisture and various Ba-OH-H_2O phases are formed after a few moments exposure to air. $BaCO_3$ also forms by reaction with CO_2 in the atmosphere. The use of $BaCO_3$ as a starting material generally results in CO_2 contamination of the products, either in the desired phase or in grain boundaries. For these reasons many researchers have employed either BaO_2 or $Ba(NO_3)_2$ as starting materials. However, BaO_2 cannot be commercially obtained without about 2-3% $BaCO_3$ contamination, and $Ba(NO_3)_2$ has the disadvantage of a very low melting point ~590-595°C. This work is, therefore, the result of an effort to understand the chemical reactions which take place when either BaO_2 or $Ba(NO_3)_2$ is heated in contact with Au or Ag.

NONSTOICHIOMETRY OF BaO_2

Several commercial sources of BaO_2 were examined by x-ray powder diffraction. All had similar diffraction patterns, essentially identical to that published [1] with a body centered tetragonal unit cell, $\underline{a}$ = 3.8154 (face centered equivalent reported as 5.3958 [2]) and $\underline{c}$ = 6.8513Å at 25°C. Previous reports in the literature [3] refer to the possibility of an unknown phase between BaO and Ba_2CuO_3 [4] when synthesized in O_2. Attempts to examine this region of the BaO-CuO-O_2 system always resulted in Ba_2CuO_3 plus a phase similar to but not equivalent to BaO_2. When pure BaO_2 was heated in O_2 at 800°C and "furnace cooled" by turning off the furnace and allowing the specimen to cool to 250°-300°C in several hours the same phase resulted, namely a BaO_2-like phase with $\underline{c} \approx 6.786$Å. It seemed most likely that the explanation for the change in the value of the $\underline{c}$-axis was due to a loss of oxygen. Therefore, a series of experiments was conducted to characterize the results from various heat treatments of BaO_2.

Several DTGA examinations were made of BaO_2 in pure O_2 (passed through a 'gettering' device to remove CO_2 and H_2O) and in 80/20 N_2/O_2 (figure 1). At 800°C in O_2, BaO_2 was found to lose weight to a value corresponding to about $BaO_{1.7}$-$BaO_{1.8}$, depending on whether the calculation is made on the original loss or on the regain of weight, respectively. As the x-ray pattern does not return to the original $\underline{c}$-axis value, ~6.824Å, the first number must be low. However, obvious $BaCO_3$ and amorphous material in the commercial BaO_2 starting material indicate the larger number is probably not low enough. The average value of $BaO_{1.75}$ probably represents the best available estimate of the minimum oxygen content in this phase before the phase transition to BaO takes place. This is shown by the DTA peak and greater weight loss at 820°C in O_2. The total weight loss in a mixture of 80/20 N_2/O_2 is less than in O_2 and the transition to BaO takes place almost 100°C lower, at ~735°C. This data differs slightly from the values which can be derived from other data [5] obtained by varying the oxygen pressure at constant temperature.

A number of experiments were performed in a quench furnace in order to measure the unit cell dimensions of BaO_{2-x} under various conditions of P_{O_2}. The specimens were generally contained in 2, 3 or 5 mm diameter Au tubes, suspended in the hot zone by a thin Pt wire and after heating for 2 or more hours, dropped into a Ni crucible which was cooled by He flowing through a Cu coiled tube immersed in liquid N_2. Several experiments were performed containing BaO_2 in a Au tube inside a larger diameter Pt tube containing a weighed amount of PtO_2 calculated to produce an O_2 atmosphere from ~1.0 to ~10 atmospheres depending on the temperature and volume of the tube. All such experiments showed that the transition to BaO occurred well above 850°C or even 900°C when the total O_2 pressure exceeded 5-10 atmospheres. The smallest $\underline{c}$-axis value or the greatest value of x in BaO_{2-x} was found when BaO_2 was heated in a sealed Pt tube with no PtO_2, at 800°C and corresponded to $\underline{c}$ = 6.666Å in equilibrium with some BaO.

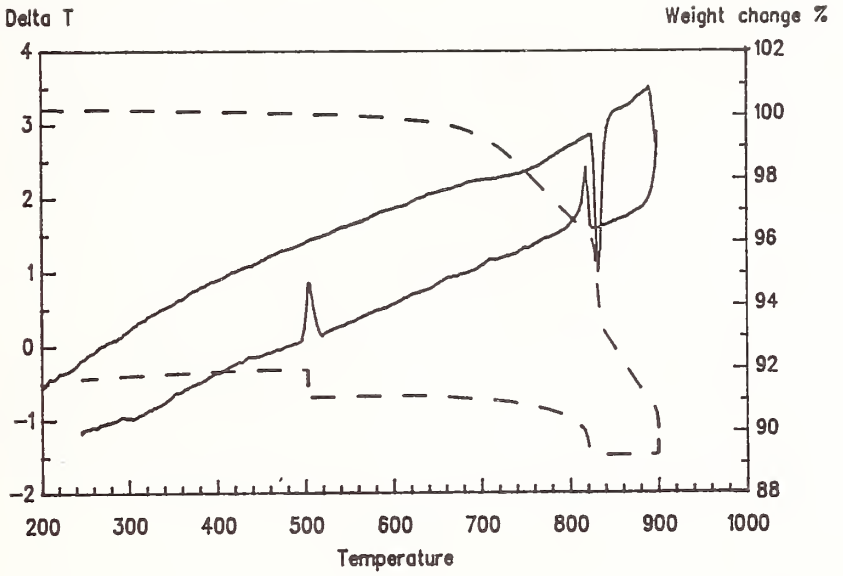

Figure 1a. DTA/TGA for BaO_2. Heating and cooling rates =5°C/min. Experiment performed in one atmosphere O_2, heated to 900°C, held for one hour, cooled to 500°C, held for one hour and cooled to 250°C.

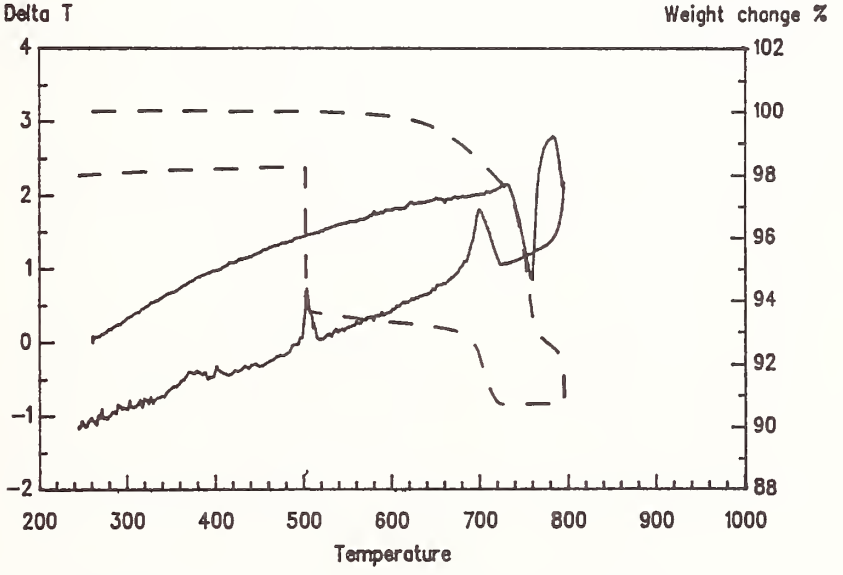

Figure 1b. DTA/TGA for BaO_2. Heating and cooling rates =5°C/min. Experiment performed in 80 N_2/20 O_2 heated to 800°C at 5°C/min, held for one hour, cooled to 500°C, held for 3 hours and cooled to 250°C.

Figure 2 shows the values of the c-axis measured from specimens quenched from various temperatures in air. A portion of the characteristic x-ray powder diffraction patterns for some of the quenched specimens are shown in figure 3.

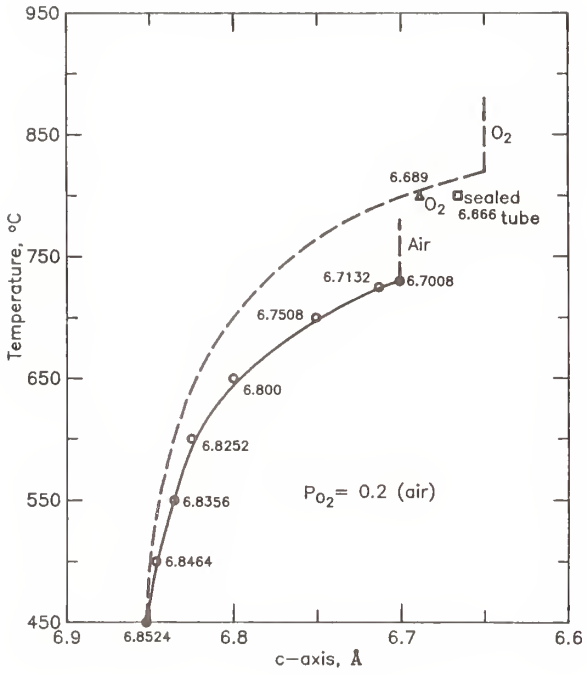

Figure 2. X-ray diffraction results of quenched BaO_{2-x} in air and "O_2". Temperature vs c-axis derived from (004) peak.

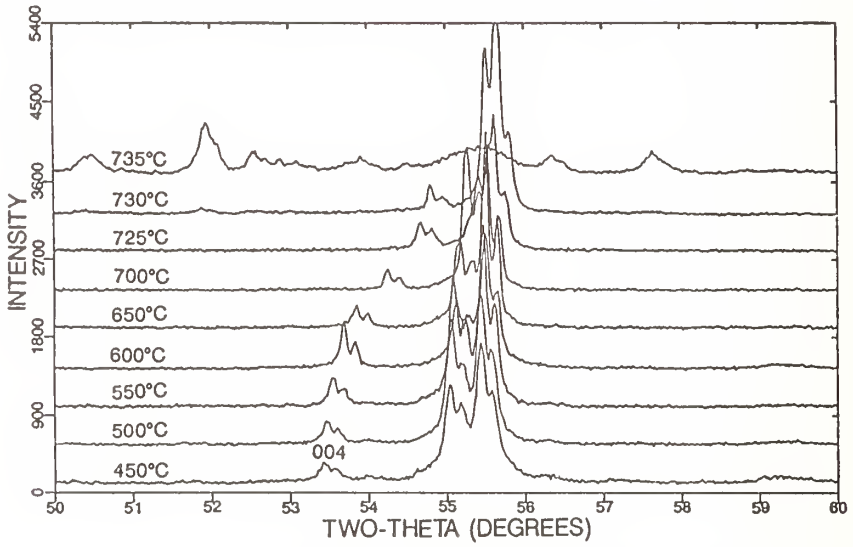

Figure 3. Portion of the x-ray powder diffraction patterns of quenched BaO_{2-x} heated at various temperatures, 450° - 735°C. Note change in the position of the (004) peak.

Attempts to prepare a large batch of BaO_{2-x} for neutron diffraction analysis have not been very successful as BaO_{2-x} in air will either hydrate and/or carbonate slightly at ≤700°C, and this causes a reaction rim to form on the Au foil. Such experiments are currently being performed in a pure oxygen atmosphere, but quenching a large batch in an enclosed atmosphere is a formidable experimental procedure. The x-ray powder diffraction pattern of the reaction product which contains unknown phases in addition to $BaCO_3$ and BaO_{2-x} is shown in figure 4.

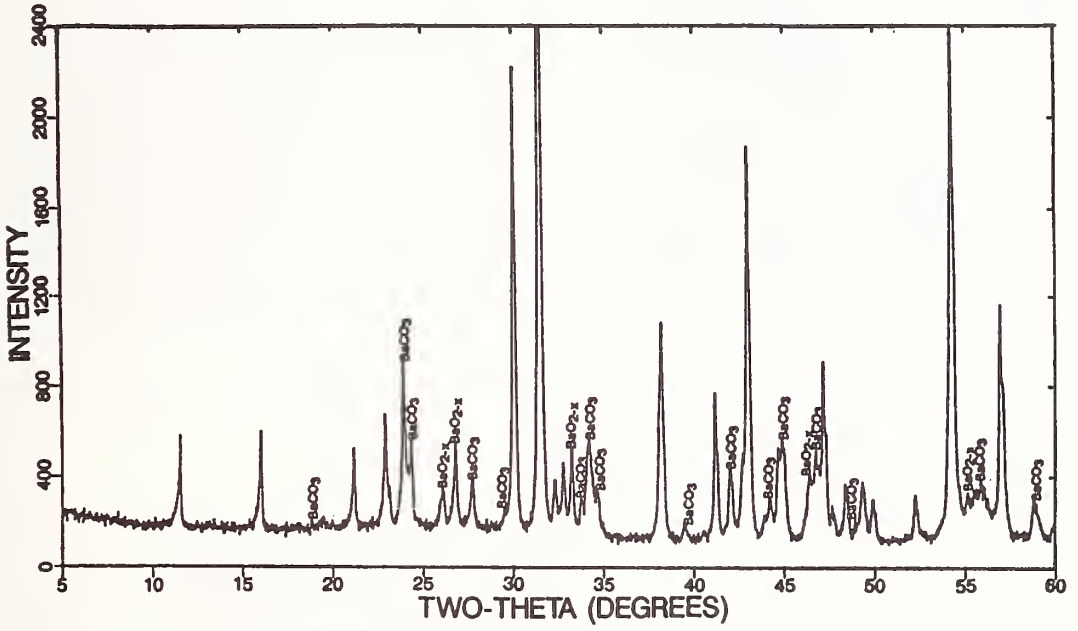

Figure 4. X-ray diffraction powder pattern of the reaction product obtained by heating a 40g batch of BaO_2 in air on Au foil at 700°C - 20 min.

DECOMPOSITION-REACTIONS OF $Ba(NO_3)_2$

Due to the impurities (generally $BaCO_3$) always found in commercial BaO_2, attempts were made to decompose $Ba(NO_3)_2$ in O_2 to form pure BaO_2. It was found, however, that $Ba(NO_3)_2$ is perfectly stable in one atmosphere of flowing O_2 at 575°C and below its melting point shows no sign of decomposition or reaction with containers of Ag, Al or Au. However, at 600°C the molten $Ba(NO_3)_2$ is very corrosive and completely destroys the Al dish.

Reactions with Au

Molten $Ba(NO_3)_2$ can be contained on Au foil or in Au tubes at 600°C, but after ~18 hours at 625°C in pure O_2, no $Ba(NO_3)_2$ or (BaO, BaO_2, etc.) is present in the x-ray powder diffraction pattern. If care is taken to avoid reaction with atmospheric moisture, etc., after removal from the furnace, an x-ray powder diffraction pattern can be obtained from the material separated from the Au foil (figure 5) which is quite different from any previously observed pattern. "Single crystal" diffraction

patterns were also obtained from some preparations, but these crystals appear to be fiber bundles rather than real single crystals, as can be seen from various x-ray precession patterns (figure 6) obtained looking down the fiber axis. At the present time it is not known if this phase is really hexagonal or orthorhomic (figure 6c). The phase is characterized by a very strong peak at ~9.75° 2θ (~9.1Å). Energy dispersive X-ray (EDX) data (figure 7) indicate that the crystals contain about one half as much Au as Ba. The composition, therefore, may be $Ba_6Au_2O_9$, although it is not possible to rule out the presence of some nitrate ions in the structure.

A second phase occurs when liquid $Ba(NO_3)_2$ has flowed over the outside of the Au tube. This phase presumably has a higher Au content than "$Ba_6Au_2O_9$", and may possibly be $BaAuO_{2.5}$. "Single crystal" x-ray precession patterns (figure 8) and a powder diffraction pattern (figure 9) show a characteristic phase with a strong low angle diffraction peak at ~8.1° 2θ and possible tetragonal symmetry. Again this may well be only a psuedo-symmetry as this compound has not been obtained as a single phase in a large enough volume to obtain a detailed x-ray powder pattern. The x-ray diffraction pattern shown in figure 9 also contains both $Ba(NO_3)_2$ and the Ba-Au-O phase with the 9.75° 2θ peak. This second phase with the characteristic peak at 8.10° 2θ is much more resistant to attack by atmospheric moisture and often will show up as the last remaining crystalline phase in a mixed phase batch after 2-3 days exposure to air.

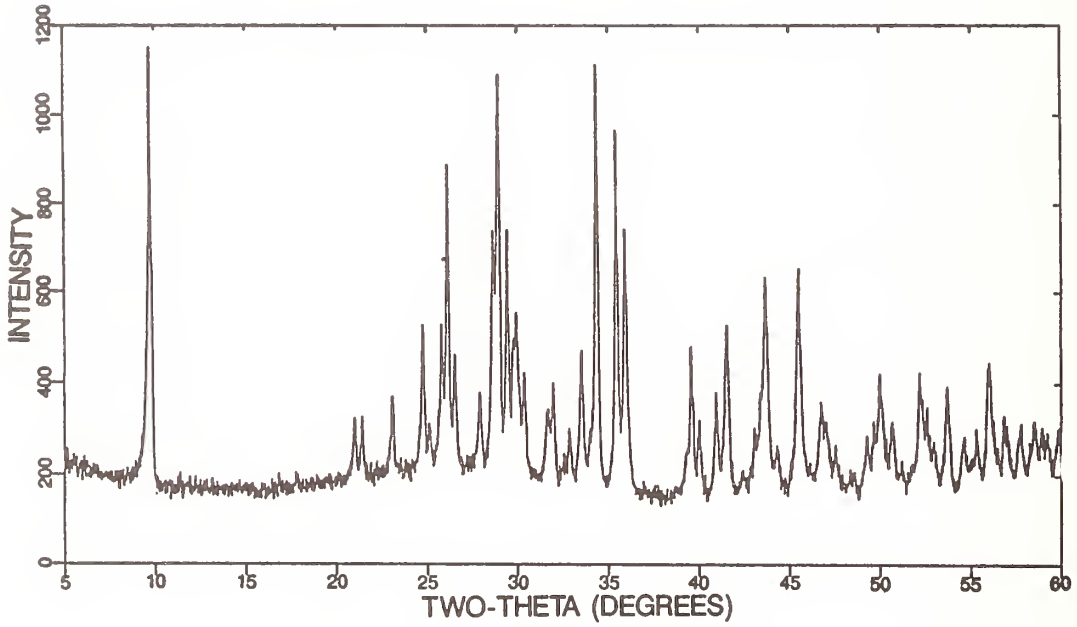

Figure 5. X-ray powder diffraction pattern of the reaction between molten $Ba(NO_3)_2$ and Au foil at 650°C in one atmosphere of O_2. This pattern shows no BaO_{2-x}, $Ba(NO_3)_2$ or Au.

Figure 6a. "multi twinned" or "fiber bundle" parallel to needle axis.

Figure 6b. "single" crystal perpendicular to needle axis.

Figure 6c. "single" crystal parallel to needed axis.

Figure 6. X-ray precession photographs of "single crystals" formed by the decomposition/reaction of $Ba(NO_3)_2$ in a Au tube or on Au foil at 600°C in O_2.

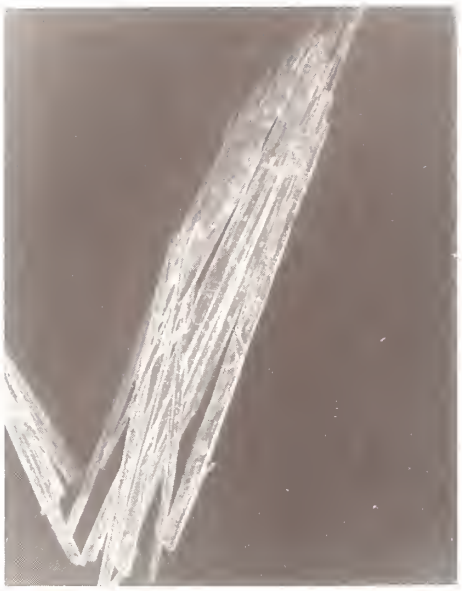

Figure 7a. 40X.

Figure 7b. 200X.

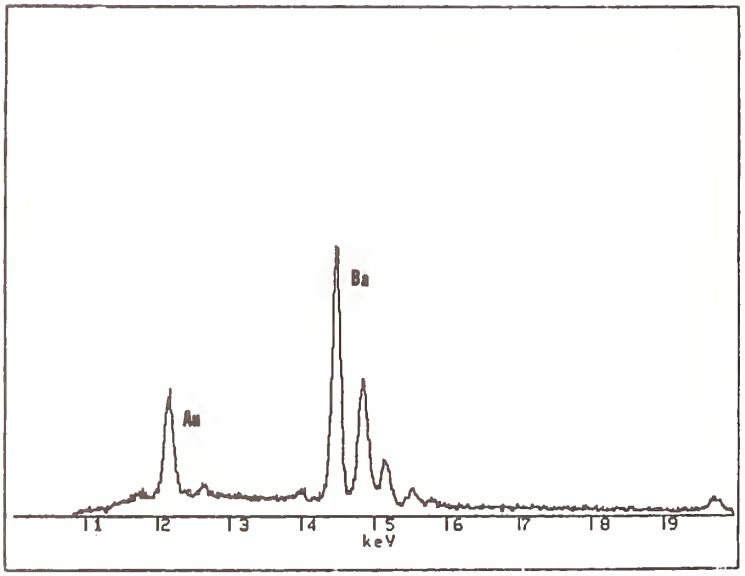

Figure 7c. EDX spectra.

Figure 7. SEM/EDX data (courtesy J. Kelly) for "$Ba_6Au_3O_9$" crystals prepared by heating $Ba(NO_3)_2$ in O_2 at 600°C - 24 hours on Au foil.

Figure 8a. Perpendicular to the needle axis.

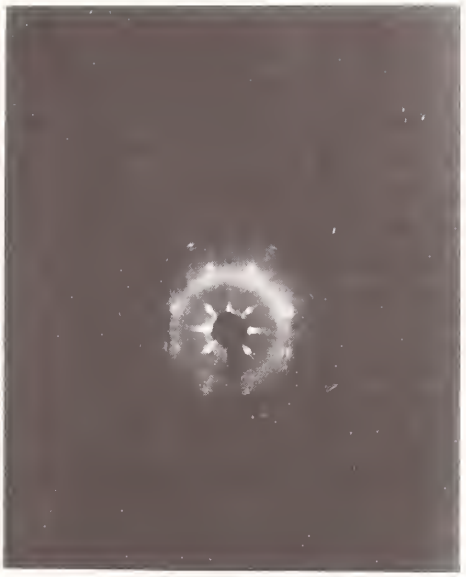

Figure 8b. Parallel to the needle axis.

Figure 8. X-ray precession photographs of "single crystals" of the phase "$BaAuO_{2.5}$" formed by a thin coating of molten $Ba(NO_3)_2$ decomposition/ reaction with the outside wall of a Au tube at 600°C in O_2.

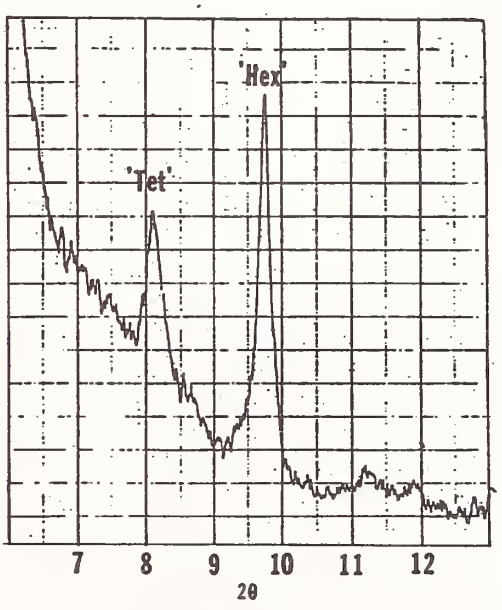

Figure 9. Low angle portion of x-ray powder diffraction pattern of reaction between a thin film of molten $Ba(NO_3)_2$ and the outer wall of a Au tube, showing two phases "Hex"- "$Ba_6Au_3O_9$" (9.75° 2θ) and "Tet" - "$BaAuO_{2.5}$" (8.1° 2θ).

Reaction with Ag

When a BaO_2 pellet is heated in air on Ag foil to ~700°C an obvious reaction rim is observed similar to that found with Au, suggesting that BaO_2 might have a melting point of about 450°C [6]. However, the DTA data illustrated in figure 1 show that BaO_2 does not melt. The reaction rim therefore must be due to impurities present in the atmosphere, as such "melting" phenomena do not occur in pure O_2 or a mixture of 80/20 N_2/O_2. Mixtures of 50/50 $BaO_2/BaCO_3$ in both Au and Ag tubes showed no sign of reaction with the containers when heated in O_2 to 700°C. It is therefore concluded that this reaction rim or "melting" phenomena is due to the presence of moisture and the formation of hydroxy or hydroxy/carbonate containing phases.

When $Ba(NO_3)_2$ is heated in Ag tubes to 700°C in pure O_2 no readily identified extra phase is found. X-ray powder diffraction patterns show mostly BaO_{2-x} plus $Ba(NO_3)_2$ and a few small extra peaks which may be due to hydration or some unidentified Ag-containing phase. However, this procedure results in the formation of quite large single crystal fragments of BaO_{2-x}. The best crystals were obtained by slow heating, 3°C/hr, from 590°C to 700°C, holding 24 hours and cooling at 6°C/hr to 500° and again holding for 24 hours. Apparently, crystal growth is initiated by the formation of BaO_{2-x} nucleation sites in the $Ba(NO_3)_2$ melt and the growth of quite large platelet crystals with rectangular shapes 2-5 mm wide and 0.2-0.5 mm thick, figure 10. The crystals often show perpendicular twin boundaries, and further twinning can be induced by pressing on the crystal face with the point of a needle. This later phenomenon indicates that the BaO_{2-x} crystals are probably ferroelastic. Single crystal x-ray precession photographs were used to characterize these crystals (figure 11) and show that the rectangular edges are (110) directions and the $\underline{c}$*-axis is perpendicular to the flat face. Crystals often show splitting of spots due to the tendency to form low angle grain boundaries either caused by growth boundaries or cleavage of the crystals perpendicular to the flat face. Twinning can often be found with 2nd and 3rd twins oriented along $\underline{hk0}$ planes with the $\underline{c}$*-axes characteristically inclined at ~76° (figure 11d).

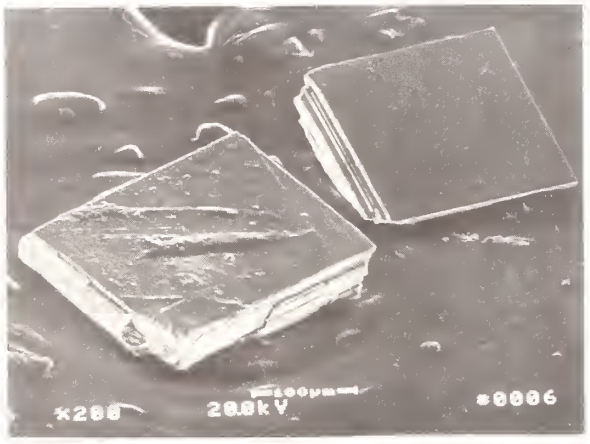

Figure 10. SEM photograph of crystals of BaO_{2-x} (courtesy J. Kelly).

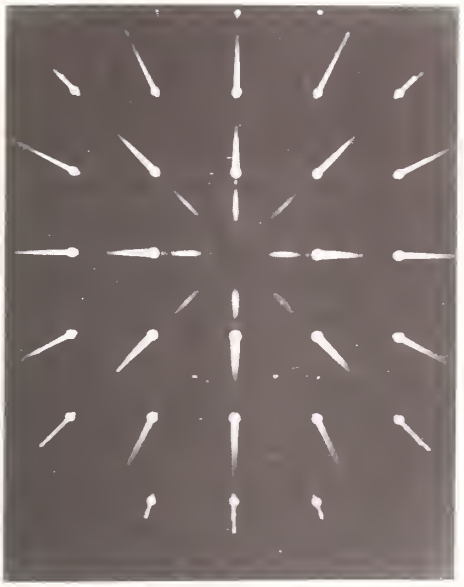

Figure 11a. hk0

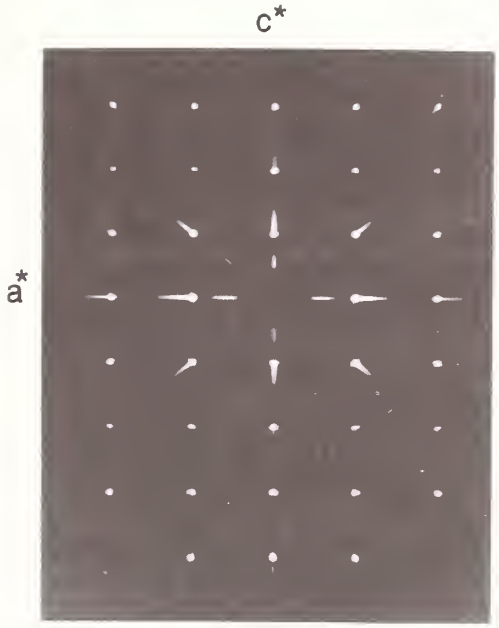

Figure 11b. h0l

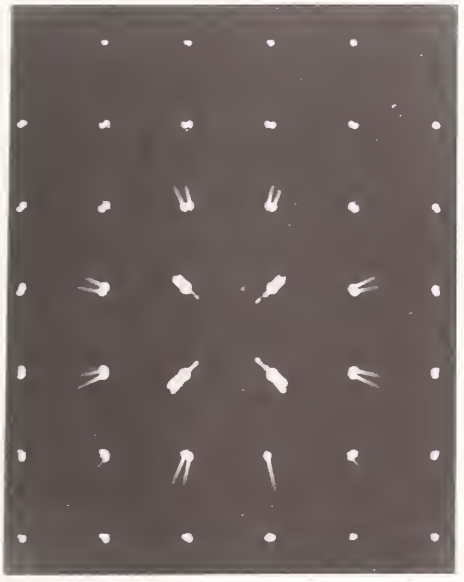

Figure 11c. hkl

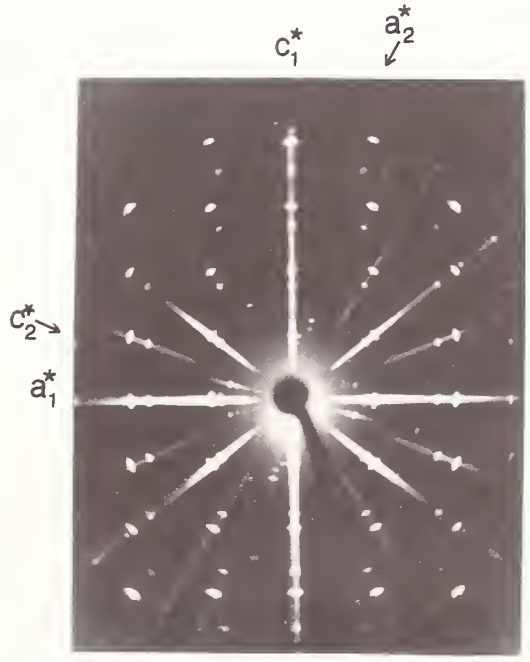

Figure 11d. h0l, unfiltered radiation, showing typical growth habit of multi (twinned?) crystals with the c*-axis always inclined at the same angle (~76°).

Figure 11. Single crystal precession photographs (Mo radition) of crystals of BaO_{2-x} prepared by decomposition of molten $Ba(NO_3)_2$ from 590°C to 700°C in O_2.

SUMMARY

Reversible nonstoichiometry in BaO_{2-x} was identified and characterized by quenching and DTGA experiments. BaO_{2-x} was found to transform to BaO at ~735°C in air and 820°C in one atmosphere O_2. $Ba(NO_3)_2$ reacts with Au in pure O_2 to form several phases identified by "single crystal" and x-ray powder diffraction and EDX analysis. No reaction with Ag could be definitely confirmed, but single crystals of BaO_{2-x} can be grown by decomposition reaction of molten $Ba(NO_3)_2$ in Ag tubes and a pure O_2 atmosphere.

REFERENCES

1. S. C. Abrahams and J. Kalnajs, "The Crystal Structure of Barium Peroxide", Acta Cryst. 7, 838-847 (1954).

2. H. E. Swanson, N. T. Gilfrich, and M. I. Cook, "Standard X-Ray Diffraction Powder Patterns", NIST Circular 539 [6], 18-19 (1956).

3. K. G. Frase and D. R. Clarke, "Phase Equilibria and Crystal Chemistry in the System Ba-Y-Cu-O", Adv. Ceram. Mat. 2 [3B], 295-302 (1987).

4. W. K. Wong-Ng, K. L. Davis, and R. S. Roth, "X-Ray Powder Study of 2BaO•CuO", J. Amer. Ceram. Soc. 71 [2] C-64-C-67 (1988).

5. O. V. Kedrovskii, P. V. Kovtunewko, E. V. Kiseleva, and A. A. Bundel Zh. Fiz. Khim. 41 [2], 414-419 (1967). (Russ.)

6. R. C. Weast, Ed. "Handbook of Chemistry and Physics". The Chemical Rubber Co., Cleveland, Ohio.

National Institute of Standards and Technology Special Publication 804, Chemistry of Electronic Ceramic Materials, Proceedings of the International Conference held in Jackson, WY, August 17-22, 1990, issued January 1991.

STRUCTURE AND PROPERTIES OF REDUCED EARLY TRANSITION METAL OXIDE SINGLE CRYSTALS GROWN FROM BORATE FLUXES

S.A. Sunshine, B. Hessen, T. Siegrist, A.T. Fiory & J.V. Waszczak
AT&T Bell Laboratories, 600 Mountain Avenue, Murray Hill, NJ 07974

Reduced ternary oxides of the early transition metals exhibit a variety of interesting physical and structural properties. Superconductivity ($LiTi_2O_4$ [1], tetragonal and hexagonal Mo and W bronzes [2]) and charge density wave behavior (Mo 'blue' bronzes [3]) have been observed in these systems. Structures range from simple perovskites like Sr_xNbO_3 [4] to complicated structures involving metal-metal bound clusters [5]. Single crystals are highly desirable for a better understanding of structure-property relations. In systems having low-melting high oxidation state ternary precursors (like A_2MO_4 and $A_2M_2O_7$; A = alkali metal, M = Mo, W) molten salt electrolysis provides a convenient route to single crystals. For other systems (particularly niobates) other methods have to be employed. Here we describe the use of borate fluxes to produce single crystals of various reduced ternary niobates and titanates in inert atmosphere. Borate fluxes have been regularly employed in the crystal growth of ferroelectrics and garnets [6], but rarely used for reduced compounds. An interesting aspect of the borates $A_nO_m \cdot xB_2O_3$ is that they can act both as a source and as a buffer for A_mO_n, allowing the product formation to be influenced by the flux composition when the A-cation is also part of the reduced ternary system. An advantage of the Ba, Sr, and La-borates is their low volatility, which allows their use under high-vacuum conditions.

THE BA-NB-O SYSTEM

Heating a mixture of NbO_2 and $BaO \cdot 3B_2O_3$ to 1100°C (10^{-6}–10^{-7} Torr), followed by slow cooling (8°C/h) produces golden crystals of the new niobate $Ba_2Nb_{15}O_{32}$ (average Nb oxidation state 4+), as well as crystals of $Ba_3Nb_5O_{15}$ [7] ($Nb^{4.8+}$) and $BaNb_8O_{14}$ [8] ($Nb^{3.25+}$) which form in a disproportionation side-reaction. The structure of $Ba_2Nb_{15}O_{32}$ (Fig. 1) contains a layer (A) of isolated octahedral $[Nb_6O_{12}]O_6$ metal-metal bound clusters, interconnected by Nb-atoms in octahedral holes in the lattice. These layers are separated by layers of Nb_3O_{13} groups (B), and layers with Ba-ions and isolated NbO_6 octahedra (C). Single crystal resistivity measurements indicate semiconducting behavior,

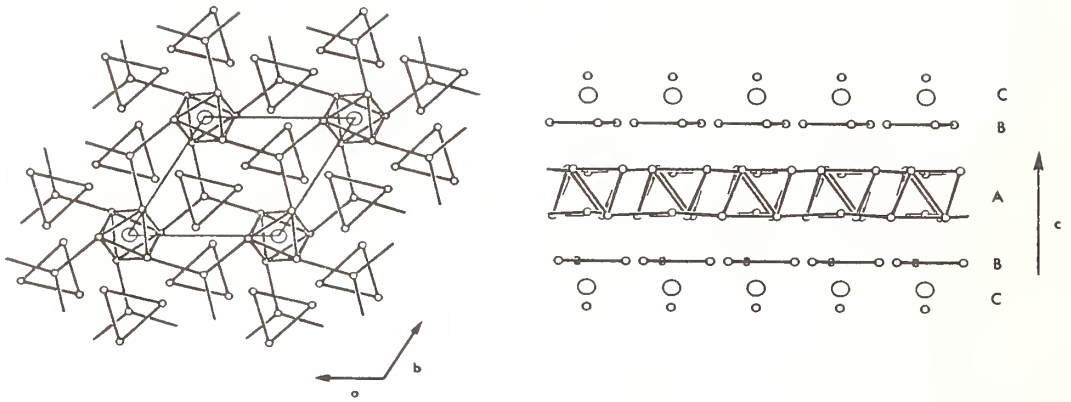

Figure 1. X-ray structure of $Ba_2Nb_{15}O_{32}$, projected along the *c*-axis (a), and perpendicular to it (b). Oxygen atoms omitted for clarity.

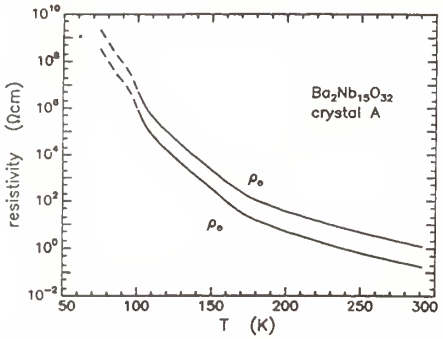

Figure 2. Single crystal resistivity data for $Ba_2Nb_{15}O_{32}$.

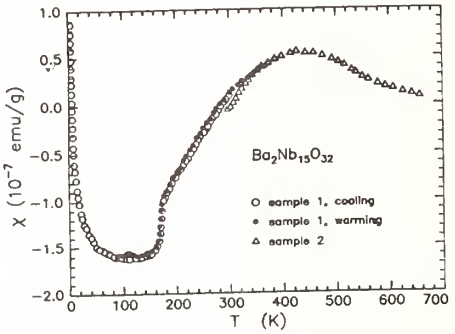

Figure 3. Magnetic susceptibility data for $Ba_2Nb_{15}O_{32}$ (uncorrected for Curie 'tail').

with a semiconductor-to-semiconductor transition at 170 K (Fig. 2). This coincides with a magnetic transition from a weakly paramagnetic state to diamagnetism below the transition temperature (Fig. 3).

The compound $Ba_3Nb_5O_{15}$ has the centrosymmetric tetragonal tungsten bronze (TTB)-type structure (Fig. 4), as observed by Magneli for $K_3W_5O_{15}$ [9]. In contrast to the isostructural (metallic) Mo and W analogues, the resistivity of $Ba_3Nb_5O_{15}$ shows a semiconducting temperature dependence, and a stronger anisotropy ($\rho_{\perp c} = 55\ \rho_{//c}$ at 300 K).

The perovskite Ba_xNbO_3 [10] has been less investigated than its Sr-analogue and appears to have a much smaller single-phase region in ceramic samples. Red metallic single crystalline $Ba_{0.95}NbO_3$ (a = 4.0853(2) Å) was obtained by recrystallizing a ceramic with nominal composition $BaNbO_3$ from the Ba-rich flux $BaO{\cdot}B_2O_3$. The refined Ba-site occupancy and cell parameter compare well with those obtained by Svensson from profile analysis on a ceramic sample [11].

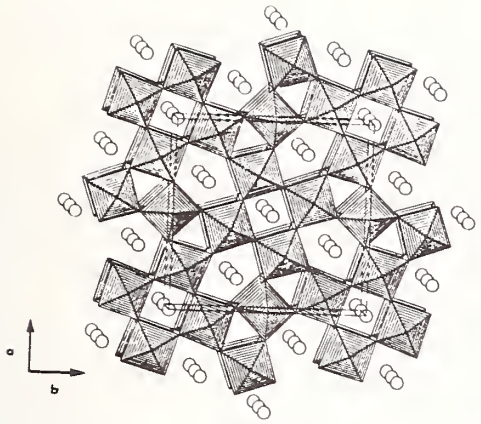

Figure 4. Polyhedral representation of the X-ray structure of $Ba_3Nb_5O_{15}$.

THE SR-NB-O SYSTEM

A broad solid-solution range, Sr_xNbO_3, is known in this system [4]. A single phase cubic perovskite exists for $0.70 \leq x \leq 0.97$, while for $0.60 < x < 0.70$ a two-phase mixture containing the TTB-type $Sr_3Nb_5O_{15}$ [12] is found. By modification of the $SrO{\cdot}nB_2O_3$ flux composition and the ternary precursor, single crystals of the perovskites $Sr_{0.72}NbO_3$ (blue, a = 3.9865(2) Å) and $Sr_{0.86}NbO_3$ (purple-red, a = 4.0077(6) Å) were obtained, the first from ceramic $Sr_5Nb_4O_{14}$ [13] and $SrO{\cdot}2B_2O_3$, the second from ceramic $SrNbO_3$ and $SrO{\cdot}B_2O_3$. Some disproportionation was observed, yielding multiply twinned crystals of $SrNb_8O_{14}$ [14], especially in relatively Sr-poor mixtures. Crystals of $Sr_5Nb_4O_{15-x}$ (dark hexagons) [13], and $Sr_2Nb_2O_{7-x}$ (black platelets) [15] were observed as side products.

Formation of the TTB-type phase in the melts is apparently less favorable for Sr than for Ba. Small crystals of $Sr_3Nb_5O_{15}$ could however be obtained by grain growth in a ceramic pellet with addition of some borate mineralizer (a = 12.3609(7) Å, c = 3.8974(3) Å).

THE SR-TI-O SYSTEM

In ceramic studies, the reduced part of the Sr-Ti-O phase diagram was found to be heavily dominated by the perovskite solid solution $SrTiO_{3-x}$ and binary oxides like Ti_nO_{2n-1}, although a strongly Sr-deficient species was suspected to exist [16]. Crystallization of a $SrTiO_{2.5}$ ceramic from $SrO{\cdot}2B_2O_3$ produces purple-blue crystals of a compound with Sr << Ti (from EDAX), together with some Ti_nO_{2n-1}. Single crystal X-ray diffraction showed the compound to be triclinic, and to have the stoichiometry $SrTi_{11}O_{20}$. Its structure (Fig. 5) can be described as consisting of two interconnected layers, A and B, perpendicular to the a-axis. The A layer contains two crystallographically independent 'double rutile' chains [17], that are sheared after every block of six TiO_6 octahedra. These chains, running parallel to the b-axis, are interconnected

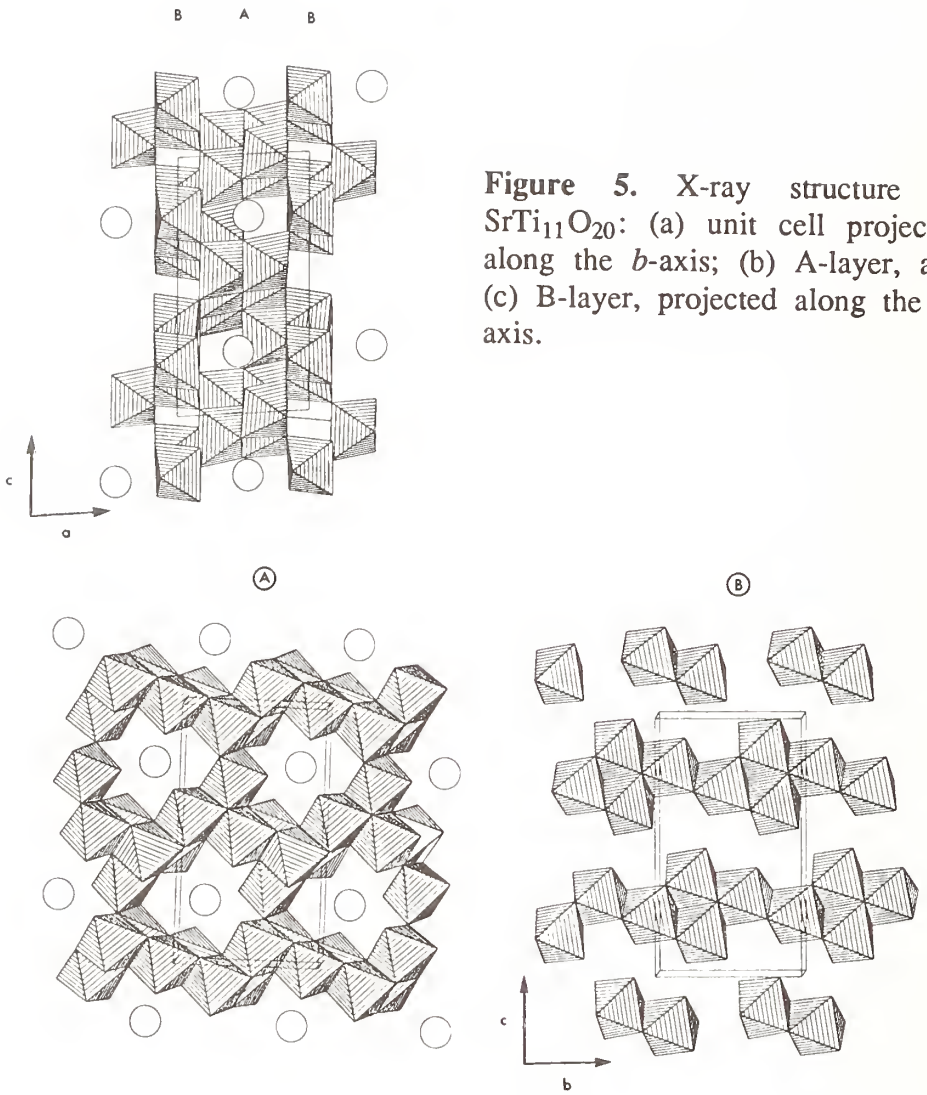

Figure 5. X-ray structure of $SrTi_{11}O_{20}$: (a) unit cell projected along the *b*-axis; (b) A-layer, and (c) B-layer, projected along the *a*-axis.

by single TiO_6 octahedra creating cavities for the Sr-ions. The B-layer contains a single rutile chain that is sheared after every block of four TiO_6-octahedra. These chains cover the cavities with the Sr-ions in the A-layer. It is unclear if this phase is identical to the proposed "$SrTi_{12}O_{19}$" from ceramic studies [16], as there are significant differences in the reported X-ray powder pattern and that calculated for $SrTi_{11}O_{20}$. The average oxidation state of Ti in $SrTi_{11}O_{20}$ is 3.45+, which implies that some oxidation of the product has occurred. Indeed all reduced titanates in molten fluxes are extremely good getters for oxygen and water. Recrystallization of $SrTiO_{2.5}$ from the Sr-rich flux $SrO{\cdot}B_2O_3$ even in vacuum produces small cubes of $SrTiO_{3-x}$ which, as a function of x, range in color from black to blue to colorless.

OTHER TITANATES

The oxophilicity of reduced titanates mentioned above is especially prominent when more volatile fluxes are used which necessitate the use of atmospheric pressure. Recrystallizing the superconducting spinel $LiTi_2O_4$ from $LiBO_2$ flux under a purified Ar atmosphere produces well-shaped blue-black octahedral crystals. The cell parameter (a = 8.3618(8) Å) indicated, however, that the product is not very reduced, and non-superconducting [1].

Lanthanide borates generally have a much higher melting point than the Sr and Ba borates, but can still be used in vacuum over a limited temperature range. Heating ceramic $LaTiO_3$ in $La_2O_3 \cdot 3B_2O_3$ to 1250°C followed by cooling to 1150°C yields a rather complicated mixture, which includes needles of a new lanthanum titanate, $La_{0.3}Ti_2O_4$, with a monoclinically distorted hollandite structure (Fig. 6). The tunnel sites are partially occupied by La. Attempts to prepare this phase as a ceramic have not been successful, but interestingly a recrystallization of a ceramic with nominal composition "$La_{0.3}Ti_2O_4$" (not containing hollandite phases) from $K_2B_4O_7$ produced needles of the tetragonal hollandite $K_xTi_2O_4$ [18].

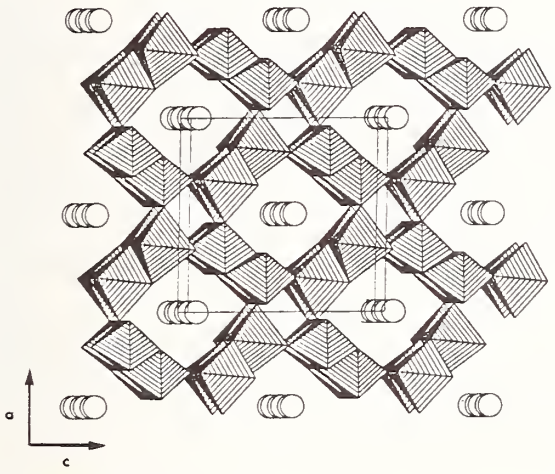

Figure 6. Polyhedral representation of the X-ray structure of $La_{0.3}Ti_2O_4$.

CONCLUSIONS

Borate fluxes are interesting media for the crystal growth of reduced ternary transition metal oxides. Modification of the flux composition provides a way of influencing the product formation. The fluxes are fairly easily removed using dilute acids at ambient temperature, whereas most of the products are inert under these conditions. In a number of cases the formation of new phases was observed. The method is however very sensitive to the quality of the atmosphere. A high-quality atmosphere control or the use of sealed molybdenum containers should enable a more efficient use of this technique.

ACKNOWLEDGMENT

BH thanks the Netherland Organization for Scientific Research (NWO) for the award of a fellowship.

REFERENCES

[1] (a) D.C. Johnson, H. Prakash, W.H. Zachariasen, and R. Viswanathan, *Mat. Res. Bull.* 8 (1973) 777; (b) M.R. Harrison, P.P. Edwards, and J.B. Goodenough, *Phil. Mag.* 52B (1985) 679; (c) Y. Ueda, T. Tanaka, K. Kosuge, M. Ishikawa, and H. Yasuoka, *J. Solid State Chem.* 77 (1988) 401.

[2] (a) Ch.J. Raub, A.R. Sweedler, M.A. Jensen, and B.T. Matthias, *Phys. Rev. Lett.* 15 (1964) 746; (b) A.R. Sweedler, Ch.J. Raub, and B.T. Matthias, *Phys. Lett.* 15 (1965)108; (c) A.W. Sleight, T.A. Bither, and P.E. Biersted, *Solid State Comm.* 7 (1969) 299.

[3] (a) M. Greenblatt, *Chem. Rev.* 88 (1988) 31; (b) C. Schlenker (ed.), "*Low-Dimensional Electronic Properties of Molybdenum Bronzes and Oxides*", Kluwer, Dordrecht (1989).

[4] D. Ridgeley, and R. Ward, *J. Am. Chem. Soc.* 77 (1955) 6132.

[5] A. Simon, *Angew. Chem. Int. Ed. Engl.* 27 (1988) 159.

[6] D. Elwell, and H.J. Scheel, "*Crystal Growth from High-Temperature Solutions*", Academic Press, London (1975).

[7] A. Feltz, and H. Langbein, *Z. Anorg. Allg. Chem.* 425 (1976) 47.

[8] S.J. Hibble, A.K. Cheetham, J. Koehler, and A. Simon, *J. Less-Common Met.* 154 (1989) 271.

[9] A. Magneli, *Ark. Khemi* 1 (1949) 213.

[10] (a) E.I. Krylov, and A.A. Sharnin, J. Gen. Chem. U.S.S.R. 25 (1955) 1637; (b) R. Kreiser, and R. Ward, *J. Solid State Chem.* 1 (1970) 368.

[11] G. Svensson, and P.E. Werner, *Mat. Res. Bull.* 25 (1990) 9.

[12] M.M. Ninh Nguyen, J. Choisnet, and B. Raveau, *C.R. Acad. Sci. Paris C* 282 (1976) 303.

[13] J.M. Carruthers, and M. Grasso, *J. Electrochem. Soc.* 117 (1970) 1426.

[14] J. Koehler, A. Simon, S.J. Hibble, and A.K. Cheetham, *J. Less-Common Met.* 142 (1988) 123.

[15] N. Ishizawa, and F. Marumo, *Acta Cryst.* B31 (1975) 1912.

[16] G.J. McCarthy, W.B. White, and R. Roy, *J. Am. Ceram. Soc.* 52 (1969) 463.

[17] A.F. Wells, "*Structural Inorganic Chemistry*", 5th ed., Clarendon Press, Oxford (1984), p. 214.

[18] T. Vogt, E. Schweda, C. Wuestfeld, J. Straehle, and A.K. Cheetham, *J. Solid State Chem.* 83 (1989) 61.

A. Navrotsky: Do you ever get any ternary or higher borates formed other than the starting material?

S. Sunshine: That is highly possible. We tend to disregard anything that remains white. If there are borates, they are oxidized borates. In these reactions what you end up with is a black reduced material and some sort of white flux or transparent flux that's left over.

The strontium borate we started with is obviously chemically altered in some way because in these reactions the flux itself is actually being used in the reaction. We've really never analyzed the left over borate after reaction. We have no evidence so far of any borate incorporation in the materials that I've described or any of the reduced materials we've looked at so far.

B. McCarroll: What did you use for a container?

S. Sunshine: In general most of these reactions were done in molybdenum foil; foil boats that we folded ourselves. I started by doing reactions in alumina, but alumina is not a good choice. I made a lot of reduced niobium aluminates that way. In general, with molybdenum we find no evidence for molybdenum incorporation in our products. If you were worried about that you could easily switch from molybdenum foil, to niobium foil, and so forth, but we've been doing the reactions in molybdenum foil.

B. McCarroll: Were you pumping on these systems?

S. Sunshine: These reactions have been done, either in inert flow or in a vacuum system. When they've done in a vacuum system they'are being pumped on continuously, even at melt temperatures. That is the advantage of the strontium, barium and lathanum borate fluxes; even at those temperatures their volatility in a vacuum is relatively low.

H. Zandbergen: If you start with potassium titanium oxide is it possible to take out all potassium leaving titanium oxide hollandite?

S. Sunshine: Well, I think that there is in general a small amount of potassium left over. I think the numbers are something like $K_{0.04}TiO_2$ or something to that effect. That's not work that I have done, so I don't know how closely they tried to analyze those numbers. They claim it to be essentially a potassium free titanium oxide, although, I think they do claim that there is a possibility for some residual potassium.

R. Shannon: How stable are these materials to oxidation?

S. Sunshine: They are very stable to oxidation at room temperature. Even when adding indium contacts at <200 degree centigrade, they seem to be stable. The compounds that you have the most problems with are the ones that have a tunnel or layered structure in which case they are much more susceptible to oxidation or reaction with water. But in general if the ion, strontium, barium or lanthanum, is well encased in the structure then they are actually quite stable.

National Institute of Standards and Technology Special Publication 804, Chemistry of Electronic Ceramic Materials, Proceedings of the International Conference held in Jackson, WY, August 17-22, 1990, issued January 1991.

THE KINETICS AND MECHANISM OF THE CRYSTALLIZATION OF $Mg_2Al_4Si_5O_{18}$ FROM $MgAl_2O_4$ AND SiO_2 IN THE PRESENCE OF A BISMUTH OXIDE FLUX

Ryan W. Dupon, Adam C. Tanous and Mark S. Thompson*

Corporate R&D, Raychem Corporation, 300 Constitution Dr., Menlo Park, CA 94025

ABSTRACT

Quantitative kinetics and mechanistic interpretation are presented for the reaction of colloidal SiO_2 and $MgAl_2O_4$ to give $Mg_2Al_4Si_5O_{18}$ in the presence of 2 atom% bismuth oxide. The active flux agent appears to be comprised predominantly of bismuth oxide and silicon oxide. The reaction proceeds through dissolution of the $MgAl_2O_4$ in the siliceous flux to produce an aluminum substituted quartz stuffed with magnesium ions as an intermediate. The stuffed quartz then converts to cordierite by a first order process. The rate constant for this conversion is $4.4x10^{-5}s^{-1}$ at 1000°C with an activation energy of 70 kcal/mole

INTRODUCTION

The preparation of cordierite($Mg_2Al_4Si_5O_{18}$) ceramics has attracted considerable attention due in large part to the small thermal expansion coefficient, good strength, and low dielectric constant of $Mg_2Al_4Si_5O_{18}$. Reported preparation methodologies have included the crystallization of glasses with the cordierite composition[1-5] and the hydrolysis of mixed, reactive intermediates such as metal alkoxides[6-8] with the cordierite composition followed by crystallization to the cordierite phase. The conversion mechanism from starting materials to cordierite for each of these processes has been investigated in some detail. Schreyer and Schairer have performed a comprehensive study of the observed

phases in the crystallization of glasses in the $MgO-Al_2O_3-SiO_2$ system around the composition of cordierite.[1] Chowdry[7] and Bernier et al[8] have followed the conversion of hydrolyzed precursors to $Mg_2Al_4Si_5O_{18}$ by X-ray diffraction. As preparative processes both the glass crystallization and sol-gel route have some drawbacks. The glass crystallization process uses common oxide starting materials but requires high temperatures and is inherently a two step process. The sol-gel process uses expensive, high energy intermediates which makes it an expensive and impractical route for bulk oxide materials. We recently reported the preparation of $Mg_2Al_4Si_5O_{18}$ below 1000°C by the reaction of SiO_2 with $MgAl_2O_4$ in the presence of a small amount of a bismuth oxide flux[9], while in the absence of bismuth oxide there is no observed reaction. In that paper we described several distinctive features of that reaction. It was observed that there was an induction period before the appearance of cordierite that was both temperature and bismuth oxide concentration dependent. Further, the induction period went to infinity at around 960°C, below which temperature no cordierite was formed. As the presence of bismuth oxide provides unique reaction paths to convert simple oxides to useful materials such as cordierite it was of interest to us to follow the phase evolution of this reaction in an attempt to understand why the bismuth oxide exerts such a strong influence on the reaction of these oxides. Additionally, we sought to obtain quantitative kinetic information on the reactions and phase transformations as they occurred. Quantitative kinetic analyses are not typically done of reactions in the solid state; however, such information could be valuable to advancing the state of preparative art in oxide systems. In order to do this, an x-ray diffractometer was fitted with a platinum hot stage to enable the collection of time-dependent diffraction data near 1000°C. The quantitative study of the kinetics for the reaction of colloidal SiO_2 with $MgAl_2O_4$ to make $Mg_2Al_4Si_5O_{18}$ in the presence of a bismuth oxide flux is presented in this paper. For purposes of comparison, data are also presented for the crystallization of a pure, non-bismuth containing glass of the cordierite composition.

EXPERIMENTAL

Powder Synthesis: A complete preparative description for this family of powders and resultant ceramics appears elsewhere.[9]
The non-bismuth containing glass with the cordierite composition was obtained from Gordon Brown of Stanford University and was prepared by conventional melt and quench processing followed by grinding to a powder.
High Temperature XRD Description: X-ray diffraction data were collected with an automated powder diffraction system[12] equipped with a high temperature attachment.[13] The cordierite precursor powder was spread in a thin layer onto a resistively heated platinum band. A Pt/Pt10%Rh thermocouple, spotwelded to the heating band, was used for temperature feedback to a Halder controller.[14] The sample was heated with a ramp of 20°C/min to the reaction temperature, and then held at that temperature until all measurements were completed. Diffraction data were collected using $CuKa_1$ radiation (50kV, 36ma), a single crystal germanium incident beam monochromator,[15] and a position sensitive detector.[16] The diffractometer was scanned from 9 to 39 degrees 2-theta at a speed of 2.5 degrees 2-theta/min after reaching the reaction temperature. Isothermal scans were repeated every 20 to 60 minutes until the reaction was complete.

The raw data were subjected to a trend oriented peak search to obtain peak positions and integrated intensities.

Kinetics Determination: All data for kinetic analyses were obtained by scanning repetitively at the desired temperature between 9° and 39°. Several peaks were selected for quantitative work. The peaks at 10.8°(100), 26.6°(112), 28.6°(202), and 29.6°(211) were used to follow the appearance of cordierite. The disappearance of the magnesium aluminate spinel was tracked at 36.7°. The presence of the SiO_2 intermediates ß-cristobalite and the substitutionally modified quartz were monitored at 35.7°and 26.5° respectively.

For rate constant calculations the integration of count intensity over angle two theta(I) was used as an expression of concentration. Simple first order rate law provided the best fit of the data and was used to determine a rate constant for the appearance of cordierite. By assuming a simple A to B reaction mechanism from a modified quartz

(1) [Intermediate]$\xrightarrow{k}$cordierite, d(cordierite)/dt = k[Intermediate]

intermediate(vida infra) to cordierite as shown in equation (1), the rate expression $\ln(1-I_t/I_\infty)=-kt$ was derived and used to determine first order rate constants for the appearance of cordierite.

RESULTS and DISCUSSION

The results of tracking the powder diffraction pattern as a function of time at 1000°C from starting materials through $Mg_2Al_4Si_5O_{18}$ formation appears in figure (1).

(2) $$2MgAl_2O_4 + 5SiO_2 \xrightarrow{Bi2O3} Mg_2Al_4Si_5O_{18}$$

Several features of these diffraction data should be noted. In the initial state (ie, 1000°C, t=0), the only crystalline species present is $MgAl_2O_4$, as the SiO_2 used

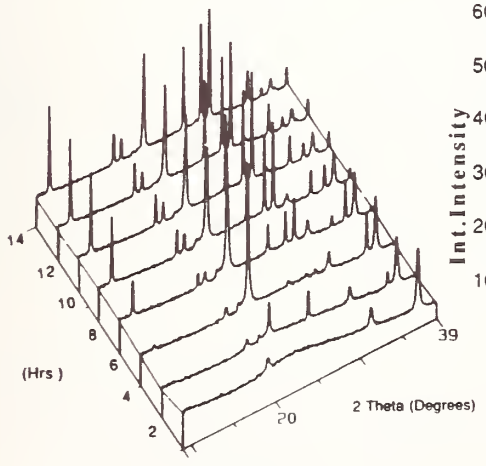

Figure 1

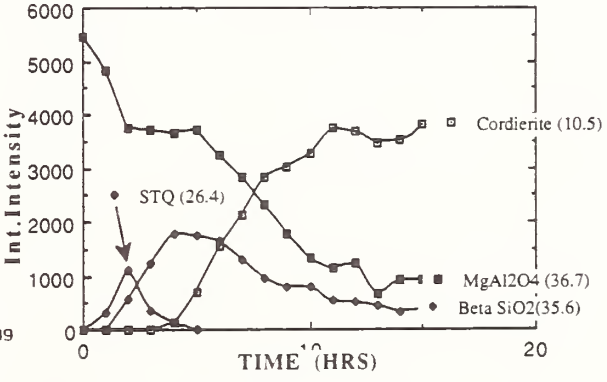

Figure 2

shows only an amorphous halo. As reported in the original paper,[9] there is an induction

period of several hours at 1000℃ before crystalline $Mg_2Al_4Si_5O_{18}$ begins to appear. By 12 hrs reaction time, the conversion to $Mg_2Al_4Si_5O_{18}$ is complete and there are no other crystalline phases present. Two transient species are observed in the intermediate scans. The intermediate with the highest abundance indexes as ß-cristobalite and the less abundant intermediate best indexes as a substituted quartz phase.[10] Discussion of the significance of the presence of these intermediates is left until later in this paper.

To monitor the progress of the reaction and to allow the determination of reaction rates, plots of integrated peak intensity as a function of time for reflections of the spinel starting material, cordierite product, and both quartz intermediates were made. These plots are shown in figure (2), with the indicated degree two theta. Qualitatively, several features are apparent from these plots. The spinel begins to disappear immediately, and then plateau before resuming its disappearance. After some induction period ß-cristobalite is observed to grow in, reach a maximum, and then disappear. The stuffed quartz also grows in and then disappears, but with an earlier maximum. Finally, the $Mg_2Al_4Si_5O_{18}$ grows in smoothly after an induction period of several hours.
The crystallization of cordierite from a glass at 960℃ as a function of time is illustrated in figure (3). This presents the growth of the 100 reflection of cordierite at 10.8°. The time dependance of this crystallization is very different from that of the cordierite formation by the bismuth oxide reaction. The glass crystallization shows two distinct stages; one with a half life of about 18 minutes and the other with a half-life of about 2 hours. One interpretation of this is that the fast process is a nucleation step, while the slow step is the consolidation of small crystalline domains into larger crystallites which scatter more efficiently.

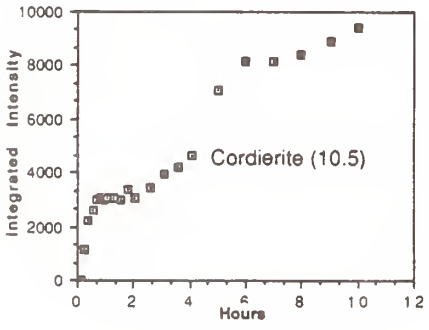

Figure 3

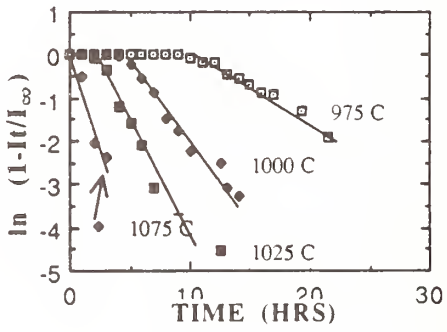

Figure 4

Using a first order rate law, rate constants for the appearance of $Mg_2Al_4Si_5O_{18}$ were obtained from the integrated intensity vs time data for the reaction containing bismuth oxide. Typical first order plots for $Mg_2Al_4Si_5O_{18}$ appearance are shown in figure (4). Rate constants for the reaction at 975℃, 1000℃, 1025℃, and 1075℃ appear in table (1). It can be observed that the rate constants for $Mg_2Al_4Si_5O_{18}$ appearance at different 2Ø are generally in good

TABLE 1

T (℃)	2Ø (hkl)	k (s^{-1})	T(℃)	2Ø (hkl)	k (s^{-1})
975	10.8 (100)	$4.0x10^{-5}$	1025	10.8 (100)	$1.6x10^{-4}$
	26.6 (112)	$4.7x10^{-5}$		26.6 (112)	$1.9x10^{-4}$
	28.6 (202)	$4.7x10^{-5}$		28.6 (202)	$1.5x10^{-4}$
	29.6 (211)	$4.2x10^{-5}$		29.6 (211)	$1.8x10^{-4}$
1000	10.8 (100)	$9.5x10^{-5}$	1075	10.8 (100)	$2.4x10^{-4}$
	26.6 (112)	$9.2x10^{-5}$		26.6 (112)	$3.4x10^{-4}$
	28.6 (202)	$1.0x10^{-4}$		28.6 (202)	$4.9x10^{-4}$
	29.6 (211)	$1.1x10^{-4}$		29.6 (211)	$4.5x10^{-4}$

agreement. The measured activation energy is 70 kcal/mole assuming an Arrhenius behavior.

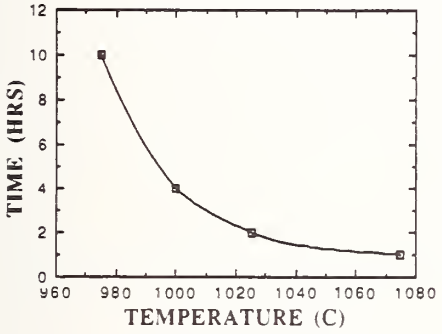

Figure 5

The temperature dependence of the induction period for the appearance of $Mg_2Al_4Si_5O_{18}$ is also shown graphically in figure (5). This curve has a roughly exponential shape, with induction period decreasing with increasing temperature. It was previously determined that below 960℃ this reaction does not proceed; that is, the induction period goes to a very large value at 960°. These two observations have some mechanistic implications for this reaction. A likely reason that the reaction to make cordierite does not proceed below 960° is that the bismuth silicate eulytite ($Bi_4(SiO_4)_3$) melts between 955° and 960°. With an excess of SiO_2 present it is expected that all the bismuth is tied up as this phase in the solid state. The exponential decrease in induction period with temperature is also consistent with the picture of a bismuth silicate flux acting as a reactive solvent in the reaction. Viscosity and diffusion are both exponential functions of temperature,[11] thus a reaction that relied on the transport through a flux to proceed would be expected to display an induction period that decreased exponentially with increasing temperature, as this one does. There is also evidence that the flux is bismuth and silica rich. Where SiO_2 is left out of the reaction there is no effect on $MgAl_2O_4$ by bismuth oxide alone. On the other hand, bismuth oxide is effective at crystallizing the amorphous SiO_2 to ß-cristobalite. Thus it is the authors' conclusion that the induction period is due to the dissolution of $MgAl_2O_4$ in the bismuth silicate flux and the diffusion required to make a suitably substituted silicate precursor to crystallize to $Mg_2Al_4Si_5O_{18}$.

(3) $SiO_2/Bi_2O_3(melt) + MgAl_2O_4 \xrightarrow{k0} [(Si_{1-x}Al_x)Mg_{x/2}O_2] \xrightarrow{k} Mg_2Al_4Si_5O_{18} + SiO_2$

The distribution of intermediates in this system is somewhat different from either the case of sol-gel or glass ceramic prepared cordierite. Both the crystallization of a glass and the

crystallization of hydrolyzed precursors with the cordierite composition show the formation of a modified, substituted quartz[7,8] as an intermediate. This quartz solid solution is described as an aluminum substituted SiO_2 with magnesium in the channels to compensate for the excess negative charge. This modified hexagonal quartz has a wide compositional range around the cordierite composition with cell parameters varying smoothly with composition. The reaction described here appears to have this substituted quartz as an intermediate. This intermediate quartz does not, however, appear to be of the cordierite composition. The observed intermediate has reflections essentially identical to a hexagonal, substituted quartz[10] with cell parameters of a=5.006Å and c=5.459Å. These cell parameters match very well with those of a quartz solid-solution from reference(1) measured at 750℃ with aluminum and magnesium content of roughly half of $Mg_2Al_4Si_5O_{18}$, which is to say it is very SiO_2 rich. This is consistent with the dynamic x-ray measurements where less than half the $MgAl_2O_4$ disappears in the early stages of the reaction where the intermediate forms . There is also a second, more abundant intermediate that appears in this reaction that does not appear in the other glass-ceramic prepared cordierite. This intermediate indexes as ß-cristobalite. It seems unlikely that this is a reactive intermediate on the reaction path to cordierite.

The mechanism by which $MgAl_2O_4$ and SiO_2 convert to $Mg_2Al_4Si_5O_{18}$ in the presence of the bismuth oxide flux thus appears to be a complex one. The initial disappearance of the $MgAl_2O_4$ is consistent with its dissolution in the flux. The bismuth oxide containing flux likely is quite rich in SiO_2, as the lower temperature limit of this process of 960℃ suggests the melting of eulytite, $Bi_4(SiO_4)_3$, which is in the range of 955℃ to 960℃. Thus the process stops below about 960℃, where there is no melt present. The stuffed quartz is clearly implicated in the conversion of starting materials to $Mg_2Al_4Si_5O_{18}$. In addition to being an intermediate in the aforementioned glass and sol-gel routes to $Mg_2Al_4Si_5O_{18}$, the stuffed quartz concentration reaches a maximum just before the appearance of crystalline cordierite in the x-ray powder pattern. As this modified quartz does not appear to be of the cordierite composition, then the crystallization products must be $Mg_2Al_4Si_5O_{18}$ and free SiO_2. The other transient species, indexed as ß-christobalite, is likely not a reactive intermediate on the path to cordierite. On the contrary, the time dependent x-ray data suggest that the formation of this crystalline species may inhibit the reaction.The initial disappearance of $MgAl_2O_4$ and its subsequent reaction with SiO_2 are believed to yield the stuffed quartz phase. The sharp decrease in the rate of spinel disappearance coincides with the appearance of crystalline ß-cristobalite. This is also coincident with the plateau of the appearance of the stuffed quartz. The slowdown in the rate of reaction is likely due to the conversion of high surface area, reactive SiO_2 to a low surface area crystalline form.

Structural analysis is in progress to determine the form of the cordierite (disordered and hexagonal or ordered and orthorhombic) and to locate bismuth in the final structure.

ACKNOWLEDGMENT Thanks to Stefan Justi and Ken Schwartz for assistance with the hot stage x-ray diffraction data collection.

REFERENCES

1) Schreyer, W. and Schairer, J. F., "Metastable Solid Solutions with Quartz-Type Structures on the Join SiO_2-$MgAl_2O_4$," *Zeitschrift fur Kristallographie,* **1961**, *116,* 60-82

2) Gregory, A. G. and Vearey, T. J., "The Crystallizaton of Cordierite Glass," *J. Mater. Sci.*, **1971**,*6,* 1312-21

3) Zdaniewski, W., "DTA and X-ray Analysis Study of Nucleation and Crystallization of MgO-Al_2O_3-SiO_2 Glasses Containing ZrO_2, TiO_2, and CeO_2," *J. Am. Ceram Soc.*, **1975**,*58,* 163-69

4) Bridge, D. R.; Holland,D.; and McMillan,P. W., "Development of the Alpha-Cordierite Phase in Glass Ceramics for Use in Electronic Devices," *Glass Technol.*, **1985**,*26,* 286-92,

5) Watanabe,K. and Giess,E., "Coalescence and Crystallization in Powdered High-cordierite ($2MgO{\cdot}2Al_2O_3{\cdot}5SiO_2$) Glass," *J. Am. Ceram. Soc.*, **1985**,*68,* C-102-3

6) Moyer,J. R.; Prunier, A. R.; Hughes,N. N.; and Winterton,R. C., *Mater. Res. Soc. Symp. Proc.*, **1986**,*73,* 117-21

7) Gensse,C. and Chowdry,U., "Non-Conventional Routes to Glass-Ceramics for Electronic Packaging," *Mater. Res. Soc. Symp. Proc.*, **1986**,*73,* 693-703

8) Bernier,J. C.; Vilminot,S.; Rehspringer,J. L.; El Hadigui,S.; and Poix,P., "Sol-Gel Processes and Synthesis of Dielectric Powders for Multilayer Ceramics," *High Tech Ceramics*, P. Vincenzini, ed, Elsevier, Amsterdam, 1987, pp 1443-50

9) Dupon,R. W.; McConville,R. L.; Musolf,D. J.; Tanous,A. C.; and Thompson,M. S., "Preparation of Cordierite Below 1000°C via Bismuth Oxide Flux," *J. Am. Ceram. Soc.*, **1990**,*73,* 335-339,

10) JCPDS file#12-708

11) R. H. Perry and C. H. Chilton ed.,*Chemical Engineers Handbook, 5th edition,* McGraw Hill, 3-247, **1973**

12) Siemens D-500

13) Anton Paar, K.G., P.O. Box 17, Graz, Austria

14) Halder Elektronik, Munich, FRG

15) Huber Diffraktionstechnik, D-8219 Rimsting, FRG

16) PSD-OED50M, Braun, Gutenbergstrasse 3, D-8046 Garching, FRG

IV. CRYSTAL CHEMISTRY

National Institute of Standards and Technology Special Publication 804, Chemistry of Electronic Ceramic Materials, Proceedings of the International Conference held in Jackson, WY, August 17-22, 1990, issued January 1991.

SOLID STATE CHEMISTRY OF PEROVSKITE AND RELATED OXIDES CONTAINING Fe^{4+}, Ni^{3+}, and Cu^{2+}

Mikio TAKANO
Institute for Chemical Research, Kyoto University,
Uji, Kyoto-fu 611, Japan

1. INTRODUCTION

Perovskites (AMO_3) and related oxides allow 3d transition metals (M) to be stabilized in unusually high formal valencies: Iron is oxidized to Fe^{4+} in $SrFeO_3$. And mixed valence states are rather easily produced by substituting La^{3+} for Sr^{2+}, for example, or by changing oxygen content. The 3d levels of an M ion lowers in energy as the atomic number of M increases and as the formal valency of M increases. This makes the M-O bond covalent, and thus the role of the oxygen lattice and, in turn, the role of the A cations bound to the oxygen atoms become important in determining the electronic properties of a material.

$SrFeO_3$ is a metallic conductor, while $CaFeO_3$ is semiconductive, though the cell volume is smaller for $CaFeO_3$. Discrete vacancy-ordered phases $SrFeO_{3-1/n}$ (n=8,4,2) are all semiconductive, even in their high temperature disordered phase.

Low dimensional M-O lattices formed in intergrowth structures generally show polaronic electric conduction. There is, however, a semiconductor-metal transition in $La_{2-x}Sr_xNiO_4$. The transition temperature T_t decreases monotonically with increasing x but with a change in dT_t/dx at x~0.6. Correlated with this is an anomalous dependence upon x of structural details, especially of the La(Sr)-O(2) bondlength. Composition x=1.4 remains metallic at least down to 10K.

Oxidation and reduction of $[CuO_2]^{2-}$ layers in intergrowth structures can give rise to high T_c superconductivity and the T_c varies depending upon details concerning composition and structure. Among the experimental parameters controlling the phase formation and crystal structure, influences of high pressures have relatively been unknown. Examples of layered phases stabilized only under high pressures will be shown.

2. PEROVSKITES CONTAINING Fe^{4+}

1) $SrFeO_3$ and $CaFeO_3$

$SrFeO_3$ retains cubic perovskite structure (a=3.850Å at 300K) and am etallic conductivity of $\sim 10^{-3}\Omega$cm down to 4K [1]. The magnetic moment estimated from magnetization measurements on $SrFe_{1-x}Co_xO_3$, which is ferromagnetic for $0.2 \leq x \leq 1$, is $\mu_{Fe^{4+}}=3.72\mu_B$ [2]. A screw spin structure with a propagation vector along the <111> direction has been found below T_N=134K [3]. This structure results from a competition of the ferromagnetic nearest neighbor interaction and the antiferromagnetic second- and fourth-nearest interactions [4] : The angle between the nearest Fe moments is only about 40° [3].

$CaFeO_3$ crystallizes in a tetramolecular tetragonal cell with a=5.325Å and c=7.579Å, and T_N=115K [5]. In contrast with $SrFeO_3$, semiconductive behavior has been found below room temperature, though there is some uncertainty caused by the small size of samples prepared under 2GPa. Further details are under investigation.

2) Microscopic electronic state of $Ca_{1-x}Sr_xFeO_3$

Mossbauer spectroscopy has proved useful to elucidating how the electronic state depends upon composition. The spectra of $SrFeO_3$ [6] are simple and beautiful in which the unique electronic state and high crystal symmetry are reflected. A narrow single peak with an isomer shift (IS) of 0.05mm/s relative to α-Fe appears at room temperature, and a single magnetic pattern is seen below T_N. The hyperfine field (Hi) is 33.1T and IS=0.146mm/s at 4K. Any quadrupole interaction has not been detected.

$CaFeO_3$ shows a single peak at 300K with IS=0.073mm/s just as for $SrFeO_3$, while, at 4K, two sets of magnetic patterns, I and II, with (Hi,IS)=(41.6, 0.34) and (27.9, 0.00) appear. And the intensity ratio of the two sets is 1:1 within experimental error as seen in Fig. 1(a). Quadrupole interactions are absent. The great difference of the parameters between the two components clearly indicates that an electronic phase transition discriminating iron into two different states occurs below 300K. Considering that both these parameters are sensitive to the d electron density of an Fe ion, a disproportionation model

$$2Fe^{4+}\ (t_{2g}{}^3\ \sigma^{*1}) \rightleftarrows Fe^{3+}(t_{2g}{}^3e_g{}^2)+Fe^{5+}(t_{2g}{}^3)$$

has been proposed, components I and II corresponding to Fe^{3+} and Fe^{5+}, respectively [7]. There are three important consequences of this model. The first is that high spin state was assumed for Fe^{4+}. The (nearly) delocalized character of the σ^* electron of e_g-orbital parentage has been understood to yield no quadrupole interaction. The spherical configurations of Fe^{3+} and Fe^{5+} have also been done so. This assumption was strongly supported by the more recent magnetic measurements on $SrFe_{1-x}Co_xO_3$ mentioned above. The second is the high content of Fe^{5+}. Iron in this high oxidation state was known at that time only as an impurity of ppm

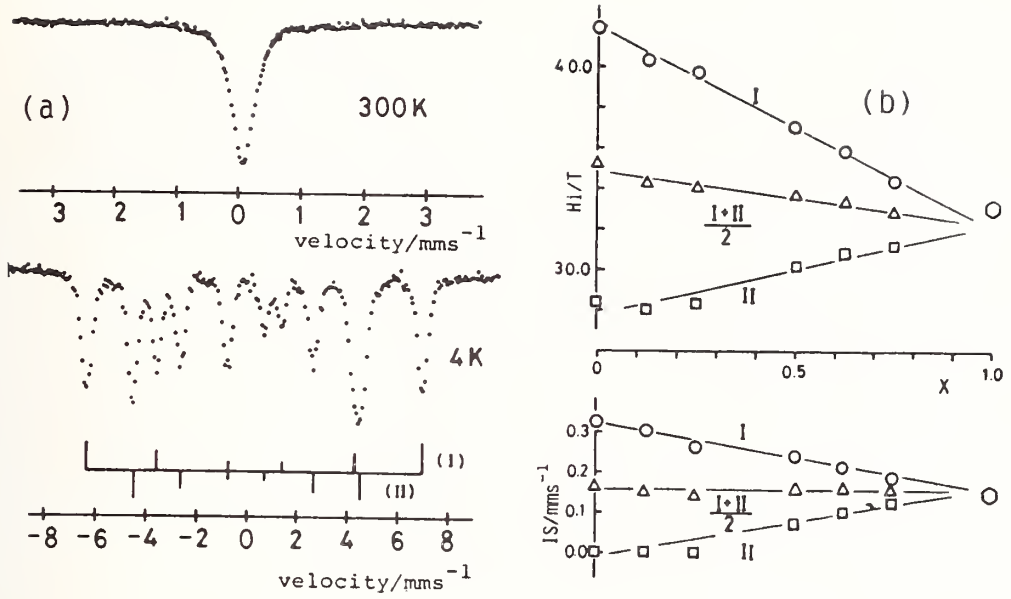

Fig. 1 Mossbauer spectra of $CaFeO_3$ (a) and IS and Hi of $Ca_{1-x}Sr_xFeO_3$ at 4K (b).

order in $SrTiO_3$ [8]. The Hi value for component II of $CaFeO_3$ at 4K just coincides with the corresponding EPR data for the $^{57}Fe^{5+}/SrTiO_3$ sample. Later Buffat et al. succeeded in stabilizing $LaLi_{0.5}Fe^{5+}{}_{0.5}O_3$ under a high oxygen pressure [9]. The third is the transition mechanism.

$Ca_{1-x}Sr_xFeO_3$ can be prepared for the whole range of x. The cell volume monotonically increases with increasing x, while the structure symmetry becomes cubic for $x \geq 0.25$. Shown in Fig. 1(b) are the composition dependence of the parameters at 4K [10]. To be noticed is that the two components gradually become similar to each other as x increases, while the mean parameter values, (I+II)/2, remain almost constant. The iron valencies may be expressed as $Fe^{(4-\delta)+}$ and $Fe^{(4+\delta)+}$, δ varying continuously from $\delta=1$ at x=0 to $\delta=0$ at x=1. Charge density wave (CDW) may be more appropriate in terminology than disproportionation.

Just the same kind of disproportionation has been found also in $Sr_{1-y}La_yFeO_3$ [11,12] as can be typically seen in the spectra for y=0.3 reproduced in Fig. 2. As a result of a rapid electron exchange the Fe ions are in an average valence state at room temperature for $y \leq 0.6$ so that IS linearly varies with y as

$$IS(y)=(1-y)IS(0)+yIS(1),$$

where IS(0)=0.05 mm/s ($SrFeO_3$) and IS(1)=0.39 mm/s ($LaFeO_3$). On the other hand, at 4 K, the spectrum for x=0.3 is composed of two components with (Hi, IS)=(46.0, 0.36) and (26.9, -0.05) with a relative intensity of I:II=66:34. The low temperature state can therefore be formulated as $Sr_{0.7}La_{0.3}Fe^{3+}{}_{0.65}Fe^{5+}{}_{0.35}O_3$.

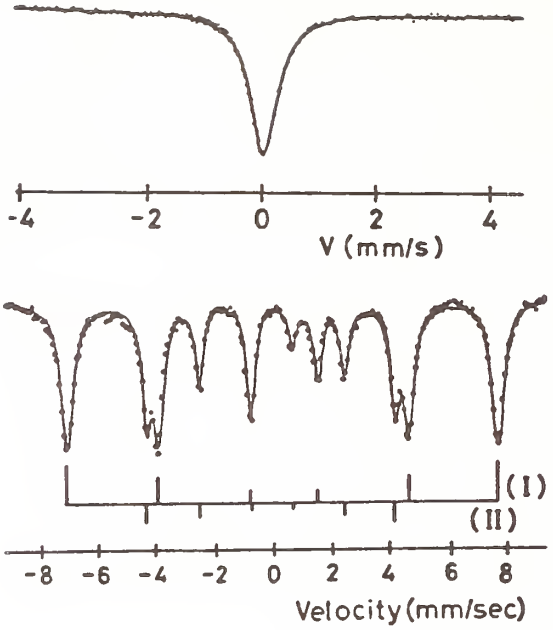

Fig. 2 Mossbauer spectra of $Sr_{0.7}La_{0.3}FeO_3$.

3) CDW, why ?

It is quite natural to suppose that the disproportion should be accompanied by a lattice distortion: The oxygen octahedron containing Fe^{3+} should be enlarged and the one containing Fe^{5+} should be compressed. However, diffraction measurements using X-ray (XRD) and neutron (ND) [13] have failed to detect any sign of such a distortion. The present author has suspected that the tran sition is set in microdomains which are so small that these diffraction measurements detect only seemingly high, averaged symmetry. Electron diffraction (ED) and transmission electron microscopic (TEM) studies at low temperatures are of great interest and are now in progress.

A theoretical calculation has been done for monometric ($[FeO_6]^{8-}$) and dimeric ($[Fe_2O_{11}]^{-14}$) clusters by a DV Xα method [14]. These clusters are embedded in a Madelung potential reflecting the perovskite structure. For either octahedron in Fig. 4(a) the Fe-O distance is 1.887Å, half the cubic root of the cell volume for $CaFeO_3$. The effective charges and the magnetic moments are given in the figure. The electron configuration is essentially such that both the $d_{x^2-y^2}$ and d_{z^2} orbitals are half occupied, which is high spin state. These orbitals each contain an oxygen 2p component weighing about 28%, while the weight is about 14% for the t_{2g} orbitals. The Fe ions carry a moment of $3.7\mu_B$, in good agreement with the extrapolated magnetization data for $SrFeO_3$. On the other hand, the Fe(I)-O(1,3) distance is elongated but the Fe(II)-O(2,3) distance is shortened, each by 0.053Å, in Fig. 3(b). As a result of this displacement the configurations are

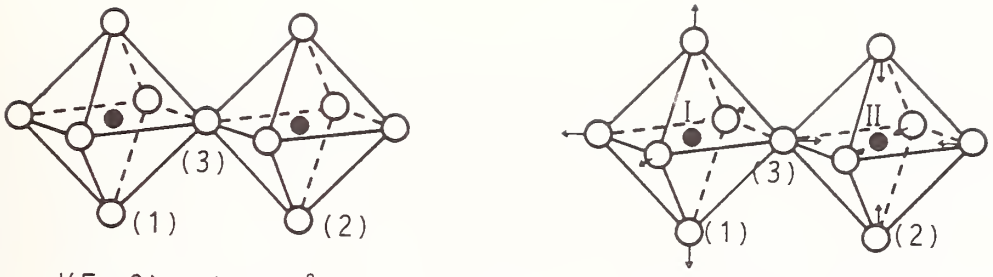

d(Fe-O) : 1.887 Å
$Fe^{2.8+}$, 3.7 μ_B
$O(1,2)^{1.83-}$,
$O(3)^{1.35-}$,

d(Fe(I)-O) : 1.940 Å
d(Fe(II)-O) : 1.834 Å
$Fe(I)^{2.7+}$, 4.1 μ_B
$Fe(II)^{2.9+}$, 3.2 μ_B
$O(1)^{1.77-}$, $O(2)^{1.88-}$
$O(3)^{1.34-}$

Fig. 3 $[Fe_2O_{11}]^{14-}$ cluster before (a) and after (b) an anion displacement.

modified as $d_{x^2-y^2}{}^1 d_{z^2}{}^{0.5}$ for Fe(I) and $d_{x^2-y^2}{}^0 d_{z^2}{}^{0.5}$ for Fe(II). The electron transfer from Fe(II) to Fe(I) reflects the opposite shifts of the level schemes for these ions. The moments differ by $0.9\mu_B$, and the hyperfine fields do by 11T according to a preliminary estimation. The experimental value is 13.7T for $CaFeO_3$ and 19.1T for $Sr_{0.7}La_{0.3}FeO_3$. The composition dependence of the d electron densities seen in $Ca_{1-x}Sr_xFeO_3$ and $Sr_{1-y}La_xFeO_3$ can thus be assigned to a smooth, composition-dependent anion displacement.

How the disproportionation can be stabilized has been explained by Goodenough [15]. The d-orbital contribution to the Fe-O interaction energy, ϕ, is assumed to have the Morse form. And the change in binding energy due to the anion displacement is divided into two parts as

$$\Delta \varepsilon = -(A-B)u^2,$$

where u is the anion displacement normalized to half the Fe-Fe separation, coefficient A is proportional to $\partial^2\phi/\partial r^2$, and Bu^2 is the elastic energy contribution. For the stabilization of disproportionation A>B is necessary. For $CaFeO_3$, in comparison with $SrFeO_3$, the Fe-O distance is shorter and the σ^* band is narrower because of the more acidic nature of Ca^{2+}. These factors have been argued to be more advantageous for $CaFeO_3$ than for $SrFeO_3$ to satisfy the above criterion of the disproportionation stabilization.

4) $CaFeO_3$ and $Sr_{0.7}La_{0.3}FeO_3$ in the transition temperature range

As seen in Fig. 4(a), the paramagnetic single peak of $CaFeO_3$ begins to be divided into two below 290K [16]. The splitting has

been interpreted to indicate the disproportionation taking place in the paramagnetic state. The separation reaches 0.32mm/s at 140K (Fig. 4(b)), which just coincides with the difference in IS between components I and II at 4K. Another reason why this splitting should not be considered as a temperature-dependent quadrupole interaction is that components I and II are not perturbed by quadrupole interactions at 4K. Below T_N a pair of magnetic patterns appear and the Hi's vary as shown in Fig. 4(c). Thus, the disproportionation proceeds gradually with decreasing temperature, and the magnetic transition follows.

Quite a different type of transition occurs for $Sr_{0.7}La_{0.3}FeO_3$ and also for $Ca_{0.5}Sr_{0.5}FeO_3$. For either phase a paramagnetic single peak and a pair of magnetic patterns are superimposed in a very wide temperature range indicating a first-order transition between the paramagnetic average valence state and the antiferromagnetic disproportioned state.

In conclusion $Ca_{1-x}Sr_xFeO_3$ and $Sr_{1-y}La_yFeO_3$ show very interesting phase transition behavior depending upon composition. The σ^* electrons in $SrFeO_3$ tend to become localized by forming CDW, the amplitude being larger as Sr is replaced more by Ca and La. It should be noted that the replacement by these elements reduces the covalency of the Fe-O bond.

Experiments in progress include measurements of XPS, Mossbauer spectroscopy under high pressures, and preparation of single crystalline films to be used for precise electric and magnetic measurements.

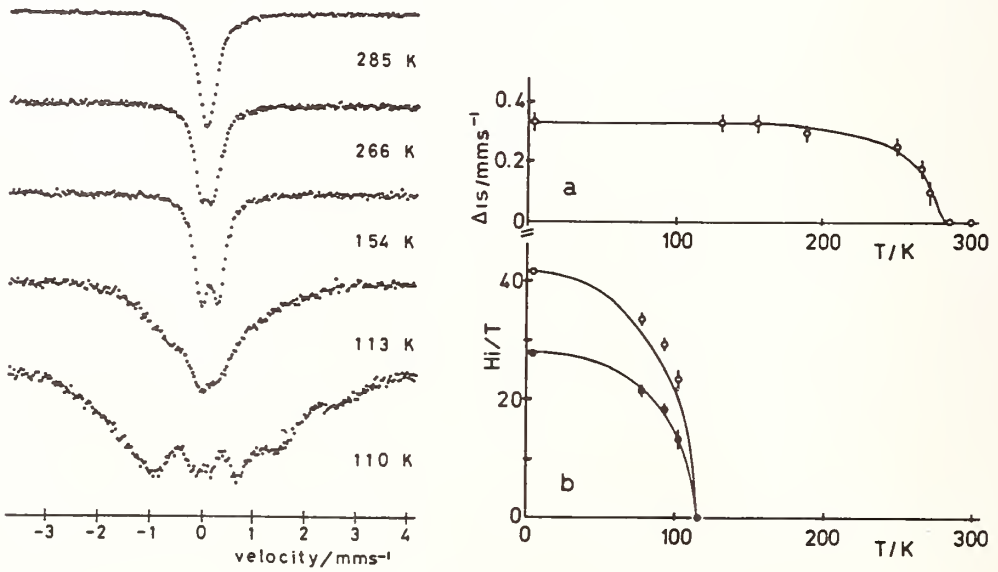

Fig. 4 Mossbauer spectra of $CaFeO_3$ (a) and the parameters (b).

5) $SrFeO_{3-1/n}$

The system $SrFeO_z$, $2.5 \leq z \leq 3$, forms a continuous solid solution at temperatures $T \geq T_t(z)$, but a series of discrete ordered-vacancy phases $SrFeO_{3-(1/n)}$ (n=8,4,2) appear below $T_t(n8)$=523K, $T_t(n4)$=598K, and $T_t(n2)$=1103K. The order-disorder transition, ordered structures, n-dependence of the electronic state were reported in refs. 18 and 19.

3. $La_{2-x}Sr_xNiO_4 (0 \leq x \leq 1.6)$

Incorporation of excess oxygen and substitution of Sr for La both introduce a mixed valency in the NiO_2 planes by lowering the Fermi energy. $La_2NiO_{4+\delta}$ shows an orthorhombic-tetragonal transition and a change in thermal expansion coefficient from weakly negative ($T<T_t$) to strongly positive at T_t~650K [20]. And a semiconductor-metal transition in the basal plane has been observed at (or near) T_t [21]. The metallic temperature region is widened by the Sr-for-La substitution [22].

1) $La_2NiO_{4+1/2n}$: Oxygen ordering

According to a recent ND study [23], there exists a two phase region in the compositional range $0.02<\delta<0.13$ and the excess oxygen in the $\delta>0.13$ phase has been located as an interstitial oxide ion O^{2-} in the tetrahedral site of the La_2O_2 layers. However, a more microscopic study using ED and TEM [24] has revealed that there are two types of homologous series of oxygen-ordered phases. These are $2a \times ka \times lc$ (k,l=n or 2n depending upon n; the most frequently observed sets are k/2=l/2=n=2 and k=l/2=n=3) and $\sqrt{2}a \times p\sqrt{2}a \times qc$ (most frequently p=2 and q=1), where $a \times a \times c$ stands for the K_2NiF_4 type cell.

The most probable ordering models are illustrated in Fig. 5. In Fig. 5(a), the interstitial oxygen atoms are aligned along the [111] direction within a (011) plane. The rows of interstitial atoms are separated from each other by 2a along the a axis. And these specific (011) planes appear with a period of na along the b axis. According to this model, δ=1/2n, i.e. δ=0.25 for n=2 and δ=0.17 for n=3. In Fig. 5(b), the interstitial atoms are separated from each other by $\sqrt{2}a$ along the [1$\bar{1}$0] direction and by $p\sqrt{2}a$ along the [110] direction within a basal plane. For p=2, the [1$\bar{1}$0] excess oxygen rows are shifted by $\sqrt{2}a$ along the [110] direction in adjacent basal planes to from a body-centered-orthorhombic lattice of $\sqrt{2}a \times 2\sqrt{2}a \times c$. For p>2 a monoclinic superlattice seems to result. Excess oxygen content is again δ=1/2p. This type of excess oxygen ordering along the [1$\bar{1}$0] direction is rather similar to that causing the structure modulation in the superconductors of the Bi-Sr-Ca-Cu-O system.

There are experimental suggestions that excess oxygen atoms are rather mobile and become ordered at low temperatures, not much

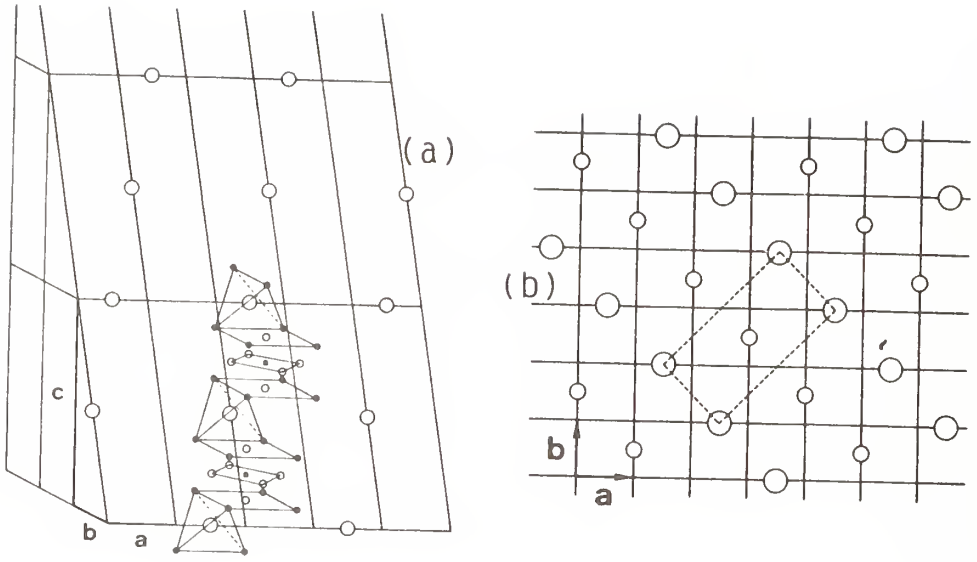

Fig. 5 Model structures of the $2a \times ka \times 1c$ type (a) and the $\sqrt{2}a \times 2\sqrt{2}a \times c$ type (b). Large and small open circles in (a) are the interstitial and normal oxygen atoms, respectively, and solid circles and squares indicate La and Cu atoms, respectively. In (b) large and small circles reprisent interstitial oxygen atoms at z=0 and c/2, respectively.

higher than room temperature. So, special attention should be paid in studying properties as a function of oxygen content and temperature.

2) $La_{2-x}Sr_xNiO_4$

Very recently samples with $x \leq 1.6$ were prepared and examined by various physical measurements [25]. The oxygen content was controlled by using suitable oxygen pressures ($10 \sim 10^7$ Pa) depending upon x. The Ni-O and La(Sr)-O bondlengths, determined by Rietveld analysis of powder XRD data, are shown Fig. 6. Ni-O(2) (apical oxygen) bondlength decreases essentially linearly with increasing x throughout the interval $0 \leq x \leq 1.4$, whereas the La(Sr)-O(2) bondlength increases linearly with x only in the interval $0 \leq x \leq 0.6$. Thus a maximum in the c-axis and the lattice axial ratio c/a appears at x=0.6 reflectng the very anisotropic change in the La(Sr)-O bondlength in the interval $0 \leq x \leq 0.6$. The axial ratio Ni-O(2)/Ni-O(1) of the NiO_6 octahedra, on the other hand, decreases linearly with increasing x throughout the interval $0 \leq x \leq 1.4$ with no obvious anomaly at x=0.6. An important shift in the relative strengths of the La(Sr)-O(2) and Ni-O(2) bonding is thus suggested.

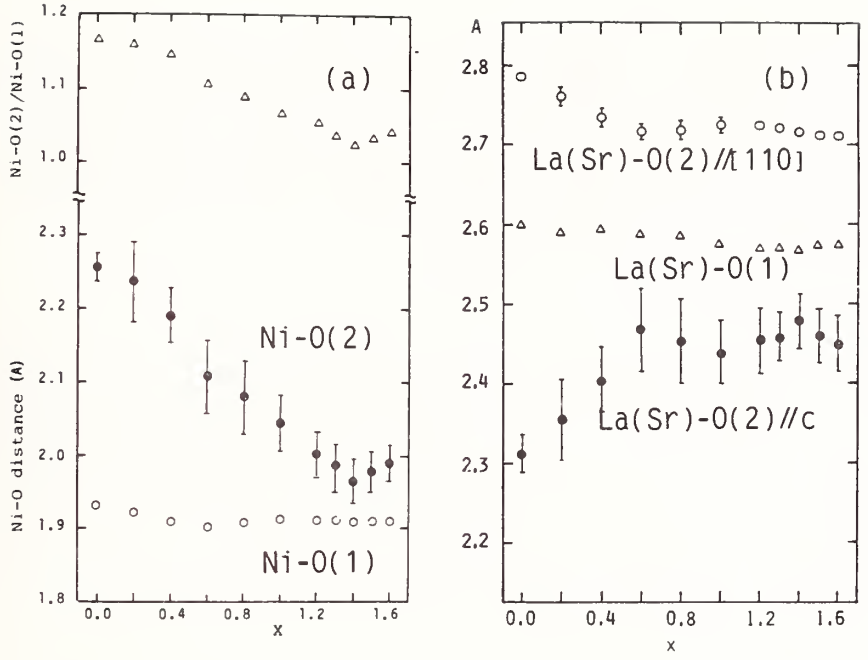

Fig. 6 Variation of the Ni-O distances and the tetragonality of the NiO_6 octahedron (a) and the variation of the La(Sr)-O distances (b).

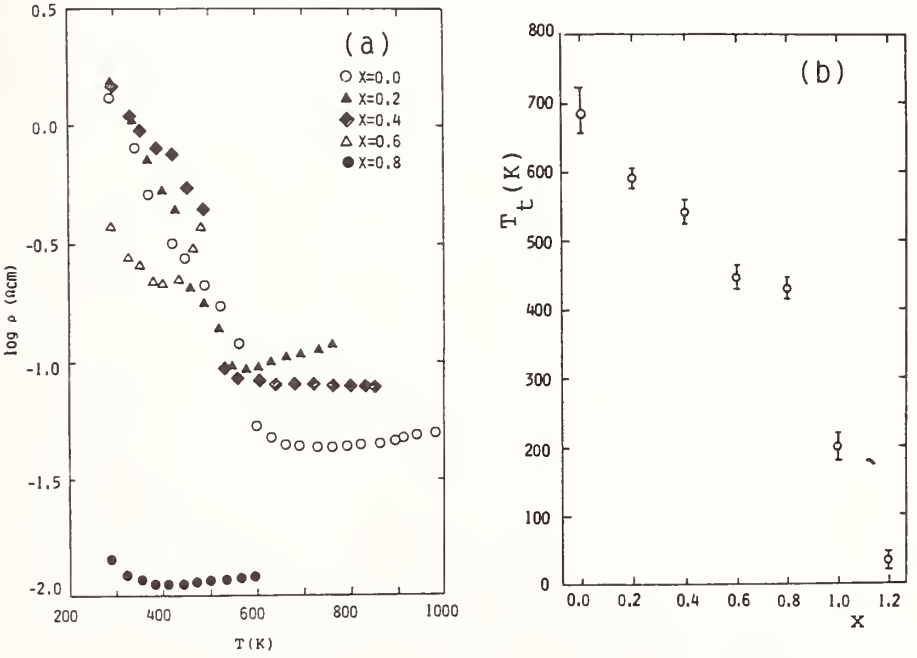

Fig. 7 Resistivity vs. T (a) and T_t vs. x (b) data for $La_{2-x}Sr_xNiO_4$.

5) $SrFeO_{3-1/n}$

The system $SrFeO_z$, $2.5 \leq z \leq 3$, forms a continuous solid solution at temperatures $T \geq T_t(z)$, but a series of discrete ordered-vacancy phases $SrFeO_{3-(1/n)}$ (n=8,4,2) appear below $T_t(n8)$=523K, $T_t(n4)$=598K, and $T_t(n2)$=1103K. The order-disorder transition, ordered structures, n-dependence of the electronic state were reported in refs. 18 and 19.

3. $La_{2-x}Sr_xNiO_4$($0 \leq x \leq 1.6$)

Incorporation of excess oxygen and substitution of Sr for La both introduce a mixed valency in the NiO_2 planes by lowering the Fermi energy. $La_2NiO_{4+\delta}$ shows an orthorhombic-tetragonal transition and a change in thermal expansion coefficient from weakly negative ($T<T_t$) to strongly positive at T_t~650K [20]. And a semiconductor-metal transition in the basal plane has been observed at (or near) T_t [21]. The metallic temperature region is widened by the Sr-for-La substitution [22].

1) $La_2NiO_{4+1/2n}$: Oxygen ordering

According to a recent ND study [23], there exists a two phase region in the compositional range $0.02<\delta<0.13$ and the excess oxygen in the $\delta>0.13$ phase has been located as an interstitial oxide ion O^{2-} in the tetrahedral site of the La_2O_2 layers. However, a more microscopic study using ED and TEM [24] has revealed that there are two types of homologous series of oxygen-ordered phases. These are $2a\times ka\times lc$ (k,l=n or 2n depending upon n; the most frequently observed sets are k/2=l/2=n=2 and k=l/2=n=3) and $\sqrt{2}a\times p\sqrt{2}a\times qc$ (most frequently p=2 and q=1), where $a\times a\times c$ stands for the K_2NiF_4 type cell.

The most probable ordering models are illustrated in Fig. 5. In Fig. 5(a), the interstitial oxygen atoms are aligned along the [111] direction within a (011) plane. The rows of interstitial atoms are separated from each other by 2a along the a axis. And these specific (011) planes appear with a period of na along the b axis. According to this model, $\delta=1/2n$, i.e. $\delta=0.25$ for n=2 and $\delta=0.17$ for n=3. In Fig. 5(b), the interstitial atoms are separated from each other by $\sqrt{2}a$ along the $[1\bar{1}0]$ direction and by $p\sqrt{2}a$ along the [110] direction within a basal plane. For p=2, the $[1\bar{1}0]$ excess oxygen rows are shifted by $\sqrt{2}a$ along the [110] direction in adjacent basal planes to from a body-centered-orthorhombic lattice of $\sqrt{2}a\times 2\sqrt{2}a\times c$. For p>2 a monoclinic superlattice seems to result. Excess oxygen content is again $\delta=1/2p$. This type of excess oxygen ordering along the $[1\bar{1}0]$ direction is rather similar to that causing the structure modulation in the superconductors of the Bi-Sr-Ca-Cu-O system.

There are experimental suggestions that excess oxygen atoms are rather mobile and become ordered at low temperatures, not much

Typical resistivity data are given for T>300K in Fig. 7(a). The data for x=0.6 is clearly anomalous above 400K and is transitional between compositions exhibiting a rather abrupt semiconductor-metal transition at T_t in the interval $0 \leq x < 0.6$, a smooth transition in the interval $0.6 < x \leq 1.2$. A plot of T_t vs. x, Fig. 7(b), shows two straight-line segments intersecting near x=0.6. This feature and the structural anomaly mentioned above suggest that there may be a significant change in the electronic state of the system at and below room temperature near the composition x~0.6 [25].

These results have been interpreted as follows. The semiconductor-metal transition at T_t in $La_2NiO_{4+\delta}$ is due to a localized-electron to itinerant electron transition among the antibonding σ^* electrons. Below T_t, this material is a small-polaron conductor and has a negative thermal-expansion coefficient consistent with increasing electron delocalization with increasing temperature. The electronic transition and the structural transition may be separated in oxygen-rich samples, the structural transition occurring at $T_t' < T_t$. In the $La_{2-x}Sr_xNiO_4$ system, the position of the O(2) atom shifts at room temperature away from its La(Sr) nearest neighbor toward its Ni nearest neighbor in the interval $0 \leq x \leq 6$ where the resistivity remains polaranic at room temperature; this shift stops for x>0.8 where the room-temperature conduction is metallic. This unusual behavior is consistent with an O(2)-displacement and polarization controlling a transition from localized-electron to itinerant-electron character at T_t in the interval $0 \leq x \leq 0.6$.

Hall effect measurements for samples in the range $1.0 \leq x \leq 1.4$ indicated that higher-mobility hole carriers are introduced; the Fermi energy drops into the π^* band at room temperature for $x \geq 1.0$ in accordance with equation $Ni^{4+} + O^{2-} \rightleftarrows Ni^{3+} + O^-$ being shifted to the right.

4. HIGH PRESSURE SYNTHESIS OF NEW Cu OXIDES CRYSTALLIZING IN LAYERED STRUCTURES

All the high Tc superconducting cupric oxides contain two-dimensional (2D) CuO_2 sheets irrespective of the sign of the carrier [26, 27]. It is an important task for solid state chemists to continue efforts to find new cupric oxides crystallizing in layered structures. For this purpose the author's group has studied how high pressure treatments influence the phase formation and crystal structure. Fine oxide powders containing appropriate metal elements were treated under 6GPa at 1300K.

It has been found that $ACuO_2$ ($A: Ba_{1/3}Sr_{2/3} \sim Sr_{1/3}Ca_{2/3}$) crystallizes in a 2D structure made of alternately stacked A and $[CuO_2]_\infty$ layers [28]. This structure was reported for the first time for $Ca_{0.84}Sr_{0.16}CuO_2$ [29]. Under ambient pressure, however,

only a narrow composition range around Ca:Sr~9:1 can be stabilized in this structure. For example, Cu-O-Cu zigzag chains are formed in $SrCuO_2$ in which CuO_4 squares share their sides, not corners. The high-pressure phase of $SrCuO_2$ has a higher specific density. As seen in Fig. 8(a) the lattice changes its size very anisotropically as a function of r_A. At relatively small r_A's both the Cu-O and A-O bonds are stretched linearly as r_A increases, while the rates are $d(Cu-O)/dr_A=0.271$ and $d(A-O)/dr_A=0.896$, reflecting the relative stiffness of the Cu-O bond. The anisotropic lattice expansion results from this difference. The expansion tends to be suppressed for $r_A>1.21$Å, more strongly for the Cu-O bond. The maximum length reaches 1.97Å, which coincides with the "ideal" length calculated from the table in ref. 30. If $CaCuO_2$ were stabilized, the lattice constants would be a=3.849Å and c=3.160Å, i.e. the Cu-O bondlength would be 1.92Å.

R_2CuO_4's containig relatively small R^{3+} ions Y, Dy, Ho, Er, and Tm have also been found to be stabilized under the pressurized conditions [31], though these are not formed at all under ambient pressure. The structure is the Nd_2CuO_4 (T') type with lattice constants plotted against the R ion radius in Fig. 8(b). It is interesting to notice that two straight-line segments intersect at R=Sm. For the R ions smaller than Sm, the $[CuO_2]_\infty$ layers probably become slightly distorted for the sake of lattice matching with the R_2O_2 sheets: The tolerance factor is too small to maintain genuinely tetragonal symmetry. In support of this ED and TEM studies of Y_2CuO_4 have revealed a complicated superlattice structure. And magnetization measurements on the R=Y and Ho phases have indicated weak ferromagnetism due to antisymmetric exchange

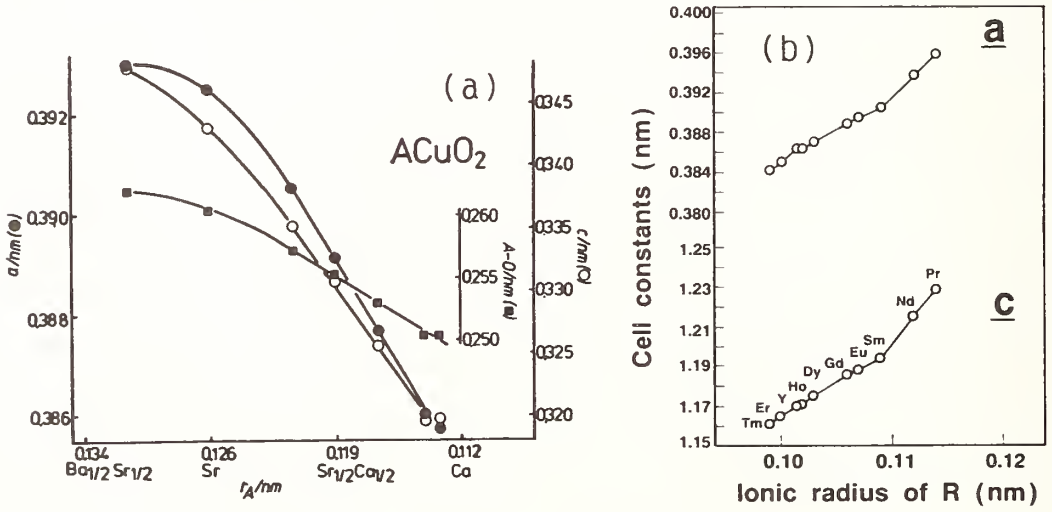

Fig. 8 Lattice constants and the A-O bondlength of $ACuO_2$ (a) and the lattice constants of R_2CuO_4 (T') (b).

interactions caused by the distortion [32]. The saturated weak ferromagnetic moment is $9\times10^{-4}\mu_B$/Cu for Y_2CuO_4. If an atomic moment of $0.5\mu_B$/Cu is assumed, the canting angle is calculated to be 0.05°.

The tolerance factor would approach unity, if the $[CuO_2]_\infty$ layers are contracted by oxidation. Injection of carrier holes, not electrons, may thus be possible. If the data for the two different structures in Fig. 8 are compared with each other, one would notice that the Cu-O bondlength in these structures overlap each other for a considerably wide range of R and A ions. $R_2A_{m-1}Cu_mO_{2m+2}$ may be formed from appropriate combinations.

REFERENCES

[1] J. B. MacChesney et al., J. Chem. Phys. 43 (1965) 1907.
[2] T. Takeda et al., J. Mag. Mag. Mater, 31-34 (1983) 797.
[3] T. Takeda et al., J. Phys. Soc. Jpn. 33 (1972) 967.
[4] T. Takeda et al., "FERRITES: Proc. Int. Conf. Sept.-Oct. 1980 Japan", (Cen. Academ. Pub., Japan, 1981) p.385.
[5] Y. Takeda et al., Mat. Res. Bull. 13 (1978) 61.
[6] P. K. Gallagher et al., J. Chem. Phys. 41 (1964) 2429.
[7] M. Takano et al., Mat. Res. Bull. 12 (1977) 923.
[8] K. A. Muller et al., Solid State Commun. 9 (1971) 1097.
[9] B. Buffet et al., C. R. Acad. Sci. 292, Ser. II (1981) 509.
[10] Y. Takeda et al., J. Phys. Colloq. 40 (1979) C2-331.
[11] M. Takano et al., J. Solid State Chem. 39 (1981) 75.
[12] P. D. Battle et al., J. Solid State Chem. 77 (1988) 124.
[13] P. D. Battle et al., J. Solid State Chem. 84 (1990) 271.
[14] H. Adachi et al., in preparation.
[15] C. Gleitzer and J. B. Goodenough, Structure and Bonding 61 (1985) 1.
[16] M. Takano et al., J. Phys. Colloq. 40 (1979) C2-313.
[17] T. Shinjo et al. "FERRITES: Proc. Int. Conf. Sept.-Oct. 1980, Japan" (Cen. Acad. Pub., Japan, 1981) 383.
[18] Y. Takeda et al., J. Solid State Chem. 63 (1986) 237.
[19] M. Takano et al., J. Solid State Chem. 73 (1988) 140.
[20] C. P. Tavares, Mat. Res. Bull. 20(1985) 979.
[21] C. N. R. Rao et al., J. Solid State Chem. 67 (1984) 266.
[22] M. Khairy et al., J. de Physique 47 (1986) C1-831.
[23] J. D. Jorgensen et al., Phys. Rev. B38 (1988) 11337.
[24] Z. Hiroi et al., Phys. Rev. B41 (1990) 11665.
[25] Y. Takeda et al., Mat. Res. Bull. 25 (1990) 293.
[26] G. Bednorz and K. A. Muller, Z. Phys. B64 (1986) 188.
[27] Y. Tokura et al., Nature 337 (1989) 345.
[28] M. Takano et al., Physica C 159 (1989) 375.
[29] T. Siegrist et al., Nature 334 (1988) 231.
[30] R. D. Shannon , Acta. Cryst. A32 (1976) 751.
[31] H. Okada et al., Physica C 166 (1990) 111.
[32] H. Okada et al., Phys. Rev. B in press.

M. Norton: Have you studied the pressure dependence of $CaFeO_3$ to find if it becomes metallic?

M. Takano: Mossbauer measurements under pressure are being done now. I suppose that the charge disproportionation will fade away and that a metallic state results.

A. Navrotsky: Are the oxygen contents of $SrFeO_3$ and $CaFeO_3$ controlled by the synthesis conditions? Did you ever get more than three oxygens?

M. Takano: $CaFeO_3$ was prepared from $CaFeO_{2.5}$ ($Ca_2Fe_2O_5$) sealed in a gold tube together with an oxygen releaser, $KClO_4$: the tube was heated at about 1000°C under 20 kb. $SrFeO_3$ needs an oxygen pressure above 500 b. For the both the oxygen content does not go beyond three.

R. J. Cava: What are the magnetic properties of $CaFeO_3$?

M. Takano: It is an antiferromagnet with a $T_N = 115$ K. The neutron diffraction pattern is quite similar to that of $SrFeO_3$. It suggests that $CaFeO_3$ also has a screw spin structure resulting from a competition between the ferromagnetic nearest neighbor interaction and the antiferromagnetic second- and fourth-nearest neighbor interactions as in $SrFeO_3$.

A. Nath: Did you observe Fe^{4+} in low spin state in any other compound?

M. Takano: Yes, in an oxygen deficient phase, $SrFeO_{2.75}$. An oxygen vacancy creates a pair of Fe^{3+} ions on either side of it, while the Fe ions coordinated octahedrally strongly attract oxygen ions and the spin state becomes low spin state. Even in the magnetically ordered state of $SrFeO_{2.75}$ the low spin Fe^{4+} ions show only a broad single line in the spectrum.

P. D. Battle: How do you recognize Fe^{4+} in low spin state?

M. Takano: From the (nearly) nonmagnetic character seen in the Mossbauer spectrum. A low spin Fe^{4+} has $S = 1$ and $L = 1$, and a nonmagnetic ground state with $J = 0$ results.

P. D. Battle: But the moment would increase quickly as a function of temperature, wouldn't it?

M. Takano: Mossbauer measurements on $SrFeO_{2.75}$ were made only at 300 K and 4 K. At 4 K the low spin state ions shows only a broad single line.

National Institute of Standards and Technology Special Publication 804, Chemistry of Electronic Ceramic Materials, Proceedings of the International Conference held in Jackson, WY, August 17-22, 1990, issued January 1991.

IMPURITY INCORPORATION MECHANISMS IN $LiNbO_3$

Dunbar P. Birnie, III
Department of Materials Science and Engineering
University of Arizona, Tucson, AZ 85721

ABSTRACT

Impurity incorporation mechanisms in lithium niobate are discussed. It is concluded that the simplistic electrical charge misfit considerations may in fact control site occupancy for impurities. Divalent Fe, Mg, and Mn are found to sit on lithium sites. Trivalent Fe sits on lithium sites and hexavalent W sits on niobium sites. The general observation of 3-fold axial defects in EPR is attributed to the internal electric field aligning point defect clusters on cooling.

INTRODUCTION

The impurity incorporation mechanism often controls the behavior of impurities in crystals. This is especially important for impurities such as Fe and Mg which have technicological importance in holographic storage and optical waveguide device studies.

Iron is interesting because of its two valence states that can be changed using oxidation and reduction treatments. This behavior activates the photo-refractive effect (PRE) that is important for optical damage in waveguide devices.

Magnesium is important in reducing optical damage in optical waveguide devices and for growing high quality single crystals without striations.

Information about other impurities may help shed light on general trends related to impurity incorporation. Therefore, this paper will review what is known about impurity substitution in lithium niobate.

Important in this discussion is knowledge about the native point defects that dominate this system. This will give us a basis for understanding what possible charge compensation mechanisms can occur when defects dissolve into lithium niobate.

UNDOPED LITHIUM NIOBATE

The low temperature, ferroelectric, phase of lithium niobate is a derivative of the hexagonal corundum structure of Al_2O_3. The lithium and niobium atoms substitute for the two octahedral Al atoms in the structure. The substitution is performed such that each near-neighbor Li-Nb pair are aligned in parallel. Thus, along the c-axis there are columns of octahedral sites which are 2/3 filled [1]. The arrangement causes the crystal to have some net spontaneous polarization characteristic of ferroelectric materials.

All three of the possible octahedral sites (lithium site, niobium site, and vacant site) along the c-axis are quasi-octahedral and thus would form quite similar spatial environment for impurity atoms.

Lithium niobate exhibits a large range of nonstoichiometry. This behavior is indicative of large levels of point defects being present in the crystal. One interesting aspect of the nonstoichiometry is that it occurs only to the Nb-rich side of the phase diagram [2-5]. The extent of nonstoichiometry can be up to several percent, depending on the temperature of equilibration.

The mechanism for the nonstoichiometry in this system has been determined using single crystal X-ray diffraction [6]. It was found that at room temperature the niobium excess is accomodated with niobium atoms sitting on lithium sites (Nb_{Li}) combined with vacant niobium sites (V_{Nb}). The concentrations of the two defects are present in levels such that global charge neutrality is maintained in the crystal. Both defects may be present in large concentrations because of the wide single phase field. The niobium antisite and niobium vacancy have net charges of +4 and -5 respectively.

One interesting consequence of these large native point defect levels is that under most circumstances lithium niobate will be intrinsic; impurity defects present at low concentrations will often be insignificant compared to the native defect concentrations. Only when the doping level becomes larger than the nonstoichiometry will the impurity start to define the defect chemistry. This is important because for low level doping we will expect that the impurity will substitute for only one of the two sites rather than a mixture of the two sites.

It is conspicuous that there is little or no nonstoichiometry to the Li-rich side of the phase diagram. This is compatible with the above stated defects being present and other defects being difficult to form

in the lattice.

With these large concentrations of charged point defects we may expect some large degree of defect association during cooling from high temperature. This rearrangement and clustering of point defects in crystals is quite common in ionic crystal structures. Clustering can occur between the native point defects and also with the impurity atoms at whatever level they are present.

The ferroelectric nature of lithium niobate may affect the orientation of defect clusters that may form on cooling. The parallel alignment of the Li-Nb pairs in the structure defines some spontaneous polarization along the c-axis direction in the lattice. This generates an internal electric field in the opposite direction which could orient defect clusters. This can occur because a clustered defect pair will consist of one positive and one negative defect, bound electrostatically which will respond as a small electrical dipole. The positive defects will tend toward the negative c-axis direction and the negative defects will tend oppositely.

In summary, we expect significant concentrations of niobium atoms sitting on lithium sites that are charge balanced by vacant niobium sites. These will be charged positive and negative, respectively. For low doping levels these two defects will define the bulk charge neutrality at room temperature. But, impurity defects that may be present in low levels may become electrostatically bound to these defects, creating cluster defects after cooling from the crystal growth condition. Also, it is possible that some preferential orientation of defect clusters will occur such that dipolar defects are aligned along the c-axis direction in the crystal.

The following sections will describe information relating to the preferred incorporation site for several impurities in lithium niobate. Clustering and charge balance considerations will be discussed for all cases. The most conclusive data comes from X-ray diffraction crystal structure determinations.

IRON

The most abundantly studied impurity in lithium niobate is iron. This is because of its importance as an identified cause of optical damage in waveguide devices. Part of the optical damage problem that arises with iron is that it has two stable oxidation states (either 2+ or 3+).

In principle these two ions could substitute in

different locations, however, it appears that both occupy lithium sites in the lattice. Field annealing has shown that both ferrous and ferric ions migrate toward the negative electrode, showing that they are indicates that they both substitute for Li [7].

For either valence of iron, substitution onto the lithium site creates a net-positive defect. At low levels of iron present the material is intrinsic so no change in the bulk charge neutrality condition will occur. However, there could be some electrostatic clustering of the positive iron defects with the negative V_{Nb} defects that will be present. If the internal electric field caused these to align primarily oriented along the c-axis, then the many of axially symmetric EPR identifications can be explained.

MAGNESIUM

Little information about the magnesium atom site is available because it has only one stable valence state which is not paramagnetic. However, one single-crystal X-ray diffraction structure determination has shown that the magnesium also substitutes for lithium [8]. The sample used had a magnesium concentration that was above "threshold" and showed magnesium atoms on lithium sites charge balanced by vacant niobium defects. The above threshold concentration indicates that the Mg_{Li} defects were controlling the defect chemistry rather than being intrinsic.

MANGANESE

Although there are many spectroscopic investigations of Mn in lithium niobate, most techniques can only say that the manganese ions sit at axially symmetric sites (which could be Li or Nb sites). However, an EXAFS determination has shown that Mn substitutes for lithium [9]. EXAFS is sensitive to some radial distribution function of neighboring atoms in the structure, including second neighbors. Therefore the Li and Nb sites can be differentiated, even though their local symmetry is identical. Charge balance should be similar to that found for low levels of iron as discussed above.

TUNGSTUN

One X-ray diffraction determination of a tungstun-containing solid solution exists [10]. The W atoms were found to occupy the niobium sites in lithium niobate. The peak intensities in powder diffraction were very

similar to those found for pure lithium niobate, whereas if the W had substituted for Li the peak intensities would have been significantly different.

This 6-valent impurity will also make a net-positive type defect when substituted for niobium. Therefore, at the large concentrations found in their crystals, the material was no longer intrinsic; likely charge balancing defects would be niobium vacancies.

DISCUSSION

The most likely simple model for site selection is based on simple considerations of charge misfit; low valence ions are often attributed to substitute for Li and high valence ions are often attributed to sit on Nb sites. Based on the few identifications above, this seems to be qualitatively true. Atom size arguments can probably be ignored because the Li and Nb sites are both octahedral and of similar size.

The charge misfit argument leaves unclear the preferred location for normally trivalent impurities which will be net two charges negative or positive, depending on substitution site.

One convenient substitution mechanism for trivalent atoms could be simultaneous substitution onto the lithium and niobium sublattices, forming near-neighbor charge-balanced pairs on adjacent Li and Nb sites. This may in-fact be happening for doping levels where the material is no longer intrinsic.

In both low and high doping levels there will be point defects present that have the opposite sign to the impurity defect. As discussed above, these can form cluster defects on cooling to room temperature. And, the internal electrical field in the ferroelectric phase can cause alignment of these dipoles along the c-axis of the crystal [11]. This can explain the axially symmetric defects often observed in various spectroscopic techniques.

Of the above impurity defects all divalent atoms (Fe, Mg, and Mn) substitute onto the lithium site. This is compatible with the charge misfit argument for site substitution. This trend might easily apply to many or all other divalent cations.

The only trivalent atom is Fe^{3+} which is found to substitute for lithium also, although the behavior at high concentrations has not been fully characterized. Since there are no other trivalent impurity atoms well enough characterized, we cannot conclude that many or most will also substitute for lithium.

There are no 4-valent atoms that have well characterized locations (although Ti is often qualitatively assigned to the niobium site). Finally, the 6-valent substitution is found on the niobium site, again in line with simple electrostatic considerations.

CONCLUSIONS

The divalent impurities, Mn, Fe, and Mg are all found to substitute for lithium. The trivalent Fe also replaces lithium. And, W replaces niobium. All of these observations are compatible with simple electrostatic charge misfit arguments. However, this still leaves uncertainty about all other ion substitutions, especially in the intermediate valence range.

REFERENCES

1) S. C. Abrahams, J. M. Reddy, and J. L. Bernstein, J. Phys. Chem. Solids 27, 997-1012 (1966).
2) J. G. Bergmann, A. Ashkin, A. A. Ballman, J. M. Dziedzic, H. J. Levinstein, and R. G. Smith, Appl. Phys. Lett. 12, 92-94, (1968).
3) P. Lerner, C. Legras, and J. P. Dugas, J. Crystal Growth 3, 231-35, (1968).
4) L.O. Svaasand, M. Ericksrud, G. Nakken, and A.P. Grande; J. Crystal Growth 22, 230-2, (1974)
5) S. G. Boyer and D. P. Birnie, III, Ceramics and Inorganic Crystals for Optics, Electro-Optics and Non-Linear Conversion, pp73-80, SPIE Proc. 968, (1988).
6) S.C. Abrahams and P. Marsh; Acta Cryst. B42, 61-8 (1986).
7) G. E. Peterson, A. M. Glass, and T. J. Negran; Appl. Phys. Lett. 19, 130 (1971).
8) H.-R. Tan, C.-F. He; Ceramics and Inorganic Crystals for Optics, Electro-Optics and Non-Linear Conversion, pp48-53, SPIE Proc. 968, (1988).
9) C. Zaldo, F. Agullo-Lopez, J. Garcia, A. Marcelli, and S. Mobilio, Sol. St. Comm. 71, 243 (1989).
10) G. Blasse and A. D. M. dePauw, J. Inorg. Nucl. Chem. 32, 3960 (1970).
11) G. H. Jonker and P. V. Lambeck, Ferroelectrics 21, 641 (1978).

National Institute of Standards and Technology Special Publication 804, Chemistry of Electronic Ceramic Materials, Proceedings of the International Conference held in Jackson, WY, August 17-22, 1990, issued January 1991.

ALKALINE EARTH NITRIDES AND HYDRIDES

Nathaniel E. Brese
Department of Chemistry
Arizona State University
Tempe, AZ 85287-1604

INTRODUCTION

Nitride and hydride materials have been overlooked in favor of oxide materials, since many are difficult to synthesize and are quite sensitive to humidity. However, their polymorphism, crystal chemistry, and physical properties (including superconductivity in transition metal nitrides such as MoN approaching 30K) are fascinating. The structures of alkaline earth nitrides and hydrides are reviewed here. The strontium system has proved the most controversial; our recent results are therefore emphasized as they are illuminating. The $PbCl_2$ structure adopted by most of the hydrides is discussed in terms of cation packing and bond valences.

NITRIDES

The composition M_3N_2 is expected for all alkaline earth nitrides as this would provide for normal oxidation states for all the atoms. The local coordination geometries required by the stoichiometry include 4- and 6-coordinated or 6- and 9-coordinated M and N atoms, respectively. The antibixbyite structure affords tetrahedral sites for the metal atoms and octahedral sites for the nitrogen atoms.

Beryllium nitride is polymorphic, although the normal form crystallizes with the antibixbyite structure (1, 2, 3, 4). The

transition temperature is roughly 1400°C (5) and the high-temperature form is based on close-packed layers of Be atoms in the sequence CCHCCH; the nitrogen atoms fill the octahedral holes (6). The local coordination geometries are preserved, but the material is no longer cubic. The high-temperature compound reported by Eckerlin contained trace amounts of Si; whether the presence of Si is an integral part of the beta form is unknown. Microscopy on the Be_3N_2-Si_3N_4 system revealed intergrowth structures in the $BeSiN_2$-Be_3N_2 system (7).

Magnesium nitride forms with the antibixbyite structure. It is easily prepared from the elements or from reactions of Mg metal with ammonia at elevated temperatures (1, 8, 9, 10).

The normal, brown calcium nitride (α-Ca_3N_2) has the antibixbyite structure (11). However, black hexagonal β-Ca_3N_2 and yellow orthorhombic γ-Ca_3N_2 are also known by their powder patterns (12). A pernitride, Ca_3N_4, has been reported (13, 14). The structure of a green subnitride, Ca_2N, was solved from single-crystal X-ray data, although the crystal was lost and impossible temperature factors resulted, since no absorption correction could be made (15, 16). A reddish-brown compound with composition $Ca_{11}N_8$ has been prepared from Ca_3N_2 at 1050°C (17); the refinement of the X-ray data was poor. Since $Ca_{11}N_8$ is extremely air-sensitive, we believe it may be an oxynitride. A nitride hydride phase with the rocksalt structure (random distribution of hydrogen atoms determined by neutron diffraction) is also reported (18, 19). The black imide, CaNH, has the rocksalt structure (20).

The strontium nitrogen system does not exhibit as many phases as the calcium one. Three nitrides have been reported, Sr_2N, Sr_3N_2, and SrN. The primary difficulty in characterizing these materials is determining the levels of oxygen and hydrogen impurity (16, 21).

Sr_2N has the anti-$CdCl_2$ structure (22) and has been the subject of considerable discussion (16). Since the conducting behavior

of Sr_2N was in question (23, 24), many assumed that hydrogen was located between the layers analogous to Ca_2NCl and Ca_2NBr (stuffed $CdCl_2$ structure) (25).

Using a very clean system, we recently prepared Sr_2N and showed by neutron diffraction that there is no hydrogen between the layers, further that Sr_2N is a weak metallic conductor, and that it exhibits temperature-independent paramagnetic behavior (26, 27). The slabs of edge-sharing NSr_6 octahedra are squashed while the vacant octahedra between slabs are elongated. (This is exactly converse to the situation in Ag_2F in which elongated FAg_6 octahedra are rationalized by Ag···Ag bonding.) We find that Sr_2N is the only stable phase in the binary system.

SrN is reported with the rocksalt structure (28), but its lattice parameter is similar to both SrO (29) and SrNH (20). Brice proposed that SrN is really a solid solution $SrN_{1-x}H_x \cdot nSrO$ ($0.02 < n < 0.08$) (16); it may also be a simple oxynitride (30). This seems likely, since the only time we observed a rocksalt phase was when the nitriding apparatus was contaminated with moisture.

The expected composition Sr_3N_2 has been observed by several workers (2, 31, 32), and its diffraction pattern has been indexed on a centered monoclinic cell (21, 33, 34). The pattern, however, closely resembles a mixture of Sr_2N and SrN (elemental analysis of an equimolar mixture would have the composition Sr_3N_2). Motte believes Sr_3N_2 to contain significant amounts of hydrogen (21). Gaudé and Lang have been unable to prepare this composition as well (35). As we have been unable to prepare this compound, I feel that the existence of Sr_3N_2 is still an open question.

Ba_3N_2 can be prepared as a stoichiometric compound (2, 31, 36, 37). Numerous workers have collected diffraction patterns (38, 39), but only Linke was able to index a hexagonal cell (13). Linke's data, however, differ significantly from those collected

by others and by us. The main problem lies in the broad peaks found on the diffraction pattern. Our attempted neutron diffraction analysis suffered from the same problem. Attempts to recrystallize Ba_3N_2 at temperatures from 700-1000°C and 4-20 kbar have so far been unsuccessful.

HYDRIDES

By comparison, the hydrogen-alkaline earth system is simple. MgH_2 crystallizes with the rutile structure (40) and CaH_2, SrH_2, and BaH_2 crystallize with the $PbCl_2$ structure (41, 42, 43, 44). The rutile structure allows for no variation in bond length, but the $PbCl_2$ ($C23$) structure type allows for unusually short and long bonds (45). Although SrH_2 was originally assigned its own structure type ($C29$) on the basis of an x-ray structure determination in 1935 (41), our neutron experiments show it to be better described as $C23$.

The $PbCl_2$ structure is generally described as cations centering tricapped trigonal prisms. However, we find that describing structures in terms of anion-centered polyhedra can be revealing (46, 47). We use SrD_2 as an example.

Figure 1 shows the traditional view of SrD_2 (cation centered polyhedra) while Figure 2 displays the hexagonal eutaxy of the cations with tetrahedral sites filled by anions.

The ratio of apparent valence (bond valence sums) of the tetrahedral and octahedral anion is much greater than unity for the alkaline earth hydrides. This ratio gets higher as one progresses down the periodic table (1.65-1.81 for Ca-Ba). It is suggested that nonbonded metal···metal interactions contribute to the stretching of the octahedral bonds (giving a low apparent valence at the octahedral site). One expects more metal···metal interactions with larger metal atoms, and this idea is supported by the valence ratio trend.

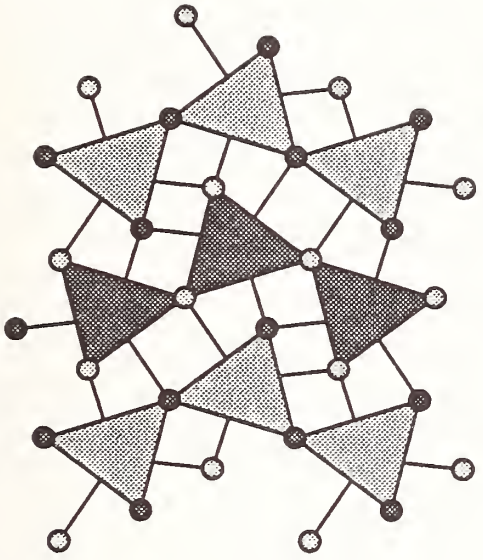

Fig. 1 SrD_2 showing Sr-centered tricapped trigonal prisms. D atoms are at 0 and 1/2.

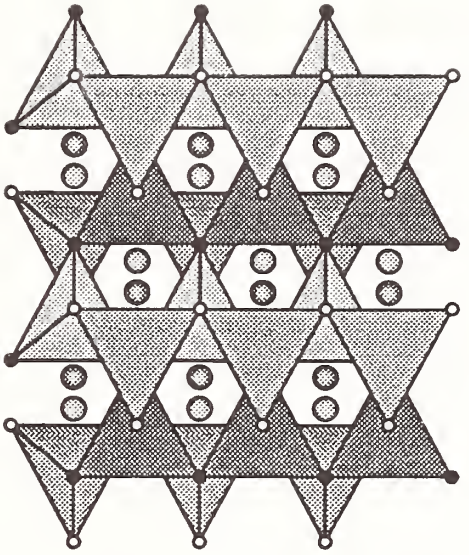

Fig. 2 SrD_2 showing $D(1)Sr_4$ tetrahedra. Large balls are D(2) atoms.

NITRIDE HYDRIDES?

The only definite compounds observed in the Sr-N-H system are those with N-H bonds, the imide (SrNH) and the amide ($SrNH_2$). Nitride hydrides, M_2NH (M=Ca,Sr,Ba), have been suggested with structures analogous to Ca_2NCl (stuffed $CdCl_2$-type structures) and rocksalt (18). The only quantitative structure determination was that for Ca_2NH which reportedly crystallizes with a superstructure of rocksalt, although H atoms partially occupy general positions (19).

ACKNOWLEDGEMENTS

This material is based upon work supported under a National Science Foundation Graduate Fellowship to NEB and is part of a continuing program in crystal chemistry supported by the National Science Foundation (grant number DMR 8813524 to M. O'Keeffe).

REFERENCES

1. B. Neumann, C. Kröger and H. Haebler, *Z. anorg. allg. Chem.* **204**, 81 (1932).
2. A. v. Antropoff and K. H. Krüger, *Z. Phys. Chem. A* **167**, 49 (1933).
3. M. v. Stackelberg and R. Paulus, *Z. Physik. Chem., Abt. B* **22**, 305 (1933).
4. P. Chiotti, *J. Amer. Ceram. Soc.* **35**, 123 (1952).
5. P. Eckerlin and A. Rabenau, *Z. anorg. allg. Chem.* **304**, 218 (1960).
6. D. Hall, G. E. Gurr and G. A. Jeffrey, *Z. anorg. allg. Chem.* **369**, 108 (1969).
7. T. M. Shaw and G. Thomas, *J. Solid State Chem.* **33**, 63 (1980).
8. J. David, Y. Laurent and J. Lang, *Bull Soc. fr. Mineral. Cristallogr.* **94**, 340 (1971).
9. J. David, *Rev. Chim. Minér.* **9**, 717 (1972).
10. D. R. Glasson and S. A. A. Jayaweera, *J. Appl. Chem.* **18**, 77 (1968).
11. P. Y. Laurent, J. Lang and M. T. LeBihan, *Acta Crystallogr.* **B 24**, 494 (1968).
12. Y. Laurent, J. David and J. Lang, *C. R. Acad. Sci. Paris* **C259**, 1132 (1964).
13. K. Linke and H. Lingmann, *Z. anorg. allg. Chem.* **366**, 89 (1969).
14. K. Linke and H. Lingmann, *Z. anorg. allg. Chem.* **366**, 82 (1969).
15. E. T. Keve and A. C. Skapski, *Inorg. Chem.* **7**, 1757 (1968).
16. J.-F. Brice, J.-P. Motte and J. Aubry, *Rev. Chim. minér.* **12**, 105 (1975).
17. Y. Laurent, J. Lang and M. T. L. Bihan, *Acta Crystallogr.* **B25**, 199 (1969).
18. J.-F. Brice, J.-P. Motte and J. Aubry, *C. R. Acad. Sci. Paris* **C276**, 1093 (1973).
19. J. Brice, J. Motte, A. Courtois, J. Protas and J. Aubry, *J. Solid State Chem.* **17**, 135 (1976).

20. H. Hartmann, H. J. Frohlich and F. Ebert, *Z. anorg. allg. Chem.* **218**, 181 (1934).
21. J. Motte, J. Brice and J. Aubry, *C. R. Acad. Sci. Paris* **C274**, 1814 (1972).
22. J. Gaudé, P. L'Haridon, Y. Laurent and J. Lang, *Bull. Soc. fr. Mineral. Cristallogr.* **95**, 56 (1972).
23. S. M. Ariya, E. A. Prokofyeva and I. I. Matveeva, *J. Gen. Chem. USSR* **25**, 609 (1955).
24. F. Hulliger, "*Structural Chemistry of Layer-type Phases*," D. Reidel, Dordrecht, Holland (1976).
25. C. H. H. Herdejürg, *Z. anorg. allg. Chem.* **545**, 177 (1987).
26. N. E. Brese and M. O'Keeffe, *J. Solid State Chem.* **87**, 134 (1990).
27. S. M. Ariya, M. S. Erofeeva and G. P. Mochaloy, *J. Gen Chem USSR* **27**, 1806 (1957).
28. J. Gaudé, P. L'Haridon, Y. Laurent and J. Lang, *Rev. Chim. Minér.* **8**, 287 (1971).
29. W. Primak, H. Kaufman and R. Ward, *J. Amer. Chem. Soc.* **70**, 2043 (1948).
30. J. Gaudé and J. Lang, *Mat. Res. Bull.* **7**, 193 (1972).
31. A. Guntz and F. Benoit, *Ann. Chim.* **20**, 5 (1923).
32. J. Gaudé and J. Lang, *C. R. Acad. Sci. Paris* **C271**, 510 (1970).
33. H. Emons, D. Anders, G. Roewer and F. Vogt, *Z. anorg. allg. Chem.* **333**, 99 (1964).
34. J. Gaudé and J. Lang, *Rev. Chim. Minér.* **7**, 1059 (1970).
35. J. Gaudé and J. Lang, *Rev. Chim. Minér.* **9**, 799 (1972).
36. Y. Okamoto and J. C. Goswami, *Inorg. Chem.* **5**, 1281 (1966).
37. R. C. Blair and Z. A. Munir, *J. Chem. Eng. Data* **16**, 232 (1971).
38. K. Torkar and H. T. Spath, *Monat. Chem.* **98**, 2020 (1967).
39. J. Gaudé and J. Lang, *C. R. Acad. Sci. Paris* **C274**, 521 (1972).
40. W. H. Zachariasen, C. E. J. Holley and J. F. J. Stamper, *Acta Crystallogr.* **16**, 352 (1963).
41. E. Zintl and A. Harder, *Z. Elektrochem.* **41**, 33 (1935).
42. J. Bergsma and B. O. Loopstra, *Acta Crystallogr.* **15**, 92 (1962).

43. A. F. Andresen, A. J. Maeland and D. Slotfeldt-Ellingsen, *J. Solid State Chem.* **20**, 93 (1977).
44. W. Bronger, S. Chi-Chien and P. Müller, *Z. anorg. allg. Chem.* **545**, 69 (1987).
45. M. O'Keeffe and N. E. Brese, *in prep* (1990).
46. M. O'Keeffe and B. G. Hyde, *J. Solid State Chem.* **44**, 24 (1982).
47. M. O'Keeffe and B. G. Hyde, *Structure Bonding* **61**, 77 (1985).

National Institute of Standards and Technology Special Publication 804, Chemistry of Electronic Ceramic Materials, Proceedings of the International Conference held in Jackson, WY, August 17-22, 1990, issued January 1991.

OXYGEN DIFFUSION IN Y_2O_3-CONTAINING TETRAGONAL ZIRCONIA POLYCRYSTALS (Y-TZP)

Yasuro Ikuma
Kanagawa Institute of Technology, Atsugi, Kanagawa 243-02, Japan

ABSTRACT

Oxygen diffusion coefficient in Y_2O_3-containing tetragonal ZrO_2 polycrystals (Y-TZP) (2.75% Y_2O_3) was determined at 600-800°C using ^{18}O as a tracer. The measurement was performed on the specimens with different grain sizes, 0.35-2.6μm, which was resulted in almost identical oxygen diffusion coefficients suggesting that there was no fast diffusion along the grain boundaries in Y-TZP. It was also found that the oxygen diffusion in Y-TZP is in good agreement with the electrical conductivity data of the same material. However, it was faster than the oxygen diffusion in tetragonal ZrO_2 doped with 14 mol% CeO_2.

INTRODUCTION

A discovery of superplasticity in Y-TZP [1,2] has introduced a new type of processing method into ceramics; In some cases ceramics could be formed by plastic deformation. This superplasticity is thought to be caused by grain boundary sliding [3]. Since diffusion is related to the grain boundary sliding and zirconia is an oxygen ion conductor, we would anticipate that the diffusion plays an important role in the superplasticity of this material. However, oxygen lattice diffusion coefficient of Y-TZP has never been determined. The objective of this study is to determine the oxygen lattice diffusion coefficient of Y-TZP and to compare with the oxygen lattice diffusion in tetragonal and cubic zirconia.

EXPERIMENTAL

ZrO_2 doped with 2.75 mol% Y_2O_3 was sintered at 1400°C for 2h and then it was pressed by HIP at 1400°C for 1.5h in an atmosphere that consists of 96% Ar and 4% O_2. Some of the specimens were

annealed at 1500 or 1600°C in air in order to grow the grain size. Grain sizes of these specimens were determined by examination of fractured surface under SEM or the observation of thin section under TEM. The x-ray diffraction analysis revealed that the original specimen consisted of 100% tetragonal ZrO_2 (t-ZrO_2). After annealing, however, the specimen consisted of 89% and 86% tetragonal ZrO_2 for 0.42μm and 2.6μm, respectively. The specimens were cut into spheres of 2mm in diameter. Their surface was finished with #1200 diamond.

Density of specimens used in the diffusion experiment was 6.08g/cm^3. The fracture stress of the specimen was 1450MPa. Microstructure of the specimen without annealing is shown in Fig. 1. The grains are uniform in size and are equiaxed. No pores are seen in the figure indicating that the specimens are closed to the theoretical density.

Specimen was placed in a Pt crucible and heated to 600-800°C in $^{16}O_2$ atmosphere until no weight change could be observed. The specimen was cooled down to room temperature and ^{18}O was introduced into the system. It was reheated to the same temperature. An exchange reaction shown by:

$$t\text{-}Zr^{16}O_2 + {}^{18}O_2 = t\text{-}Zr^{18}O_2 + {}^{16}O_2 \qquad (1)$$

took place, which was followed by a subsequent diffusion of ^{18}O into the bulk of specimen. The whole process was monitored by a microbalance. Readers are referred to elsewhere [4,5] for the experimental detail.

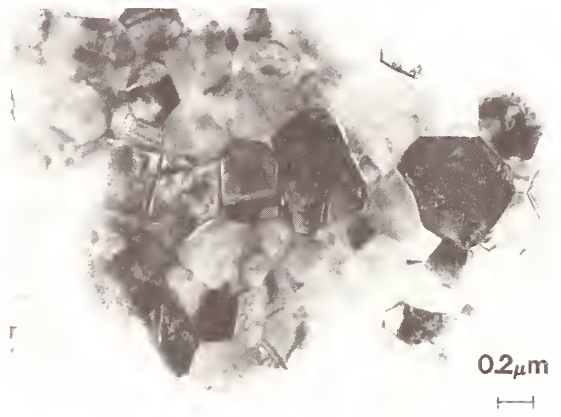

Figure 1. Transmission electron micrograph of Y-TZP (2.75 mol% Y_2O_3, grain size = 0.35μm).

RESULTS AND DISCUSSION

Typical results of diffusional annealing of specimens were shown in Fig. 2 for the specimens with 0.35μm in grain size. M_t in the figure is the total amount of ^{18}O in a specimen at time t and M_∞ is the corresponding quantity after an infinite time. Consequently if the diffusion was completed, M_t/M_∞ would be unity. The data points are concave up within a short annealing time. This implies that the exchange reaction at the surface of specimen was not fast enough as compared to the diffusion process in the bulk. The consequence of this is that we have to use an equation [6] for diffusion from a well-stirred solution of limited volume into a sphere when the equilibrium at the surface proceeds at a finite rate. We tried to fit the data to the equation. The curves in the figure were the results of such calculation. Since the calculated results were in good agreement with experimental data, the value of D (diffusion coefficient) used for the calculation of the curve was assigned [7] to the oxygen diffusion coefficient at the experimental condition.

The diffusion coefficients obtained in this manner are plotted in Fig. 3. The diffusion coefficients from various grain sizes are shown in the figure. It is evident that the grain size has little effect on the diffusion coefficient of this material [8]. This is one of the experimental results which indicate that the grain boundary diffusion in t-ZrO_2 is not enhanced over the lattice diffusion coefficient. A similar observation was reported [9,10] for cubic ZrO_2 (c-ZrO_2). The result in this study,

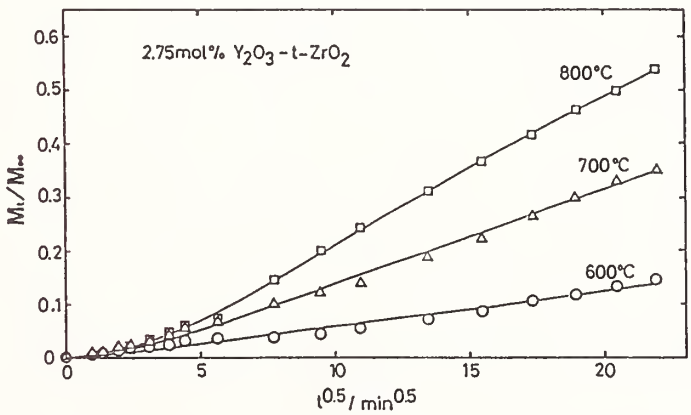

Figure 2. Typical results of diffusional annealing of Y-TZP (2.75 mol% Y_2O_3, grain size = 0.35μm).

consequently, is the oxygen lattice diffusion coefficient ($D_{l,O}$) in Y-TZP. There is some scatter in the data at low temperatures (600-650°C). According to the phase diagram [11] of this system, 600°C at 2.75mol% Y_2O_3 is really in a contradictory region. The system may have crossed into the two-phase region (tetragonal and monoclinic). The concentration of Y_2O_3 in monoclinic ZrO_2 (m-ZrO_2) would be smaller than the concentration of it in tetragonal ZrO_2. This might be one of the factors that contribute to the low oxygen diffusivity in m-ZrO_2. That could be the cause of the scatter in the data. A least square fit to the data yields:

$$D_{l,O} = 1.24 \times 10^{-1} \exp[-137 kJmol^{-1}/RT] \ cm^2 s^{-1} \qquad (2)$$

It is the oxygen lattice diffusion coefficients in Y-TZP.

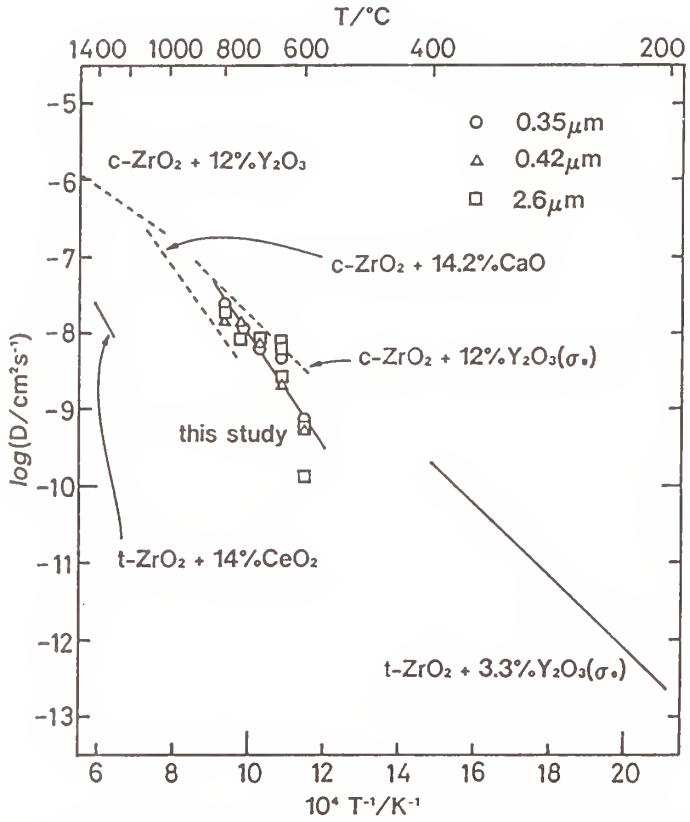

Figure 3. The diffusion coefficients in Y-TZP. Also shown are tracer diffusion in t-ZrO_2 doped with 14% CeO_2 [12], c-ZrO_2 doped with 12% Y_2O_3 [10] and c-ZrO_2 doped with 14.2% CaO [9] and diffusivity calculated from electrical conductivity of Y-TZP (3.3 mol% Y_2O_3) [14] and c-ZrO_2 doped with 12% Y_2O_3 [13].

In Figure 3 also shown are the oxygen lattice diffusion coefficients in cubic ZrO_2 doped with Y_2O_3 [10] and CaO [9] and tetragonal ZrO_2 doped with CeO_2 [12]. The diffusion coefficients calculated from the electrical conductivity data of cubic zirconia doped with Y_2O_3 [13] and tetragonal zirconia doped with Y_2O_3 (Y-TZP) [14] are also included in the figure. The results of current study are in good agreement with the electrical conductivity data for Y-TZP (3.3 mol% Y_2O_3) [14]. In calculating the diffusion coefficients with the use of Nernst-Einstein equation, it was assumed that correlation factor was unity. That may have shifted the diffusivity from the electrical conductivity to higher value by a factor of about 4. Considering that the measurements were not performed over the same temperature range, the agreement of these data is excellent.

Extending the diffusion data of t-ZrO_2 doped with 14% CeO_2 [12] to the lower temperature we found that it is smaller than the results of this study. Doping ZrO_2 with Y_2O_3

$$Y_2O_3 = 2Y_{Zr}' + 3O_O^X + V_O^{\cdot\cdot} \qquad (3)$$

the concentration of $V_O^{\cdot\cdot}$ would be increased [15]. That would in tern enhance the oxygen lattice diffusion. Doping ZrO_2 with CeO_2 will not have this kind of effect. Some cerium atoms in ZrO_2 could be in 3+. However, the results in the figure 3 suggest that most of cerium atoms are in 4+.

Oxygen lattice diffusion in c-ZrO_2 doped with Y_2O_3 [10] was determined at temperatures higher than 1000°C. Extending their results to lower temperatures, it agrees well with the data of Stratton et al. [13] who have determined the electrical conductivity of c-ZrO_2 doped with 12 mol% Y_2O_3. The diffusivity calculated from the conductivity for c-ZrO_2 agrees fairly well with the current results. This is rather surprising because the concentration of impurities are quite different among these two oxides; 2.75% vs. 12%. Since the oxygen lattice diffusion in calcia stabilized ZrO_2 at 14.2 mol% CaO [9] is also in the same orders of magnitude, there might be a saturated value for the diffusion of oxygen in ZrO_2. It will be increased to a higher value if zirconia is doped with Y_2O_3. However, the concentration of Y_2O_3 seems to have little effect on diffusivity once certain amount of Y_2O_3 is exceeded. This is true for any kinds of additives. At higher concentration of additives, a defect complex would be formed. It is one of the factors which limit the diffusivity at high concentration of additives.

CONCLUSIONS

The oxygen lattice diffusion coefficient in Y-TZP is determined over the temperature range, 600-800°C. It did not depend upon the grain size of the specimen suggesting that there is no fast diffusion along the grain boundaries. The diffusivity is in good agreement with the diffusion coefficient calculated from the electrical conductivity measurement in Y-TZP. It was also in the same orders of magnitude as the diffusion of c-ZrO_2 doped with Y_2O_3 or CaO.

ACKNOWLEDGMENTS

The author acknowledges Dr. T. Masaki of Toray Industries, Inc. for providing the samples and Y. Tsubaki for carrying out the experiments. This work was supported in part by the Japanese Ministry of Education, Science and Culture under contract of Priority Areas "Advanced Inorganic Materials."

REFERENCES

1. F. Wakai, S. Sakaguchi, Y. Matsuno, Adv. Ceram. Mater., 1[3] 259 (1986).
2. F. Wakai, S. Sakaguchi, H. Kato, Yogyo-Kyokai-Shi, 94[8] 721 (1986).
3. F. Wakai, T. Nagano, J. Mater. Sci., in press.
4. W. Komatsu, Y. Ikuma, Z. Phys. Chem. N. F., 131, 79 (1982).
5. Y. Ikuma, W. Komatsu, Adv. Ceram., 10, 464 (1984).
6. H. S. Edwards, A. F. Rosenberg, J. T. Bittel, Report No. ASD-TDR-63-635 (1963) Wright-Patterson Air Force, Ohio.
7. Y. Ikuma, W. Komatsu, Mater. Sci. Forum, 29, 199 (1988).
8. Y. Ikuma, Y. Tsubaki, J. Ceram. Soc. Japan, submitted.
9. L. A. Simpson, R. E. Carter, J. Am. Ceram. Soc., 49[3] 139 (1966).
10. Y. Oishi, K. Ando, in "Transport in Nonstoichiometric Compounds", eds. G. Simkovich and V. S. Stubican (Plenum Publ., 1985), p. 189.
11. H. G. Scott, J. Mater. Sci., 10[9] 1527 (1975).
12. K. Ando, S. Morita, R. Watanabe, Yogyo-Kyokai-Shi, 94[8] 732 (1986).
13. T. G. Stratton, D. Reed, H. L. Tuller, Adv. Ceram., 1, 114 (1981).
14. N. Bonanos, E. P. Butler, J. Mater. Sci. Lett., 4, 561 (1985).
15. Y. Ikuma, K. Komatsu, W. Komatsu, Adv. Ceram., 24, 749 (1988).

National Institute of Standards and Technology Special Publication 804, Chemistry of Electronic Ceramic Materials, Proceedings of the International Conference held in Jackson, WY, August 17-22, 1990, issued January 1991.

A STRUCTURAL BASIS FOR THE DIFFERENT DIRECTIONS OF OXYGEN NONSTOICHIOMETRY IN La_2CuO_4 AND Nd_2CuO_4

D. J. L. Hong and D. M. Smyth, Materials Research Center
Whitaker Lab #5, Lehigh University, Bethlehem, PA 18015

ABSTRACT

La_2CuO_4 is an oxygen-excess, p-type semiconductor while Nd_2CuO_4 is oxygen-deficient and n-type. Since they contain the same amount of the same oxidizable and reducible cation, their different behavior must be attributed to their different crystal structures. It is shown that the major distinction is that there is a favorable site for interstitial oxygen in the La_2CuO_4 structure, but not in the closely-related structure of Nd_2CuO_4.

INTRODUCTION

La_2CuO_4 and Nd_2CuO_4 have played important roles in the development of high temperature superconductors based on complex Cu oxides. Ba-doped La_2CuO_4 was the first such material discovered (1), and was the forerunner of an extensive family of cuprate superconductors whose chemistry is dominated by acceptor-doped, oxygen-excess, p-type compositions. Superconductivity has subsequently been discovered in Nd_2CuO_4 that was donor-doped and reduced (2). This was the first n-type copper oxide to exhibit superconductivity.

The different treatments given to La_2CuO_4 and Nd_2CuO_4 to achieve a superconducting state are also reflected in their different tendencies to become nonstoichiometric. Their high temperature, equilibrium conductivities as a function of oxygen activity are displayed in Fig. 1. It is seen that the equilibrium conductivity of La_2CuO_4 increases with increasing oxygen activity indicating oxygen-excess, p-type behavior, while that of Nd_2CuO_4 increases with decreasing oxygen activity indicating oxygen-deficient, n-type behavior. Clearly, the stoichiometric compositions for these two oxides are displaced laterally along the oxygen activity axis such that Nd_2CuO_4 is stoichiometric at a much higher oxygen activity than is La_2CuO_4. The superconducting states are achieved by doping and equilibrating these materials in a way that augments their natural tendency toward nonstoichiometry.

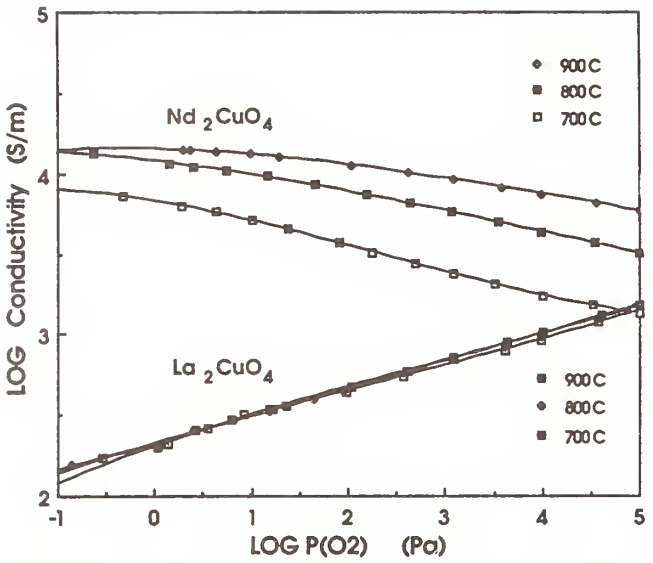

Figure 1. The equilibrium electrical conductivities of undoped La_2CuO_4 and Nd_2CuO_4 measured as a function of oxygen activity.

The stoichiometric composition of an oxide corresponds to the condition that the electron and hole concentrations are equal ($n = p$), and is the boundary between oxygen-excess nonstoichiometry with excess holes, and oxygen-deficient nonstoichiometry with excess electrons (3). The equilibrium conductivity will have its minimum value at the oxygen activity corresponding to the stoichiometric composition, insofar that the electron and hole mobilities are equal. It is possible to derive an expression for the equilibrium oxygen activity at the stoichiometric composition from the mass-action expressions for the equilibrium oxidation and reduction reactions. If it is assumed that anion Frenkel defects are the most favorable lattice defects, and that the ionic defects are fully ionized, the oxidation reaction can be written as

$$V_I + 1/2\ O_2 \rightleftharpoons O_I'' + 2h^{\bullet} \qquad (1)$$

and the corresponding mass-action expression is

$$[O_I'']\ p^2 / [V_I] = K_{ox} e^{-\Delta H_{ox}/kT} P(O_2)^{1/2} \qquad (2)$$

The appropriate reduction reaction is

$$O_o \rightleftharpoons 1/2\ O_2 + V_o^{\cdot\cdot} + 2e' \qquad (3)$$

with the mass-action expression

$$[V_o^{\cdot\cdot}]\ n^2/[O_o] = K_{red}\ e^{-\Delta H_{red}/kT}\ P(O_2)^{-1/2} \qquad (4)$$

The two mass-action expressions can be equated for the stoichiometric condition n = p, and solved for the corresponding equilibrium oxygen partial pressure, $P(O_2)^o$, i.e. the oxygen partial pressure at the conductivity minima (4)

$$P(O_2)^o = \left\{ \frac{[O_I'']^o [O_o]^o}{[V_I]^o [V_p^{\cdot\cdot}]^o} \right\} \frac{K_{red}}{K_{ox}} \exp\ [\Delta H_{ox} - \Delta H_{red})/kT] \qquad (5)$$

where the superscript zero denotes the situation at the stoichiometric composition. The term in braces is a small factor near unity. It is seen that the dominant factor is the relative magnitude of the enthalpies of oxidation and reduction. If the enthalpic cost of oxidation is large relative to that of reduction, then the stoichiometric composition will occur at relatively high oxygen activities, and the material will favor oxygen-deficient, n-type behavior at oxygen partial pressures of 1 atm and below.

The magnitudes of the enthalpies will depend on two main factors:

1. The ease with which the ionic components of the material can be chemically oxidized or reduced, i.e. a redox factor.

2. The ease with which the ionic defects that result from nonstoichiometry can be accommodated within the lattice, i.e. a structural factor.

If the individual enthalpies can be taken as the sum of these two components, then $\Delta H_{ox} = h_p + h_{int}$, where the latter two terms represent the enthalpic contributions from the formation of holes and of oxygen interstitials, and $\Delta H_{red} = h_n + h_{vac}$, where the latter two terms correspond to the formation of electrons and oxygen vacancies. Comparison of the exponential terms in Eq. (5) for La_2CuO_4 (unprimed symbols) and Nd_2CuO_4 (primed symbols) can be written as

$$h_p + h_{int} - h_n - h_{vac} \quad \underline{vs.} \quad h'_p + h'_{int} - h'_n - h'_{vac} \tag{6}$$

Since both compounds contain exactly the same amount of the same oxidizable and reducible species, Cu^{++}, the h_p and h_n terms should be similar for both and the comparison is reduced to only the structural contributions

$$h_{int} - h_{vac} \quad \underline{vs.} \quad h'_{int} - h'_{vac} \tag{7}$$

Their different behavior would then seem to result primarily from their different crystal structures. Even though the two compounds have the same generic formula, and their rare earth ions differ in size by less than 5%, they do have different structures, as shown in Fig. 2. It is instructive to examine these structures in some detail to see if there is any apparent reason for a difference in the enthalpic cost of the lattice defects.

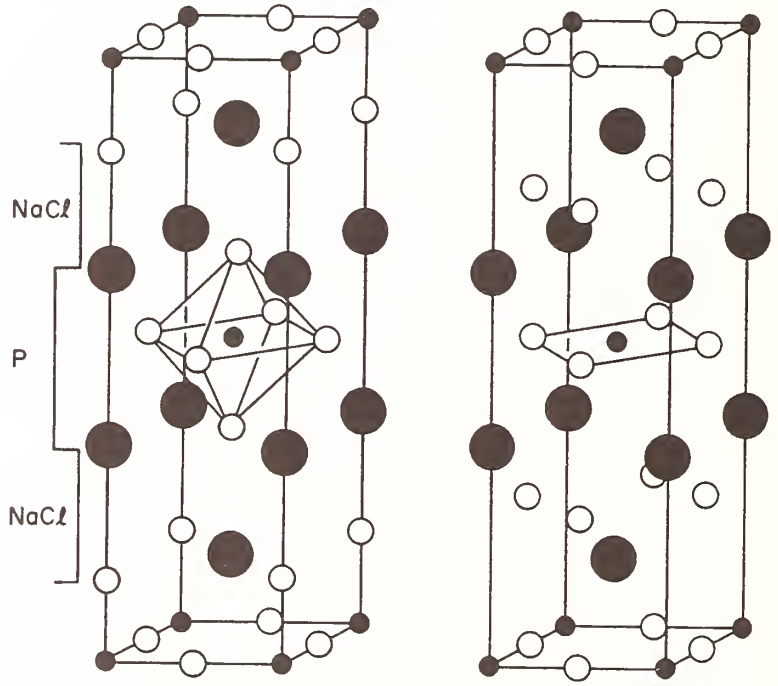

Figure 2. The crystal structures of La_2CuO_4 and Nd_2CuO_4. Small solid circles are Cu; large solid circles are rare earth cations; open circles are oxygens. The alternate NaCl and perovskite (P) layers are indicated for La_2CuO_4.

La_2CuO_4

Undoped La_2CuO_4 has a stoichiometric excess of oxygen when equilibrated in an oxidizing atmosphere such as air or pure oxygen, and can be represented by the more general formula La_2CuO_{4+y}. Recent thermogravimetric studies by Li and Alcock, using hydrogen reduction to La_2O_3 and Cu to obtain absolute compositions, showed that $y > 0$ for oxygen partial pressures between 10^{-4} and 1 atm over the temperature range 750-950°C (5). Appelman et al. found by iodometric titration that $y = 0.007$ for samples equilibrated in air at 1000°C (6). The equilibrium conductivity is in good agreement with these findings, as shown in Fig. 1. The observed dependence of the conductivity on $P(O_2)^{1/6}$ corresponds to the mass-action expression for the oxidation reaction, Eq (2), when this reaction is the major source of charged defects such that $p = 2[O_I'']$. This will be discussed in greater detail elsewhere.

A stoichiometric excess of oxygen can be incorporated either as interstitial ions, as assumed in Eq. (1), or by the formation of cation vacancies. The latter would require vacancies of both cation species, or the exsolution of the oxide of the cation whose vacancy is less-favored. Experimental evidence to be discussed shortly shows that interstitial oxygen is the favored mode of incorporation. The structure of La_2CuO_4, sometimes referred to as the K_2NiF_4 structure, can be viewed as a coherent intergrowth of the NaCl and perovskite structures (7). The corresponding parts of the structure are indicated in Fig. 2. However, interstitial anions are never observed as majority defects in compounds having either the NaCl or perovskite structures, so their presence in La_2CuO_4 appears to be anomalous. This has been resolved recently by powder neutron diffraction studies on the isostructural La_2NiO_{4+y} by Jorgensen et al. (8). Since Ni^{+2} is more easily oxidized than Cu^{+2}, the nickel analog has much higher contents of excess oxygen, with $0.13 < y < 0.18$. This proved to be sufficient to locate the excess oxygen, and it was found to be in the NaCl part of the structure, as shown in Fig. 3. This site corresponds to the tetrahedrally coordinated site in the NaCl part of the structure. In the ideal NaCl structure with close-packed anions of radius R_a, the tetrahedrally coordinated site will accommodate an ion of radius $0.225R_a$. This should be much too small to accommodate an interstitial anion. However, in La_2CuO_4, the NaCl part of the structure is far from the close-packed prototype in which the octahedral sites contain an ideal cation of radius $0.414R_a$. In fact, La^{+3} is approximately the same size as O^{--}, and the anion sublattice is forced to expand far beyond the close-packed case. Thus instead of having the ideal NaCl packing as shown in

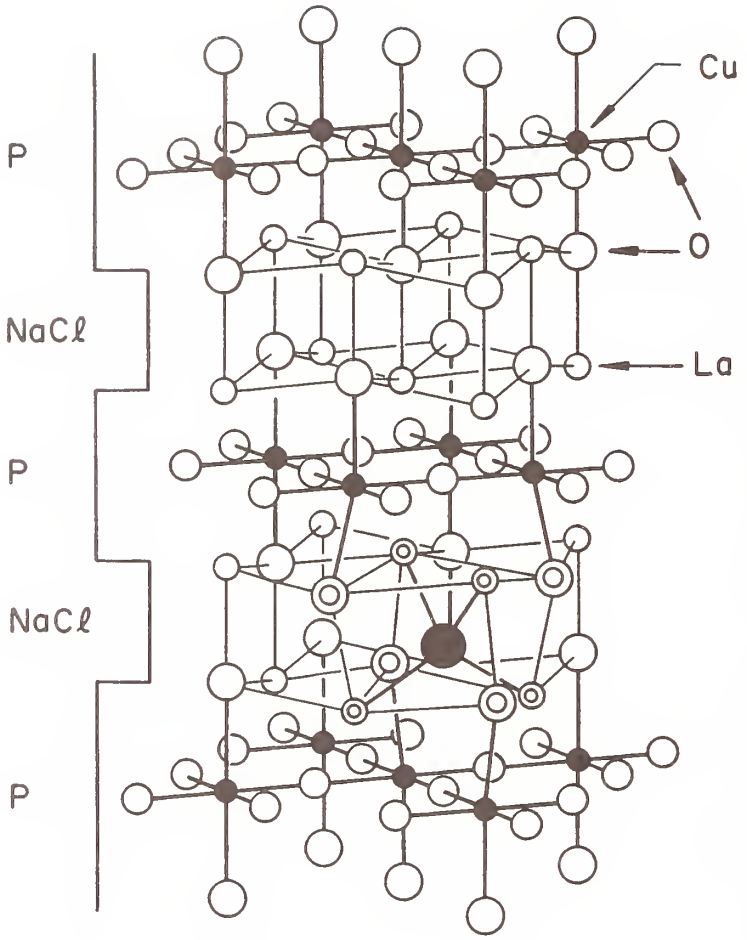

Figure 3. La_2NiO_4 showing the interstitial oxygen (large solid circle) and the distorted cube of nearest neighbors (double circles). Adapted from Ref. (8).

Fig. 4a, the situation is more accurately represented by Fig. 4b. As the cation in the NaCl structure approaches the anion in size, the tetrahedrally coordinated sites expand by more than a factor of 3 to a radius of $0.732R_a$. In other words, the tetrahedrally coordinated site takes on the character of the body-centered site in a simple cubic structure with the cube corners alternately occupied by cations and anions. This relieves the size constraints on the incorporation of interstitial anions. Jorgensen et al. also found that the surroundings of the interstitial anion are distorted so that the four cations are closer (average distance 0.2395 nm) than the four anions (average distance 0.2625 nm) so that the electrostatic environment is more hospitable for the interstitial anion. The observed oxygen-excess, p-type behavior of La_2CuO_4 is related to the presence of an accessible interstitial site for excess anions.

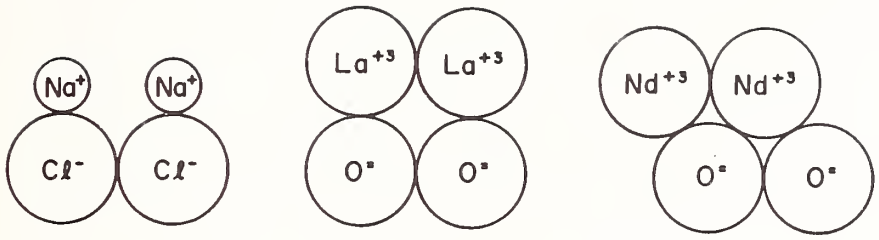

a. NaCℓ (220) b. La_2CuO_4 c. Nd_2CuO_4

Figure 4. (a) Side view (220 plane) of the ideal NaCl structure with $R_c = 0.414R_a$. (b) Side view of NaCl-type part of the La_2CuO_4 structure with $R_c = R_a$. (c) The lateral shift of a pair of ions that gives the more effective space-filling of the Nd_2CuO_4 structure.

When La_2CuO_4 is acceptor-doped, as in $La_{2-x}Sr_xCuO_{4-x/2}$, the material is even more easily oxidized to an oxygen-excess, p-type state, because of the ease of filling the extrinsic oxygen vacancies

$$V_o^{\cdot\cdot} + 1/2\ O_2 \rightleftharpoons O_o + 2h^{\bullet} \qquad (8)$$

This oxidation reaction actually reduces the concentration of lattice defects and is thus energetically more favorable than the oxidation of the undoped material where the number of lattice defects is increased, as shown in Eq. (1). Thus while Fig. 1 shows that there is essentially no temperature dependence to the equilibrium conductivity for the undoped material, indicating that $\Delta H_{ox} \approx 0$, the oxidation of the acceptor-doped material is exothermic, so that the oxygen content increases with decreasing temperature. This is another example of the importance of the enthalpic cost of forming the lattice defects.

Nd_2CuO_4

The equilibrium conductivity of undoped Nd_2CuO_4 shows oxygen-deficient, n-type behavior as shown in Fig. 1. The conductivity increases with decreasing oxygen partial pressure as expected for the loss of oxygen according to Eq (3).

When the cations and anions are about the same size, the NaCl structure is not an effective way to fill space, as shown in Fig. 4b. More efficient packing can be accomplished by

translating adjacent layers so that the ions in one layer fit into the interstices of the next, as shown in Fig. 4c. This is approximately the response of the Nd_2CuO_4 structure where the anions on the cell edges in one of the NaCl layers in La_2CuO_4 move onto the faces where they can move up between the large cations in the adjacent layer. Since this increases the net anion occupancy in this layer to 2 (4 anions on faces instead of on edges), the apex anions from the CuO_6 octahedra in La_2CuO_4 have dropped into this anion layer in Nd_2CuO_4, leaving the Cu in four-fold, planar coordination. Schematic cross-sections through these anion planes are shown for the two structures in Fig. 5. In La_2CuO_4, there is a La^{+3} in the center of the four edge oxygens. In Nd_2CuO_4, the oxygens on the faces intrude further toward the center, and the Nd^{+3} is extruded from the remaining restricted space in this plane toward the adjacent Cu-O plane. As a result of the rearrangement of the NaCl pattern in La_2CuO_4 to the more effective packing of Nd_2CuO_4, the c-axis of the latter is shorter by 7.6%, more than can be accounted for by the replacement of La^{+3} by the slightly smaller Nd^{+3}.

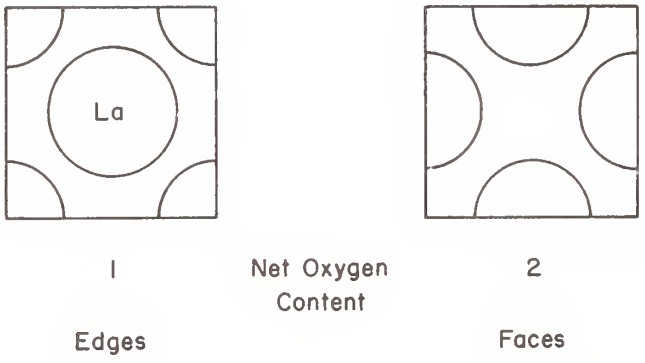

Fig. 5. (a) Cross-section through a NaCl-type layer in La_2CuO_4 with oxide ions on the cell edges and lanthanum in the center. (b) The corresponding shifted layer of oxide ions in Nd_2CuO_4 that have moved to the faces without a central cation.

In Nd_2CuO_4, the space that was available for interstitial anions in La_2CuO_4 is now occupied by the shifted oxygens and can no longer accommodate excess oxygen. By this reasoning, one might look for a possible interstitial site back at the vacated edge in Nd_2CuO_4. However, as shown in Fig. 6, this site is now electrostatically very unfavorable because it is surrounded by 8 other anions and a single Cu in the adjacent plane. The large

cations "see" the interstitial site thrcugh the space between four oxygens and are thus quite well screened from the site. Thus this interstitial site is much less favorable than the one in La_2CuO_4.

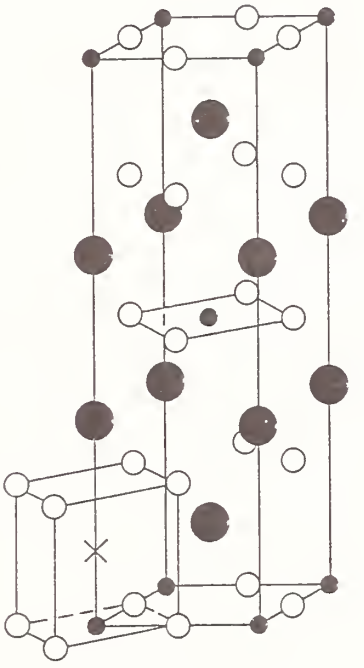

Figure 6. A possible interstitial site (X) in Nd_2CuO_4 near a site normally occupied by oxygen in La_2CuO_4.

One might also consider the apical oxygen sites that are filled in the perovskite layers of La_2CuO_4, but that have been vacated in Nd_2CuO_4, as possible interstitial oxygen sites in the latter compound. However, the adjacent anion layer in Nd_2CuO_4 has twice the anionic charge it has in La_2CuO_4, and it has moved closer to the apical site, making this interstitial site much less favorable. Thus the potential sites for interstitial oxygen in Nd_2CuO_4 are much less favorable than the site in La_2CuO_4. As a result, h'_{int} for Nd_2CuO_4 in Eq. (7) is much larger than h_{int} for La_2CuO_4. Assuming that the h_{vac} terms are comparable, this will displace the stoichiometric composition for Nd_2CuO_4 to much higher oxygen activities so that in the normal experimental range below 1 atm, this material shows only oxygen-deficient, n-type behavior.

When Nd_2CuO_4 is donor-doped, the stoichiometric composition, corresponding to a combination of stoichiometric binaries, will be of the type $Nd_{2-x}Ce_xCuO_{4+x/2}$. Since there is no favorable site in the structure for the excess oxygen, it is expelled under usual conditions, leaving behind electrons

$$2CeO_2 \xrightarrow{(Nd_2O_3)} 2Ce'_{Nd} + 3O_o + 1/2\ O_2 + 2e' \qquad (9)$$

This gives the characteristic n-type behavior of the donor-doped material.

RELATED COMPOUNDS

It has recently been shown that Nd_2NiO_{4+y} normally exists with a stoichiometric excess of oxygen, i.e. with positive values of y (9). Since this compound is isostructural with La_2CuO_4, this is to be expected according to the arguments of this paper, and confirms that the oxygen-deficient, n-type behavior of Nd_2CuO_4 is not related to its Nd content, but to its structure. The major difference between La_2CuO_4 and Nd_2NiO_4 is that the amount of excess oxygen is much greater in the nickelate, because Ni^{+2} is more easily oxidized than is Cu^{+2}

Lightfoot et al. recently determined that $La_{1.25}Dy_{0.75}CuO_{3.75}F_{0.5}$ has the so-called T* structure, in which one end of the unit cell has the La_2CuO_4 structure while the other end has the Nd_2CuO_4 structure (10). Thus the material has favorable sites for interstitial oxygen, but only half as many as in La_2CuO_4. The material was found to exist with a stoichiometric excess of oxygen which was determined by powder neutron diffraction to exist as interstitial oxygen only in the NaCl part of the La_2CuO_4-end of the unit cell. Thus when the unit cells contain elements of both types of structure, the availability of a favorable interstitial site for excess oxygen determines the basic redox balance of the material.

CONCLUSIONS

Since La_2CuO_4 and Nd_2CuO_4 have the same type of formula, and contain the same amount of the same oxidizable and reducible cation, the chemical tendency to oxidize or reduce should be the same. Thus the different directions of oxygen nonstoichiometry observed for the two undoped materials must be attributed to their different crystal structures. It is shown that the primary distinction is that there is a favorable site for interstitial oxygen in the La_2CuO_4 lattice, but not in the Nd_2CuO_4 lattice.

ACKNOWLEDGEMENT

This research was supported by the Division of Materials Research of the National Science Foundation.

REFERENCES

1. J. G. Bednorz and K. A. Müller, Z. für Physik B - Condensed Matter, 64, 189 (1986).

2. E. K. Takayama-Muromachi, Y. Matsui, Y. Uchida, F. Izumi, M. Onoda, and K. Kato, Jap. J. Appl. Phys., 27(12), L2283 (1988).

3. D. M. Smyth, in Selected Topics in High Temperature Chemistry: Defect Chemistry of Solids, O. Johannesen, and A. G. Andersen, Eds., Elsevier, Amsterdam (1989), pp. 1-27.

4. N.-H. Chan, R. K. Sharma, and D. M. Smyth, J. Am. Ceram. Soc., 65(3), 167 (1982).

5. B. Li, Ph.D. Dissertation, University of Notre Dame, March 1990.

6. E. H. Appelman, L. R. Morss, A. M. Kini, U. Geiser, A. Umezama, G. W. Crabtree, and K. D. Carlson, Inorg. Chem., 26, 3237 (1987).

7. D. M. Smyth, in Ceramic Superconductors II, Research Update, 1988, M. F. Yan, Ed., The American Ceramic Society, Inc., Westerville, OH (1988), pp. 1-12.

8. J. D. Jorgensen, B. Dabrowski, S. Pei, D. R. Richards, and D. G. Hinks, Phys. Rev. B, Condensed Matter, 40(4), 2187 (1989).

9. B. W. Arbuckle, K. V. Ramanujachary, Z. Zhang, and M. Greenblatt, to appear in J. Sol. State Chem., 88 (1990).

10. P. Lightfoot, S. Pei, and J. D. Jorgensen, Physica, C169, 15 (1990).

R. Cava: So, Don, you would predict that the neodymium cuprate or any neodymium cuprate structure type cannot be made into a P-type superconductor.

D. Smyth: No, I wouldn't say that. It's just that everything is displaced in oxygen pressure space, and you would have to equilibrate the material in high oxygen pressures.

B. Wuensch: Don, this is not a sling or an arrow. This is support. I don't think you have to be quite so apologetic for an interstitial oxygen in a rock salt-type oxide. There is fragmentary evidence, but a lot of evidence, from creep data and diffusion data that there may be oxygen interstitial as the predominant effect, and also there is the peroxi-center, for example, in barium oxide.

D. Smyth: The peroxide ion is quite a different thing. What type of materials for the creep data?

B. Wuensch: MgO, MgO types, and solid solutions.

D. Smyth: There are processes, like creep or sintering, that require transport of a minority defect. However, I know of no case in which interstitial anion are majority defects in the rock-salt structure.

A. Macker: These materials are also potential candidates for high temperature reagents in solid oxide fuel cells. While we have studied the lanthanum strontium cuprate, but the neodymium cerium cuprate, is also that material which has no phase transition below room temmperature.

D. Smyth: Well, there is some phase separation behavior at low temperatures. We've done our conductivity measurements above 500°C where I don't think that's the case. I don't know whether those types of phase separation at lower temperatures would affect your properties or not.

B. Scott: I want to mention that the Johnson group at Ohio State reported a lanthanum copper oxide, which they get to in quite an unusual way, but reported lanthanum copper oxide with excess oxygen ions in the structure, and it has as much as, I think, 4.33 oxygen.

D. Smyth: I believe that this material is made by a low temperature process, and that the excess oxygen is not thermodynamically stable.

B. Scott: Yes.

National Institute of Standards and Technology Special Publication 804, Chemistry of Electronic Ceramic Materials, Proceedings of the International Conference held in Jackson, WY, August 17-22, 1990, issued January 1991.

RUDDLESDEN-POPPER PHASES $A_{n+1}M_nO_{3n+1}$: STRUCTURES AND PROPERTIES

J.S. Kim, J.Y. Lee, J.S. Swinnea, and H. Steinfink
Materials Science and Engineering, Department of Chemical Engineering,
The University of Texas, Austin, TX 78712,
W.M. Reiff, Department of Chemistry,
Northeastern University, Boston, MA 02115, and
P. Lightfoot, S. Pei, and J.D. Jorgensen,
Argonne National Laboratory, Argonne, IL 60439

INTRODUCTION

Intergrowth crystal structures in inorganic systems have provided a fertile field of solid state chemical research for many years and the discovery of high-T_c superconducting cuprates has focused attention on intergrowth structures based on perovskite blocks. Ruddlesden and Popper (R-P hereafter) (1) have described intergrowth structures with the general formula $Sr_{n+1}Ti_nO_{3n+1}$ where n is the number of perovskite layers separated by SrO layers. Indeed, La_2CuO_4 corresponds to the n = 1 phase in which the decreased ionic charge of the octahedral ion is compensated by the increased ionic charge of the dodecahedral ion.

Numerous structures have been derived from these parent compounds by the replacement of Ti^{4+} with lower valent transition metals and charge compensation with higher valent ions on the alkaline earth site. In this manner the series of compounds $Ln_2AM_2O_7$, Ln^{3+} = La, Nd, Sm, Eu, Gd, Tb, A^{2+} = Sr, Ba, M^{3+} = Mn, Fe, has been synthesized and they are isomorphous with the n = 2 R-P phase (2,3). The replacement of Ti^{4+} by Cu^{2+} to form $La_2SrCu_2O_6$ requires the removal of an oxygen ion for overall charge neutrality. The apical oxygen bridging the two octahedra is missing resulting in layers of copper pyramids whose bases face each other (4). The lowering of the valence of the octahedral ion from 4+ to 3+ is charge compensated by trivalent rare earth ions and maintains the octahedral double layer. However, the replacement of the 4+ ion with Cu^{2+} introduces a modification in the structure by the removal of the apical O^{2-} to create separate copper pyramids. The replacement of $2Ti^{4+}$ in the parent compound by $Fe^{3+}Cu^{2+}$, to create an intermediate valence state +2.5, again causes the removal of an oxygen ion, but now the unshared apex of the octahedron is lost. The structure of $YBaFeCuO_5$ contains double layers of apex-sharing Fe/Cu pyramids separated by a single layer of Y in 8-fold coordination - a fluorite unit (5). Its structural relationship to the R-P parent compound with n=2 is not apparent from the stoichiometry. To emphasize it requires the formula to be written as

$(YBa\square)(FeCu)O_{7-\delta}$, but no cation vacancies exist in this structure. We synthesized a compound that contains the apex-sharing double pyramidal layer as a structural motif and has all the alkaline earth sites filled.

Relatively few compounds with n=3 have been investigated. We have synthesized and investigated the properties of $LaSr_3Fe_3O_{9\pm\delta}$ and report here some of the results.

$Y_2SrFeCuO_{6.5}$

The substitution of 2Y and FeCu for 2Sr and 2Ti in $Sr_3Ti_2O_7$ led to a new phase $Y_2SrFeCuO_{6.5}$. Its crystal structure and magnetic properties were investigated using single crystal X-ray diffraction, powder neutron diffraction, Mössbauer spectroscopy, and magnetic susceptibility measurements. $Y_2SrFeCuO_{6.5}$ is orthorhombic, Ibam, a = 5.4036(8) [5.4149(1)] Å, b = 10.702(1) [10.7244(1)] Å, c = 20.250(2) [20.2799(2)] Å; values in square brackets are neutron data. The structure is derived from the R-P phase $Sr_{n+1}Ti_nO_{3n+1}$ with n = 2. The Fe/Cu atoms occupy randomly the approximate center of oxygen pyramids. The pyramids share the apical bridging oxygen and articulate laterally by corner sharing of oxygen to form a double pyramidal layer perpendicular to *c*. The pyramidal slabs are separated by double layers of Y that are in 7-fold coordination to oxygen, forming a defect fluorite unit, Fig. 1.

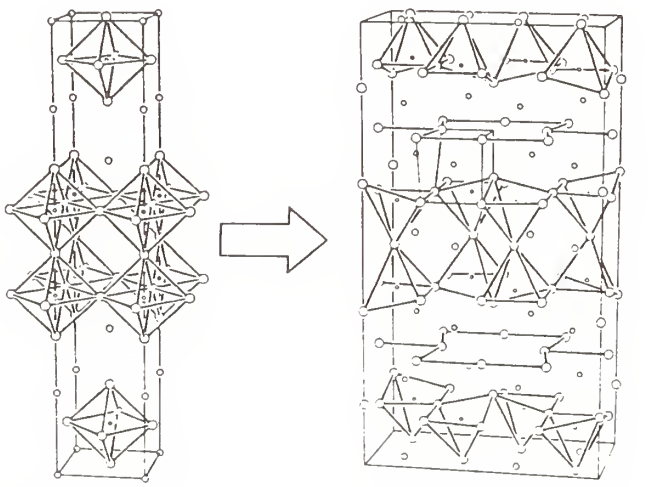

Fig. 1. The evolution of the $Y_2SrCuFeO_{6.5}$ from the parent compound. Large circles are O, smaller circles are Y, and the smallest are Fe/Cu. The defect fluorite unit is outlined around one Y.

The oxygen layer between the Y layers contains a vacant site. The surrounding oxygen ions within the layer and oxygen ions from the pyramidal bases situated above and below the vacant site are displaced toward it and distort the pyramids. The average bond length Sr-10 O is 2.793(10)Å and for Y-7 O is 2.331(6)Å. The Fe/Cu-O distances vary from 1.940(6) to 2.002(2)Å.

Mössbauer spectra indicate a unique iron environment and magnetic ordering at about 265 K. The paramagnetic phase coexists with the magnetic phase over an approximate temperature range 300 - 263 K, characteristic of low dimensionality (1 or 2D) magnetic interactions. The temperature dependence of the molar magnetic susceptibility is consistent with the Mössbauer data and also suggests low-dimensionality with a broad maximum in χ_M vs. T at 260 K. The isomer shift and quadrupole splitting are consistent with Fe^{3+} in 5-fold coordination and H_{int} values also indicate classic high spin Fe^{3+}, Table 1, Fig. 2.

Table 1. Isomer shifts δ*, quadrupole splittings ΔE, and internal fields H_{int} for $Y_2SrFeCuO_{6.5}$.

Temperature (K)	ΔE (mm/sec)	δ	H_{int} (kG)
306	0.56	0.26	0
295.7	0.57	0.25	0
295	0.54	0.25	0
285	0.61	0.28	>0
253.4			252
241.2			270
216.8			333
199.3			362
181.7			385
181.1			382
145.7			418
120.7			440
77			467
4.8			499

*Relative to natural iron metal foil.

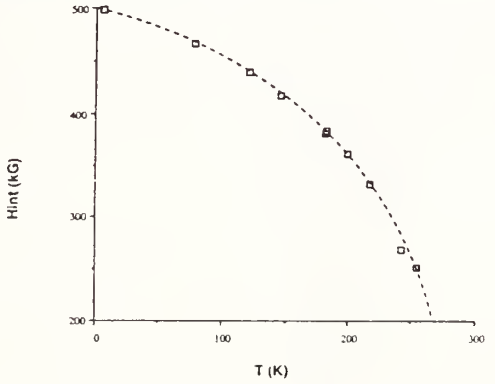

Fig. 2. Internal magnetic field vs. temperature for $Y_2SrFeCuO_{6.5}$

Powder neutron diffraction data at 10K show several new peaks that were absent in the room temperature data. They could be indexed on the basis of a *primitive* unit cell of the same dimensions as the original body-centered cell. Numerous models for the magnetic structure were tried but none accounted satisfactorily for the observed magnetic line intensities. It is interesting to note that no magnetic structural studies of R-P related phases have been reported. These structures ($AO{\cdot}2ABO_3$) may be regarded as intermediate between the 3D perovskite (ABO_3) and 2D Sr_2FeO_4 ($AO{\cdot}ABO_3$) structure types and would be of interest in studying pseudo-2D magnetic properties.

This phase does not display detectable deviation from the 1:1 Fe-Cu ratio. Substitution of 0.20 Ca for Y is possible. This phase can also be synthesized with Gd and Er. It is a semiconductor.

$LaSr_3Fe_3O_{9\pm\delta}$

Compounds based on the parent structure with n = 3, $Sr_4Ti_3O_{10}$, have not been investigated extensively. Brisi and Rolando (6) studied the system Sr-Fe-O and report an oxygen deficient $Sr_4Fe_3O_{10-x}$ phase. We prepared $LaSr_3Fe_3O_x$ by standard ceramic techniques as single phase material by reacting the oxides and carbonates at about 1450°C. A single crystal from the reaction product was selected for the determination of the crystal structure by X-ray diffraction. The compound is isostructural with $Sr_4Ti_3O_{10}$, Fig. 3, but is oxygen deficient, with composition $LaSr_3Fe_3O_{9\pm\delta}$.

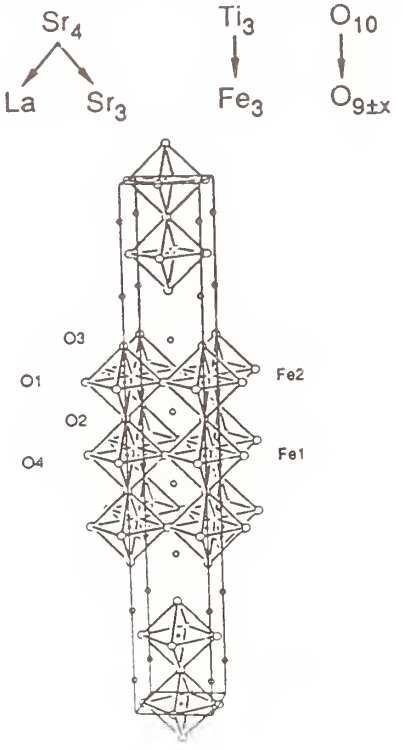

Fig. 3. The structure of $LaSr_3Fe_3O_{9\pm\delta}$. The oxygen vacancies are primarily in the equatorial plane of Fe1. The crystallographically distinct atoms are labled. Sr are shown as small non-bonded circles.

The value of δ is approximately ± 0.25. The oxygen vacancies are concentrated around the central Fe1 octahedron and oxygen can be reversibly intercalated. The equatorial Fe-O lengths for the octahedra are equal, 1.939(5)Å, but the apical Fe1 - O2 lengths for the central octahedron are significantly shorter, 1.8785(2)Å, than for the flanking octahedra. The Fe2 - O2 length of 2.0982(15)Å to the shared O2 is also significantly longer than Fe2 - O3, 2.058(8)Å, to the unshared apex. One La/Sr is in a dodecahedral site and the other crystallographically independent La/Sr is in 9-fold coordination, a monocapped square antiprism. Bond-valence calculations (7) using the expression $V = \sum_i \exp\left(\frac{r_o - r_i}{0.37}\right)$, $r_o\ (Fe^{3+}) = 1.759$, $r_o\ (\frac{1}{4} La^{3+} + \frac{3}{4} Sr^{2+}) = 2.132$, yield +3.92 for Fe1, +3.33 for Fe2, +2.28 for La/Sr1, and +2.20 for La/Sr2. If the oxygen stoichiometry for this phase can be increased to 9.5, the Fe1 most likely becomes the tetravalent ion. The valence sums for La/Sr are equal to the weighted value for the site occupant in the structure.

Mössbauer spectra and magnetic susceptibility data indicate 3D antiferromagnetic ordering temperatures of ~75K for the low oxygen content material and 150 K for the high oxygen content phase. The compound decomposes when oxygen content is less than about 8.6. We have determined that the Sr/La ratio is 3:1 within the limits of second-phase detection by powder X-ray diffraction. This phase forms with La, Nd, Pr, and Gd but not with Er; Ca and Ba do not substitute for Sr.

ACKNOWLEDGMENTS

The first four authors acknowledge the support of the Robert A. Welch Foundation of Houston, Texas, and the Microelectronics and Computer Technology Corporation (MCC) of Austin, Texas. W.M.R. thanks the Northeastern University Research and Scholarship Development and Biomedical Support Funds for support to purchase a cobalt-57 Mössbauer spectroscopy source. The research by P. L., S.P. and J.D.J. is supported by the US Department of Energy, Basic Energy Sciences/Materials Sciences under Contract No. W-31-109-ENG-38 and by NSF Science and Technology Center for Superconductivity Grant No. DMR88-09854. We thank Dr. Joel S. Miller and Mr. Scott McClean of the Central Research and Development Laboratory, DuPont Co., Wilmington, DE for the magnetic susceptibility measurements.

References

1. S. N. Ruddlesden and P. Popper, Acta Cryst., 11, 54 (1958).

2. D. Samaras, A. Collomb, and J. Joubert, J. Solid State Chemistry 7, 337 (1973).

3. M. N. Deschizeaux Cheruy and J. C. Joubert, J. Solid State Chemistry, 40, 14 (1981).

4. N. Nguyen, L. Er-Rakho, C. Michel, J. Choisnet, and B. Raveau, Mat. Res. Bull. 15, 891 (1980).

5. L. Er-Rakho, C. Michel, Ph. Lacorre and B. Raveau, J. Solid State Chemistry, 73, 531 (1988).

6. C. Brisi and P. Rolando, Ann. Chim. (Rome), 59, 385 (1969).

7. I. D. Brown and D. Altermatt, Acta Cryst. B41, 244 (1985).

V. SUPERCONDUCTORS

National Institute of Standards and Technology Special Publication 804, Chemistry of Electronic Ceramic Materials, Proceedings of the International Conference held in Jackson, WY, August 17-22, 1990, issued January 1991.

MICROSTRUCTURES IN HIGH TEMPERATURE SUPERCONDUCTORS

H.W. Zandbergen
National Centre for HREM, Laboratory of Materials Science, Delft University of Technology, Rotterdamseweg 137, 2628 AL Delft, The Netherlands

ABSTRACT

Electron microscopy results of a number of research projects are reviewed, showing the important role electron microscopy can play: studies of several defects in $YBa_2Cu_3O_7$, $(Bi,Tl)_2(Sr,Ba)_2Ca_nCu_{1+n}O_{6+2n}$, and $Pb_2Sr_2(Ca_{1-x}Y_x)_nCu_{2+n}O_{6+2n+\partial}$ have led to successful synthesis of a number of compounds; a high density of [100] 90° rotation twin boundaries in $YBa_2Cu_3O_7$ leads to a decrease in Tc and the superconducting fraction, structural features at the grain boundary can explain the cause of the low critical currents in polycrystalline materials; using detailed analysis of superstructures in $(Bi,Pb)_2Sr_2CaCu_2O_{8+\partial}$ models were postulated, which were confirmed with other techniques.

INTRODUCTION

Microstructures, such as grain boundaries and defects, determine for a major part the properties of materials. For instance grain boundaries in $YBa_2Cu_3O_7$ appear to have a strongly negative effect on the critical current. Unique data can be obtained with electron microscopy, in particular when high resolution electron microscopy (HREM) is combined with element analysis on a nanometer scale.

From different types of research on superconductors quite a number of questions are raised, which can at least partly be answered using electron microscopy. A number of these questions are listed in Table 1.

Table 1. Several questions concerning (micro)structures of superconductors.

Question	Type of EM research required
Which compositions have a change to be stable as new single phase materials?	HREM and Eelement analysis (determine defects)
Can specific physical properties be correlated to a given defect?	TEM, HREM (quantization of defects in well characterized samples)
What are the reasons for the low Jc's in polycrystalline materials?	HREM (study of grain boundaries)
Which defects have good pinning properties?	TEM, HREM (determine density of defects)
What is the nature of thin film/substrate interfaces	HREM and element analysis
What is the cause of the modulated structures, and how can we influence it?	HREM, electron diffraction
What are the solubility ranges?	element analysis, TEM, HREM
What is the distribution of elements over the sample?	element analysis
What are the exact atom positions?	detailed HREM, image processing
What is the valency of the ions?	EELS (but difficult)

For many applications the performance of large scale manifactured high temperature oxide superconductors is still too poor. Thin films, obtained by laser ablation or off-axis sputtering, meet the requirements, but these techniques are often too time-consuming and too expensive. Single crystals are interesting for fundamental research studies but will also be too expensive and too complicated for application. Consequently it is very worthwhile to try to understand the reasons of the poor performance of many of the superconducting materials, in particular polycrystalline materials. Concerning the latter it is important to understand why it shows to have such low critical currents and to find a method of grain boundary engineering to obtain high Jc polycrystalline material.

HREM was carried out with a Jeol 200CX (200 kV, ±10° tilt), a Jeol 4000EX (400 kV, ±20° tilt) or a Philips CM30ST (300 kV, ±25° double tilt). The last electron microscope is equipped with a Link EDX element analysis system. Thin foils for the study of grain boundaries were obtained from pellets by mechanical thinning with dry grinding paper to about 80 μm and further thinning by ion milling. Ion milling was performed on liquid nitrogen cooled specimens with Argon and was started with 20°, 5-6 kV, 2mA and finished with 12°, 3-4 kV, 0.8 mA. For other electron microscopy studies thin specimens were obtained by mounting grounded crystal fragments on carbon coated perforated polymer films supported by a Cu or Au grid.

DEFECTS AS INDICATIONS FOR EXISTANCE OF NEW COMPOUNDS

In Table 2 compounds are listed which were observed as defects in superconductors before the compound itself was synthesized. Only defects in the first two compounds will be discussed here.

Table 2. Defects occurring in parent compounds indicating a new stable compound

Parent compound	Defect observed	New compound	References
$YBa_2Cu_4O_8$	$(CuO)_2$ double layers	$YBa_2Cu_4O_8$	1,2,3
$Bi_2Sr_2CaCuO_2$	extra Ca and CuO_2 layers	$Bi_2Sr_2Ca_2Cu_3O_{10}$	4,5
$Tl_2Ba_2Ca_nCu_{1+n}O_{6+2n}$	single TlO layer	$TlBa_2Ca_nCu_{1+n}O_{5+2n}$	6,7
$Pb_2SrLaCaCu_3O_{8+\partial}$	Ca, CuO_2 layers absent	$Pb_2SrLaCu_2O_{6+\partial}$	8,9
	PbO, Cu layers absent	$Pb_{1-x}Sr_{2+x}(Ca,Y)Cu_2O_6$	10,11

The most frequently observed planar stacking fault in $YBa_2Cu_3O_7$ is a $(CuO)_2$ double layer formed by insertion of an extra CuO layer at the CuO layer between the two BaO layers [1,12,13]. Detailed analysis of HREM images [1] showed that at the defect Cu-O-Cu-O... chains occur in the direction of the displacement required to accommodate the extra CuO layer. These planar stacking faults were observed first as defects formed in $YBa_2Cu_3O_7$ when it is exposed to air at room temperature for some time [1,12] and it was suggested that the formation of these defects is due to the thermodynamical instability of this material in the temperature range 20-500°C. Recently data were published showing $YBa_2Cu_3O_7$ to be unstable below 800°C. Regular intercalation results in a superstructure, which has been observed first in thin films [14-16] and

films [14-15] and near grain boundaries in dense sintered material [14]. Later, it has been found possible to synthesize materials having a regular incorporation of extra CuO layers. Bordet et al [16] reported the existence of $YBa_2Cu_{3.5}O_{7.5}$, in which every second CuO layer is replaced by a $(CuO)_2$ double layer. The existence of such a structure was predicted in one of our early papers [12]. $YBa_2Cu_4O_8$, in which every CuO layer is replaced by a $(CuO)_2$ double layer, has also been synthesized [2,3,17].

When we started our research [4,18] on the superconducting phases in the system Bi_2O_3-SrO-CaO-CuO only the compounds with n=0 (Tc=20K) [19] and n=1 (Tc=80K) [20,21] were known. HREM on a sample partly containing material having a Tc of 110 K, showed the existence of regions having a longer c-axis (3.7 nm), suggesting the existence of a n=2 type material with a Tc of 110 K, which was confirmed by many researchers. Analytical electron microscopy on this sample showed the existence of crystals with a range of compositions, in agreement with the intergrowth of the n=1 and n=2 phase. Further research has revealed that the compounds in these series show a strong intergrowth of lamellae of each of the phases in this system.

STRUCTURE/PROPERTY RELATIONS

Direct evidence of structure property relations in oxide superconductors is still quite scarce. In this paper an example will be given of the influence of [100] 90° rotation twins (see figure 1) on the superconducting properties. Another example reported in literature [22,23] is the presence of many edge dislocations due to interruptions of planar stacking faults, which occur in many thin films and which seem to lead to enhanced flux pinning.

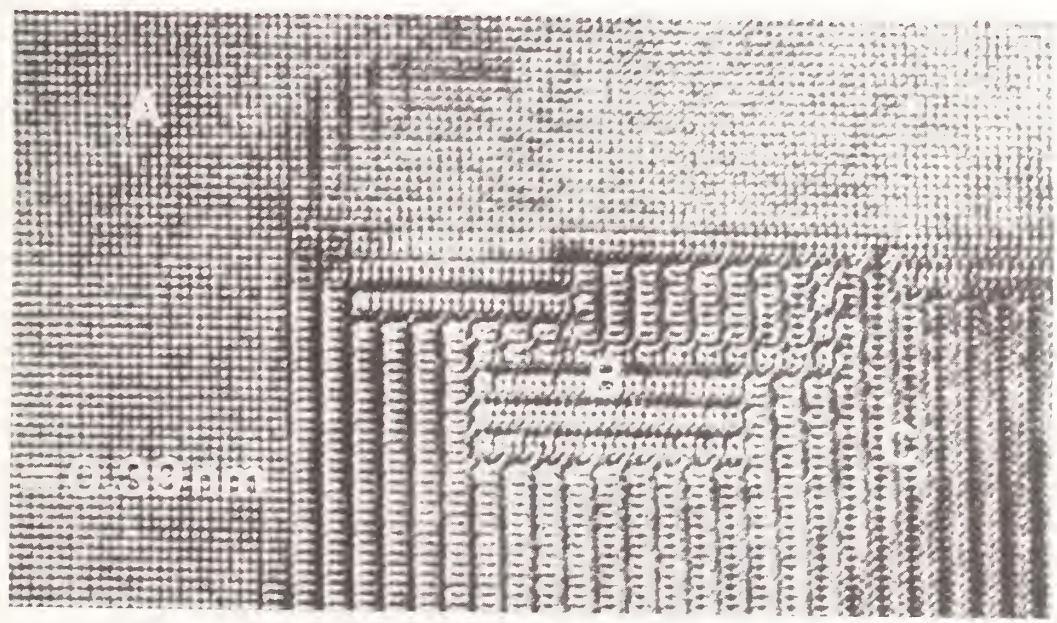

Figure 1. Micrograph of $YBa_2Cu_3O_{7-\partial}$ showing [100] 90° rotation twin boundaries. For A, B, and C regions the c axis is out of the plane, vertical and horizontal respectively.

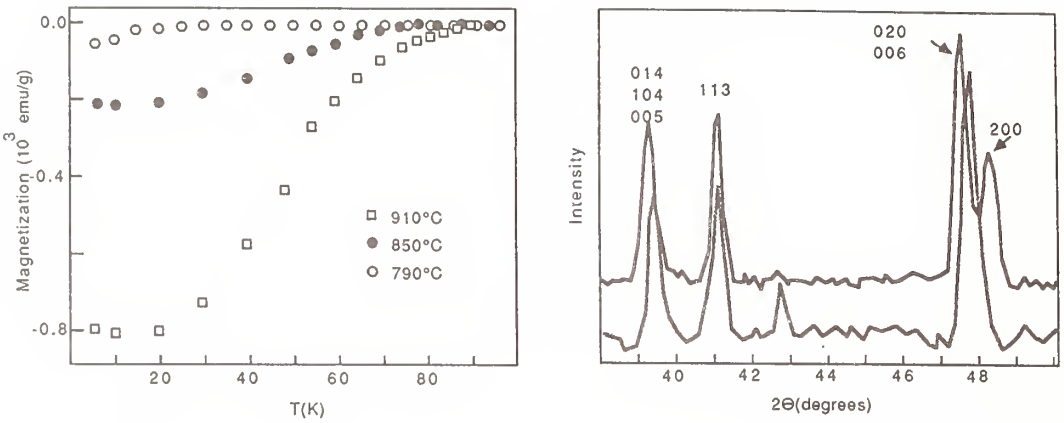

Figure 2. Magnetic susceptibility and X-ray diffraction data of samples of $YBa_2Cu_3O_{7-\delta}$ obtained by heating at various temperatures resulting in different densities of [100] 90° rotation twin boundaries. For high densities the superconducting fraction is very small and the material remains tetragonal (bottom line in X-ray plot).

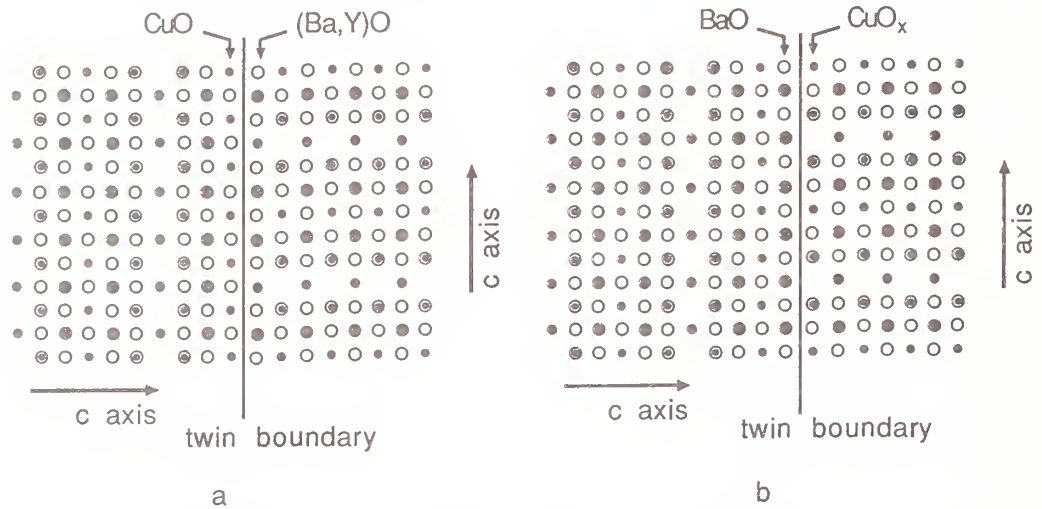

Figure 3. Atomic arrangement at [100] 90° rotation twin boundaries. From HREM images it cannot be determined which one of both structures occurs.

[100] 90° rotation twins occur when the c/a ratio in $YBa_2Cu_3O_7$ -like materials is close to 3. An electron microscopy study has shown [24] that the number of [100] 90° rotation twins increases with decreasing calcination temperature. These twins are formed during the growth of the (tetragonal) crystal are not the result of impinged grain growth.

The presence of pre-existing [100] 90° rotation twins in the tetragonal phase has significant implications. Such twin boundaries act as impediments to the complete transformation the high temperature tetragonal phase to the low temperatur orthorhombic one. This is mainly due to the mismatch between the a axis on the one hand and the b and c/3 axes on the other hand, which will lead to a high number of dislocations, as is observed experimentally [24]. The required

strain energy will at least reduce the free energy decrease accompanying the tetragonal-to-orthorhombic transformation and can completely inhibit the transformation for sufficiently high [100] 90° rotation twin densities. Indeed the larger the twin density the poorer the superconductivity properties are found to be, as can be in figure 2. When the synthesis [25] is done in nitrogen at about 650°C good superconducting orthorhombic $YBa_2Cu_3O_{7-\partial}$ can be obtained after annealing at about 450°C. This shows that the formation of these twins is not due to low diffusion rates at 800°C but must be due to a difference in the structures with various oxygen contents.

The atomic arrangement of these twin boundaries is given in figure 3. Across the twin boundary the sublattice of the Cu ions is continued [26]. Many grain boundaries on a axis oriented thin film have a similar atomic arrangement because many grains have a [100] 90° twin relation. Because the sublattice of the Cu ions are continued across the grain boundary with only a change in direction of the (Ba,Y) sublattice and the oxygen sublattice, this type of grain boundary is expected to be not a weak link. Indeed still high critical currents are observed for a axis oriented thin films [27], even when these films consist of multilayers of superconducting $YBa_2Cu_3O_7$ and non-superconducting $PrBa_2Cu_3O_7$ [28]. Babcock et al [29] report similar results for a bicrystal with one [100] 90° rotation twin boundary.

THE CAUSE OF LOW J_c's IN POLYCRYSTALLINE MATERIALS

Grain boundaries can act as strong pinning centers if the Lorentz force is almost exactly perpendicular to the grain boundary, but they can also act as weak links for currents crossing the grain boundary. Small deviations, inherent to grain boundaries, can strongly influence the performance of superconducting materials. Since the coherence lengths of superconductivity in copper oxides are very small (e.g. 0.4 nm parallel to the c axis and 3 nm perpendicular to the c axis) the wave function of the condensate will decay very rapidly at the grain boundary. Consequently the grain boundary has to be studied on an atomic scale, in order to determine its possible influences on superconducting properties.

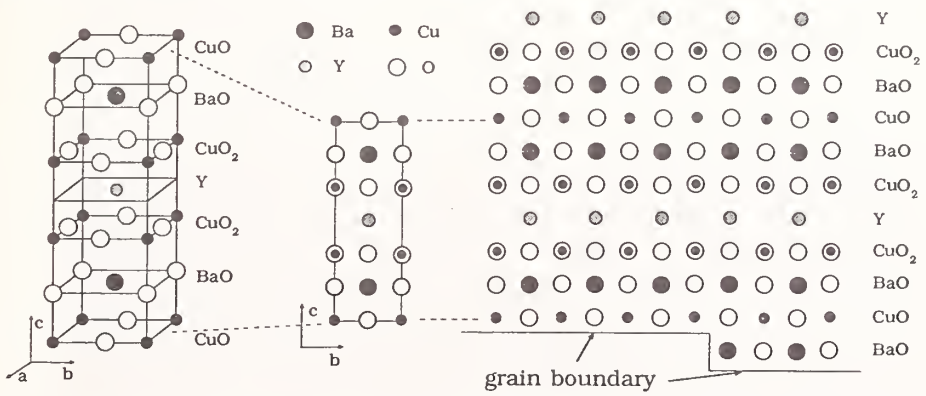

Figure 4. Representation of the atomic arrangement at a (001) grain boundary. The unit cell in perspective view and in [100] projection are given on the left. The grain boundary is either between the BaO and CuO planes or between the CuO_2 and BaO planes.

Electron microscopy studies on grain boundaries in $YBa_2Cu_3O_{7-\partial}$ have been reported by many groups [30-34]. During sintering no amorphous phase is formed [30-32], but such a phase can be formed during annealing [35]. Also agreement exists on the occurrence of dislocations at a number of grain boundaries [32-33], the presence of planar defects near the grain boundaries [35], and cracks, being perpendicular to [001], with a width of 2-8 nm [30,34].

Dimos et al [36] have suggested that dislocations present at low angle grain boundaries are the cause the large drop in J_c of maximum 50 times, as observed in studies of thin films of $YBa_2Cu_3O_{7-\partial}$ on $SrTiO_3$ bicrystals. Babcock et al [29] have reported similar results. It should be noted that the grain boundaries Dimos et al investigated occur only scarcely in polycrystalline $YBa_2Cu_3O_{7-\partial}$. Most of the grain boundaries in $YBa_2Cu_3O_{7-\partial}$ are parallel to (001) of one of the adjacent grains. Also the drop, observed by Dimos et al, is mucl less than the one found for polycrystalline materials (about 1000 times). Consequently other structural features in randomly oriented polycrystalline material must be the cause the very considerable extra drop in J_c.

In randomly oriented $YBa_2Cu_3O_{7-\partial}$ the connecting grain boundaries are for more than 90% parallel to (001) of one of the adjacent grains (see figure 4). It is very plausible that it is this type of grain boundary indeed strongly deteriorates the critical current [35], because the coherence length along the c axis, and thus over (001) grain boundaries, is very small, so that such grain

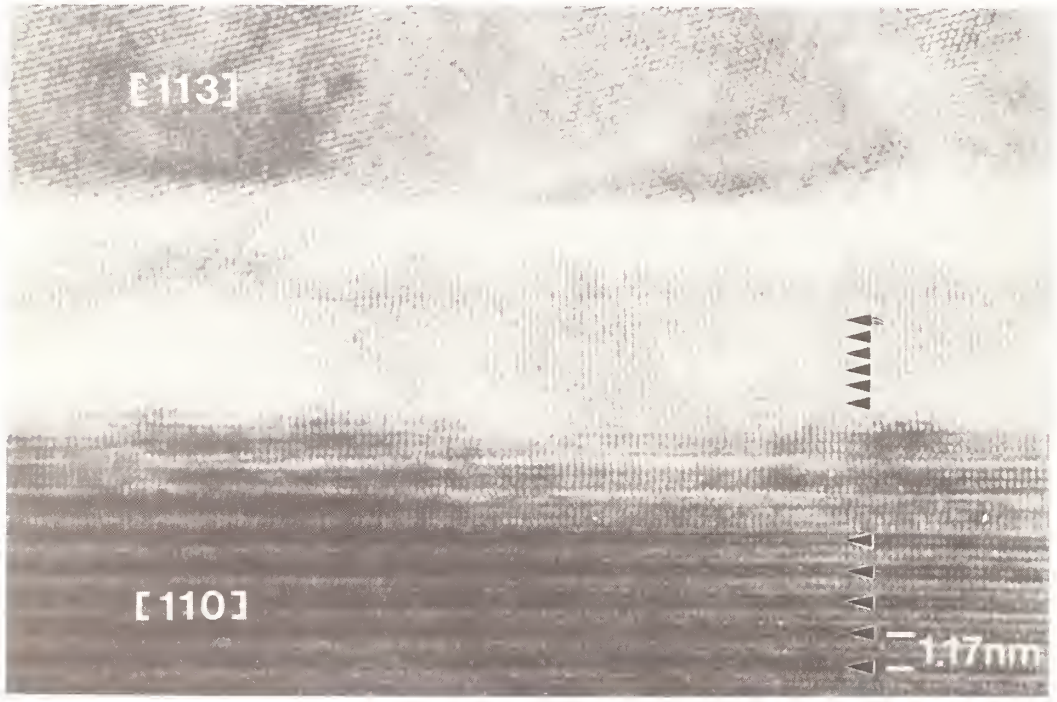

Figure 5. Micrograph of a grain boundary in $La_{1.25}Ba_{1.75}Cu_3O_{7-\partial}$, heated in nitrogen at 950°C for 24 hours, showing the presence of $La_{2-x}Ba_xCuO_4$ at the grain boundary. When this material is heated in oxygen atmosphere no second phase is formed.

boundaries may very well act as a weak links. Also grain boundaries are effected by a decomposition due to the thermodynamical instability of $YBa_2Cu_3O_{7-\partial}$ below 800°C. This is seen most pronounced for $La_{1+x}Ca_{1-x}BaCu_3O_{7-\partial}$, which after annealing at 450°C in air or insufficiently dried oxygen, shows formation of amorphous and crystalline material at many of the grain boundaries (see Figure 5). Similar effects, although less pronounced, are observed for $YBa_2Cu_3O_{7-\partial}$. The thermodynamical instability can also lead to the formation of planar defects, caused by the intercalation of an extra CuO layer.

In this respect the question arises whether grain boundary engineering will finally lead to materials with critical currents high enough for applications. As is shown above, the low critical currents in polycrystalline materials are probably caused by a combination of factors: a dead layer at (001) grain boundaries, dislocations at grain boundaries, and degradation at grain boundaries. It will be difficult to overcome all problems completely. Dominancy of (001) grain boundaries can possibly be prevented using $La_{1+x}Ca_{1-x}BaCu_3O_{7-\partial}$, or sintering at lower temperatures. The structure degradation at grain boundaries is due to the thermodynamic instability below 800°C and is difficult to prevent completely. But a careful choice of annealing temperature, time and atmosphere is expected to lead to an acceptable minimization of the degradation. Dislocations at grain boundaries will be rather difficult to prevent in polycrystalline materials and will be also generated by difference in thermal expansion along the crystal axes.

STRUCTURE ANALYSIS USING HREM IMAGES

In general analysis of defectless structures can be done best with X-ray single crystal diffraction or neutron powder diffraction. However HREM can be very useful in situations where no good diffraction data can be obtained e.g. because no single crystals are present and the material is not suited for powder diffraction because the crystallites are too small, multiply twinned, or contain a superstructure (often not observable with powder diffraction techniques). This will be discussed using the superstructures in the compounds $Bi_2Sr_2CaCu_2O_{8+\partial}$ and $Bi_{1.5}Pb_{0.5}Sr_2CaCu_2O_{8+\partial}$.

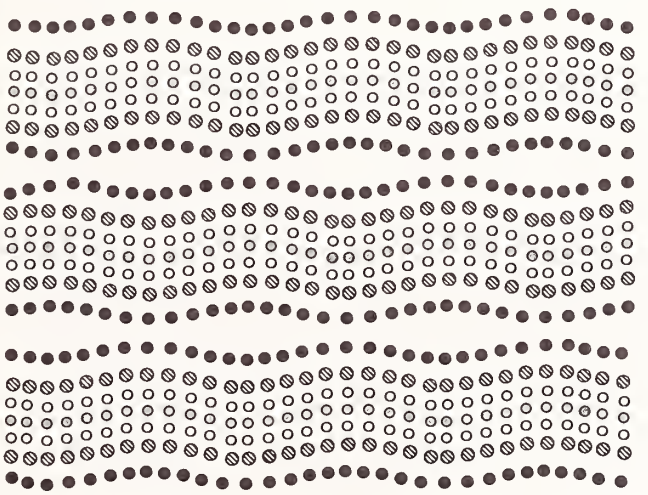

Figure 6. Schematic representation of the modulated structure of $Bi_2Sr_2CaCu_2O_{8+\partial}$. Only the cations are shown (black=Bi, white=Cu, small shaded=Ca, large shaded=Sr).

Since superconductivity at high temperatures was discovered in the systems Bi_2O_3-SrO-CaO-CuO [37] much structural research has been done on these compounds. It was quickly established that T_c's of 80 and 110 K were related to the phases $Bi_2Sr_2CaCu_2O_{8+\partial}$ [38,39] and $Bi_2Sr_2Ca_2Cu_3O_{10+\partial}$ [40], which are the n=1 and n=2 members of the series $Bi_2Sr_2Ca_nCu_{1+n}O_{6+2n+\partial}$. The structures of the Bi containing high temperature superconductors are modulated (see references in [41]), which can be described with a modulation vector, $\mathbf{k}_1$, which can vary between 3.5**b** and 5.0**b**, **b** being the b axis. It is schematically represented in Figure 6. Concensus is growing on the position and the occupation of the oxygen atoms in or near the Bi double layer. Most of the latest results [42-46] seem to confirm the presence of extra oxygen atoms in the BiO layers, which was first suggested by us [47] from electron microscopy observations. We explained the superstructure with an insertion of extra oxygen in the BiO layer to adjust partially the mismatch of the BiO double layers and the perovskite block between the BiO double layers.

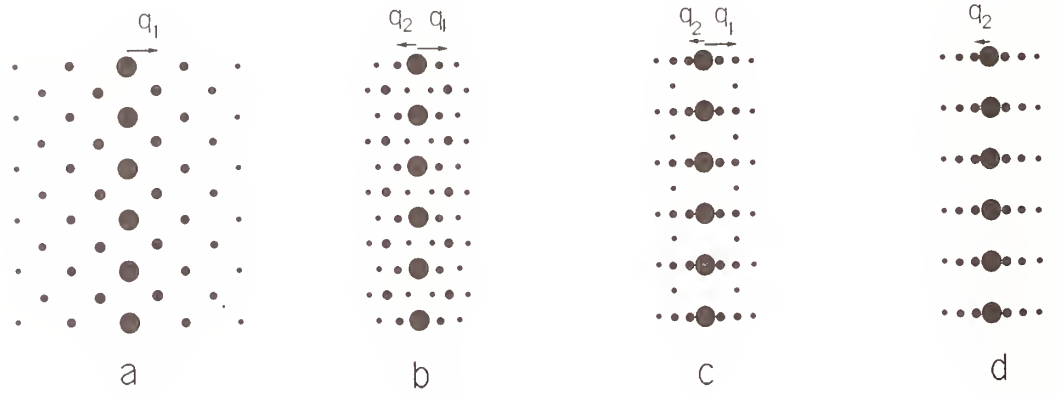

Figure 7. Schematic representation of [100] diffraction patterns of $Bi_{2-x}Pb_xSr_2Ca_{1-y}Y_yCu_2O_{8+\partial}$ with a) x=0,y=0.6, b) x=0.3,y=0.3, c) x=0.3,y=0.0, and d) x=0.6,y=0.0, showing a) the Bi-type of modulation, b) and c) the mixed Bi/Pb type of modulation, d) the Pb-type of modulation.

Pb substitution for Bi is reported [48] to have a positive effect of the formation of the n=2 phase, which has a Tc of about 110K. A number of groups [41] have shown that partial substitution of Bi by Pb leads to the formation of a superstructure which is different from that of the pure Bi compounds. Schematic representations of the diffraction patterns are shown in Figure 7. The modulation can be represented with a vector $\mathbf{k}_2$, being approximately 8**b**, and will be called hereafter the Pb-type of modulation. No sudden change occurs from the Bi-type to the Pb-type of modulation with increasing Pb content. Over a considerable region both modulations coexist. Both modulations interact as is evident from the presence of combined modulation vectors $\mathbf{k}_1+\mathbf{k}_2$ and $\mathbf{k}_1-\mathbf{k}_2$ [see ref 41]. The presence of the combinations of q_1 and q_2 indicates that both modulations occur in the same region.

The model we proposed for the modulated structure consists of two aspects. First, incorporation of clusters of extra oxygen in the BiO layer, as

depicted in figure 8, is assumed in order to get a better lattice match of the perovskite block and the BiO layers. The clusters of neighbouring BiO layers within one $(BiO)_2$ double layer are located at the same positions along the b axis, this forming double clusters. This leads to the modulation in neighbouring BiO layers to be in anti-phase (see figure 9). The oxygen rich clusters form strings along the a axis. The insertion of the oxygen rich clusters will lead to a local expansion of the BiO layers, which allows contraction elsewhere, thus resulting in a modulation of the structure. Second, a shift of the atoms in the BiO layers in the [100] direction is suggested to be caused by the lone pairs. In that model both aspects were not directly correlated to each other.

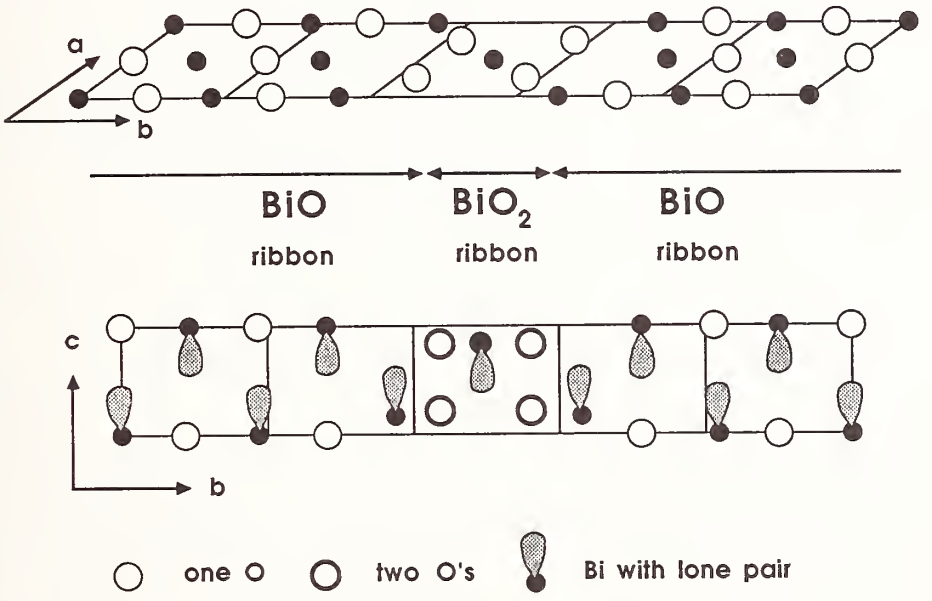

Figure 8. Schematic representation of the effect of the introduction of extra oxygen in the BiO layer. In the oxygen rich region the lone pairs point no longer to an oxygen of the adjacent BiO layer allowing a shorter BiO-BiO layer distance as is indicated in b).

The basic idea in the model for the Bi modulation is the compensation for the lattice mismatch by patches with extra oxygen. The model of the Pb type of modulation should be based on the same principle. Because the substitution of Bi^{3+}--> Pb^{2+} will probably result in less oxygen in the (Bi,Pb)O layers the Pb-type of modulation must be correlated to a smaller amount of oxygen rich clusters. These oxygen rich clusters cannot be ordered as in the Bi-type of modulation, in which double clusters occur, because the oxygen rich regions would be too far apart. This leads to a model for the Pb-type of modulation in which oxygen rich regions in adjacent BiO layers are separated as much as possible resulting in the model as shown in Figure 9.

Electron diffraction patterns (see Figure 7) show superreflections q_1+q_2 and similar combinations and also that q_2/q_1 is either close to 2/3 or 1/2. Interaction between both modulations without any changes in these modulations is

difficult to imagine, because the displacements along the c axis of the two types of modulations are incommensurate with each other. However interaction can still occur in a matrix in which the atoms are displaced in the c direction according to a Pb-type of modulation. This situation is schematically represented in figure 9c. With such a model of the mixed modulation one would expect that for a dominant Pb-type of modulation the amplitude along the c axis of the Bi-type of modulation is much smaller than that for the pure Bi-type of modulation. This is because the c components of both modulations are not compatible. This expectation is in agreement with a recent publication of Gao et al [49] on a X-ray single crystal diffraction study on $Bi_{2-x}Pb_xSr_2CuO_{6+\partial}$ with x=0.3 showing that the c component of the Bi type modulation in the BiO layer is almost zero.

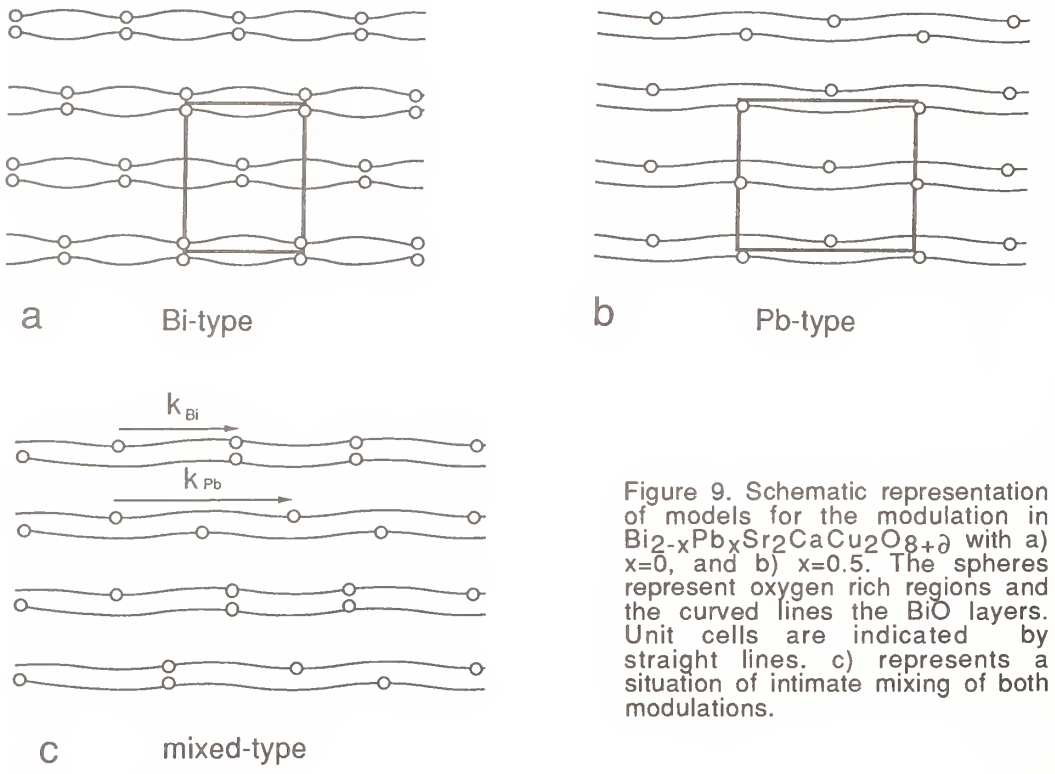

Figure 9. Schematic representation of models for the modulation in $Bi_{2-x}Pb_xSr_2CaCu_2O_{8+\partial}$ with a) x=0, and b) x=0.5. The spheres represent oxygen rich regions and the curved lines the BiO layers. Unit cells are indicated by straight lines. c) represents a situation of intimate mixing of both modulations.

DISCUSSION

The analysis of HREM images has to be done very carefully, because the observed image is not a direct image of the structure, but an image, modified by the electron microscope. This is done partly by the imperfections of the microscope and partly by the defocus of the microscope, which is chosen by the microscopist, because specific structural features are observed best at well defined defocus values. For experimental images the exact defocus value is not known exactly. At best the defocus can be determined with an accuracy of about 10 nm. This shows that careful calculations are necessary, and that conclusions

regarding the positions of atoms should never be done using one experimental image, but always using several images of a through focus series, for which the defocus step is known.

Mostly the comparison between calculated and experimental images is done by eye. However, the printing of the experimental images as well as the calculated images is mostly not a linear process. Thus, comparison by digitized gray values is much more accurate, an example of which is given in ref. 1. Nevertheless, using comparison by eye several conclusions can be made in combination with other data from the high resolution images. In the first place the positions of the mirror planes is not effected by the printing. Also symmetry properties of the crystal can be lost because of misalignments of the microscope but not gained. Consequently the symmetry in the experimental image is the minimum symmetry of the structure. By comparison of experimental and calculated images it is very often possible to correlate the existing mirror planes unambiguously. Thus, when defects or intergrowth occur, the symmetry in the experimental image can be used to rule out a large number of locations of these defects. Secondly in the case of planar defects, the increase or decrease in the period perpendicular to the planar defect also restricts the number of models and image calculations can help with a further restriction. Often the high resolution image often allows one to determine the number of layers which are added or omitted in the defect.

Since the structure determination using image calculations is a trial and error method, whereby accurate atomic positions are not obtained, it is evident that it is tried to obtain a direct image of the structure. This is in principle possible if one knows how the microscope transforms the image. Knowing the transfer function of the microscope, the experimental image can be deconvoluted, to obtain the wave function at the exit of the crystal. Next the projected potential has te be retrieved using a sophisticated computer program, tracing the electron back to the entrance of the crystal. Having thprojected potential, atomic positions can determined much more accurately. It is expected that such a procedure will be available in near future making structure determination with high resolution electron microscopy much more reliable. When one is able to retrieve the projected potential, the only important characteristic of the microscope will be the information limit.

The advantages of the possibility to do electron microscopy with EDX element analysis are large in the search for new superconductors and in the determination whether intended substitutions are realized. For instance, many papers have been published on the substitutions in $YBa_2Cu_3O_7$, without a verification whether the substitution was completely successful. Performing EDX element analysis on crystals, which have the 1-2-3 structure according to electron diffraction, can show very easily whether the substitution was complete.

In this paper some clear examples of structure/property relations are given. However, this relation between many defects of various nature and their influence on the properties have not been established. The determination of such relations will be difficult because a given material will contain various defects. Small changes in composition, not detectable with electron microscopy, will further complicate such a determination. Evidently very careful studies are necessary on well characterized samples with different physical properties.

Acknowledgement
The author wish to thank Prof. G. van Tendeloo (University of Antwerp) and Prof. R. Gronsky (Lawrence Berkeley Laboratory) for the use of some electron microscopes and valuable discussions.

REFERENCES

1. H.W. Zandbergen et al, Nature 331, 596 (1988)
2. P. March et al, Nature 334 141 (1988)
3. E. Kaldis et al, Physica C 159, 668 (1989)
4. H.W. Zandbergen et al, Nature 332, 620 (1988)
5. H.W. Zandbergen et al, Solid State Comm. 66, 397 (1988)
6. H.W. Zandbergen et al, Appl Phys. A46, 233 (1988)
7. R. Beyers, et al, Appl. Phys. Lett. A 53, 432 (1988)
8. H.W. Zandbergen et al, Physica C 158, 155 (1988)
9. H.W. Zandbergen et al, Physica C 159, 81 (1989)
10. H.W. Zandbergen, and G. van Tendeloo, Phys. Rev B40, 11300 (1989)
11. T. Rouillon et al, Physica C 159, 201 (1989)
12. H.W. Zandbergen, R. Gronsky and G. Thomas, Phys. Stat. Sol. (a) 105, 207 (1988)
13. D.J. Li, et al, Physica C, 156, 204 (1988)
14. H.W. Zandbergen and G Thomas, Phys. Stat Sol (a) 107, 825 (1988)
15. A.F. Marshall, Phys. Rev B, 37, 9353 (1988)
16. P. Bordet et al, Nature 334, 596 (1988)
17. R.J. Cava et al, Nature 338, 338 (1989)
18. H.W.Zandbergen et al, Appl. Phys. A46, 153 (1988)
19.. C. Michel et al, Z. Phys. B68, 421 (1987)
20. M.A. Subramanian et al, Science 239, 1015 (1988)
21. J.M. Tarascon et al, Phys. Rev. B57, 9882 (1988)
22. R. Ramesh et al, Science 247, 57 (1990)
23. L.A. Tietz, J. Mater. Res. 4. 1072 (1989)
24. H.W. Zandbergen et al, Physica C, 166, 255 (1990)
25. M.S. Horowitz et al, Science 243, 66 (1989)
26. H.W. Zandbergen, J. van der Berg, and P.H. Kes, Cryogenics 1990, 633 (1990)
27. R.Feenstra et al, Appl. Phys. Lett. 54, 1063 (1989)
28. C.B. Eom et al, presentation at MRS Spring Meeting San Francisco 1990
29. S.E. Babcock et al, Proc. Int. Conf. Cryogenic Materials, Garmisch Partenkirchen, May 9-11 (199)
30. H.W. Zandbergen and G. van Tendeloo, Mat. Res. Soc. Proc. Vol 156, 209 (1989)
31. T. Kogura et al, Physica C, 156, 707 (1988)
32. S.E. Babcock, D.C. Larbalestier, J. Mater. Res. 5, 919 (1990)
33. H.W. Zandbergen, and G. Thomas, Acta Cryst A44, 772 (1988)
34. T. Yamamoto et al, Supercond. Sci. Technol. 1, 153 (1988)
35. H.W. Zandbergen et al, Cryogenics 1990, 628 (1990)
36. D. Dimos et al, Phys. Rev. Lett. 61, 219 (1988)
37. H. Maeda, Y. Tanaka, M. Fukutomi, T. Asano, Jap. J. Appl. Phys. 27 (1988) L209
38. J.M. Tarascon et al, Phys. Rev. (1988)
39. H.G. von Schnering et al, Angewante Chemie 27, 574 (1988)
40. H.W. Zandbergen et al, Nature 332, 620 (1988)
41. H.W. Zandbergen et al, Physica C, 168, 426 (1990)
42. V. Petricek, Y. Gao, P. Lee, P. Coppens, preprint
43. G. Calestani, C. Rizzoli,M.G. Francesconi,G.D. Andreetti, Physica C 161 (1989) 598
44. A. Yamamoto, M. Onoda, E. Takayama-Muromachi, F. Izumi, T. Ishigaki, H. Asano, Phys. Rev. B preprint
45. Y. le Page et al, Phys. Rev. B40, 6810 (1989)
46. J.M. Tarascon et al, Phys. Rev. B39, 11587 (1989)
47. H.W. Zandbergen, Physica C, 156, 325 (1988)
48. S.A. Sunshine, et al, Phys. Rev. B **38** (1988) 893
49. S.M. Green, C. Jiang, Y. Mei, H.L. Luo, C. Politis, Phys. Rev. B **38** (1988) 5016
50. H.W. Zandbergen and W.A. Groen, Physica C 166 (1990) 282

A. Sleight: Many people have, of course, made 123 at low temperatures and have seen the Meissner effect disappear, even though it looks like it's still exactly 123-oxygen 7. But when we did specific heat measurements on those samples we found they were completely superconducting. The Meissner effect disappears because the particle size gets smaller than the penetration depth of the magnetic field. So I would assume that your materials are really superconducting although the Meissner effect is not indicating superconductivity. It is disappearing just because the particles are becoming smaller than the penetration depth.

H. Zandbergen: In our experiments with changing preparation temperatures we tried to keep the particles at the same size by variation of the time of preparation. Still I expect that the material prepared at low temperature will contain many weak links because of the many [100] 90 degree rotation twin boundaries. The magnetic field can penetrate the particles through the weak links which will result in a situation as if you have very small particles.

A. Sleight: The field can penetrate?

H. Zandbergen: Can penetrate, yes, along the [100] 90 degree rotation twin boundaries.

A. Sleight: I think the only way to check the presence of superconductivity in such samples is by doing specific heat measurements.

H. Zandbergen: I agree.

M. Marezio: It's very dangerous to determine by measuring the Meissner effect whether a compound is superconducting, as Sleight has already said. I suggest you check this with other types of measurements.

I would like to ask you what the valency of the Bi atoms is when you put extra oxygen in the BiO layer and you make BiO_2 patches. The Bi-O distances are very short and my guess is that the Bi is probably five-valent. In that case you don't need a lone pair chemistry since Bi^{5+} does not have a lone pair. The Bi-O distance has been determined with X-ray diffraction, but the errors are so big that one cannot decide on the valency of that Bi atom. My feeling is that in the model with the extra oxygens the BiO distances are rather short.

R. Cava: Yes, they are. I have no idea about the lone pair effect. What I do know is that the structure is slightly or even more complicated.

H. Zandbergen: We cannot isolate the bismuth oxide layer from the rest of the structure. We know that Bi can partially substitute Sr. If you put extra oxygen in the BiO layer one would expect that the Bi in the SrO layer is situated around the position of the extra

oxygen. Thus you do not need very much charge compensation for the extra oxygen if there is extra Bi on the Sr sites near that regon. Concerning the exact distances I have no good values because they will depend on the amplitude of the modulation.

M. Marezio: But the Bi-O distance will be close to half of the diagonal of the average structure and that is short.

H. Zandbergen: Yes, it's short but the distance from a Bi atom to its nearest neighbor oxygen atom in the SrO layer is also very short, so it is a funny structure anyway.

R. Roth: Has anybody done calculations of the bond valence sum around Bi based on good X-ray data?

D. Brown: Because of the incommensurate structure of the Cu compounds no one has been able to look at it properly. I can't remember exactly but I must have calculated the bond valence sums. I don't think there is any reason to believe the Bi atoms are anything other than trivalent. The extra oxygen results in extra charge on the CuO_2 layer and not on the BiO layer.

M. Marezio: X-ray absorption edge measurements have been done and no Bi^{5+} is observed. The value of this result depends of course on the accuracy of the technique.

D. Smyth: If you look at the actual detailed compositions of these materials which Art Sleight has described several times and add up the cations you find that it is positive charge deficient relative to the ideal composition that you show here, which probably means that it is oxygen deficient. So it should be relatively easy to slip some more oxygen into this material.

M. Marezio: It is a combination of the two. This has been discussed at Bordeaux during the International Meeting of Crystallography. Coppens, who observed the cation vacancies with X-ray diffraction, and others, who described the superstructure based on X-ray diffraction, agreed that the complicated structure is due to a mixture of excess oxygen and cation vacancies. On the other hand there are quite a number of reports which state that the various sites are fully occupied.

H. Zandbergen: The problem with the determination of the occupancies with diffraction techniques is the variety of possible substitutions: Ca on the Sr site, Bi on the Sr and Ca sites, Sr on the Ca site. So it is very difficult to determine whether cation vacancies do occur.

R. Cava: But there is virtually no crystallographic study which is consistent with the cation ratio that you give here.

H. Zandbergen: No, that is right.

R. Cava: Virtually none.

H. Zandbergen: Right. I and many others are only using this notation for reasons of simplicity.

P. Davies: I thought that AEM work has shown very convincingly that the Bi phase is quite Sr deficient.

H. Zandbergen: That's why I said that Sr is partly substituted by Bi thus probably stabilizing the structure and leading to Sr deficient material.

P. Davies: My other question relates to the Pb doped phase, when you go from the "in-phase" to the "out-phase" type of modulation due to the reduction in the number of oxygen ions in the Bi layer. When you take a little oxygen out of the Bi material do you see any change in the nature of the modulation?

H. Zandbergen: You cannot take enough oxygen out of pure Bi compounds to change the type of modulation. But the oxygen content can be increased easily by partial substitution of calcium by yttrium or another trivalent atom. With such a substitution you have to put in extra oxygen in the structure. Indeed with this substitution the modulation vector is decreasing which is consistent with an increase of oxygen in the bismuth oxide layer.

A. Nath: There are many groups which have been heating the 123 compounds between 500 and 700°C for long times. Could you eleborate on your statement that the compound is not stable in oxygen below 800°C? What kinds of effects do you expect?

H. Zandbergen: I am expecting mainly amorphization. Apart from many clean grain boundaries we have also seen many grain boundaries (in particular for $LaBa_2Cu_3O_7$) with contained amorphous phases at the grain boundary and some small CuO crystallites.

National Institute of Standards and Technology Special Publication 804, Chemistry of Electronic Ceramic Materials, Proceedings of the International Conference held in Jackson, WY, August 17-22, 1990, issued January 1991.

CRYSTAL CHEMISTRY OF OXIDE SUPERCONDUCTORS

Arthur W. Sleight
Oregon State Univ., Corvallis, OR

INTRODUCTION

This paper discusses some recent results for copper oxides which contain the CuO_2 sheets that are present in all of the copper oxide based superconductors. Another aspect of this paper is to discuss oxidation state stabilization and oxidation state fluctuations as they might relate to a mechanism for superconductivity.

NEW MATERIALS

Bednorz and Müller discovered (1) superconductivity in doped La_2CuO_4. However, our attempts to produce superconductivity in several closely related materials have been met with many disappointments. The R_2CuO_4 (R = Pr - Gd) phases could not be doped p-type to become superconducting (2), but they were eventually doped n-type to become superconducting (3).

The two layer analog of La_2CuO_4 has been known for several years (4), but the doping of $La_2CaCu_2O_6$ to produce superconductivity was reported only very recently (5). There had been a suggestion (6) of structural reasons for this apparent inability to produce superconductivity, but these reasons were not substantiated by detailed structural studies (7).

Another structure very closely related to La_2CuO_4 is that of the $A_2CuO_2X_2$ series where A can be Ca or Sr and X may be Cl or Br (8). Attempts to produce superconductivity by either p- or n-type doping have failed to date. We have recently (9) expanded this oxyhalide family to include the two-layer versions, $Ca_3Cu_2O_4Cl_2$ and $Ca_3Cu_2O_4Br_2$ (Figure 1). It is interesting that attempts to prepare three-layer structures of the type $A_4Cu_3O_6X_2$ or $A_4Cu_3O_8$ have so far failed. Our attempts to dope $Ca_3Cu_2O_4X_2$ phases p-type have not succeeded. However, $Ca_{3-x}Y_xCu_2O_4X_2$ phases have been prepared which are presumably n-type (9). Superconductivity has not yet been observed in this two-layer structure.

MIXED VALENCY AND THE PARTIALLY FILLED BAND

A feature common to both bismuth and copper oxides is the availability of three consecutive oxidation states: Cu^{I}, Cu^{II}, Cu^{III} and Bi^{III}, Bi^{IV}, Bi^{V}. All of these oxidation states are well known to

chemists, with the exception of Bi^{IV}. We know that s^1 cations such as Bi^{IV} are unstable when concentrated. Thus, we do not normally find discrete compounds where bismuth is entirely in the tetravalent state. However, we do find Bi^{IV} in dilute systems, both insulating and metallic systems (10).

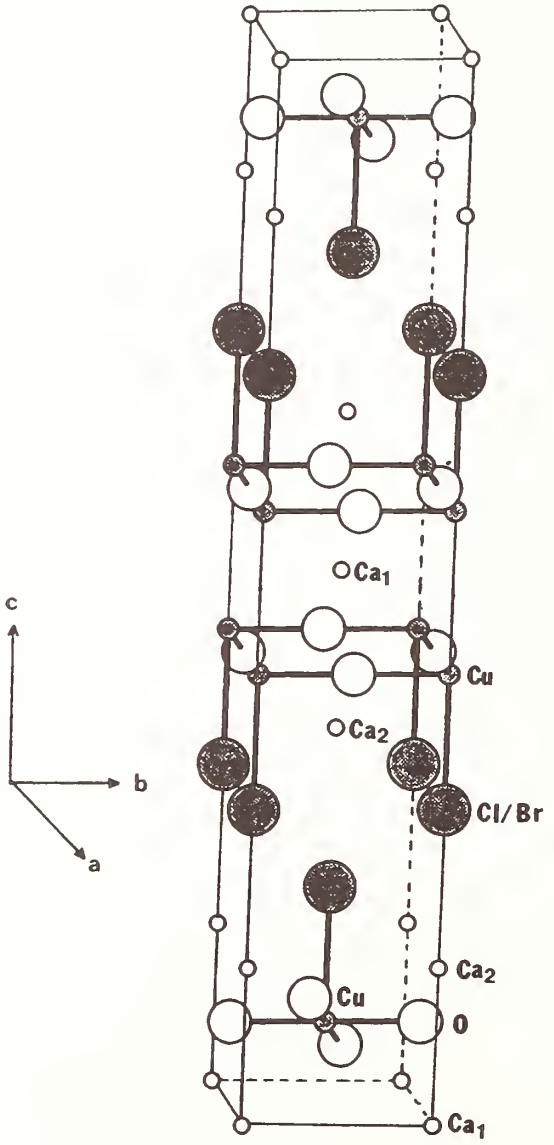

Figure 1

Structure of $Ca_3Cu_2O_4Cl_2$ and $Ca_3Cu_2O_4Br_2$.

The lowest oxidation states for copper, $Cu^{I}(3d^{10})$, and for bismuth, $Bi^{III}(6s^{2})$, are diamagnetic. The middle valency, $Cu^{II}(3d^{9})$ or $Bi^{VI}(6s^{1})$, is always a one electron state. The highest oxidation state is always diamagnetic in the case of bismuth, $Bi^{V}(6s^{0})$. However, the $3d^{8}$ state for Cu^{III} is paramagnetic for cubic (octahedral or tetrahedral) copper but is diamagnetic for square planar copper. It would seem significant that all copper oxide superconductors have a square planar arrangement of oxygens around copper. There may be a fifth, or a fifth and sixth oxygen, ligand; however, these are always at much longer distances. Thus, the mixed valency analogy between bismuth and copper is complete for the structures where superconductivity is observed. Both the lower and upper oxidation states are diamagnetic and the middle oxidation state is spin one half.

The mixed valency in any given superconductor may be viewed as involving just two oxidation states: $Cu^{II,III}$ in $La_{2-x}Sr_xCuO_4$, $Cu^{I,II}$ in $Nd_{2-x}Ce_xCuO_4$ and $Bi^{IV,V}$ in $Ba_{1-x}K_xBiO_3$. It is essential for metallic properties and for superconductivity that the two oxidation states be present on one crystallographic site. Thus, $YBa_2Cu_3O_6$ is neither metallic nor superconducting because Cu^{I} and Cu^{II} occupy distinct crystallographic sites and there is no mixed valency on either site. On the other hand, $YBa_2Cu_3O_7$ is metallic and superconducting, and this is related to $Cu^{II,III}$ mixed valency in the CuO_2 sheet sites.

The mixed valency situation may be equally well described in terms of bands. The band to be considered in the case of bismuth is the Bi*6s* - O*2p* band. The band in the case of copper is the Cu$3d_{x^2-y^2}$ - O*2p* band. Both of these are σ^* bands. For the lowest oxidation state (Cu^{I} or Bi^{III}), these bands are filled; for the highest oxidation state (Cu^{III} or Bi^{V}), these bands are empty. According to simple band structure considerations, we would expect metallic properties for any partial filling of these σ^* bands in bismuth and copper oxides. While metallic properties are indeed observed for most of the intermediate band fillings, insulating properties are always found for the half-filled band in both cases, *i.e.*, the situation for pure Bi^{IV} or pure Cu^{II}.

There are two competing mechanisms to produce an insulating state for the half-filled σ^* band. One is through valency disproportionation, and this is the case for $BaBiO_3$, *i.e.*, $2Bi^{IV} \rightarrow Bi^{III} + Bi^{V}$. If Bi^{IV} had not disproportionated in $BaBiO_3$, we would expect this compound to be metallic because it would have a half-filled band. Many have been confused by this disproportionation description because of confusion about the meaning of valent states as opposed to real charges (10).

Disproportionation of Bi^{IV} in $BaBiO_3$ leads to two distinct sites for Bi^{III} and Bi^{V}. Thus, we formulate this compound as $Ba_2Bi^{III}Bi^{V}O_6$. The Bi-O distances are those expected of these oxidation states (10). The real charges on Bi^{III} and Bi^{V} are very much lower than the oxidation states due to covalency effects. Thus, the real charge difference between Bi^{III} and Bi^{V} is much less than two. An equivalent description of the disproportionation situation in $BaBiO_3$ is the term charge density wave (CDW).

There is another way to achieve an insulating state for the half-filled band, and that is through antiferromagnetic ordering. This happens for all of the copper oxides which contain copper only as Cu^{II}. Thus, spin pairing of electrons on Cu or Bi sites is always related to the insulating state of the Cu^{II} and Bi^{IV} oxides. For the copper oxides, it is spin pairing between adjacent Cu^{II} sites. In the case of Bi^{IV}, spin pairing occurs on alternate Bi sites creating Bi^{III} and Bi^{V}. The magnetic situation in the Cu^{II} oxides may also be described as a spin density wave (SDW).

We will refer to the two competing mechanisms for localization at the half-filled band as disproportionation and magnetic. We could say that if $BaBiO_3$ did not become insulating through disproportionation, it would have become a $BaBi^{IV}O_3$ antiferromagnetic insulator. However, muon spin rotation experiments have completely ruled out that unlikely possibility (11). We could also say that if Cu^{II} oxides did not become antiferromagnetic insulators, disproportionation into Cu^{I} and Cu^{III} would have occurred. This is, of course, exactly what usually happens for Ag^{II} and Au^{II}. For AgO, the oxidation state of silver is clearly not two. This compound is instead $Ag^{I}Ag^{III}O_2$.

Schematic band structures for the copper and bismuth oxides just discussed are given in Figure 2. The hypothetical half-filled band metals do not exist due to electron-electron correlations which cause band spliting. The π^* band is placed so that it is always below the Fermi level. This is consistent with all band structure calculations. However, band structure calculations are not reliable on this issue because they ignore the electron-electron correlations which split the σ^* band and which could cause the filled portion of the σ^* band to drop below the top of the π^* band. The primary assurance that the π^* band always lies below the Fermi level is that an obvious symmetry exists at the Fermi level, *i.e.*, doping either p- or n-type produces essentially the same result (Figure 3). This would not be expected if the π band overlaped the Fermi level. The consensus from nuclear resonance studies is also that there are carriers in only the σ^* band (12).

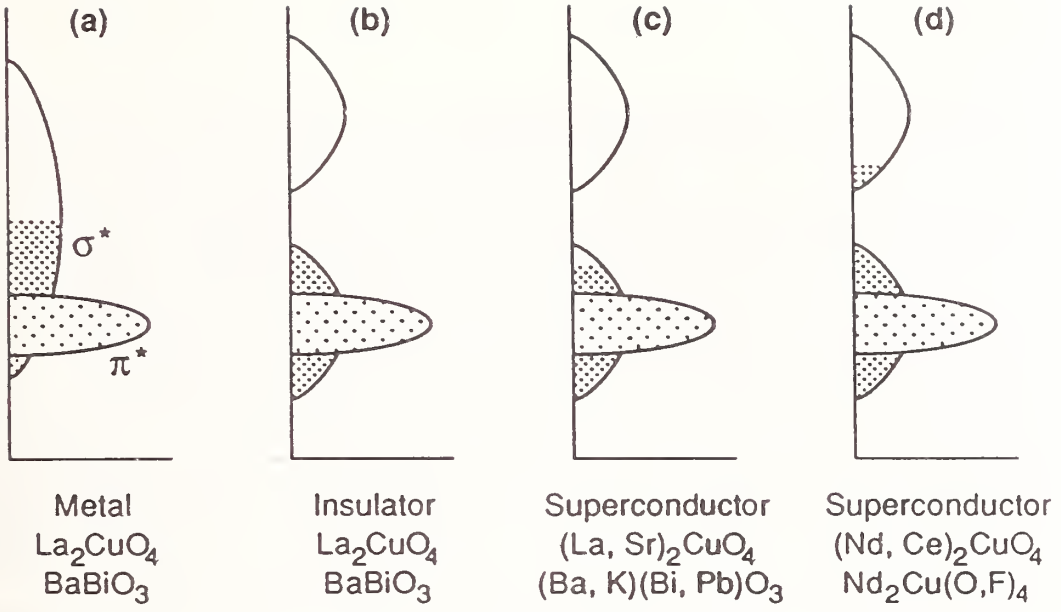

Figure 2

Schematic band structures for pure and doped $BaBiO_3$ and La_2CuO_4. The metallic compounds are hypothetical materials without disproportionation or magnetic interactions which cause band splitting when the σ* band is half filled. Both the p-type (c) and n-type (d) conductors are shown.

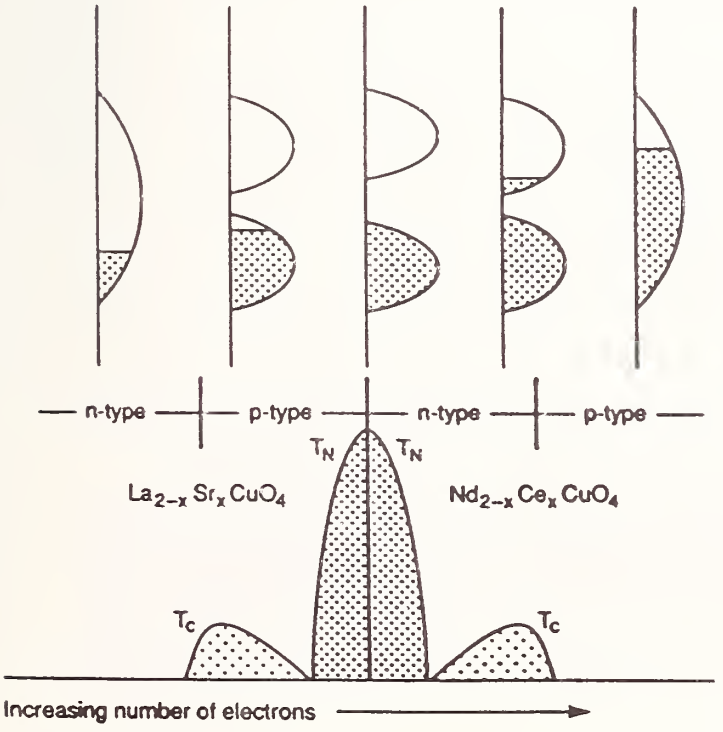

Figure 3

Schematic phase diagram (lower) and schematic band structures (upper) for A_2CuO_4 phases, both n- and p-types.

STABILIZATION OF OXIDATION STATES

We know that the O^{-2} ion is not stable in the gas phase. Such a species would spontaneously loose an electron and become O^{-1}. Nonetheless, we correctly conclude that oxygen is a divalent in nearly all of its compounds, including O_2 and O_2^{-2}. This is not surprising in view of the differences in real charges, oxidation states and valent states just discussed. However, there are two very different ways to describe the stabilization of divalent oxygen. One way has a covalent approach, the other an ionic approach. In highly covalent compounds such as O_2, CO_2, SO_3, and OsO_4, we would refer to oxygen as divalent even though the real charge on oxygen is zero or just slightly negative. Thus in this case, the problem of stabilizing the O^{-2} ion never occurs because the real charge on oxygen never approaches two.

In oxides of high ionicity, it is useful to employ another approach to rationalize the existence of divalent oxygen. This alternative approach has particular relevance to the copper and bismuth oxides despite the covalency of the Cu-O and Bi-O bonds. Although the O^{-1} ion is not stable in the gas phase, it can be stabilized as a fully doubly negatively charged O^{-2} ion in a solid through Madelung forces. The cations surrounding oxygen in a solid produce an electrostatic field intense enough to capture the second electron. This means that we have so stabilized the oxygen *2p* levels that the second electron may be added despite the strong on-site Columbic forces which repel this second electron.

One of the common features of the copper and bismuth oxides superconductors is the presence of highly electropositive cations such as Ba^{II}. These cations may have several important roles such as enabling certain framework structures and increasing the covalency of the Cu-O or Bi-O bonds (13). One very crucial role of the electropositive cations is the stabilization of oxygen *2p* levels to an extent which allows for unusually high oxidation states for copper and bismuth. We know that in the binary Cu/O and Bi/O systems neither $Cu_2^{III}O_3$ nor $Bi_2^{V}O_5$ can be produced even at high oxygen pressure. However, introduction of highly electropositive cations stabilize oxygen *2p* states to such an extent that Cu^{III} and Bi^{V} can exist. Lacking the electropositive cations, Cu^{III} or Bi^{V} would readily oxidize O^{II} to O_2^{-II} or O_2. Good examples of Cu^{III} and Bi^{V} are in $KCuO_2$ and $KBiO_3$ where potassium serves the role of stabilization of oxygen *2p* states sufficiently to allow Cu^{III} or Bi^{V} to exist. Highly

electropositive cations might also play a role in stablizing Cl^{-I} in the presence of Cu^{III} or of I^{-I} in the presence of Cu^{II}.

The disproportionation of Bi^{IV} and Cu^{II} is shown schematically in Figure 4. This disproportionation can only be understood if one takes into account the high covalency and the stabilization of Bi^{V} and Cu^{III} by highly electropositive cations such as Ba^{II}. The main point is that their is a redistribution of electrons in the Bi-O and Cu-O bonds. Although a charge density wave is produced, the magnitude of the charges is much less than would be implied in an ionic model. The situation is in fact very much analogous to what occurs in $BaTiO_3$ on going through its ferroelectric transition (Figure 4). The main difference is that disproportionation is an antiferroelectric, rather than ferroelectric, process.

MECHANISM FOR HIGH T_c

There is still no consensus for a mechanism for the high T_c in the cuprate superconductors. Nonetheless, we have learned much about the electronic structure of such materials. Some proposed theories may now be discarded. The discovery of the n-type cuprate superconductors was the clinching evidence needed to discard theories based on some unique feature of an oxygen *2p* band, a π^* band, or overlapping bands. The central question now for the cuprate superconductors is the fate of spin correlations as the Cu^{II} based insulators are doped. Certainly, these spin correlations are diminished with either n-type or p-type doping. Long range magnetic order disappears, and the materials become metallic. One line of thinking is that it is a vestige of this magnetic state which is indirectly responsible for superconductivity. A more traditional view is that magnetism and superconductivity tend to be mutually exclusive phenomena. The first role of doping is then to weaken the spin correlations sufficiently so that charge fluctuations can then dominate and produce superconductivity. Only this latter view is compatible with both the Bi-based and the Cu-based superconductors, and only this view will be further discussed here.

Some of the features common to both the copper-based and bismuth-based superconductors have been discussed earlier in this chapter. One might say that these two types of superconductor differ in their isotope effects in a way that suggests a different mechanism, but this is not really the case. It is now generally agreed that the oxygen isotope effect in $YBa_2Cu_3O_7$ is finite but quite small. However, it is also known

Disproportionation of Bi^{IV} and Cu^{II}

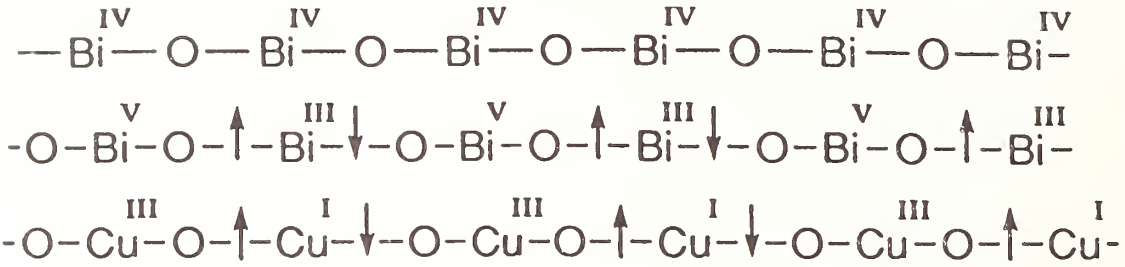

Bond Disproportionation in $BaTiO_3$ (d^0)

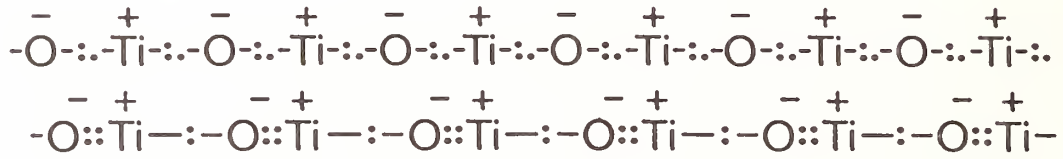

Distortions with filled *d* shell

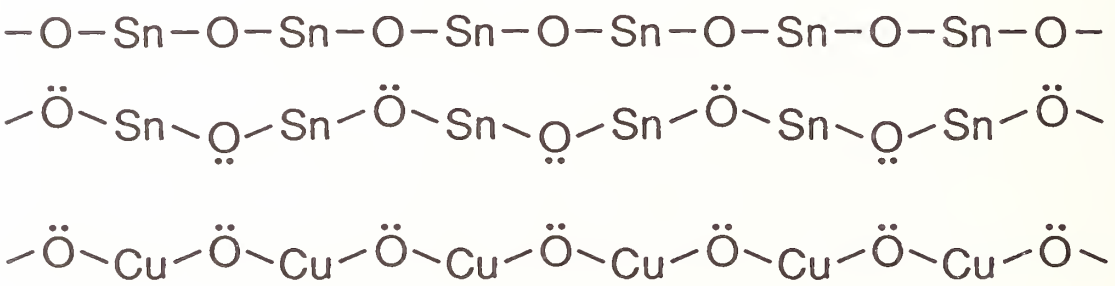

Figure 4

Disproportionation and distortions in the perovskite structure. Arrows represent the spin of antibonding electrons in the Bi^{III}-O^{-II} and Cu^{I}-O^{-II} bonds. For $BaTiO_3$, the dots represent bonding electrons, σ and π. For Sn and Cu, the pair of dots represent a pair of nonbonding electrons resulting from bond bending.

that this fact alone cannot be used to discount a possible critical importance of the electron-phonon interaction in such superconductors. The oxygen isotope effect is pronounced in both $La_{2-x}A_xCuO_4$ and $Ba_{1-x}K_xBiO_3$ superconductors (14,15). Thus, we can be rather certain that the electron-phonon interaction is important for all these superconductors, including the cuprate superconductors with T_c's above 100 K.

I continue to believe that the mechanism for high T_c lies in the tendency for disproportionation of the middle valence state, *i.e.*, Cu^{II} or Bi^{IV} (Figure 3). Such a tendency is well known in chemistry, as previously discussed in this chapter. A problem has been, and remains, that this tendency to disproportionate is not well understood in terms of physics. Nonetheless, this is a real phenomenum which inherently gives the electron-electron attraction required for superconductivity. Such an approach to forming Cooper pairs necessarily means that there will be an electron-phonon interaction. Still, there may be important charge fluctuations that are not so strongly coupled to phonons, *e.g.*, on site polarizibility. This may also make a significant contribution to increasing T_c . A serious problem in developing this view is that charge fluctuations in ferroelectrics such as $BaTiO_3$ (Figure 4) have never been well understood from a physics perspective.

References

1. Bednorz, J. G. and Müller, K. A. *Z. Phys.* B64:198-193 (1986).

2. Gopalakrishnan, J., Subramanian, M.A., Torardi, C.C., Attfield, J.P., and Sleight, A.W., *Mat. Res. Bull.,* 24:321-330, (1989).

3. Tokura, Y., Takagi, H. and Uchida, S. *Nature* 337:345 (1989).

4. N. Nguyen, N., Er-Rakho, L., Michel, C., and Choisnet, J., *Mat. Res. Bull.* 15:891, (1980).

5. Cava, R.J., Batlogg, B., van Dover, R.B., Krajewski, J.J., Waszczak, J.V., Fleming, R.M., Peck, Jr., W.F., Rupp, Jr., L.W., Marsh, P., James, A.C.W.P., and Schneemeyer, L.F., *Nature*, 345:602-603 (1990).

6. Hervieu, M., Maignan, A., Martin, C., Michel, C., Provost, J., and Baveau, B., *J. Solid State Chem.*, 75:925 (1988).

7. J. Huang and A.W. Sleight, *Physica C*,169:169-173 (1990).

8. Grande, Von B. and Müller-Buschbaum. *A. Anorg. Allg. Chem.*, 429:88 (1977).

9. Huang, J., Hoffmann, R.-D., and Sleight, A.W., *Mat. Res. Bull.*, in press.

10. Sleight, A.W., *Valency Considerations in Oxide Superconductors*, Proc. Welch Conf. on Chem. Res., XXXII. Valency, p. 123, 1989.

11. Uemura,Y.J., Sternlieb,B.J., Cox, D.E., Brewer, J.H., Kadono, R. Kempton, J.R., Kiefl, R.F., Kreitzman, S.R., Luke, G.M., Riseman, T., Williams, D.L., Kossler, W.J., Yu, X.H., Stronach, C.E., Subramanian, M.A., Gopalakrishnanan, J., and Sleight, A.W., *Nature,* 335:151(1988).

12. Walsted, R.E. and Warren, W.W., *Science,* 248:1082 (1990).

13. Sleight, A.W., *High-Temperature Superconductivity in Oxides* in Chemistry of High-Temperature Superconductors, (Nelson, Whittingham, George, eds.) p. 2, Amer. Chem. Soc., Wash. D.C.,(1987).

14. Crawford, M.K., Kunchur, M.N., Farneth, W.E., McCarron, E.M., and Poon, S.J., *Phys. Rev. B.*, 41:282 (1990).

15. Hinks, D.G., Richards, D.R., Dabrowski, B., Marx, D.T., and Mitchell, A.W., Nature 335: 419 (1988); Batlogg, B. Cava, R.J., Rupp, L.W., Mujsce, A.W., Krajewski, J.J., Remeika, J.P., Peck, W.F., Cooper, A.S., and Espinosa, G.P. *Phys. Rev. B* 61:1670 (1988).

H. Zandbergen: You showed a correlation between T_c and modulation periodicity for the $Bi_2Sr_{2-x}Y_xCaCu_2O_{8+y}$ type phases, but what was the actual compositional variation?

A. Sleight: Both yttrium content and oxygen content are varied to obtain the entire range of modulation periodicity from 5.0 to 4.1. The phase with the periodicity of 5.0 contains no yttrium and is obtained by extracting oxygen from the lattice. Increasing the yttrium content results in a decrease in the modulation periodicity, but 4.0 is never quite achieved.

H. Zandbergen: The most important thing you are changing is probably the Cu-O distance along the c axis.

A. Sleight: Perhaps, but we do not have the adequate crystallographic data to comment on that. We might infer the Cu-O distance within the CuO_2 sheets from the a and b cell dimensions. This approach indicates the expected decrease in this Cu-O distance as the copper is oxidized. However, this is complicated by the fact that the CuO_2 sheets are not flat. Thus, the a and b cell dimensions do not accurately reflect the Cu-O distances in the sheets.

B. Dobrowski: In the case of EXAFS data from the $Ba(Bi,Pb)O_3$ system, you still see two Bi-O distances for the metallic $BaPb_{0.75}Bi_{0.25}O_3$ composition. How then can you explain the metallic properties?

A. Sleight: I agree that I would not have expected two Bi-O distances in the metallic region. Perhaps the $BaPb_{0.75}Bi_{0.25}O_3$ sample has regions where bismuth has disproportionated and regions where it has not disproportionated. Homogeneity is an issue here. Some optical studies also suggest that the charge density wave extends into the metallic region.

B. Dabrowski: We did the same EXAFS experiment for the $(Ba,K)BiO_3$ system. There you see disproportionation in the nonsuperconducting region but only one Bi-O distance for the superconductors.

A. Sleight: That is what I would expect to see. We are planning to reexamine the EXAFS of superconducting $Ba(Pb,Bi)O_3$ on another sample.

P. Davies: Do you actually know the carrier type in your oxychlorides?

A. Sleight: Our only evidence is based on the changes in unit cell dimensions on substitution of yttrium. Because Y^{3+} is smaller than Ca^{2+}, we see the expected decrease in the c axis on replacing some Ca with Y. However, this substitution causes an expansion of the a axis and thus the Cu-O distance. This expansion is only expected if

the average copper oxidation state has decreased below two. This is probably a more significant result than a Hall or Seebeck measurement.

M. Takano: This is not a question but a comment. I want to say something on disproportionation. We have looked at the disproportionation of iron(IV) into iron (III) and iron(V), and found the effective charges of iron(III) and iron(V) to be +2.7 and +2.9, respectively.

A. Sleight: Right. I liked your comment on what happens when covalency is introduced. The reason that oxidation state arguments work, even though real charges are totally dfferent than oxidation state values, is because the covalent mixing gives new orbitals with the same symmetry as before mixing. Thus, the fact that real charges are very much smaller than oxidation state values does not perturb our argument about disproportionation.

You find a real charge difference of only 2.0 for an oxidation state difference of two. That seems about right to me given such high covalency.

National Institute of Standards and Technology Special Publication 804, Chemistry of Electronic Ceramic Materials, Proceedings of the International Conference held in Jackson, WY, August 17-22, 1990, issued January 1991.

OUT OF PLANE DISPLACEMENTS OF OXYGEN FROM THE CUO_2 SHEETS IN $CA_{.85}SR_{.15}CUO_2$ BY ATOM–PAIR DISTRIBUTION FUNCTION ANALYSIS

S. J. L. Billinge, P. K. Davies and T. Egami
Department of Materials Science and Engineering
University of Pennsylvania,Philadelphia, PA 19104-6272.
C. R. A. Catlow
Royal Institution,21, Albemarle Street, London W1X 4BS,U.K.

ABSTRACT

Atom–pair distribution function (PDF) analysis of neutron powder diffraction data has been carried out on the layered material $Ca_{.85}Sr_{.15}CuO_2$. The result indicates that the CuO_2 sheets in this material are not flat but distort locally with oxygens displacing up and down from their average positions in the plane by 0.1 ± 0.03Å. A static lattice energy minimisation calculation, using central force pair potentials, indicates that, in this ionic approximation, such a distortion is energetically favourable with respect to the flat planes. Thermal factors have been refined from the PDF for the case of displaced oxygens and their temperature variation is in good agreement with Debye theory. The distortions can be explained using ionic arguments and are predicted by bond valence theory. The importance of these distortions and the in–plane bonding environment, to the superconducting cuprates is discussed.

INTRODUCTION

$Ca_{.85}Sr_{.15}CuO_2$ has a structure of infinitely repeating CuO_2 planes, separated by the alkaline earth ions Ca^{2+} and Sr^{2+}.[1] These planes are essentially the same as those that occur in all of the high Tc cuprate superconductors. $Ca_{.85}Sr_{.15}CuO_2$ is the endmember of the $A_2B_2Ca_{n-1}Cu_nO_{4+2n}$ (A=Tl,Bi, B=Ba,Sr, n=1,2,3...) family of materials as $n \rightarrow \infty$. It has no complicated intergrowths, which are characteristic of the superconductors, and the unit cell contains just four atoms. It is thus of interest to be studied as a model compound for the CuO_2 planes. The average structure is tetragonal with space group P4/mmm with a = b = 3.8611Å c = 3.2052Å and has been refined from an x–ray single crystal

study.[1] In common with the superconductors, large thermal factors (up to $<u^2>= 13x10^{-3}Å^2$) were required on the in–plane copper and oxygen sites, even though the average structure is apparently so simple.

The purpose of this work is to study the intrinsic local structure of the CuO_2 plane. A local probe of structure, the PDF analysis of neutron powder diffraction data has been used. This analysis presumes no periodicity and yields information about short range correlations between atoms. A brief description of the analysis procedure will be given, before the results are presented. The structure has been modelled using a static lattice energy minimisation routine and a summary of these results is also presented.

PAIR DISTRIBUTION FUNCTION ANALYSIS

The method is widely used for structural studies of glasses and liquids but more recently has been successfully applied to crystalline systems, where its utility is in elucidating non–periodic order in the structure.[2]The relationship of the PDF to scattered intensity is through a fourier transform. The raw diffraction data is reduced to the total scattering function, S(Q), after correcting for background, absorbtion and detector efficiency. This is then fourier transformed to get the PDF.

These PDFs can then be compared to simulated PDFs, calculated from model structures, which are determined in real space, directly from the atom positions in the model, with no recourse to scattering theory. An agreement factor (A–factor) was defined to describe the fit of simulated PDF to data;

$$A = \left[\frac{\int_{r_{min}}^{r_{max}} [\rho_{dat}(r) - \rho_{sim}(r; a_k)]^2 \, dr}{\int \rho_0^2 \, dr} \right]^{\frac{1}{2}},$$

$\rho_{dat}(r)$ is the value of the measured PDF and $\rho_{sim}(r; a_k)$ is the value of the simulated PDF, at r. This function was minimised with respect to variation of thermal factors, a_k, to produce a best–fit of model to data. An example of PDFs from the 10K data and model are shown in fig 1.

EXPERIMENTS AND RESULTS

$Ca_{.85}Sr_{.15}CuO_2$ was prepared in powder form by solid state reaction of $CaCO_3$, $SrCO_3$ and CuO. This mixture was decarbonated at 850°C for eight hours, then baked at temperatures up to 980°C for up to 60 hours, with frequent grindings.

Neutron powder diffraction data were collected at the Intense Pulsed Neutron Source (IPNS) at Argonne Natl. Lab. using the time–of–flight, Special Environment Powder Diffractometer (SEPD).[3] Fifteen grams of

sample were sealed in a vanadium sample holder with He exchange gas and cooled using a Displex closed loop He refrigerator. Data were collected at 10K, 150K and 298K.

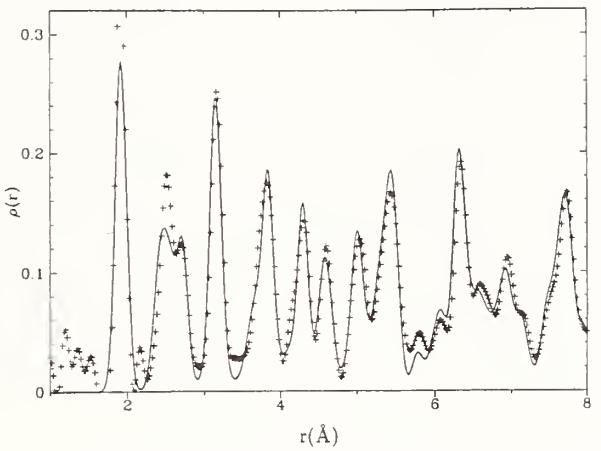

Figure 1. PDFs for $Ca_{.85}Sr_{.15}CuO_2$ from data taken at 10K (crosses) and best–fit model (line).

A Rietveld full profile refinement was carried out on the data. Refinements were carried out in two space groups; P4/mmm and $P\bar{4}m2$. In the latter group, displacements of atoms out of the plane are allowed. No improvement in R_w was obtained in the $P\bar{4}m2$ group, though oxygen atoms did refine off their in–plane sites by a small amount. There is little evidence from Rietveld results for any deviations from planarity of these planes though the possibility that this is occurring is not discounted by these results.

The neutron powder data were then converted to PDFs. A model structure was constructed and atoms displaced from their average positions systematically. Various possible distortions are suggested by the large thermal factors refined during conventional crystallographic analyses. Each of these was tried in the current modelling. The distortions were: A shift of oxygen up and down parallel to z, a shift of copper up and down parallel to z, a shift of oxygen in–plane along directions perpendicular to the Cu–O bond and a shift of oxygen parallel to $<101>$ type directions. The last distortion is suggested by the possibility of the disorder being some kind of lattice dilation to accommodate the oversize strontium ions. In each case atoms were displaced up and down on alternating sites by a value $\pm\Delta$ and the thermal factors refined by least squares minimisation of the A–factor. Δ was then increased in a stepwise fashion, repeating the process at each step. In this way graphs of best–fit A–factor vs. Δ were plotted for each distortion.

The A–factor curves diverge when peaks in the model are shifted to such an extent with respect to the experimental PDF that only a poor fit is possible. This provides a stringent test for the maximum extent of a distortion. It was found that the best–fit A–factor diverged for $\Delta \leq 0.04$Å for all of the distortions tried except when oxygen was displaced up and down along the z–direction. This will be referred to as the Oz distortion. Thus all of the distortions introduce peaks into the PDF which are not compatible with the experimentally derived PDF, except for the Oz case. The results for Oz are shown in figs. 2a and 2b. Fig. 2a plots the best–fit A–factors determined when isotropic thermal factors were used on all sites. The advantage of this constraint is that the number of fitting parameters is only three in each refinement. The curves do not diverge before $\Delta = 0.11$Å and fall to a minimum before diverging. From this we can infer that the PDFs indicate that a distortion of O along z up and down by 0.10 ± 0.03Å from the plane is probably occurring.

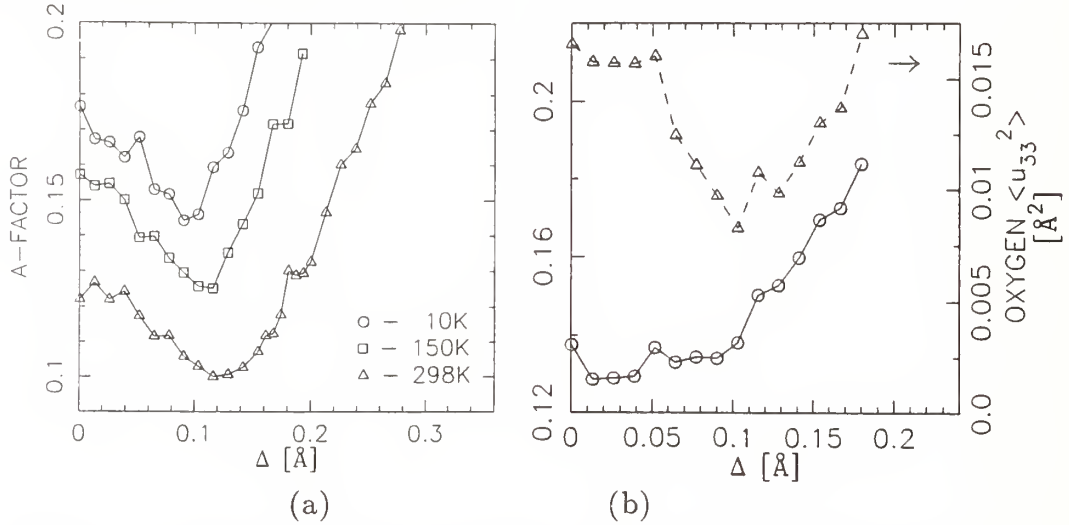

figure 2. (a)Best fit A–factors for fit of model PDF to data at three temperatures for the case of modelling using isotropic thermal factors. (b) Lower curve is the A–factor curve for 10K data using anisotropic thermal factors. The upper curve shows the refined value of $<u_{33}^2>$ from the oxygen site as a function of static displacement of oxygen along z.

The modelling was then repeated with anisotropic thermal factors and the results for the 10K data are shown in fig. 2b. In this case there are seven independent thermal parameters. There is no obvious minimum in the best–fit A–factor curve however it does show a plateau extending beyond $\Delta = 0.1$Å which diverges sharply thereafter. Also plotted are values of the oxygen $<u_{33}^2>$ mean square displacement parameter refined from the PDF.

This falls by a factor of two from the case of no oxygen displacement to a that of a 0.1Å Oz displacement.

The truly dynamic nature of a refined thermal factor may be gauged by its temperature dependence, an estimate of which is possible using Debye theory.[4] The isotropically averaged mean square displacement values refined on oxygens sites from the PDF, were plotted as a function of temperature for the cases of no distortion and for an Oz distortion of 0.1Å. Using the Debye expression for $< u^2 >$, the 10K data point was fitted to determine a Debye temperature Θ_D and the expected temperature dependence was plotted. The behaviour of the $< u^2 >$ values refined with the Oz distortion accord much better with the theory than do those refined for no distortion.

A static lattice energy minimisation calculation has been carried out to investigate the nature and extent of atomic reorganisations around the strontium ions which may be the cause of the observed disorder. An ionic model was used with two–body central–force pair potentials of the Buckingham form with the shell model of Dick and Overhauser[5] used to describe polarizability. The potential parameters were transferred from CuO, CaO and SrO. They predicted well the phonon density of states of the real material and thus appear to provide a good approximation to the real potentials. Strontium ions were then introduced into a nominally pure $CaCuO_2$ compound which took the layered structure of $Ca_{.85}Sr_{.15}CuO_2$. The results indicated that the strontium ion could be accommodated with minimal atomic displacements around it. Nearest neighbour copper and oxygen ions were seen to move by no more than 0.06Å and atoms beyond this first shell moved by an order of magnitude less. These deviations are much less in extent than those observed in the PDF.

A perfect lattice energy minimisation calculation was carried out on an idealised $CaCuO_2$ structure. It was found that this had a lattice energy minimum, E falling from -74.253 to -74.430eV/formula unit, when oxygen displaced up and down from the plane, along z by 0.3Å, in a correlated fashion from site to site. Thus the calculation predicts the Oz distortion, though it overestimates the effect.

DISCUSSION AND CONCLUSIONS

A driving force for the Oz distortion must also explain the lattice calculations which predicted it within an ionic approximation. Such a driving force may derive from the fact that the Ca–O bond length in the material is longer than the ideal CaO bond length as determined from ionic radii considerations. The ideal Ca–O distance is calculated to be 2.47Å[6]and the distance in the crystal is 2.51Å. If the shape of the crystal potential is

convex in this region then a splitting of the bonds to become equally longer and shorter would produce an overall saving in energy since the shorter bonds would gain a greater saving in energy than the longer bonds would lose. For a value of $\Delta = 0.1$Å the short Ca–O bond becomes 2.44Å and the long bond becomes 2.57Å, placing the shorter bond close to the ideal Ca–O ionic separation. This can also be thought of in terms of bond–valence theory.[7] For Ca^{2+} in $Ca_{.85}Sr_{.15}CuO_2$ in ideal 8–fold coordination the average bond valence will be 0.25 valence units. The non–linearity of the relationship between bond valence and bond length has been used to predict the occurrence of distortions in situations where ions cannot take up their ideal bond length, since an equal lengthening and shortening of bonds leads to an increase in the average bond valence. In the present case the undistorted bond length R = 2.51Å gives s = 0.230 valence units, somewhat lower than the expected value. If the oxygens displace up and down by 0.3Å then there are four bonds of length R = 2.33Å, s = 0.341, and four bonds of R = 2.71Å, s = 0.151 valence units, thus the average bond valence is raised, simply by introducing the distortion, to 0.246 valence units. The real distortion is closer to $\Delta = 0.1$Å, however this still raises the average bond valence towards the ideal value.

The properties of the plane, if not the detailed structure, will be similar in all of the CuO_2 planes in the superconducting cuprate materials. These studies indicate that there is an ionic driving force tending to shift oxygen off its average position in the plane. In the more complex superconducting structures it is likely that other structural elements in the intergrowth regions between the planes will dictate the exact configuration taken up by the planes. It appears, however, that there is no strong restoring force holding the oxygen in the plane and thus both the static and dynamic nature of the planes are able to be significantly affected even by small second order interactions.

REFERENCES

[1] T. Siegrist et. al., Nature **334**, 231 (1988).
[2] T. Egami et. al., Materials Transactions, JIM, **31**, 163 (1990).
[3] J. D. Jorgensen, et. al., J. Appl. Cryst. **22**, 321 (1988).
[4] P. P. Debye, Ann. Phys. Lpz. **43**, 49 (1914).
[5] see "Computer Simulation in Solids" (C. R. A. Catlow, W. C. Mackrodt, eds.), Springer–Verlag, (1982).
[6] R. D. Shannon and C. T. Prewitt, Acta. Cryst.,**925**, 946 (1969).
[7] I. D. Brown in "Structure and Bonding in Crystals, Vol II" (M. O'Keefe and A. Navrotsky, eds.) Academic Press (1981).

National Institute of Standards and Technology Special Publication 804, Chemistry of Electronic Ceramic Materials, Proceedings of the International Conference held in Jackson, WY, August 17-22, 1990, issued January 1991.

CRYSTAL CHEMISTRY AND OXYGEN ACTIVITY EFFECTS ON T, T′ AND T* PHASE STABILITIES IN $(La,RE)_2CuO_4$ SYSTEMS

JOSEPH F. BRINGLEY, BRUCE A. SCOTT AND STEVEN S. TRAIL
IBM Research Division, Thomas J. Watson Research Center Yorktown Heights, NY 10598

ABSTRACT

$La_{2-x}RE_xCuO_4$ (RE = Nd-Y) solid solution systems have been investigated to determine the factors stabilizing the T (La_2CuO_4), T′ (Nd_2CuO_4) and hybrid T*-type structures. A simple ionic model with a perovskite-like tolerance factor is found to accurately define the existence field of each. A remarkably sharp boundary is found to separate the T and T′ stability fields, while the T* structure occurs in a narrow region adjacent to this boundary. The formation of the T* phase is viewed as resulting from a thermodynamic competition between the T and T′ phases, due to a tendency toward T/T′ site ordering. Oxygen activity is found to have a strong influence on phase selection in $(RE)_2CuO_4$ systems to the extent that two different structure-types can be stabilized at a fixed cation composition, but slightly different oxygen stoichiometries. It is found that near the phase boundaries in $La_{2-x}RE_xCuO_4$, the T and T* structure-types are stable for $\delta > 0$, while the T′ structure is stable for $\delta < 0$.

INTRODUCTION

There are three closely related phases with stoichiometry RE_2CuO_4 (whose structures are shown in Fig. 1), all of which can be made superconducting under the appropriate doping and/or processing conditions (1-3). The cation positions in these structures are to a first order approximation identical, so that the only difference between the three structure-types is in the arrangement of oxygen about the cation framework. The different oxygen arrangements determine the Cu-O coordination framework which varies from either 4-fold (T′-structure), 5-fold (T*-structure) or 6-fold (T-structure) Cu-O coordination. The RE-O framework changes from nine-fold coordinate, rock-salt-like layers in T, to 8-fold, fluorite-like layers in T′ or a mixture of the two (T*). Most striking, however, is the varying substitutional preferences of these materials and the manifestation of these preferences in their physical properties. The T-structure (Fig. 1a)

becomes superconducting when hole-doped, and furthermore, can only be doped with holes (and not with electrons). In contrast, The T′-structure (Fig. 1b) becomes superconducting when electron-doped, and can only be doped with electrons. The T* phase, which can be considered a hybrid of the T and T′ phases, might then be expected to exhibit both hole and electron superconductivity, but has thus far been found to exhibit only hole superconductivity (4,5).

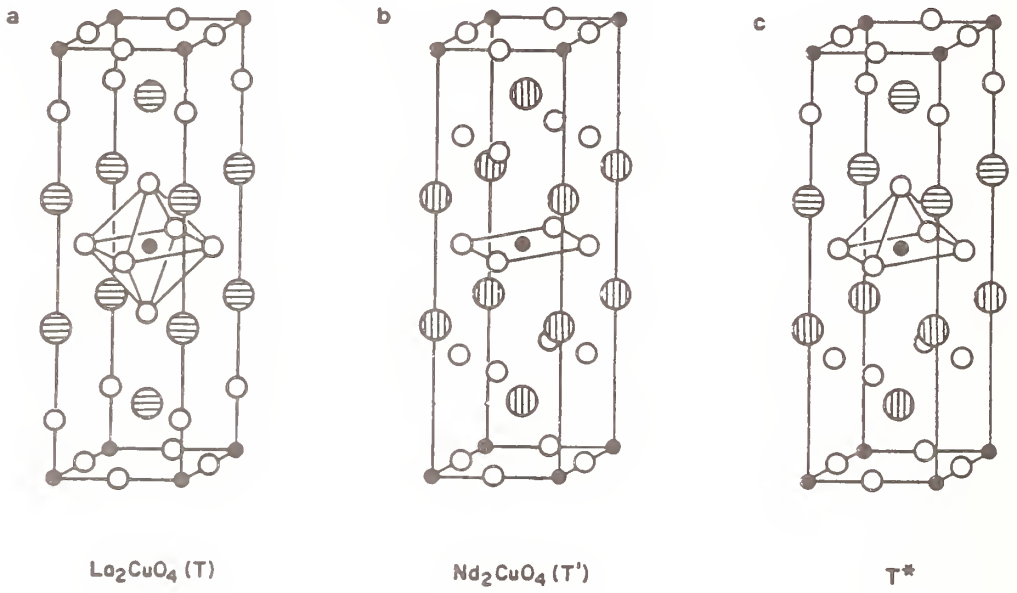

Fig. 1. The T, T′ and T* structures, Cu = solid circles, O = open circles and RE = shaded circles.

In an effort to understand their crystal chemistry and phase stability, and to gain insight into the nature of the specific substitutional preferences of the T, T′ and T* phases, solid solutions and phase relationships in the systems $La_{2-x}RE_xCuO_4$ (RE = Nd-Y) have been investigated. These mixed rare earth systems allow us to evaluate how ionic size and ordering affect structure and stability. The results are explained within the framework of a simple ionic model in which a perovskite-like tolerance factor (t) is found to be a remarkable predictor of T, T′ and T* stability limits (6). In addition, we have examined the effect of oxygen activity (PO_2) on solid solutions of the type $La_{2-x}Nd_xCuO_4$ and $La_{2-x}Dy_xCuO_4$ (Ce and Th-doped). We have found that subtle changes occur in the oxygen sublattice depending upon temperature and oxygen partial pressure (P_{O_2}) during processing. These observations allow the stabilization of two different structure types (either T/T′ or T′/T*) at a fixed cation composition, and allow the stability fields of the T, T′ and T* phases to be manipulated considerably (7).

EXPERIMENTAL

Powdered mixtures of rare-earth and copper oxides, or coprecipitated hydroxides, were heated in Pt crucibles for 24h, ground, pelletized, and reheated, at temperatures from 900-1150°C (48-72h). They were cooled slowly or quenched from reaction temperature. Experiments were performed in air, oxygen, or in a high-pressure oxygen environment using an externally heated René alloy vessel. Powder X-ray diffraction data were obtained on a Siemens D500 diffractometer using CuKα radiation. Full experimental details are provided elsewhere (6).

RESULTS & DISCUSSION

Extensive study of solid solution formation was performed on several $La_{2-x}RE_xCuO_4$ systems, with particular attention paid to $La_{2-x}Nd_xCuO_4$. Although there is some disagreement in the literature (6-9), we find that the equilibrium phase diagram of $La_{2-x}Nd_xCuO_4$ consists of a binary system containing the T-structure for $0.0 \leq x \leq 0.4$, and the T′ structure for $0.5 \leq x \leq 2.0$, separated by a narrow two-phase region. In addition, a non-equilibrium T* phase near $x = 1$ and a fourth phase denoted T″ near $x = 0.5$ have also been reported (6,9). For all the rare earths examined (6), however, it is found that the T-structure of La_2CuO_4 becomes unstable and a transition occurs to either a single-phase T′-structure or a two phase T/T′ mixture as the RE radius decreases from La→Yb. In fact, if the limiting solid solution concentrations of RE in the T-structure of $La_{2-x}RE_xCuO_4$ from this work and from other literature sources are compared (6), it is found that the transition occurs sharply at an average cation radius of 1.204(4) Å. Below this value, the T′-structure becomes stable for the stoichiometry RE_2CuO_4. These trends can be understood within the framework of the following simple ionic packing model.

A complete summary of the results of the present work are collected in Fig. 2, where solid solution compositions are plotted vs. a tolerance factor (t), calculated in all cases for a "reference state" of 9-fold RE-O coordination. The tolerance factor, defined as $t = (r_A + r_O)/\sqrt{2}(r_B + r_O)$, has long been used to describe the stability of the related perovskites, and is a measure of the periodic match of the RE-O and metal oxide layers which comprise these structures (6). It is found that T, T′ and T* phases fall into separate regions having quite discrete boundaries or transition points. The T →T′ transition takes place sharply at a tolerance factor $t = 0.865$. This defines the lower stability limit of the K_2NiF_4 (T-type) structure. Further, if all of the known metallates having the T-structure are tabulated, it is found that the structure is stable over the range $0.865 \leq t \leq 0.993$ (6). However, for clarity, only the regions where the cuprates occur are emphasized here. The T-structure orthorhombically distorts at the lower boundary of its range, $0.873 \geq t \geq 0.865$ (dashed line of Fig. 2), before undergoing transformation to the T′-form, which is stable over the interval

$0.865 \geq t \geq 0.832$. Combinations of copper, oxygen and rare earth cations with $t < 0.832$ do not form RE_2CuO_4 compounds. $RE_2Cu_2O_5$ phases, in which the rare earth is 6-fold coordinated, are the only known cuprates to form in these mixed oxide systems (11), although the T′ phase has been stabilized at high pressures for the smallest rare earth cations (12).

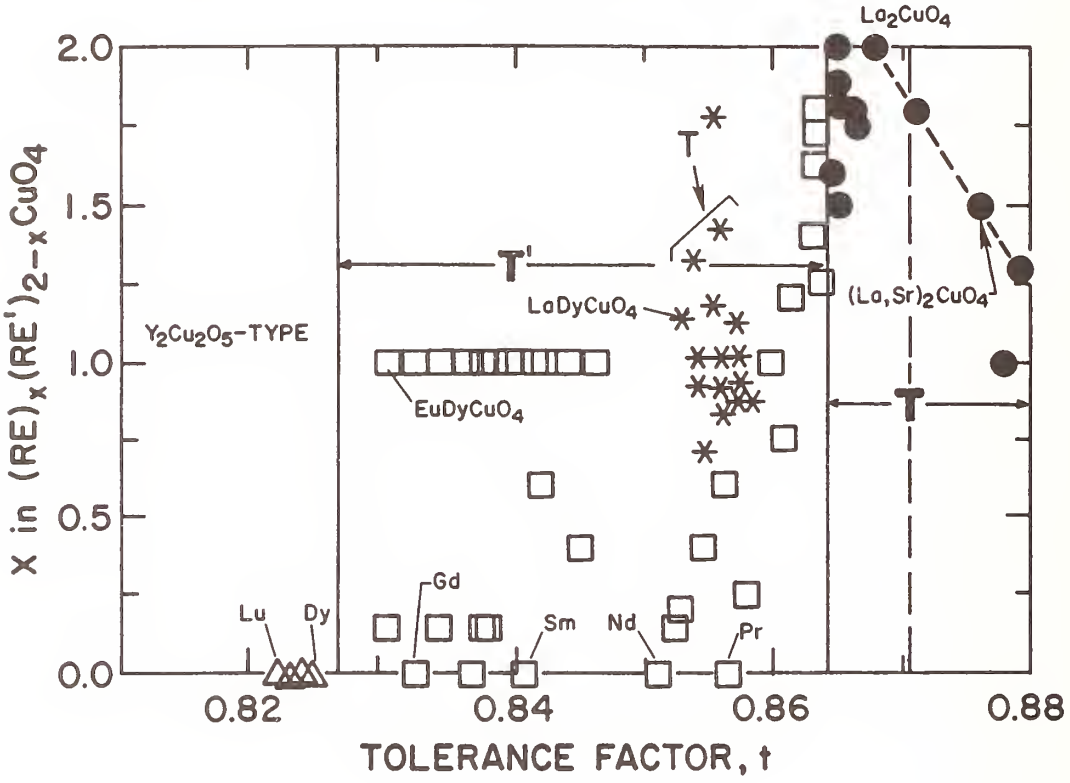

Fig. 2. Compositions of discrete phases and solid solutions having the T, T′ and T* structures. Boundaries are based on the present results; for clarity, not all points are represented.

The data of Fig. 2 show the hybrid T*-phase falling in a very narrow region near the T/T′ phase boundary. This is not surprising in view of its close relationship to both the T and T′ structure-types. We have investigated the systems $La_{2-x}RE_xCuO_4$ (RE = Sm - Yb, Y) near x = 1, to examine how rare-earth size and cation ordering govern the formation of the T* phase. It was found that metastable T* phases form for RE = Sm - Gd but they could not be isolated as single phases. However, T* does becomes quite stable for the smaller rare earths Tb (13) and Dy and can be isolated as single phases for $0.6 \leq x \leq 1.0$ and $0.8 \leq x \leq 1.0$, respectively. We have recently shown that the T* phase occurs only when there is an appreciable disparity in size between La and the smaller RE cation with

which it is matched (6), and that this provides a driving force for A-site cation ordering.

Oxygen Activity Effects

All three phases in the RE_2CuO_4 system are known to exhibit non-stoichiometry in the anion sublattice. We have examined the effect of oxygen activity on solid-solutions of the type $La_{2-x}Nd_xCuO_4$ and $La_{2-x}Dy_xCuO_4$ (Ce and Th doped) to determine its effect upon the crystal chemistry and phase stability in RE_2CuO_4. We find that subtle stoichiometry changes occur in the oxygen sublattice depending upon oxygen activity and temperature during processing. These small variations in oxygen content influence the precise location of the T/T′ or T′/T* phase boundaries in these systems, thereby stabilizing two different structure-types at a A-site cation content.

The solid solution limit of Nd in the T-phase of $La_{2-x}Nd_xCuO_4$ in *air* at 1050°C occurs at x = 0.4. However, if the samples are prepared at 910°C in 400 bar O_2, the solid solution limit extends to x = 0.7. Figure 2 shows the X-ray powder diffraction patterns of (a) $La_{1.4}Nd_{.6}CuO_{4+\delta}$ prepared in 400 bar O_2 at 910°C, and (b) the same sample heated in air and quenched from 1050°C. The pattern of the sample prepared in 400 bar O_2 is that of a single phase material having the T structure, while the phase prepared in air is T′. The oxygen stoichiometries of the two samples differ by only $\delta = 0.06$. Thermogravimetric analysis of solid-solution compositions close to the phase boundary indicate that, in general, the T-phase is stable for $\delta > 0$ and T′ for $\delta < 0$, with the T → T′ transition occuring for $\delta \approx 0$. The transitions are also found to be reversible (7).

A similar result was observed in solutions of the type $La_{1.2}Dy_{.8-x}M_xCuO_{4+\delta}$ (M = Ce, Th), where unique cation compositions could be prepared in either the T′ or T* structure-type depending upon the oxygen activity. For example, a sample of composition $La_{1.2}Dy_{.7}Ce_{.1}CuO_{4+\delta}$ was found to exhibit the T* structure when prepared in 1 atm O_2, but was converted to the T′ structure when heated at 950°C in pure N_2.

The oxygen activity effects observed in our experiments occur for compositions adjacent to the transition boundaries determined in air. Since two phases will have similar free energies near their phase boundary, it is perhaps not surprising that the resulting small shifts in oxygen stoichiometry are so effective in steering phase selection. A substoichiometric oxygen content is destabilizing to the T structure with its higher cation-oxygen coordination numbers, while this favors the T′ structure. A similar argument can be made for T* vs T′. These effects are also consistent with the observed doping preferences of the T, T′ and T* phases and may be be related to electronic factors.

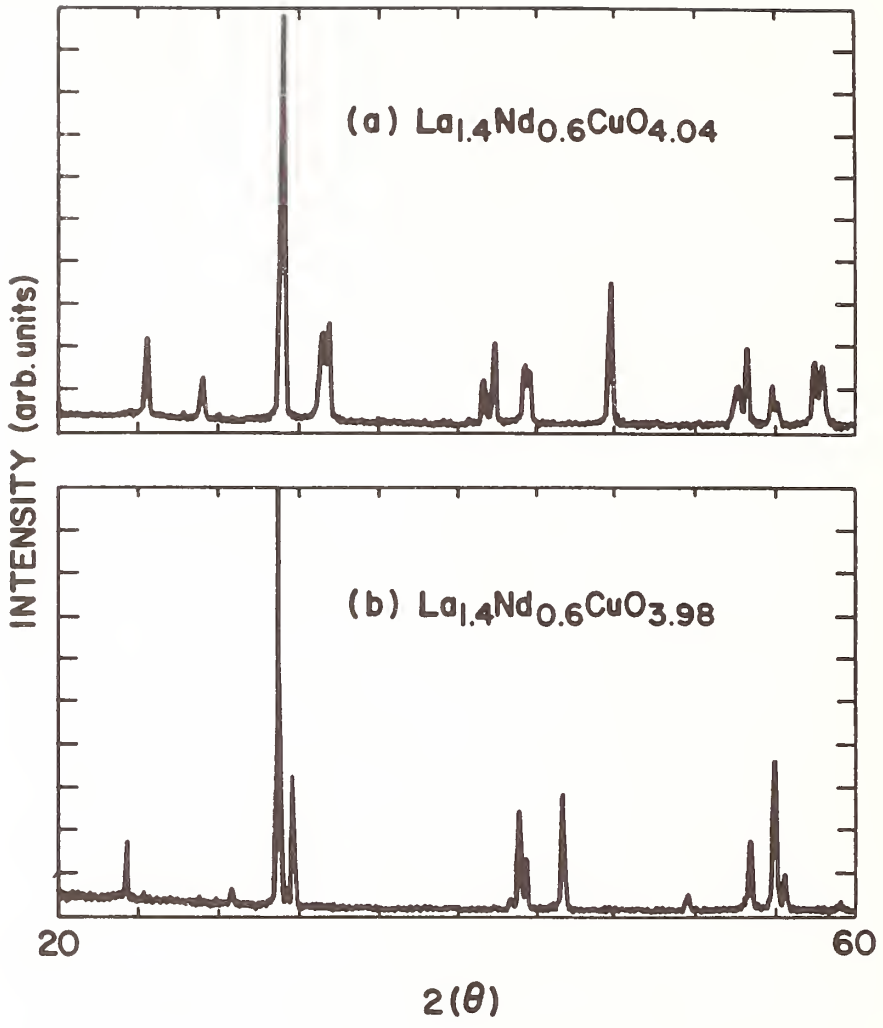

Fig. 3. X-ray powder diffraction profiles of (a) the T and (b) the T′ phase at x = 0.6. The oxygen stoichiometries are given.

SUMMARY AND CONCLUSIONS

The following picture emerges from our study of $La_{2-x}RE_xCuO_4$ systems. As the value of x increases, the average rare earth ionic radius declines and the 9-fold coordinated site of the T structure becomes unstable. Structural changes are first manifested by the transition in T-phase symmetry from tetragonal to orthorhombic. With further increase in x, the average rare earth cation radius becomes too small to support the

orthorhombically-distorted structure, and a major transformation takes place to T′. Near this boundary both T and T′ are of comparable thermodynamic stability, as is T*, so this hybrid structure also makes an appearance. At first, T* is metastable, but it begins to compete favorably with T′ when the mismatch in RE size becomes sufficient to provide a driving force for cation ordering. We estimate that approximately a 10% difference in average rare earth radius between the 9- and 8-fold coordinated sites is required to fully stabilize T*. At larger values of x (or for the smaller rare earths) this difference is exceeded and T′ becomes the stable phase. Eventually, the average RE radius becomes too small to support 8-fold coordination, lowering the tolerance factor further, and RE_2CuO_4 phases are no longer found at ambient pressure. The stability fields, and therefore the phase boundaries, can be manipulated considerably by careful control of temperature and oxygen activity, thereby allowing two different structure types to occur at a fixed cation composition, albeit a slightly different oxygen stoichiometry. Near the phase boundaries in $La_{2-x}RE_xCuO_4$, the T and T* structure-types are stable for $\delta > 0$, while the T′ structure is stable for $\delta < 0$. These results, in combination with the tolerance factor model, can be very useful in the design of selective synthetic routes to the T, T′ and T* phases.

REFERENCES

1. H. Müller-Buschbaum, Angew. Chem. Int. Ed. 16, 674 (1977).
2. Y. Tokura, H. Takagi, and S. Uchida, Nature 337, 345 (1989).
3. A. C. W. P. James, S. M. Zahurak and D. W. Murphy, Nature 338, 240 (1989).
4. H. Sawa et al. Nature 337, 347 (1989).
5. M. F. Hundley, J. D. Thompson, S.-W. Cheong, Z. Fisk, R. Scharwz and J. E. Schirber, Phys. Rev. B. B40, 5251 (1989).
6. J. F. Bringley, S. S. Trail and B. A. Scott, J. Solid State Chem. 86, 310 (1990).
7. J. F. Bringley, S.S. Trail and B.A. Scott, J. Solid State Chem. in-press (1990).
8. K. K. Singh, P. Ganguly and C. N. R. Rao, Mat. Res. Bull. 17, 493 (1982).
9. A. Manthiram and J.B. Goodenough. J. Solid State Chem. in-press (1990).
10. R. Shannon, Acta Cryst. A32, 751 (1976).
11. N. Kimizuka, E. Takayama and S. Horiuchi, J. Solid State Chem. 42, 322 (1982).
12. H. Okada, M. Takano and Y. Takeda, *Physica C* **166**, 111 (1990).
13. T. Kenjo and S. Yajima, Bull. Chem Soc. Jpn. 50, 2847 (1977).

B. Dabrowski: Have you seen other members of this family, namely the Ruddleson-Popper phases, in high pressure samples?

J. Bringley: No, we didn't. We tried to prepare them directly, but were never able to.

B. Dabrowski: But they have been reported in the literature?

J. Bringley: Yes, there are two reports. Frankly, I don't believe that they exist although they may be present as intergrowths in some samples.

R. Cava: But they're from I.B.M.

J. Bringley: I think they observed them by electron microscopy; correct? So they appear to exist as intergrowths.

H. Zandbergen: Have you any idea about the reason why the Demazean phase of $LaCuO_3$ is rhombohedral, because it's prepared at the same temperature?

J. Bringley: Well, it appears to be the high pressure polymorph of $LaCuO_3$ and is prepared at 65 kilobar, versus a hundred fold less pressure in this case. So I think that would perhaps explain why it has different symmetry. Actually if you look at the two structures they are almost identical, the tetragonal and rhombohedral distortions are very small. Both are quite close to cubic symmetry.

H. Zandbergen: Is there a difference in volume?

J. Bringley: Yes, the volume of the tetragonal form is about five percent larger as you would expect for a low pressure polymorph.

A. Navrotsky: You mentioned two phase regions. Do you definitely see two phases coexisting in the x-ray patterns?

J. Bringley: Yes, we do. And let me just comment that I was a little bit hesitant to show that slide because it is not really a phase diagram at all. The way we came up with that diagram is that we determined lattice parameters from a collection of samples, which were prepared under different conditions, so it really is only to show the evolution of the lattice parameters and the approximate homogeneity ranges of these phases. But, in fact, one can, by playing tricks at lower temperatures prepare, for example, the tetragonal phase with a much lower oxygen stoichiometry. So those two-phase regions, yes, we did see both phases growing in under these conditions.

National Institute of Standards and Technology Special Publication 804, Chemistry of Electronic Ceramic Materials, Proceedings of the International Conference held in Jackson, WY, August 17-22, 1990, issued January 1991.

ROOM TEMPERATURE MOBILITY and DIFFUSION COEFFICIENT of OXYGEN in POLYCRYSTALLINE $YBa_2Cu_3O_{7-x}$

Yosef Scolnik*, Michael Schwartz#, Eyal Sabatani, and David Cahen*

the Weizmann Institute of Science, Rehovot ,Israel 76100

ABSTRACT. The practical diffusion coefficient of oxygen in $YBa_2Cu_3O_{7-x}$ at room temperature, as measured by a current decay method in a wet electrochemical set-up was found to be 4 ± $2x10^{-12}cm^2/sec$, essentially independent of grain size (in polycrystalline thin films or bulk pellet) and of surface properties. Therefore it is concluded that the rate-determining step in the diffusion process, the movement of the oxygen inside the grain, is much faster than what would be expected on the basis of extrapolation of high temperature data. This explains our ability to use RT reduction to form metastable 123 variants.

INTRODUCTION

Oxygen-deficient $YBa_2Cu_3O_{7-x}$(123) has been prepared by several methods, mostly by reducing at, or quenching from high temperatures. Such high temperature methods of (de)oxygenation change not only content but also the arrangement of oxygens (1). This makes it difficult to distinguish between structural effects and electronic ones (change of number of charge carriers due to change in oxygen content) on the superconducting properties of 123. Earlier we have shown (2,3) that 123 can be reduced at RT in a wet electrochemical cell and that this provides a way to separate the electronic and structural effects. This can lead to unique behaviour including material showing a 20°K T_c (3) [recently confirmed by the elegant experiments of Jorgensen et al.(4)]. In view of this possibility of RT reduction the question of oxygen mobility in this, relatively low, temperature regime becomes important.

EXPERIMENTAL

Material Preparation: 123 was prepared using in situ prepared nitrate precursors, as described in refs. 2 and 3. X-ray powder diffraction showed the orthorhombic pattern of 123. The material showed reproducibly an oxygen content of 6.97 ± 0.02 as determined by iodometric titration. $La_{0,5}Sr_{0,5}CoO_{3-x}$ was

prepared according to ref. 5 and was single phase as determined by X-ray powder diffraction. The parameter 'x' was determined to be 0.01 by iodometric titration. The thin films used were prepared at Tel Aviv University by e^-- gun sputtering of 123 targets, using alumina (α-corundum) substrates. The films were non-epitaxial, polycrystalline and 1μm thick. In some of the experiments special treatments were done on the pellets before electrochemical reduction. The density and average grain size of pellets could be changed by varying the heat treatment during the final sintering stage. The effect of porosity was examined using pellets which were reground and repressed without sintering. Porosity was further increased by preparing pellets which contained tetra-butyl ammonium perchlorate (tBAP) which was removed by soaking. Porosity was decreased artificially by covering the working side of the pellet with a microporous membrane. Porosity was estimated by SEM. The surfaces of some pellets were modified by etching with a Br_2/ethanol solution (1% by weight) for 10 to 40 minutes, to remove insulating hydroxide and carbonate formed by air exposure (6). Also, Ag was evaporated onto the pellets because of the reported decrease in activation energy for oxygen out-diffusion from samples coated with Ag (7).

The wet electrochemical reductions were performed in a standard 3-electrode cell. Generally, propylene carbonate/(0.1M tBAP) was used as the electrolyte. In some cases we used dry acetonitrile as the solvent. Pressed pellets were 8 mm in diameter and 0.5 mm thick, with a density of 4.6-5.0 g/cm^3. Contacts to all samples were prepared by attaching a Cu wire to the sample with Ag paint and insulating epoxy cement. Two Pt wires were used as counter and quasi-reference electrodes. Ar was bubbled through the solution before the reduction. During the experiment a stream of Ar, blanketing the solution surface, was maintained. Standard electrochemical equipment including a coulometer, was used. Magnetic susceptibility measurements were done using the a.c. mutual inductance technique at a frequency of 75 Hz and a field of approximately 1/3 Gauss.

We performed cyclic voltammogramms of pellets treated with ethanol/Br_2 and impedance measurements to determine the porous diffusion coefficient of the pellets. The experiments were done in a 3-electrode system with a platinum counter electrode, a Ag/0.1M Ag^+ reference electrode and a pellet as the working electrode. For this experiment we used an acetonitrile solution that contained 0.5mM tetramethyl ammonium methyl ferrocene($TmamFe^{+/2+}$).

Method of Analysis The diffusion coefficient of oxygen in 123 was determined using the method of Van Buren et al. (5) for polycrystalline samples, in which the time decay of the current is measured. This method can be used for the determination of oxygen diffusion coefficients in porous pellets. It is based on a bounded 3-dimensional diffusion model under potentiostatic conditions. A plot of I vs. $1/\sqrt{t}$ was made and from the intercept on the $1/\sqrt{t}$ axis (=> t_o) D could be determined from the following equation:

$$\lambda = a/\sqrt{(Dt_o)} \qquad (1)$$

where a is the average grain size (determined by SEM) and λ is a shape parameter taken to be 2 as intermediate between a sphere and a cube. In order to test the applicability of the method to our set-up and the organic solutions, the experiment was also performed with $La_{0,5}Sr_{0,5}CoO_{3-x}$ in aqueous KOH as reported in ref.(5). The diffusion coefficients that we obtained were similar to those reported in ref. 5. Impedance measurements were in the form of complex impedance plots and were analyzed by the method of ref. 8.

RESULTS

EVIDENCE FOR ELECTROCHEMICAL REDUCTION OF 123: There are several indications that the currents measured in these reduction experiments are indeed due to oxygen reduction, and are not the result of some corrosion or surface catalysis process.

- **Structural evidence:** The X-ray diffraction patterns show shifts, especially in the region of the (200) and [(020) + (006)] reflections, that are similar to those reported for high temperature reduction of 123, in the case of thin films. For the pellets there are some differences and the reflections are broadened upon reduction, as compared to those for non-reduced ones (cf. ref. 3). In the thin films this broadening did not occur. Since the X-ray patterns for pellets are measured on reground pellets, we concluded that we measure a phenomenon representative of the bulk of the pellets.
- **Stochiometric evidence:** A second result which supports oxygen removal (in the form of O^{-2}) from the bulk of the pellet is the exact agreement between the quantity of oxygen removed as determined by coulometry and the final oxygen content of the sample as determined by iodometric titration. This analysis could be done only on pellets. When the experiment was done in the same way with a pellet of $YBa_2Cu_3O_6$ (1236) essentially no current could be passed, again indicating that the reaction in 123(7) is not a surface phenomenon.

- **Atomic Absorption spectroscopy** was used to check for copper in the electrolyte solutions after reduction. Because the amount of copper that we found could account for less than 0.2% of the charge that was passed, corrosion of the material cannot be responsible for the current during the experiment.
- **Magnetic susceptibility of reduced samples:** The transition to the superconducting state is broadened in reduced pellets relative to starting material. The degree of broadening increases with increasing degree of reduction (for a full description of these and electrical resistivity results, see refs. 2 and 3).
- **Impedance measurements:** The frequency plots that we obtained are very close to those expected from theory (8). The calculated porous diffusion coefficient is of the order of 10^{-7}-10^{-8} cm^2/sec, which shows that porous diffusion is **NOT** limiting.

DIFFUSION COEFFICIENT: The practical diffusion coefficient, determined by potentiostatic current decay, was found to be:

$$4 \pm 2 \times 10^{-12} \text{ cm}^2/\text{sec}$$

for pellets and thin films. In order to test whether the measured effective diffusion coefficient was actually due to oxygen diffusion within a grain or due to some surface or solution process, the preparation conditions were varied (as described in the Experimental Section) to obtain pellets with modified physical properties. The grain size was varied from 5-10 μm (as shown by SEM) and pellets with densities of 4.2-5.0 g/cm^3 were used. The changes in grain size and density resulted in pellets with different porosities as observed by SEM. Porosity was also varied with the use of a microporous membrane on the working surface. In addition, the working voltage was varied from -1.0 to -0.5 V in various experiments. Pellets were also used in which the surfaces had been modified by an etching process and by Ag evaporation as described above. Cyclic voltammograms clearly showed an influence of the etching process on the surface properties of the pellets (as expressed by improved electrode behaviour). In all these experiments the measured diffusion coefficient of 123 at room temperature was found to be independent of the different treatments. Samples that were partially reduced by high temperature methods, to oxygen contents similar to those obtained by RT reduction, gave similar results, within the scatter of the experimental data. The thin film results were similar to those obtained for the pellets. Their analysis was done assuming a grain size of 1μm. The polycrystalline nature of these thin films is what allowed us to use this current decay method for them.

DISCUSSION

It was already found that the diffusion coefficient for oxygen in this material is very high. For example a value of $5x10^{-8}$ cm^2/sec was reported at 550°C (9). Extrapolation of high temperature results to room temperature gives a value for D of approximately 10^{-20} cm^2/s. Such a small diffusion coefficient would limit oxygen loss to a very narrow surface region and cannot explain our results. As stated before our results give a much higher practical diffusion coefficient. These results should be compared to the values of: 1.4×10^{-11} cm^2/s and 5×10^{-15} cm^2/s at 25°C for D in other perovskites, namely $La_{0,5}Sr_{0,5}CoO_{3-x}$ and $Nd_{0,5}Sr_{0,5}CoO_{3-x}$ (5). These values are also orders of magnitude larger than those obtained by extrapolation from high temperatures. We note that Yoshida et al. (10), using a plasma-oxidation technique, found a diffusion coefficient of the order of 10^{-12} cm^2/sec for 123 films below 160°C.

CONCLUSIONS

The effective diffusion coefficient of oxygen in polycrystalline 123 at room temperature, as found by the current decay method, was found to be independent of the sample form (polycrystalline thin films or bulk pellets) and of the various treatments given to the pellets. In particular the changes in porosity, density and surface treatments do not affect the measured effective diffusion coefficient. These results lead to the conclusion that the rate-determining step in the diffusion process is the diffusion of oxygen inside the grain, rather than a surface reaction, and that at room temperature this diffusion is unexpectedly facile. This explains the ability to modify the O-content at room temperature, a process that allows the formation of metastable variants of 123.

Acknowledgements: We thank the US-Israel Binational Science Foundation, Jerusalem, Israel, for financial support. We are grateful to G. Deutscher, U. Dai and M. Has from Tel Aviv University for providing us with thin films.

Present adress: Xsirius, Hamada 4, Jerusalem ,Israel
* Authors for correspondence

REFERENCES

1. Manthiram, A.; Swinnea, J.S.; Sui, Z. T.; Steinfink, H.; Goodenough, J. B.; J. Am. Chem. Soc. 1987, 109, 6667.

2. Schwartz, M.; Rappaport, M.; Hodes, G.; Cahen, D.; Physica C 1988, 153-155, 1457.
Schwartz, M.; Cahen, D.; Rappaport, M.; Hodes, G.; Solid State Ionics 1989, 32-33, 1137.

3. Schwartz, M.; Rappaport, M.; Hodes, G.; Reich, S.; Cahen, D.; Mat. Lett. 1989, 7, 411.

4. Jorgensen, J. D.; Pei, S.; Lightfoot, P; Shi, H.; Paulikas, A. P.; Veal, B. W.; Physica C
1990 167,571.

5. van Buren, F. R.; Broers, G. H. J.; Bouman, A. J.; Boesveld, C.; J. Electroanal. Chem. 1978, 88, 353.

6. Vasquez, R. P.; Hunt, B. D.; Foote, M. C.; Appl. Phys. Lett. 1988, 53, 2692.

7. Schrott, A. G.; Tu, K. N.; Yeh, N. C.; Singco, G.; Levi, A.; Tsuei, C. C.; Phys. Rev. B 1989, 39, 2910.

8. De Levie, R.; Electrochimica Acta 1963, 8 ,751.

9. Ginley, D. S.; Nigrey, P. J.; Venturini, E. L.; Morosin, B.; Kwak, J. F.; J. Mater. Res. 1987, 2, 732.

10. Yoshida, A.; Tamura, H.; Morohashi, S.; Hasuo, S.; Appl. Phys. Lett. 1988, 53, 811.

National Institute of Standards and Technology Special Publication 804, Chemistry of Electronic Ceramic Materials, Proceedings of the International Conference held in Jackson, WY, August 17-22, 1990, issued January 1991.

PHASE SEPARATION IN $Nd_{2-x}Ce_xCuO_4$*

B. Dabrowski, P. Lightfoot, D.R. Richards, D.G. Hinks, J.D. Jorgensen, Shiyou Pei, Y. Zheng, D.T. Marx and A.W. Mitchell, Materials Science Division, Argonne National Laboratory, Argonne, IL 60439, USA

ABSTRACT

A series of $Nd_{2-x}Ce_xCuO_4$ samples with starting compositions $0 \leq x \leq 0.25$ have been prepared in several different oxygen partial pressures at 990-1100°C. The high resolution neutron and synchrotron X-ray diffraction data show that single-phase material is formed only for the x=0.0 and x~0.165 compositions. For the x=0.165 sample there is a strong dependence of cerium solubility on synthesis temperature.

INTRODUCTION

The $Nd_{2-x}Ce_xCuO_4$ system is unique among the superconducting copper oxides because the charge carries are considered to be electrons instead of holes[1]. The assignment of electrons as charge carriers was based on structural considerations[2], chemical analysis[3], X-ray absorption spectroscopy[4] and Hall and Seebeck coefficient measurements[1,5]. However, several experimental facts remain ambiguous. For example, some authors reported conflicting results for the sign of the Hall coefficient[6] and for the total oxygen content of the samples[7]. The presence of two or even more phases in the same sample were reported in electron diffraction studies[8]. Moreover, reducing synthesis conditions (as used for the synthesis of superconducting $Nd_{2-x}Ce_xCuO_4$ and try to dope the system with electrons via oxygen vacancy generation) are now frequently used for preparation of hole doped superconducting systems like Sr-Ca-Y-Pb-Cu-O[9] and to improve the superconducting properties in the Bi-Sr-Ca-Cu-O system[10].

We have recently shown[11] that consideration of phase separation is required before the superconducting properties of $Nd_{2-x}Ce_xCuO_4$ can be uniquely determined. Our high resolution neutron and synchrotron X-ray diffraction data show that single phase material is

formed only for the x=0.0 and x~0.165 compositions. Other samples contain a mixture of the x~0.165 composition, which is superconducting, and other compositions which are nonsuperconducting. In this article we review our previous results and provide some additional data for the temperature dependence of the observed phase separation for samples with fixed starting cerium content (x=0.165).

EXPERIMENTAL

Powder samples of $Nd_{2-x}Ce_xCuO_4$ with $0 \leq x \leq 0.25$ were prepared from the metal oxides in several different oxygen partial pressures in the temperatures range 990-1100^{0}C, followed by quenching. Annealing in high purity argon at 900^{0}C followed by quenching produces superconducting material. Neutron powder diffraction data were obtained using the Special Environment Powder Diffractometer (SEPD) at Argonne National Laboratory's Intense Pulsed Neutron Source. High resolution X-ray data were collected on the powder diffractometer on line X7A at Brookhaven's National Light Source. The superconducting properties were studied by AC susceptibility using a Lake Shore Cryotronics, Inc. Model 7000 AC susceptometer.

RESULTS AND DISCUSSION

Our synthesis conditions for samples with different cerium content were typical (fired in air at 1080^{0}C and annealed in argon at 900^{0}C) to that used in previous studies[1-3]. We found that firing in air at higher temperatures frequently led to partial melting, especially for low cerium content samples. Our results for T_c and superconducting phase fraction, shown in Fig. 1a, are also similar to the previously reported data[12] and show bulk superconductivity occurring only in a narrow range of composition ($\Delta x \sim 0.01$) centered at x=0.16. The superconducting fraction was determined from the zero field cooled AC susceptibility at 4.5K and is normalized to the largest fraction occurring for x=0.16 sample (which is about 0.6 of the full diamagnetic signal). The superconducting T_c, determined from the onset of the diamagnetic signal, appears to remain almost constant for $x \leq 0.16$ at 24K, then decreasing by only a few degrees at larger cerium concentrations.

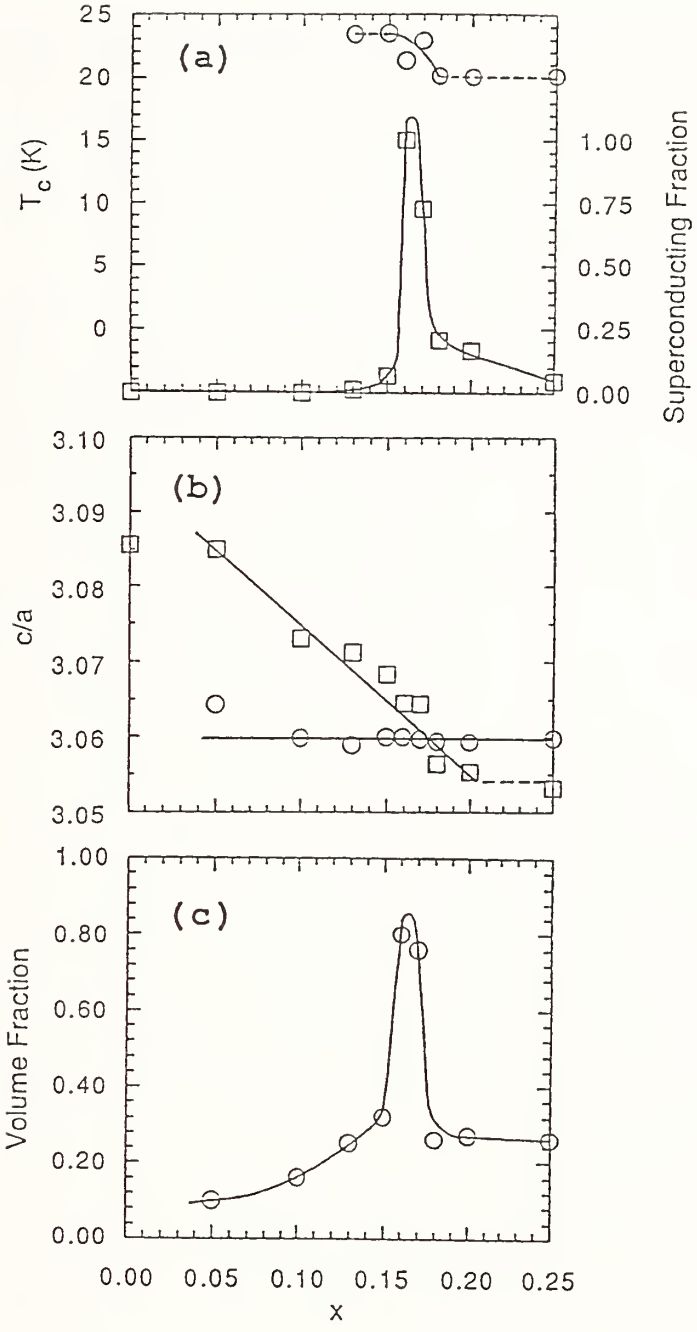

Fig. 1. Superconducting T_c and volume fraction (a), lattice parameters ratio c/a (b) and volume phase fraction (c) as a function of starting cerium content for $Nd_{2-x}Ce_xCuO_4$.

The neutron diffraction data, analyzed initially by the Rietveld method based on a single-phase model, have been used to refine the structure in the tetragonal I4/mmm space group as previously reported[13]. However, substantially better fits, which accounted for the distinct shoulders on many of the Bragg diffraction peaks, were obtained when a two-phase model was used for the x=0.05, 0.1, 0.13 and 0.15 samples. The model consisted of two tetragonal phases for which only the lattice parameters and the phase fractions were allowed to refine. For other samples the multiphase behavior was not clearly evident in the diffraction data. The refined lattice parameters ratio c/a and the volume phase fraction for each of the two phases are shown in Fig. 1b and 1c, respectively. The c/a ratio displays an almost linear decrease with x for one phase while remaining practically constant for the other phase. The volume fraction of the phase with the constant c/a ratio peaks sharply for x=0.16 and 0.17 samples coinciding with the peak in the superconducting phase fraction (Fig. 1a). This behavior suggests that only one composition, x~0.165, is superconducting and traces of superconductivity in other samples result from the presence of a small amount of that phase.

The high-resolution X-ray data confirmed, in principle, these initial findings. However, while X-ray data show relatively sharp peaks, broad shoulders are observed extending to higher values of x. This may be interpreted as the presence of several phases extending to the solubility limit.

To understand the phase separation process better, we have performed a structural study as a function of firing temperature and oxygen partial pressure for samples with fixed starting cerium content (x=0.165). Figure 2 shows portion of the Rietveld refinement profiles for a sample fired in air at 1000^{0}C (a) and at 1080^{0}C (b) followed by quenching. Firing at 1000^{0}C leaves some unreacted Ce(Nd)O_2 oxide leading to the lower final cerium content in the compound. The sample also shows phase separation in agreement with the previous observations (shoulders are clearly visible on several of the diffraction peaks). All the cerium is incorporated into the compound at 1080^{0}C and the sample is single phase (the two-phase refinement shown on Fig. 2b is only marginally better than single-phase refinement).

Although the shape of the observed miscibility gap is not yet fully determined, several interesting

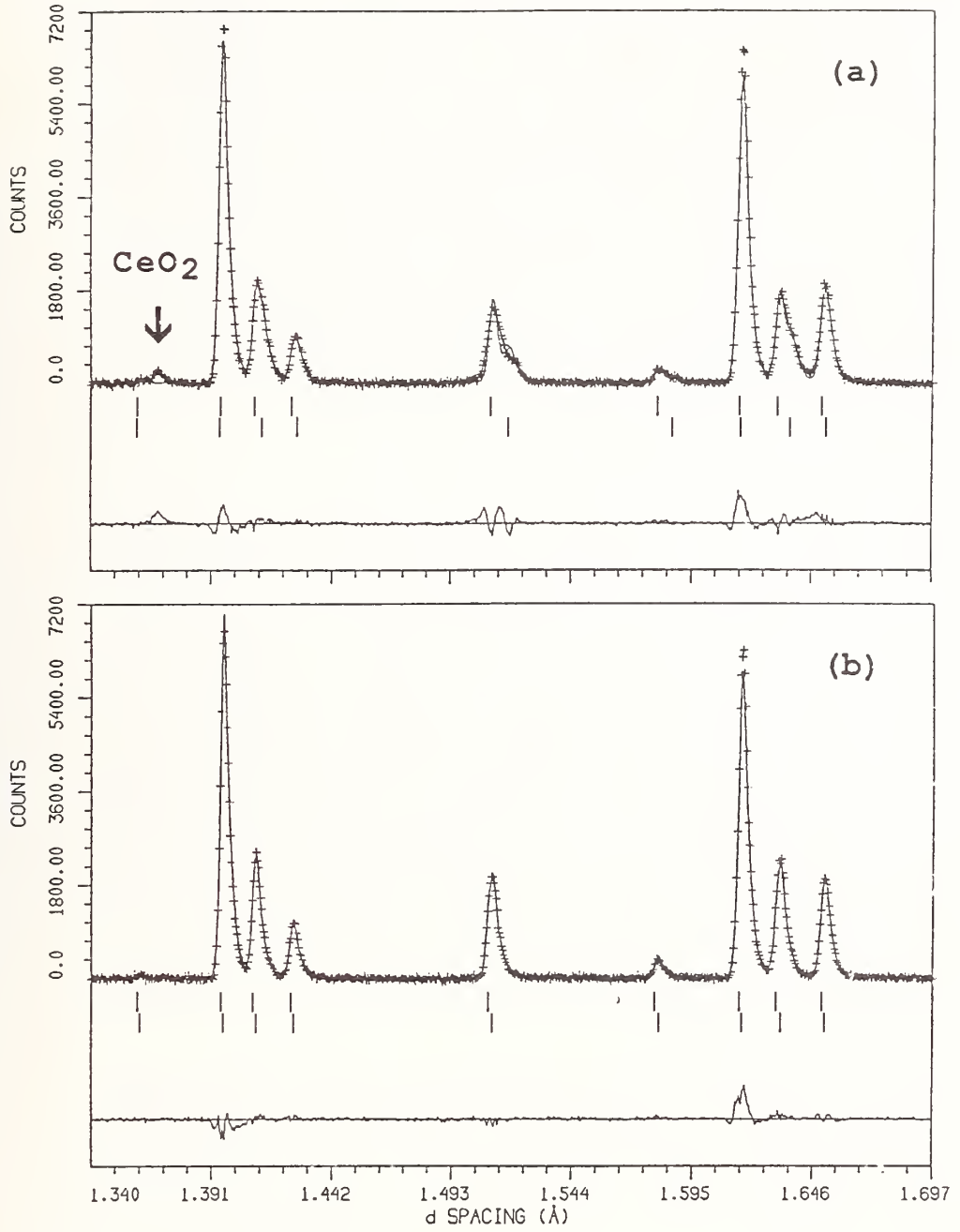

Fig. 2. Portion of the Rietveld refinement profiles for sample fired in air at 1000°C (a) and at 1080°C (b) followed by quenching.

conclusions can be made. The miscibility gap appears to have one limit around ~0.05-0.10 and the other limit at 0.15 for temperatures near 1000^{0}C. The phase separation is an intrinsic characteristic for this system, thus, similar behavior must be present for samples studied in other laboratories. Any conclusions regarding continuous variation of the normal and superconducting state properties as a function of cerium content must be reconsidered. The presence of two phases in most samples may be the cause of disagreement reported in the literature because properties of the compounds on both sides of the miscibility gap may be very different, and, in particular, one compound may be electron doped while the other hole doped.

CONCLUSION

We have examined a series of $Nd_{2-x}Ce_xCuO_4$ samples with nominal compositions $0 \leq x \leq 0.25$ using high resolution neutron and synchrotron X-ray powder diffraction and AC susceptibility. Bulk superconductivity, with onset T_c~24K, as determined by AC susceptibility, occurs only in a narrow range of composition (Δx~0.01) centered at x=0.16. The diffraction data show that samples of $Nd_{2-x}Ce_xCuO_4$ are not single phase except near x=0 and x~0.165. Two-phase Rietveld refinements indicate that other starting compositions contain a fraction of the superconducting composition in an amount proportional to the observed diamagnetic fraction. The cerium solubility is strongly dependent on the synthesis temperature. Our results imply that interpretation of past results has to be taken with caution and great care has to be taken before the superconducting properties of $Nd_{2-x}Ce_xCuO_4$ can be uniquely determined.

*Supported by NSF-Office of Science and Technology Centers under contract #STC-8809854 (BD, PL, SP, DTM) and U.S. Department of Energy, BES, under contract #W-31-109-ENG-38 (DGH, JDJ, YZ, AWM).

REFERENCES

1. H. Takagi, S. Uchida, and Y. Tokura, Phys. Rev. Lett. 62, 1197 (1989).
2. Y. Tokura, H. Takagi, and S. Uchida, Nature 337, 345 (1989).

3. J.T. Market, E.A., Early, T. Bjonholm, S. Ghamaty, B.W. Lee, J.J. Neumeier, R.D. Price, C.L. Seaman and M.B. Maple, Physica C158, 178 (1989).
4. J.M. Tranquada, S.M. Heald, A.R. Moodenbaugh, G. Liang and M. Croft, Nature 337, 720 (1989); E.E. Alp, S.M. Mini, M. Ramanathan, B. Dabrowski, D.R. Richards and D.G. Hinks, Phys Rev. B40, 2617 (1989).
5. Y. Hidaka and M. Suzuki, Nature 338, 635 (1989).
6. Z.Z. Wang, T.R. Chien, N.P. Ong, J.M. Taraskon and E. Wang, (preprint).
7. E. Wang, J.-M. Tarascon, L.H. Greene, G.W. Hull and W.R. McKinnon, Phys. Rev. B41, 6582 (1990).
8. F. Izumi, Y. Matsui, H. Takagi, S. Uchida, Y. Tokura, and H. Asano, Physica C 158, 433 (1989); C. H. Chen, D. J. Werder, A. C. W. P. James, D. W. Murphy, S. Zahurak, R. M. Fleming, B. Batlogg, and L. F. Schneemeyer, Physica C 160, 375 (1989); T. Williams, Y. Maeno, I Mangelshots, A. Reller, and G. Bednorz, Physica C 161, 331 (1989).
9. R.J. Cava at al., Nature 336, 211 (1988).
10. S. Koyama, U. Endo and T. Kawai, J. Appl Phys. 27, L1861 (1988).
11. P. Lightfoot, D.R. Richards, B. Dabrowski, D.G. Hinks, S. Pei, D.T. Marx, A.W. Michell, Y. Zheng and J.D. Jorgensen, Physica C168, 627 (1990).
12. G. Liang, J. Chen, M. Croft, K V. Ramanujachary, M. Greenblatt, and M. Hedge, Phys. Rev. B 40, 2646 (1989).
13. H. K. Muller-Buschbaum and W. Wallschlager, Z. Anorg. Allg. Chem. 414, 76 (1975).

National Institute of Standards and Technology Special Publication 804, Chemistry of Electronic Ceramic Materials, Proceedings of the International Conference held in Jackson, WY, August 17-22, 1990, issued January 1991.

NEW RARE-EARTH CUPRATES WITH THE $NaCuO_2$ STRUCTURE

P.K. Davies, E. Caignol, and T. King
Department of Materials Science and Engineering,
University of Pennsylvania, Philadelphia, PA 19104-6272.

INTRODUCTION

With the reports of n-type superconductivity in Ce and Th-doped Nd_2CuO_4, the isolation of new Nd-containing cuprates is of considerable scientific interest.[1] Our original aim in this work was to investigate the formation of double-Cu sheet compounds with the T'-type Nd_2CuO_4 structure. In the corresponding lanthanum systems it is well known that a simple "Ruddlesden-Popper" T-type phase, $La_2MCu_2O_6$, in which Cu ions in square-pyramidal coordination form 2-dimensional double sheets, is stabilized by the intra-sheet cation M, where M=Ca or Sr.[2] In this structure the pairs of Cu-sheets are separated by a single LaO rocksalt-related layer and the 9-fold coordination of La is essentially identical to that in the La_2CuO_4 T-type structure. Extensive p-doping of $La_2MCu_2O_6$ is quite difficult, however recent work by Cava et al has shown that by using high pressure techniques superconducting transitions on the order of 60K can be produced in samples with $(La_{1.6}Sr_{0.4})CaCu_2O_6$.[3] The T' analog of this compound, in which the double Cu-sheets - with Cu in square-planar coordination - would be separated by fluorite-related intergrowths with Nd retaining the cubic coordination adopted in Nd_2CuO_4, should also have the nominal stoichiometry $Nd_2MCu_2O_6$. For M=Sr a single phase compound does form, however it crystallizes with a T-type structure, with Nd in 9-fold coordination, and is isostructural with the corresponding La compound.

The apparent instability of a double-sheet T' cuprate with the $Nd_2SrCu_2O_6$ stoichiometry, is most likely due to an effective increase in the size of the ions on the "Nd" site resulting from a distribution of Sr on both the intra-Cu sheet site and the Nd site. To reduce the effective size of the ions in the Nd-site we synthesized a series of compositions of $Nd_2MCu_2O_6$ with M = $(Sr_{1-x}Ca_x)$, hoping that the smaller Ca ions would favor the formation of a T'-type $Nd_2MCu_2O_6$ phase. Despite the apparent logic of this approach, no evidence was found for a double-sheet T' cuprate phase. As the concentration of M approached pure calcium the x-ray patterns were multi-phase, and contained reflections from a new insulating phase, with a non-perovskite-related structure, with the stoichiometry $Ca_{2\pm x}Nd_{2\pm x}Cu_5O_{10}$. Isostructural phases were also found in the corresponding Y_2O_3-CaO-CuO and Gd_2O_3-CaO-CuO systems. The structures of these new phases, which are closely related to that of $NaCuO_2$, are the subject of this paper.

STRUCTURAL STUDIES OF $Ca_{2\pm x}M_{2\pm x}Cu_5O_{10}$ (M = Nd, Gd,Y)

All the specimens were prepared by standard solid state techniques at 1000°C in air. The samples were investigated by powder x-ray diffraction using an automated Rigaku DMaxB diffractometer with CuK_α radiation generated at 50kV and 40mA, and by TEM using a Philips 400T electron microscope operated at 120kV. For M = Y, a single phase solid solution is formed for $0 \leq x \leq 0.8$. X-ray patterns collected from a series of samples within this range are shown in figure 1. With the exception of those indicated in the figure, all of the remaining peaks could be indexed using an orthorhombic cell with, for x=0, a = 2.817(1)Å, b = 6.185(1)Å, c = 10.594(1)Å and V = 184.63(7)Å^3. This cell, space group Fmmm, is the same as that reported by Seigrist et al[4] for the sub-cell of the low temperature phase $Ca_{0.8}CuO_2$, which is isostructural with $NaCuO_2$. This structure, first reported by Hoppe[5], consists of one-dimensional chains of edge-sharing Cu square planes, linked by sodium ions in octahedral coordination, see figure 2. In $NaCuO_2$ the octahedral sites are fully occupied; however, both $Ca_{0.8}CuO_2$ and the ternary $Ca_{2\pm x}M_{2\pm x}Cu_5O_{10}$ cuprates are cation deficient, and the strong additional

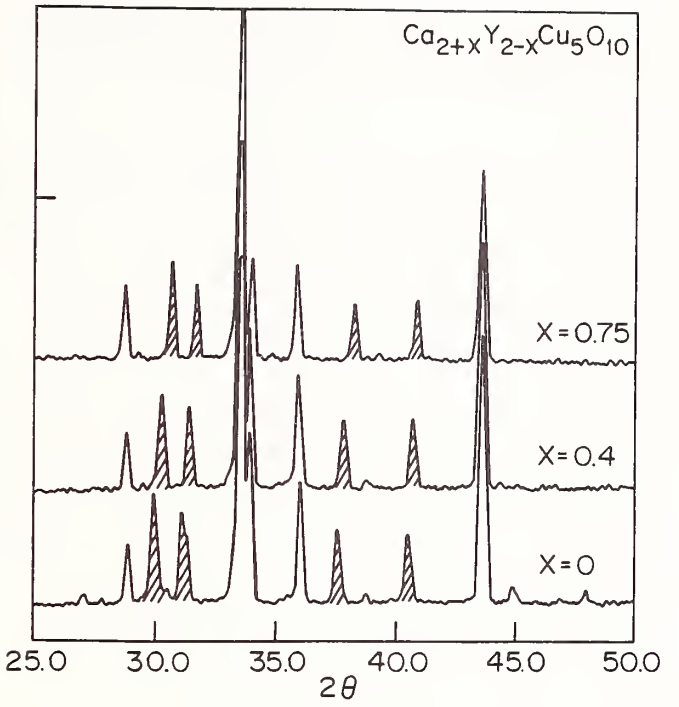

Figure 1. X-ray patterns for $Ca_{2\pm x}Y_{2\pm x}Cu_5O_{10}$ with x = 0, 0.4, 0.75. Shaded peaks due to incommensurate superstructures.

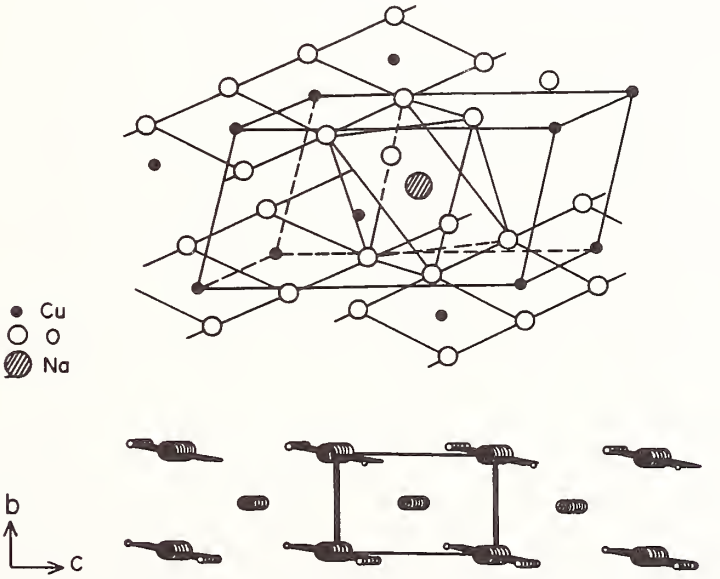

Figure 2. Schematic of $NaCuO_2$ structure. Edge-shared Cu square planes form 1-D chains along a axis. These are linked by larger cations located in channels.

reflections in the x-ray patterns result from commensurate and incommensurate ordering of the Ca/M cations in the channels of the $NaCuO_2$-type cell.

The positions of the reflections corresponding to the orthorhombic sub-cell show little variation as the composition of the solid solution is changed. However, the positions of the extra "un-indexable", superlattice diffraction peaks exhibit a large and systematic variation across the solid solution region - see figure 1. By using fractional Miller indices based on an orthorhombic "$NaCuO_2$-type" sub-cell, we have found that it is possible to index all the diffraction peaks in the powder patterns of the $Ca_{2\pm x}M_{2\pm x}Cu_5O_{10}$ phases. For example, the two strong reflections close to $2\theta = 30°$, can be indexed as $(1-\delta a,1,1-\delta c)$ and $(1-\delta a,1,1+\delta c)$ respectively. Using this type of indexing scheme we find that for $Ca_2Y_2Cu_5O_{10}$, $\delta a = 0.201(1)$ and $\delta c = 0.243(3)$; relative to the orthorhombic sub-cell, this corresponds to a supercell with $a = 5a_{sub}$, $c = 4.12c_{sub}$. A more complete indexing scheme for $Ca_2Y_2Cu_5O_{10}$ is shown below.

$Ca_2Y_2Cu_5O_{10}$: sub-cell; a=2.817, b = 6.185, c = 10.594 Å
$\delta a = 0.201$, $\delta c = 0.243$; $a = 5a_{sub}$, $c = 4.12c_{sub}$

$2\Theta_{obs}$	$2\Theta_{calc}$	I	h	k	l
16.65	16.72	6	0	0	2
28.85	28.84	13	0	2	0
29.83	29.83	24	1-δa	1	1-δc
31.03	31.00	20	1-δa	1	1+δc
33.53	33.52	100	0	2	2
33.81	33.81	30	0	0	4
35.99	36.01	23	1	1	1
37.53	37.52	18	1-δa	1	3-δc
40.37	40.33	17	1-δa	1	3+δc
43.61	43.59	42	1	1	3

This indexing scheme was successfully extended to the powder patterns of all the compositions in the solid solution series. For example, for a Ca-rich sample with $x = 0.75$, $\delta a = 0.171(1)$ and $\delta c = 0.227(1)$, which corresponds to an

incommensurate orthorhombic supercell with $a = 5.848a_{sub}$, $c = 4.41c_{sub}$. A summary of the range of superstructures characterized for the Nd, Y and Gd systems is shown below.

System	Ca/M	1/δa	1/δc
$Ca_{2+x}Y_{2-x}Cu_5O_{10}$	1.0	5.0	4.03
	1.5	5.405	4.17
	2.25	5.848	4.405
$Ca_{2+x}Gd_{2-x}Cu_5O_{10}$	0.77	4.524	5.0
	1.0	4.878	4.566
	1.5	5.263	4.484
$Ca_{2+x}Nd_{2-x}Cu_5O_{10}$	0.625	4.0	0.0
	1.0	4.76	5.714
	1.33	5.0	5.0

The validity of this indexing scheme was further confirmed by electron diffraction. Although a detailed description of the electron diffraction patterns will be described elsewhere, in figure 3 we show electron diffraction patterns collected from the same samples shown in figure 1. These patterns were collected along the b axis of the orthorhombic sub-cell, and clearly show the superlattice reflections originating from the ordering along the a and c directions of the sub-cell. The periodicities of the supercells, which are indicated on the patterns for the a* direction, are in excellent agreement with those calculated from the x-ray patterns.

STOICHIOMETRY RANGE, VALENCE CHANGES.

The limits of single phase formation for the $Ca_{2\pm x}M_{2\pm x}Cu_5O_{10}$ systems are a function of the chemistry of the trivalent M ions. In all three systems Ca-rich samples can be prepared at 1000°C, with the solid solution moving toward a $Ca_4Cu_5O_{10}$ end-member. It was found that the range of solution increases with Y>Gd>Nd. For all the Ca-rich samples the oxygen stoichiometry remains

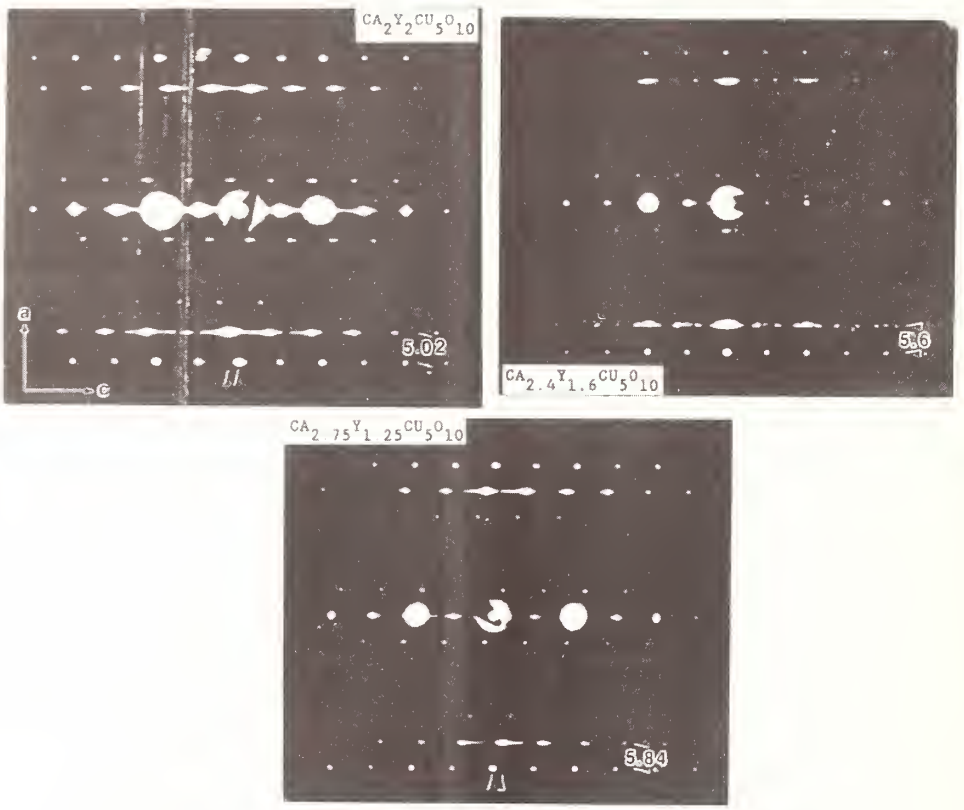

Figure 3. [010] diffraction patterns for a series of samples in the $Ca_{2\pm x}Y_{2\pm x}Cu_5O_{10}$ system.

constant, implying a stabilization of the 3+ state for Cu. However, in all cases the samples remain non-conducting. Trivalent-rich samples could only be synthesized for Nd and Gd, and the range of solution increased in accordance with the ionic radius of the cation, with Nd>Gd. In contrast to the stoichiometric 225 and Ca-rich compositions, for the M^{3+}-rich samples the (Ca+M):Cu ratio was < 4:5, and the composition of the solution proceeded toward an $M_{3.33}Cu_5O_{10}$ (i.e. $Nd_2Cu_3O_6$) end-member, with the copper ions remaining in the divalent state. These compositional variations were reflected by an abrupt change in the lattice parameters of the sub-cells in the Nd and Gd systems at Ca/M<1, with a in particular becoming shorter. At the limit of the Nd solution, with an approximate composition $Nd_{2.5}Ca_{1.25}Cu_5O_{10}$, i.e. $Nd_2CaCu_4O_8$, the supercell is commensurate with a= $4a_{sub}$, c = c, see figure 4.

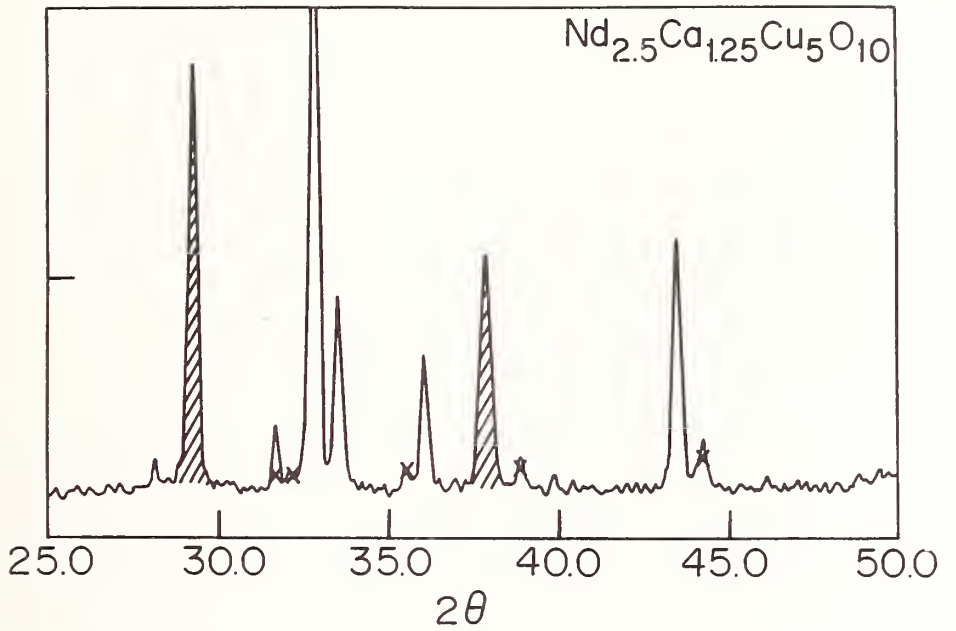

Figure 4. X-ray pattern of $Nd_{2.5}Ca_{1.25}Cu_5O_{10}$. Commensurate superlattice, peaks shaded, with a = 4asub, b=b, c=c.

SUMMARY.

In summary, we have been unable to stabilize double-sheet T' analogs of the $La_2SrCu_2O_6$ structure. . Phase equilibria studies conducted at 1000°C in air indicate that the M_2O_3-CaO-CuO systems (M=Y,Nd,Gd) are dominated by a new ternary phase $Ca_{2\pm x}M_{2\pm x}Cu_5O_{10}$. The structures of these layered cuprates are related to that of $NaCuO_2$ and contain linear chains of edge-shared Cu square planes. These structures exhibit complex x-ray and electron diffraction patterns that can be indexed using incommensurate supercells. It is possible to stabilize valences of Cu >2^+, however all of the phases are non-metallic.

We acknowledge support from the National Science Foundation through grants DMR-88-19027, and through the MRL program, grant DMR88-19885.

REFERENCES.

(1) Y. Tokura, H. Takagi, and S Uchida, Nature, *337*, 345 (1989)
(2) N. Nyugen et al., Mat. Res. Bull., *15*, 891 (1980)
(3) R.J. Cava et. al., Nature, *345*, 602 (1990)
(4) T. Siegrist, R.S. Roth, C.J. Rawn, and J.J. Ritter, Chemistry of Materials, *2*, 192 (1990)
(5) K. Hestermann and R. Hoppe, Z. Anorg. Allg. Chem., *367*, 261 (1969)

National Institute of Standards and Technology Special Publication 804, Chemistry of Electronic Ceramic Materials, Proceedings of the International Conference held in Jackson, WY, August 17-22, 1990, issued January 1991.

THERMODYNAMIC MEASUREMENTS IN THE Y-BA-CU-O SYSTEM

Fernando H. Garzon and Ian D. Raistrick
Los Alamos National Laboratory

The discovery of three high temperature superconducting phases: $YBa_2Cu_3O_{7-x}$, $YBa_2Cu_{3.5}O_{15-x}$ and $YBa_2Cu_4O_8$ within the ytrrium-barium-copper-oxygen system has aroused interest in the thermochemistry of these compounds and other coexisting, non-superconducting phases. Measurement of thermodynamic values of the formation of these compounds such as enthalpies ($\Delta H°$), entropies ($\Delta S°$) and Gibbs free energies ($\Delta G°$) can lead to a better understanding of the phase equilibria, reactivity and chemical bonding within these novel materials. Enthalpies of formation are of particular value as they may be evaluated together with heat capacity data to provide $\Delta G°$ and $\Delta S°$. The enthalpy of formation of the $YBa_2Cu_3O_{7-x}$ phase has been measured by Morss et al. using isoperibol solution calorimetry [1]. The focus of this work is on enthalpic measurements of compounds that exist within the Y-Ba-Cu-O quaternary system using precision isothermal solution calorimetry.

EXPERIMENTAL

Samples of $YBa_2Cu_3O_{7-x}$, Y_2BaCuO_5, and $BaCuO_2$ were synthesized from Y_2O_3, CuO and $BaCO_3$ by grinding the components in a mortar and pestle, and firing at 900°C for 10 hours in flowing dry oxygen. The samples were then quenched to room temperature, reground, pelletized and re-annealed for 10 more hours. The $YBa_2Cu_3O_{7-x}$ sample was reheated at 400°C in oxygen for three hours then slow-cooled to room temperature. The $YBa_2Cu_4O_8$ sample was produced by mixing $YBa_2Cu_3O_{7-x}$ and CuO and heating for 10 days at 850°C at 1 atm of oxygen pressure. X-ray diffraction was used to check the phase purity of the samples. The only impurity found was trace amounts of CuO in the $YBa_2Cu_4O_8$ sample. Oxygen stoichiometry analysis of the $YBa_2Cu_3O_{7-x}$ sample was performed by hydrogen reduction of the compound in a Perkin Elmer TGA7 thermogravimetric analyzer. The mass change of the sample corresponded to an initial oxygen content of 6.96.

A Tronac 558 isothermal solution calorimeter, modified for perchloric acid calorimetry, was used for the determination of the enthalpies of solution of $YBa_2Cu_3O_{7-x}$, Y_2BaCuO_5, $YBa_2Cu_4O_8$ and $BaCuO_2$ in 4.00 M perchloric acid(Baker Ultrex grade) at 25°C . The Tronac calorimeter consists of a stirred teflon and platinum isothermal calorimetric vessel that maintains bath temperature

by a combination of thermoelectric cooling and resistive heating. Heat events occurring within the vessel are compensated by an automatic adjustment of the resistive heater power, thus providing a direct method of measuring the magnitude of the heat event. The calorimeter operates submerged in a high stability isothermal bath (±0.001°C/week). The advantages of this technique over the more commonly used quasi-adiabatic calorimetry (isoperibol) are: a) During the course of the experiment, the calorimetric vessel temperature does not deviate appreciably from the bath temperature thus vessel heat leak corrections are almost negligible. b) The heat flux is also measured directly rather than back-calculated from the temperature rise of a quasi-adiabatic vessel.

The calorimetric measurement procedure consists of the following steps. The samples (3-5 determinations per compound) are first encapsulated in borosilicate glass ampoules, which are attached to the stirring rod of the isothermal vessel that contained 25 ml of 4.00 M $HClO_4$. The calorimetric vessel is submerged in the bath and allowed to reach thermal equilibrium. An electrical calibration is made by the addition of a known amount of joule heat from a calibration resistor immersed in the solution within the vessel. The sample-containing ampoule is broken by a translation of the stirring rod downward against the bottom of the isothermal vessel. The heat of dissolution is then determined by automatic electrical compensation. After the system reaches thermal equilibrium a second joule heat calibration is made. As $\Delta H°$ is a state function, standard-state enthalpies of formation may be calculated by the combination of enthalpies of appropriate chemical reactions whose net summation yields the elemental formation reaction for the compound at standard state conditions.

RESULTS

The enthalpies of dissolution of the measured compounds are listed in Table 1. The enthalpy of solution of the $YBa_2Cu_3O_{7-x}$ compound was in excellent agreement with Morss et al.[1]. Thermodynamic data for heats of solution of other compounds used in the thermodynamic cycles were taken from ref. [1].

Compound	ΔH^o_{298} solution (kJ/mole)
$YBa_2Cu_3O_{7-x}$ (x=0.04)	-796.1± 5
$YBa_2Cu_4O_8$	-847.5 ± 5
Y_2BaCuO_5	-655.5 ± 19
$BaCuO_2$	-249.1± 0.2

Table 1. Heats of dissolution of listed compounds in 4.00 M $HCLO_4$ at 298 K.

$YBa_2Cu_3O_{7-x}$:

{1} $Y(ClO_4)_{3(aq)}+2Ba(ClO_4)_{2(aq)}+3Cu(ClO_4)_{2(aq)}+6.5H_2O_{(aq)}+0.23O_2 = YBa_2Cu_3O_{6.96}+13HClO_{4(aq)}$
$\Delta H_{\{1\}} = 796 \pm 5$ kJ/mole

{2} $Y_{(s)} + 3/4O_{2(g)} = 0.5Y_2O_{3(s)}$
$\Delta H_{\{2\}} = 0.5(-1905.6 \pm 2.0$ kJ/mole)

{3} $0.5Y_2O_{3(s)} + 3HClO_{4\,(aq)} = Y(ClO_4)_{3(aq)} + 1.5H_2O_{(aq)}$
$\Delta H_{\{3\}} = 0.5(-365.7 \pm 2.0$ kJ/mole)

{4} $2Ba_{(s)} + 2Cl_{2(g)} + 22/2O_{2(g)} + 6H_{2(g)} = 2Ba(ClO_4)_2 \cdot 3H_2O_{(s)}$
$\Delta H_{\{4\}} = 2(-1691.6 \pm 3.0$ kJ/mole)

{5} $2Ba(ClO_4)_2 \cdot 3H_2O_{(s)} = 2Ba(ClO_4)_{2(aq)} + 6H_2O_{(aq)}$
$\Delta H_{\{5\}} = 2(+32.1 \pm 3.6$ kJ/mole)

{6} $3Cu_{(s)} + 3Cl_{2(g)} + 21O_{2(g)} + 18H_{2(g)} = 3Cu(ClO_4)_2 \cdot 6H_2O_{(s)}$
$\Delta H_{\{6\}} = 3(-1928.4 \pm 1.0$ kJ/mole)

{7} $3Cu(ClO_4)_2 \cdot 6H_2O_{(s)} = 3Cu(ClO_4)_{2(aq)} + 18H_2O_{(aq)}$
$\Delta H_{\{7\}} = 3(+5.7 \pm 0.2$ kJ/mole)

{8} $10HClO_{4(aq)} = 5Cl_{2(g)} + 20O_{2(g)} + 5H_{2(g)}$
$\Delta H_{\{8\}} = 10(+127.1 \pm 1.0$ kJ/mole)

{9} $19H_2O_{(aq)} = 19H_{2(g)} + 19/2O_{2(g)}$
$19(+286.10 \pm 0.5$ kJ/mole)

$\Delta H^\circ_{\{f\}123} = Y_{(s)} + 2Ba_{(s)} + 3Cu_{(s)} + 6.96/2O_{2(g)} = YBa_2Cu_3O_{6.96(s)}$
$\Delta H^\circ_{\{f\}123} = \sum \Delta H_{\{1\text{-}9\}} = -2718 \pm 20$ kJ/mole

$YBa_2Cu_4O_8$:

{1} $Y(ClO_4)_{3(aq)}+2Ba(ClO_4)_{2(aq)}+4Cu(ClO_4)_{2(aq)}+7.5H_2O_{(aq)}+0.5O_2 = YBa_2Cu_4O_{8(s)} + 15HClO_{4(aq)}$
$\Delta H_{\{1\}} = 847.5 \pm 5$ kJ/mole

{2} $Y_{(s)} + 3/4O_{2(g)} = 0.5Y_2O_{3(s)}$
$\Delta H_{\{2\}} = 0.5(-1905.6 \pm 2.0$ kJ/mole)

{3} $0.5Y_2O_{3(s)} + 3HClO_{4\,(aq)} = Y(ClO_4)_{3(aq)} + 1.5H_2O_{(aq)}$
$\Delta H_{\{3\}} = 0.5(-365.7 \pm 2.0$ kJ/mole)

{4} $2Ba_{(s)} + 2Cl_{2(g)} + 22/2O_{2(g)} + 6H_{2(g)} = 2Ba(ClO_4)_2 \cdot 3H_2O_{(s)}$
$\Delta H_{\{4\}} = 2(-1691.6 \pm 3.0$ kJ/mole)

{5} $2Ba(ClO_4)_2 \cdot 3H_2O_{(s)} = 2Ba(ClO_4)_{2(aq)} + 6H_2O_{(aq)}$
$\Delta H_{\{5\}} = 2(+32.1 \pm 3.6$ kJ/mole)

{6} $4Cu_{(s)} + 4Cl_{2(g)} + 28O_{2(g)} + 24H_{2(g)} = 4Cu(ClO_4)_2 \cdot 6H_2O_{(s)}$
$\Delta H_{\{6\}} = 4(-1928.4 \pm 1.0$ kJ/mole)

{7} $4Cu(ClO_4)_2 \cdot 6H_2O_{(s)} = 4Cu(ClO_4)_{2(aq)} + 24H_2O_{(aq)}$
$\Delta H_{\{7\}} = 4(+5.7 \pm 0.2$ kJ/mole)

{8} $12HClO_{4(aq)} = 6Cl_{2(g)} + 24O_{2(g)} + 6H_{2(g)}$
$\Delta H_{\{8\}} = 12(+127.1 \pm 1.0$ kJ/mole)

{9} $24H_2O_{(aq)} = 24H_{2(g)} + 24/2O_{2(g)}$
$24(+286.10 \pm 0.5$ kJ/mole)

$\Delta H^\circ_{\{f\}124} = Y_{(s)} + 2Ba_{(s)} + 4Cu_{(s)} + 4O_{2(g)} = YBa_2Cu_4O_{8(s)}$
$\Delta H^\circ_{\{f\}124} = \sum \Delta H_{\{1\text{-}9\}} = -2906.4$ kJ/mole ± 25 kJ/mole

Y_2BaCuO_5:

{1} $2Y(ClO_4)_{3(aq)} + Ba(ClO_4)_{2(aq)} + Cu(ClO_4)_{2(aq)} + 5H_2O_{(aq)} = Y_2BaCuO_{5(s)} + 10HClO_{4(aq)}$
$\Delta H_{\{1\}} = 655.5 \pm 19$ kJ/mole

{2} $2Y_{(s)} + 3/2O_{2(g)} = Y_2O_{3(s)}$
$\Delta H_{\{2\}} = -1905.6 \pm 2.0$ kJ/mole

{3} $Y_2O_{3(s)} + 6HClO_{4\,(aq)} = 2Y(ClO_4)_{3(aq)} + 3H_2O_{(aq)}$
$\Delta H_{\{3\}} = -365.7 \pm 2.0$ kJ/mole

{4} $Ba_{(s)} + Cl_{2(g)} + 11/2O_{2(g)} + 3H_{2(g)} = Ba(ClO_4)_2 \cdot 3H_2O_{(s)}$
$\Delta H_{\{4\}} = -1691.6 \pm 3.0$ kJ/mole

{5} $Ba(ClO_4)_2 \cdot 3H_2O_{(s)} = Ba(ClO_4)_{2(aq)} + 3H_2O_{(aq)}$
$\Delta H_{\{5\}} = +32.1 \pm 3.6$ kJ/mole

{6} $Cu_{(s)} + Cl_{2(g)} + 7O_{2(g)} + 6H_{2(g)} = Cu(ClO_4)_2 \cdot 6H_2O_{(s)}$
$\Delta H_{\{6\}} = -1928.4 \pm 1.0$ kJ/mole

{7} $Cu(ClO_4)_2 \cdot 6H_2O_{(s)} = Cu(ClO_4)_{2(aq)} + 6H_2O_{(aq)}$
$\Delta H_{\{7\}} = +5.7 \pm 0.2$ kJ/mole

{8} $4HClO_{4(aq)} = 2Cl_{2(g)} + 8O_{2(g)} + 2H_{2(g)}$
$\Delta H_{\{8\}} = 4(+127.1 \pm 1.0$ kJ/mole)

{9} $7H_2O_{(aq)} = 7H_{2(g)} + 7/2O_{2(g)}$
$7(+286.10\pm0.5$ kJ/mole)

$\Delta H^\circ_{\{f\}2115} = 2Y_{(s)} + Ba_{(s)} + Cu_{(s)} + 5/2\ O_{2(g)} = Y_2BaCuO_{5(s)}$
$\Delta H^\circ_{\{f\}2115} = \Sigma\Delta H_{\{1\text{-}9\}} = -2686.9 \pm 22$ kJ/mole

$BaCuO_2$:

{1} $Ba(ClO_4)_{2(aq)} + Cu(ClO_4)_{2(aq)} + 2H_2O_{(aq)} = BaCuO_{2(s)} + 4HClO_{4(aq)}$
$\Delta H_{\{1\}} = 249.1\pm0.2$ kJ/mole

{2} $Ba_{(s)} + Cl_{2(g)} + 11/2O_{2(g)} + 3H_{2(g)} = Ba(ClO_4)_2 \cdot 3H_2O_{(s)}$
$\Delta H_{\{2\}} = -1691.6\pm3.0$kJ/mole

{3} $Ba(ClO_4)_2 \cdot 3H_2O_{(s)} = Ba(ClO_4)_{2(aq)} + 3H_2O_{(aq)}$
$\Delta H_{\{3\}} = +32.1\pm3.6$ kJ/mole

{4} $Cu_{(s)} + Cl_{2(g)} + 7O_{2(g)} + 6H_{2(g)} = Cu(ClO_4)_2 \cdot 6H_2O_{(s)}$
$\Delta H_{\{4\}} = -1928.4\pm1.0$ kJ/mole

{5} $Cu(ClO_4)_2 \cdot 6H_2O_{(s)} = Cu(ClO_4)_{2(aq)} + 6H_2O_{(aq)}$
$\Delta H_{\{5\}} = +5.7\pm 0.2$ kJ/mole

{6} $4HClO_{4(aq)} = 2Cl_{2(g)} + 8O_{2(g)} + 2H_{2(g)}$
$\Delta H_{\{8\}} = 4(+127.1\pm1.0$ kJ/mole)

{7} $7H_2O_{(aq)} = 7H_{2(g)} + 7/2O_{2(g)}$
$7(+286.10\pm0.5$ kJ/mole)

$\Delta H^\circ_{\{f\}0112} = Ba_{(s)} + Cu_{(s)} + O_{2(g)} = BaCuO_{2(s)}$
$\Delta H^\circ_{\{f\}0112} = \Sigma\Delta H_{\{1\text{-}7\}} = -822.3\pm7.9$ kJ/mole

We have analyzed the following two possible decomposition reactions at the 1:2:4 and the 1:2:3 cation ratio compositions using a value of -155.2 kJ for the heat of formation of CuO[2] and a partial molar enthalpy of oxidation of -190 kJ/mole O_2 for the $YBa_2Cu_3O_{7-x}$ compound[1] :

$YBa_2Cu_3O_{7-x} + CuO + x/2\ O_2 = YBa_2Cu_4O_8$ (I)
$4YBa_2Cu_3O_{7-x} + (2x-1/2)O_2 = 2YBa_2Cu_4O_8 + Y_2BaCuO_5 + 3BaCuO_2$ (II)

The decomposition reaction represented by reaction (I) at 298 K and 1 atm P_{O_2} does not involve oxygen gas at x=0; under these circumstances $\Delta G_{(I)} \approx \Delta H_{(I)}$. The value obtained (-38 kJ/mole) clearly indicates that $YBa_2Cu_3O_{7-x}$ and CuO will transform into $YBa_2Cu_4O_8$ at low temperatures under equilibrium conditions.This has been experimentally observed by a number of researchers [3-7]

Reaction (II) is a completely solid-state reaction at the x= 0.25 composition. This is the equilibrium $YBa_2Cu_3O_{7-x}$ stoichiometry at approximately 873 K and 1 atm of oxygen pressure [8]. The $\Delta G_{rx} \approx \Delta H_{rx}$ value of ~44 kJ/mole indicates that, at this pressure and temperature, $YBa_2Cu_3O_{7-x}$ is thermodynamically unstable with respect to $YBa_2Cu_4O_8$, Y_2BaCuO_5, and $BaCuO_2$. At higher temperatures reactions (I) and (II) will no longer be favorable due to the increasingly positive entropic contribution of the change of state of oxygen gas to lattice oxygen. This effect will eventually change the sign of the ΔG_{rx} and thus $YBa_2Cu_3O_{7-x}$ will become stable, as is observed experimentally.

The implications of the thermodynamic instability of the $YBa_2Cu_3O_{7-x}$ structure limit the ability to synthesize the $YBa_2Cu_3O_{7-x}$ compound at low temperatures and may effect the electronic properties of the materials by the appearance of microscopic defects within the $YBa_2Cu_3O_{7-x}$ lattice as the material is cooled below its boundary of thermodynamic stability.

The authors would like to thank Dr. David S. Ginley of Sandia National Laboratories and Dr John W. Halloran of CPS Corporation for supplying the $YBa_2Cu_4O_8$ material and helpful discussions.

REFERENCES

[1] L. R. Morss, D. C. Sonnenberger, R. J. Thorn, *Inorg.Chem.* **27**, 2106-2110 (1988)

[2] O. Kubaschewski, C. B. Alcock, *Metallurgical Thermochemistry 5th Ed.*, Pergamon Press, Oxford, 282, (1979)

[3] R.J. Cava, J.J. Krajewski, W.F. Peck, B.Batlogg, L.W. Rupp, R.M. Fleming, A.C.W.P. James, P. Marsh , *Nature* **334** 328-330 (1989)

[4] D.E. Morris, N. G. Asmar, J. H. Nickel, R. L. Sid, J. Y. T.Wei, J. E. Post, *Physica C,* **159**, 287-294 (1989)

[5] J. Karpinski, S. Rusiecki, E. Kaldis, B. Bucher, E. Jilek, *Physica C,* **160**, 449-457 (1989)

[6] J. Karpinski, S. Rusiecki, E. Kaldis, B. Bucher, E. Jilek, Physica C, 161, 618-625 (1989)

[7] S. Jin, H. M. O'Bryan, P.K. Galagher, T.H.Tiefel, R.J. Cava, R.A. Fastnacht, G.W. Kammlott, *Physica C*, **165**, 415-418 (1990)

[8] K. Kishio,, T. Hasegawa, K. Suzuki, K. Kitazawa, K. Fueki, *Mat. Res. Soc. Symp. Proc.* **156**, 91-97(1989)

National Institute of Standards and Technology Special Publication 804, Chemistry of Electronic Ceramic Materials, Proceedings of the International Conference held in Jackson, WY, August 17-22, 1990, issued January 1991.

CALORIMETRIC STUDIES OF CERAMICS

Alexandra Navrotsky
Department of Geological and Geophysical Sciences
and Princeton Materials Institute
Princeton University
Princeton NJ 08544

ABSTRACT

High temperature reaction calorimetry is used to study a variety of ceramic problems. Lead borate solution calorimetry near 973 K and transposed temperature drop and scanning calorimetry to 1773 K are complementary techniques. This paper illustrates two diverse applications: the energetics of oxide superconductor phases in both the YBCO and doped lanthanum cuprate systems and *in situ* studies of melting and crystallization in a glass-forming silicate, $CaMgSi_2O_6$.

CALORIMETRY

Recent advances, in both isothermal and scanning experiments (see Table 1), make possible direct study of ceramic processes and processing at 873-1773 K. Three types of calorimeters are in use in our laboratory. Custom built Calvet twin microcalorimeters operate isothermally, typically near 973 K. Two sample chambers, roughly 2.5 cm in diameter by 15 cm high, each surrounded by sensitive thermopiles, are embedded in an alloy block maintained at constant temperature (1). Chemical reactions (e.g dissolution of a sample into molten lead borate solvent) take place in the sample chamber and heat flow is monitored. The relatively large size of the sample chamber permits the introduction of sample into solvent through a mechanical stirring device. The high sensitivity allows the measurement of small heat effects (0.3 to 1 J per experiment) and the use of small samples (10-50 mg of sample dissolving into 20-30 g of solvent). Samples can also be dropped into this calorimeter from room temperature. When no solvent is present, a transposed temperature drop experiment

Table 1 High Temperature Calorimetric Experiments

- Calorimeter essentially isothermal
  - Solvent present
    - Solution calorimetry: sample equilibrated in hot calorimeter, then dissolved. Differences in heats of solution give heat of reaction at calorimeter T
    - Drop solution calorimetry: sample dropped from room T. Sample may be encapsulated in Pt, pyrex glass (which dissolves) or lead borate glass (same as solvent), or as unencapsulated chunks. Differences in heats of drop-solution give heat of reaction at room T.
    - Differential drop solution calorimetry: sample in lead borate capsule dropped on one side simultaneously with matched empty capsule on other side, improved sensitivity for 5 mg samples
  - Solvent absent
    - Transposed temperature drop calorimetry
      - No permanent change in sample: heat content measurement, includes heat of any reversible phase change
      - Sample changes oxidation state: difference between first and second drop gives heat of redox reaction
      - Sample loses H_2O, CO_2 or other volatiles: difference gives heat of devolatilization
      - Sample undergoes irreversible phase change:difference gives heat of transformation at room T.
      - Sample undergoes change in degree of order or other structural parameters: difference gives ordering energy.
- Calorimeter changes temperature
  - At constant rate
    - Scanning calorimetry: generally semiquantitative measure of heat capacity and phase change or decomposition
  - In steps separated by isothermal periods
    - Step scanning calorimetry: best measurement of heat capacity and reversible phase transition enthalpies

measures the heat content of the sample and any transformation which occurs rapidly at calorimeter temperature (e.g. oxidation, dehydration, rapid phase transition, melting, or structural change) (1,2,3). When solvent is present, the drop solution experiment measures the sum of heat content and heat of solution (2). Drop solution calorimetry is useful when the sample in question can not be equilibrated at calorimetric temperature prior to dissolution because of decomposition, as is often the case with metastable or readily oxidized or reduced materials (2,3).

A commercial Setaram HT 1500 calorimeter also uses a thermopile to measure heat flow. Rather than being embedded in a massive alloy block, this much smaller calorimetric detector hangs free in a furnace, and can perform transposed temperature drop experiments at any temperature from about 873 to 1773 K (4). It can also be operated in scanning mode (continuous heating or cooling) or step-scanning mode (rapid temperature change by a small increment followed by an isothermal equilibration period) (5). For the latter experiments, using about 1 g of sample, we have made significant modifications to the original sample assembly and general operating procedure, as well as written our own software.

This calorimeter is too small for easy use for solution calorimetry. Furthermore, its calibration factor is sensitive to sample geometry and to detector positioning in the furnace, which changes slightly from run to run because the entire detector must be removed to change samples. We are presently constructing a calorimeter which should overcome some of these difficulties, combining features of our solution calorimeters with scanning capability using a thermopile permanently positioned in a furnace.

A commercial Setaram DSC 111 uses a very miniaturized thermopile detector in a silver block for differential scanning calorimetry from about 200 to 1073 K. It can measure heat capacities on 50-100 mg samples and detect phase transitions, oxidation, and other changes. Optimum heat capacity measurements using this instrument take considerable attention to detail. We use our own software rather than the commercially available package.

The DSC 111 is most useful as a semi=quantitative exploratory tool, as is the HT 1500 when used at a rapid scan rate (10 K/min). Once transitions are located, they can be studied in quantitative detail. Enthalpies of formation of complex oxides from their binary oxide components and of mixing in solid solutions are best determined using solution or drop solution calorimetry (1). Enthalpies of phase transitions can be determined by these two methods if both phases in question can be quenched to ambient (1,2). If a phase transition is rapid and reversible, scanning or step-scanning can be used (6). The ability to scan to 1773 K opens many new ceramic applications (e.g. melting, glass transitions, rapid displacive phase transitions, order-disorder.

ENERGETICS OF PHASES IN DOPED LANTHANUM CUPRATE AND YBCO SYSTEMS

Systems $La_{2-x}A_xCuO_{4-y}$ (A = Ba, Sr, Ca, Pb)

In these phases with structures derived from the K_2NiF_4 type, the substitution of a divalent ion for trivalent La is compensated by oxidation of copper from formal 2+ to formal 3+ oxidation state and/or by the creation of oxygen vacancies. We performed solution calorimetry on a series of single phase materials for Ba, Sr, Ca, and Pb, after having characterized their crystallographic parameters, metal ratios and oxygen contents (8).

X-ray diffraction data show that at room temperature, an orthorhombic to tetragonal phase change is observed at x=0.1 for Ba, Sr, and Ca. Johnston et al. reported that La_2CuO_4 undergoes a second order orthorhombic to tetragonal phase transformation between 506-536 K (7). Since solution calorimetry was performed at 977 K , the data obtained pertain to the tetragonal K_2NiF_4 structure for all samples. Oxygen contents, obtained by iodometric titration and/or thermogravimetry, for samples equilibrated in air at 973 K are shown in Fig. (1a). For Ba, Sr, and Ca. Initial substitution retains the stoichiometric oxygen content ($y<0.02$ for $x<0.10$), but increasing substitution causes oxygen vacancy formation to approximately the same extent for all three cations. Lead substitution results in oxygen loss for all values of x to the extent

Fig.1 Doped Lanthanum Cuprates

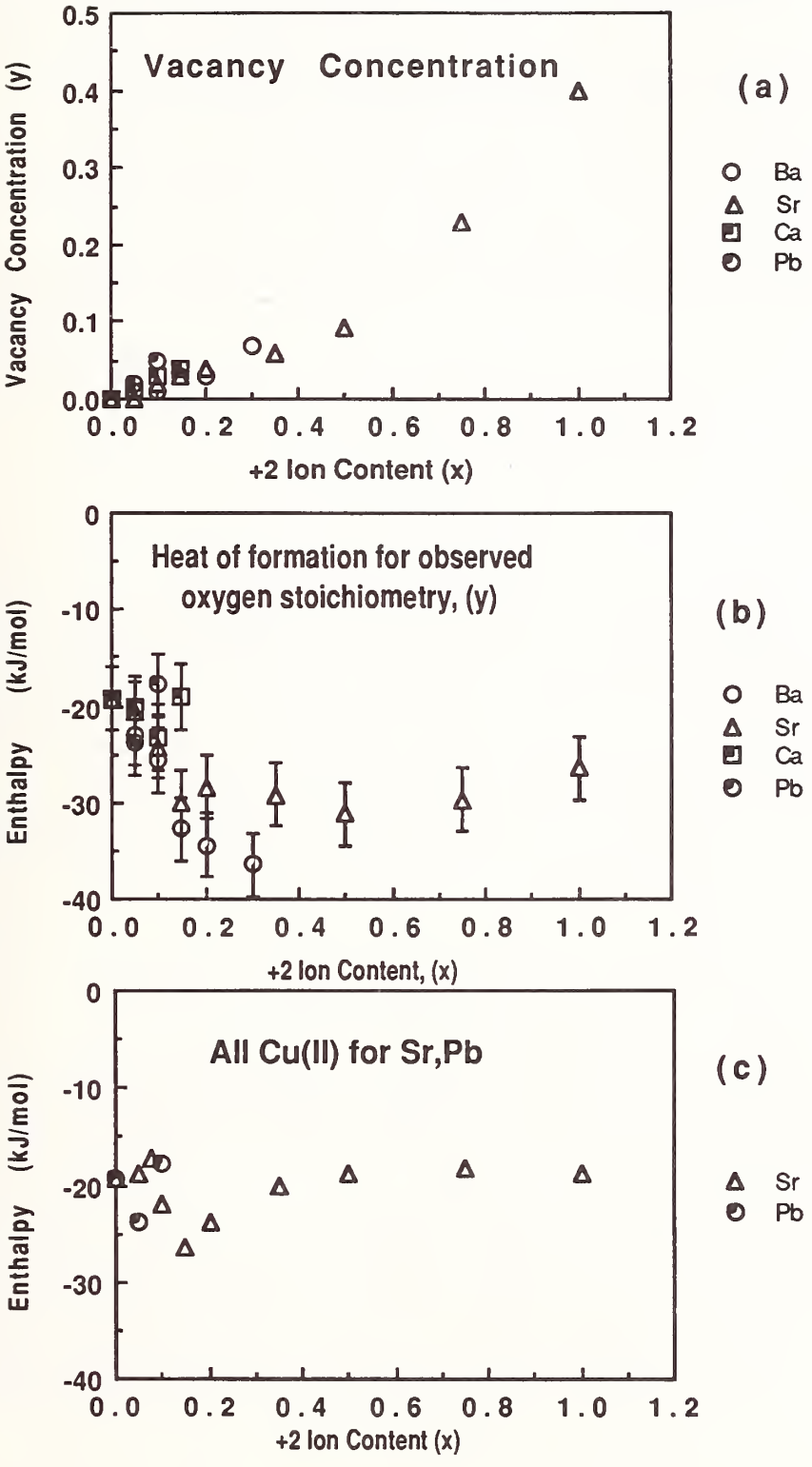

the enthalpy of formation of the Sr-substituted compound (ΔH_4) from the binary oxides remains very similar to that of pure La_2CuO_4. ΔH_4 in turn reflects the balance of two factors: (a) differences in the intrinsic properties of La and Sr (ionic size, charge, "basicity") which affect the energetics of the substitution of Sr for La, and (b) the enthalpy of oxygen vacancy formation. The nearly constant value of ΔH_4 suggests either that these two effects cancel each other in the Sr-La substitution, or that both terms are small.

If the same calculation is done for Ba-La using ΔH_3 derived from the Sr system, then values of ΔH_4 are slightly negative. This may be because ΔH_3, is actually more exothermic or that ΔH_4 is more exothermic for the Ba system.

If only enthalpies are considered, all these phases should have y values of zero because oxidation is clearly exothermic. Oxidation involves a large negative entropy due to fixing molecular oxygen into a crystal structure. A typical value for the entropy of oxidation for transition metals is -92 J/mol·K (9). At 977 K, this entropy can compensate the large negative enthalpy to yield non-zero y values. This entropy argument also explains why, as T increases (at given imposed external oxygen fugacity) the degree of oxidation of a given phase generally decreases.

Thermodynamics of Phases in the Y-Ba-Cu-O System

High temperature reaction calorimetry has been done on $YBa_2Cu_3O_x$ and related phases in the Y-Ba-Cu-O system. (3,14). Preliminary analysis of the oxidation state of Cu in lead borate indicates that the reaction during drop solution calorimetry is :

$$YBa_2Cu_3O_x\ (298\ K) + (6.5-x)/2\ O_2\ (g, 975\ K) = \{1/2\ Y_2O_3 + 2\ BaO + 3\ CuO\}\ (soln, 975\ K) \qquad (5)$$

that no formal oxidation states greater than Cu^{2+} (and Pb^{2+}, O^{2-}) are detected.

Heats of solution represent the reaction (at 977 K):

$$La_{2-x}A_xCuO_{4-y}\ (xl) = x\ AO\ (soln) + (1-x/2)\ La_2O_3\ (soln) + CuO\ (soln) + ((x-2y)/4)\ O_2\ (g) \quad (1)$$

From these values and the heats of solution of the component oxides the heat of formation at 977 K can be calculated:

$$(1-x/2)\ La_2O_3\ (xl) + (x)AO\ (xl) + CuO\ (xl) + ((x-2y)/4)O_2\ (g) = La_{2-x}A_xCuO_{4-y}\ (xl) \quad (2)$$

Fig. (1b) shows the heat of formation, ΔH_f, at 977 K as a function of divalent substitution, x. As x increases to about 0.15, ΔH_f becomes more exothermic, with the magnitude of the effect decreasing in the order Ba > Sr > Ca > Pb. At higher concentrations, the heats of formation for Ba and Sr level off, while those for Ca and Pb become more endothermic.

These observations can be interpreted as follows. The enthalpy of formation (Eq. (2)) can be divided into two steps:

$$A_xLa_{2-x}CuO_{4-(x-2y)/2} + (x-2y)/4\ O_2 = A_xLa_{2-x}CuO_4 \quad (3)$$

$$x\ AO + (1-x)/2\ La_2O_3 + CuO = A_xLa_{2-x}CuO_{4-(x-2y)/2} \quad (4)$$

Eq. (3) represents oxidation of an oxygen deficient phase containing only Cu^{2+} to a fully oxidized phase free of oxygen vacancies and containing the maximum amount of (formal) Cu^{3+}. The enthalpy associated with this process has been estimated as -157 ± 10 kJ per mol of O_2) by comparing the transposed temperature drop enthalpies of two samples, each having different oxygen contents, of both $La_{1.25}Sr_{0.75}CuO_{4-y}$ and of $LaSrCuO_{4-y}$. The enthalpy of step (4) can then be calculated by subtracting ΔH_3 from ΔH_2. The results (see Fig.(1c)) show that, when the effect due to oxidation is removed,

Data for the same system were obtained previously by transposed temperature drop calorimetry to 1057 K (3). Both show a linear dependence of enthalpy on oxygen content, x. The two lines are almost parallel, and give a partial molar enthalpy of oxygen (oxidation enthalpy), ΔH_{ox} = -209±7 kJ mol^{-1} per O_2 (present data) and ΔH_{ox} = -190±5 kJ/mol (3). The intercalation of oxygen is exothermic and energetically stabilizes structures with higher oxygen contents. The constancy of ΔH_{ox} with composition implies that the oxygen energetics are insensitive to the orthorhombic tetragonal transition and that the exact distribution of valence states changes continuously, with no titration end-point at x=6.5 (3).

Measured enthalpies of formation of $YBa_2Cu_3O_x$ and related phases are listed in Table 2. Large exothermic enthalpies of formation from simple oxides are due to the basicity of BaO. $Y_2Cu_2O_5$ has a small endothermic

Table 2 The Enthalpies of Formation of $YBa_2Cu_3O_x$ and Related Phases from Oxides and from Elements

Compound	ΔH_f (kJ/mol) from oxides	from elements
$YBa_2Cu_3O_x$ (295 K)		
x=6.33	-79.4±7.3 [a]	-2575±9
x=6.45	-76.8±4.9 [a]	-2590±7
x=6.48	-74.1±6.1 [a]	-2592±8
x=6.64	-86.8±7.2 [b]	-2608±9
x=6.87	-101.8±6.4 [b]	-2623±9
x=6.92	-110.3±9.5 [b]	-2631±11
Y_2BaCuO_5 (295 K)	-52.9±3.0 [c]	-2664±5
Y_2BaCuO_5 (975 K)	-59.3±3.0 [c]	
$Y_2Cu_2O_5$ (295 K)	+9.2±3.2 [c]	-2211±5
$Y_2Cu_2O_5$ (975 K)	+6.6±2.9 [c]	
$BaCuO_{2.01}$ (295 K)	-83.8±3.1 [b]	-789±4
$YBa_2Cu_4O_8$ (295 K)	-145.8±10.4 [b]	-2824±12

a. from BaO Y_2O_3, CuO and Cu_2O
b. from BaO, Y_2O_3, CuO and O_2
c. from BaO, Y_2O_3, CuO

enthalpy of formation from the oxides, implying that it is entropy-stabilized.

To estimate the stability of various phases to possible decomposition, we choose reactions involving neither oxidation nor reduction, so that enthalpy can be taken as an estimate of free energy, since entropy changes of solid-solid reactions are usually small.For the reaction:

$$YBa_2Cu_3O_7 + CuO = YBa_2Cu_4O_8 \qquad (6)$$

ΔH_{298} = -78.1±5.3 kJ/mol. This implies that the 1:2:4 phase is indeed more stable at its own composition than a mixture of fully oxygenated 1:2:3 and CuO.

For the reaction:

$$1/2\ Y_2BaCuO_5 + 3/2\ BaCuO_{2.01} + CuO = YBa_2Cu_3O_{6.515} \qquad (7)$$

ΔH_{298} = 28.9±4.5 kJ/mol. This suggests that the 1:2:3 compound with intermediate oxygen content near x=6.5 may be unstable with respect to a mixture of "green phase" and "$BaCuO_2$", and may explain why these phases are often found as impurities in the 1:2:3 material. We are investigating whether the fully oxygenated 1:2:3 phase has any stability field in T- $f(O_2)$ space.

DIRECT MELTING AND CRYSTALLIZATION OF $CaMgSi_2O_6$

$CaMgSi_2O_6$, diopside, is a common mineral and constituent of natural and synthetic silicate melts and glasses. Its nominal melting point is 1665 K but some incongruency below that temperature is now established (4,5). Rapid cooling (>100 K/min) produces a glass; slower cooling (1-100 K/hr) produces crystallization of a mixture of phases at 50-100 K below the liquidus. Using step-scanning mode in the HT 1500 calorimeter, we traced the melting of diopside and determined that, for a stoichiometric crystalline sample, incongruent melting begins at 1606 K.(5). The first 20% of melting occurs over a 44 K interval, and the remaining 80% within 15 K. Scanning calorimetry is a very sensitive tool for detecting small amounts of melting (see Fig. (2)). The enthalpy of fusion, 137.7 kJ/mol, (see Fig. (2)) is in excellent agreement with previous measurements by transposed temperature drop calorimetry

Fig. 2
Diopside melting:step scanning calorimetry

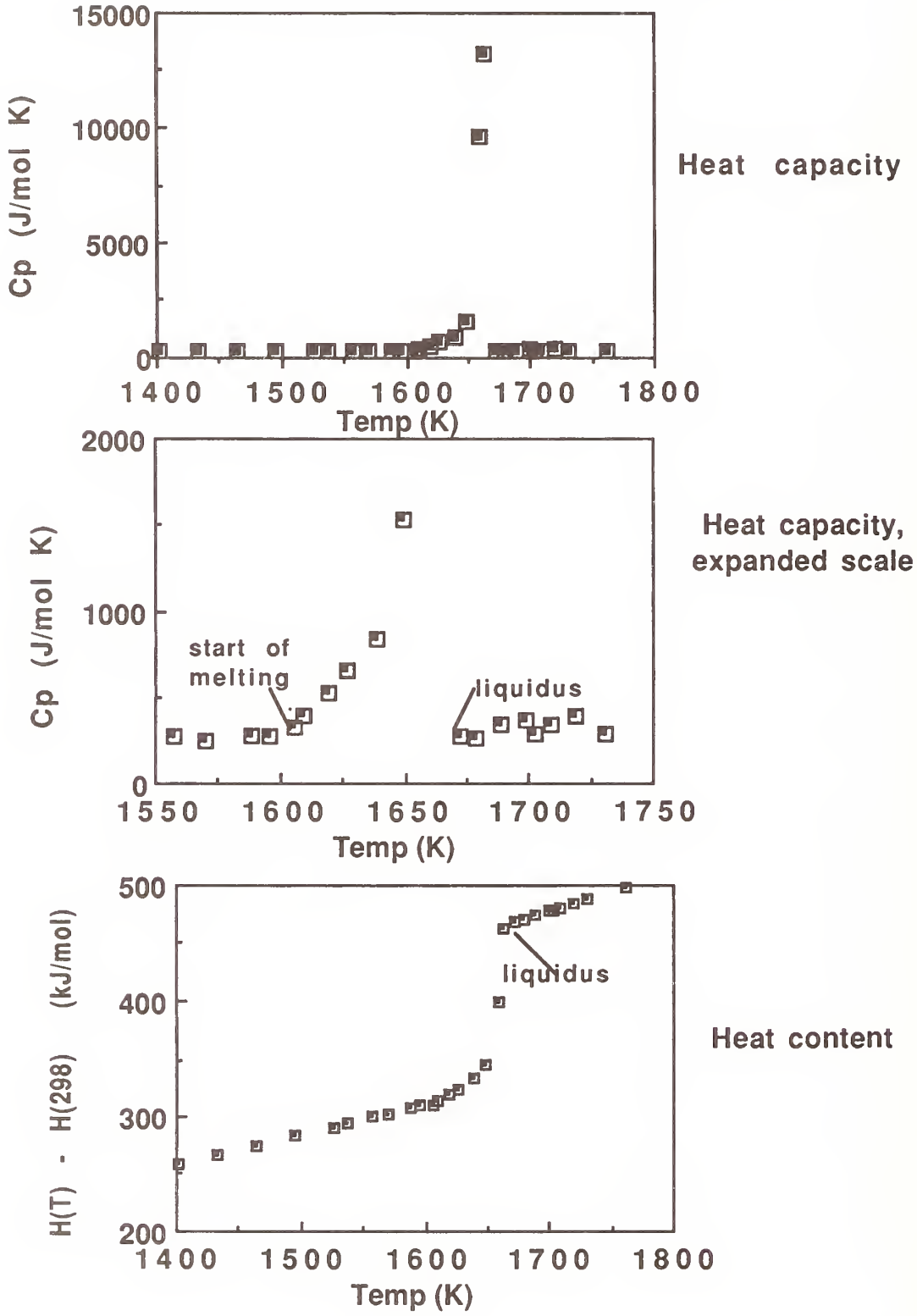

(5) and by thermochemical cycles involving the glassy phase (10). The heat capacities derived for the crystalline and liquid phases are in good agreement with previous values obtained by conventional drop calorimetry (10). Step scanning provides a sensitive and accurate way of determining the heat capacities of silicate liquids . We are currently studying a series of Fe_2O_3-bearing molten silicates.

We performed crystallization experiments in the calorimeter using continuous cooling at different rates (5). An initial experiment at 30 K/hr starting at 1715 K produced a single large exotherm at 1545 K. The product was fully crystalline, consisting of two phases, a magnesium-rich diopside solid solution $Ca_{1-x}Mg_{1+x}Si_2O_6$ and a slightly magnesian wollastonite $Ca_{1-x}Mg_xSiO_3$. Three experiments were done at a cooling rate of 10 K/hr, starting at 1691 K. Each produced single exotherms, but, though the conditions were nominally identical, the exotherms occurred at somewhat different temperatures, 1576, 1534, and 1566 K. Our experiments are in general agreement with the kinetic crystallization study of Kirkpatrick et al. (11), although we could not confirm the small amounts of forsterite, Mg_2SiO_4, which they reported.

In situ studies of crystallization in glass ceramics should now be possible. Since the enthalpy released is a sensitive indicator of crystallization, scanning calorimetry can be used directly to construct time-temperature-transformation (T-T-T) curves. When a metastable phase is initially formed (e.g. beta-quartz in a cordierite ceramic), its subsequent annealing and transformation can be followed. The incubation or pre-nucleation stages of crystallization (during which no crystallization is detected by bulk methods such as diffraction) may nevertheless involve significant changes in glass structure. Since much of the energy difference between glass and crystal may come from changes in local environments rather than from long range order per se (12), we propose that a significant part of the enthalpy of vitrification may be released before crystallization becomes detectable by conventional means. This hypothesis should be tested in glasses for which homogeneous rather than heterogeneous nucleation is suggested.

ACKNOWLEDGEMENTS

This work was supported by the National Science Foundation, the Department of Energy, and IBM Corporation. The following people participated in these studies at Princeton: C. Bennett, J. Bularzik, J. DeYoreo, J. DiCarlo, R. Lange, K. Mocala, M. Parks, L. Topor, Z. Zhou, D. Ziegler. The following collaborators were involved: J. Bringley, P. Davies, A. Jacobson, B. Scott, E. Takayama-Muromachi, S.Trail.

REFERENCES

1. Navrotsky, A. Phys. Chem. Min. 2, 89 (1977).

2. Ashida, T., Kume, S., Ito, E., Navrotsky, A. Phys. Chem. Miner. 16 239 (1988).

3. Parks, M. E., Navrotsky, A., Mocala, M., Takayama-Muromachi, E., Jacobson, A., and Davies, P. J. Solid State Chem. 79, 53 (1989). Erratum (in press).

4. Ziegler,D., Navrotsky,A. Geochim. Cosmochim. Acta 50, 2461 (1986).

5. Lange, R.A., DeYoreo, J.J., Navrotsky, A. Amer. Mineral. (in press).

6. Redfern, S.A.T., Salje, E., Navrotsky, A. Contrib. Mineral. Petrol. 101, 479 (1989).

7. Johnston, D.C., Stokes, J.P., Goshorn, D.P., Lewandowski, J.T., Phys. Rev. B 36, 4007 (1987).

8. Bularzik, J., Navrotsky, A. DiCarlo, J. Bringley, J., Scott, B., and Trail, S. submitted, Fall 1990 Materials Research Society Meeting.

9. Navrotsky, A., in "M. T. P. Reviews of Science: Inorganic Chemistry Series 2" (D.W.A. Sharp, Ed.), P. 29, Butterworth-Univ. Park Press, Baltimore, MD (1974).

10. Stebbins, J.F., Carmichael, I.S.E., Weill, D.F., Amer. Mineral. 68, 717 (1983).

11. Kirkpatrick, R.J., Kuo, L.C., Melchoir, J. Amer. Mineral. 66, 223 (1981).

12. Navrotsky, A., Geisinger, K.L., McMillan, P.F., Gibbs, G.V. Phys. Chem. Mineral. 11, 284 (1985)

13. Zhou, Z., Navrotsky, A., Scott, B., Trail, S., submitted Fall 1990 Materials Research Society Meeting.

P. D. Davies: One thing that we both well know is the advantage of calorimetric sensitivity to probing short-range order, which is quite difficult to quantify using structural techniques. The ferroelectric relaxors discussed by Bob Newnham and other speakers exhibit quite complex microstructural ordering phenomena. When these are made at very low temperatures, say 600°C, by sol-gel techniques you might expect the short range order to be different to that in samples prepared by conventional techniques at high temperatures. Do you have any plans to examine these compounds to see whether different synthesis methods lead to differing degrees of short-range order?

A. Navrotsky: Well, in fact, that was sort of behind some questions that I raised in my talk. Certainly something like magnesium and niobium ordering, although the electrostatic argument says the size of the domain is going to remain small, could well vary with T. The ratio of ordered to disordered regions may be strongly dependent on the preparation techniques.

Niobium is not an easy element to dissolve in high temperature oxide fluxes. We've actually made some progress in this technique. Interestingly enough, this progress shows the interplay of different fields. We first got started dissolving lanthanum, niobium and titanium, for looking at glass structures, looking at the behavior of highly-charged cations in glasses, partly for chemical systematics and partly for rad waste reasons. Yes, we can do it now and, yes, if somebody had some well-characterized samples, we'd be delighted to try.

National Institute of Standards and Technology Special Publication 804, Chemistry of Electronic Ceramic Materials, Proceedings of the International Conference held in Jackson, WY, August 17-22, 1990, issued January 1991.

SYNTHESIS AND PROPERTIES OF Ba-FREE SUPERCONDUCTIVE $(Eu,Ce)_4(Eu,Sr)_4Cu_{6-x}M_xO_z$ (M:Fe,Co,Al)

Ataru Ichinose, Takahiro Wada, Yuji Yaegashi, Akiko Nara
H. Yamauchi and Shoji Tanaka

Superconductivity Research Laboratory, ISTEC
10-13, Shinonome 1-Chome, Koto-Ku, Tokyo 135, Japan

Ba-free "446" [$(Eu,Ce)_4(Eu,Sr)_4Cu_6O_z$-type] samples were synthesized by partially substituting Fe, Co or Al for Cu. We prepared Ba-free $(Eu_{3/4}Ce_{1/4})_4(Eu_{1/3}Sr_{2/3})_4Cu_{6-x}M_xO_z$ samples (M=Fe, Co and Al and x=0.5, 1.0, 1.5 and 2.0). All the samples were of near single phase and the crystal structure was tetragonal. As x increased, the length of the a axis increased, while that of the c axis decreased. The samples with x=0.5 and M=Fe and Co exhibited superconductivity with zero-resistance temperatures at 23 and 28 K, respectively. None of the samples with M=Al exhibited zero resistances, but those with x=0.5 and 1.0 exhibited superconductivity onsets around 20 K. The appearance of superconductivity for the series of the samples with Al was explained in terms of the carrier density. However, the appearance of superconductivity for both series of samples with Fe and Co was indifferent of the carrier density.

I. INTRODUCTION

Sawa et al.[1] discovered cuprate superconductors of a new type with Tc's around 40 K. These cuprates are represented by a general formula, $(Ln,Ce)_4(Ln,Ba)_4Cu_6O_z$ (Ln=Nd, Sm and Eu), and are termed as 446 oxides in the present paper. The structure of this family of cuprates is perovskite- and fluorite-related and similar to both the triperovskite structure of $YBa_2Cu_3O_z$ and the Nd_2CuO_4 structure. The crystal structure is illustrated in Fig. 1. In the unit cell of this structure, two different types of sites exist for lanthanide ions: the "A1" sites are occupied by small ions, i.e., Ce^{4+}, and medium-sized ions, i.e., Nd^{3+}, Sm^{3+} and Eu^{3+}, while the "A2" sites are occupied by large ions, i.e., Ba^{2+}, as well as by the medium-sized ions. The oxygen site on the Cu(1)-O(1) plane was found to be partially occupied[1]. That is, oxygen vacancies are randomly

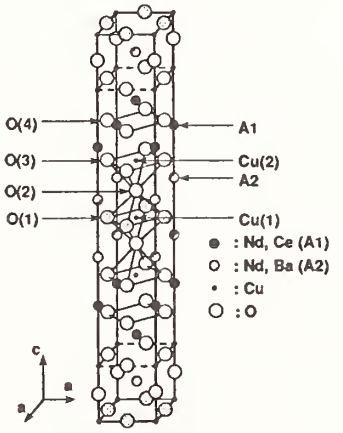

Fig. 1. Crystal structure of the 446 compound.

distributed on the Cu(1)-O(1) plane such that the crystal system of this cuprate be tetragonal. Previously, we reported on 446 materials with Sr^{2+} which partially substituted for Ba^{2+} in the A2 site[2]. We also reported that 446 oxides with two different ions for medium-sized ion sites, i. e. , $(Ln, Ce)_4(La, Ba, Sr)_4Cu_6O_Z$ (Ln=Eu, Gd, Dy, Ho and Y),[3],[4] were able to be prepared. In the present work, we synthesize Ba-free 446 oxides by substituting metallic ions such as Fe, Co or Al ions for copper ions. The samples studied are given by the formula $(Eu_{3/4}Ce_{1/4})_4(Eu_{1/3}Sr_{2/3})_4Cu_{6-x}M_xO_Z$, where M=Fe, Co and Al, and x=0.5, 1.0, 1.5 and 2.0.

II. EXPERIMENTAL PROCEDURE

The starting materials were Eu_2O_3, CeO_2, $SrCO_3$, CuO, Fe_2O_3, $CoCO_3$ and $Al(NO_3)_39H_2O$ powders. The powders were weighed to nominal compositions of $(Eu_{3/4}Ce_{1/4})_4(Eu_{1/3}Sr_{2/3})_4Cu_{6-x}M_xO_Z$ in which M=Fe, Co and Al and x=0.5, 1.0, 1.5 and 2.0. The mixed powder was calcined at 1000-1020 ℃ in air, and then pulverized and pressed into parallelepiped bars. The bars were sintered at 1040 ℃ in O_2 gas flow and slowly cooled. These samples were reheated at 400-600 ℃ at a high oxygen partial pressure, $P(O_2)$=200 atm.

The lattice constants were determined by x-ray powder diffraction using CuKα radiation. A curved graphite monochrometor was placed in the scattering beam path. The oxygen contents of the samples were determined by a coulometric titration method[5],[6]. Electrical resistivity was measured from room temperature down to the He boiling point by a conventional dc four-probe method.

III. RESULTS & DISCUSSION

Figure 2 shows of the x-ray diffraction pattern for $(Eu_{3/4}Ce_{1/4})_4(Eu_{1/3}Sr_{2/3})_4Cu_4Co_2O_Z$ annealed at PO_2=200 atm. The peaks in the pattern are indexed for a tetragonal unit cell with the lattice constants, a=3.860 Å and c=27.95 Å. The peaks which are not identified as those of 446 phase are marked with asterisks. All the samples were of near single phase and the crystal system of each sample was tetragonal. The peaks marked with asterisks in Fig. 2 were larger for the samples with the smaller values of the metallic ion content, x. The samples with x=0 were of multi phases and peaks for a 446 phase were hardly observed. The relationship between the oxygen content, z, and the metallic ion content, x, is given in Figs. 3(a), (b) and (c) for three different series of samples

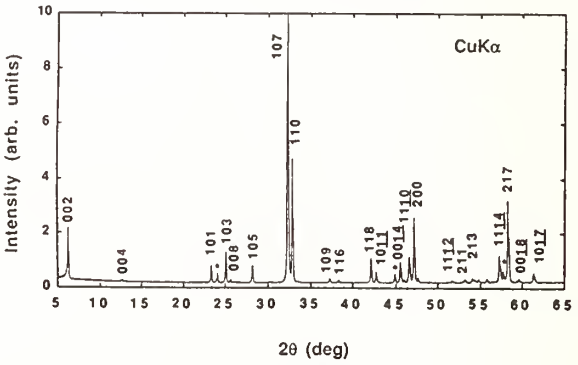

Fig. 2. X-ray diffraction pattern for $(Eu_{3/4}Ce_{1/4})_4(Eu_{1/3}Sr_{2/3})_4Cu_4Co_2O_z$ annealed at high oxygen partial pressure of 200 atm.

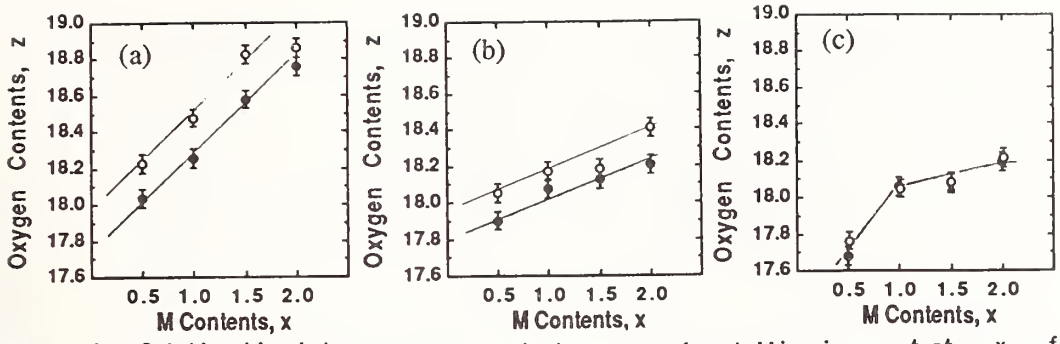

Fig. 3. Relationship between oxygen content, z, and metallic ion content, x, for $(Eu_{3/4}Ce_{1/4})_4(Eu_{1/3}Sr_{2/3})_4Cu_{6-x}M_xO_z$ with (a)M=Fe, (b)M=Co and (c)M=Al. Close circles are for as-sintered samples and open circles for annealed samples at high oxygen partial pressure of 200 atm.

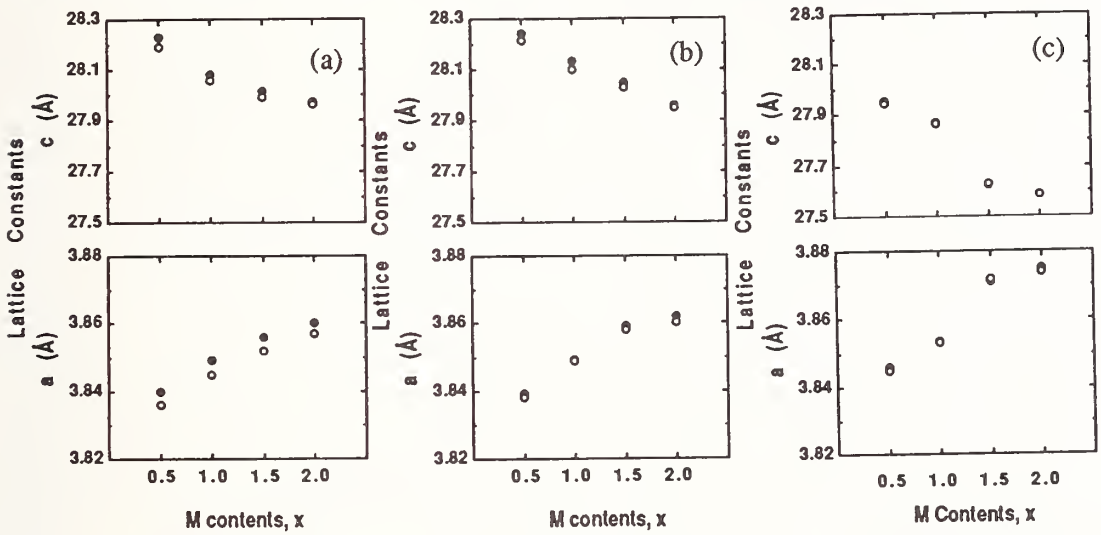

Fig. 4. Relationship between lattice constants and metallic ion content, x, for $(Eu_{3/4}Ce_{1/4})_4(Eu_{1/3}Sr_{2/3})_4Cu_{6-x}M_xO_z$ with (a)M=Fe, (b)M=Co and (c)M=Al. Close circles are for as-sintered samples and open circles for annealed samples at high oxygen partial pressure of 200 atm.

containing Fe, Co and Al ions, respectively. The oxygen content increased as x increased for each of the three series. For the series of samples containing Al, as x increased, the oxygen content, z, was initially low and leveled off at a constant value around 18.2. The oxygen contents of the high-O_2-pressure annealed samples were larger than those of as-sintered samples for the series containing Fe and Co. On the contrary, for the series of samples containing Al, the oxygen contents were nearly identical before and after high-O_2-pressure annealing. These observations suggested that the oxygen contents for the series of samples containing Al were hard to be increased by high-O_2-pressure annealing. This was probably because the ionic radius of Al^{3+}(0.535 Å)[7] was much smaller than that of Cu^{2+}(0.73 Å)[7]. Figures 4(a)-(c) show the relationships between the lattice constants, a and c, and the metallic ion content, x. For the series

of 446 samples containing Fe and Co, as metallic ion content, x, increased, the c-axis length decreased monotonically, while the a-axis length increased. It should be noted that both a and c axes were shorter after high-O_2-pressure annealing for these two series of samples (Figs. 4(a) and (b)). Both lattice constants, a and c, for the series of samples containing Al abruptly changed between x=1.0 and 1.5. However, the changes in the a- and c-axis length before and after high-O_2-pressure annealing were minimal (Fig. 4(c)). Thus, it is likely that the changes in the lattice constants were caused by the oxygen added by the high-O_2-pressure annealing procedure.

The temperature dependence of electrical resistivity is given in Figs. 5(a), (b) and (c) for the three series of the high-O_2-pressure annealed samples containing Fe, Co and Al for M, respectively. Among the samples with M=Fe, superconductivity clearly appeared for the sample with x=0.5 and the zero-resistance temperature, $T_c^{R=0}$, for this sample was 23 K. The magnitude of resistivity of each sample was lower than that of the same sample without high-O_2-pressure annealing. The zero-resistance temperature, $T_c^{R=0}$, and the superconductivity onset temperature, T_c^{on}, of the sample with M=Co and x=0.5 increased respectively from 10 to 28 K and from 25 to 39 K by high-O_2-pressure annealing. The magnitude of resistivity of each sample in the series containing Co was lowered by high-O_2-pressure annealing. For the series of samples containing Al, even if the samples were annealed at high-O_2-partial pressure, the superconducting transition temperature and the magnitude of resistivity in normal state were not much altered.

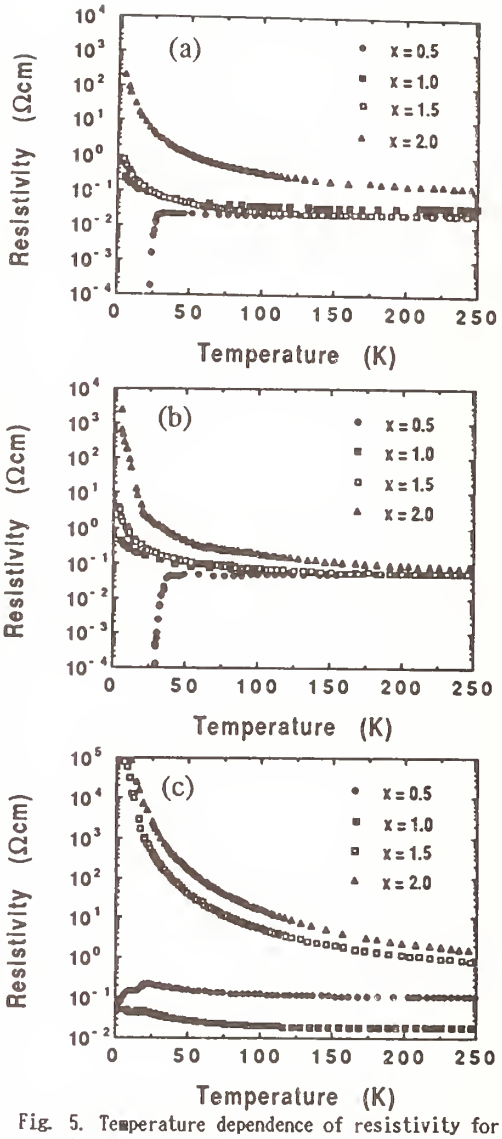

Fig. 5. Temperature dependence of resistivity for $(Eu_{3/4}Ce_{1/4})_4(Eu_{1/3}Sr_{2/3})_4Cu_{6-x}M_xO_z$ annealed at high oxygen partial pressure of 200 atm with (a)M=Fe, (b)M=Co and (c)M=Al.

Sunshine et al.[8] reported that in $YSr_2Cu_{3-x}M_xO_z$ (123 structure), Fe, Co or Al for M occupied Cu(1) sites located between two Sr sites along the c axis. Because of the similarity

of the 446 structure to the 123 structure, we anticipated that Fe, Co or Al when doped into the 446 structure would occupy the Cu(1) sites (Fig. 1). Then the oxygen occupancy for the O(1) sites which surrounded a Cu(1) site should be altered to maintain the local electro-neutrality condition when Fe, Co or Al ions are substituted for Cu(1) ions. Therefore, if the valence of a Cu(1) ions is assumed to be 2+, and the metallic ion content, x, increases by 1.0, the oxygen content, z, increases by 0.5 for M with the valence of 3+, while z remain unchanged if the valence of M is 2+. From this point of view, "3+" is resulted for the valence of a Fe ion (which is one of the most possible valence numbers for a Fe ion), because the gradient of the z-vs-x curve given in Fig. 3(a) is approximately equal to 0.5. Similarly, a valence between 2+ and 3+ is resulted for the valence of a Co ion (which is possible for a Co ion in a resonating valence state between 2+ and 3+), since the gradient of the z-vs-x curve given in Fig. 3(b) is ~0.2. Therefore, it is likely that the metallic ion (M) substitution for copper in the Ba-free 446 compounds, $(Eu_{3/4}Ce_{1/4})_4(Eu_{1/3}Sr_{2/3})_4Cu_{6-x}M_xO_z$, does not alter the carrier density for x up to 2.0 when M=Fe or Co. For each of the series of samples with M=Fe and x up to 1.5 and those with M=Co and x up to 2.0, the magnitudes of resistivity at room temperature are nearly identical. It seems that the carrier density for every sample of each of the series is nearly constant regardless the value of x. If so, we cannot employ the carrier density as the crucial factor the appearance of superconductivity. On the contrary, for the series of samples with M=Al as shown in Fig. 3(c), the oxygen content did not increase enough to offset the positive charge due to the substitution of Al^{3+} at the Cu(1) site. The excess positive charge would reduce the hole (carrier) concentration. Therefore, for the samples with M=Al, it is likely that the disappearance of superconductivity is due to the decrease in the carrier density.

For the series of samples with M=Fe or Co, the disappearance of the superconductivity might be caused by the magnetic interference due to the substituted metallic ions, i.e., Fe or Co ions. However, presently we have no experimental evidence to support this speculation.

So far, two cases were distinguished for the disappearance of superconductivity in 446 compounds with metallic ions which were partially substituted for Cu ions : (1) Disappearance of superconductivity in the 446 compounds with Fe or Co ions doped was hardly related to the change in the carrier density. (2) In the 446 compounds with Al ions doped, superconductivity disappeared when the carrier (hole) density was reduced. Case (2) corresponds to the mechanism proposed by Tokura et al.[9] Case (1) seems to remain puzzled. There have been reported experimental data that the a-axis dimension which represents the Cu-O bond length on the Cu-O plane is crucially important for the appearance of supercon-

ductivity in such systems as $(La_{1-x}M_x)_2CuO_4$ (M=Ba, Sr or Ca)[10] and $(Pb,Cu)Sr_2(Y,Ca)Cu_2O_z$[11]. Actually, among the samples with M=Fe or Co, superconductivity showed only for those which had the a-axis length shorter than ~3.84 Å, and among the samples with M=Al, superconductivity was observed for those whose a-axis length was shorter than 3.85 Å. From these observations, it may be said that for the present 446 compounds containing Fe, Co and Al, superconductivity showed when the a-axis length was shorter than a threshold value around 3.845 Å.

IV. CONCLUSION

We successfully synthesized Ba-free 446 [$(Eu,Ce)_4(Eu,Sr)_4Cu_6O_z$-type] samples by partially substituting Fe, Co or Al for Cu. It was demonstrated that without substitution of metallic ions such as Fe, Co and Al ions for Cu ions , Ba-free 446 structure was not formed. The a axis increased and the c axis decreased with increasing x for $(Eu_{3/4}Ce_{1/4})_4(Eu_{1/3}Sr_{2/3})_4Cu_{6-x}M_xO_z$. The samples with x=0.5 and M=Fe and Co exhibited superconductivity. The superconductivity transition temperature of these samples were raised when the samples were annealed at a high oxygen pressure of 200 atm. The superconductivity of the sample with x=0.5 and M=Al was significantly improved by annealing at high oxygen partial pressure. For the samples with M=Al, the disappearance of superconductivity was explained by the reduction in the carrier density. For the samples with M=Fe and Co, the disappearance of superconductivity was not related to a change in the carrier density which rather remained constant. For all the samples studied in this work, it seemed that there might be a threshold value for the dimension of the a axis : only samples with the a axis shorter than the threshold value (3.845 Å) exhibited superconductivity.

ACKNOWLEDGMENT

We are indebted Dr. S. Tajima of SRL for her helpful discussions.

REFERENCE

[1] H. Sawa, K. Obara, J. Akimitsu, Y. Matsui and S. Horiuchi, J. Phys. Soc. Jpn., 58, 2252(1989).

[2] A. Ichinose, T. Wada, Y. Yaegashi, H. Yamauchi and S. Tanaka, Jpn. J. Appl. Phys., 28, L1765(1989).

[3] T. Wada, A. Ichinose, Y. Yaegashi, H. Yamauchi and S. Tanaka, Phys. Rev. B37, 5912(1989).

[4] T. Wada, A. Ichinose, Y. Yaegashi, H. Yamauchi and S. Tanaka, Jpn. J. Appl. Phys., 29, L266(1990).

[5] K. Kurusu, H. Takami and K. Shintomi, Analyst, 114, 1341(1989).

[6] M. Kosuge and K. Kurusu, Jpn. J. Appl. Phys., 28, L810(1989).

[7] R. D. Shannon, Acta Crystallogr. A32, 751(1976).

[8] S. A. Sunshine, L. F. Schneemeyer, T. Siegrist, D. C. Douglass, J. V. Waszczak, R. J. Cava, E. M. Gyorgy and D. W. Murphy, Chem. Mater., 1, 331(1989).

[9] Y. Tokura, J. B. Torrance, T. C. Huang and A. I. Nazzal, Phys. Rev. B38, 7156(1988).

[10] K. Kishio, K. Kitazawa, N. Sugii, S. Kanbe, K. Fueki, H. Takagi and S. Tanaka, Chem. Lett., 635(1987).

[11] T. Maeda, K. Sakuyama, S. Koriyama, H. Yamauchi and S. Tanaka, to be published.

National Institute of Standards and Technology Special Publication 804, Chemistry of Electronic Ceramic Materials, Proceedings of the International Conference held in Jackson, WY, August 17-22, 1990, issued January 1991.

EXCESS OXYGEN DEFECTS IN LAYERED CUPRATES

P. Lightfoot[1], Shiyou Pei[1], J. D. Jorgensen[2], X.-X.Tang[3], A. Manthiram[3] and J. B. Goodenough[3], (1)Science and Technology Center for Superconductivity and (2) Materials Science Division, Argonne National Laboratory, Argonne, IL 60439 and (3) Center for Materials Science and Engineering, University of Texas at Austin, Austin, TX 78712.

ABSTRACT

Neutron powder diffraction has been used to study the oxygen defect chemistry of two non-superconducting layered cuprates, $La_{1.25}Dy_{0.75}CuO_{3.75}F_{0.5}$, having a T*-related structure, and $La_{1.85}Sr_{1.15}Cu_2O_{6.25}$, having a structure related to the that of the newly discovered double-layer superconductor $La_{2-x}Sr_xCaCu_2O_6$. The role played by oxygen defects in determining the superconducting properties of layered cuprates is discussed.

INTRODUCTION

Defects are known to play a critical role in the synthesis and superconducting properties of the high T_c oxide superconductors (1). The unique role played by excess oxygen doping has been elegantly demonstrated in the $La_2CuO_{4+\delta}$ system by Jorgensen et al. (2), who showed that superconductivity in this system in fact results from a subtle phase separation into an oxygen-rich superconducting phase and a stoichiometric non-superconducting phase, both having orthorhombic structures based on the K_2NiF_4, or T structure. Due to the relatively small defect concentration, it was not possible to locate the excess oxygen defect in the neutron powder diffraction study of $La_2CuO_{4+\delta}$. However, a later study of the isostructural La_2NiO_{4+y} ($y \sim 0.18$) unambiguously determined the excess oxygen to be located in an interstitial site in the La_2O_2 rock-salt like layers of the structure (3).

Two structures closely related to the T structure are the T' and T* structures, differing only in the positions of the oxygen atoms within the lattice,

leading to square planar and square pyramidally coordinated copper, respectively. In view of the similarities between these structures, it may be expected that similar interstitial oxygen defects could also occur in these systems, and may indeed play a critical role in determining the electronic behaviour of these systems, both of which have been made superconductive (4,5). In this paper we describe the observation, by neutron powder diffraction, of such a defect in the T* phase $La_{1.25}Dy_{0.75}CuO_{3.75}F_{0.5}$ (6). We also describe the identification of the excess oxygen location in the double-layer phase $La_{1.85}Sr_{1.15}Cu_2O_{6.25}$ (7), and discuss this in the light of the related, recently discovered (8) superconducting phase $La_{1.6}Sr_{0.4}CaCu_2O_6$.

EXPERIMENTAL

A powder sample of $La_{1.25}Dy_{0.75}CuO_4$ was obtained from stoichiometric quantities of La_2O_3, Dy_2O_3 and CuO, fired at 950°C for 12h and then at 1050°C for a further 20h. Fluorination was achieved by a low-temperature anion exchange reaction, by reacting $La_{1.25}Dy_{0.75}CuO_4$ with ZnF_2 in an evacuated sealed tube at 280°C for 48h.

$La_{1.85}Sr_{1.15}Cu_2O_{6.25}$ was obtained by firing intimately mixed La_2O_3, $SrCO_3$ and CuO in 1 atm O_2 according to the following scheme: 1000°C (20h), 1050°C (20h), 500°C (12h), 450°C (12h), 400°C (12h), 350°C (12h) and 300°C (12h). This procedure was found to maximise the oxygen content for a 1 atm O_2 anneal. Neutron powder diffraction data were collected on the Special Environment Powder Diffractometer at Argonne's Intense Pulsed Neutron Source. Data were analysed by the Rietveld method.

RESULTS AND DISCUSSION

$La_{1.25}Dy_{0.75}CuO_{3.75}F_{0.5}$. Our refinement (6) shows that this phase adopts an orthorhombically distorted structure based on that of the T* phases (9). Incorporation of the excess anion content occurs in an interstitial site in the La_2O_2 rocksalt layers of the

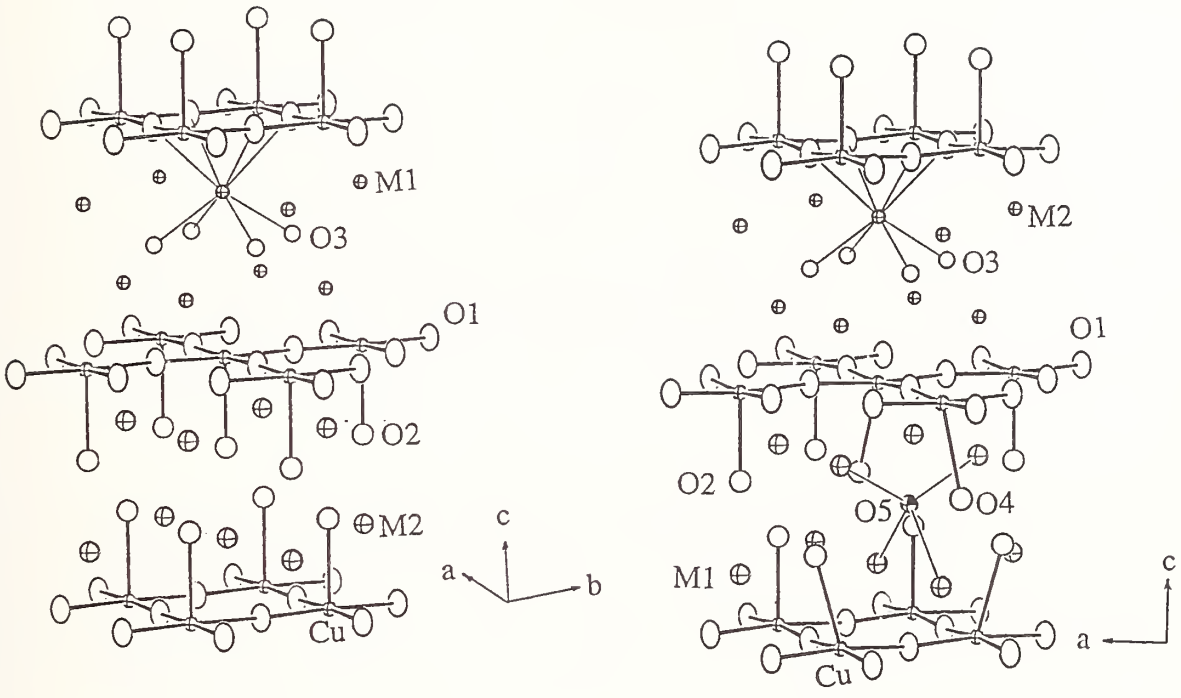

(a) (b)

Figure 1. (a) Idealized tetragonal T* structure, showing alternating T' (top half) and T (bottom half) layers. (b) The distorted T* structure of $La_{1.25}Dy_{0.75}CuO_{3.75}F_{0.5}$, showing incorporation of the interstitial defect, O(5). Favorable coordination of O(5) to four M(1) and four displaced anion, O(4), sites occurs. Note that only half of the true unit cell (which is rotated by 45° around the c-axis, relative to (a)) is shown, for ease of comparison of the two structures.

structure, and not in the vacant "apical" position in the T' -type half of the structure. This type of interstitial defect is directly analogous to that previously observed in $La_2NiO_{4.18}$ (3) and that thought to be the doping mechanism responsible for superconductivity in $La_2CuO_{4+\delta}$ (2).Accommodation of the defect requires displacement of the four neighboring apical oxygens on to new sites, in order to provide favorable anion-anion contacts. A comparison of the undistorted (tetragonal) $La_{1.25}Dy_{0.75}CuO_4$ and the distorted $La_{1.25}Dy_{0.75}CuO_{3.75}F_{0.5}$, showing incorporation of the anion defect, is presented in Figure 1. Interestingly, high oxygen partial pressures are often found necessary to make the T* phases superconducting (10,11). Hence, although the present phase does not superconduct, it is not unreasonable that a similar type of defect may again turn out to be the doping mechanism responsible for superconducting behavior in the T* phases.

$La_{1.85}Sr_{1.15}Cu_2O_{6.25}$.The structure adopted by this phase (7) is an oxygen-deficient variant of the well-known $Sr_3Ti_2O_7$ structure (n=2 member of the Ruddlesden-Popper series $AO.nABO_3$). A view of the structure is shown in Figure 2. Previous refinements of the structures of cuprates of this type, $La_2SrCu_2O_6$ (12) and $La_{1.9}Ca_{1.1}Cu_2O_6$ (13), have suggested a zero, or very small occupancy of the O(3) site between neighboring CuO_5 pyramidal layers. For the present case, where a significantly higher oxygen content has been obtained, we have shown unambiguously that the inter-layer site can accommodate a high concentration of excess oxygen. Indeed, our work suggests transfer of a small, but significant amount of the in-plane oxygen (O1) to the inter-layer site. It is interesting to compare this phase with the recently discovered (8) superconducting system $La_{2-x}Sr_xCaCu_2O_6$ (maximum T_c = 60K at x = 0.4). Izumi et al. (13) showed that in $La_{1.9}Ca_{1.1}Cu_2O_6$, Ca has a strong preference for the smaller, M(1) site between the CuO_2 layers. Thus it would be expected that in $La_{2-x}Sr_xCaCu_2O_6$ the Ca would also adopt the M(1) site, thus leading to a relatively short (~3.3Å) Cu-Cu distance, and inhibiting the occupancy of the O(3) site. This system, therefore,

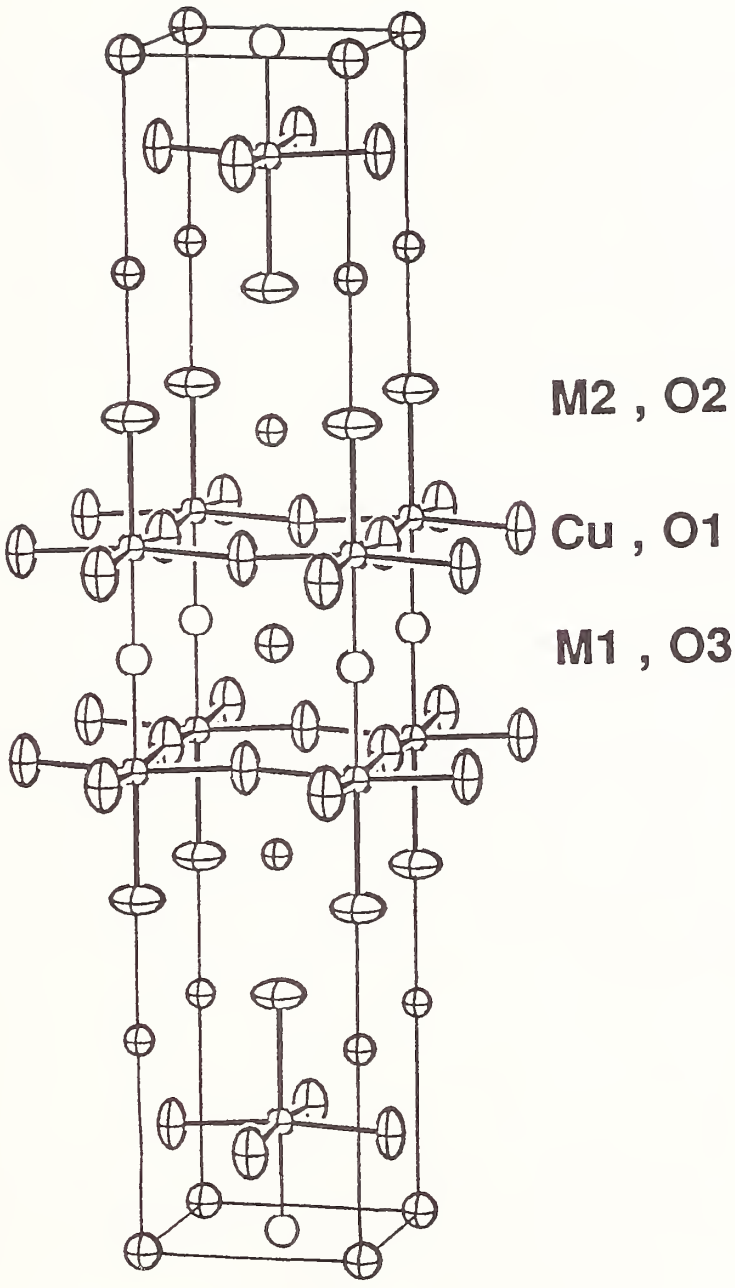

Figure 2. Structure of $La_{1.85}Sr_{1.15}Cu_2O_{6.25}$. Note that the O(3) site, which is completely vacant in the case of $La_{1.9}Ca_{1.1}Cu_2O6$, is partially occupied in the present case.

easily maintains the pseudo-two-dimensional nature believed to be required for superconductivity. In $La_{1.85}Sr_{1.15}Cu_2O_{6.25}$, the Cu-Cu distance is correspondingly greater (3.756Å), facilitating the occupancy of the inter-layer O(3) site, and thus leading to the partial breakdown of the 2D nature of the structure. Further careful structural work will show whether such ideas may help to explain the absence of superconductivity in $La_{1.85}Sr_{1.15}Cu_2O_{6.25}$ and related phases (14).

CONCLUSIONS

We have presented two examples of the way in which oxygen defects play a critical role in the structural chemistry of the layered cuprates, and suggest that such defects may have a profound effect on the electronic properties of these systems. Clearly, before any definitive statements relating defect chemistry to superconductivity may be made, more structural data will be required. We have so far only examined the simplest systems. Neutron powder diffraction will play a central role in the elucidation of the defect structures of more complex systems. However, it is also clear, for example in the $Nd_{2-x}Ce_xCuO_4$ system (15, 16), that the differences between superconducting and non-superconducting samples is very subtle, and defect chemistry on a local scale may provide the key to the understanding of these systems in the future.

ACKNOWLEDGEMENTS

This work was supported by the NSF-Office of Science and Technology Centers under contract #STC-8809854 (PL, SP), U.S. Department of Energy, BES, under contract #W-31-109-ENG-38 (JDJ) and the R.A. Welch Foundation, Houston, TX (XXT, AM, JBG).

REFERENCES

1. J. D. Jorgensen and D. G. Hinks, Neutron News, 1, 24 (1990).

2. J. D. Jorgensen, B. Dabrowski, S. Pei, D. G. Hinks, L. Soderholm, B. Morosin, J. E. Schirber, E. L. Venturini and D. S. Ginley, Phys. Rev. B., 38, 11337, (1988).
3. J. D. Jorgensen, B. Dabrowski, S. Pei, D. R. Richards and D. G. Hinks, Phys. Rev. B., 40, 2187 (1989).
4. Y. Tokura, H. Takagi and S. Uchida, Nature, 337, 345 (1989).
5. J. Akimitsu, S. Suzuki, M. Watanabe and H. Sawa, Jpn. J. Appl. Phys., 27, L1859 (1988).
6. P. Lightfoot, S. Pei, J. D. Jorgensen, X.-X. Tang, A. Manthiram and J. B. Goodenough, Physica C, 169, 15 (1990).
7. P. Lightfoot, S. Pei, J. D. Jorgensen, X.-X. Tang, A. Manthiram and J. B. Goodenough, Physica C, in press.
8. R. J. Cava, B. Batlogg, R. B. van Dover, J. J. Krajewski, J. V. Waszczak, R. M. Fleming, W. F. Peck Jr. L. W. Rupp Jr., P. Marsh, A. C. W. P. James and L. F. Schneemeyer, Nature, 345, 602 (1990).
9. H. Sawa, S. Suzuki, M. Watanabe, J. Akimitsu, H. Matsubara, H. Watabe, S. Uchida, K. Kokusho, H. Asano, F. Izumi and E. Takayama-Muromachi, Nature, 337, 347 (1989).
10. M. F. Hundley, J. D. Thompson, S. W. Cheong, Z. Fisk, R. B. Schwartz and J. E. Schirber, Phys. Rev. B., 40, 5251 (1989).
11. Z. Fisk, S. W. Cheong, J. D. Thompson, M. F.Hundley, R. B. Schwartz, G. H. Kwei and J. E. Schirber, Physica C, 162-164, 1681 (1989).
12. V. Caignaert, N. Nguyen and B. Raveau, Mater. Res. Bull., 25, 199 (1990).
13. F. Izumi, E. Takayama-Muromachi, Y. Nakai and H. Asano, Physica C, 157, 89 (1989).
14. J. B. Torrance, Y. Tokura, A. Nazzal and S. S. P. Parkin, Phys. Rev. Lett., 60, 542 (1988).
15. P. Lightfoot, D. R. Richards, B. Dabrowski, D. G. Hinks, S. Pei, D. T. Marx, A. W. Mitchell, Y. Zheng and J. D. Jorgensen, Physica C, 168, 627 (1990).
16. B. Dabrowski et al. (this meeting).

National Institute of Standards and Technology Special Publication 804, Chemistry of Electronic Ceramic Materials, Proceedings of the International Conference held in Jackson, WY, August 17-22, 1990, issued January 1991.

CAN Co(Fe) SUBSTITUENT IN $YBa_2Cu_3O_{7-\delta}$ MIGRATE BACK AND FORTH BETWEEN Cu(1) AND Cu(2) SITES?

Amar Nath, Zoltán Homonnay, Guang-Way Jang, Sandor I. Nagy, Yen Wei and Chi C. Chan
Department of Chemistry, Drexel University, Philadelphia, PA 19104

Cobalt and iron substitute preponderantly at the Cu(1) site especially if present in low concentrations [1]. In the oxygen-deficient 1-2-3 compound containing less than $O_{6.4}$, the Cu^{2+} ions in the sheets order antiferromagnetically [2]. Cu on Cu(1) site is monovalent and non-magnetic and therefore do not participate in the magnetic ordering. The neighboring Cu^{2+} ions along the sheets are strongly coupled antiferromagnetically, while there is weaker coupling between the sheets along the **c**-axis. $^{57}Fe(^{57}Co)$ on Cu(1) sites do not sense the magnetic field as the chain sites are sandwiched between the two neighboring sheets and they are symmetrically disposed with respect to the spins aligned antiparallel. Consequently, observation of a Zeeman split sextet in oxygen-deficient 1-2-3 compound is generally regarded as a signature for Mössbauer probe being situated on the sheet (i.e. Cu(2)) site[3-14]. However, we had mentioned earlier of the possibility that the Mössbauer probe be situated at neither the Cu(1) nor Cu(2) site but occupy an interstitial position [12,13].

We created a large amount (~50 %) of the magnetic species by thermal treatment of $YBa_2Cu_3(^{57}Co)O_{7-\delta}$ (containing ~30 ppm ^{57}Co substituent) at 800 °C for 5 h under Ar flow. This species is created at the expense of the square planar species A situated at Cu(1) site (Fig. 1). It manifests itself as a Zeeman split sextet (designated M) in the deoxygenated compound, and as a doublet (M') in the oxygenated sample -- the oxygen loading being carried out at a relatively low temperature of 450 °C. The doublet M' has Mössbauer parameters characteristic of ionic Fe^{3+}. The Mössbauer spectra change drastically after the thermal treatment at 800 °C and followed by oxygen loading (Fig. 1). However, it may be mentioned that superconducting properties of this thermally treated sample are identical to the original one, not having undergone any thermal treatment. This was verified by non-resonant microwave absorption studies. M' (or M) consitutes about 50 % of the total area of the spectra. The other major component is the square planar species A (Fig.1). If M'

really represents 50 % of the ^{57}Co being situated at the Cu(2) site, then it is a great blessing. We can probe both copper sites simultaneously for varying oxygen contents, and increasing amounts of substituents like Fe, Co, Ni and Zn in the fully oxygenated state. These investigations could provide very valuable information regarding the role of Cu-O chains vis-a-vis the Cu-O sheets, especially with respect to the charge transfer between the two sites. This apparent migration of Co or Fe substituent from Cu(1) to Cu(2) site during thermal treatment at high temperatures in an inert ambient was originally proposed by Takayama-Muromachi et al. [15] and later observed by Mössbauer researchers[3,12-14]. We report here that a thermal treatment at 700 °C under oxygen flow converts the M' doublet to species A mainly (Fig. 1).

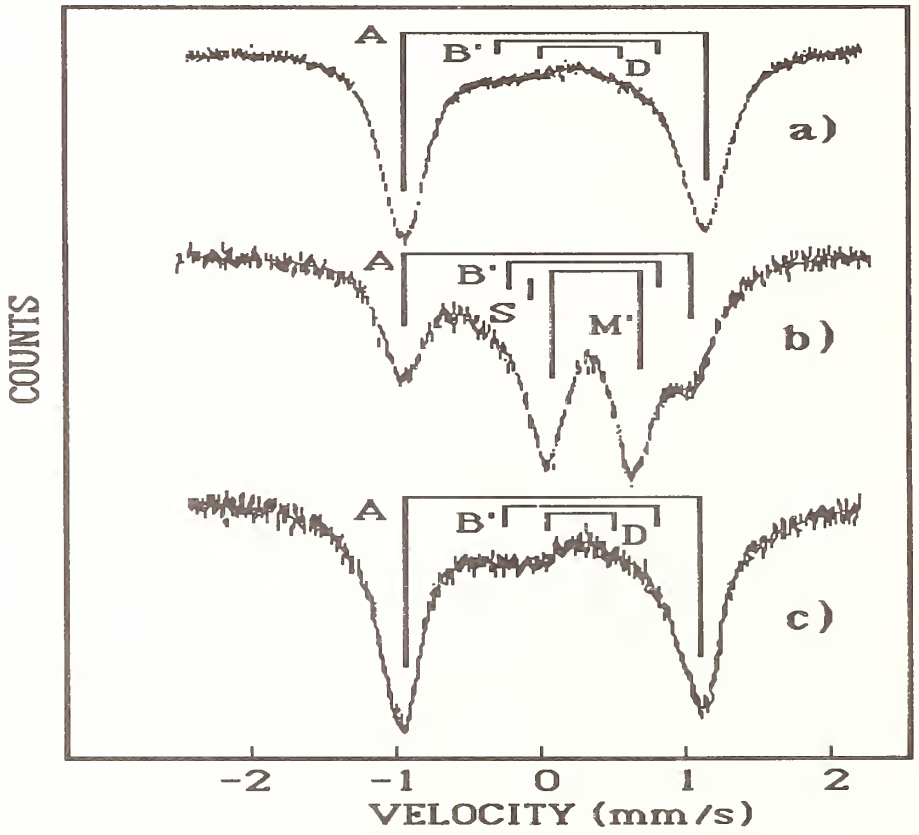

Figure 1. Emission Mössbauer spectra of $YBa_2Cu_3(^{57}Co)O_{6.87\pm0.02}$ (obtained by heating fully oxygenated material at 410 °C under Ar flow to convert 5-fold coordinated species to the 4-fold one) with differing thermal history. (a) The sample was subjected to thermal treatment with O_2 flow at 950 °C and then oxygenated at 450 °C; (b) thermal treatment of sample (a) with Ar flow at 800 °C (to generate the magnetic species) and then oxygenation at 450 °C; (c) thermal treatment of sample (b) with O_2 flow at 700 °C for ~40 h followed by oxygenation at 450 °C.

So the question is whether Fe and Co substituents can really migrate back and forth between Cu(1) and Cu(2) sites with the help of different thermal treatments. Takayama-Muromachi and co-workers[15] reason that the chains would lose all their oxygen above 750 °C in an inert ambient, and that Fe originally present in the chains would seek the oxygen rich environment (5-fold coordination) of the Cu(2) site.

Our detailed investigations do not bear out this scenario. On the other hand, our observations discussed below, lead us to the conclusion that species M(M') is situated at an interstitial site and not at the Cu(2) site.

Firstly, the species M' (doublet) or M (sextet) hardly shows any change in isomer shift on deoxygenation of the 1-2-3 compound. It is generally believed that during deoxygenation, electrons are transferred from the chains to the sheets, thereby, weakening the hole superconductivity in the sheets. The probe site is apparently oblivious to the charge transfer between the two Cu sites. If one assumes that the holes are primarily localized on the oxygen atoms and that the oxygen band is the one responsible for the metallic and superconducting behavior[16], then the microprobe on Cu(2) site would not sense any charge transfers, and neither would it sense the transition from metallic to insulating state. However, recent photoemission studies indicate that there is significant Cu 3d character in the density of states at the Fermi level suggesting strong O 2p and Cu 3d hybridization[17]. Therefore, the absence of changes in the isomer shift of species M'(M), in contrast with that of species A at Cu(1) site where significant changes are observed (Fig. 2), strongly suggest an interstitial site for M'(M).

Secondly, thermal treatment at 700 °C in presence of O_2 converts species M'(M) into species A which is situated at Cu(1) site. Under these conditions, Fe and Co can form only 4-fold coordinated species at Cu(1) site with the limited amount of oxygen available. The question arises as to why the substituent if situated at Cu(2) site would want to forgo the 5-fold coordination site and migrate to a 4-fold coordination Cu(1) site. On the other hand, if species M(M') constitute interstitials, they can diffuse to nearby Cu(1) site and form 4-fold coordinated species A, which partly converts to 5-coordinated species during cooling in O_2 ambient.

Thirdly, the outermost peaks of the sextet are quite broad and their widths decrease as one proceeds inwards. This is a signature for distribution of hyperfine magnetic fields, which would be expected of interstitial occupancy.

The following scenario emerges from the above observations. The dopant ^{57}Co or ^{57}Fe with 4 or 5 oxygen neighbors in oxygen rich microdomains at the chain site, when subjected to further deoxygenation at temperatures > 700 °C under Ar flow would tend to break loose, as it can not form stable 2-coordinate linkages with oxygen, unlike Cu. When the

substituent is present in macroscopic amounts e.g. 1 % or more (as is generally the case for ^{57}Fe substitution, as absorption Mössbauer spectroscopy is much less sensitive than emission Mössbauer spectroscopy, where 20 to 30 ppm substitution of ^{57}Co may be adequate), clustering occurs and 5-coordinate linkages are formed which are more reluctant to part with the bound oxygen and resist dissociation. The dissociated Co or Fe ion migrates to a nearby potential well and is trapped there during cooling. The interstitial $^{57}Co^{2+}$ ($^{57}Fe^{3+}$) is situated on a site which can not be equidistant from the two neighboring sheets and would sense a net magnetic field in an oxygen-deficient sample. It would also probe the Neel temperature characteristic of the lattice, viz. 415±5 K for $O_{6.0}$ stoichiometry, which is in harmony with the one determined by neutron diffraction(2). The interstitials acquire some mobility above 600 °C and in the presence of oxygen would tend to settle down at nearby Cu(1) site as 4-coordinated species.

A detailed account of this work will be published elsewhere.

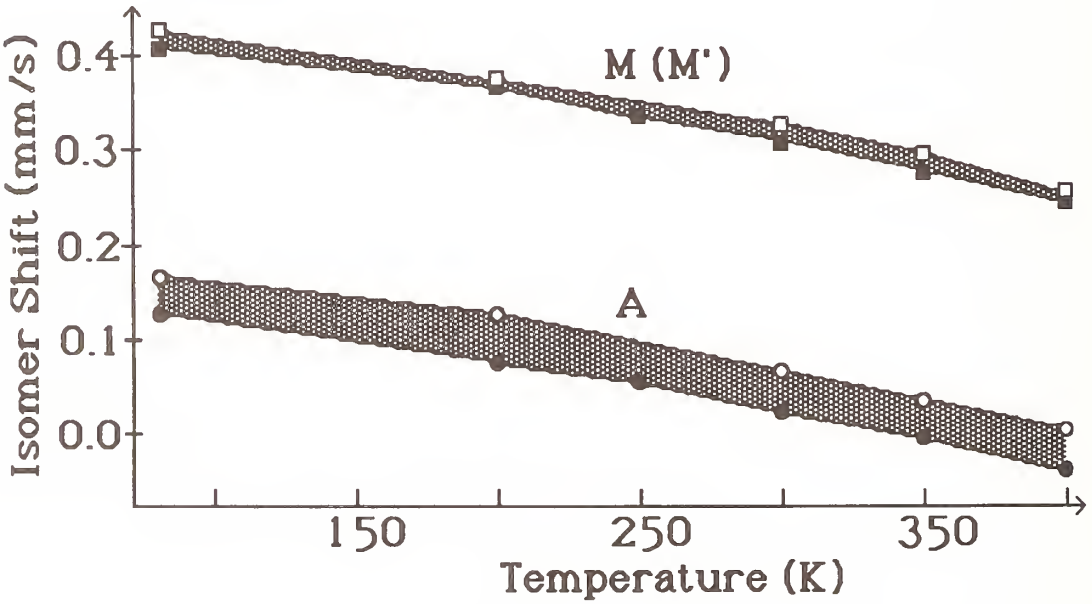

Figure 2. Mössbauer isomer shifts (relative to α-Fe) for cobalt species A and M'(M) in $YBa_2Cu_3(^{57}Co)O_{6.27}$ (open) and $YBa_2Cu_3(^{57}Co)O_{6.87}$ (solid) as a function of temperature. Shaded areas are a guide to the magnitude of changes.

REFERENCES

(1) L. H. Greene and B.G. Bagley in *"Physical Properties of High Temperature Superconductivity II"*,D. M. Ginsberg, edit., p. 509, World Scientific, Singapore (1990)

(2) J. M. Tranquada in "Earlier and Recent Aspects of Superconductivity", J. G. Bednorz and K. A. Müller, eds. p. 422, Springer-Verlag (1990)
(3) Z. Q. Qiu, Y. W. Du, H. Tang and J. C. Walker, *Journal of Magnetism & Magnetic Materials* **78**, 359 (1989)
(4) R. A. Brand, Ch. Sauer, H. Lütgemeier, P. M. Meuffels and W. Zinn, Proc. ICAME'89, *Hyperfine Interactions* ,in press.
(5) L. Bottyan, R. A. Brand, J. Dengler, B. Molnar, D. L. Nagy, G. Ritter, and J. Schober, in *"Proc. XIV Zakopane School on Physics "*, World Scientific Publ. (1990).
(6) T. Shinjo and S. Nasu, in *"Mechanism of High Temperature Superconductivity"*, H. Kamimura & A. Oshiyama, eds., p. 166 (1989)
(7) S. Nasu, M. Yoshida, Y. Oda, T. Kohara, T. Shinjo, K. Asayama, F.E. Fujita, S. Katsuyama, Y. Ueda and K. Kosuge, *J. Magn. Mag. Mat.*, in press
(8) L. J. Swartzendruber, L. H. Bennett, M. Z. Harford and M. Rubinstein, *J. Supercond.* **1**, 219 (1988)
(9) Yu. T. Pavlyuhin, N. G. Hainovsky, Y. Y. Medikov and A. I. Rykov, *Pramana* **31**, L 445 (1988)
(10) K. Donnelly, J. M. D. Coey, S. Tomlinson and J. M. Greneche, *Physica C* **156**, 579 (1988)
(11) I. Nowik, M. Kowitt, I. Felner, and E. R. Bauminger, *Phys, Rev. B* **38**, 6677 (1988).
(12) A. Nath, S. Nagy, M Barsoum, S. D. Tyagi and Y. Wei, *Solid State Commun.* **68**, 181 (1988)
(13) Z. Homonnay, S. Nagy , G. W. Jang, Y. Wei, S. Tyagi and A. Nath, Proc. ICAME'89, *Hyperfine Interactions,* in press
(14) S. Katsuyama, Y. Ueda and K. Kosuge, *Physica C* **165**, 404 (1990)
(15) E. Takayama-Muromachi, Y. Uchida and K. Kato, *Jap. J. Appl. Phys.* **26**, L2087 (1987)
(16) "Earlier and Recent Aspects of Superconductivity", J. G. Bednorz and K. A. Müller, eds., Springer-Verlag (1990)
(17) R.S. List, A.J. Arko, R.J. Bartlett, C.G. Olson, A.B. Yang, R. Liu, C. Gu, B.W. Veal, J.Z. Liu, K. Vandervoort, A.P. Paulikas and J.C. Campuzano, J. Magn. Mag. Mat. **81**, 151 (1989)

National Institute of Standards and Technology Special Publication 804, Chemistry of Electronic Ceramic Materials, Proceedings of the International Conference held in Jackson, WY, August 17-22, 1990, issued January 1991.

ELECTROCRYSTALLIZATION IN THE Ba-K-Bi-O SYSTEM

Michael L Norton and Horng-Yi Tang
Department of Chemistry, University of Georgia, Athens, GA.
and
Judith Eglin
Chemistry Department, Michigan State University, East Lansing, Michigan

ABSTRACT

A technique for the low temperature, isothermal, isopotential electrochemical deposition of superconducting, highly crystalline materials in the Ba-K-Bi-O system has been developed. The current status of this method of producing large (2mm diameter), well facetted crystals in this system is presented in detail.

INTRODUCTION

The Bismuth based system (Ba-M-Bi-O) (1,2), given sufficient development, may provide higher temperature superconductors. This conclusion is supported from two quite different approaches. First, the electron-phonon interaction is so strong in $BaBiO_3$ that the frozen phonon mode or commensurate charge density wave is stable to 800 K (3). The Tc of a system may be considered to have as its upper limit the temperature of this phase transition. A second approach utilizes the relationship between average electronegativity and Tc (4) to predict that the Tc of the 3-D members of this system should approach 180 K (5). Few other systems currently display this high probability of future rises in Tc.

The Ba-K-Bi-O system displays several modes of instability. At high temperatures, the potassium oxide component is volatile under standard oxide ceramic synthesis conditions (6). At intermediate temperatures, the potassium becomes insoluble in the perovskite phase (7), and at lower temperatures, the oxygen content becomes unstable (6). This system is thus not amenable to high temperature crystal growth. The utilization of low temperature synthetic techniques allows for the exploration of new regions of the phase diagram of chemical systems, and allows the discovery of materials not accessible via high temperature techniques due to the presence of large activation energies intrinsic to massively reconstructive phase transformations.

The molten salt electrocrystallization method has a number of potential advantages to offer in the synthesis of novel conducting materials. Conducting phases are preferentially synthesized in electrocrystallization because electrochemical potential losses (IR drop) are minimal in such phases. Growth of non-conductors is self limited by a process commonly referred to as electrode passivation. There is nearly instantaneous nucleation of the desired phase under proper conditions. Because nucleation and growth

occurs only on the selected electrode area, there are only a limited number of nucleation sites, leading to a reduced number of nucleated crystals, in comparison to many crystallization techniques. The relative supersaturation can be set electronically (potentiostatically), and the reaction can be stopped or quenched quickly. All crystalline product can be readily and quickly extracted from the growth solution.

The anodic electrocrystallization technique is exceptionally well suited for the preparation of large single crystals in the Ba-K-Bi-O system for at least two reasons. First, a successful flux or solution based growth technique requires significant solubility of the reagents to enable diffusion to provide significant mass transport. The product phases (BKBO's) are not very soluble in KOH, and therefore would cause recrystallization of BKBO to be a slow crystal growth process in this system. However, $Ba(OH)_2$ and Bi_2O_3 are relatively soluble in KOH. The electrochemical oxidation of Bi from an average formal +3 to a >+4 oxidation state yields an insoluble product which grows on the substrate. The large change in solubility accompanying the rather large change in average formal Bi oxidation state may readily be understood in terms of the associated change in Madelung energy. The second most important feature impacting crystal growth in this system is the intrinsic necessity of oxygen or oxidizing agent transport to the growing crystal/solution interface. Such oxidative power is readily delivered electrically, but chemical oxidation requires diffusion of oxygen across the ambient gas/condensed phase interface. This results, in our experience, in formation of a solid polycrystalline surface barrier film of the oxidized product phase, which impedes further oxygen transport. In the electrochemical system, oxidative power is delivered only to the desired crystal/solution interface.

PREPARATION

Low temperature electrodeposition experiments are performed in readily obtainable Teflon sample containers (Cole-Parmer). Teflon is the only container material we have identified which does not contaminate the melt with long term contact. Potentiostatic deposition is performed utilizing a three electrode, one compartment cell geometry. A high current synthetic potentiostat (Bioanalytical Systems, SP-2) system was employed for these studies. The working electrode (positive, or biased anodically) can be platinum, gold, or silver. The deposited film protects this electrode from anodic dissolution. A 1 mm diameter silver wire electrode (Aesar, 99.9%) is most commonly used. The counter electrode (negative or biased cathodically) used is a 1 mm diameter platinum wire (Aesar, 99.99%), which is rapidly coated with a thick polycrystalline layer of bismuth metal during use. The reference electrode, which is placed in close proximity to the working electrode, appears to be relatively stable and is particularly appropriate to this system, consists of a polycrystalline Bismuth metal rod, cast to a diameter of 1 mm.

The stability of this reference electrode's potential is related to the pO_2 and to the Bismuth salt concentration in the solution. This electrode system does not introduce impurities detectable by EDX (energy dispersive X-ray analysis) into the product phase. The temperature of the cell, its envelope, and a large heat capacity metal thermal ballast cup holding the assembly is maintained using a controller (Omega) to drive a hotplate. In an average deposition, 20 grams of KOH is placed in a 15 cc teflon crucible and melted at the reduced melting point of 180 C. The lowered melting point is presumed to result from the known high water content of commercial KOH. After raising the temperature to 200 C, the other components of the melt, 1.60 grams of $Ba(OH)_2*8H_2O$ and 2.37 grams of Bi_2O_3 are added with stirring to aid dissolution. A quiescent solution is maintained during deposition. Maintenance of an inert atmosphere is necessary in order to avoid "spontaneous" or air oxidation of the chemical system. This "spontaneous " oxidation can be quite rapid at elevated temperatures. A quartz cell holder contains the cell, supports the electrodes, and allows maintenance of a water vapor saturated nitrogen cover gas flow over the cell. The constant pH_2O may influence the long term stability of the reference electrode potential.

Upon sedimentation of excess, undissolved Bi_2O_3, electrolysis of the crystal clear solution is begun at an applied potential of 0.7 V vs the Bi reference electrode. Deposition begins immediately, and is terminated by withdrawing the crystal laden electrode from the melt after any desired period of time. The useable time is limited by the depletion of Bi from the solution through deposition of Bi metal (cathodic) and Bi oxides (anodic), to periods on the order of 48 hours for the system described here. Samples are air cooled, rinsed and ultrasonically cleaned in distilled water, then allowed to air dry.

CHARACTERIZATION

Morphological observations are made using an inverted optical metallograph (Leco).

Scanning electron microscopy and energy dispersive x-ray analyses are performed using a Phillips model 505 SEM equipped with a Tracor Northern 5500 data aquisition system and semiquantitative analysis software. Multiple sites are probed with 25kV excitation and 100 nm spot size. Data collected over the range 0 - 25 kV are collected. The M line of Ba, the K line of K, and the L line of Ba are fit to yield atomic percentages of these elements.

X-ray diffraction patterns are acquired using a Scintag XDS 2000 Theta/Theta X-ray Powder Diffraction system. Data were taken for two-theta values in the range 15 - 60 degrees, and analyzed on the systems Microvax. Profile analysis utilized a Rietveld Analysis program modified by Hill and Howard (8).

Magnetommetry was performed using a SQUID Magnetometer (S.H.E.).

RESULTS AND DISCUSSION

Optical Microscopy: Materials prepared with deposition times of 6 hours have been observed to grow as dendrites along 111. The nuclei and earliest grown crystals are metallic bronze in color. The later grown crystals are bright blue in reflection. It could be expected that these colors reflect the electronic properties of the material, which are governed by their K content.

SEM/EDX: One of the larger crystals grown is shown in figure 1.

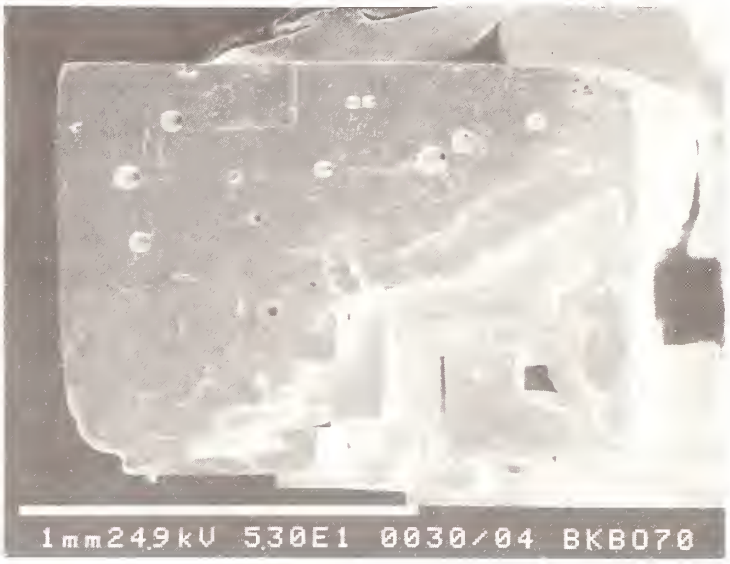

Figure 1 Scanning Electron Micrograph of BKBO Crystal

EDX analysis shows that the bronze colored early crystalline material displays a composition roughly corresponding to $Ba_{.8}K_{.2}BiO_3$. The later material, which composes the bulk of the material displays the stoichiometry $Ba_{.6}K_{.4}BiO_3$, the well known superconducting composition. Although mapping of the composition along the growth direction has not been performed, it is anticipated that there is a K concentration gradient along this line.

X-ray Diffraction: Analysis of the X-ray diffraction pattern indicates significant broadening of the peaks, which are readily indexed as cubic. The pattern is not readily refined, and indicates some spread in lattice constants, consistent with the EDX and optical observations that the material is not homogeneous.

Magnetic Susceptibility: AC Squid measurements indicate that the product does contain substantial ammounts of superconducting material (ca 20%). The magnetic transition, displayed in Fig. 2,

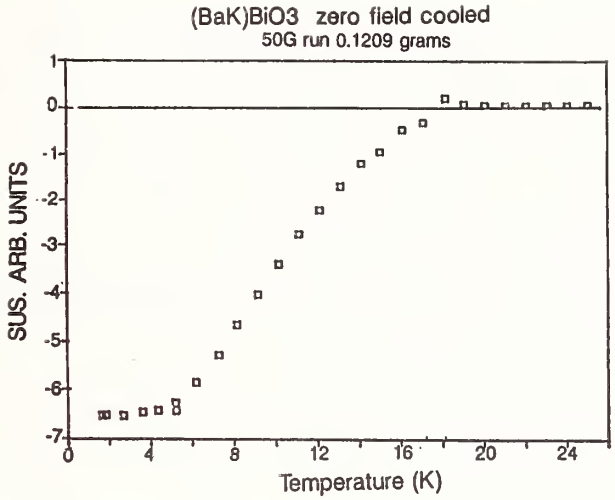

Figure 2 Susceptibility Plot for BKBO Polycrystalline Mass

is not sharp, and the onset (ca 18 K) is far below transition temperatures reported for powders of this material (30 K) (7). These findings support the conclusions that the crystalline product is inhomogeneous, contains nonsuperconducting stoichiometries, and likely is strained by the gradient in lattice parameter. The lack of evidence for the highest Tc material is unexpected, and difficult to explain.

DISCUSSION AND CONCLUSION

The electrodeposition reaction can be viewed as a Bismuth oxide polymerization process resulting in a 3-D polymer stuffed with cations. That is, a polymer crosslinked in two dimensions perpendicular to the growth direction is formed, and incorporates ions from the melt as growth progresses. The reason for utilizing potentiostatic control of the electrode process rather than the constant current deposition previously employed (9) was to maintain a constant rate of polymerization, and therefore to maintain a steady state doping rate. It would appear that, over relatively long deposition times, this control breaks down. Solution or local depletion of Ba content may be responsible for the dopant profile. Higher temperature deposition experiments in larger volumes of solution will lead to higher diffusion constants for Ba, and less perturbation of solution Ba content during cell operation. Sample homogenization via thermal annealing does not appear practical in view of the thermal sensitivity of these materials. Inhomogeneity appears to be a general problem in the Ba-K-Bi-O system, and has been observed in crystals ranging from .3 mm to 5 microns in diameter (10).

As well as the graded concentrations inferred in these materials, it may be possible to form block copolymers and dopant superlattices by modifying the deposition rate by controlling the deposition potential.

Large regions (100's of microns) of the grown crystals do appear to be homogeneous via EDX analysis, and small single crystals grown quickly may be quite homogeneous. Therefore, although this method will require further development to deliver extraordinarily large, perfect crystals, the products readily obtainable may be of great value for optical studies, which are highly surface sensitive, and temperature dependent X-ray structural studies, which require reasonably small samples.

This work was partially supported by SURA. We acknowledge the use and staff support of the Center for Ultrastructural Studies at UGA, and X-ray diffraction studies performed by B. Chakomaukos at Oak Ridge National Laboratory.

REFERENCES:

1. A.W. Sleight, J.L. Gilson, and P.E. Bierstedt, Solid State Commun. **17**, 27 (1975).
2. L.F. Mattheiss, E.M. Gyorgy, and D.W. Johnson,Jr., Phys. Rev. B **37**, 3745 (1988).
3. D.E. Cox and A.W. Sleight, Acta Cryst. B **35**, 1 (1979).
4. D.A. Nepela and J.M. McKay, Physica C **158**, 65 (1989).
5. D. Tseng and E. Ruckenstein, J. Mater. Res., **5**, 742 (1990).
6. D.G. Hinks, B. Dabrowski, J.D. Jorgensen, A.W. Mitchell, D.R. Richards, S. Pei, and D. Shi, Nature, **333**, 836 (1988).
7. D.G. Hinks, J.D. Jorgensen, D.R. Richards, B. Dabrowski, Y. Zheng and S. Pei, preprint, Mol. Cryst. Liq. Cryst. (1990).
8. R.J. Hill and C.J. Howard, program LHPM1, CSIRO Div. of Mineral Chemistry, P.O. Box 124, Port Melbourne 3207.
9. M.L. Norton, Mat. Res. Bull., **24**, 1391 (1989).
10. L.F. Schneemeyer, J.K. Thomas, T. Siegrist, B. Batlogg, L.W. Rupp, R.L. Opila, R.J. Cava, and D.W. Murphy, Nature, **335**, 421 (1988).

National Institute of Standards and Technology Special Publication 804, Chemistry of Electronic Ceramic Materials, Proceedings of the International Conference held in Jackson, WY, August 17-22, 1990, issued January 1991.

STRUCTURAL DIVERSITY IN OXYGEN-DEFICIENT PEROVSKITES

J.T. Vaughey and K.R. Poeppelmeier
Department of Chemistry and The Science and Technology Center for Superconductivity, Northwestern University, Evanston, IL 60208

The discovery of high temperature superconductivity in several perovskite-related copper oxides which exhibit variable oxygen stoichiometry has initiated renewed interest in the structures of oxygen deficient perovskites and related compounds[1,2]. For example, it has been suggested that in the $YBa_2Cu_3O_{7-\delta}$ system, the reported plateau in the plot of oxygen content versus T_c at 60K is due to an ordering of the oxygen vacancies[3]. Therefore the determination of possible structures originating from the removal of oxygen and ordering of the anion vacancies is essential. There are several known perovskite-related oxides where the ordering of vacancies have been well determined by either X-ray single crystal or neutron powder diffraction structure determinations. In this paper, we will compare the structures of $LaSrCuAlO_5$[4], $Ca_2Mn_2O_5$[5], $LaSrCuGaO_5$[6], and $YBaCuFeO_5$[7]. These examples demonstrate that compounds which exhibit a large fraction ($\approx$ 17%) of anion vacancies adopt nonrandom vacancy distributions that reflect the coordination chemistry of the B-cation(s). Each exhibits a unique way to remove one oxygen from a double perovskite ($A_2B_2O_6$). The synthesis and X-ray single crystal structure for $YBaCuFeO_5$ are reported and compared with an earlier neutron powder diffraction study[7].

CRYSTAL STRUCTURE

Single crystals of the compound $YBaCuFeO_5$ were isolated as small black plates from a flux of the general composition $YBa_4Cu_{10}FeO_x$ that was slowly cooled (6°C/hr) from 1000°C in an alumina crucible. Energy Dispersive X-ray Analysis (EDX) confirmed the presence of all four cations in an approximate 1:1:1:1 ratio. No contamination from the alumina crucible could be detected. The unit cell was determined from 25 independent reflections collected on a Enraf-Nonius CAD4 diffractometer collected at -120°C. The cell was determined to be tetragonal with a = 3.865(1) Å, and c = 7.6425(8) Å. There was no evidence from Weissenberg photos of a supercell in agreement with the unit cell determined by the diffractometer. From analysis of the data collected (h k l and $\bar{h}$ $\bar{k}$ $\bar{l}$), the compound

was found to be acentric with no observable systematic absences. These reflection conditions lead to five possible space groups. Structural solution was undertaken using the X-ray crystallography package TEXSAN[8]. The final space group chosen was P4mm (#99) based on the refinement from a double perovskite model where the Y^{+3}/Ba^{+2} and Fe^{+3}/Cu^{+2} could be ordered in alternate AO and BO_2 layers, respectively. To determine the position of the oxygen vacancy, each B-cation was assumed to be six coordinate and the occupancies of each oxygen were allowed to vary. The vacant oxygen sites occur at (1/2, 1/2, 1/2), which results in square pyramidal coordination of both the copper and iron sites. Refined positional parameters and temperature factors are in Table 1. The final R-factor was 0.092, R_w = 0.103. An ORTEP of the structure is shown in figure 1.

TABLE 1. Positional and temperature factors for $YBaCuFeO_5$

Atom	x	y	z		B (Å^2)
Ba	0	0	0	[0.0226]*	0.61(3) [0.82]
Y	0	0	0.4910(8)	[0.5112]	0.43(3) [0.58]
Cu	0.5	0.5	0.7157(7)	[0.2738]	0.68(7) [0.47]
Fe	0.5	0.5	0.254(1)	[0.7387]	0.26(7) [0.86]
O(1)	0.5	0.5	0.990(5)	[0.0149]	0.9(2) [1.68]
O(2)	0.5	0	0.301(2)	[0.3331]	0.3(2) [1.09]
O(3)	0.5	0	0.669(3)	[0.7028]	0.5(2) [0.89]

(* = brackets indicate neutron diffraction study[7])

The refined structure is similar to that reported by Er-Rakho, Michel, Lacorre, and Raveau when the placement of barium at the origin is taken into account.[7] Although copper and iron could not be distinguished based on X-ray diffraction methods, the copper was placed on the z = 0.75 site because of a more distorted coordination on that position consistent with the Jahn-Teller d^9 copper cation. In contrast, in the neutron diffraction study, iron was placed predominantly on the z = 0.75 site (62%). The neutron scattering lengths for copper and iron are 0.772 x 10^{-12} cm and 0.954 x 10^{-12} cm, respectively. Mossbauer spectroscopy showed iron was present on both sites. The distorted coordination environment found for iron (+3) was consistent with other compounds, such as $LaSrFeO_4$[9].

DISCUSSION

A wide variety of physical methods, including high resolution electron microscopy, single crystal X-ray diffraction, and powder neutron diffraction have been used to investigate oxygen deficient perovskites. This paper will concentrate on

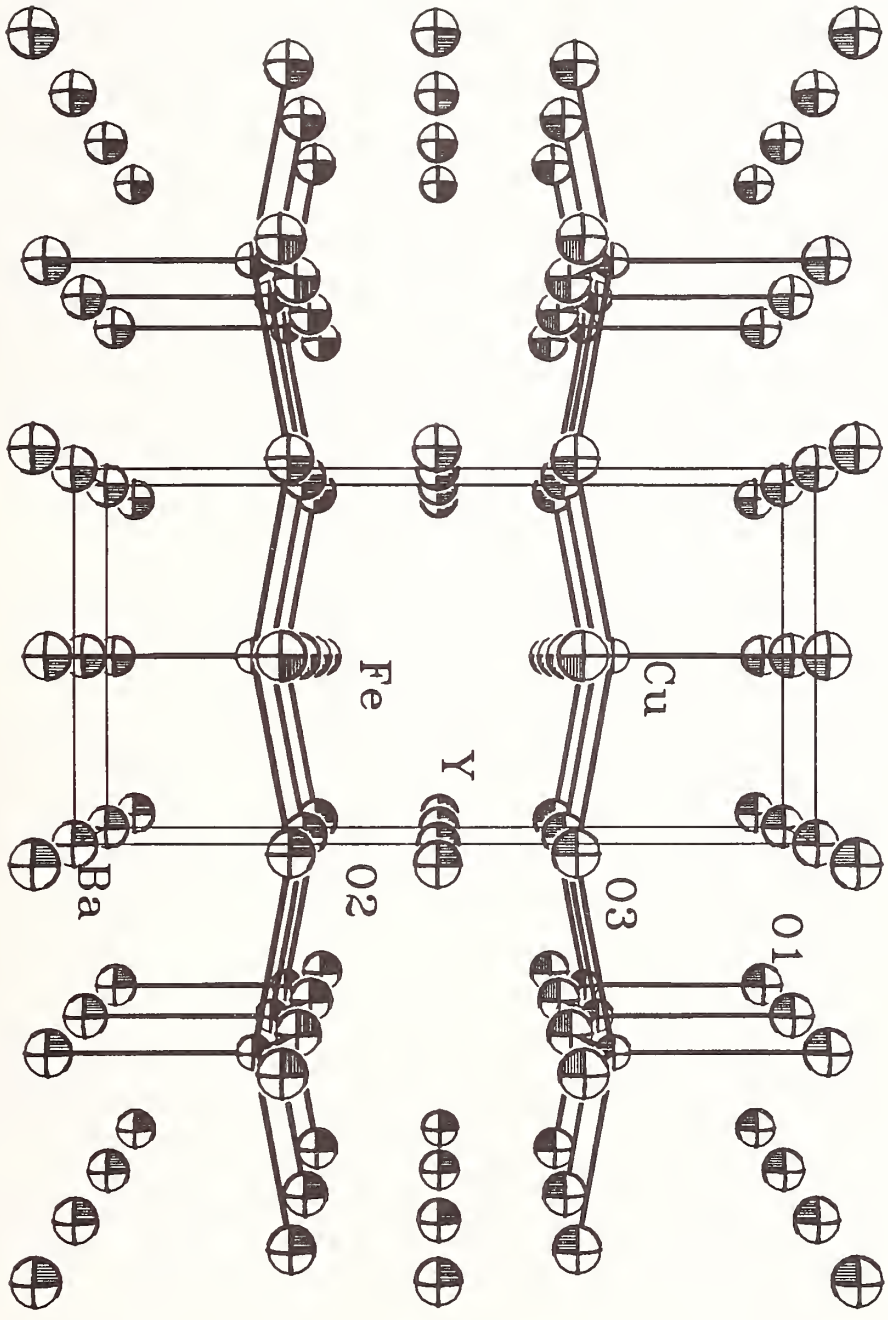

FIGURE 1 The structure of $YBaCuFeO_5$ viewed down the a-axis.
(atom sizes are arbitrary)

compounds with an oxygen deficiency that has manifested itself in some well ordered arrangement of oxygen vacancies and is still easily compared to the perovskite structure. In general, the ordering of anion vacancies is due to the coordinational and redox chemistry of the B-cation[10]. One of the earliest discovered and most studied members of this class of compounds is the mineral brownmillerite, Ca_2FeAlO_5 (ABO_{3-x}; x = 0.5)[11]. It has been found that the aluminum and iron unequally mix over the tetrahedral and octahedral sites, with aluminum having a preference for the tetrahedral site[12]. In oxygen-deficient perovskite compounds, the structures of possible compounds are limited by the coordination environment of the B-cation. The four compounds $Ca_2Mn_2O_5$, $YBaCuFeO_5$, $LaSrCuGaO_5$, and $LaSrCuAlO_5$ will be used to illustrate the structural variation that has been observed in oxygen deficient perovskites with the composition $ABO_{2.5}$ ($A_2B_2O_5$). Two involve only square pyramidal coordination of the B-cation while two others involve tetrahedral and octahedral coordination. Figure 2 shows the relationship of the four structures to be compared to the parent perovskite structure. The crystallographic relationships of the four compounds and perovskite are listed in table 2.

TABLE 2. Relation of unit cells to perovskite

	a (Å)	b (Å)	c (Å)	V (Å^3)	V*(Å^3)
$LaSrCuGaO_5$	16.383 ($4a_p$)	5.533 ($\sqrt{2}a_p$)	5.330 ($\sqrt{2}a_p$)	483.1	60.4
$LaSrCuAlO_5$	7.922 ($2a_p$)	11.020 ($2\sqrt{2}a_p$)	5.424 ($\sqrt{2}a_p$)	473.5	59.2
$YBaCuFeO_5$	3.865 (a_p)	3.865 (a_p)	7.643 ($2a_p$)	114.2	57.1
$Ca_2Mn_2O_5$	5.43 ($\sqrt{2}a_p$)	10.24 ($2\sqrt{2}a_p$)	3.74 (a_p)	208.0	52.0

* = volume per one perovskite formula unit

$Ca_2Mn_2O_5$ was first reported in 1982 as the end product of the reversible oxygenation of $CaMnO_3$[5]. Under a reducing atmosphere the compound $CaMnO_{3-\delta}$ ($0 \leq \delta \leq 0.5$) was found to evolve oxygen and form a series of stable, oxygen deficient compounds. Using powder neutron diffraction, the structure of $CaMnO_{2.5}$ (or $Ca_2Mn_2O_5$) was determined to consist of square pyramidal manganese (d^4 - Mn^{3+}, $(t_{2g})^3$ $(e_g)^1$). The structure of $CaMnO_{2.5}$ is characterized by oxygen vacancies generated by the reduction of Mn^{4+} to Mn^{3+} that order as shown in figure 2. The intermediate members of the series contain various ordering patterns of square pyramids and octahedra[13].

$YBaCuFeO_5$ was first reported in 1988[7]. One description of the structure is that the oxygen vacancy occurs in the AO layer to form square pyramids of copper

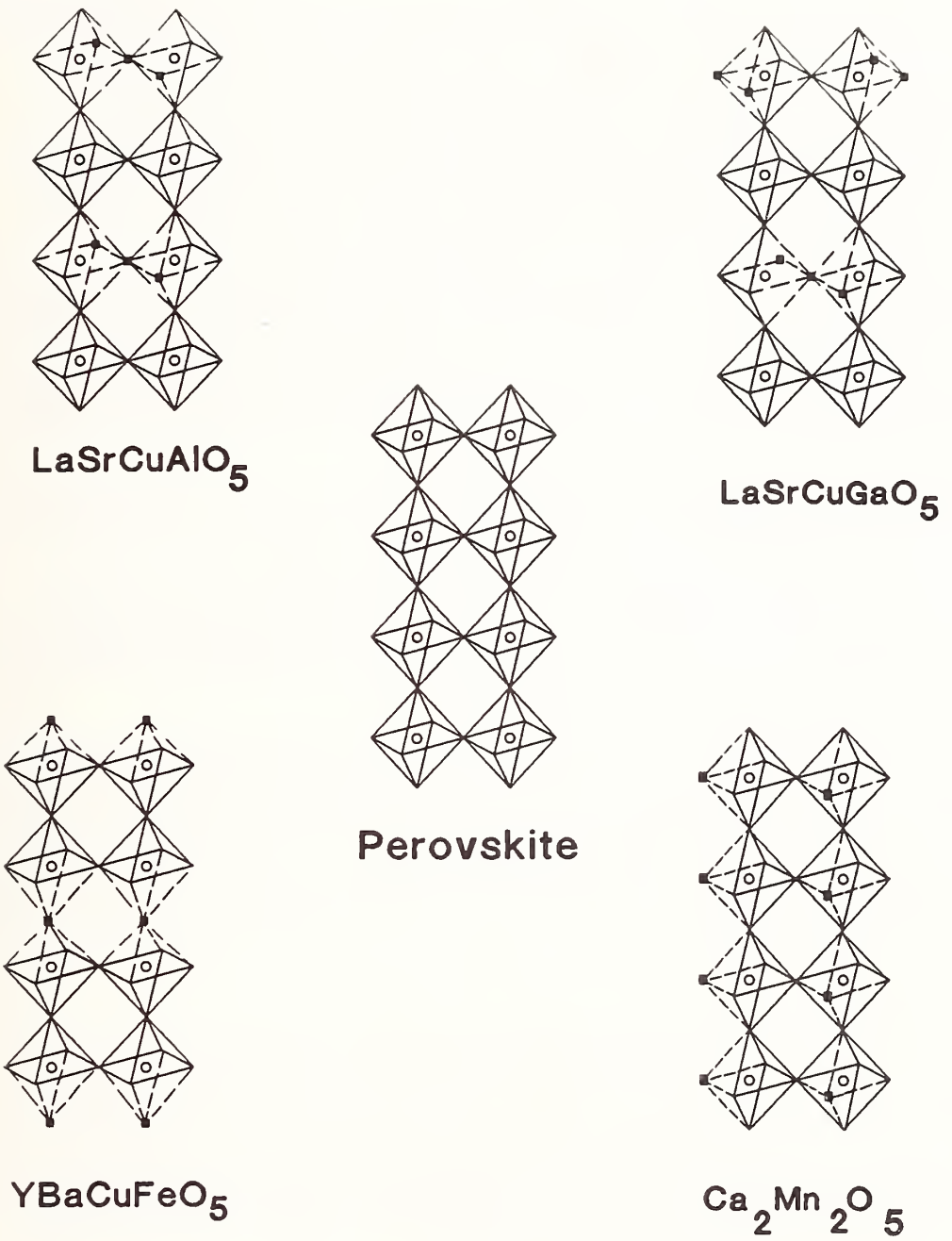

FIGURE 2 A structural comparison of the compounds to perovskite

(d^9 - Cu^{+2}) and iron (d^5 - Fe^{3+}). $YBaCuFeO_5$ is of considerable interest because it can also be viewed as the first member of the structural family that includes $YBa_2Cu_3O_{7-\delta}$, the 93K superconductor[14]. However, the structure of $YBaCuFeO_5$ is closely related to $Ca_2Mn_2O_5$. To illustrate the similarity of $Ca_2Mn_2O_5$ and $YBaCuFeO_5$ the oxygen vacancy should be viewed to be in the mixed $(Fe,Cu)O_2$ layer. In $CaMnO_{2.5}$ one-half of the oxygen atoms in alternate [110] rows are missing, whereas in $YBaCuFeO_5$, one-quarter of the oxygen atoms sites are vacant in every [110] row. A reason for the different ordering patterns is the ionic radii of the A-cations. Whereas yttrium (1.16Å) and calcium (1.26Å) are approximately the same size and often substitute for one another, barium (1.56Å)[15] is larger, and requires a higher coordination number. As predicted[5], the coordination of the A and B cations together determines the overall structure. In $YBaCuFeO_5$, the yttrium site is 8-coordinate and the barium site is 12-coordinate, in contrast to $CaMnO_{2.5}$, where the calcium is 10-coordinate.

$LaSrCuGaO_5$ was recently discovered[6] and shown to have the brownmillerite structure with octahedral and tetrahedral coordination of the mixed B-cations, respectively. The oxygen vacancies are ordered within the gallium - oxygen layer as shown in figure 2. This arrangement of vacancies is probably the most commonly seen in oxygen deficient perovskites. A large number of compounds have been isolated and studied with this general structure encompassing several late transition metals (Co, Fe) and the group IIIB cations (Al, Ga, In)[16] .

$LaSrCuAlO_5$ is an another example[4] where oxygen vacancies order to form tetrahedrally coordinated aluminum. However compared with $LaSrCuGaO_5$, the vacancies are in the same location layer to layer with respect to the copper plane. It is closely related to the brownmillerite structure, but as is evident from table 2 and figure 2, there is a doubling of the a-axis, instead of the quadrupling seen in the $LaSrCuGaO_5$ structure.

CONCLUSION

The structures of four distinct variations that result from the removal of one oxygen from the double perovskite formulation $A_2B_2O_6$ (i.e. $A_2B_2O_5$) have been discussed. The importance of the electronic structure, the coordinational preferences of the B-cation, and the coordinational number of the A-cation have been shown to be the factors in understanding the arrangement of oxygen vacancies that each structure has adopted. These results present a clear picture of the possible structural variations, and provide the basis for understanding structure/property relationships in areas as diverse as catalysis and superconductivity.

ACKNOWLEDGMENTS

Support for this research was from the Science and Technology Center for Superconductivity (NSF DMR-8809854).

REFERENCES

1. Bednorz, J. G.; Müller, K. A. *Z. Phys.* **1986**, *B64*, 189.

2. (a) Nguyen, N.; Choisnet, J.; Hervieu, M.; Raveau, B. *J. Solid State Chem.* **1981**, *39*, 120. (b) Goodenough, J.B.; Demazeau, G.; Pouchard, M.; Hagenmuller,P. *J. Solid State Chem.* **1973**, *8*, 325.

3. (a) Renault, A.; Burdett, J.K.; Pouget, J.P. *J. Solid State Chem.* **1987**, *71*, 587. (b) Lin, Y.P.; Greedan, J.E.; O'Reilly, A.H.; Reimers, J.N.; Stager, C.V.; Post, M.L. *J.Solid State Chem.* **1990**, *84(2)*, 226.

4. Wiley, J.B.; Sabat, M.;Hwu, S.-J.; Poeppelmeier, K.R.; Reller, A.; Williams, T. *J. Solid State Chem.* **1990**, *88(1)*, 250.

5. Poeppelmeier, K.R.; Leonowicz, M.E.; Longo, J.M. *J.Solid State Chem* **1982**, *44(1)*, 89.

6. Vaughey, J.T.; Wiley, J.B.; Poeppelmeier, K.R. *Z.anorg.allg.Chem*, **1990**, submitted.

7. Er-Rakho, L.; Michel, C.; Lacorre, P; Raveau, B. *J. Solid State Chem.* **1988**, *73*, 531.

8. "TEXSAN"; Molecular Structure Corp.: College Station , TX 77843.

9. Soubeyroux, J.L.; Courbin, P.; Fournes, L.; Fruchart, D.; Le Flem, G. *J. Solid State Chem.* **1980**, *31*, 313.

10.(a) Poeppelmeier, K.R.; Leonowicz, M.E.; Scanlon, J.C.; Longo, J.M.; Yelon, W.B. *J. Solid State Chem.* **1982**, *45(1)*, 71. (b) Leonowicz, M.E.; Poeppelmeier, K.R.; Longo, J.M. *J. Solid State Chem.* **1985**, *59*, 71.

11. Hansen, W.C.; Brownmiller, L.T. *Amer. J. Sci.* **1928**, *15*, 224.

12. Smith, D.; *Acta Cryst.* **1962**, *15*, 1146.

13.(a)Chiang, C.K.; Ph.D. Thesis, Northwestern University, Evanston, IL, 1989. (b)Reller, A.; Thomas, J. M.; Jefferson, D.A. *Proc. R. Soc. London* **1984**, *A394*, 223.

14. Cava, R.J.; *Sci. Amer.*, **1990**, *263(2)*, 42.

15. Shannon, R.D. *Acta Cryst.* **1976**, *A32*, 751.

16.(a) Schenck, V.R.; Muller-Buschbaum, H. *Z. anorg allg. Chem.* **1973**, *395*, 280.
(b) Battle, P.D.; Gibb, T.C.; Nixon, S. *J. Solid State Chem.* **1988**, *73*, 330.
(c) Harder, R.; Muller-Buschbaum, H. *Z. anorg allg. Chem.* **1980**, *464*, 169.
(d) Colville, A.A.; Geller, S. *Acta Cryst.*, **1971**, *B27*, 2311.

National Institute of Standards and Technology Special Publication 804, Chemistry of Electronic Ceramic Materials, Proceedings of the International Conference held in Jackson, WY, August 17-22, 1990, issued January 1991.

NEW $LaCuO_{3-\delta}$ PEROVSKITES PREPARED AT HIGH OXYGEN PRESSURE

J. F. BRINGLEY, B. A. SCOTT, S. J. LA PLACA, R. F. BOEHME
M. W. McElFRESH, T. M. SHAW, S. S. TRAIL and D. E. COX†.
IBM Research Division, Thomas J. Watson Research Center, Yorktown Heights, NY 10598. †National Synchrotron Light Source, Brookhaven National Laboratory, Upton, NY 11973.

INTRODUCTION

The transport and physical properties of the perovskite-related superconducting cuprates are known to be strongly correlated with hole concentration (p), i.e., the oxidation state of the Cu-O matrix (1, 2). Although a large number of cuprates with intermediate hole concentrations, p = 0.0 -0.5 (Cu^{2+} - $Cu^{2.5+}$), have been extensively characterized, relatively little work has been reported on materials with higher hole concentrations, p = 0.5 - 1.0. Although a number of such cuprates are known, in which copper occurs formally as Cu^{3+} (3, 4), most of these are structurally unrelated to the superconductors, and a direct comparison of their chemical and physical properties may not be appropriate. The synthesis of a cuprate exhibiting a wide oxygen stoichiometry range, while maintaining the basic perovskite structure, would therefore be of great value for elucidating the nature of Cu/O hole states, determining how magnetic and transport properties change with carrier concentration, and for establishing a complete set of "standards" for the spectroscopy of Cu^{3+}, Cu^{2+} and intermediate valence states. In this paper, we report the synthesis, structure and preliminary characterization of a new oxygen-defect perovskite, $LaCuO_{3-\delta}$, related directly to the superconducting cuprates. Although superconductivity has not been observed in this system, its oxygen stoichiometry range, $0.0 \leq \delta \leq 0.5$, is the widest yet found in a cuprate, allowing the formal oxidation state of copper to be varied from +2 to +3 within the same basic perovskite framework. As a result of these features and of those described below, this may represent a model system with which to address the above questions and to probe the subtle interplay of

the crystal-chemical and physical properties of the superconducting and related cuprates.

The perovskite $LaCuO_3$ can be considered the fully-oxidized, three-dimensional prototype of the layered high-T_c materials. This compound was first prepared by Demazeau et al. at 900 °C and 65 kbar using $KClO_3$ as an oxygen buffer (5). Its x-ray powder diffraction pattern was indexed on the basis of a rhombohedrally-distorted perovskite cell and it was reported to be fully stoichiometric and to display metallic properties down to 77 K. Because of the very high pressure and other complexities of its synthesis, however, further characterization of this important phase has not been forthcoming. In examining whether $LaCuO_3$ can be prepared under milder synthetic conditions, we have discovered a new series of oxygen defect $LaCuO_{3-\delta}$ perovskites, with $0 \leq \delta \leq 0.5$.

EXPERIMENTAL:

High-pressure oxygen reactions were performed in an externally heated René alloy vessel pressurized at or below room-temperature with high-purity gas. Reaction temperatures were measured at a shallow recess in the reactor wall at the sample position, and pressure measured with an uncalibrated gauge. Phases in the $LaCuO_{3-\delta}$ system were prepared at 900 °C at oxygen pressures from 0.2 - 1 kbar using coprecipitated La and Cu hydroxide precursors. The precursors were decomposed by slow heating to 650°C under O_2 prior to reacting them in high pressure oxygen. Exclusion of CO_2 and other organic impurities from the starting materials and the oxidizing atmosphere was necessary in order to obtain single-phase, homogeneously oxidized materials. Compositions were established by thermogravimetric analyses with an accuracy in δ of $\pm$ 0.02. High-resolution X-ray powder diffraction data for the various phases in the $LaCuO_{3-\delta}$ system were collected at the Brookhaven National Synchrotron Light Source. Structural refinements were performed with a modified Rietveld program.

RESULTS AND DISCUSSION:

Syntheses performed under oxygen pressures ranging from 0.4 - 1 kbar yield a tetragonal phase with $0.0 \lesssim \delta \lesssim 0.2$. Its structure is a simple tetragonal distortion of a cubic perovskite with a = 3.81875(5) Å and c = 3.97270(7) Å at δ = 0.05, space group P4/m. The tetragonal distortion is brought about by a slight Jahn-Teller-like elongation of the CuO_6 octahedra, in which there are four in-plane Cu-O bonds at 1.909 Å, and two apical Cu-O bonds at 1.986 Å. This is in contrast to the rhombohedral form in which all Cu-O distances are equal at 1.94 Å (3). The lanthanum cations are twelve-fold coordinated by oxide ions with

bond distances ranging from 2.70 -2.75 Å. In addition, electron diffraction data indicate a very weak and diffuse supercell with multiplicity $2c$, however, this was not observed in the synchrotron data and is not included in the structural refinement. The unit cell volume of the tetragonal phase is $\approx$ 5% larger than that of the rhombohedral form (5), which suggests that the latter is the high-pressure and the former the low-pressure polymorph of $LaCuO_3$.

The tetragonal form of $LaCuO_{3-\delta}$ can be made oxygen deficient either by lowering the synthetic pressure or by reducing it in 1 atm O_2 or N_2 at 400 - 600 °C. Below its homogeneity range, $0.0 \lesssim \delta \lesssim 0.2$, the ordering of oxygen vacancies results in the formation of a monoclinic perovskite stable over the range $0.2 \lesssim \delta \lesssim 0.4$. The structure of this phase is shown in Fig. 1. The vacancies order along the pseudo-cubic {021} axes, giving rise to a new $a \times \sqrt{5}a_p \times \sqrt{5}a_p$ cell with lattice parameters a = 3.83076(2) Å, b = 8.62884(5) Å and c = 8.65149(5) Å for δ = 0.33, space group P2/m. The synchrotron diffraction peaks of this phase are extremely sharp (about 0.025° FWHM) so that the monoclinic distortion from orthorhombic symmetry can be readily distinguished, although it is very small (β = 90.214(4)°). The unit cell composition is $La_5Cu_5O_{13.35}$.

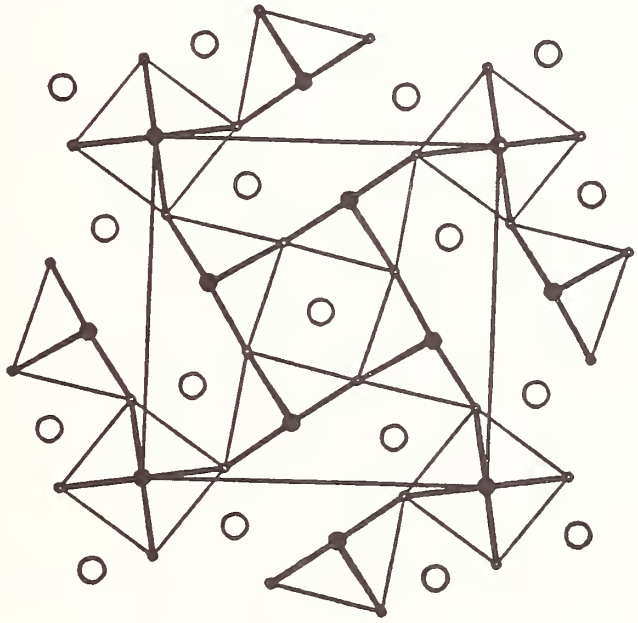

Fig. 1. Projection onto the (100) plane of the crystal structure of $La_5Cu_5O_{13+y}$, with the unit cell indicated. La = large open circles, Cu = filled circles.

The structure of this phase closely resembles that of $BaLa_4Cu_5O_{13+x}$ (6), although the latter is tetragonal, space group P4/m. It is comprised of one-dimensional chains of CuO_6 octahedra oriented along *c* which share corners with four CuO_5 square-pyramids in the (100) planes. The CuO_5 pyramids share corners with four other square pyramids but are oriented with their basal faces at 90° to one another. In contrast to $BaLa_4Cu_5O_{13}$, the structure is significantly distorted from tetragonal symmetry, and the Cu-O-Cu bonds adjoining octahedra and pyramids are bent considerably below their ideal 180° bond angle.

Yet a third phase can be isolated in the $LaCuO_{3-\delta}$ system by heating the tetragonal form to 725 °C in N_2. This perovskite is orthorhombic and exhibits a homogeneity range of $0.43 \leq \delta \leq 0.5$. Rietveld refinement shows that oxygen vacancy ordering in the (010) plane, which is complete at $\delta = 0.5$, creates a cell with lattice parameters related to those of the pseudo cubic perovskite by $a \simeq 2\sqrt{2}a_p$, $b \simeq a_p$ and $c \simeq \sqrt{2}a_p$. Cell parameters obtained from the refinement are $a = 10.4782(2)$ Å, $b = 3.87956(7)$ Å and $c = 5.5491(1)$ Å for a sample of composition $LaCuO_{2.53}$. The orthorombic perovskite, whose structure shown in Fig. 2 is isostructural with $CaMnO_{2.5}$ (7) and is entirely composed of corner-shared CuO_5 pyramids which form pairs by sharing oxygen vacancies in the (010) planes. The structure can be derived from a pseudo-cubic perovskite by placing an oxygen vacancy on the face of the cubic cell and rotating the cube 90° around its four-fold axis, thereby generating all possible pyramid orientations with a repeat of 4*a*.

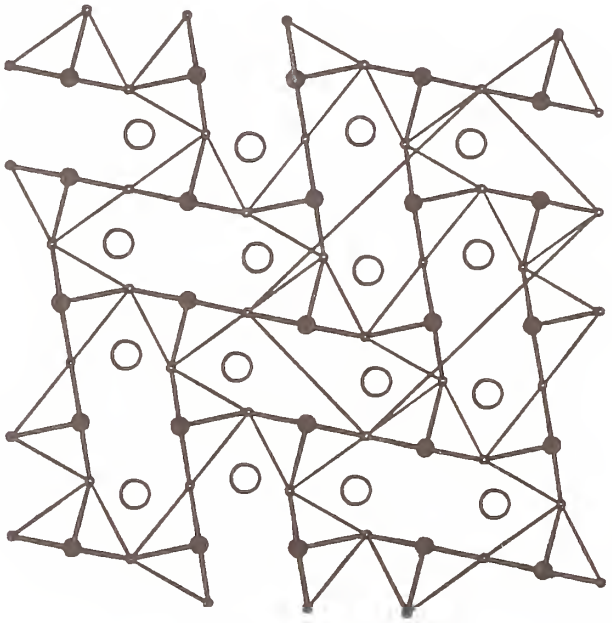

Fig. 2. Projection onto the (010) plane of the crystal structure of $LaCuO_{2.5}$. The unit cell is drawn, see note to Fig. 1.

A summary of the phase and crystallographic data for $LaCuO_{3-\delta}$ are collected in Fig. 3. The phase fields shown were obtained from samples prepared directly, or modified by reduction of a $\delta = 0.1$ composition in N_2 or O_2 (1 atm) at 300 - 750°C. Therefore, Fig. 3 is not an equilibrium phase diagram. Indeed, we have found it is possible to change the ranges somewhat by varying the preparation or processing conditions. Depending upon composition, three distinct ordered arrangements of oxygen (or vacancies) are observed. A tetragonal perovskite with a homogeneity range $0 \lesssim \delta \lesssim 0.2$ occurs at 900°C and $P_{O_2} = 0.4$ - 1 kbar. At lower oxygen pressures, $P_{O_2} = 0.2$ - 0.4 kbar, the degree of oxidation decreases leading to the formation of a monoclinic phase stable over the interval $0.2 \lesssim \delta \lesssim 0.4$. Both forms are metallic, with room temperature resistivities of 100 $\mu\Omega$cm and 300 $\mu\Omega$cm for $\delta = 0.14$ (tetragonal) and $\delta = 0.33$ (monoclinic), respectively. Superconductivity has not been observed in either case down to 4.2 K. Lastly, an orthorhombic perovskite can be prepared in this system by heating the tetragonal form to 700-800 °C in N_2. This phase has a homogeneity range between $0.43 \leq \delta \leq 0.5$ and appears to be an insulator.

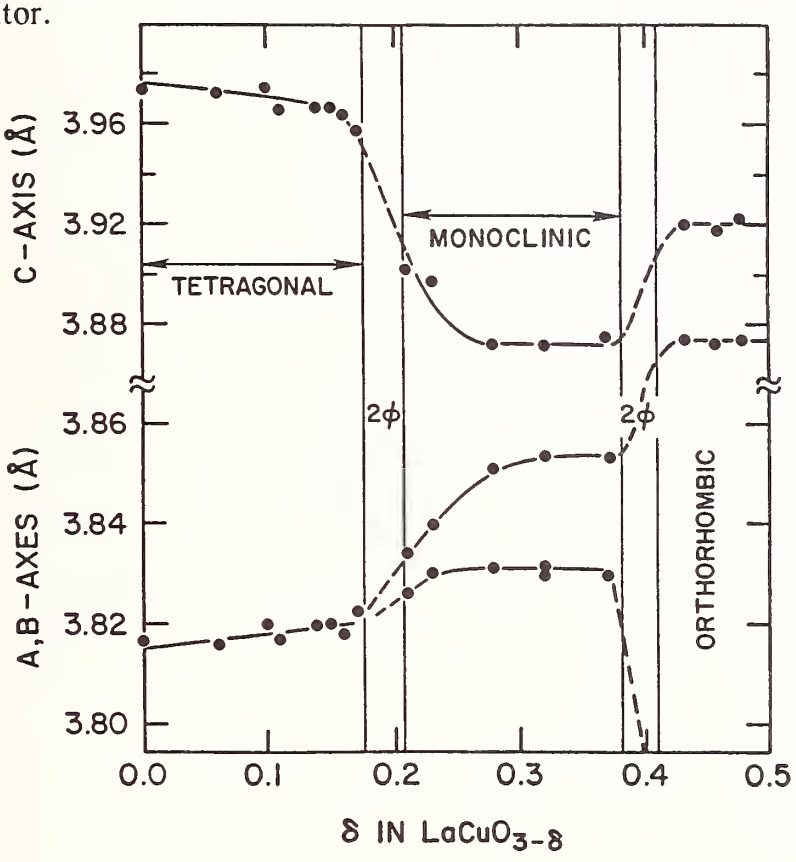

Fig. 3. The variation of the perovskite subcell parameters with oxygen content in $LaCuO_{3-\delta}$. The subcell a-axis of the orthorhombic phase (3.70 Å) is not shown for clarity, 2ϕ = approx. two phase region.

As oxygen is removed from the tetragonal $\delta = 0$ phase, two CuO_5 pyramids and two formally "Cu^{2+} sites" are created in the form of square-pyramidal pairs per each vacancy inserted. The result is that Cu is found only in octahedral and/or square-pyramidal coordination throughout the homogeneity range of $LaCuO_{3-\delta}$, and that fortuitously, the number of holes (i.e., "Cu^{3+}-sites") will be formally equal to the number of octahedral coordination sites in the system. This aspect of the structure means that the +3 and +2 valence states of Cu in $LaCuO_{3-\delta}$ are "tagged," a feature which can be used to great advantage in unravelling the electronic structure of the cuprates. For example, this fact has been exploited to gain insight into factors governing the "missing" electron paramagnetic resonance in the superconducting cuprates (8, 9). A detailed study of the effects of systematic valence changes on the electrical and magnetic properties in the $LaCuO_{3-\delta}$ system will be reported elsewhere.

REFERENCES

1. M. W. Shafer, T. Penney and B. L. Olson, *Phys. Rev. B.* **36**, 4047 (1987).
2. J. B. Torrance, Y. Tokura, A. I. Nazzal, A. Bezinge, T. C. Huang and S. P. Parkin, *Phys. Rev. Lett.* **61** 1127 (1988).
3. K. Hestermann and R. Hoppe, *Z. Anorg. Allg. Chem.* **367**, 249 (1969).
4. N. ER. Brese, M. O'Keefe, R. B. Von Dreele and V. G. Young, *J. Sol. St. Chem.* **83**, 1 (1989).
5. G. Demazeau, C. Parent, M. Pouchard, and P. Hagenmuller, *Mat. Res. Bull.* 7, 913 (1972).
6. C. Michel, L. Er Rahko, M. Hervieu, J. Pannetier and B. Raveau, *J. Sol. St. Chem.* **68**, 143 (1987).
7. K.R. Poeppelmeier, M.E. Leonowicz, J.C. Scanlon and J.M. Longo, *J. Solid State Chem.* **45**, 71 (1982).
8. F. Mehran and P. W. Anderson, *Solid State Comm.* **71**, 29 (1989).
9. F. Mehran, J. F. Bringley, B. A. Scott and T. R. McGuire, submitted to *Nature*.

VI. SURFACE CHEMISTRY

National Institute of Standards and Technology Special Publication 804, Chemistry of Electronic Ceramic Materials, Proceedings of the International Conference held in Jackson, WY, August 17-22, 1990, issued January 1991.

SURFACE ENERGY BARRIER FORMED BY ADSORBED OXYGEN IN POROUS ZnO

Satoru FUJITSU, Kunihito KOUMOTO* and Hiroaki YANAGIDA**
Department of Materials Science and Ceramics Technology,
Shonan Institute of Technology, 1-1-25 Tsujido-Nishikaigan,
Fujisawa, Kanagawa 251, Japan
* Department of Industrial Chemistry, the University of Tokyo,
7-3-1 Hongo, Bunkyo-ku, Tokyo 113, Japan
** Research Center for Advanced Science and Technology,
the University of Tokyo, 4-6-1 Komaba, Meguro-ku, Tokyo 154, Japan

The surface energy barrier formed by the chemisorbed oxygen on porous ZnO has been measured. The height of the barrier decreases by holding the sample at room temperature. This is due to the change in the oxidation state of the chemisorbed oxygen. The doping of CoO into porous ZnO enhances the saturated amount of chemisorbed oxygen and stabilizes the high temperature type of oxidation state into the low temperature.

Introduction

It is known that ZnO based varistor is the typical functional ceramics using the energy barrier along the grain boundary[1]. This characteristic depends on the atmosphere, especially oxygen, during its fabrication process. When the material is heated in the reducing ambient, the large non-ohmic characteristic cannot be observed, while this property is restored by heating in air or oxygen.

The authors have pointed out that the acceptor state to form such an energy barrier was brought about by the excess ionized oxygen along the grain boundaries[2-4]. Though such a state along the grain boundary cannot be detected, the analogous state can be recognized on the surface as the chemisorbed oxygen.

When oxygen atom or molecule adsorbs on n-type semiconducting oxide as ZnO, it traps a conduction electron from the bulk to acquire a negative charge. The carrier density then decreases, and, to compensate for the negative charges on the surface, the electron depletion layer is generated simultaneously. This depletion layer acts as the conduction barrier. In the case of a

porous body (see Fig.1), the average neck radius connecting the grains is supposedly very small, and the effect of a depletion layer on total conduction behavior cannot be ignored[2,5,6]. It is also considered that the energy barrier along the grain neck formed by penetrated oxygen contributes to control the total conduction behavior.

The authors reported that the electrical conductivity of porous ZnO having 50% porosity was controlled by the energy barrier formed by the chemisorbed and penetrated oxygen at the neck area. And the non-ohmic properties were observed at room temperature when the sample was quenched after annealing >400°C in air[7]. These phenomena can be explained by the proposed theoretical model to estimate the surface energy barrier formed by chemisorbed oxygen. The effect of the penetrated oxygen has not been clarified yet.

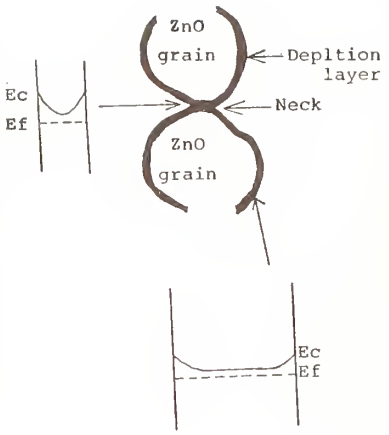

Fig.1 Cross Section of a connecting neck in a porous ZnO and its energy band.

In this study, the formation of the surface energy barrier and its stability are examined from the viewpoint of the chemisorption of oxygen and the change in its oxidation state. The effect of CoO doping is also examined on the energy barrier which is an important dopant to modify the varistor.

Experimental Procedure

(1)Sample Preparation

Nominally pure ZnO powder was dispersed in an aqueous solution of $Al(NO_3)_3$ (and $Co(NO_3)_2$), and dried. The resulting powder was calcined at 600°C to decompose aluminum nitrate into 0.5mol% Al_2O_3 oxide (and cobalt nitrate into 0.5mol% CoO oxide). The powder was then pressed into a rectangular bar in a steel die and sintered at 800°C for 1 h in air. This type of Al_2O_3-doped sample will be denoted as S-n. And Al_2O_3-CoO-doped sample will be called S-Co. Aluminum oxide was added to make the ZnO body porous. When pure ZnO was sintered by the same procedure, the relative density attained >80%. Of course, trace amount of Al_2O_3 dissolved into ZnO as a donor. The prepared samples had surface areas, of $3.2m^2/g$(S-n) and $2.8m^2/g$(S-Co) and 50% relative density (S-n and S-Co). No CoO, Al_2O_3 and the other compounds than ZnO were indicated by X-ray diffraction or EPMA. It is expected from the reported phase diagram that CoO dissolved into ZnO completely while considerable amount of Al_2O_3 precipitated in the grain boundary.

(2)Non-ohmic Properties

After annealing at 500°C in air for 1 h, the samples were quenched into liq.N_2. An In-Ga alloy was painted on each sample to achieve ohmic contact. The current-voltage (I-V) and capacitance-voltage (C-V) characteristics were then estimated at 25 C using a curve tracer (Kikusui 5802) at 50Hz and an LCZ meter (HP-4274A) at 100kHz, respectively. The samples were enclosed in the quartz tube during heating and quenching. And they were put into dry air during the electrical measurements.

(3)ESR measurement

The paramagnetic centers on the surface and in the bulk of the sample after heating, quenching and holding were measured using an ESR spectrometer at X-band frequency(JEOL JES-PE-3X), with the pressure in the sample tube below 130Pa and a field modulation of 100kHz. The spectra were recorded at 20°C. The intensity of the signal was corrected by that of Mn-marker which was inserted into the cavity with the sample tube.

Results and Discussion

(1)Non-ohmic properties

The S-n and S-Co both quenched from 500 C in air showed non-ohmic exponent, α, expressed as $I=(V/C)^{\alpha}$, of 2.8 and 6.2, respectively. The energy barrier heights estimated by C-V characteristic were 4900 and 29500V/cm for S-n and S-Co, respectively. At 500°C, the saturated amount of chemisorbed oxygen was 4.8μlSTP/cm^2 for S-n and that was 7.8μlSTP/cm^2 for S-Co.

The height of the surface energy barrier (ϕ_s) can be expressed as[8]

$$\phi_s=(2eN_{ss}^{\ 2})/\varepsilon\varepsilon_o N_d) \qquad (1)$$

where N_{ss} is the surface state density, which should be proportional to the amount of chemisorbed oxygen in the present case; N_d is the carrier density; and the other symbols have their usual meanings. Since the chemisorbed oxygen forms the electron trap state on the surface, the high energy barrier is generated when the large amount of oxygen chemisorbs on the sample.

The height of energy barrier and the saturated amount of chemisorbed oxygen for S-Co were larger than those for S-n in other temperature region.[7]

Figure 2 shows changes in α and current density for samples held at 25°C in dry air: The non-ohmic exponent decreased and the current density under the bias of 1 V/cm increased with increased holding time. Since the I-V relation was non-ohmic, conductivity could not be determined using Ohm's law. The non-ohmic exponent of the S-n decreased to 1 within 100 h, whereas the value for S-Co

decreased more slowly. This decrease in the non-ohmic exponent and increase in current density are due to the decrease in barrier height predicted by the C-V relation.

Equation (1) indicates that either increased carrier density or decreased surface state density with holding time at room temperature should explain decreases in barrier height. The decrease in the carrier density and the desorption of oxygen were not observed.

The decrease in the barrier height was due to the change in the oxidation state of chemisorbed oxygen. At high temperature (>400°C), the oxidation state of the chemisorbed oxygen can be represented as O^{2-}. According to the literature[9], O^{2-}, O^{-}, and O_2^{-} are stable above 300°C, at 150° to 300°C, and below 150°C, respectively. Even if the amount of oxygen chemisorbed at high temperature is frozen by quenching, its oxidation state may become more stable, with fewer electrons leading to a decrease in barrier height, when the sample is held at room temperature, as expressed by

$$O^{2-} \rightarrow O^{-} + e \quad (2)$$

$$O^{2-} + (1/2)O_2(g) \rightarrow 2O_2 + e \quad (3)$$

where e represents the released conduction electron.

(2)ESR Measurement

Change in the oxidation state of the chemisorbed

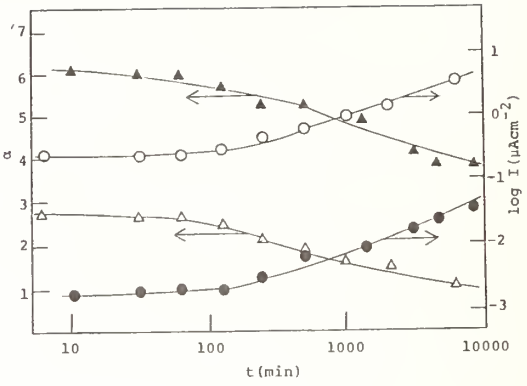

Fig.2 Change in the non-ohmic exponent(△, ▲) and the current density under the bias(1V/cm) (○, ●) with holding time at 25°C in dry air. Open and closed marks show the S-n and S-Co, respectively. The sample were prepared by quenching from 500°C into liq.N_2

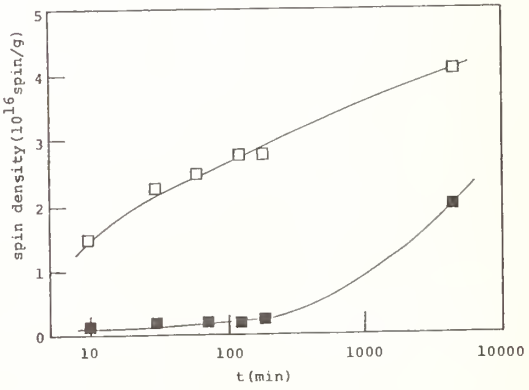

Fig.3 Change in the spin density resulting from O_2^{-} and O^{-} for S-n(○) and S-Co(●).

oxygen were observed directly by ESR spectroscopy. The ESR signals assigned to the chemisorbed oxygen (O_2^-[10] and O^-[11]) were observed in both S-n and S-Co, and its intensity increased with increased holding time at room temperature. To evaluate the increased intensity of the signals, the spin concentration was calculated by double integration of the spectra. Since the signals could not be clearly divided into O^- and O_2^-, only the total spin concentration was estimated in the present calculation. As shown in Fig.3, the spin concentration increased with holding time at room temperature, similar to the changes in the non-ohmic exponent and current density in Fig.2. This result indicates that the decreased barrier height resulted from the reactions expressed in Eqs. (2) and (3), in which trapped electrons were released, hence decreasing the surface state density. The slow decrease in S-Co energy barrier height with holding time at room temperature apparently corresponds to the slow increase in spin concentration.

The considerable difference in ESR spectra for S-n and S-Co is the signal at a g-value of 1.96. Though this signal can be observed in S-n after any treatment, that was never observed in S-Co. The 1.96 line is attributed to mobile electrons in the conduction band and/or a trapped hole in the shallow donor band, which probably arises from defects such as interstitial zinc and/or oxygen vacancies[12]. Since the difference of the electrical conductivity in both samples was not as great as that in the intensity of the ESR signals of the two samples with g=1.96, this signal should be assigned not to the conduction electron but to the paramagnetic defects as oxygen vacancies, zinc atoms at the interstitial site trapping one hole. The substituted aluminum ion is a candidate of the paramagnetic center, but aluminum ion was doped in both samples. Probably, CoO doping forms the donor state that is undetectable by ESR spectroscopy as doubly ionized oxygen vacancies and/or the zinc atom at the interstitial site.

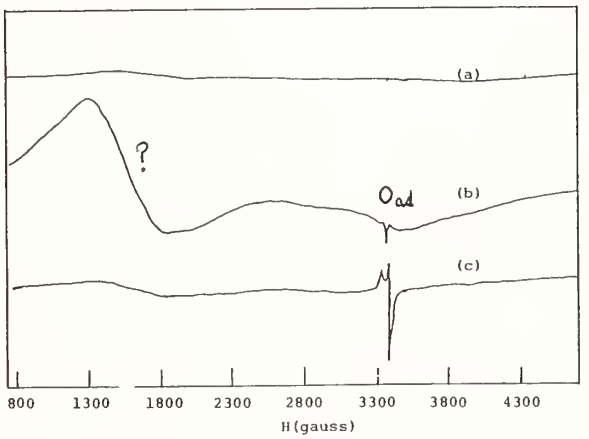

Fig.4 ESR spectra for S-Co
(a)spectrum for the sample evacuated at 600°C for 10 h. No signal was observed in this spectrum.
(b)spectrum for the sample annealed at 500°C for 1 h in 130Pa of oxygen pressure and (c)spectrum for the sample exposed in 130Pa of oxygen pressure at 25°C after evacuation.

As shown in Fig.4

(a), evacuated S-Co exhibited no signal by ESR measurement at room temperature. Oxidized S-Co showed the signals assigned to chemisorbed oxygen and also a broad band at 1500 gauss (g 4.25). Since this broad band was observed in the sample oxidized at room temperature where the oxidation of CoO in grain bulk cannot be expected, the formation of such a signal is resulted from the change in the oxidation state of Co ion near the surface. The enhancement of the saturated amount of chemisorbed oxygen and the stability of O^{2-} should be supported by the formation of complex of Co ion and chemisorbed oxygen. In the present experiment, it is impossible to assign this unknown signal at 1500 gauss.

References

[1] K.Mukae et al., Jpn.J.Appl.Phys., 16,1361(1977).
[2] S.Fujitsu et al., Bull.Chem.Soc.Jpn., 61,1979(1988).
[3] S.Fujitsu et al., Solid State Ionics., 32/33,482(1989).
[4] S.Fujitsu et al., J.Am.Ceram.Soc., 70,C-71(1987).
[5] N.M.Beekmans, J.Chem.Soc.,Faraday Trans.1, 74,31(1978).
[6] M.Takata et al., Yogyo Kyokaishi, 87,19(1979).
[7] S.Fujitsu et al., J.Am.Ceram.Soc., to be published.
[8] S.R.Morrison, Advanced Catalysis, 7,259(1955).
[9] M.Sedaka et al., Bull.Chem.Soc.Jpn., 38,1414(1965).
[10]J.O.Cope et al., J.Chem.Soc.,Faraday Trans.1, 69,1(1973).
[11]N.B.Wong et al., J.Chem.Phys., 60,2148(1974).
[12]G.Neumann, "Paramagnetic Properties", p.269 in Current Topics in Material Science ed. by E.Kaldis 7,(1981), North-Holland Amsterdam.

National Institute of Standards and Technology Special Publication 804, Chemistry of Electronic Ceramic Materials, Proceedings of the International Conference held in Jackson, WY, August 17-22, 1990, issued January 1991.

SURFACE PROPERTIES OF $BaTiO_3$ AT ELEVATED TEMPERATURES

J. Nowotny[1] and M. Sloma[2]
(1) Australian Nuclear Science & Technology Organisation
Advanced Materials, Menai, NSW 2234, Australia
(2) Max-Planck-Institute for Solid State Research
7000 Suttgart 80, FR Germany

ABSTRACT

Surface electrical properties of undoped $BaTiO_3$ have been studied by using the High Temperature Kelvin Probe. Changes in work function have been measured during oxidation and reduction processes under controlled oxygen activity. Experimental data are considered in terms of changes in nonstoichiometry of the $BaTiO_3$ surface layer and structural reconstructions within this layer. Impact of the observed phenomena on properties of ceramic materials based on $BaTiO_3$ is discussed.

INTRODUCTION

Segregation causes the chemical composition, crystalline ordering and electrical properties at interfaces, such as external surfaces and grain boundaries, to differ from those of the bulk. The effects of segregation have been the subject of extensive studies for metals and alloys and have been confirmed for ceramic compounds such as binary metal oxides and their solid solutions [1]. Thus it is expected that segregation at interfaces will also affect the properties of ternary oxides such as $BaTiO_3$ [2].

Several properties of $BaTiO_3$, which are important for application, such as dielectric properties and temperature characteristics of resistivity, are strongly influenced by interfaces. So far, however, little is known about the effect of segregation on surface properties of $BaTiO_3$ and its impact on interface properties.

The predominant lattice defects in $BaTiO_3$ are oxygen vacancies [3,4]. Their bulk concentration is determined by oxygen activity in the gas phase. The relationship between oxygen partial pressure and oxygen nonstoichiometry of $BaTiO_{3-x}$, in equilibrium state, is described in several publications. Similar relationships may also be expected for the surface layer. However, as a result of segregation the concentration of defects in this layer

may be higher than that in the bulk. If this is the case, the resulting enrichment may lead to the formation of low dimensional surface structures.

Electrical properties are very sensitive to nonstoichiometry and related defect structure. The most frequently applied methods in studies of defect structure are electrical conductivity and thermopower. Unfortunately, both these methods are bulk sensitive and show very little, or no sensitivity to the surface. On the other hand, the work function is a very surface sensitive parameter. It can be determined using a High Temperature Kelvin Probe [5] which enables studies of solids at elevated temperatures and under controlled gas atmosphere.

The purpose of this work is to study surface properties of $BaTiO_3$ at elevated temperatures under controlled oxygen activity by using work function measurements.

WORK FUNCTION AND DEFECT STRUCTURE

The work function (WF) of $BaTiO_3$ was measured by the Kelvin method [5].

The Kelvin method involves taking measurements of the contact potential difference (CPD) between two surfaces (1) and (2):

$$CPD = 1/e\ (\varphi_1-\varphi_2) \qquad (1)$$

where e is the elementary charge and φ is WF. Accordingly, WF changes may be expressed as:

$$\Delta\varphi_1 = e(CPD) + \Delta\varphi_2 \qquad (2)$$

Changes in the WF of semiconducting compound caused by the variations in nonstoichiometry can be directly related to the concentration of defects. For a p-type semiconductor we have:

$$\Delta\varphi = -kT\ \ln\ (N/[h^{\cdot}] \qquad (3)$$

where N is the density of states, $[h^{\cdot}]$ is the concentration of electron holes, k is the Boltzmann constant and T is absolute temperature. Work function changes can also be related to the Fermi energy level of the surface layer:

$$\Delta\varphi = -E_{F.} \qquad (4)$$

The relationship (3) is only valid for WF data taken at elevated temperatures when an equilibrium between the gas phase and the solid has been established. If this condi-

tion is satisfied, then differences in the WF can be directly related to the defect structure of the boundary layer.

The defect structure of nonstoichiometric oxides is determined by the oxygen activity of the gas phase. Then changes in oxygen partial pressure results in variations of defects concentration which can be considered either as acceptor or donor centers. Usually, increases in $p(O_2)$ results in either increases in the concentration of acceptors or decreases in the concentration of donors. Both result in the decrease of E_F and, consequently, in the increase of WF assuming that the crystal ordering remains unchanged.

Changes in the oxide nonstoichiometry and resulting concentration of electronic defects within the p-type composition range with $p(O_2)$ can be expressed by the following relationship

$$[h^{\cdot}] = \text{const}\ p(O_2)^{1/n} \qquad (5)$$

where n is the parameter related to the valency of defects. For doubly ionized oxygen vacancies, n is 6. If predominant lattice defects are singly ionized oxygen vacancies or acceptor-type impurities then, according to the mass action law, in both cases the oxygen exponent is equal 1/4.

Combination of Eq. (3) and (5) results in the following dependence between the exponent 1/n and WF:

$$1/n = (1/kT)\{\partial\varphi/\partial \ln p(O_2)\} \qquad (6)$$

Hence the parameter n is related to the surface layer.

It has been reported that the parameter n for undoped $BaTiO_3$ within the p-type region is equal to 4 [4]. This value is consistent with several defect models including: the intrinsic model, which is based on singly ionized oxygen vacancies, extrinsic model based on acceptor type impurities and the cation nonstoichiometry model[4].

EXPERIMENTAL

The High Temperature Kelvin Probe [5] enabled the performance of WF measurements on both single crystals and polycrystalline specimens up to 1273 K under gas atmosphere of controlled oxygen activity. The measurements involve the determination of the CPD between the studied specimen and Pt reference electrode. The oxygen partial pressure in the gas phase was imposed by using a $Ar-O_2$ mixture. Its activity was determined by using a zirconia gauge.

$BaTiO_3$ specimens were prepared by coprecipitation of Ba and TiO oxalates. Details of the preparation were described in ref. [6].

WF measurements were performed on specimens initially standardized at 1123 K in argon of oxygen activity $p(O_2)=10^2$ Pa and then cooled down to the temperature of the measurements. The applied experimental procedure involved the isothermal determination of WF changes as a function of time after $p(O_2)$ was suddenly changed to a new value (6.9×10^3 Pa). The measurements were performed within the range 473-1019 K.

RESULTS

Figs. 1 and 2 illustrate the WF changes while cooling (first part of figures) and WF changes during successive oxidation and reduction runs (second part of figures) at 325 and 590°C, respectively. The WF changes on cooling are caused by several processes including the chemisorption of oxygen and surface nonstoichiometry. The sign of measured $\Delta\varphi$ values for the two runs at both temperatures are different. At 325°C; during the oxidation and reduction runs, $\Delta\varphi$ is positive and negative, respectively. At 590°C a reverse effect is observed.

DISCUSSION

Measured WF changes at 590°C (Fig. 2) are in accordance with theoretical predictions described above. One may therefore presume that the oxidation run causes oxygen incorporation and results in the formation of donor centers such as oxygen vacancies:

$$O_O \rightleftharpoons V_O^{z} + zh \qquad (7)$$

Corcondantly, the reduction run leads to evolvment of oxygen and disappearance of the donors. It can therefore be assumed that the equilibrium (7) is shifted into the right and left by oxidation and reduction runs, respectively. The model is fully consistent with experimental data illustrated in Fig. 2. In contrast, the WF data in Fig. 1 suggest, that surface electrical properties at 325°C are controlled by some other surface process. These data can be explained in terms of crystalline reordering induced by changes in oxygen activity. One possible explanation involves the tetragonal/cubic (t/c) transition. In air bulk $BaTiO_3$ transforms at 120°C. However, it has been reported that the grain boundary layer of $BaTiO_3$ exhibits the cubic structure at room temperature [7]. It is not known at what temperature the t/c transition may take within the boundary layer but one may expect that

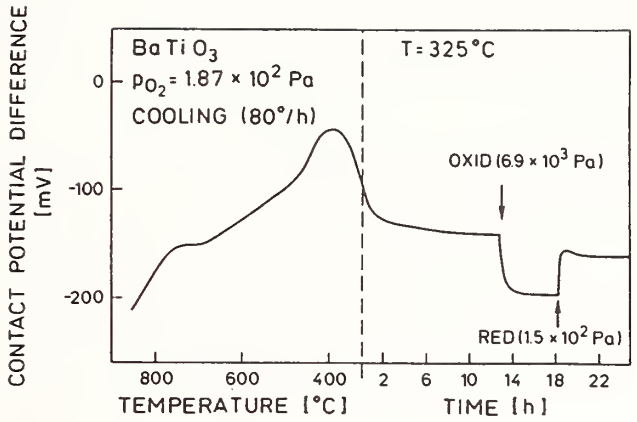

Fig. 1. CPD vs. T (cooling) and vs. time at 325°C

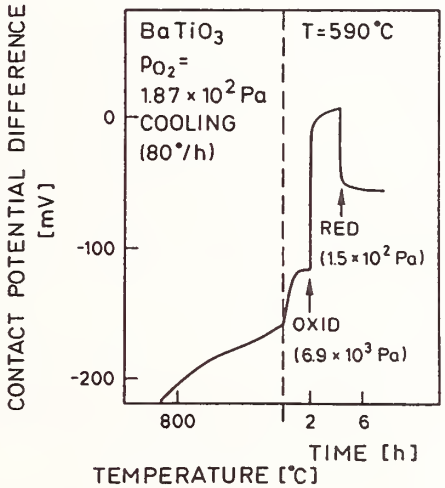

Fig. 2. CPD vs. T (cooling) and vs. time at 590°C

the Curie temperature for the interface layer depends on the oxygen activity. Thus, the effect observed in Fig. 1 may be ascribed to the interfacial structural reordering between the tetragonal structure to the cubic structure stable at higher oxygen activity. The tetragonal/monoclinic reordering has also been taken into account [8].

There is a lack of experimental data which could confirm the oxygen induced interface transition model described above. Electron microscopy of $BaTiO_3$ standardized under controlled oxygen activity may be helpful in this matter.

The sign of WF changes taken at 590°C is in agreement

with the model of nonstoichiometry for $BaTiO_3$ which involves oxygen vacancies as predominant defects. The value of the parameter n determined here (n=4) can be considered along with several defect models mentioned above.

CONCLUSIONS

Work function studies indicate that the oxygen pressure exponent for the surface layer at 590°C is essentially the same as that reported for the bulk of $BaTiO_3$. Its absolute value (1/n = 1/4) is in agreement with several defect models considered for this compound.

WF measurements at 325°C are inconsistent with the above defect models and indicate that changes in oxygen activity result from structural reordering of the surface layer. It is expected that the reordering involves the t/c transition which is limited to the boundary layer. On the basis of the results in this study, it is likely that the structural reordering takes place when $BaTiO_3$ and $BaTiO_3$-base dielectric materials are cooled below 325°C. Up until now, the interface properties of the dielectrics have been considered in terms of oxygen chemisorption and nonstoichiometry. The results in Fig. 1 indicate that the structural evolution of interfaces during cooling also must be taken into account. It is well known that the crystalline structure at interfaces changes when the density of defects exceeds some critical value. Thus it is probable that the reordering which occurs at the surface of $BaTiO_3$ is related to segregation.

AKCNOWLEDGEMENTS

This work has been supported by the European Community within the BRITE/EURAM Project, Grant No BE-3595/89. Thanks are due to Kath Smith for proofreading.

REFERENCES

[1] J. Nowotny, "Surface & Interfaces of Ceramic Materials", L.-C. Dufour et al., Eds., Kluwer Acad., Dordrecht, 1989, p. 205-239
[2] S. Desu, "Interfacial Segregation in Perovskites and Applications to Boundary Layer Devices", PhD thesis, University of Illinois, Urbana, 1982
[3] A.M.J.H. Seuter, Philips Res.Rep.Supl., 3, 1-84 (1974)
[4] J. Nowotny and M. Rekas, J.Europ.Cer.Soc., 5, 173-182 (1989)
[5] J. Nowotny, M. Sloma and W. Weppner, J.Am.Ceram.Soc., 72 [4] 564-70 (1989)
[6] M. Rekas and M. Wierzbicka, Solid State Ionics 20, 51-54 (1986)
[7] J.-C. Niepce, Ref. [1], p. 521-533
[8] K. Smith, unpublished results.

National Institute of Standards and Technology Special Publication 804, Chemistry of Electronic Ceramic Materials, Proceedings of the International Conference held in Jackson, WY, August 17-22, 1990, issued January 1991.

A SCANNING TUNNELING MICROSCOPY STUDY OF SINGLE CRYSTAL ZnO AND TiO_2 SURFACES

Gregory S. Rohrer
Carnegie Mellon University
Dept. of Metallurgical Eng. and Materials Science
Pittsburgh PA 15213
and
Dawn A. Bonnell
University of Pennsylvania
Dept. of Materials Science and Engineering
Philadelphia PA 19104

ABSTRACT

The surfaces of ZnO and TiO_2 single crystals have been imaged in ultrahigh-vacuum with a scanning tunneling microscope. Constant current images of the polar ZnO faces show that single crystal surfaces cleaned by vacuum heating have numerous steps consisting mainly of $(10\bar{1}0)$ and $(11\bar{2}0)$ faces. Images of the reduced $TiO_2(110)$ surface indicate that crystallographic shear planes in the bulk strongly influence the surface structure. Local variations in stoichiometry ranging from Ti_3O_5 to Ti_6O_{11} have been determined by directly measuring the spacing between the periodic intersections of adjacent shear planes with the $TiO_2(110)$ surface. The results in this paper demonstrates that it is possible to resolve atomic-scale features on the surfaces of wide bandgap semiconductors using the scanning tunneling microscope.

INTRODUCTION

The reactions at transition metal oxide surfaces which underlie complex phenomena such as heterogeneous catalysis [1] and gas sensing [2] are strongly influenced by the geometric and electronic surface structure. The application low energy electron diffraction (LEED) [3] and high resolution transmission electron microscopy [4] have provided the first insights

into the structures of these surfaces, but the current information is still rather limited and many systems have not yet been investigated. We have used a scanning tunneling microscope (STM), an instrument which has had enormous impact on the study of metal and covalently bonded semiconductor surfaces, to study the surfaces of two transition metal oxides. From topographic maps of these surfaces, we have been able to identify the types of facets which form on the ZnO polar faces and determine the influence of bulk, planar defects on the atomic structure of the TiO_2(110) surface.

EXPERIMENTAL DETAILS

The anisotropic etching of the ZnO $(000\bar{1})$ and (0001) faces was used to determine the polarity of the single crystal. The polar faces were mechanically polished until there were no optically visible defects by sequentially reducing the size of abrasive alumina grinding media down to 0.05 micron. After heating the sample in ultrahigh-vacuum (UHV) at 600-700 °C for 2 hours, sharp LEED patterns were observed and Auger electron spectroscopy indicated that the surfaces were free of carbon contamination. Previous work has indicated that such a treatment produces steps and facets on the surface. [5] The titania surface, prepared in a similar way, was first polished and then reduced by heating in UHV at a temperature above 900 K for 36 hrs. Following this treatment, the dark grey, opaque crystal was argon ion milled and then annealed at 823 K for 30 min in 1 X 10^{-7} torr of O_2 in order to re-oxidize the surface and anneal out the damage produced by ion bombardment. LEED patterns indicated that this preparation method produced a well ordered, relatively defect free surface. [6] The crystal was then exposed to air for several days before being introduced into the UHV STM chamber, where it was heated at approximately 673 K for 2 min and then 'flashed' at approximately 973 K for 5 sec. Following this treatment, a (1X1) LEED pattern was found, identical to that observed following the initial preparation.

The microscope consisted of a commercial STM head [7] controlled by 'home made' feedback electronics and software of conventional design. The images were collected in the constant current mode using sample biases of -1.5 to -3.0 V and tunnel currents between 0.1 and 1.0 nA and are presented after the subtraction of a

background plane which eliminates the tilt of the sample that would otherwise overwhelm small variations and make atomic features undetectable. Other experimental details have been described previously. [8]

RESULTS AND DISCUSSION

The constant current image of the ZnO($000\bar{1}$) oxygen terminated face, shown in Fig. 1, demonstrates that surfaces prepared by *in situ* annealing have a high step density. However, unannealed surfaces appeared even more disordered, presumably due to polishing damage. Atomically smooth flat areas are separated from one another by either single or multiple steps which are aligned predominantly in the either the [$10\bar{1}0$] or [$11\bar{2}0$] direction. This is reasonable, since these are the nonpolar faces and are known to be thermodynamically stable. [2] The height of the step which forms the large hexagonal plateau in the lower left part of the image is 5.21 Å, which agrees well with the ideal spacing between the oxygen planes along the [0001] direction which is 5.25 Å. Similar results were obtained for the (0001) surface. Spatially resolved tunneling spectroscopy has been used to detect mid-gap defect states associated with these steps, a result described in a more detailed paper. [9] In the majority of the regions imaged, the atomically smooth areas were only about 100 Å in diameter. This high density of edge sites is likely to affect the electronic properties and reactivity of this surface.

No atomic-resolution images of the ZnO surfaces have yet been recorded. However, we have examined only intrinsic (not intentionally doped) crystals with low electronic conductivities and the resolution of the images was undoubtedly space charge limited. [10] This was not the case for the reduced titania crystal which we have also examined.

Fourier analysis and direct measurement of the images of the TiO_2(110) surface (see Fig. 2a) indicate that the rows oriented in the [$1\bar{1}1$] direction have an 8.5 Å periodicity and a 1 Å corrugation height. The corrugation directed along the rows has a 3.4 Å periodicity and a 0.2 Å amplitude. The width of these rows seems to vary somewhat and there are also numerous "missing cells". The bulk terminated rutile lattice

Fig. 1. Constant current image of the ZnO(000$\bar{1}$) face. Steps are visible which form (10$\bar{1}$0) and (11$\bar{2}$0) faces. The image is 771 Å X 771 Å and was acquired at -1.5 V sample bias and 0.3 nA. The vertical resolution is 36 Å from black to white.

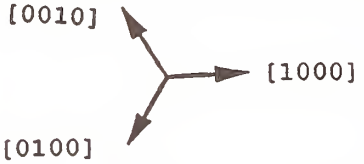

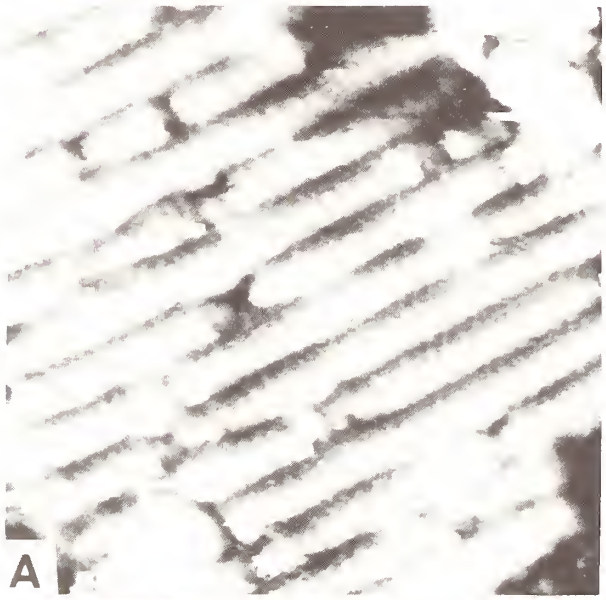

Fig. 2.a)109 Å X 109 Å image of titania(110). acquired at -2.0 V and 0.1 nA. Vertical resolution is 2 Å from black to white and the rows are oriented in the [1$\bar{1}$1] direction. b) 273 Å X 108 Å image of a different region acquired using the same conditions. The vertical resolution is 9 Å and the rows are oriented in the [$\bar{1}$13] direction.

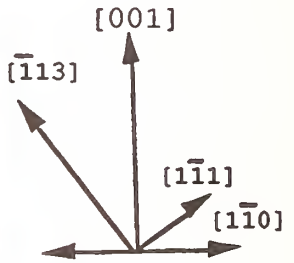

vectors have been added for comparison. Other images of this area show ledges which occur approximately every 100 Å and some regions of the images are either disordered or covered with adsorbates. The image in Fig. 2b, acquired on another area of the surface, shows rows oriented along the [$\bar{1}$13] direction with an approximately 20 Å spacing. It is clear from these observations that the surface structure can not be

described by a simple termination of the bulk unit cell or some combination of unit cells.

The orientation and spacing of the rows on the crystal surface suggest that they are caused by the intersection of crystallographic shear (CS) planes with the (110) surface. The (121) family of planes are among those along which the CS displacements can occur. [11] The (121) plane intersects the (110) surface along the $[1\bar{1}1]$ direction, the same direction that the rows in Fig. 2a are oriented. The intersection of the $(1\bar{2}1)$ plane and the (110) surface is in the direction $[\bar{1}13]$, the direction in which rows in Fig. 2b are aligned. Because the CS displacement is always of the type $^1/_2[0\bar{1}1]$, adjacent sections of the crystal are vertically displaced 1.6 Å with respect to one another along the line normal to the (110) surface. Because the plane subtraction applied to each image removes any global slope, a stepped structure appears saw-toothed, so that the intersection of each CS plane with the surface appears as a depression or dark spot on the image. The spacing of the rows in Fig. 2a suggests that every sixth anion (121) plane is a CS plane and that the local composition in this area is Ti_3O_5, while the spacing of the rows in Fig. 2b suggests that CS occurs at every twelfth anion $(1\bar{2}1)$ plane and that the local composition is Ti_6O_{11}. The 0.2 Å corrugations within the rows of Fig. 2a have a 3.4 Å spacing which is very close to the spacing of titanium atoms (3.5 Å) along this same direction in the ideal rutile unit cell.

It should also be noted that the presence of excess titanium along the CS planes should result in an electronic density of states corrugation which is opposite to the geometric effect. However, corrugations in the electronic density of states are usually some tenths of angstroms, so this effect should not be able to cancel the larger geometric effect. In fact, the observation that the corrugations in Fig. 2a are about 1 Å, less than the expected value of 1.6 Å, suggests that the presence of excess titanium in these positions compensates somewhat for the geometric effect. Although previous models of the reduced $TiO_2(110)$ surface have not considered the possible existence of CS planes or their effect on the titania surface structure [12], the existence of these planar defects has been proposed by Firment et al. [13] to explain angle-resolved UPS data

from the reduced $MoO_3(010)$ surface, another transition metal oxide which forms a variety of CS structures.

CONCLUSION

This work demonstrates that the STM is capable of determining the surface structure of ionic materials, such as TiO_2 and ZnO, and that these oxides have unusual surface structures which undoubtedly play a role in determining their activity as catalysts and sensors.

ACKNOWLEDGEMENTS

The authors acknowledge J. Vohs for providing the ZnO crystal. Also, V. Henrich and Z. Zhang are acknowledged for preparing and providing the rutile sample. This work was funded by IBM and the Nation Science Foundation.

REFERENCES

[1] W. E. Farneth, E. M. McCarron III, A. W. Sleight, and R. H. Staley, *Langmuir* **3**, 217 (1987).
[2] W. Gopel, *Prog. Surf. Sci.* **20**,9 (1985).
[3] V. Henrich, *Rep. Prog. Phys.* **48**, 1481 (1985).
[4] Z. C. Kang, D. J. Smith, and L. Eyring, *Surf. Sci.* **175**, 684 (1986).
[5] M. Grunze, W. Hirschwald, and D. Hofmann, *J. Cryst. Growth* **52**, 241 (1981).
[6] H. R. Sadeghi and V. E. Henrich, *Appl. Surf. Sci.* **19**, 330 (1984).
[7] The STM head was manufactured by WA technologies, England.
[8] G. Rohrer and D. Bonnell, *J. Am. Ceram. Soc.*, in press.; G. Rohrer, V. Henrich and D. Bonnell, submitted to *Science*.
[9] G. S. Rohrer and D. A. Bonnell, in preparation
[10] F. Flores. and N. Garcia, *Phys. Rev.* **B 30**, 2289 (1984).
[11] L. A. Bursill and B. G. Hyde, Prog. in Solid State Chem. Reiss and McCaldin, Ed (Pergamon Press, New Jersey, 1972), Vol. 7, p. 177.
[12]W. Göpel, G. Rocker, and R. Feierabend, *Phys. Rev.* **B 28**, 3427 (1983).
[13] L. E. Firment, A. Ferretti, M. R. Cohen, and R. P. Merrill, *Langmuir* **1**, 166 (1985).

DISCUSSION

J. Nowotny: In the Max Planck Institute for Solid State Research in Stuttgart, there has been research on the electrical properties of titanium oxide involving measurements of electrical conductivity as a bulk property and work function as a surface property under the same conditions. What has been observed is that the same material, under the same conditions is n-type in the bulk and is p-type at the surface. So we have p-type conditions coming from the bulk to the surface. Is it known how the surface might become the type as you have mentioned?

G. S. Rohrer: Yes, under some circumstances I think it's quite possible for there to be an accumulation layer at the surface that could actually transform the material from one type to the other. However, that did not appear to be the case during these measurements.

D. Cahen: Could it be possible that when you try to compare the results from UPS, XPS and STM, you see problems that are associated with desorption and adsorption of oxygen? Because unless you work consistently at very low pressures you will get oxygen very quickly, on most of these surfaces.

G. S. Rohrer: I have to say that's always a possibility, because I don't know exactly the chemistry of the edge sites. But I'd also have to point out that these surfaces stay very clean in the UHV pressure range. In fact, they only interact weakly with most gases, so that once you clean them off they are very stable. These experiments were carried out in roughly the $5x10^{-10}$ torr pressure range.

R. Newnham: What are the prospects of using STM for real ceramics?

G. S. Rohrer: For nonconductive ceramics, the prospects are very poor right now. We've made preliminary efforts to do this at Penn, by photo-exciting surfaces. Another approach is to dope an insulating surface and make it conductive, but then, of course, you might change the chemical properties of the surface.

We've already put out some papers on polycrystalline zinc oxide ceramics and there is a lot of promise for probing grain-boundary interactions. But the key thing right now is that the crystal has to have some kind of conductivity.

D. Cahen: I'm a little bit concerned about your remark that you have clean surfaces, because in all papers which I know there's always a question of oxygen and water absorption. How do you know that you have clean surfaces?

G. S. Rohrer: Well, with respect to oxygen and water absorption, it's difficult to say absolutely. However, I followed instructions from the literature for cleaning procedures which produced one-by-one surfaces as determined by LEED.

As far as the chemistry and possible absorption at the edge sites, I have to try to deduce that from the experimental results. However with respect to carbon-containing species, my experiments indicate that once I cleaned the surfaces, they stayed clean in UHV.

VII. THEORY AND MODELING

National Institute of Standards and Technology Special Publication 804, Chemistry of Electronic Ceramic Materials, Proceedings of the International Conference held in Jackson, WY, August 17-22, 1990, issued January 1991.

FACTORS DETERMINING THE DIELECTRIC CONSTANTS OF OXIDES AND FLUORIDES

R. D. SHANNON
E. I. Du Pont de Nemours and Co., Inc.
Central Research and Development Department
Experimental Station
Wilmington, DE 19880-0356

ABSTRACT

A preliminary set of 16 ion dielectric polarizabilities was derived from the dielectric constants of 63 oxides and 4 fluorides using a least squares fitting procedure and the ion additivity rule in conjunction with the Clausius-Mosotti equation and accurately determined dielectric constants and molar volumes. Assuming an arbitrary value for $\alpha_D(B^{3+}) = 0.05$ Å^3 anion polarizabilities of 2.01, 2.18, and 1.63 Å^3 are found for $O^=$, OH^-, and F^-, respectively. Typical cation polarizabilities are 0.79, 0.85, 1.31 and 3.15 Å^3 for Al^{3+}, Si^{4+}, Mg^{2+} and Ca^{2+}, respectively. The agreement between measured dielectric polarizabilities as determined from the Clausius-Mosotti equation and those calculated from the sum of oxide polarizabilities and the sum of ion polarizabilities is ~ 0.5% for 18 oxides. The effects of composition, structure, polar impurities, mixed valence and defects on total polarizability are demonstrated.

INTRODUCTION

Recent efforts to replace Al_2O_3 as an electronic packaging material have generated an interest in a better understanding of the factors which determine the dielectric constant of oxide materials (Chowdhry and Sleight, 1987; Kawakami et al., 1987; Kondo et al., 1987; Tummala, 1988). Olhoeft (1981), in a study of a wide variety of silicates found the dielectric constant, $\kappa' = 1.91^d$ where d = density in g/mL. However, plots of κ' vs. d for a variety of borates, aluminates, silicates and phosphates show considerable scatter.

Another approach used to systematize dielectric constant data for many decades involves the use of polarizabilities. The

dielectric polarizability, α_D, is related to the measured dielectric constant by the Clausius-Mosotti equation:

$$\alpha_D = 1/b\ [(V_m)\ (\kappa'-1)/(\kappa'+2)] \qquad (1)$$

where V_m is the molar volume in $\mathring{A}^3$, b is assumed to be $4\pi/3$, and κ', the real part of the complex dielectric constant, is measured in the range 1 KHz to 10 MHz (Roberts 1950,1951). The dielectric polarizability includes both ionic, α_i, and electronic, α_e, components. The electronic polarizability, α_e, is related to the refractive index, n, by the Lorenz-Lorentz equation (Lorentz 1880; Lorenz 1880):

$$\alpha_e = 1/b\ [(V_m)\ (n^2 -1)/(n^2 +2)] \qquad (2)$$

Although the Clausius-Mosotti equation is strictly valid only for compounds where the molecule or ion has cubic symmetry (Szigeti, 1949; Bosman and Havinga, 1963; Dunmur, 1972; Megaw, 1975; and Roberts, 1949,1950,1951), it has been shown to be approximately valid for a number of noncubic crystals by Roberts (1949, 1951) and Lasaga and Cygan (1982).

The concept of additivity of molecular polarizabilities whereby the molecular polarizability of a complex compound A_2BX_4 can be broken up into the molecular polarizabilities of the simpler compounds AX and BX_2 according to:

$$\alpha_D(A_2BX_4) = 2\ \alpha_D(AX) + \alpha_D(BX_2) \qquad (3)$$

is useful in systematizing dielectric constant data and has been discussed by Heydweiller (1920), Cheng (1940), Jonker and Van Santen (1947), Roberts (1949, 1950, 1951), and Lasaga and Cygan (1982). It has recently been demonstrated that the oxide additivity rule, in conjunction with simple oxide polarizabilities, accurate dielectric constants and molar volumes, results in agreement between observed and calculated polarizabilities of $\sim$ 1% for a wide variety of oxides (Shannon and Subramanian, 1989; Shannon et al., 1989; Shannon et al., 1990a,b).

Molecular polarizabilities of complex substances can also be broken up into ion polarizabilities according to:

$$\alpha(A_2BX_4) = 2\ \alpha(A^{2+}) + \alpha(B^{4+}) + 4\ \alpha(X^{=}) \qquad (4)$$

Ion polarizabilities are potentially more useful and easier to use for predictive purposes than simple oxide polarizabilities. Many sets of empirical electronic ion polarizabilities, α_e, have been derived from the C-M equation and the additivity rule using the

alkali halides and alkaline earth chalcogenides (Tessman, Kahn and Shockley (TKS), 1953; Pirenne and Kartheuser, 1964; Wilson and Curtis, 1970; Boswarva, 1970; Coker, 1976; Claro, 1978) and using a variety of minerals (Lasaga and Cygan, 1982). These polarizabilities were found to be useful in predicting refractive indices. A set of 18 dielectric ion polarizabilities, α_D, derived from cubic compounds by Roberts (1949), assuming $\alpha_D(O^{=}) = 2.387$ Å^3 was found to give agreement between observed and calculated polarizabilities of ~ 5%. A second set of 11 dielectric ion polarizabilities was derived for application to minerals by Lasaga and Cygan (1982), assuming $\alpha_D(O^{=}) = 2.37$ Å^3. Using these ion polarizabilities agreement between observed and calculated total polarizabilities of 24 common minerals was ~ 10% with some individual deviations as large as 20%.

In this paper we derive a set of preliminary dielectric ion polarizabilities that can be used to predict total polarizabilities of a variety of oxides and fluorides to an accuracy of about 0.5%. We then summarize recent data showing the validity of the oxide additivity rule and compare the results from the oxide additivity rule with those from the ion additivity rule. Finally, we show that large deviations from additivity can sometimes be traced to certain physical characteristics such as ionic or electronic conductivity, the presence of dipolar impurities or piezoelectric resonance.

PROCEDURE

The data set includes only single crystal dielectric constants of estimated precision < 1%; data from noncubic crystals is included only if the dielectric anisotropy was determined. Sources include Westphal and Sils (1972), Young and Frederickse (1973), Olhoeft (1981), Shannon et al. (1989, 1990a, 1990b, 1990c), Shannon and Subramanian (1989) and Subramanian et al. (1989). Many of the data found in the earlier compilations (Keller, 1966; Westphal and Sils, 1972; Young and Frederickse, 1973; and Olhoeft, 1981) were not useful because of poor accuracy, poor knowledge of chemical composition or cell dimensions, polycrystalline nature of the samples or lack of complete anisotropic data for noncubic materials. Where mineral dielectric constants were used, efforts were made to include only data on gem quality crystals with accurate cell dimensions and whose composition was not in question. A few dielectric constants obtained from infrared reflectance data were used; accuracies of ~ 1% were assumed (Gaskell and Johnson, 1974). Dielectric data from ionic conductors and ferroelectrics as well as data from polycrystalline samples were avoided.

If it is assumed that the total molar dielectric polarizability of a compound can be calculated (α_{calc}) as a simple linear combination of individual ionic polarizabilities, α(ion), then:

$$\alpha_{calc} = \sum_{I=1}^{N} n \cdot \alpha_D(ion) \qquad (5)$$

where, I varies over the total number (N) of types of ions (I) in the formula unit and n is the number of ions of type I in the formula unit, and α_D(ion), can be used as a set of refinable parameters in a least squares procedure which minimizes the function:

$$\sum_{i=1}^{M} w_i \, (\alpha_{obs} - \alpha_{calc})^2 \qquad (6)$$

Here i varies over the number of measurements of α_{obs} for a variety of compounds and $w_i = \sigma_i^{-2}$, where σ_i is the estimated % error in the experimental dielectric constant.

The standard deviation of a refined value of α_D(ion) is calculated as:

$$\sigma\left[\alpha_D(ion)\right] = M_I^{-1/2} \qquad (7)$$

where M_I is the diagonal element of the inverted normal matrix corresponding to the ionic polarizability for ion "I" varied in the least squares procedure.

In practice it is necessary to fix one polarizability as done for electronic polarizabilities by TKS ($\alpha_e(Li^+)$), Wilson and Curtis ($\alpha_e(Li^+)$), Coker ($\alpha_e(Li^+)$), and Boswarva ($\alpha_e(Mg^{2+})$), and for dielectric polarizabilities by Roberts ($\alpha_D(O^=)$). We have arbitrarily assumed the value for $\alpha_D(B^{3+}) = .05$ Å^3. This assumption results in a value for $\alpha_D(O^=) = 2.01$ Å^3, close to values obtained by assuming an $\alpha(O^=)/r^3$ law (Shanker et al., 1973) with either crystal radii ($\alpha_D(O^=) = 2.15$-2.87 Å^3; Shannon, 1976) or bonded radii ($\alpha_D(O^=) = 1.97$-2.55 Å^3; Gibbs and Boisen, 1986).

Empirical and theoretical studies of electronic polarizabilities show that cation electronic polarizabilities are

constant and anion polarizabilities vary approximately with lattice constant and anion molar volume (TKS, 1953; Kirsch et al., 1974; Coker, 1976; Mahan, 1980; Fowler and Madden, 1984a,b). In the refinements carried out here, a slight linear dependence of α_D on oxygen molar volume was found. However, because of the limited set of data used, this dependence was ignored in the set of ion polarizabilities reported in Table 1.

RESULTS

The results from refinements of α_D(ion) made using experimental polarizability data from 63 oxides and 4 fluorides are given in Table 1. The ratio of observables to variables is only 2.4; desirable values are of the order of 3-6. Most of the calculated uncertainties in refined ion polarizabilities are small, i.e., 0.001-.005 $\AA^3$. These uncertainties are unrealistically low; a more reasonable estimate of the uncertainty is probably ± 0.02 $\AA^3$ for the smaller ions such as Al^{3+} and Si^{4+} and ± 0.05 $\AA^3$ for larger ions such as Ca^{2+}, Y^{3+} and Zr^{4+}.

Table 1

Ion Dielectric Polarizabilities

Ion	α_D, $\AA^3$	σ
F-1	1.63	0.001
O-2	2.01	0.002
OH-1	2.18	0.005
Be+2	0.30	0.003
Mg+2	1.31	0.002
Fe+2	2.22	0.005
Mn+2	2.64	0.005
Ca+2	3.15	0.002
B+3	0.05	---
Al+3	0.79	0.003
Ga+3	1.49	0.003
Sc+3	2.81	0.004
Y+3	3.79	0.003
Gd+3	4.36	0.003
Si+4	0.85	0.004
Zr+4	3.27	0.013

Table 2 compares total molecular polarizabilities of a variety of borates, aluminates, gallates and silicates determined from the measured dielectric constants using the Clausius-Mosotti relation and from the oxide and ion additivity rules. In general both the

oxide and ion additivity rules are obeyed to ± 0.5%. The rules hold for simple oxides such as $BeAl_2O_4$ and Be_2SiO_4 as well as for more complex compositions such as $CaB_2Si_2O_8$ and $Y_3Sc_2Ga_3O_{12}$.

Table 2.

Comparison of Observed and Predicted Single Crystal Dielectric Polarizabilities

Compound	$\langle\kappa'\rangle$	Pred.[a] α_T	Pred.[b] α_T	exp[c] α_T	$\Delta\%^a$	$\Delta\%^b$
$Al_{.99}Fe_{.01}OOH$	8.44	---	4.99	5.02	---	+ 0.6
$Mg_{.98}Fe_{.02}AlBO_4$	8.075	10.24	10.21	10.18	- 0.6	- 0.3
$CaB_2Si_2O_8$	6.73	21.13	21.05	21.29	+ 0.8	+ 1.1
$BeAl_2O_4$	8.93	9.84	9.92	9.87	+ 0.3	- 0.5
Be_2BO_3OH	4.82	---	8.84	8.80	---	- 0.5
$BeAlSiO_4OH$	6.64	12.11	12.17	12.16	+ 0.4	- 0.1
$MgAl_2O_4$	8.18	10.96	10.94	11.10	+ 1.3	+ 1.4
$Y_3Al_5O_{12}$	10.60	39.79	39.48	39.38	- 1.0	- 0.2
$Y_3Sc_2Al_3O_{12}$:Nd	12.20	43.64	43.60	43.48	- 0.4	- 0.3
$Gd_3Sc_2Al_3O_{12}$	12.71	45.73	45.23	45.35	- 0.8	+ 0.3
$Gd_{3.03}Ga_{4.97}O_{12}$	12.18	44.83	44.78	44.66	- 0.4	- 0.3
$Y_3Sc_2Ga_3O_{12}$	12.94	45.30	45.63	45.42	+ 0.3	- 0.5
Be_2SiO_4	6.21	9.31	9.49	9.35	+ 0.5	- 1.5
Mg_2SiO_4	7.00	11.54	11.53	11.54	0.0	0.0
$Mg_{1.80}Fe_{.22}SiO_4$	7.27	11.78	11.76	11.80	+ 0.2	+ 0.3
Fe_2SiO_4	8.77	13.28	13.24	13.24	- 0.3	0.0
$ZrSiO_4$	11.5	12.16	12.17	12.12	- 0.3	- 0.4
				$\langle\Delta\rangle$ =	0.5%	0.5%

a. Oxide additivity rule
b. Ion additivity rule
c. Using the Clausius-Mosotti relationship; polarizabilities in $Å^3$

DISCUSSION

The set of dielectric polarizabilities found in Table 1 is significantly different from the sets of Roberts (1949) and Lasaga and Cygan (1982). The differences arise primarily because of the large difference in $\alpha_D(O^=)$: 2.01 $Å^3$ (our set) vs. 2.387 $Å^3$

(Roberts; Lasaga and Cygan). Their higher value occurred because they had no data from borates or beryllates; use of $\alpha_D(O^=) = 2.387$ $Å^3$ results in negative polarizabilities for B^{3+} and Be^{2+}. Our polarizabilities are more reliable because of more accurate dielectric constants from a larger number of compounds involving more ions. The problem of relative values of cation and anion polarizability still remains, but based on the α_D/r^3 relationship and the concept of bonded radii, the values obtained from the least squares procedure seem reasonable.

The Clausius-Mosotti equation shows explicitly how dielectric constant depends on composition and crystal structure through polarizability and molar volume. Low dielectric constants are clearly favored in compounds containing ions of low polarizability.

Figure 1

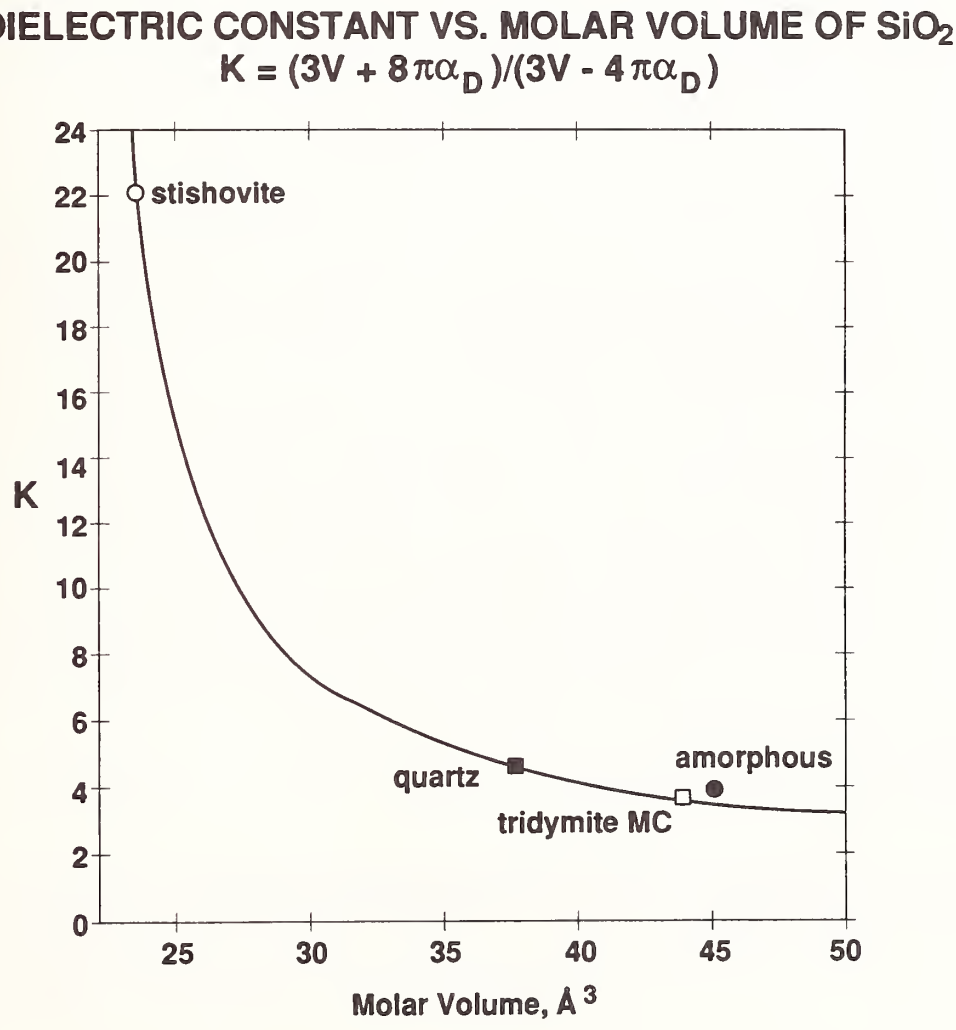

Crystal structure is generally important in determining κ only insofar as it determines molar volume. The effect of the molar volume term is shown for the SiO_2 polymorphs in Figure 1 where V_m is plotted vs. the calculated dielectric constant, κ(calc). There is a rapid decrease in κ(calc) as V_m increases. Thus, the more open the structure, the lower the value of the dielectric constant. The dielectric constant of stishovite, although not yet determined, would be predicted to be approximately 22. The more open tridymite and amorphous structures have lower κ than the more dense quartz polymorph.

The excellent agreement between observed and calculated total polarizabilities in Table 2 implies a good degree of predictability using the C-M equation for well-behaved compounds. Some of the poor agreement between calculated and predicted κ's in more complex structures indicated in Table 3 can be traced to factors which are known to increase κ: ionic and electronic conductivity, H_2O or CO_2

Table 3.

Deviations from the Additivity Rule

Type and Composition		<κ'>	Pred.[a] α_T	Exp.[b] α_T	Δ,%	Ref.
$LiGaO_2$	$LiGaO_2$	7.27	6.47	6.96	+7.0	1
fayalite	$Fe_{1.86}Mn_{.07}Mg_{.02}Al_{.01}Si_{1.01}O_4$	14.1	13.25	15.0	+11.8	2
cordierite	$Na_{.03}Mg_{1.97}Fe_{.03}Al_{3.97}Fe_{.03}Si_5O_{18}\cdot[(H_2O)_{.28}(CO_2)_{.08}]$	5.81	46.4[c]	55.8	+16.8	3
			57.0[d]	55.8	+2.1	
fluorite	CaF_2:Er (3%)	8.28	6.48	6.90	+6.1	4
akermanite	$Ca_2CoSi_2O_7$	11.29	23.88	28.58	+16.4	5
pyrope	$Mg_{1.95}Fe_{.99}Ca_{.09}Mn_{.01}Al_{1.98}Si_3O_{12}$	12.20	33.54	35.72	+6.1	6
almandine	$Fe_{1.45}Mg_{1.18}Ca_{.20}Mn_{.04}Al_{2.00}Si_3O_{12}$	11.96	33.65	35.99	+6.5	6
grossular	$Ca_{2.98}Mn_{.01}Al_{1.97}Fe_{.02}Si_{2.94}O_{12}$	8.53	37.59	35.67	-5.4	6

a. Oxide additivity rule
b. Using the Clausius-Mosotti relationship; polarizabilities in $Å^3$
c. Omitting contributions of H_2O and CO_2
d. Including contributions of H_2O and CO_2: $\alpha_D(H_2O) = \alpha_e + \alpha_i + p^2/3kT = 3.5 + 28.4 = 31.9$ $Å^3$/mole H_2O

1. Shannon et al., 1990a 2. Suwa, 1964 3. Shannon and Subramanian, unpublished 4. Fontanella and Andeen, 1976 5. Shannon et al. (1990d) 6. Shannon et al. (1990c).

in channels or large cavities. Thus, poor agreement in the case of $LiGaO_2$ is probably caused by Li mobility (Shannon et al., 1990a). Dielectric constants of Fe_2SiO_4 vary widely; deviations from a mean value of about 8.8 are associated with high losses and can be associated with the presence of Fe^{3+} and space charge polarization. Poor agreement between α_D(calc) and α_D(exp) in cordierite is caused by lack of consideration of the presence of H_2O and CO_2 in the channels (Shannon et al., 1989). The increased polarizability of CaF_2:Er is caused by the formation of Er^{3+}-F_i dipoles (Fontanella and Andeen, 1976). The unusually large deviation of the observed dielectric constant of Co akermanite from the calculated value is probably associated with piezoelectric resonance and possibly also the incommensurate structure and possible local displacements of the Ca ions from their mirror planes (Hemingway et al.,1986).

Positive deviations of pyrope and almandine and the negative deviation of grossular appear to be related to structural peculiarities of the garnet family. Similar deviations from additivity were found by Holland (1989) in a study of the thermodynamic quantities of silicate minerals, who found the entropy contributions of Mg^{2+} and Fe^{2+} in pyrope and Ca^{2+} in grossular to be larger and smaller, respectively, than expected for these cations in eight-coordination.

Garnet structural anomalies include: (1) an unusual amount of edge sharing and (2) octahedral edges shared with the dodecahedral edges which are longer than the unshared edges (Novak and Gibbs,1971). These constraints cause changes in what are normally invariant bond distances. For example, the mean Al-O distance, d<Al-O> is 1.886 Å in pyrope, but is 1.924 Å in grossular. The mean <Al-O> distance varies continuously in the series pyrope-almandine-spessartite-grossular (Novak and Gibbs, 1971) and is inversely proportional to the garnet polarizability deviations. The differences between shared and unshared O-O distances lead to bond strain as defined by Novak and Gibbs. The deviation from additivity of polarizability is approximately proportional to the bond strain. Thus, instead of anomalies only at the pyrope and grossular end members, the polarizability deviations are seen to be a gradual function of both d<Al-O> and bond strain. The polarizability additivity deviations seem, therefore, to be related to the rigidity of the garnet framework.

ACKNOWLEDGEMENTS

I wish to thank A. J. Owens and J. B. Parise for the least squares program, M. A. Subramanian, R. A. Oswald and R. W. Shiffer for sample preparation and dielectric constant measurements, J. T. Armstrong and G. R. Rossman for electron microprobe analyses, and C. Foris and A. Brown for cell dimensions.

REFERENCES

Bosman AJ, Havinga EE (1963) Phys. Rev. 129:1593-1600.
Boswarva, IM (1970) Phys. Rev. B1:1698-1701.
Cheng CK (1940) Phil. Mag. 30:505-515.
Chowdhry U, Sleight AW (1987) Ann. Rev. Mater. Sci. 17:323-340.
Claro FH (1978) Phys. Rev. B18:7058-7061.
Coker H (1976) J. Phys. Chem. 80:2078-2084.
Dunmur DA (1972) Molec. Phys. 23:109-115.
Fontanella J, Andeen C (1976) J. Phys. C. 9:1055-1064.
Fowler PW, Madden PA (1984) Phys. Rev. B29:1035-1042.
Fowler PW, Madden PA (1985) J. Phys.Chem. 89:2581-2585.
Gaskell PH, Johnson DW (1974) J. Noncryst. Solids 20:153-169.
Gibbs GV, Boisen MB (1986) Better Ceramics Through Chemistry II, Mat. Res. Soc., Pittsburgh 73:515-527.
Hemingway BS, Evans HT, Nord GL, Haselton HT, Robie RA, McGee JJ (1986) Can. Miner. 24:425-433.
Heydweiller A (1920) Z. Phys. 3:308-317.
Holland TJB (1989) Amer. Mineral. 74:5-13.
Jonker GH, Van Santen JH (1947) Chemisches Weekblad 43:672-679.
Kawakami K, Takabatake M, Minowa T, Chiba J, Sasaki M (1987) Adv. Ceram. 19:95-102.
Keller JV (1966) Handbook of Physical Constants, Eds. SP Clark Jr. Geological Soc. Amer. Memoir 97, Geological Soc. Amer. pp. 553-577.
Kirsch R, Gerard A, Wautelet M (1974) J. Phys. C: Solid State Phys. 7:3633-3644.
Kondo K, Okuyama M, Shibata Y (1987) Adv. Ceram. 19:77-87.
Lasaga AC, Cygan RT (1982) Am. Mineral. 67:328-334.
Lorentz L (1880) Ann. Phys. Chem. 11:70-103.
Lorenz HA (1880) Ann. Phys. Chem. 9:641-645.
Mahan GD (1980) Solid State Ionics 1:29-45.
Megaw HD (1975) Ferroelectricity in Crystals. Methuen, London. pp. 165-178.
Novak GA, Gibbs GV (1971) Amer. Mineral. 56:791-825.
Olhoeft GR (1981) Physical Properties of Rocks and Minerals.Y.S. Touloukian et al. Eds. McGraw-Hill, New York. pp.257-329.
Pirenne J, Kartheuser E (1964) Physica 30:2005-2018.
Roberts R (1949) Phys. Rev. 76:1215-1220.
Roberts R (1950) Phys. Rev. 77:258-263.
Roberts R (1951) Phys. Rev. 81:865-868.
Shanker J, Kumar N, Verma MP (1973) Ind. J. Pure Appl. Phys. 11:644-647.
Shannon RD (1976) Acta. Cryst. A32:751-767.
Shannon RD, Subramanian MA (1989) Phys. Chem. Minerals 16:747-751.
Shannon RD, Subramanian MA, Mariano AM, Rossman GR (1989) Proc. Mater. Res. Soc. Symposium on Materials for Magneto-Optic Data Storage, San Diego, April 24-27.

Shannon RD, Subramanian MA, Allik TH, Kimura H, Kokta MR, Randles MH, Rossman GR (1990a) J. Appl. Phys. 67:3798-3802.
Shannon RD, Subramanian MA, Hosoya S, Rossman GR (1990b),to be published.
Shannon RD, Subramanian MA, Rossman GR (1990c), to be published.
Shannon RD, Subramanian MA, Iishi K, Rossman GR (1990d), to be published.
Subramanian MA, Shannon RD (1989) Mater. Res. Bull. 24:1477-1483.
Subramanian MA, Shannon RD, Chai BHT, Abraham MM, Wintersgill MC (1989) Phys. Chem. Minerals 16:741-746.
Suwa K (1964) J. Earth Sci. Nagoya Univ. 12:129-134.
Szigeti B (1949) Trans. Farad. Soc. 45:155-166.
Tessman JR, Kahn AH, Shockley W (1953) Phys. Rev. 92:890-895.
Tummala RR (1988) Ceram. Bull. 67:752-758.
Westphal WB, Sils A (1972) Dielectric constant and loss data. US National Technical Information Service AFML-TR-72-39.
Wilson JN, Curtis RM (1970) J. Phys. Chem. 74:187-196.
Young KF, Frederickse HP (1973) J. Phys.Chem.Ref.Data 2:313-409.

B. Wuensch: Bob, based on a hazy recollection of what lies behind the Clausius-Mosotti equation, I believe that it hinged on an assumption by Lorentz of polarization of point dipoles. Your oxide additivity relations nicely finesses the variation of individual ion polarizabilities from structure to structure. Yet, in other calculations such as the Mott-Littleton-type calculations of defect formation energies (Yamashita and Kurosawa, J. Phys. Soc. Japan 89,944,1954) problems were encountered with ionic polarizabilities when attempting to extend the calculations from simple ionic compounds such as the alkali halides to oxides. Is there any correlation between the extent to which the original Lorentz assumption is followed and your deviations from additivity?

R. Shannon: The Yashita-Kurosawa calculations showed that it was necessary to introduce variable oxygen polarizability in order to obtain meaningful results in calculations of defect formation energies in MgO, CaO and SrO. Variable oxygen polarizability was found by Tessman, Kahn and Shockley (Phys. Rev. 92,890,1953) and also by others (Mahan, Solid State Ionics, 1,29,1980; Fowler and Madden, J. Phys. Chem. 89,2581,1985) in studies of electronic ion polarizabilities. However, my studies of dielectric polarizabilities show little or no dependence of oxygen polarizability on oxygen molar volume. At the present time I do not see a clear correlation between the additivity relationship deviations and oxygen molar volume.

M. O'Keeffe: In pyrope the bond valence sum at Mg is much less than two and in grossular the bond valence sum is much greater than two. Such deviations from ideal values may serve as warnings that the additivity relations will not hold.

R. Shannon: I agree. The unusual bond valence sums around the X ions in silicate garnets are a result of structural constraints imposed by the unusual extent of edge-sharing. This results in bond distances and bond valences that give rise to unusual polarizabilities that may be characteristic of "rattling" Mg ions and "compressed" Ca ions.

M. O'Keeffe: (1) Dielectric constants depend strongly on frequency and temperature. Did you carry out your experiments at a standard temperature and frequency? (2) The electronic part of the dielectric constant depends on collective properties, i.e., charge. Perhaps an electronegativity correction might be useful.

R. Shannon: The experiments were carried out at room temperature and over a frequency range of 30 KHz to 3 MHz but the results are reported at 1 MHz. Over that frequency range there is generally less than 0.2% deviation for the samples that I have looked at so far.

D. Cahen: Did you also note only a 0.2% variation in the dielectric constant of $LiGaO_2$ over the frequency range 30 KHz to 3 MHz? If your explanation for the additivity deviation in $LiGaO_2$ is correct, ionic migration will be expressed in a variation of K with frequency.

R. Shannon: The dielectric constants reported for $LiGaO_2$ were obtained at BTL and were not reported at different frequencies. However, Grant et al. (J. Am. Ceram. Soc. 60,226,1977) showed a variation in K with frequency at 482°C.

R. Newnham: In going from the total polarizabilities for the simple oxides such as SiO_2 and CaO to the polarizabilities for individual ions, do we have the same problem here that we have with ionic radii, where we must arbitrarily fix the radius of one ion? If so, do these individual polarizabilities mean that much?

R. Shannon: We have all the same problems with ion polarizabilities that we have with ionic radii. Although it is necessary to make some arbitrary choices, there are limits. For example, it is not possible to choose the polarizabilitiy of oxygen to be 2.4 A^3 because that results in negative polarizabilities for B^{3+} or Be^{2+}. I have picked an arbitrary value for the dielectric polarizability of B^{3+} (.005 A^3) that seems reasonable when you look at calculated values for electronic polarizabilities. I don't know if that's a good assumption but at the present time it is the best I can do.

R. Newnham: So there might be something like a 10% limit for the polarizabilities or is it higher than that?

R. Shannon: It could be larger than 10%.

National Institute of Standards and Technology Special Publication 804, Chemistry of Electronic Ceramic Materials, Proceedings of the International Conference held in Jackson, WY, August 17-22, 1990, issued January 1991.

INTERNAL STRAIN IN PEROVSKITE RELATED MATERIALS

I.D.Brown
Institute for Materials Research, McMaster University,
Hamilton, Ontario, Canada L8S 4M1

1. INTRODUCTION

Many simple inorganic structures can be built from AO and BO_2 layers (Figure 1), where A and B are cations (metals) and O is an anion which in this paper is assumed to be oxygen. Five additional types of layers may be created by removing either oxygen atoms (to give the layers A, B and BO) or cations (to give the layers O and O_2).

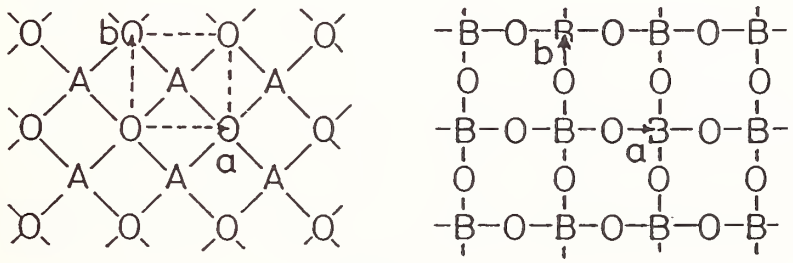

Figure 1

By stacking the layers together in different sequences, a large variety of different structures can be generated. Rocksalt has the sequence (AO.AO.AO), fluorite the sequence ($A.O_2.A.O_2$) and perovskite the sequence ($BO_2.AO.BO_2.AO$). The number of different sequences that are found in nature is limited by crystal chemical constraints. The sequence must be electrically neutral for the given composition and the cations must be in sites with appropriate coordination environments. The layers must also have the same in-plane spacing which, given that no two cations have exactly the same size, means that the bonds in some layers will be stretched while those in others will be compressed. A variety of mechanisms is available for relaxing these strains depending on the size and nature of the cations present, and it is this variety that leads to the rich crystal chemistry that these systems display. In some cases the strain is not completely relaxed and the resulting residual strain itself may have important effects on the properties.

The three most important crystal chemical constraints are discussed in the next section which is followed by a detailed description of the relaxation mechanisms. Four examples are then considered and the paper concludes with speculations on the relation between the strain and the superconducting transition temperature.

2 THE CRYSTAL CHEMICAL CONSTRAINTS

1. The sequence must provide a site whose coordination number is close to the Average Observed Coordination Number (AOCN) of the cation.

The average observed coordination numbers (AOCN) for many cations surrounded by oxygen have been determined by examining all the compounds stored in the Inorganic Crystal Structure Database[1]. In the majority its of compounds, a cation is found with a coordination number that lies within 1, or possibly 2, of its average, i.e. its AOCN.

Cation environments with almost any desired coordination number can be created in structures composed of AO and BO_2 layers by selecting a suitable sequence. Examples of coordination numbers and the sequences that give rise to them are:

2	AO.B.AO	
4	AO.BO.AO	$A.BO_2.A$
5	$AO.BO_2.A$	AO.AO.B
6	$AO.BO_2.AO$	AO.AO.AO
7	AO.AO.BO	
8	$BO_2.A.BO_2$	$BO_2.A.O_2$
9	$AO.AO.BO_2$	
10	$BO_2.AO.BO$	
12	$BO_2.AO.BO_2$	

In each case the coordination number refers to the cation in the center of the triplet.

2. The compound must be charge neutral.

This is an absolute constraint for the whole compound but local charge neutrality is also expected. For example, $BaBiO_3$ is composed of alternating BaO and BiO_2 layers, each of which is charge neutral, but $Cu^{++}O_2$ carries a double negative charge, and is expected to be surrounded by positively charged layers. A perovskite sequence ($CuO_2.AO.CuO_2.AO$) cannot occur since no quadrivalent A cations have a coordination number of 12. The sequence ($CuO_2.A.CuO_2.A$) requires only a divalent ion with a coordination number of 8. Ca (AOCN = 7.3) is a good candidate and is the cation most often found in this sequence.

3. Each layer in the sequence must have the same in-plane lattice spacing.

If the layers are to stack to form a commensurate crystal, they must all have exactly the same in-plane lattice spacings (a and b). Since each cation has its own distinctive size, commensurability can only be achieved by compressing some and stretching other bonds. The fascinating and extensive crystal chemistry shown by these compounds largely results from the different ways in which these strains are (or are not) relaxed. The different relaxation mechanisms are discussed in more detail in the next section.

3. FITTING THE LAYERS TO A PROCRUSTEAN BED

Bond valences[2] provide a quantitative method of analyzing the bonding requirements of different cations. They also provide a convenient tool for modelling the relaxations. The crystal is treated as a network of bonds that link nodes (atoms). The important properties of this network are the valences (oxidation states) of the atoms and the valences associated with the bonds. These are related by two Kirchhoff-like network equations:

1. The sum of bond valences at each node equals the atomic valence of the node

2. The sum of bond valences around any loop is zero.

Bond valences are found empirically to be inversely related to bond length[3]. By solving the Kirchhoff equations for a given bond network, bond valences can be predicted and from these the expected bond lengths can be calculated. Even if the bonding network is not known, it is possible to predict the average length of the bonds formed by a cation by recognising, from rule 1, that the average bond valence is equal to (atomic valence)/(coordination number). Average bond lengths calculated in this manner have been used to determine the ideal in-plane lattice spacings for various cations in the coordinations close to their average observed coordination number (Fig. 2).

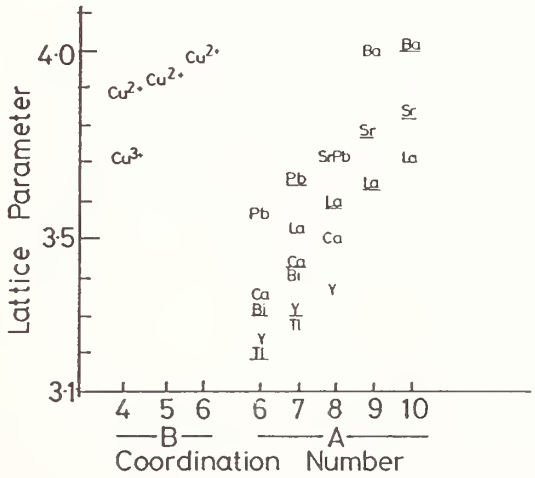

Figure 2. Lattice parameters expected for various AO and BO_2 layers with A and B cations in coordinations close to their AOCN (underlined).

BaO and SrO layers match the CuO_2 layers in size, but most cations have ideal in-plane spacings that are considerably smaller than those of the CuO_2 layers. A variety of mechanisms is available for compressing or, more usually, stretching a layer to provide a match.

1. Buckling. Buckling a layer results in non-planar bonding and brings the B (or A) atoms closer together. The effect is not large, a 0.3Å displacement of the O atoms perpendicular to the layer reduces a by only 0.05Å. This is generally not an effective way of reducing the in-plane spacing of a layer because buckling is usually controlled by stronger constraints on the inter-layer bonding.

2. Changing the inter-layer spacing. Any coordination environment can be expanded within a layer by compressing it perpendicular to the layer (and vice versa). There are two ways in which the bonding environment of a cation can be compressed to increase the in-plane lattice spacing:

i) For octahedrally coordinated A cations shortening the bonds between layers results in lengthening the bonds within the layers. The effectiveness of this mechanism is shown in Fig. 3 (top) for A = Tl^{+++} in octahedral coordination. The broken line indicates regular coordination. To match the spacing of the CuO_2 layer (3.85Å), the inter-layer spacing would have to be reduced by 0.3Å leaving Tl with a coordination that most chemists would describe as linear.

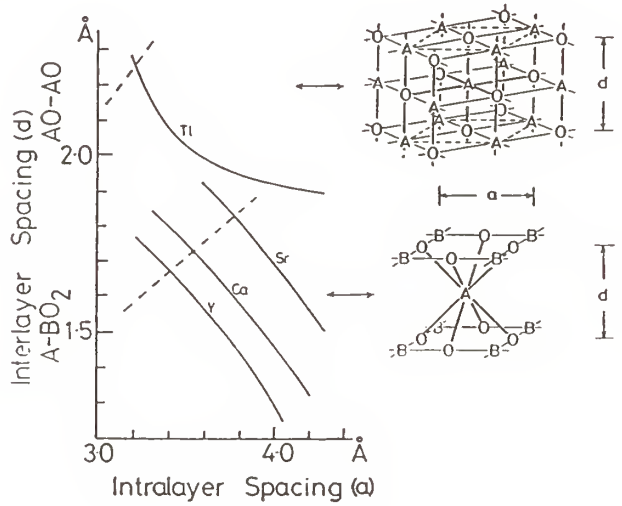

Figure 3

ii) For 8-coordinate A cations, changing the bond angles at the cation can change the ratio of in-plane (a) to inter-layer spacing (d) without changing the bond lengths. The effect, which depends only on geometry, is shown in Fig. 3 (bottom) for A = Y, Ca and Sr.

Changing the inter-layer spacing is effective in changing the in-plane spacing when only one kind of bond bridges the layers, as found, for example, between two TlO layers or around a Ca layer that contains no anions. When two different kinds of bond bridge the layers, they are usually in competition, one bond attempting to decrease, the other increase, the inter-layer spacing (see, for example, Fig. 6).

3. Moving the cation off the center of its coordination sphere. As shown elsewhere[4], if the bonds formed by a cation are changed from their average value by making some longer and some shorter, the average bond length increases. If a cation is moved within its layer away from the center of its coordination sphere, the ligand atoms will move further apart. Rule 1 can be used to calculate how the bond valences, and hence the bond lengths, vary as the environment is distorted. Its effectiveness is shown by

the broken line in Fig. 4, which shows the changes in the bond lengths and lattice spacing produced by a trigonal distortion of octahedrally coordinated Bi^{+++}. The increase in lattice spacing is negligible for small distortions but is significant for the kinds of distortions typically shown by cations with stereoactive lone pairs of electrons in their valence shells (e.g. Tl^{+}, Pb^{++} and Bi^{+++}).

4. Charge transfer between cations. Increasing the charge on a cation shortens the bonds that it forms. Since charge is conserved, increasing the charge on one cation means decreasing the charge, hence lengthening the bonds, of another cation in the structure. This is modelled in Fig. 5 which shows the effects of moving positive charge from Tl^{+++} to Cu^{++}. The effect is large but this mechanism is restricted to compounds that have two different cations both capable of changing oxidation states.

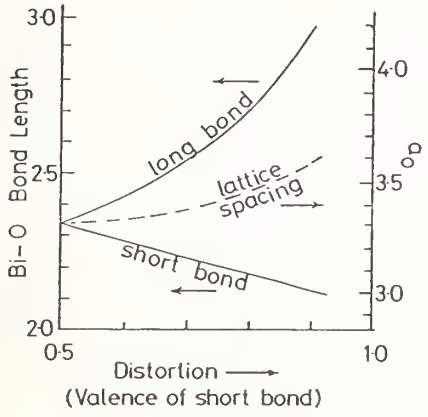

Figure 4

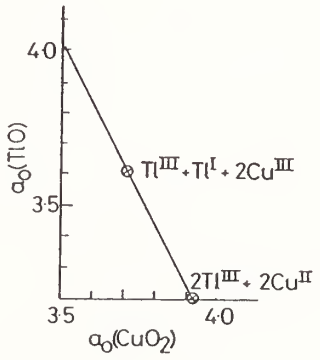

Figure 5

5. Addition of interstitial oxygen atoms. Adding one oxygen atom to every fifth or sixth unit cell in the layer will lead to a superstructure with a larger average spacing between the cations. The negative charge of the additional oxygen must be balanced by additional positive charge at the cation sites.

4. CONSTRUCTING THE LAYER SEQUENCE

Local charge neutrality will favour certain sequences. Neutral layers (e.g. $A^{++}O$) can be stacked in any order but, in the copper oxides with which this paper is chiefly concerned, the BO_2 layers usually contain copper and therefore carry a charge of -2, more or less, depending on the Cu oxidation state. This requires the presence nearby of positively charged layers such as $A^{+++}O$, A^{+++} or A^{++}. Among the sequences that provide charge neutrality are $(CuO_2.A^{++}.CuO_2.A^{++})$ and $(A^{+++}O.CuO_2.A^{+++}O)$, both of which are commonly found. The coordination number of Cu is 4 in the first sequence and 6 in the second, both acceptable coordination numbers for copper. The coordination number of A is 8 in first sequence (Ca and Sr are candidate cations, see Fig. 2) and 9 or 10 in the second, the obvious candidate for this site being La (AOCN = 8.5).

Sequences of AO layers give rise to a rocksalt structure and can be referred to

as 'An' sequences where n is the number of layers in the sequence. The alternating CuO_2.A.CuO_2.A.CuO_2 sequences are perovskite-like and can be referred to as 'Bm' sequences where the total number of CuO_2 layers in the sequence is m and the number of A layers sandwiched between the CuO_2 layers is (m-1). A third type of sequence (A.O_2.A) can be derived from an A2 sequence by rearranging the O atoms. It has the fluorite structure and can be labelled 'Fn', where n is the number of A layers in the sequence. To maintain the fluorite structure, an F sequence will always be bounded by BO_2 layers. Most copper oxide layer compounds are composed of combinations of A, B and F sequences and can be labelled 'An-Bm' etc. Any such sequence must be electrically neutral and must contain coordination environments appropriate to the cations present. Some examples of observed sequences are:

A2-B1	AO.AO.BO_2	La_2CuO_4
A2-B2-F2-B2	AO.AO.BO_2.A.O_2.A.BO_2	$NdSrCuO_4$
$A3^1$-B2	AO.BO.AO.BO_2.A.BO_2	$Ba_2YCu_3O_7$
A3-B3	AO.AO.AO.BO_2.A.BO_2.A.BO_2	$TlBa_2CaCu_3O_9$
A4-B2	AO.AO.AO.AO.BO_2.A.BO_2	$Tl_2Sr_2Ca_2Cu_2O_8$

The superscript in the third example indicates that one layer in the AO sequence has been replaced by a BO layer. The A cations in the B sequences are 8 coordinate (from Fig. 2, Ca^{++}, Sr^{++}, Pb^{++}, La^{+++} and Y^{+++} are candidates). The A cations at the ends of the A sequence are 9-coordinate (La^{+++}, Sr^{++} and Ba^{++} are candidates). Those in the middle of the A sequence are 6-coordinate (Tl^{+++}, Bi^{+++}, Y^{+++}, Pb^{++} and Ca^{++} are candidates). The 6-coordinate layers, which contain the smallest cations, will be the most strained by the requirements of commensurability, and any cations (e.g. Ca and Y) that can occupy sites with higher coordination numbers will tend to do so.

5. A SIMPLE MODEL OF THE RELAXATION: THE A4-B2 STRUCTURES

All the layers are subject to some strain as a result of the different cation sizes, but the strain is seen most dramatically around Bi and Tl. Although both cations have oxidation states of +3, Bi contains a lone pair of electrons in its valence shell and so responds to the strain differently from Tl. Fig. 2 shows that the TlO layer has to expand by 0.64Å to match the lattice parameter of the CuO_2 layer. In $Tl_2Ba_2CaCu_2O_8$[5] the largest relaxation observed is a reduction of the TlO-TlO inter-layer spacing from 2.25Å to 2.00Å resulting in an expansion of the in-plane spacing by 0.40Å (Fig. 3). Transfer of about 0.20 electrons from Cu to Tl results in a further accommodation of 0.10A (Fig. 5). The remaining relaxation is achieved by the Tl atom going off center in its coordination sphere in a way not yet fully understood, an effect that is both assisted and complicated by the presence of Tl^+ produced by the charge transfer.

The macroscopic effects of the strain relaxation are thick, chunky crystals resulting from the strong interplanar bonding, and superconductivity resulting from the holes on the CuO_2 layers. In the observed structure the bond valence sum around Ba is larger than expected (2.2 valence units (v.u.) instead of 2.0) and that around Cu is smaller, suggesting that there is a residual strain in which the Ba is in compression and the Cu in tension.

The change required in the lattice spacing of the nominally isostructural $Bi_2Sr_2CaCu_2O_{8.2}$ is smaller, totalling only 0.50Å (Fig. 2). The lone pair distortion of the Bi environment relaxes about 0.2Å of this (Fig. 4) and the rest is relaxed by the incorporation of about one extra O atom in every tenth unit cell. The additional oxygen raises the oxidation state of Cu to +2.2 and hence leads to superconductivity, but, in contrast to the Tl compound, the lone pair environment of Bi leads to very weak bonding between the BiO layers making the crystals thin and flaky.

These two examples show that even in nominally isostructural compounds the strain can be relaxed in different ways, leading, in general, to different physical properties. The similarity in the superconducting properties is deceptive; quite different mechanisms are responsible for its occurrence.

6. A MORE SOPHISTICATED APPROACH TO RELAXATION: THE KIRCHHOFF EQUATIONS.

The above analysis is rather crude, being based on a model in which all the bonds around a cation are initially assumed to be equal. This will not, in general, be the case even in a completely unconstrained crystal because the bonding around the anions will be different. A better set of starting bond lengths can be determined using the Kirchhoff rules given in Section 3 above. This approach will be illustrated with two examples.

6.1 THE A2-B1 STRUCTURE: $La_{1.85}Sr_{0.15}CuO_4$

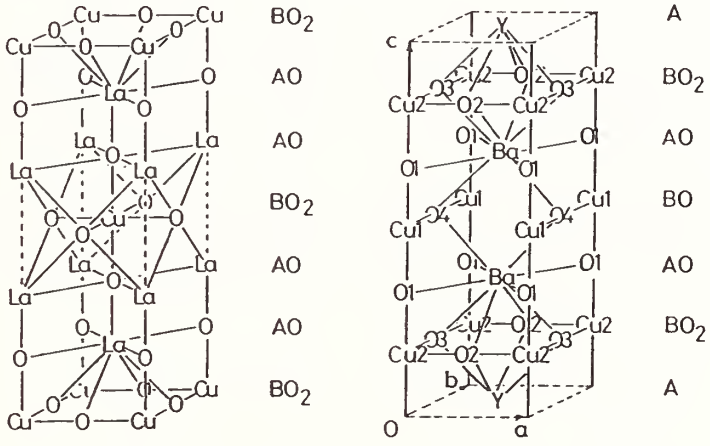

Figure 6

La_2CuO_4 (Fig. 6a) is a stoichiometric compound in which the copper is divalent. The bond valence sums (c.f. Table I Col. C) indicate that it is highly strained with the lanthanum in tension and the copper in compression. The trivalent lanthanum can be substituted by the larger divalent strontium atom, simultaneously increasing the oxidation state of Cu, both of which effects help to relieve the strain. The Kirchhoff equations are used to predict the bond lengths and bond valence sums shown in Col. A of Table I for the doped sample.

The strain is relieved in part by bringing the two LaO layers closer together. The consequences of shortening the inter-layer La-O bond to the observed length and

adjusting the in-plane La-O2 bonds to give the correct valence sum around La are shown in Col. B. The in-plane La-O2 bond is lengthened, but only by about a third of the required amount. The observed bond lengths[8] are shown in Col. C and the residual strain in Col. D. It is seen that considerable strain remains; the in-plane La-O2 bonds are stretched by 0.14Å and the Cu-O1 bonds compressed by 0.08Å.

Table I

		A	B	C	D	
Bond Lengths						
La/Sr-O2		2.53Å	2.37Å	2.37Å	0.00Å	
La/Sr-O1	(x4)	2.65	2.65	2.64	0.01	compression
La/Sr-O2	(x4)	2.53	2.59	2.73	0.14	tension
Cu-O1	(x4)	1.97	1.97	1.89	0.08	compression
Cu-O2	(x2)	2.40	2.40	2.40		(assumed)
Valence Sums						
La		2.92	2.92	2.58	-0.34	
Cu		2.15	2.15	2.62	+0.47	
O1		2.00	2.00	2.28	+0.28	
O2		2.00	1.85	1.61	-0.39	(Col C - Col A)

Table I. Bond lengths and valence sums in $La_{2\cdot85}Sr_{0\cdot15}CuO_4$.
Col A: Predictions of Kirchhoff equations (the long Cu-O2 bond is fixed at the observed value to simulate the Jahn-Teller distortion. Col B: After relaxation of the short La-O2 bond. Col C: Observed[8]. Col D: Residual strain (Col C - Col B).

6.2 THE A3[1]-B2 STRUCTURE, $Ba_2YCu_3O_x$ (x = 6-7)

Modelling this structure (Fig. 6b) is more complex than modelling La_2CuO_4 because, in order to use the Kirchhoff rules, one needs to make some assumptions about the distribution of charge between the two Cu atoms[9].

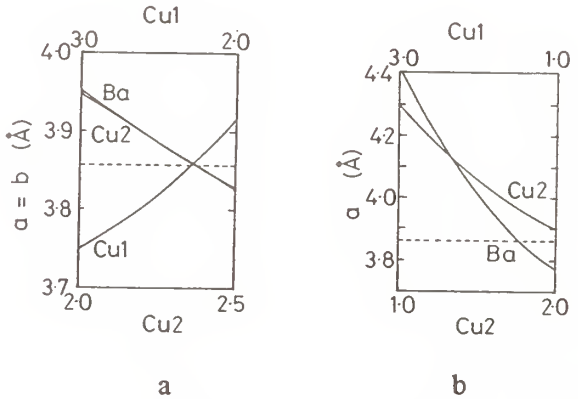

Figure 7. Modelled in-plane lattice spacings for the different layers of $Ba_2YCu_3O_x$ assuming different distributions of the charge. a) for x = 7

and b) for x = 6. The observed spacing is indicated by the broken line.

Fig. 7a shows the in-plane lattice spacings predicted for the BaO, CuO (Cu1) and CuO_2 (Cu2) layers for various distributions of charge between Cu1 and Cu2. A distribution with a charge of +2.33 on all copper atoms leads to complete commensurability between all three layers and this is the structure observed. However, a similar modelling of $Ba_2YCu_3O_6$ (Fig. 7b) gives a different result. The charge transfer required to achieve commensurate layers would leave the 2-coordinate Cu1 with a charge of +2.3 and the 5-coordinate Cu2 with a charge of +1.35, both of which are incompatible with the coordination environment. In this case the observed oxidation states remain close to those expected from the coordination numbers (+1 for Cu1 and +2 for Cu2). As a result the bonds are strained. This is shown by the average bond valence sum around copper being 0.2 v.u. too large (Cu-O in compression), and that around Ba being 0.2 v.u. too small (Ba-O in tension). In this case there is no effective relaxation mechanism and a residual strain remains[9].

Between these two extreme compositions, one can predict the charge distribution by noting that, as each oxygen atom is added to the Cu1 layer, it forms Cu-O bonds that contribute only about +1 v.u. to the oxidation state of Cu1 while adding -2 to the charge of the crystal. The additional positive charge is supplied by Cu2. The predicted oxidation states of the two copper atoms (the lines) are compared with those observed (crosses[10] and open figures[11]) in Fig. 8.

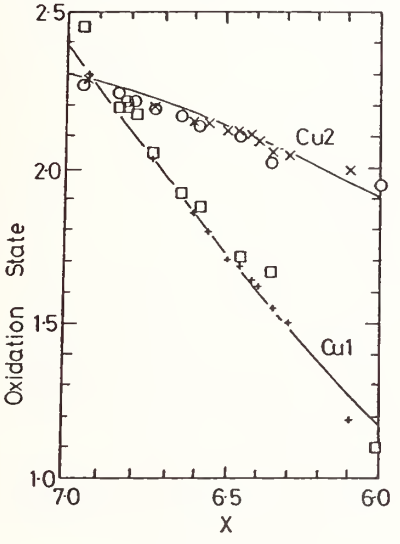

Figure 8

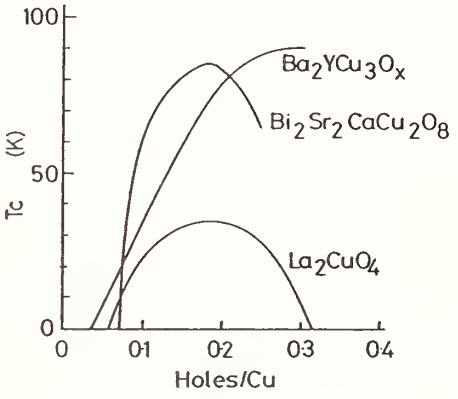

Figure 9

7. CONCLUSION

La_2CuO_4 becomes superconducting when holes are introduced into the CuO_2 layer by doping the crystal with Sr, but in some structures the size of the cations, and hence the natural incommensurability of the different layers, results in relaxations that also introduce electron holes into the copper planes. Since the presence of holes is a sine qua non for superconductivity there is a natural relationship between the expectation of strain in the bonds and the presence of superconductivity.

Studies of several systems[9,12,13,14] have shown that Tc reaches a maximum at a hole concentration of about 0.2 to 0.3 holes/Cu, falling off as the hole concentration is either decreased or increased from this value (see Fig. 9). Recently de Leeuw et al.[15] have shown that the maximum value of Tc (Tc(max)) in these systems is higher for those compounds in which the bond valence sums around the Cu atom are smaller than expected and lower for those compounds in which the valence sums are larger. The structures of many of these crystals are not accurately known and the calculation of the valence sums by de Leeuw et al. was fairly crude, but, since the valence sums should all be close to 2.2 - 2.3, the differences which they calculate (ranging from 2.06 to 2.53) suggest that Tc(max) is determined by the presence of residual internal strain[16]. If the CuO_2 layers are in tension (valence sums around Cu low) Tc(max) will be above 90K; if they are in compression (valence sums at Cu high) Tc(max) will be lower. As discussed above, $Ba_2YCu_3O_7$, which has Tc(max) = 90K, has its strain fully relaxed. On the other hand $Tl_2Ba_2CaCu_2O_8$, with Tc(max) = 125K, has residual strain in which the CuO_2 layers are in tension. The valence sum around Cu in $La_{1.85}Sr_{0.15}CuO_4$ is 2.62 (Table I), a surprisingly high value that is indicative of considerable compression. Tc(max) for this structure is only 35K.

7. ACKNOWLEDGEMENTS

I would like to thank the Natural Science and Engineering Research Council of Canada for a research operating grant.

8. REFERENCES

1. I.D.Brown Acta Cryst. B44 (1988) 545-553.

2. I.D.Brown, Phys. Chem. Miner. 15 (1987) 30-34.

3. I.D.Brown and D.Altermatt Acta Cryst. B41 (1985) 244-247.

4. I.D.Brown and R.D.Shannon, Acta Cryst. A29 (1972) 266-282.

5. A.W.Hewat, E.A.Hewat, J.Brynestad, H.S.Mook and E.D.Specht, Physica C 152 (1988) 438-444.

6. J.M.Tarascon, Y.LePage, P.Barboux, B.G.Bagley. L.H.Greene, W.R.McKinnon, G.W.Hull, M.Giroud and D.M.Hwang, Phys. Rev. B37 (1988) 9382-9389.

7. Y.LePage, W.R.McKinnon, J-M.Tarascon and P.Barboux, Phys.Rev. B40 (1990) 6810-6816.

8. S.Pei, J.D.Jorgensen, D.G.Hinks, B.Dabrowski, P.Lightfoot and D.R.Richards, Physica C (1990) submitted.

9. I.D.Brown J. Solid State Chem. (1990) submitted

10. J.D.Jorgensen, B.W.Veal, A.P.Paulikas, L.J.Nowicki, G.W.Crabtree, H.Claus and W.K.Kwok, Phys. Rev. B41 (1990) 1863-1877.

11. R.J.Cava, A.W.Hewat, E.A.Hewat, B.Batlogg, M.Marezio, K.M.Rabe, J.J.Krajewski, W.F.Peck Jr. and L.W.Rupp Jr. Physica C 165 (1990) 419-433.

12. J.B.Torrance, Y.Tojura, A.I.Nazzal. A.Bezinga, T.C.Huang and S.S.P.Parkin, Phys. Rev. Letts 61 (1988) 1127-1130.

13. Y.Tokura, J.B.Torrance,T.C.Huang and A.I.Nazzal, Phys. Rev. B38 (1988) 7156-7159.

14. W.A.Groen, D.M.de Leeuw and L.F.Feiner, Physica C 165 (1990) 55-61.

15. D.M.de Leeuw, W.A.Groen, L.F.Feiner and E.E.Havinga Physica C 166 (1990) 133-139.

16. I.D.Brown, Physica C (1990) in press.

R. Cava: There are two experimental observations that we made in oxygen deficient 123. These involved discontinuities in two things that are independent of the model. One of these things is the bond length between the copper in the plane and the apical oxygen, and the other thing is the variation of T_c as a function of oxygen content, both of which show discontinuities at places where T_c changes, either an abrupt change where it goes away or a gradual change where it goes from 90 K to 60 K. And I know you're aware of that. The picture you showed for your corrected values of copper valence implies a continuous variation of bond valence sum at the Cu(II) site as a function of x. You must have some explanation as to why the properties are discontinuous when you have an apparently continuous change in valence.

I. D. Brown: There are three circles in Fig. 8 that are critical and which don't lie on that line, the points for $6.0 < x < 6.5$. And the reason is that you were studying a rather ordered sample. What happens is that there is a phase at $x = 6.5$ in which the oxygen atoms are ordered. And because your sample is particularly ordered it means that you create this ordered phase. And that ordered phase will have a higher T_c (60K). This phase comes in, in your case, a little earlier and stays around a little longer as x is varied. In the Jorgenson study the samples were prepared a different way, and are more disordered. And, in fact, I have modeled the T_cs based on the idea that the presence of the ordered phase is responsible for the discontinuity.

P. Lightfoot: In support of this picture, if you look at our samples which have been prepared without allowing the lattice to relax at room temperature, we do not see evidence for a discontinuity until we heat the samples back to two to three hundred degrees, so probably your model is closer to such an unrelaxed state.

I. D. Brown: That's right. The model is completely unrelaxed, it represents a completely disordered state.

M. O'Keeffe: Your prediction for the change of T_c with stress or strain can be mirrored by the effect of the pressure on the T_c; is that, in fact, true?

I. D. Brown: Yes, we looked at that, but the problem is that you're working in one system. That other graph that I showed (not reproduced in the printed text) represents only the maxima in Fig. 9 plotted against the bond valence sum at Cu. If you take any one sample and you subject it to pressure (for instance, if you subject $Ba_2YCu_3O_x$ to pressure) you change the charge distribution. The distortion theorem predicts that what will happen when you compress the 123 compound is that the oxygen that bridges the planes and the chains, which is asymmetric to begin with, will actually become more symmetric. The effect of that is to transfer holes into the planes and therefore to move you to the right in Fig. 9. And if you make a sample in the left hand part of the curve then you get quite a large change in T_c. If you make a sample near the top of the curve the change in T_c with pressure is very small because you're on the top of the curve.

A. Navrotsky: Going back to your theorem that if the bond lengths deviate from the average, the average will then deviate positively to a longer bond length, that seems to me to fundamentally mirror the nature of the interatomic potential and its anharmonicity; that, in fact, it's easier to stretch than to compress. Is there any way of getting quantitative data on the nature of that potential from looking systematically at bond length variations?

I. D. Brown: If you look at the expression relating bond valence and bond length you can see that the bond valence is very like a Born repulsion potential. So basically, in a sense, what we're looking at here is the repulsive term as we bring two atoms up to each other. If we put more electrons into the bond we compress it. We press the two atoms closer together and the distance is determined really by the repulsion between the atoms. So there is some relationship here. Bob Shannon and I, in the first paper in this series (Acta Cryst. A29, 266 (1973)), showed that there was a relationship between that exponent and the Born exponent from pressure measurements.

B. Dabrowski: Relating to dependence of T_c and the amount of ordering, there are several papers which showed the same behavior. In a recent paper, Jim Jorgenson and coworkers (Physica C 167, 571 (1990)) showed room temperature relaxation after disorder, changing T_c. For this composition it takes a period of 20 to 30 days, and it involved local ordering of oxygen around copper in the chain. There is agreement between copper band-valence differences when the data was taken after the samples relaxed.

The other problem is oxygen content, x. One of the Xs in Fig. 8 suggests there is some impurity. Low oxygen content samples may therefore shift in the graph and make it much steeper.

B. Cava: It is well established that there is a distinct difference between samples that are prepared by quenching from a high temperature and samples that are annealed over long periods of time at low temperature. We're not the only people that now see this very sharp disappearance of superconductivity. There's data from Switzerland, as well, that shows extremely sharp changes of T_c vs x when the samples are annealed for a very long time. It all has to do with the perfection of the ordering.

I. D. Brown: I think that's right. So the graphs I've shown of T_c vs x (not given in text, see Fig. 8 in I. D. Brown, J. Solid State Chem. in press) are what one would expect just for a completely disordered structure. What you're saying is, when you allow these things to relax they order and this discontinuity begins to appear. Is that right?

B. Dabrowski: Right. I do observe this taking place, also. At room temperature it takes about 30 days. It may take two months.

I. D. Brown: Yes, it takes longer.

National Institute of Standards and Technology Special Publication 804, Chemistry of Electronic Ceramic Materials, Proceedings of the International Conference held in Jackson, WY, August 17-22, 1990, issued January 1991.

EMPIRICAL METHODS IN OXIDE CRYSTAL CHEMISTRY

Michael O'Keeffe
Chemistry Department, Arizona State University,
Tempe, AZ 85287, U.S.A.

INTRODUCTION

It is clear that Solid State Chemistry in general, and oxide chemistry in particular, will remain an experimental science for the foreseeable future. We cannot predict what compositions will occur as stable compounds and we cannot predict what crystal structures they will adopt when they do occur. Our deficiency in the latter regard has been called a "continuing scandal" (*1*) perhaps without a full appreciation of the daunting complexity of the crystal structures sometimes found for compounds with simple chemical compositions. While awaiting the millennium, we must make do with empirical and semi-empirical rules that allow some generalizations about crystal chemistry; it is with a review of some of these from a personal, possibly minority, perspective that this paper is concerned.

In particular, although the goal of structure prediction is still over the horizon, we can make some statements about expected bond lengths, and to a lesser degree about bond angles and coordination numbers in crystal structures.

THE BOND VALENCE METHOD

Until recently bond lengths in crystals were described as sums of a bewildering variety of radii of limited and specialized applicability (*covalent, ionic, metallic, etc.* radii). More recently the *bond valence* method, which has a long history, has come to the fore as it presents a number of distinct advantages over the use of radii both for the prediction and interpretation of bond lengths in crystals (*2*). These advantages become particularly apparent in crystals with irregular coordination polyhedra and/or mixed anions. The method utilizes two empirical observations.

The first of these, associated particularly with the names of Pauling and of Zachariasen, is that the bond valence, defined such that the sum of the valences of the bonds from a given atom is equal to the atomic valence, is a unique function of the bond length. Recent work (*3,4*) has used a "standard" form for the bond length d_{ij} of a bond of valence v_{ij}:

$$d_{ij} = R_{ij} - b\ln v_{ij} \qquad (1)$$

Here b is a "universal" parameter equal to 0.37 Å, and R_{ij} is a parameter unique to the pair of atoms i and j forming the bond. R_{ij} is, in a formal sense, the length of a single (unit bond order) bond; however the range of applicability of eq. (1) is strictly limited to the range of bond valences normally encountered in crystal structures. Extensive tables of R_{ij} are now available (*3,4*).

Except in the simplest cases, the constraints that bond valence sums are equal to atomic valences are insufficient to uniquely determine individual bond valences. An important step was taken by Brown (*5*) in introducing

the second principle (*Brown's Ansatz*) that, subject to those constraints, bonds between pairs of atoms of a given kind will be as nearly equal as possible. For example in a complex magnesium oxide, bonds from a given Mg atom to crystallographically-distinct O atoms will be as nearly equal in valence as possible. It transpires that this principle always results in an unique set of expected valences (*2*) and a computer algorithm for deriving them for complex crystals has been described (*6*).

IMPLICATIONS OF BROWN'S ANSATZ

The principle that bond valences for bonds from an atom to others of the same chemical kind are as nearly equal as possible suggest the following corollary: structures in which bonds from an atom to chemically-equal atoms are forced by bond valence constraints to be very unequal are unlikely to be stable. I (*2*) consider this to be an updated and more-generally applicable restatement of Pauling's celebrated electrostatic valence rule. There is space for just one simple example of its use.

In the sesquioxides M_2O_3 the average coordination number of O is 2/3 that of the metal atom *M*. Thus unless the coordination number of *M* is 3, 6, 9,… there must be oxygen atoms with more than one coordination number. In particular for 4-coordinated *M* (coordination number indicated by a preceding superscript roman numeral) one must have $^{iv}M_2{}^{iii}O(1)_2{}^{ii}O(2)$. The valence sums require that *M*-O(1) bonds have valence 2/3 and that the *M*-O(2) bonds have a valence 1. It is noteworthy that the only known sesquioxide with tetrahedrally-coordinated metal is in the high-pressure form of B_2O_3 which indeed has has long and short bonds in the BO_4 tetrahedron. (Note in passing that the ionic radius approach would predict four bonds of equal length and that the zero pressure

structure of B_2O_3 has 3-coordinated B). On the other hand there are at least 33 sesquioxides with 6-coordinated metal atoms. There are also five compounds with 7-coordinated metal atoms (*A* rare earth structure) but these have very anomalous bond lengths (*2*).

EXCEPTIONAL ELEMENTS

Sufficient examples have now been adduced in the literature to show that the principles outlined above successfully predict bond lengths in a wide variety of crystals. It is therefore rewarding to identify the cases where the Brown ansatz fails to predict observed bond lengths. Most of these cases can be identified with three kinds of cation.

(a) "Jahn-Teller" cations. These are notably d^4 and d^9 electronic configurations of the transition elements [*e.g.* Mn(III) and Cu(II)]. Here configurations such as octahedra with four short and two long bonds are found for generally well-understood reasons.

(b) "Lone pair" cations. These are characterized by a ns^2 valence configuration found in lower oxidation states of the heavier elements of groups 13-16. Tl(I), Pb(II) and Bi(III) are common examples.

(c) "d^0" cations. This category refers to the early transition elements (groups 3,4,and 5) in their maximum oxidation states. Examples are Ti(IV), Nb(V), W(VI). Oxides of these elements often (but not always) contain a wide range of bond lengths even when not required by valence sum constraints. A striking example is afforded by the low temperature structure of WO_3 with each O bonded to two metal atoms, but which contains a wide

range of W-O bond lengths in contrast to the topologically-identical structures of ReO_3 (d^1) and TeO_3 (d^{10}) in which all bond lengths are equal.

The predilection of cations in this third category to irregular coordination is manifest in their ubiquity in ferro- and antiferro-electric crystals with distorted MO_6 octahedra. It is also in accordance with their occurrence in structures with oxygen atoms with different coordination numbers. Notable among these last are the "shear" structures such as Ti_nO_{2n-1} (with ^{iii}O and ^{iv}O) and W_nO_{3n-1} (with ^{ii}O and ^{iii}O). It possibly relevant also to oxidation catalysts which require an easy transition between M=O and M-O-H at the surface.

BONDING RADII

It has recently been found (7) that bond valence parameters R_{ij} for a wide variety of bonds can be expressed to a good approximation in terms of two atomic parameters r_i and c_i:

$$R_{ij} = r_i + r_j - [r_i r_j(\sqrt{c_i}-\sqrt{c_j})^2]/(c_i r_i + c_j r_j) \qquad (2)$$

An expression of this form was proposed in a somewhat different context by Ray, Samuels and Parr (*8*) in which the parameters c were the atomic electronegativities. It was indeed found that the empirically-determined c parameters did in fact correlate very well with atomic electronegativities. The parameters r in Eq. (2) are interpreted as bonding radii, with the last term being a correction for bond shortening in heteropolar bonds. This last term is generally rather small, with an average value of 1% of R_{ij} and a maximum value of 11% for Cs-F bonds.

In determining the parameters in Eq (2), no data were included for metallic bonds, nevertheless it was found that the derived parameters predicted the bond lengths in elemental metals rather well (largest error 10%). This suggests that the bonding radii, together with the "electonegativity" parameters, can be used for all types of bond (covalent, ionic, metallic). It should be noted that as data for homopolar bonds are included, there is not an arbitrary division into "cations" and "anions", and one has an unambiguous scale of "size". Typical bonding radii, *r*, are (in Å):

Li	Be	B	C	N	O	F
1.00	0.81	0.79	0.78	0.72	0.63	0.58

Na	Mg	Al	Si	P	S	Cl
1.36	1.21	1.13	1.12	1.09	1.03	0.99

NON-BONDED INTERACTIONS

It might generally be conceded that coordination numbers in crystals are controlled to some extent by next-nearest (non-bonded) interactions. However, the relative importance of cation...cation and anion...anion interactions in crystals such as oxides remains a somewhat contentious issue. It is my opinion that the rôle of cation...cation interactions has generally been greatly discounted: some reasons for this opinion are summarized here.

Early attempts (*9*) to characterize non-bonded interactions focussed on *A...B* distances in $A^{X}B$ moities ("geminal" or "one-angle" configurations) in molecules. It was found that, to a good approximation, the distances could be expressed as a sum of non-bonded radii.

Extensions to crystals (*10*) followed; a set of such radii for comparison with the bonding radii given above follows (in Å).

Li	Be	B	C	N	O	F
1.5	1.35	1.26	1.25	1.14	1.12	1.10

Na	Mg	Al	Si	P	S	Cl
1.68	1.66	1.62	1.53	1.46	1.45	1.44

The scale of these radii has now been provided with a sound theoretical basis (*11*). As discussed below, I feel that they are now mainly of historical interest, although they do illustrate the same periodic trends as the bonding radii. In particular O and F are again the "smallest" atoms.

Another observation that leads to the belief that metal...metal interactions are of importance in oxide crystal chemistry is that many oxide structures, including some apparently complex ones, may be elegantly described as a "stuffing" of simple cation arrays (*12*). Indeed, in far too many cases to be merely a coincidence, the metal arrays in complex oxides are those of common alloy types. [The noted crystal psychologist, P. B. Moore (*13*) has remarked that, if these observations are to be ascribed to coincidence, we must "declare that Nature's dice are loaded"].

Particularly when the crystal- and thermo-chemistry of compounds rich in alkali and alkaline earth elements is examined, one is lead to the observation that these elements behave *as if* they strongly repel each other. This is manifest in unusually long (*14*) and weak (*15*) bonds in oxides and related crystals involving these elements. This idea, coupled with a realization of the

important rôle of stoichiometry, leads to an explanation (*16*) of the occurrence of unusual oxidation states and coordination numbers in such metal-rich compounds, as well as the apparent nonexistence of compounds such as Na_3N. The importance of large "cations" in stabilizing high oxidation states in copper oxide superconductors has also been emphasized (*17*).

SIMULATING CRYSTAL STRUCTURES

This not the place for a review of the extensive literature on simulation of crystal structure. However, it needs to be stated that the information content of structure is generally less than commonly supposed. Thus the apparently complex crystal structure of the garnets $A_3B_2C_3O_{12}$ is completely determined by four parameters (the cubic cell edge and oxygen coordinates) and one can already get a good approximation (better than many "sophisticated" simulations) to the structure simply by using metal-oxygen distances from tables of ionic radii (*10*). To test simulation methods, particularly if they are to lead to any useful generalizations, one must do very well in predicting both interatomic distances *and* lattice parameters. A possibly useful approach to the problem, still actively under development is outlined here.

As a starting point, for a given topology, one can predict expected valences and hence bond lengths. In exceptional cases, these are sufficient to determine a crystal structure (see the contribution by I. D. Brown to these proceedings). In this case one could minimize the difference between calculated valences v_c and predicted valences v_p. This corresponds to minimizing for all bonded distances d_k the sum

$$\Sigma|v_c - v_p| = \Sigma_k|\exp[(R_{ij}-d_k)/b] - v_p| \qquad (3)$$

More generally there will be more structural parameters than bond lengths. A simple example is afforded by the familiar corundum structure of Al_2O_3 which has two lattice parameters and an O parameter, but from the point of view of the bond valence method, only one predicted Al-O distance. There are in fact two independent (and in this case significantly different) Al-O distances, and to reproduce them one needs to include the effect of O...O and Al...Al repulsions.

Non-bonded repulsion energies are commonly, and with some theoretical justification, expressed as (*11*):

$$E_k = A_{ij}\exp(-d_k/a_{ij}) \qquad (4)$$

Here d_k is the kth non-bonded distance and A_{ij} and a_{ij} are constants for the atom pair under consideration and have been determined for a number of more electronegative element pairs empirically from molecular properties [see (*11*) for references]. Minimizing the repulsion energy can be expressed as minimizing the sum

$$\Sigma_k\exp[(S_{ij}-d_k)/a_{ij}] \qquad (5)$$

Where $S_{ij} = a_{ij}\ln A_{ij}$. The expression (5) is written in this way to illustrate the suggestive similarity to (3). To determine an optimal structure (3) and (5) have to be minimized simultaneously.

One needs to find parameters S and a for atom pairs that reproduce known crystal structures, and a start has been made. A large number of structures has to be examined and a consistent set of parameters extracted - a large task. To test whether the proposed method has any

merit, to date a somewhat arbitrarily chosen constant value of a = 0.25 Å has been chosen (in the same spirit as a constant b = 0.37 Å is used for bonded interactions) and S found for non-bonded interactions. Typical values are S_{AlAl} = 3.0 Å and S_{OO} = 2.7 Å.

As those who have attempted to model structures by similar methods (*e.g.* so-called DLS methods which are close in spirit) will know, the derived structures can be very sensitive to the values of the input parameters. It is observed that for many oxide structures, especially those with several different types of cation, that the valence sums at O are very close to 2.0 even though the sums at the individual cations deviate significantly from the atomic valences. I have found that the structure simulation procedure for oxides is much more robust (and significantly more difficult to implement) if one constrains the valence sums at O atoms to be exactly 2.0.

As a hint of the possible utility of the method very preliminary results (Table 1.) are given for the simulation of three $A_3B_2C_3O_{12}$ compounds with the garnet structure by this method. In this work a constant value of S = 3.2 Å was used for all metal...metal interactions and S = 2.7 Å for O...O interactions. Despite the simplicity of the model several distinctive features of the structures are reproduced. For example the short Al-O bond lengths in $Mg_3Al_2Si_3O_{12}$ and the long Al-O bond lengths in $Ca_3Al_2Si_3O_{12}$ (compare the contribution of R. D. Shannon to these proceedings) are reproduced. To be noted also is that the two independent A-O bonds in the structure are calculated to have significantly different lengths in accord with observation, even though the simple bond valence method predicts that they have the same valence. Finally the low valence sum at Mg and the high valence sum at Ca is reproduced.

Table 1. Comparison of observed and simulated (calc) structures for three garnets. a and x, y, z are the lattice parameter and oxygen coordinates. V'_A is the valence sum at Mg, Ca or Sr.

	$Mg_3Al_2Si_3O_{12}$		$Ca_3Al_2Si_3O_{12}$		$Sr_3Y_2Ge_3O_{12}$	
	calc	obs	calc	obs	calc	obs
a	11.412	11.546	11.912	11.846	13.081	13.087
x	-0.0347	-0.0329	-0.0433	-0.0381	-0.0434	-0.0395
y	0.0502	0.0502	0.0459	0.0449	0.0542	0.0517
z	0.1547	0.1534	0.1510	0.1514	0.1591	0.1591
$d(A\text{-}O)_1$	2.198	2.197	2.390	2.320	2.603	2.551
$d(A\text{-}O)_2$	2.340	2.342	2.505	2.503	2.661	2.684
$d(B\text{-}O)$	1.898	1.887	1.949	1.933	2.270	2.250
$d(C\text{-}O)$	1.603	1.634	1.624	1.653	1.748	1.768
V'_A	1.72	1.72	2.21	2.48	2.00	2.12

It is interesting that in this example, as in many others, it is found that the contribution of cation...cation and anion...anion repulsions to the total repulsion energy is comparable, and that omitting one or the other invariably leads to unsatisfactory structures. Thus the answer to the question of whether cation repulsions or anion repulsions are important in oxide chemistry is (as is so often the case with such questions) that both are important and that both must be considered.

Acknowledgment. This work was supported by a grant (DMR 8813524) from the National Science Foundation.

REFERENCES

1. J. Maddox, *Nature*, **335**, 201 (1988).
2. M. O'Keeffe, *Structure and Bonding*, **71**, 162 (1989).
3. I. D. Brown and D. Altermatt, *Acta Crystallogr.* B**41**, 240 (1985).
4. N. E. Brese and M. O'Keeffe, *Acta Crystallogr.* in press.
5. I. D. Brown, *Acta Crystallogr.* B**33**, 1305 (1977).
6. M. O'Keeffe, *Acta Crystallogr.* A**46**, 138 (1990).
7. M. O'Keeffe and N.E.Brese, to be published.
8. N. K. Ray, L. Samuels and R. G. Parr, *J. Chem. Phys.* **70**, 3680 (1979).
9. L. S. Bartell, *J. Chem. Phys.* **32**, 827 (1960).
10. M. O'Keeffe and B. G. Hyde, in *Structure and Bonding in Crystals* (M.O'Keeffe and A.Navrotsky, eds.) Wiley, New York (1981).
11. M. A. Spackman, *J. Chem. Phys.* **85**, 6579 (1986).
12. M. O'Keeffe and B. G. Hyde, *Structure and Bonding*, **61**, 77 (1985).
13. P. B. Moore, *Mineralogical Record*, **20**, 339 (1989).
14. N. K. McGuire and M. O'Keeffe, *J. Solid State Chem.* **54**, 49 (1984).
15. M. O'Keeffe and J. A. Stuart, *Inorg. Chem.* **22**, 177 (1983).
16. M. O'Keeffe and B. G.Hyde, *Nature*, **309**, 411 (1984).
17. M. O'Keeffe and S. Hansen, *J. Am. Chem. Soc.* **110**, 1506 (1988).

R. Cava: Why is it that the D zero ions have this peculiar property of not working?

M. O'Keeffe: I don't know really, however, I can give you a glib answer. In a TiO_6 regular octahedron there are empty states, the D manifold, which are non-bonding in octahedral symmetry. If the symmetry is reduced these states mix in with the bonding states, the unbonded energy states go up and the bonded energy states go down, producing a 2nd order Jahn-Teller effect. The exact distortion type cannot be predicted, but any distortion from octahedral symmetry will make the non-bonding states mix with the bonding states. Then if there is one electron in the d-band the whole statistics of the occupied states goes up. Presumably as you go further across the d-level the anti-d-states get higher and higher energy.

A. Nath: The deviations which you mentioned in garnet, for example, would they be explained by the features which you mentioned in your last slide?

M. O'Keeffe: No, I think they're fully explained just by the repulsions within the crystal, the metal-metal and oxygen-oxygen repulsions.

A. Nath: That would explain all the deviations?

M. O'Keeffe: That's what I tried to show in my simulations. In this calculated structure, the valence sum at oxygen is constrained to be two. That is the only arbitrary nature of the calculation. We have predicted bond lengths for all the bonds in the structure, or predicted valences, and we also have non-bonded interactions. What we do is minimize the deviation from the predicted valences and the non-bonded repulsions together. What you come up with is the observed structure.

I. Brown: In that last calculation do you use the idea of equal valences between the bonds?

M. O'Keeffe: Yes. For example, calcium is eight coordinated and all the bonds should be the same. Each bond should have a valence of a quarter, so the deviations from a quarter are what is implicated.

I. Brown: Then you constrain the oxygen to be two and after that put in the repulsions.

M. O'Keeffe: Yes. Where the parameters come from, of course, is important. We have looked at a large number of structures like corundum to find out what sort of aluminum-aluminum and oxygen-oxygen repulsions must be put in to get the observed structure. This is well defined, and these parameters are simply then transferred to more complex crystals.

D. Cahen: Your earlier slides of magnesium oxide showed first a cut through the electron density along the magnesium oxygen bond. I assume it was the valence electron density?

M. O'Keeffe: No, total electron density. That was on a logarithmic scale.

D. Cahen: So afterwards you took the total electron density in your equation to get the potential?

M. O'Keeffe: Yes.

D. Cahen: I wonder what would happen if you can, in a pseudo-potential like way, just take the valence electron density.

M. O'Keeffe: You get very similar plots actually. The core electrons are so close to the nucleus that the effect of their electrostatic potential would be very small. So you get a very similar curve.

B. Dabrowski: In your equation the single parameter R_o is expressed as a function of R_1, R_2; are you including also the dependence on thermodynamic functions like temperature and pressure?

M. O'Keeffe: No.

B. Dabrowski: Can you explain phase transition temperatures?

M. O'Keeffe: These parameters are average room temperature zero pressure parameters. Bond lengths don't change that much with temperature except for alkali metals where there is very large bonding. All parameters are for zero pressure. I think that's all I can say.

R. Roth: I would like to make a comment regarding some recent work from NIST and DuPont on the coordination number of the Bi^{+3} ion, that relates to the subjects discussed by O'Keeffe and Brown as well as the earlier talk by Shannon. The crystal structures of three Bi^{+3} containing phases have recently been solved by x-ray single crystal structure analyses and neutron powder diffraction Rietveld analyses. In $Ca_4Bi_6O_{13}$ (Chem. Mater. 2 454, 1990), although 2/3 of the Bi^{+3} ions are in 5-fold coordination (with the lone pair electrons presumably in the 6th direction to complete an octahedron) 1/3 of the Bi^{+3} ions are in 3-fold coordination with oxygen. In $Ca_2Bi_2O_5$, 1/3 of the Bi^{+3} ions are in 5-fold coordination with 2/3 of the Bi^{+3} ions in an unusual 'saw-horse' 4-fold configuration, with the 5-fold polyhedron bridging two 4-fold ions in a U-shaped Bi_3O_{11} unit. In $Sr_2Bi_2O_5$ all of the Bi^{+3} ions are in 3-fold coordination. Thus the coordination polyhedra formed by the Bi^{+3} ion are not 6-, 8-, or 12-fold as might be expected but rather form strange and entirely unexpected patterns. Many more such structures need to be examined before we can feel that we understand and can predict the oxygen coordination of the Bi^{+3} ion.

National Institute of Standards and Technology Special Publication 804, Chemistry of Electronic Ceramic Materials, Proceedings of the International Conference held in Jackson, WY, August 17-22, 1990, issued January 1991.

COMPUTER SIMULATION STUDIES OF ELECTRONIC CERAMICS

A.N. Cormack
NY State College of Ceramics
Alfred University, Alfred, NY 14802

INTRODUCTION

The detailed chemistry of electronic ceramics is often rather complicated, either by "accident" or design. By "accident," we mean that a compound with a complex stoichiometry, such as the $YBa_2Cu_3O_{6+x}$ or $Bi_2Sr_2CaCu_2O_{8+x}$ high T_c ceramic superconductors, is found to have useful properties. By design, on the other hand, we mean that a basically simple composition, such as ZnO or $BaTiO_3$, has a number of other components added to it in order to control more precisely the desirable electronic properties.

As so often with ceramic materials, processing is a key issue and control of the chemistry and stoichiometry is an essential part of the processing conditions. From a crystal chemical point of view, incorporation of minor components, or maintenance of a complex stoichiometry, each require control and hence an understanding of the defect properties of the material. The objective of computer simulation studies is to provide a theoretical basis from which to understand defect properties, especially in situations where experimental access to these properties is limited in one way or another. In this short review, we will describe the methodology behind the calculations and aim to demonstrate the efficacy of the approach using a number of recent examples and illustrations.

METHODOLOGY

The basic physics of our type of simulations is embodied in the Born Model of the solids, supplemented by a representation of ion polarisability for which the Shell Model, due to Dick and Overhauser, is used. The Shell Model treats each ion in terms of two point components: a core in which the mass of the ion is contained on a mass-less shell which may be loosely taken to represent the valence electrons. The total formal charge on the ion is divided between the core and the shell which are coupled

together via a harmonic spring so that the polarisability (which depends on the shell charge and the harmonic spring constant) is modeled correctly. (In fact, what one strives to reproduce is the dielectric behaviour of the solid which is governed by the ion polarisabilities).

In addition to the coulombic term, there is a contribution to the overall interatomic potential from short-range effects, notably the repulsions that come into play when ions approach each other too closely. Since most of the chemistry--by which I mean the differing behaviour of different ions or indeed compounds, such as MgO and CaO--is predicated on the validity of the interatomic potential the way in which the short range terms are modeled is of some importance. There is no single, correct formula; indeed, one could use computed values stored numerically in the computer. The most common approach, however, is to use a parametrised analytical form usually of the Born-Mayer or Buckingham type:

$$V(r) = A.\exp(-r/\rho) - Cr^{-6}$$

where the parameters A, ρ and c are appropriate for any given interaction.

The lattice energy, from which the properties such as structural equilibrium, elastic and dielectric tensors may be derived is then just the sum of pair potential interactions: Defect energies are obtained, at least in principle, by summing the interactions of the defect species with all the other ions in the crystal. Clearly, this is impossible in practice, so a two-region strategy is used. In this approach an inner region I, which is treated atomistically using appropriate interatomic potential models, is embedded in a dielectric continuum in which the polarisation due to the net charge on the defect may be evaluated according to Mott-Littleton theory.

A key point, both with respect to the defect energy calculations and in determining structural equilibrium is the use of energy minimisation (with respect to ion position) to ensure that, in the case of the defect calculation, the structure around the defect is in equilibrium with the defect and that, for perfect lattice calculations, the whole unit cell is the equilibrium.

A more complete description of the computational and theoretical details may be found in ref (1).

ALKALINE EARTH EXCESS ALKALINE EARTH TITANATES

The alkaline earth titanates are widely used in the electronic ceramics industry in a number of different applications. A key property to be controlled during their processing is the

TABLE 1 BASIC POINT DEFECT ENERGIES (IN EV) IN ALKALINE EARTH TITANATES

Defect	$BaTiO_3$	$SrTiO_3$	$CaTiO_3$
V_O	17.79	18.95	18.96
V_A	16.73	19.82	21.15
V_{Ti}	81.77	86.52	86.26
A_{Ti}	66.30	66.29	63.79
Ca_{Ti}	59.75	62.52	63.79

A/Ti cation ratio. Of interest in this regard is the ease with which these compounds may become nonstoichiometric and by what mechanism. A review of the literature suggests that $BaTiO_3$, $SrTiO_3$ and $CaTiO_3$ each behave somewhat differently with respect to incorporation of excess alkaline earths. In summary, $BaTiO_3$ tolerates virtually no excess Ba, $SrTiO_3$ accommodates some via point defect formation and more through the formation of planar defect structures, but for $CaTiO_3$, the situation is less clear, with conflicting data.

Our interest here was to see whether these differing observations could be explained in terms of a single defect model common to the three compounds or whether different mechanisms might be operating. Accordingly, using a consistent set of interatomic potentials, we calculated the basic defect energies for the three compounds.[2] Note that these are the energies required to produce the defect. For example, oxygen vacancy formation involves the removal of an oxide ion from the structure to infinity and this is the energy recorded in table (1). Using these energies, one may obtain the energies of the various defect reactions that may occur, allowing one to determine which processes may be the more favourable.

For instance, excess alkaline earths may be incorporated via two principle mechanisms according to the reactions given in Table 2. The first involves Ti vacancies whilst the second produces A_{Ti} defects. Our results indicate that reaction (1) is

TABLE 2 REACTION ENERGIES (IN EV) FOR EXCESS ALKALINE EARTH INCORPORATION

	Reaction	$BaTiO_3$	$SrTiO_3$	$CaTiO_3$
(1)	$AO \rightarrow A_A + O_O + V_{Ti} + 2V_O$	4.14	10.25	10.11
(2)	$2AO \rightarrow A_A + A_{Ti} + 2O_O + V_O$	2.25	0.91	4.80

energetically unfavourable for all three titantates, whereas for $SrTiO_3$ reaction (2) has a low energy of 0.91 eV associated with it. In $BaTiO_3$ and $CaTiO_3$, A_{Ti} defects are not expected to form, again becasue of high reaction energies (see Table (2)).

Another way to consider solubility limits is to examine the energetics of second phase formation. In the case of the orthotitanates, A_2TiO_4 it is interesting to note that whilst Ba_2TiO_4 adopts the K_2SO_4 structure, Sr_2TiO_4 has the K_2NiF_4 structure whereas Ca_2TiO_4 is not known as a single phase. We calculated the energies of orthotitanate formation assuming, for each compound, both structure types. For Ba_2TiO_4 we predict that the K_2SO_4 structure will be preferred whereas for Sr_2TiO_4, the K_2NiF_4 structure will be adopted. For Ca_2TiO_4 we find a positive reaction energy for both structure types, indicating that either will be energetically unstable with respect to disproportionation to CaO and $CaTiO_3$. All of these results concord with the experimental observations and taken together with the point defect calculations indicate that there are sufficient differences in the energetics of each alkaline earth to account for their varying behaviours.

DOPED MANGANESE FLUORIDE

In this example, the simulations were aimed at addressing two principle questions arising from some experimental observations. Ling and Nowick,[3] measuring the ionic conductivity, noted a degree of anisotropy that was less than expected given the tetragonal symmetry of the rutile structure which is adopted by MnF_2. This was ascribed to the mechanism of ion transport in the material but a detailed and quantitative explanation could not be extracted from their data. Secondly, in doped samples, but not in pure samples, low temperature dielectric loss peaks were observed that have associated energies too small to be assigned to ions jumping between lattice sites. Since these peaks were associated with impurity (or dopant) defect structures, it seemed natural to undertake a set of defect calculations, with the objective of uncovering a suitable migration mechanism and elucidating the nature of the defect structure causing the dielectric loss.

In summary, our findings[4] were as follows: The intrinsic disorder is predicted to be of anion Frenkel type, and, interestingly, that the anion interstitial would adopt a "split interstitial" structure, that is an anion in an interstitial site would displace an adjacent lattice anion into another interstitial position. Thus the interstitial would be split between two sites bridged by a vacant lattice anion site. This has important consequences for both of the experimental observations described above. Firstly, it provides for a low energy pathway in the basal plan in addition to the empty channels in the c direction, thus

suggesting an explanation for the lack of anisotropy seen in the conductivity. Secondly, the calculations reveal that when bound to an dopant ion such as Y^{3+} or Er^{3r+} sitting substitutionally on an Mn site, the split interstitial configuration is able to relax further into a low symmetry arrangement in which one of the interstitial fluorine moves to a site above the basal plane, whilst the other moves to a position below the basal plane with the dopant remaining in the basal plane. A "flip-flop" orientation of this defect complex, switching the F ions which lie above and below the basal plane, accounts for the dielectric loss measurements.

Note that the dopant is required for the split interstitial structure to go off-symmetry: a somewhat subtle chemical influence which has been elucidated from the computer simulations.

Our last example concerns a rather complex system with the potential for an extensive range of nonstoichioimetries; hence, an ideal subject for attack by atomistic computer simulations.

NONSTOICHIOMETRY IN $LaMgAl_{11}O_{19}$

$LaMgAl_{11}O_{19}$ has the magnetoplumbite structure, which is related to the β-alumina family of structures in that both consist of slabs with the spinel structure stacked together. The basic differences occur in the structure of the inter-slab region. These differences can be crucial: magnetoplumbites do not exhibit cation conductivity whereas β-aluminas are very good fast ion conductors.

In this review, we will focus on just one aspect of the crystal chemistry of these materials. The following formulae have been variously suggested to describe the nonstoichiometry in $LaMgAl_{11}O_{19}$: $La_{1-x}MgAl_{11+x}O_{19}$; $LaMg_xAl_{11}O_{18+x}$; $La_{1-x}Al_{11+2/3+x}O_{19}$; $La_{1-x}MgAl_{11+5x/3}O_{19+x}$; $LaMg_xAl_{11+2/3(1-x)}O_{19}$ and $La_{1-x}Mg_yAl_{11+x+2/3(1-y)}O_{19}$. Each formula represents the creation of a different set of point defects and thus, using computer simulations to calculate the energies of these different point defects, it is possible to give some quantitative indication of the relative ease of producing these nonstoichiometries.[5] The results are not altogether surprising. For example, changing the La to Al ratio occurs relatively easily by substituting Al on La sites, and this nonstoichiometry can be facilitated by losing magnesium. The formation of defect complexes can, however, change the energetics somewhat as we discuss next.

An interesting result of our calculations concerns the incorporation of excess oxygen. The basic principles of crystal chemistry dictate that substituting an anion in place of a cation is not a sensible thing to do. However, when Stevels first

proposed that oxygen would substitute for lanthanum, he noted that there were likely to be additional defect interactions because of the diffuse scattering he observed. We have found that, not surprisingly, attempts to replace a single lanthanum by oxygen is not energetically favourable; indeed, it is difficult to get the oxygen to remain in the same vicinity as the lanthanum site. However, if additional defect species are introduced, such as those depicted in figure (1), then the O_{La} defect can, in fact, be stabilised, and moreover, the binding energy of such a defect cluster renders this mode of nonstoichiometry energetically compatible with other likely mechanisms. Thus, the computer simulation studies, in addition to discriminating between possible modes of nonstoichiometry, can also lend support to the structure of defect complexes inferred from x-ray scattering studies.

References

1. C.R.A. Catlow and W.C. Mackrodt, "Computer Simulation of Solids" Lecture Notes in Physics, vol. 166, Springer, Berlin (1982).
2. K.R. Udayakumar and A.N. Cormack, J. Phys. Chem. Solids, 50, 55 (1989).
3. S. Ling and A.S. Nowick, Phys. Rev. B40, 3266 (1989).
4. A.N. Cormack, C.R.A. Catlow and S. Ling, Phys. Rev. B40, 3278 (1989).
5. Like Xie and A.N. Cormack, J. Solid State Chem. 88, (October) (1990).

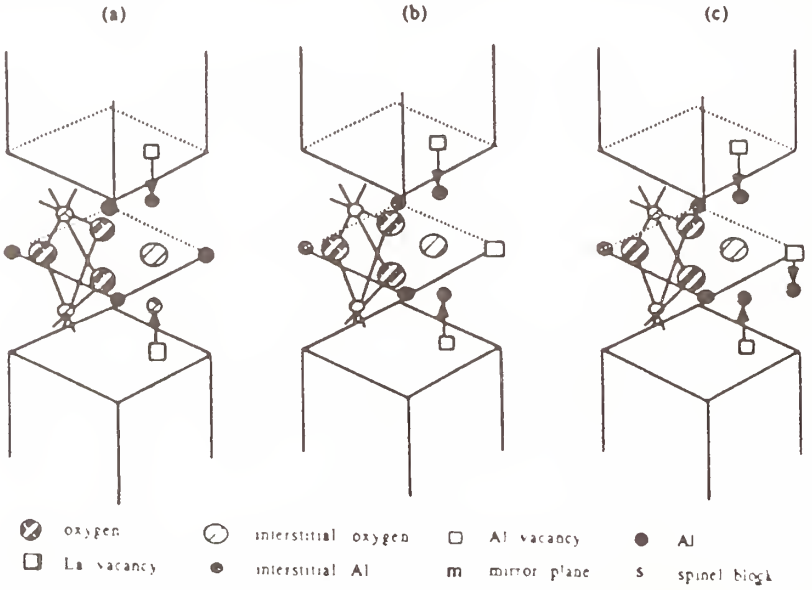

Figure 1. Defect complexes associated with the stabilisation of O_{La} defects. Note that displacement, but not complete removal, of a mirror plane Al, increases the stability of the cluster.

proposed that oxygen would substitute for lanthanum, he noted that there were likely to be additional defect interactions because of the diffuse scattering he observed. We have found that, not surprisingly, attempts to replace a single lanthanum by oxygen is not energetically favourable; indeed, it is difficult to get the oxygen to remain in the same vicinity as the lanthanum site. However, if additional defect species are introduced, such as those depicted in figure (1), then the O_{La} defect can, in fact, be stabilised, and moreover, the binding energy of such a defect cluster renders this mode of nonstoichiometry energetically compatible with other likely mechanisms. Thus, the computer simulation studies, in addition to discriminating between possible modes of nonstoichiometry, can also lend support to the structure of defect complexes inferred from x-ray scattering studies.

References

1. C.R.A. Catlow and W.C. Mackrodt, "Computer Simulation of Solids" Lecture Notes in Physics, vol. 166, Springer, Berlin (1982).
2. K.R. Udayakumar and A.N. Cormack, J. Phys. Chem. Solids, 50, 55 (1989).
3. S. Ling and A.S. Nowick, Phys. Rev. B40, 3266 (1989).
4. A.N. Cormack, C.R.A. Catlow and S. Ling, Phys. Rev. B40, 3278 (1989).
5. Like Xie and A.N. Cormack, J. Solid State Chem. 88, (October) (1990).

DISCUSSION

(Unknown): My first question concerns the model that you used: Is it a pure ionic model? I may have missed that. But my real question is that you showed a list with defect formation energies. How do they compare to experimental? They seemed to be awfully large.

A. Cormack: The individual defect formation energies bear no resemblance to what you measure experimentally. What you measure, if you can, is the Scottley or Frenkel disorder energy or some antisite reaction energy. These energies involve a combination of the raw energies given in that table.

(Unknown): There are experimental data that you can compare to.

A. Cormack: Not directly for the alkaline earth titanates. I think one thing we can compare here is what we would predict the defect concentration such as strontium or titanium sites in strontium titanate, and our energies predict the concentration which is in the same ballpark as seen experimentally.

Just to comment on the first question about the model; I prefer to use the term Born model instead of a purely ionic model because the model consists of both point charges and short range repulsive interactions and is not just purely an electrostatic model.

National Institute of Standards and Technology Special Publication 804, Chemistry of Electronic Ceramic Materials, Proceedings of the International Conference held in Jackson, WY, August 17-22, 1990, issued January 1991.

COMPUTER SIMULATION OF DOPANT SUBSTITUTION IN $YBa_2Cu_3O_7$

M.S. Islam and C. Ananthamohan
Department of Chemistry, University of Surrey
Guildford GU2 5XH, UK

ABSTRACT

Atomistic simulation techniques are used to investigate dopant substitution on the Cu sublattice in $YBa_2Cu_3O_7$. The techniques are based on the Mott–Littleton methodology which effectively treats lattice relaxation around defects or impurity species. Solution energetics are calculated for both divalent and trivalent dopant ions. Correlations between particular bond distances and T_c are also examined.

INTRODUCTION

Since the discovery of the $YBa_2Cu_3O_7$ superconductor, the effect of substitution by dopant ions on its properties has been extensively studied to investigate the origin of the superconductivity. Such studies have demonstrated that rare–earth substitution for Y has almost no effect on the critical temperature (T_c) [1], whereas substitution for the Cu sites by 3d transition elements results in a decrease in T_c, the magnitude being dependent on the particular ion [e.g. 2–7]. As is now well known, $YBa_2Cu_3O_7$ adopts a perovskite–like structure with two distinct copper sites : Cu(1) chain and Cu(2) plane. In evaluating the influence of substituting ions it is apparent that the precise lattice location is important. In some cases, however, the preferred site has not been clearly established, particularly for the Cu(1) versus Cu(2) sites. This partly arises from differences in experimental conditions and difficulties in characterizing the exact oxygen stoichiometry.

In this paper the energetics of dopant incorporation are examined using atomistic simulation techniques. These methods have been successful in describing defect properties of ceramic oxides [8–10] and have been applied to the cuprate superconductors [11–14]. This study extends our recent studies of defects [12] and oxygen migration [13] in $YBa_2Cu_3O_7$, by focusing on cation substitution within the Cu sublattice.

THEORETICAL METHODS

The present account of these widely used techniques will be brief since detailed reviews are given elsewhere [9,10]. The calculations are formulated within the framework of the Born model and are based on two–body potentials to represent short–range forces, which include the shell description of ionic polarization. The essential feature of the

lattice simulations is the relaxation of ions in the vicinity of the defect or dopant. The Mott–Littleton approach is to divide the crystal into two regions so that ions in the inner region surrounding the defect are relaxed explicitly, whereas the remainder of the crystal is treated by continuum approximations. The potentials for $YBa_2Cu_3O_7$ are the same as in the previous studies [12,13], which reproduced the structure to within 0.03 Å. Full details of all the potential parameters and computed crystal properties are given by Baetzold [12].

RESULTS AND DISCUSSION

The principal dopants or impurities in $YBa_2Cu_3O_7$ are divalent and trivalent cations. The simulation approach is based on the calculation of the energetics of dissolution in the oxide, which are obtained by combining appropriate cohesive energies with energy terms accompanying the formation of the substitutional species.

We first consider the dissolution of divalent impurities into the Cu^{2+} sublattice, which can be represented by the defect equation:

$$MO + Cu_{Cu}^{x} \longrightarrow M_{Cu}^{x} + CuO \qquad (1)$$

The calculated energies of solution, ΔE, for the two nonequivalent copper sites are listed in Table I, where our sign convention is such that a positive value indicates an endothermic process. The calculations suggest that the transition–metal cations Fe^{2+}, Co^{2+}, Ni^{2+}, Zn^{2+} and Cd^{2+} preferentially substitute for Cu(2). Most notably, the highly favourable solution energies for NiO and ZnO are in line with the observation that these oxides dissolve readily in $YBa_2Cu_3O_7$. The results generally agree with diffraction studies that find Ni^{2+} and Zn^{2+} on the Cu(2) plane. As expected the larger alkaline–earth ions Ca^{2+} and Sr^{2+} have high and unfavourable energies. Note that experimentally, Fe and Co are considered to be in the 3+ charge state, which will be examined below.

TABLE I. Calculated energies of solution (in eV per dopant ion).

MO	$\Delta E_{Cu(1)}$	$\Delta E_{Cu(2)}$
MgO	1.20	0.18
CaO	1.28	1.15
SrO	2.28	2.94
FeO	0.91	0.02
CoO	0.85	–0.10
NiO	–1.86	–3.19
ZnO	–1.96	–3.18
CdO	–0.82	–1.23

In Fig. 1 the calculated energies of solution are plotted versus the ionic radius of the dopant ion; a strong correlation between the two is found with an energy minimum observed at Ni^{2+}. Such variation with ion size is explained in terms of the relaxation of the surrounding ions, and suggests that changes in local structural ordering may be important in the observed depressions in T_c.

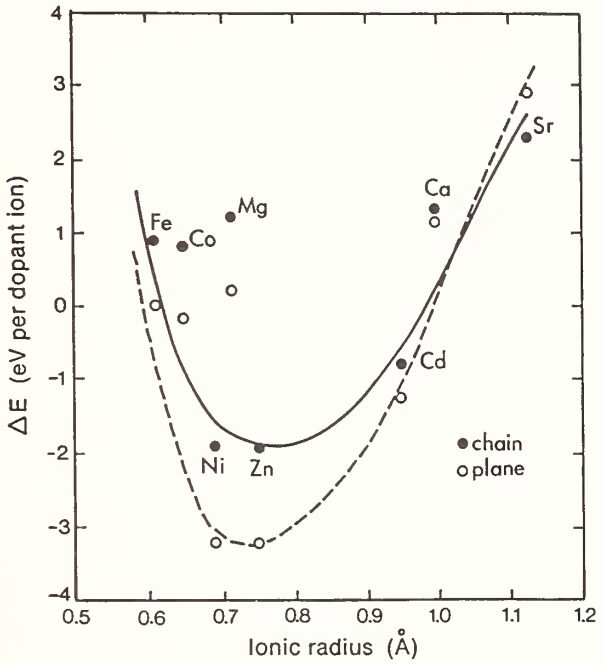

Fig. 1. Calculated solution energies versus divalent dopant radius

The simulation program used in this study also provides detailed information on the relaxed positions of host–lattice ions. From our structural analysis we find significant ion displacements around the dopant ion. In Table II, the calculated M^{2+}–Cu(1) and Cu(1)–O(4) bond distances for the 3d dopant ions (M^{2+}) are summarized. It has been proposed that the Cu–O bonds that link the chains to the planes provide a sensitive probe of charge transfer effects. Indeed, from neutron diffraction experiments correlations of certain average bond lengths with T_c have been discussed. Therefore, to illustrate the behaviour of our computed bond distances we plotted both the M^{2+}–Cu(1) and the Cu(1)–O(4) distances versus T_c, shown in Fig. 2. A trend towards decreasing T_c with increasing M^{2+}–Cu(1) and decreasing Cu(1)–O(4) bond distances is found. We recognize, however, that the observed value of T_c is strongly dependent on the precise dopant concentration. Nonetheless, diffraction measurements [5] have similarly found T_c decreasing systematically with decreasing Cu(1)–O(4) bond distance, for both Co–doped and oxygen–deficient materials.

TABLE II. Calculated bond distances (in Å) for divalent dopant substitution on the Cu(2) site.

M^{2+}	M–Cu(1)	Cu(1)–O(4)
Fe	4.2748	1.8430
Co	4.2806	1.8434
Ni	4.1936	1.8614
Cu[a]	4.2560	1.8741
Zn	4.1835	1.8514

a Undoped lattice

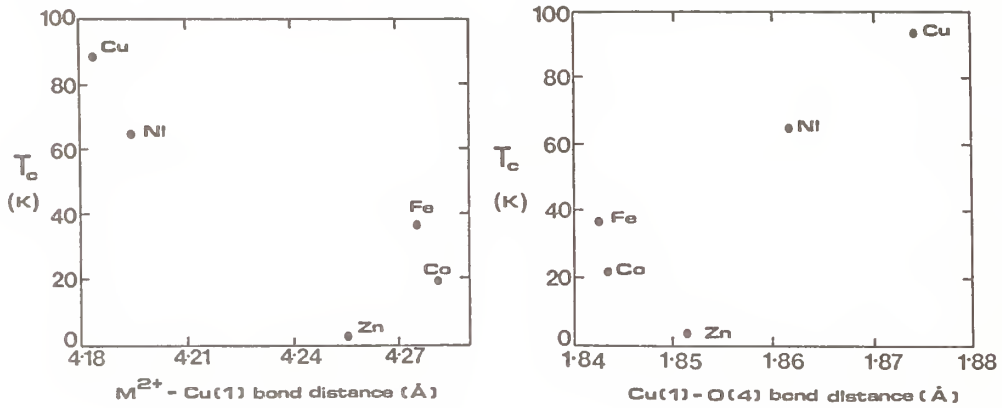

Fig. 2. Variation of T_c with calculated bond distances for dopants on Cu(2). Observed values of T_c from [2]

For trivalent impurities substituting at Cu^{2+} sites there are two alternative charge–compensating defects: oxygen interstitials or copper vacancies. The corresponding defect reactions are

$$M_2O_3 + 2Cu_{Cu}^{x} \longrightarrow 2M_{Cu}^{\cdot} + O_i'' + 2CuO \qquad (3)$$

or

$$M_2O_3 + 3Cu_{Cu}^{x} \longrightarrow 2M_{Cu}^{\cdot} + V_i'' + 3CuO \qquad (4)$$

The former process involving oxygen incorporation is calculated to have the lowest energy [12] and is, therefore, predicted to be the majority compensating mechanism. This result is in accord with thermogravimetric measurements that show an increase in oxygen content with increasing Al^{3+}, Fe^{3+} and Co^{3+} dopant concentration [4]. Note that oxygen uptake accounts for the observed increase in unit–cell volume even though Al^{3+}, Fe^{3+} and Co^{3+} are all smaller than Cu^{2+}.

The calculated energies of solution for the trivalent ions Al, Sc, Fe, Ga and Bi are presented in Table III. Examination of these energies reveals that the trivalent dopants are predicted to favor substitution at the Cu(2) site. Diffraction experiments have, in general, suggested that Al and Fe substitute predominantly for Cu(1), although recent neutron studies find significant Fe occupancy of Cu(2) sites even for low dopant content [6,7]. Note that in this study we have considered systems at high dilution i.e. the solution energies are for isolated dopant ions. At higher concentrations the clustering of dopants may play an increasingly crucial role, which could clearly effect the calculated solution energies. These defect interactions obviously are subjects for further study.

TABLE III. Calculated energies of solution (in eV per dopant ion).

M_2O_3	$\Delta E_{Cu(1)}$	$\Delta E_{Cu(2)}$
Al_2O_3	0.10	–1.66
Sc_2O_3	0.75	–1.44
Fe_2O_3	–0.31	–1.84
Ga_2O_3	–0.25	NC[a]
Bi_2O_3	4.23	4.22

[a] Calculation not converged

CONCLUSIONS

We have shown that the application of atomistic simulation techniques can provide a useful way of investigating dopant phenomena in the $YBa_2Cu_3O_7$ ceramic oxide. While there may remain some uncertainties in the calculated solution energies for this complex system, our study demonstrates the ability of the method to distinguish between alternative modes of dopant substitution and compensation mechanisms. From our analysis of local ion displacements immediately surrounding the dopant ion, we find a trend towards decreasing T_c with increasing M^{2+}–Cu(1) and decreasing Cu(1)–O(4) bond distances, which is consistent with results of neutron–diffraction measurements.

ACKNOWLEDGEMENTS

MSI would like to thank Roger Baetzold at the Kodak Research Laboratories NY, for many useful discussions.

REFERENCES

[1] P.H. Hor, R.L. Meng, Y.Q. Wang, L. Gao, Z.J. Huang, J. Bechtold, K. Forster and C.W. Chu, Phys. Rev. Lett. 58, 1891 (1987).

[2] G. Xiao, F.H. Streitz, A. Garvin, Y.W. Du and C.L. Chien, Phys. Rev. B **35**, 8782 (1987).

[3] Y. Maeno, T. Tomita, M. Kyogoku, S. Awaji, Y. Aoki, K. Hosino, A. Minami and T. Fujita, Nature 328, 512 (1987).

[4] J.M. Tarascon, P. Barboux, P.F. Miceli, L.H. Greene, G.W. Hull, M. Eibschutz and S.A. Sunshine, Phys. Rev. B **37**, 7458 (1988).

[5] P.F. Miceli, J.M. Tarascon, L.H. Greene, P. Barboux, F.J. Rotella and J.D. Jorgensen, Phys. Rev. B **37**, 5932 (1988).

[6] S. Katano, T. Matsumoto, A. Matsushita, T. Hatano and S. Funahashi, Phys. Rev. B **41**, 2009 (1990).

[7] S. Katsuyama, Y. Ueda and K. Kosuge, Physica C. **165**, 404 (1990).

[8] C.R.A. Catlow, R. James, W.C. Mackrodt and R.F. Stewart, Phys. Rev. B **25**, 1106 (1982).

[9] C.R.A. Catlow, Annu. Rev. Mater. Sci. **16**, 517 (1986).

[10] C.R.A. Catlow, in *Solid–State Chemistry: Techniques*, edited by A.K. Cheetham and P. Day (Clarendon, Oxford, 1987), Chap. 7.

[11] M.S. Islam, M. Leslie, S.M. Tomlinson and C.R.A. Catlow, J. Phys. C **21**, L109 (1988); C.R.A. Catlow, S.M. Tomlinson, M.S. Islam and M. Leslie, *ibid.* **21**, L1085 (1988).

[12] R.C. Baetzold, Phys. Rev. B **38**, 11304 (1988); M.S. Islam and R.C. Baetzold, *ibid.* **40**, 10926 (1989)

[13] M.S. Islam, Supercond. Sci. Technol. (to be published).

[14] W.C. Mackrodt, Supercond. Sci. Technol. **1**, 343 (1989).

National Institute of Standards and Technology Special Publication 804, Chemistry of Electronic Ceramic Materials, Proceedings of the International Conference held in Jackson, WY, August 17-22, 1990, issued January 1991.

MOLECULAR DYNAMICS SIMULATIONS OF ION MOTION IN DIVALENT AND MIXED MONOVALENT-DIVALENT BETA''- ALUMINA

C. A. Lane and G. C. Farrington
University of Pennsylvania, Philadelphia, PA 19104

INTRODUCTION

The ability to design materials with specified properties is an intriguing goal, one which may become obtainable with the growing accessibility of fast computers. To reach this goal, however, computer models must be developed which can accurately reproduce experimentally observed properties of known materials before they can be trusted as design tools. Beta''-alumina is a particularly good material for testing such models. Well-known for its ability to undergo ion exchange with a variety of mono, di, and trivalent cations (1), beta''- alumina exhibits different structural, optical, and transport properties depending on its mobile ion content. Therefore, a reasonable computer model for beta''- alumina should be able to reproduce the properties of any of its isomorphs.

Prior studies have been carried out on pure Na(I)-beta''- alumina using molecular dynamics (MD) (2,3). This work explores how well MD represents other beta''-alumina isomorphs, in particular mixed Na(I)-Ba(II)-, mixed Na(I)-Sr(II)-, and pure Sr(II)- beta''- alumina. Simulation results will be discussed in light of a.c. impedance measurements and structural data.

MD SIMULATION

The MD code used in this work is loosely based on a constant volume, number, and energy code written by Walker (4). Since the MD technique has been described

in great detail elsewhere (5), only those aspects particular to this study are presented here.

Interionic Potentials. All ions were treated as rigid spheres to minimize computation time. The coulombic contribution to the interionic potentials was calculated by an Ewald summation. Short-range potentials were in the Born-Mayer-Huggins form. The values of the parameters, A, rho, and C, were taken from several sources. The parameters for the pairs of ions present in beta- alumina were taken from a fit to bulk properties of Na(I)- beta- alumina (6), the parameters for the Mg-O, Sr-O, and Ba-O pairs were taken from a fit to bulk properties of their native oxides (7), and the Sr- and Ba- related cation-cation potentials were calculated using the electron gas approximation (8).

Equilibration. For the simulations of the mixed monovalent-divalent systems, the MD box included 9 full unit cells or approximately 800 atoms. The Sr(II) simulations included 36 unit cells. Initially, the mobile cations were placed randomly in the two-dimensional conduction layers while all other ions were placed in their crystallographic sites. The velocities and lattice parameters were scaled periodically until a stable target temperature was reached and the internal stresses were negligible. The volume of the box was then held fixed for the rest of the simulation. The equilibration period typically took several thousand timesteps, where each timestep was 5×10^{-15} sec long for the mixed systems and 3.5×10^{-15} sec long for the Sr(II) system.

Diffusion. The tracer diffusion coefficient was obtained from the two-dimensional random walk equation. The mean square distance travelled was calculated by averaging over the number of mobile cations and over time origins (9). Values of the Haven ratio as a function of composition were taken from (10).

SIMULATION RESULTS AND DISCUSSION

Simulations of the mixed Na(I)-Ba(II)- system were quite successful at reproducing expected microscopic ordering processes and conductivity trends. Thomas et al. have already reported preliminary MD simulations of one composition of Na(I)-Ba(II)- beta''- alumina, where they examined the influence of a single Ba(II) on its

local environment (11). Simulations presented here were done at 927°C for $Na_{1.67-2x}Ba_xMg_{0.67}Al_{10.33}O_{17}$, where x = 0.0-0.78.

Our simulations showed that the cations in the conduction layers were quite mobile at low Ba(II)/Na(I) ratios. However, near 80% replacement of Na(I) by Ba(II), the cations and vacancies assumed an ordered arrangement in which either a Na(I) or a Ba(II) occupied one of the two possible tetrahedral, low potential energy sites, known as the BR sites. Simulations of this ordered structure indicated that its ionic conductivity was much lower than that of compositions containing more Na(I). In fact, experimental

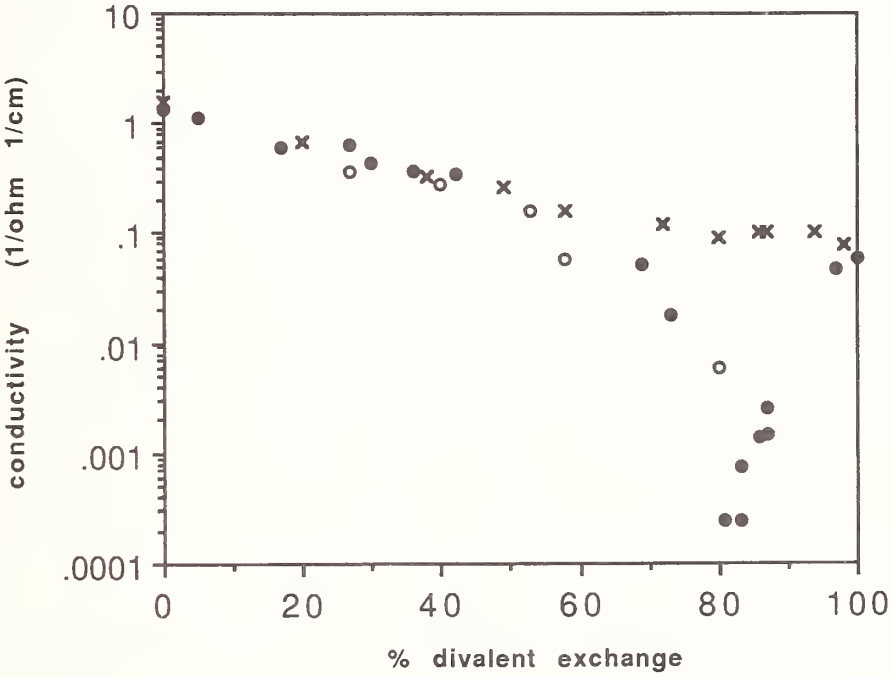

Figure 1 Simulated and experimental conductivity as a function of composition in mixed Na(I)-Ba(II)- and mixed Na(I)-Sr(II)- beta''- alumina. Closed circles and X's represent experimental data for the Na(I)-Ba(II) and the Na(I)-Sr(II) systems respectively at 400°C. Open circles represent Na(I)-Ba(II) conductivity values calculated from MD simulations at 927°C.

measurements of the ionic conductivity of Na(I)-Ba(II)-beta''- alumina as a function of composition showed that the conductivity passes through a pronounced minimum at this composition (12). The simulated and experimental conductivity data are shown in Figure 1.

Difficulties with the simulations arose near the end compositions, pure Na(I)- and pure Ba(II)-beta''-alumina. The simulations at the high target temperature we used became unstable at low Ba(II) content, below about 20% exchange of Ba(II) for Na(I). In addition, above 80% exchange, the Ba(II) ions were essentially immobile during the relatively short time span, 30 psec, of the simulation. The resulting meager statistics made it impossible to calculate a meaningful value of the diffusion coefficient. Therefore, the simulations did not predict the experimentally observed increase in conductivity above 80% exchange.

The results of a.c. impedance measurements of mixed Na(I)-Sr(II)-beta''- alumina as a function of composition are also shown in Figure 1. In this case, the pronounced minimum exhibited in the Na(I)-Ba(II) system is not observed. It is conjectured that this is because Sr(II) has been experimentally observed to prefer an alternative octahedral site, the mid-oxygen site, (14) and, therefore, would not be in competition with the Na(I) cations for their preferred BR sites. Simulations of 80% exchanged Na(I)-Sr(II)-beta''-alumina, however, have incorrectly placed the Sr(II) cations in the same locations as the Ba(II) cations and, therefore, have incorrectly reproduced the conductivity that has been observed experimentally.

Simulations of pure Sr(II)-beta''- alumina showed a small percentage of the Sr(II) cations either at the mid-oxygen sites or off-centered from the BR sites. The cations in these sites served as boundaries dividing domains of ordered regions over which the Sr(II) occupied one or the other of the two possible BR sites. These boundaries were very short-lived as the Sr(II) cations rapidly moved to the tetrahedral sites, and did not convincingly reproduce the expected high occupation of the octahedral sites.

CONCLUSION

The goal of this work has been to predict with some accuracy the properties of several beta''- alumina

isomorphs, with a clear eye on the possibility of ultimately being able to predict the properties of unknown isomorphs. Our work illustrates the potential opportunities as well as the current pitfalls which accompany MD simulations.

First, it is gratifying that MD is quite successful as a structural probe in the cases of Na(I)- and Na(I)-Ba(II)-beta''- alumina, but rather disconcerting that it fails with the Sr(II) systems. It is likely that this is due to both a problem with transporting cation-oxygen potentials from their simple native oxides to the more complex beta''- alumina structure, as well as a problem with the simple assumption that all of the atoms are fully charged ionic spheres. To remedy the latter problem, we are in the process of simulating the mixed Na(I)-Sr(II) system allowing for polarizability of Sr(II) and neighboring oxygens by incorporating the shell model.

Second, the time-scale of MD simulations is extremely short when compared to the time-scale of real-life ionic transport. As shown in this work, MD performed quite well predicting the general decrease in ionic conductivity for low Ba(II) concentrations in the mixed Na(I)-Ba(II) system, but failed to predict the subsequent increase in conductivity at the high Ba(II) content end where fewer mobile cations are present and jumps are infrequent.

ACKNOWLEDGEMENTS

This work was supported by the Office of Naval Research and by the NSF-MRL program under Grant No. DMR-8819885. Simulations were carried out primarily on the Pittsburgh Supercomputing Center Y-MP. C. Lane would like to thank H. Hummel for providing the Sr- and Ba-related cation-cation potentials.

REFERENCES

1. Y.-F.Y. Yao & J.T. Kummer, J. Inorg. Nucl. Chem., 29 (1967) 2453; G.C. Farrington & J.L. Briant, Science, 204 (1979) 1371; G.C. Farrington & B. Dunn, Solid State

Ionics, 7 (1982) 267; G.C. Farrington, B. Dunn, & J.O. Thomas, Appl. Phys. A, 32 (1983) 159.
2. M.L. Wolf, J.R. Walker, & C.R.A. Catlow, Solid State Ionics, 13 (1984) 33.
3. M.A. Zendejas & J.O. Thomas, Solid State Ionics, 28-30 (1988) 46; J.O. Thomas & M.A. Zendejas, submitted for publication.
4. J.R. Walker, in: Computer Simulation of Solids, 166, Lecture Notes in Physics, C.R.A. Catlow & W.C. Mackrodt, (eds.), Springer, Berlin (1982).
5. M.J.L. Sangster & M. Dixon, Advances in Physics, 25, 3 (1976) 247.
6. J.R. Walker & C.R.A. Catlow, J. Phys. C15 (1982) 6151.
7. G.V. Lewis, Physica 131B (1985) 114.
8. R.G. Gordon & Y.S. Kim, J.Chem. Phys., 56, 6 (1972) 3122.
9. M.J. Gillan, Physica 131B (1985) 157.
10. G.E. Murch & R.J. Thorn, Phil. Mag., 36, 3 (1977) 529.
11. J.O. Thomas, M. Alden, & G.C. Farrington, Solid State Ionics, 9&10 (1983) 301.
12. C. Lane, G.C. Farrington, J.O. Thomas, & M.A. Zendejas, Solid State Ionics, in press.

AUTHOR INDEX

Batllo, F.
Battle, P. D.
Billinge, S. J. L.
Birnie, D. P.
Brese, N.
Bringley, J. F.
Brown, I. D.
Bursill, L. A.
Cahen, D.
Cava, R. J.
Christoffersen, R.
Clark, T.
Cormack, A. N.
Dabrowski, B.
Davies, P. K.
Dickens, P. G.
Dimos, D.
Farley, T.
Feist, T. P.
Fitzgerald, J. J.
Fujitsu, S.
Garzon, F. H.
Greenblatt, M.
Huebner, W.
Ichinose, A.
Ikuma, Y.
Islam, M. S.
Jacobson, A. J.
Kao, H. C. I.
Kauzlarich, S. M.
Klavins, P.
Kolar, D.
Lane, C. A.
Lessing, P.
Lightfoot, P.
Lukasiewicz, S.
Macker, A.
Marezio, M.
McCarroll, W.
McHale, A.
Nasrallah, M. M.
Nath, A.
Navrotsky, A.
Negas, T.
Newnham, R. E.
Norton, M. L.
Nowotny, J.
O'Keeffe, M.
Owen, A. E.
Payne, D. A.
Piffard, Y.
Poeppelmeier, K.
Raistrick, I. D.
Rawn, C. J.
Ritter, J. J.
Rohrer, G. S.
Rosenfeld, H. D.
Roth, R. S.
Roth, S.
Sasaki, Y.
Scott, B. A.
Shannon, R. D.
Shrout, T. R.
Sleight, A. W.
Smyth, D. M.
Steinfink, H.
Subramanian, M. A.
Sunshine, S. A.
Sunstrom, J. E.
Switzer, J. A.
Takano, M.
Tanzawa, T.
Thomas, T.
Thompson, M. S.
Trontelj, M.
Wilson, G.
Wuensch, B. J.
Zandbergen, H. W.

☆ U.S. GOVERNMENT PRINTING OFFICE : 1991 O - 288-456 : QL3

NIST-114A
(REV. 3-89)

U.S. DEPARTMENT OF COMMERCE
NATIONAL INSTITUTE OF STANDARDS AND TECHNOLOGY

BIBLIOGRAPHIC DATA SHEET

1. PUBLICATION OR REPORT NUMBER
NIST/SP-804

2. PERFORMING ORGANIZATION REPORT NUMBER

3. PUBLICATION DATE
January 1991

4. TITLE AND SUBTITLE

CHEMISTRY OF ELECTRONIC CERAMIC MATERIALS

5. AUTHOR(S)

Peter K. Davies and Robert S. Roth

6. PERFORMING ORGANIZATION (IF JOINT OR OTHER THAN NIST, SEE INSTRUCTIONS)

U.S. DEPARTMENT OF COMMERCE
NATIONAL INSTITUTE OF STANDARDS AND TECHNOLOGY
GAITHERSBURG, MD 20899

7. CONTRACT/GRANT NUMBER

8. TYPE OF REPORT AND PERIOD COVERED
Final

9. SPONSORING ORGANIZATION NAME AND COMPLETE ADDRESS (STREET, CITY, STATE, ZIP)

NASA, ONR, DuPont, Idaho National Engineering Laboratory, and University of Pennsylvania

10. SUPPLEMENTARY NOTES

[ ] DOCUMENT DESCRIBES A COMPUTER PROGRAM; SF-185, FIPS SOFTWARE SUMMARY, IS ATTACHED.

11. ABSTRACT (A 200-WORD OR LESS FACTUAL SUMMARY OF MOST SIGNIFICANT INFORMATION. IF DOCUMENT INCLUDES A SIGNIFICANT BIBLIOGRAPHY OR LITERATURE SURVEY, MENTION IT HERE.)

The International Conference on The Chemistry of Electronic Ceramic Materials was held at the Sojourner Inn, in the Teton Village, Jackson Hole, Wyoming from August 17-22, 1990. In an attempt to maximize the development of this rapidly moving, multidisciplinary field, this conference brought together major national and international researchers to bridge the gap between those primarily interested in the pure Chemistry of Inorganic Solids and those interested in the Physical and Electronic Properties of Ceramics. With the many major discoveries that have occurred over the last decade, one of the goals of this meeting was to evaluate our current understanding of the Chemistry of Electronic Ceramic Materials, and to assess the state of a field that has become one of the most important areas of Advanced Materials Research.

12. KEY WORDS (6 TO 12 ENTRIES; ALPHABETICAL ORDER; CAPITALIZE ONLY PROPER NAMES; AND SEPARATE KEY WORDS BY SEMICOLONS)

crystal chemistry; dielectric ceramics; low temperature synthesis and characterization; solid state synthesis and characterization; surface chemistry; superconductors; theory and modelling

13. AVAILABILITY

[X] UNLIMITED

[ ] FOR OFFICIAL DISTRIBUTION. DO NOT RELEASE TO NATIONAL TECHNICAL INFORMATION SERVICE (NTIS).

[X] ORDER FROM SUPERINTENDENT OF DOCUMENTS, U.S. GOVERNMENT PRINTING OFFICE, WASHINGTON, DC 20402.

[X] ORDER FROM NATIONAL TECHNICAL INFORMATION SERVICE (NTIS), SPRINGFIELD, VA 22161.

14. NUMBER OF PRINTED PAGES
513

15. PRICE

ELECTRONIC FORM

NIST Technical Publications

Periodical

Journal of Research of the National Institute of Standards and Technology—Reports NIST research and development in those disciplines of the physical and engineering sciences in which the Institute is active. These include physics, chemistry, engineering, mathematics, and computer sciences. Papers cover a broad range of subjects, with major emphasis on measurement methodology and the basic technology underlying standardization. Also included from time to time are survey articles on topics closely related to the Institute's technical and scientific programs. Issued six times a year.

Nonperiodicals

Monographs—Major contributions to the technical literature on various subjects related to the Institute's scientific and technical activities.

Handbooks—Recommended codes of engineering and industrial practice (including safety codes) developed in cooperation with interested industries, professional organizations, and regulatory bodies.

Special Publications—Include proceedings of conferences sponsored by NIST, NIST annual reports, and other special publications appropriate to this grouping such as wall charts, pocket cards, and bibliographies.

Applied Mathematics Series—Mathematical tables, manuals, and studies of special interest to physicists, engineers, chemists, biologists, mathematicians, computer programmers, and others engaged in scientific and technical work.

National Standard Reference Data Series—Provides quantitative data on the physical and chemical properties of materials, compiled from the world's literature and critically evaluated. Developed under a worldwide program coordinated by NIST under the authority of the National Standard Data Act (Public Law 90-396). NOTE: The Journal of Physical and Chemical Reference Data (JPCRD) is published quarterly for NIST by the American Chemical Society (ACS) and the American Institute of Physics (AIP). Subscriptions, reprints, and supplements are available from ACS, 1155 Sixteenth St., NW., Washington, DC 20056.

Building Science Series—Disseminates technical information developed at the Institute on building materials, components, systems, and whole structures. The series presents research results, test methods, and performance criteria related to the structural and environmental functions and the durability and safety characteristics of building elements and systems.

Technical Notes—Studies or reports which are complete in themselves but restrictive in their treatment of a subject. Analogous to monographs but not so comprehensive in scope or definitive in treatment of the subject area. Often serve as a vehicle for final reports of work performed at NIST under the sponsorship of other government agencies.

Voluntary Product Standards—Developed under procedures published by the Department of Commerce in Part 10, Title 15, of the Code of Federal Regulations. The standards establish nationally recognized requirements for products, and provide all concerned interests with a basis for common understanding of the characteristics of the products. NIST administers this program as a supplement to the activities of the private sector standardizing organizations.

Consumer Information Series—Practical information, based on NIST research and experience, covering areas of interest to the consumer. Easily understandable language and illustrations provide useful background knowledge for shopping in today's technological marketplace.

Order the **above** *NIST publications from: Superintendent of Documents, Government Printing Office, Washington, DC 20402.*

Order the **following** *NIST publications—FIPS and NISTIRs—from the National Technical Information Service, Springfield, VA 22161.*

Federal Information Processing Standards Publications (FIPS PUB)—Publications in this series collectively constitute the Federal Information Processing Standards Register. The Register serves as the official source of information in the Federal Government regarding standards issued by NIST pursuant to the Federal Property and Administrative Services Act of 1949 as amended, Public Law 89-306 (79 Stat. 1127), and as implemented by Executive Order 11717 (38 FR 12315, dated May 11, 1973) and Part 6 of Title 15 CFR (Code of Federal Regulations).

NIST Interagency Reports (NISTIR)—A special series of interim or final reports on work performed by NIST for outside sponsors (both government and non-government). In general, initial distribution is handled by the sponsor; public distribution is by the National Technical Information Service, Springfield, VA 22161, in paper copy or microfiche form.

U.S. Department of Commerce
National Institute of Standards and Technology
(formerly National Bureau of Standards)
Gaithersburg, MD 20899